University of Pretoria

The development and microstructural evolution of the bulk γ-Ti-45Al-2Nb (Sn, Cr, Mn & Si)-doped intermetallic alloys and their mechanical properties

by

Maria Ntsoaki Mathabathe

Supervised

by

Prof. C. W. Siyasiya, Prof. R. J. Mostert, and Dr. A.S. Bolokang

Submitted in partial fulfilment of the requirement for the degree

PhD (Applied Science) Metallurgy

In the

Department of Material Science and Metallurgical Engineering

Faculty of Engineering, Built Environment, and Information Technology

University of Pretoria

South Africa

2019

Declaration

I declare that this thesis was composed by myself and that it is solely the result of my own original work, except where explicitly stated otherwise in the text. It is being presented for the Doctoral degree in Applied Science Metallurgy, in the Faculty of Engineering, Built Environment and Information Technology of the University of Pretoria. It has not been submitted for any other degree or professional qualification at any other University.

Parts of this work have been published in (1) Journal of Alloys and Compounds (REF:79 &115); (2) Vacuum (REF:78); (3) Materials Characterization (Mentioned in pg. VI); (4) Advanced Powder Technology (pg. VI); and (5) IOP Conference Series: Materials Science and Engineering (pg. VI). The articles have a total of 23 citations.

Acknowledgements

This journey would not have been possible without the support of my family, professors, mentors, and friends. I am deeply indebted to my adviser Prof. W.E. Stumpf for the fundamental role he played, in the beginning of my research work. Completion of this Doctoral Thesis was possible with the support of several personnel of which I express my sincere gratitude too. I am extremely grateful to my research guides, Dr. A. S. Bolokang, Dr. G. Govender, Prof. C.W. Siyasiya, and Prof. R. J. Mostert for their valuable guidance, scholarly inputs and consistent encouragement I received throughout the research work. In particular, Dr. G. Govender, for believing in me, the patient guidance, encouragement, and advice he has provided throughout my time as his student. Special mention goes to my supervisor Dr. A. S. Bolokang, for unconditional support, with an amicable and positive disposition, for the effort invested in publishing some parts of the work.

This work would not have been possible without the financial support provided by the Counsil of Scientific Industrial Research (CSIR), the Department of Science and Technology (DST), and NRF. Finally the technical assistance from the University of Pretoria, Mintek, University of Western Cape, mainly for the provision of some of the laboratory equipment; and lastly, the management services provided by Mr. William Matlala and Mr. Mondli Ntshona from the CSIR are appreciated.

Dedication

This work is dedicated to God the Father of my Lord Jesus Christ, the pillar of my strength.

To my dearest family

Sesie, Elias and Jerry Mathabathe

Thank you for your unqualified genuine support towards my studies.

This dissertation is insolently dedicated to you.

Ngiyabonga kakhulu!

Abstract

The γ-TiAl based intermetallic alloys play an important role in structural applications, such as aerospace and automotive industries. The current work studied the novel development and microstructural evolution, along with their mechanical properties of the γ-TiAl based alloys viz. the binary (Ti--48Al), ternary (Ti--48Al-2Nb), quaternary (Ti--48Al-2Nb-0.7Cr) and quinary (Ti--48Al-2Nb-0.7Cr-0.3Si). The alloys were fabricated employing both powder and ingot metallurgy routes. Consolidation of the alloys was achieved by vacuum arc melting. As-cast and thermally treated sections of sample ingots were characterized using optical microscopy (OM) and scanning electron microscopy (SEM), X-ray diffraction (XRD), X-ray photo-electron spectroscopy (XPS), atomic force microscopy (AFM), Raman spectroscopy (RS), transmission electron microscopy (TEM), electron backscattered diffraction (EBSD). Thermal analysis, such as differential scanning calorimetry (DSC) and differential thermal analysis (DTA) were employed in order to give insight into phase transformations. Moreover, hardness, room temperature tensile testing with subsequent fractography, cyclic oxidation, nitriding treatment and incorporating first principle calculations with orientation relationships were some of the property behaviors studied in the dissertation.

The key findings of the research were: 1) the addition of Nb and Cr to the γ-TiAl based alloys promoted grain refinement and induced phase transformation, 2) slight overall Al loss of the γ-TiAl based alloys was observed due to the compaction method prior to melting. Uni-axial cold pressing of the blended metal powders indicated that Al particles migrated to the surface in contact with the die facets, 3) of all the alloys studied, the quinary (Ti-48Al-2Nb-0.7Cr-0.3Si) alloy exhibited good mechanical properties, 4) phase transformation and microstructural evolution of an α-solidifying quinary alloy illustrated a homogeneous microstructure with Spheriodized/Widmanstätten laths, 5) it has been shown that the formation of $\gamma/\alpha_2/Ti_5Si_3$ in the Ti-48Al-2Nb-0.7Cr-0.3Si intermetallic alloy followed the Blackburn orientation relationship of both the as-cast (β-solidifying) and heat-treated (α-solidifying) phases, 6) surface cladding in a N/Ar atmosphere indicated that the oxidation properties of the ternary and quinary showed improved significance compared to the binary and quaternary alloys and, 7) Sn and Mn, were some of the doping elements added to the quinary alloy excluding the Cr due to its inducement of the brittle β-phase which exhibits low mechanical properties. As a result, γ-TiAl based Ti-48Al-2Nb-0.3Si, Ti-48Al-2Nb-1Sn-0.3Si, and Ti-48Al-2Nb-1Sn-0.7Mn-0.3Si intermetallic alloys were developed and investigated.

Graphical Abstract

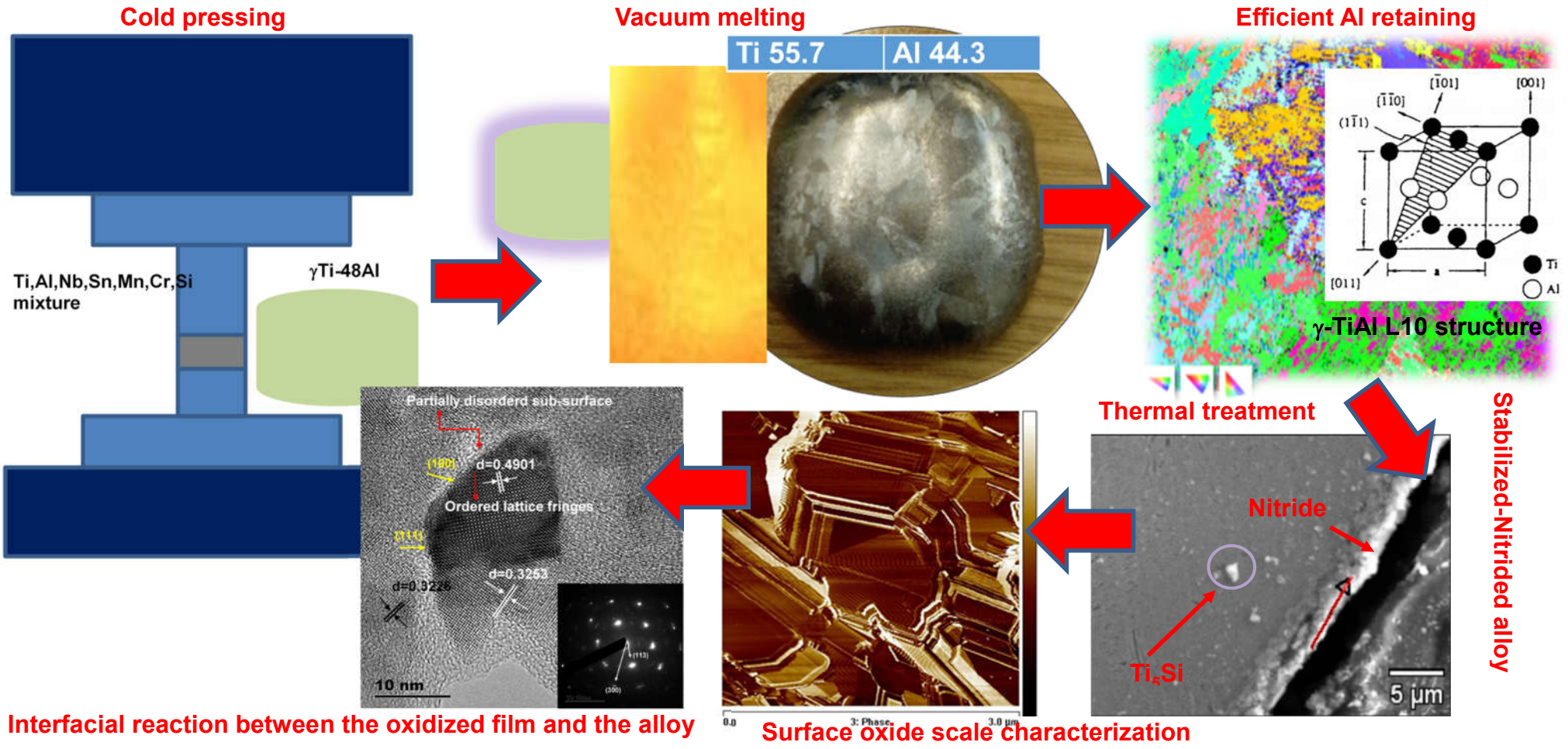

List of articles included in the Thesis

Published articles

1. Mathabathe, M. N., Bolokang, A. S., Govender, G., Mostert, R. J., & Siyasiya, C. W. (2018). The vacuum melted ɣ -TiAl (Nb, Cr, Si) –doped alloys and their cyclic oxidation properties. Vacuum, 154, 82–89.
2. Mathabathe, M. N., Govender, G., Bolokang, A. S., Mostert, R. J., & Siyasiya, C. W. (2018). Phase transformation and microstructural control of the alpha-solidifying γ-Ti-45Al-2Nb-0.7Cr-0.3Si intermetallic alloy. Journal of Alloys and Compounds, 757, 8–15.
3. Mathabathe, M. N., Bolokang, A. S., Govender, G., Mostert, R. J., & Siyasiya, C. W. (2018). Structure-property orientation relationship of a $\gamma/\alpha_2/Ti_5Si_3$ in as-cast Ti-45Al-2Nb-0.7Cr-0.3Si intermetallic alloy. Journal of Alloys and Compounds, 765, 690-699.
4. Mathabathe, M. N., Govender, G., Siyasiya, C. W., Mostert, R. J. & Bolokang, A. S., (2019). Surface characterization of the cyclically oxidized γ-Ti-45Al-2Nb-0.7Cr alloy after nitridation. Journal of Materials Characterization, 154, 94-102.
5. Mathabathe, M. N., Bolokang, A. S., Govender, G., Siyasiya, C. W & Mostert, R. J. Cold pressing and vacuum arc melting of γ-TiAl based alloys. Advanced Powder Technology, https://doi.org/10.1016/j.apt.2019.08.038.
6. Mathabathe, M. N., Bolokang, A. S., Govender, G., Siyasiya, C. W & Mostert, R. J. EBSD characterisation of the B2 orientation in γ-TiAl based. IOP conference series: Materials Science and Engineering, 655:1. Advanced Powder Technology, https://doi.org/10.1016/j.apt.2019.08.038.

Conferences

1. Mathabathe, M. N., Govender, G., Mostert, R. J., & Siyasiya, C. W. (2017). Microstructure Characterization of As-cast Gamma-Titanium Aluminide Based Intermetallic Alloy. MSSA, Bela Bela, South Africa, 4-7 October 2017.
2. Mathabathe, M. N., Bolokang, A. S., Govender, G., Mostert, R. J., & Siyasiya, C. W. Effect of Nb, Cr, and Si alloying on the microstructure and fracture behavior of the γ-TiAl-based alloys. Mechanics, Aberdeen, UK, 9-12 July 2018.
3. Mathabathe, M. N., Bolokang, A. S., Govender, G., Siyasiya, C. W & Mostert, R. J., Effect of nitridation treatment on cyclic oxidation of the γ-Ti-48Al-2Nb and Ti-48Al-2Nb-0.7Cr-0.3Si intermetallic alloys. 3rd International Conference on Applied Surface Science, Pisa Palazzo dei Congressi, Italy, 17-20 June 2019.
4. Mathabathe, M. N., Bolokang, A. S., Govender, G., Siyasiya, C. W & Mostert, R. J., EBSD characterization of a β/B2 orientation in Ti-48Al-2Nb-0.3Si alloy. COSAAMI, South Africa, 23-26 October 2019. Status: Abstract accepted for publication and oral presentation.

Nomenclature

Symbol	Units	Description
a, b, c	nm	Lattice parameters
β/B2		BCC-A2 parent phase
α2		Ti_3Al
γ		TiAl
c', c_{11}, c_{12}	GPa	Elastic constants
σ_{UTS}	MPa	Ultimate tensile stress
ε		True strain

Abbreviations	Definitions
BCC	Body centred cubic lattice
BSI	Backscattered electron imaging
DSC	Differential scanning calorimetry
DTA	Differential thermal analysis
HREBSD	High resolution electron backscattered diffraction
ED	Electron diffraction
EDS/EDX	Energy dispersive X-ray spectroscopy
FCC	Face centred cubic lattice
FCT	Face centred tetragonal cubic lattice
HCP	Hexagonal close-packed

RHL	Rhombohedral
SEI	Secondary electron imaging
SEM	Scanning electron microscopy
TEM	Transmission electron microscopy
XPS	X-ray photoelectron spectroscopy
XRD	X-ray diffraction
AFM	Atomic force microscopy
BOR	Blackburn orientation relationship
SADP	Selected area diffraction pattern
CRSS	Critical resolved shear stress
LAGB	Low angle grain boundary
HAGB	High angle grain boundary
T	Temperature
K	Kelvin

Table of Contents

List of Figures

List of Tables

1. CHAPTER 1: GENERAL BACKGROUND

1.1. Introduction

Gamma-titanium aluminide alloys constitute a vital class of structural materials, which thanks to their excellent physical and mechanical properties, potentially may play an important role in the aerospace and automotive industries [1,2]. In particular, as recognized by Abdallah et al. [1], they uphold attention due to their attractive balance of properties for engineering applications where weight reduction, improved fuel consumption, and high-temperature efficiency are essential requirements. Of relevant importance to gas turbine designers, the γ-TiAl based alloys are an attractive replacement to nickel-based superalloys. This is due to their low density 4g/cm^3 (approximately half of that of nickel-based alloys: 8g/cm^3) as well as their high temperature proficiency (mainly at temperatures which surpass the capability of conventional titanium alloys), resulting in a higher combustion efficiency and thus fuel savings [1,2]. Substitution of Ni-based superalloy parts with titanium aluminides is supposedly to reduce the structural weight of gas turbine engines by 20–30%. Hence, a significant increase in engine performance, fuel efficiency and reduction in emissions may be realized by utilizing titanium aluminides in gas turbine engines [3].

In addition to these properties, γ-TiAl alloys are of interest for the production of rotating parts in aerospace engines and for automotive industries such as engine valves and turbine wheels of turbochargers [2]. These engineering usage and material description for titanium aluminides are delineated by Kothari et al. [3]. In particular to this research study, γ-TiAl are used for turbocharger applications for passenger vehicles. Materials for turbocharger turbines have to exhibit high-temperature strength, and be resistant to fatigue, creep and oxidation. The prime property necessary for the turbine wheel is endurance against centrifugal stresses generated during rotation. Since centrifugal stress is proportional to specific gravity, therefore specific strength is an appropriate measure [2]. Tetsui [4] showed that TiAl alloys with the suitable composition and microstructure demonstrated outstanding specific strength when compared to current superalloys (such as Inconel 713C) in the contemplated temperature range.

Despite the appealing mechanical properties of γ-TiAl alloys, crucial drawbacks have been described, such as in the work by Lasalmonie [5]. In particular, Liu et al. [6] emphasized the poor ductility and low fracture toughness of γ-TiAl at room temperature which limits their practical applications, and due to these poor properties, high rates of crack propagation at low and intermediate temperatures, remain a concern for the utilization of these alloys in engineering structures. In addition, Baudana et al. [2] emphasized the fact that γ-TiAl alloys suffer severe oxidation at temperatures above 700 °C, creating harmful titanium oxides. This oxidation behavior is a drawback for automotive applications as the turbochargers operate in

the temperature range of 700-950 °C. The oxidation behavior of γ-TiAl based alloys was explained in detail by Pflumm [7]. Therefore, ongoing research of these alloys is required to understand and consider their mechanical behavior, as emphasized by Abdallah et al. [1].

However, owing to the inherent poor ductility and fracture toughness of γ-TiAl based intermetallic alloys at room temperature, Zhan et al. [8] recommended that these properties can be enhanced by the addition of alloying elements and thermo-mechanical treatments. The present study will focus on employing the modified composition of the well-known Ti-48Al-2Nb-2Cr alloy to a composition of Ti-48Al-2Nb-0.7Cr-0.3Si alloy for automotive engine application such as the turbine wheels of turbochargers. Moreover, Baudana [2] stated that Nb and Si are added to increase oxidation resistance, but that the Nb content should be kept to a minimum since higher contents can reduce ductility at room temperature (RT), resulting in poor machinability [9]. Furthermore, Lapin and Nazmy (2004) [10] reported that the coherent Ti_5Si_3 particles that form through eutectoid transformation along lamellar interfaces, enhance creep resistance and inhibit dynamic recrystallization of TiAl alloys.

Novel experimental approaches have been investigated that could characterize the applicable deformation mechanisms. The combination of these results with the attributes of continuum mechanics and thermodynamics has permitted developing models to describe thermo-mechanically controlled processes [11], therefore a selection of such frameworks is introduced and explained in a comprehensive way, respectively.

Due to poor castability of the γ-TiAl alloy, Biamino et al. [12] reported that this alloy is the most recent material demonstrated to be processed by Electron Beam Melting (EBM) which overcomes the processing issues related to conventional techniques. However, Yang et al. [9] reported that the investment casting process is the favored method of producing TiAl alloys, which could produce fine cast products with little or no machining after the casting process. Furthermore, Bystrzanowski et al. [13] reported that, since γ-TiAl based alloys are considered as high-temperature structural materials for aerospace and automotive industries, their creep resistance is of importance for successful applications. For instance, low-pressure turbine blades must not creep more than 1% within 10 000h at temperatures of about 700ºC under tensile stresses of 100-150 MPa [13].

The as-cast microstructure of TiAlNb-based alloys consists of lamellar phase structures, and the mechanical and creep properties have a close relationship with the microstructure and deformation mechanism, such as dislocation slip, twinning and so on [14]. In addition, various microstructures of γ-TiAl alloys may be obtained by different heat-treatment regimes, for different creep resistances due to differences in deformation mechanisms [14]. However, Thomas and Bacos [15] pointed out that the creep resistance can further be increased by

adjusting the lamellar microstructures. Both primary and secondary creep characteristics depend on the average lamellar spacing, which can be achieved by subsequent heat-treatment processes after the casting process. Furthermore, the authors mentioned that heat-treatment above α-transus temperature results in a fully lamellar microstructure where the holding time controls the lamellar colony size, while the cooling rate controls the lamellar spacing [15]. In addition, for Ti40Al-10Nb alloys studied by Zhan et al. [8] showed that the structure of Widmanstätten laths was more creep resistant than the lamellar structure owing to its short mean free path of dislocation slip.

Zhang et al. [16], reported that significant improvements in room temperature ductility and fracture toughness of γ-TiAl based alloys have been attained by the addition of β-phase stabilization elements like Cr, Nb, Mo and V. Moreover, the addition of Si enhances the creep resistance, oxidation resistance, and increases the fluidity of the melt. Although generally these alloying elements alter the microstructure, however, the combined effect of silicon and β-stabilization elements on phase transformations is not fully understood.

In this research study, the influence of heat treatment on the microstructure and mechanical properties of Ti-48Al-2Nb-0.7Cr-0.3Si alloy was investigated, combined with microstructural observations to provide the theoretical basis for the development and application of these intermetallic alloys for turbocharger applications used in passenger vehicles. Additionally, the study sought to address the creep behavior of the microstructure consisting of Widmanstätten laths, which has not been investigated to date. In addition, in this work, the influence of the addition of Sn, and Mn alloying elements in the Ti-48Al-2Nb-0.7Cr-0.3Si alloy were also investigated.

1.2. Research Problem Statement and Objectives

1.2.1. Problem Statement

The γ-TiAl based phase with a tetragonal ($L1_0$) structure was studied. According to Qiu Cong-Zhang et al. [16], this phase comprises a certain amount of α_2-Ti_3Al with a closed-packed hexagonal DO_{19} structure. The reason for this was reported by Huang and Hall [17] that duplex alloys are more ductile than single phase alloys. In addition, the α_2, especially in the form of lamellar laths transformed from α-phase, has the tendency to resist deformation. As mentioned above, the alloy comprises of $\gamma/\alpha/Ti_5Si_3$ phases at room temperature. This study endeavoured to assimilate knowledge of why, how, and what joint effect do the $\gamma/\alpha_2/Ti_5Si_3$ have on the arc button melted γ-TiAl based intermetallic alloy. Furthermore, high-resolution electron backscatter diffraction (EBSD) was employed to analyze the orientation relationship of the various phase in the as-cast condition of the alloys.

In the manufacture of bulk TiAl-based alloys, castability is essential for industrial applications as many TiAl components are manufactured by casting. However, the cost of production is increased by a variety of casting defects, which makes their application challenging. To overcome this obstacle, extensive work [3], [15], [18] has been dedicated to preparing TiAl with refined and homogeneous microstructure by alloying, heat-treatment, thermo-mechanical treatment, including isothermal and pack forging, and rolling processes. Another aspect limiting bulk TiAl-based alloy applications is their poor oxidation resistance above 800 °C. When these alloys are subjected to oxidation conditions, the scale is not a protective Al_2O_3 layer, but a mixture of Al_2O_3 and TiO_2. The oxidation resistance of bulk TiAl-based alloys is enhanced by the addition of ternary elements such as Nb, W, and Mo. Moreover, the positive effect of Nb and Mo is mostly described in terms of the doping effect and their effect in increasing aluminium activity and diffusivity. Brotzu et al. [19] referred to a doping effect as a reduction of oxygen concentration in rutile lattice, whereas the increase of aluminium activity and diffusion results in the development of a compact and protective passive alumina layer in the scale. However, as far as the other alloying elements are concerned, both their individual and their collective effects are still not completely understood. Therefore, this study sought to explore the effects of some alloying elements on microstructural evolution, hardness, tensile ductility, fractography and high temperature oxidation resistance of these bulk TiAl-based alloys manufactured by arc button melting with the aim of finding an alloy composition that could improve room temperature (RT) workability, as well as hot corrosion resistance.

As discussed above, structural materials such as γ-TiAl based alloys, are lightweight with properties similar and in some instances more superior to those of the heavy materials resulting in less fuel consumption, higher impact in vehicle efficiency and reduction in CO_2 emissions. In other words, TiAl bulk alloys find their application mainly in turbochargers of passenger vehicles or turbine blades where they operate at an elevated temperature in the range of (700-950 °C). Their durability is measured by their resistance to thermal cracking, creep, and oxidation at these elevated temperatures. Therefore, this study also focused on the optimization of some of these properties through alloy design and microstructural optimization by heat treatment. With regards to the latter, the lamellar structure of γ-TiAl/α_2-Ti_3Al was studied.

1.2.2. Research Objectives

The main objectives of the study were:

- To develop γ- Ti-48Al-2Nb alloyed with (Sn, Mn, Cr, and Si at. (%) intermetallic alloys using a small vacuum arc re-melting technique, and to investigate the effect of these alloying elements in terms of mechanical properties viz. tensile ductility (at ambient

temperature) with subsequent determination of fracture modes; and hardness properties.

- To evaluate the behavior of as-cast alloys; i.e. to determine crystallographic domains of the stable phases at room temperature, i.e. $\gamma/\alpha/Ti_5Si_3$, analyze their orientation mapping and solidification textures using high-resolution backscatter diffraction (EBSD).
- To study phase transformations employing thermal techniques using differential thermal analysis (DTA) and differential scanning calorimetry (DSC) in order to determine critical temperatures in order to ascertain microstructural evolution (fully lamellar + Widmanstätten laths + spheriodized) via the heat treatment process.
- To determine cyclic oxidation in air at 900 °C for the as-cast and the nitrided alloys viz. Ti-48Al (binary alloy), Ti-48Al-2Nb (ternary alloy), Ti-48Al-2Nb-0.7Cr (quaternary alloy) and Ti-48Al-2Nb-0.7Cr-0.3Si (quinary alloy) in (at %), all stabilized at 1100 °C using environmentally controlled tube furnace.

1.2.3. Research Questions

This study addressed the following research questions:

- Can the γ-TiAlNb based intermetallic alloy be successfully developed with minimal Al vaporization by the vacuum arc melting technique?
- Which microstructure described above provides the better mechanical properties?
- What influence does doping γ-TiAlNb based alloys with, Sn, Mn, Cr and Si have on phase transformation behaviors, interms of lamellar spacing, inter-lamellar phases, tetragonal interface types etc.?
- Can the as-cast dendritic structures of the γ-TiAl based alloys be microstructurally evolved with the subsequent heat-treatment process?
- Can pre-nitridation treatment of the γ-TiAl based alloys improve cyclic oxidation?

1.2.4. Scope of the Study

The focus of this research study was to investigate the development of γ-TiAlNb based alloys doped with Sn, Mn, Cr, Si, and their mechanical properties. The research investigated the development of six alloys of nominal compositions Ti-48Al, Ti-48Al-2Nb, Ti-48Al-2Nb-0.7Cr, Ti-48Al-2Nb-0.7Cr-0.3Si, Ti-48Al-2Nb-0.3Si, and Ti48Al-2Nb-1Sn-0.7Mn-0.3Si (at. %). The fabrication process of the alloys involved both the powder and ingot metallurgy i.e., precursor metallic powders with subsequent consolidation technique by vacuum arc melting. The as-cast γ-Ti-48Al-2Nb-(Sn, Mn, Cr, Si)-doped intermetallic alloys were thermally treated to examine microstructural evolution. Microstructure revealed spheriodized and Widmanstätten laths embedded in the lamellar structure ($\alpha_2+\gamma$), the latter, however, was observed as

cross/needle-like laths with spatial orientation with respect to the lamellar structure. Furthermore, the evolution of texture disclosed that the formation of $\gamma/\alpha_2/Ti_5Si_3$ follows the Blackburn orientation relationship [16]:

$\{111\}_\gamma \parallel (0002)_\alpha$ and

$\langle 1\ \bar{1}\ 0\rangle_\gamma \parallel \langle 1\ 1\ \bar{2}\ 0\rangle_\alpha$.

The research study also demonstrated the determination of six tetragonal γ-variants performed under transmission electron microscopy (TEM). The work was carried out within the CSIR Light Metal (LM) competency area to develop the titanium industry in South Africa. However, the fabrication processes, i.e. the casting technique via the vacuum arc melting was outsourced to Mintek. The EBSD work was performed at the University of Pretoria, whereas the TEM analysis was conducted at the University of Western Cape.

1.3. Research Hypothesis

- It would be possible to develop a novel production process of γ-TiAl based alloys doped with Nb, Sn, Mn, Cr and Si elements whereby the Al vaporization is minimized in a vacuum arc melting furnace. The predicted stable phases at room temperature would be γ, β/β2, α2, α, Ti_5Si_3.
- Pre-nitridation of the γ-TiAl based alloys would improve cyclic oxidation properties. As-heat treated Widmanstätten lath microstructure of the Ti-45Al-2Nb-0.7Cr-0.3Si alloy (at. %) fabricated by vacuum arc button melting, would exhibit increased mechanical properties when compared to an as-cast, spheriodized and fully lamellar microstructures.

1.4. Type of Research

This research study comprised the following components:

- Theory building research – **70%**
- Theory testing research – **20%**
- Theory application research – **10%**

1.5. Limitations of the research study

The limitations of the research study were the following:

- The challenge of not able to add alloying elements during the melting process
- The Al loss during arc melting had to be controlled by a precursor with a higher Al content.

2. CHAPTER 2: THEORY AND RESEARCH REVIEW

2.1. Background to the bulk TiAl intermetallic alloys

Fig. 2.1 shows a section of the Ti-Al binary phase diagram, from which it is comprehensible that at lower Al contents the higher temperature beta phase is enlarged, allowing easier hot working and if high-temperature properties are not required, this should be a considered approach for lower cost processing [20].

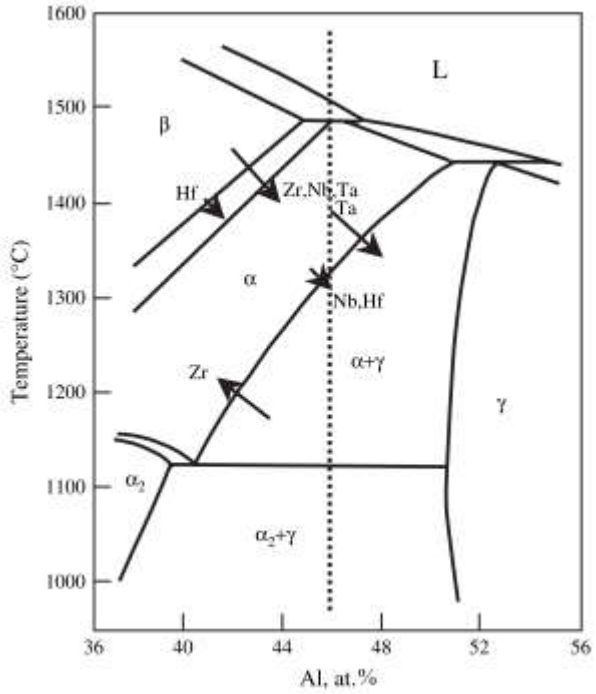

Figure 2.1. Ti-Al binary phase section. The arrows indicate the movement of the phase boundaries for ternary alloying additions, while the length of the arrows indicate the strength of each element [20].

Wu [20] reported that most applications which are anticipated for TiAl based alloys require high-temperature strength and such a case requires an Al-content closer to 46 at.% [20]. However, if Ti-46Al is cooled quickly from the alpha phase field (**Fig. 2.1**), a fully lamellar structure is generated as the γ-phase is precipitated on the (0001) planes of the α. However, if cooling is slightly slower, a near fully lamellar structure is formed, where some gamma phase coarsening takes place, giving rise to lamellae with neighboring γ grains.

2.2. The Crystallography and phase equilibria of bulk TiAl intermetallics

The mechanical properties of the bulk γ-TiAl based alloys are greatly reliant upon both the chemical composition and microstructure. Creep is no exception and, it has been shown that of the three possible microstructures: near-γ, duplex and fully lamellar- which are comprised of colonies of discrete platelets of mainly γ-TiAl with a smaller number of α_2-Ti_3Al lamellae of

which the latter is most creep resistant. These studies have demonstrated that creep deformation behavior of lamellar structures is independent on colony size in the range of 600-1200 μm and, that γ grains situated at the colony boundaries impair the creep resistance until their volume fraction exceeds 20% whereupon the gamma grains dominate the creep behavior [21].

The currently-accepted TiAl phase diagram for alloys with compositions near TiAl is shown in **Fig. 2.2** by Mishin and Herzig [22].

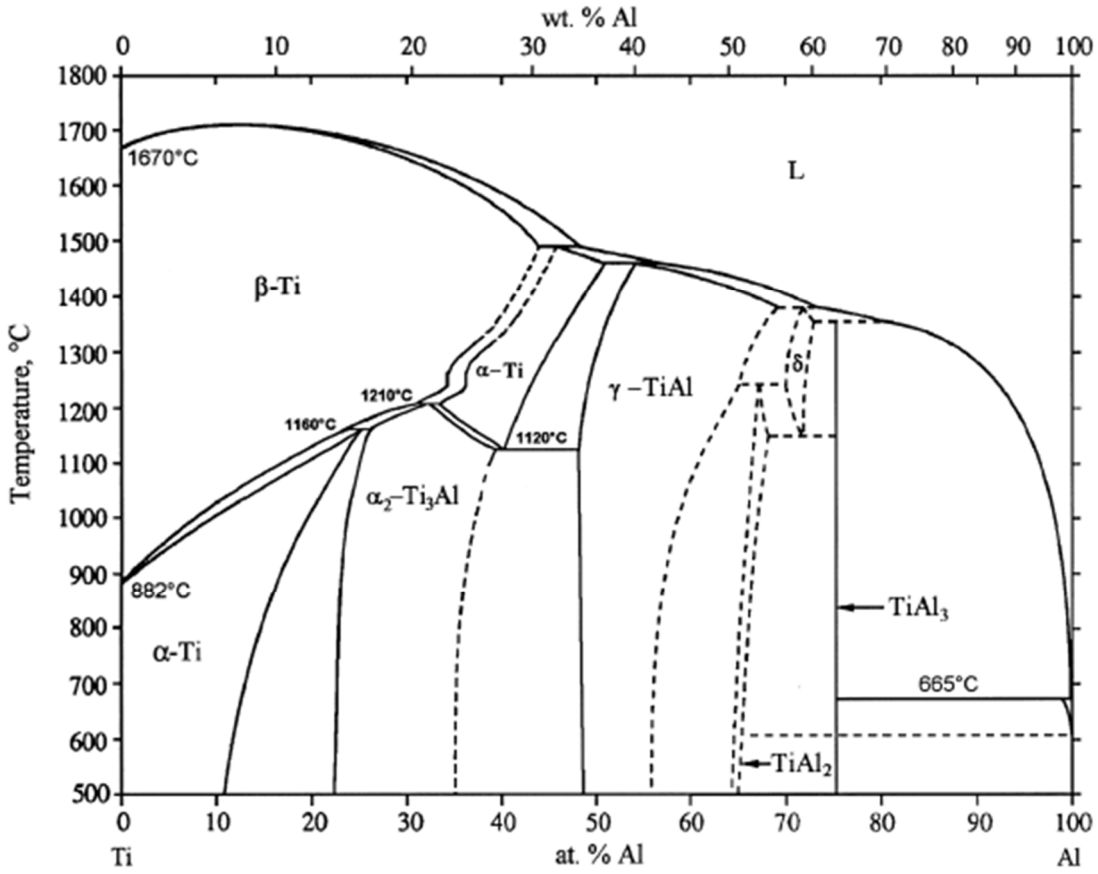

Figure 2.2. TiAl phase diagram [22].

The γ-phase Ti-(50-56)Al has an ordered face centered tetragonal $L1_0$ structure up to the melting point of 1460°C, with *c*/*a* = 1.02, **Fig. 2.3** [23].

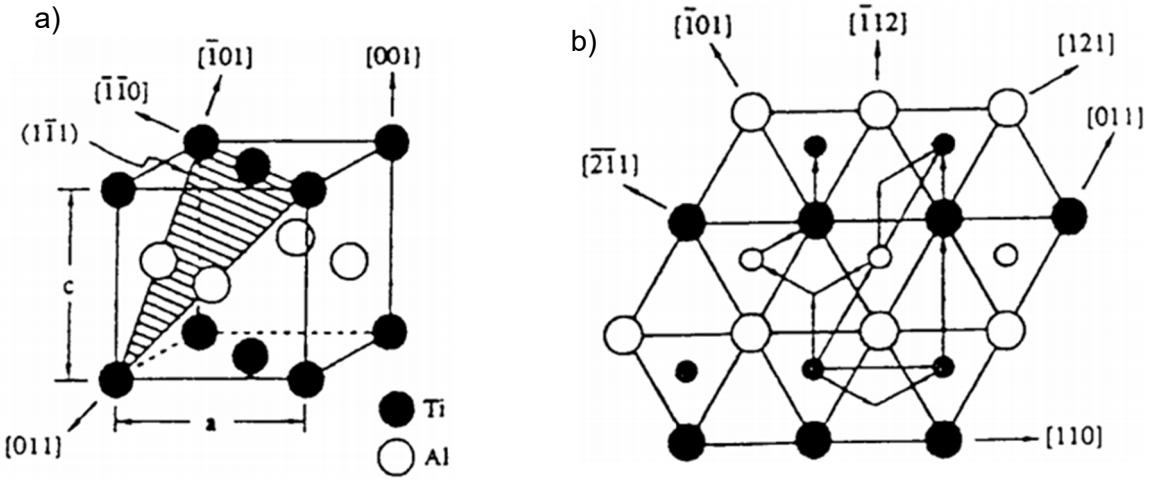

Figure 2.3. Structure of (a) TiAl $L1_0$, and (b) (111) plane showing slip vectors for feasible dissociation reaction, such as: ordinary dislocations ½ [110], super dislocations [011] and ½ [112], and twin dislocations $1/6$ [112] [23].

Similar work has been done by Jiang, [24] whereby the crystal structures of $L1_0$, $D0_{19}$, and B2 were investigated stipulated in **Fig. 2.4. Table 2.1** represents crystallographic data on these constituencies viz. the geometry and symmetry information.

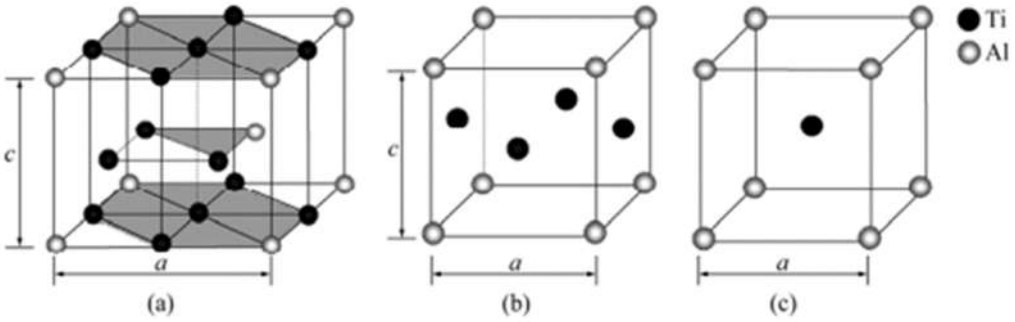

Figure 2.4. Crystal structures in B2-contained TiAl alloy: (a) Hexagonal α_2-Ti_3Al phase (DO_{19}); (b) Tetragonal γ-TiAl phase (L10); (c) Cubic B2 phase [24].

Qiu Cong Zang et al. [16] reported the on the fundamental of phase diagrams, especially Ti-Al multi-component system in their applicability of phase transition, design and control of heat-treatment operations. **Table 2.1** represents some crystallographic data of stable and meta-stable succeeding in the Ti-Al-X system [16].

Table 2.1. Crystal data for the Ti-Al-X system [16].

Alloy	Density/ ($mg.m^{-3}$)	Cell parameter			Pearson symbol	Space group	Crystal structure
		a/nm	c/nm	γ/(°)			
β(ht Ti)	4.31	0.333	0.333	90	cI2	*Im3m*	BCC-A2
α(RT tI)	4.12	0.289.	0.464	120	hP2	$P6_3/mmc$	HCP-A3
α2(Ti_3Al)	4.22	0.578	0.465	120	hP8	$P6_3/mmc$	DO_{19}
γ(TiAl)	3.82	0.283	0.407	90	tP2	*P4/mmm*	$L1_0$
B2($TiMo_{0.5}Al_{0.5}$)	5.63	0.318	0.318	-	-	-	-
B2($TiNb_{0.5}$ $Al_{0.5}$)	4.75	0.324	0.324	90	cP2	*Pm3m*	B2
B2($TiCr_{0.3}$ $Al_{0.7}$)	4.55	0.312	0.312	-	-	-	-

*$a=b$ and $\alpha=\beta=90^0$. The values of density and (a,b,c) will change after alloying with some other different elements

As discussed above TiAl has an $L1_0$ crystal structure shown in **Fig. 2.3a**, which comprises of layers of Al and Ti atoms on alternate planes of (001). Furthermore, Robert and Haasen [25] reported that the c-axis of TiAl will always be the [001] direction. The *c*/*a* ratio is 1.02 at the stoichiometric composition and extends to 1.03 with Al-rich compositions. Thus, the structure can be considered to be an fcc-derivative structure with a nearly-cubic unit cell. In the present study, the investigated alloy, whose nominal composition was Ti-48Al-2Nb-0.7Cr-0.3Si (at. %) invariably comprised of the Ti_5Si_3 precipitate in as-cast condition, whose crystal structure is hexagonal and its prototype is Mn_5Si_3 with a space group of $P6_3/mcm$, shown in **Fig. 2.5**. In addition, extensive work has been done by researchers to determine the lattice parameters of titanium silicate (Ti_5Si_3), **Table 2.2**.

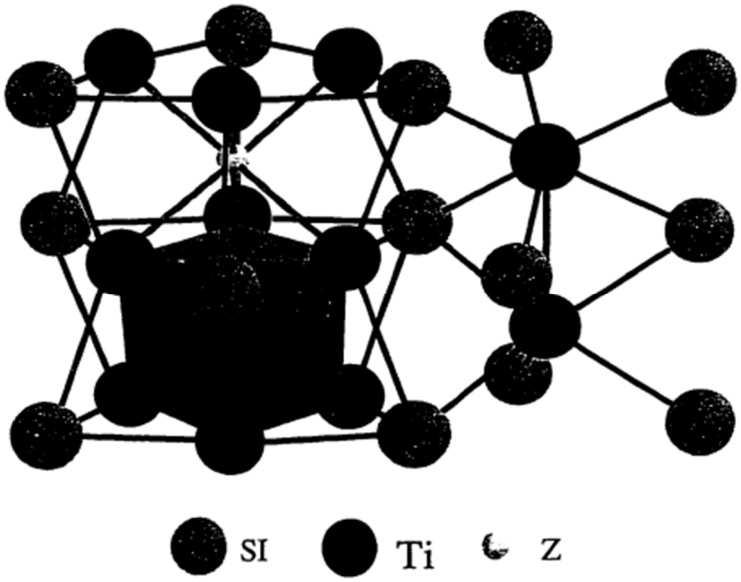

Figure 2.5. Partial crystal structure of Ti_5Si_3Zx. The interstitial atom Z sit at the center of the irregular, face-sharing octahedral of Ti atoms [26].

Table 2.2. Lattice parameters of Ti_5Si_3 [26].

a, Å	c, Å	References
7.465	5.162	Pietrokowsky et al. 1951
7.429	5.139	Swanson et al. 1959
7.444	5.143	Quakernaat et al. 1974
7.454	5.147	Thom et al. 1995
7.461	5.150	Kajitani et al. 1986

Sun et al [27] demonstrated that the *c*/*a* ratio of the Ti_5Si_3 is 0.6899. Furthermore, the TEM micrographs of the Ti_5Si_3 particles illustrated a polygonal shape in Ti_{52}-Al_{48}-$3Si_2Cr$ and Ti-45Al-2Nb-0.7Cr-0.3Si alloys, **Fig. 2.6**.

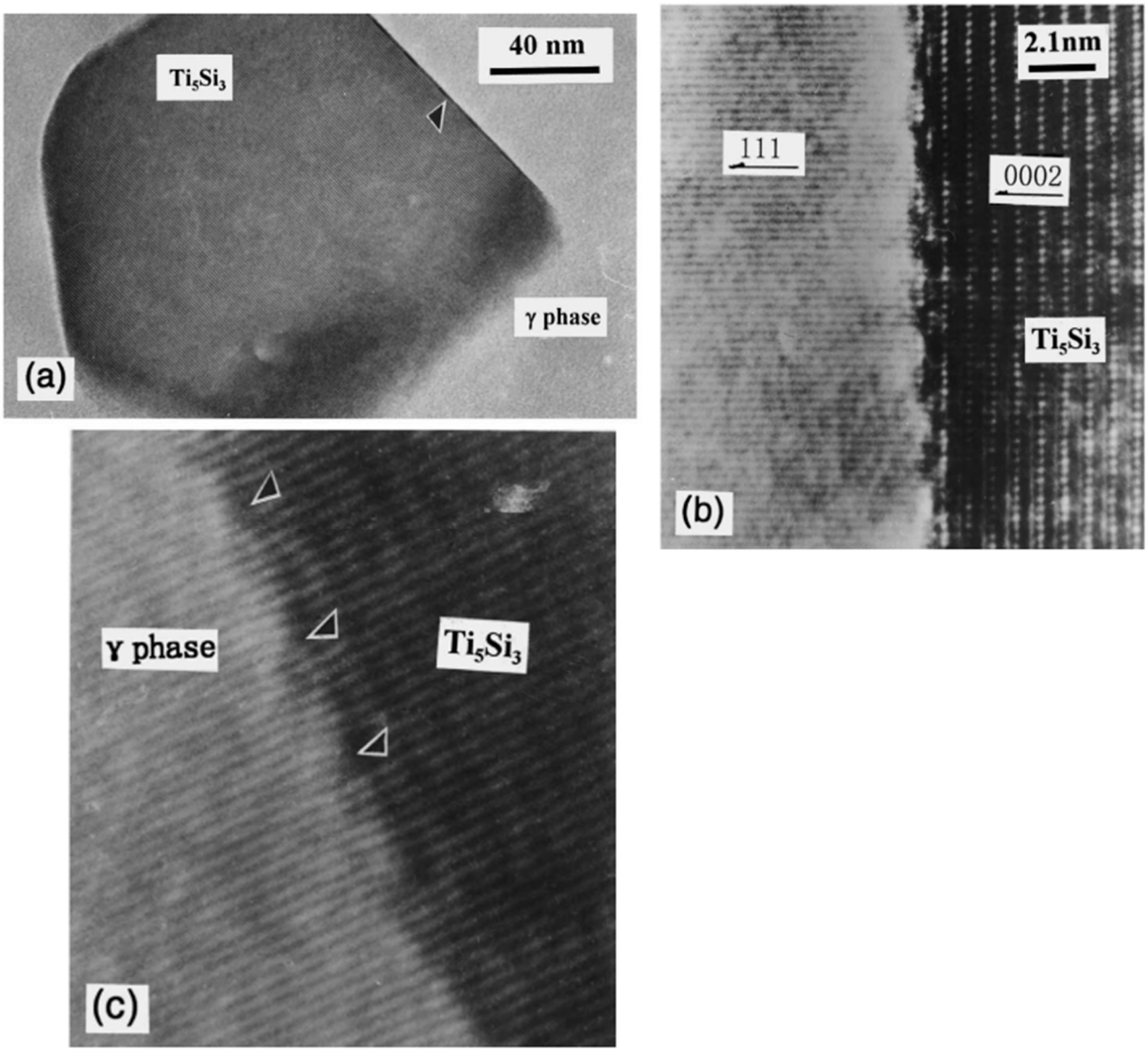

Figure 2.6. (a) HRTEM images showing incoherent Ti_5Si_3/γ interface in Ti_{52}-Al_{48}-3Si2Cr, (b) a semi-coherent Ti_5Si_3/γ interface in Ti_{52}-Al_{48}-3Si2V, and c) a semi-coherent Ti_5Si_3/γ interface in Ti_{52}-Al_{48}-3Si2Cr alloy [27].

The Ti_5Si_3/γ interface has an orientation relationship of $(011)_\gamma$ || $(0110)_{Ti5Si3}$ and $(233)_\gamma$ || $(0002)_{Ti5Si3}$. This was validated by the selected area diffraction pattern (SADP) and the corresponding schematic diagram of a Ti_5Si_3/γ interface in Ti_{52}-Al_{48}-3Si_2Cr represented in **Fig. 2.7**. It is important to also note that the needle-like Ti_5Si_3 particles precipitated along the γ/γ boundaries which has an orientation relationship $(101)_\gamma$ || $(1010)_{Ti5Si3}$.

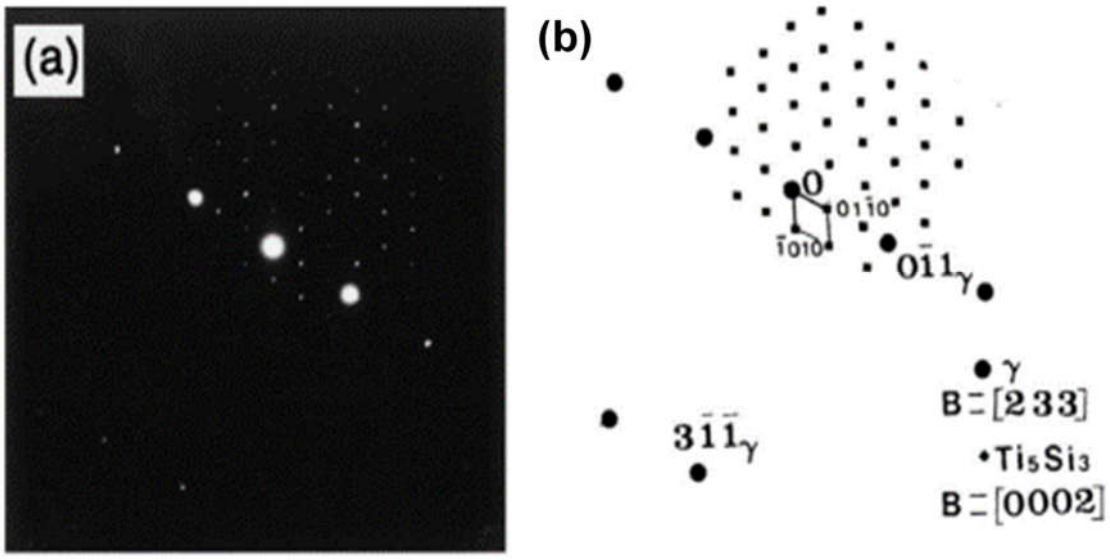

Figure 2.7. Selected area diffraction pattern (SADP) and b) corresponding schematic of Ti_5Si_3/γ in Ti_{52}-Al_{48}-3Si2Cr [27].

According to Qiu Cong-Zhang et al. [16], the γ-TiAl based phase comprises a certain amount of α_2-Ti_3Al with a closed-packed hexagonal DO_{19} structure. However, the inherent poor ductility affecting forming processes, even at elevated temperatures, has been the major concern in the manufacture of γ-TiAl based alloys. However, alloying with strong beta-stabilizing elements such as (Cr, Nb, W and Mo) may refine the grain structure and improve high-temperature deformation ability as a result of stabilized metastable B2 phase (ordered phase of β at low temperature). However, Fan et al. [28] reported that small additions of silicon enhance high-temperature oxidation resistance, in the fine coherent Ti_5Si_3 particles formed during a eutectoid reaction along lamellar interfaces intensifies creep resistance. Moreover, the authors [28] also reported that the presence of coarse Ti_5Si_3 particles in the microstructure suggests that the particles may have precipitated directly from the liquid saturated with brittle β-phase, that consequently reduces tensile properties.

Deformation by slip occurs on {111} planes (shown in **Fig. 2.3b**) and, due to tetragonality, there are two types of dislocations, particularly the ordinary ½ (110) and super-dislocations (011) = ½ (011) + ½ (011); these will, however, have slightly larger Burgers vectors as these directions are not fully closed packed. At ambient temperature, deformation occurs by both ordinary and super-dislocations. However, the [011] and [101] super-dislocations are mostly stationary because segments of the trailing super-partials 1/6 (112)-type form altered dipoles. Meanwhile, the dissociated ½ (110) dislocations of stacking faults are largely sessile due to Peierls stress [23]. Moreover, as the temperature increases up to 600°C, the flow stress rises,

due to the mobility of super-partials and cross-slip from {111} to {100} to form K–W-type locks, meanwhile the ½ (110) slip activity piles-up and twinning is favored, as explained by Smallman and Bishop [23].

However, the two-phase (γ+α) Ti-Al based alloys have better ductility than single-phase γ with a maximum at 48 at. (%) Al. This enhancement has been ascribed to the reduced c/a with decreased Al, with the effect of further promoting twinning and withdrawing of O_2 and N_2 interstitials by α_2. Additions of V, Cr or Mn, reduce the lattice parameter, and promote better ductility [23]. Furthermore, the two-phase microstructure contribute in optimizing the mechanical properties such as (tensile, creep and the fracture toughness properties). In addition, the volume fraction and morphology of the lamellar α_2 structure plays a significant, and at about ~30% of it contribute to mechanical properties [23].

2.3. General properties of bulk TiAl intermetallic compounds

Intermetallic compounds are generally regarded as having bonding of a mixture of metallic and covalent [23]. The strong bonding and ordered structure give rise to high elastic moduli, lower self-diffusion coefficients and therefore give rise to greater stability of diffusion-controlled properties [23]. Some of the intermetallic compounds which are of interest are summarized in **Table 2.3**.

Table 2.3. Comparison of the physical properties of some intermetallic compounds [23].

Compound	*Crystal structure*	*Melting temp. (°C)*	*Density ($kg\ m^{-3}$)*	*Young's modulus/density*
Ni_3Al	$L1_2$ (ordered fcc)	1400	7500	45
Ni_3Si	$L1_2$ (ordered fcc)	1140	7300	
NiAl	B2 (ordered bcc	1640	5860	35
Ti_3Si	$D0_{19}$ (ordered cph)	1600	4200	50
TiAl	$L1_0$ (ordered tetragonal)	1460	3910	24
FeAl	B2 (ordered bcc)	1300	5560	47

Smallman [23] also reported that bulk titanium aluminides intermetallics alloyed with Al or Si exhibit resistance to oxidation and corrosion because of their adhesive surface oxides. According to Boehlert [29], titanium aluminides containing orthorhombic (O) phase based on Ti_2AlNb are important for elevated-temperature structural applications, essentially exhibiting good specific strength and stiffness, and additionally their creep and oxidation resistance.

2.3.1. The advantages of bulk γ-TiAl based intermetallic alloys

Dimiduk [30] evaluated γ-TiAl based alloys with other structural materials for aerospace applications, and showed that modern opportunities have become forthcoming due to their interesting properties. The most important payoffs include the following [30]:

- High melting point due to the stable ordered structure;
- Low density;
- High specific strengths and moduli;
- Low diffusivity;
- A good structural stability;
- Good resistance against oxidation and corrosion;
- High ignition resistance (when compared with conventional titanium alloys);
- Good thermal stability and small sensitivity to structural coarsening [5].

Good creep properties of TiAl when compared to βNiAl which has a BCC based ordered structure where diffusion is rapid. However, a limitation in creep resistance occurs at high temperatures (T>1250 ºC) in Ni-based superalloys [5], compared to TiAl-based alloys which offer competitive or improved creep properties at temperatures above ~1000K.

Fig. 2.8 illustrates the specific modulus and specific strength (as a function of temperature) of γ-TiAl alloys compared to other materials. Consequently, γ-TiAl based alloys could essentially be employed in a wide range of components in the automotive, aerospace engine and power plant turbine industries [30].

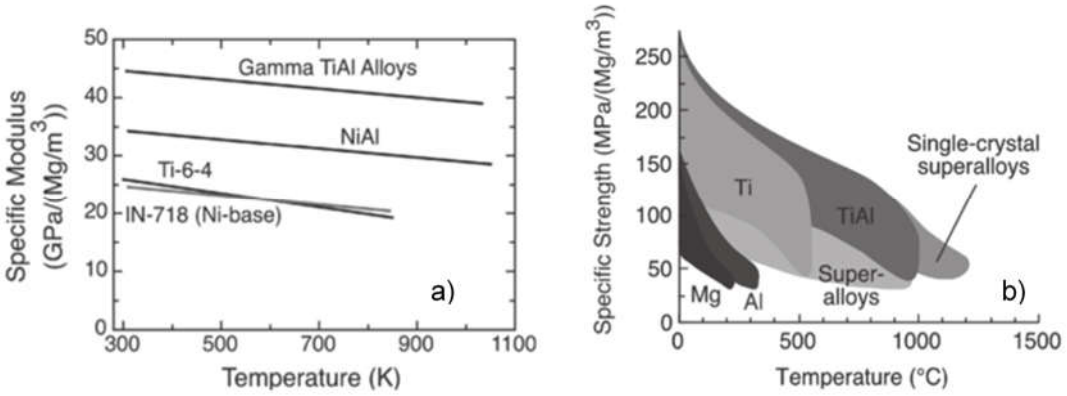

Figure 2.8. Graphs showing the (a) specific moduli and (b) specific strengths of TiAl and other structural materials, as a function of temperature [30].

This specific data in **Fig. 2.8** indicate that TiAl compares approvingly with the other materials. However, Lancaster et al. [31] mentioned that γ-TiAl alloys provide appealing properties for various jet engine components subjected to elevated temperatures, disregarding their inherent brittleness at room temperatures.

Wu [20] illustrated in **Fig. 2.9a**, the tensile properties of TiAl, NiAl & steel alloys as a function of temperature between room temperature and 800 °C is shown, and the data indicate that the bulk TiAl alloys have a higher specific strength when compared to other alloys. Whilst, this is so, the author pointed out that the ambient temperature ductility is inadequate, and is

particularly about 1% for all TiAl alloys [20]. This property (low ductility) shown in **Fig. 2.9b** is a major drawback, especially for structural components, since 1% elongation is commonly an accepted minimum value, and cast components in particular rarely reach this level.

Johnson et al [32] described that machining from an ingot comprised of the lamellar colony (α_2/γ) of TiA-based alloys, have disclosed that the mechanical properties are highly anisotropic. In addition, if the loading axis is perpendicular to the lamellar boundaries, the material is completely brittle even for tests conducted at 1000 °C. However, when the loading axis is parallel to the lamellar boundaries, the best combination of strength and toughness is acquired, not only at room temperature but also at elevated temperatures. Hence, materials with such an aligned microstructure may also have excellent creep strength.

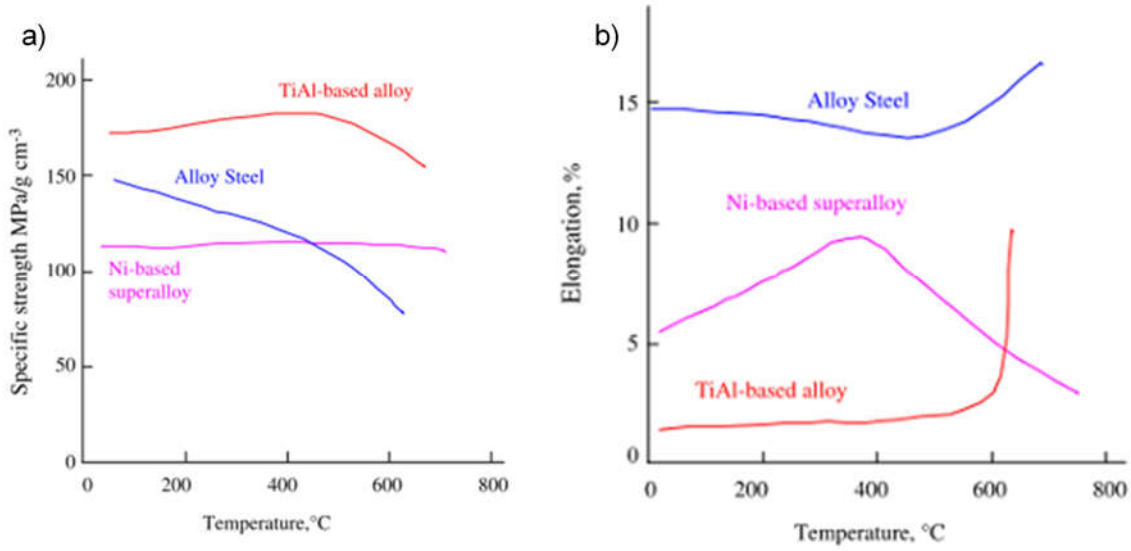

Figure 2.9. Specific strength and b) ductility as a function of temperature for a TiAl based alloy, a NiAl based alloy and an alloy steel [20].

2.3.2. The drawbacks of γ-TiAl intermetallic alloys

The following shows the common drawbacks of intermetallics which result directly from their structure as indicated by Lasalmonie [5]:

- These ordered compounds have a high sensitivity to the composition which therefore influences the mechanical properties.
- Low fracture toughness, particularly at room temperature, is a problem since it limits the size of acceptable cracks to very small values.
- Strength at low and intermediate temperatures is small and strengthening by deformation (such as forging) is a challenge, due to low ductility.
- Corrosion is a problem in systems without chromium at intermediate temperatures (500-900 °C).

- The high content of elements with different melting temperatures makes the production of good quality ingots difficult and costly.

Smallman [23] also explained the reasons for the lack of ductility particularly at low and intermediate temperatures included the following:

- A limited number of easy deformation modes to satisfy the von Mises yielding criterion.
- Operation of dislocations with large Burgers vectors.
- Restricted cross-slip, instead stress concentration, can activate slip in the next grain via pile-up of dislocations at the grain boundary.
- Intrinsic grain boundary weakness, and segregation of deleterious solutes to grain boundaries.

However, Smallman [23] further reported that intermetallic compounds can be made more ductile by small alloying additions. In addition, ductility of these bulk intermetallics is also enhanced at very small grain sizes, typically in the 5μm range which typically follows the stress Hall Petch relationship **Eq. 1**:

$$\sigma_y = \sigma_o + Kd^{-1/2} \quad (1)$$

where σ_y is yield strength for permanent deformation of the material, σ_o and K are constants for the alloy and d is the average diameter of the grains. This has motivated the current research and development of γ-TiAl intermetallics to increase the likelihood of applications of these materials.

2.4. The applications of bulk TiAl intermetallic alloys

2.4.1. Applications in turbo-chargers for passenger vehicles

Fig. 2.10 shows a schematic illustration of how a turbocharger functions. Tetsui [4] described a turbocharger as a device in which heat energy from the engine exhaust gas turns a turbine along with a compressor, to a point that the inflow air is pressurized by the compressor and supplied to the engine, thereby improving the engine's combustion efficiency. Additionally, in order to comply with near-future environmental regulations pertaining to exhaust emissions from passenger vehicles, as well as to improve vehicle acceleration, improved response has been put forth as a priority for turbochargers in recent years. The simplest way to improve the response is to make rotating parts lighter in weight, and this approach is most effective with respect to turbine wheels that make use of Ni-based superalloys (Inconel 713C) having a specific gravity of approximately 8 g/cm^3. However, as turbines are subject to long-term exposure to high temperature exhaust gases of at least 850 °C, heat resistance is an essential prerequisite for turbine wheel materials, such that conventional lightweight metallic materials (Al or Ti-based alloys) cannot be used.

Furthermore, the work done Tetsui [4] on a new high-response turbocharger using this TiAl alloy for its turbine wheel, showed that performance and endurance of the TiAl turbocharger were confirmed through numerous engine tests, leading to the first successful commercial applications of TiAl alloys.

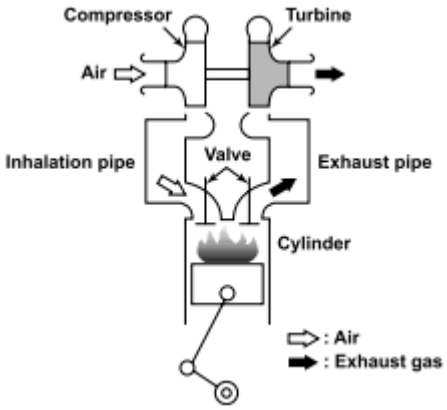

Figure 2.10. Schematic illustration of the action of a passenger vehicle [4].

2.4.2. Applications in gas turbines

The choice of material is always based on the best properties. The temperature ranges for NiAl and TiAl applications are indicated by **Fig. 2.11**:

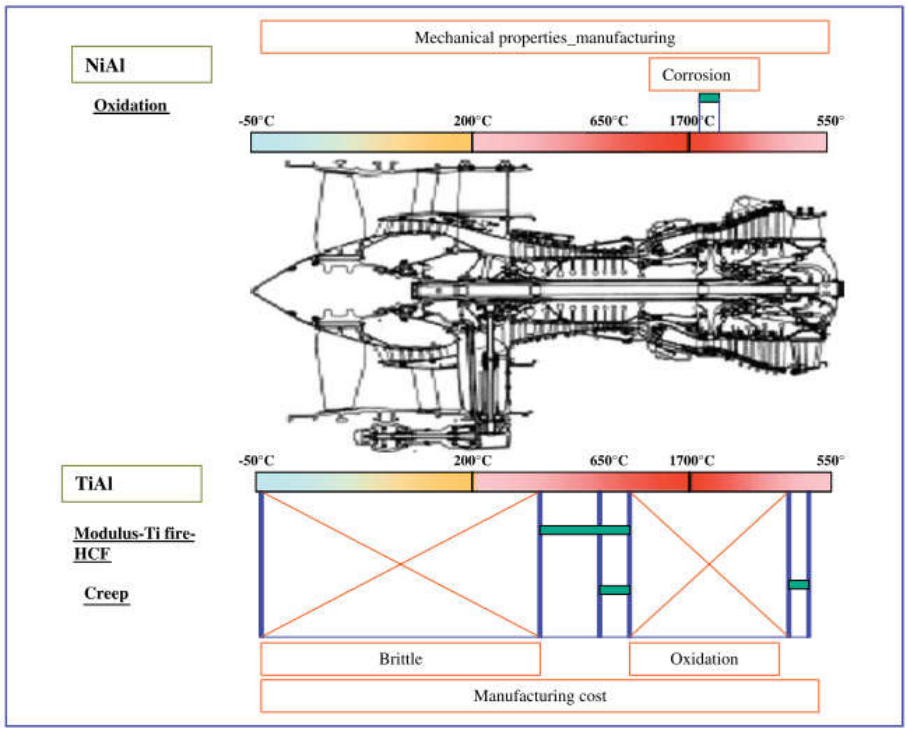

Figure 2.11. Temperature ranges for NiAl and TiAl applications. Limiting factors are indicated in frames parallel to the temperature ranges [5].

Lasalmonie [5] compared the specific strength of γ-TiAl to conventional Ti and Ni based alloys and found the following:

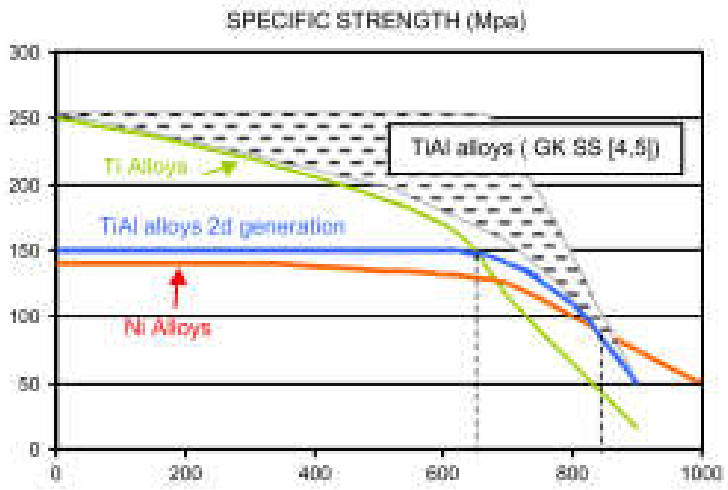

Figure 2.12. Specific strength of TiAl alloys compared to Ti and Ni based alloys [5].

Fig. 2.12 shows that the second generation of γ-alloys cannot replace Ti alloys fully and that is an improvement over Ni alloys only in the limiting temperature range of 650-800 ºC, i.e. due to oxidation sensitivity, this range for long term applications should be limited to 650-750 ºC. As a result, this explains the two types of applications based on creep strength, indicated in **Fig. 2.11**, which are components (blades and vanes) at the end of the high pressure compressor and in the low pressure turbine. However, γ-TiAl alloys exhibit a high Young's modulus at lower temperatures, shown in **Fig. 2.13 (a)**, and its resistance to titanium combustion shown in **Fig. 2.13 (b)**, which illustrates very low burning velocity of γ as recognized out by Lasalmonie [5].

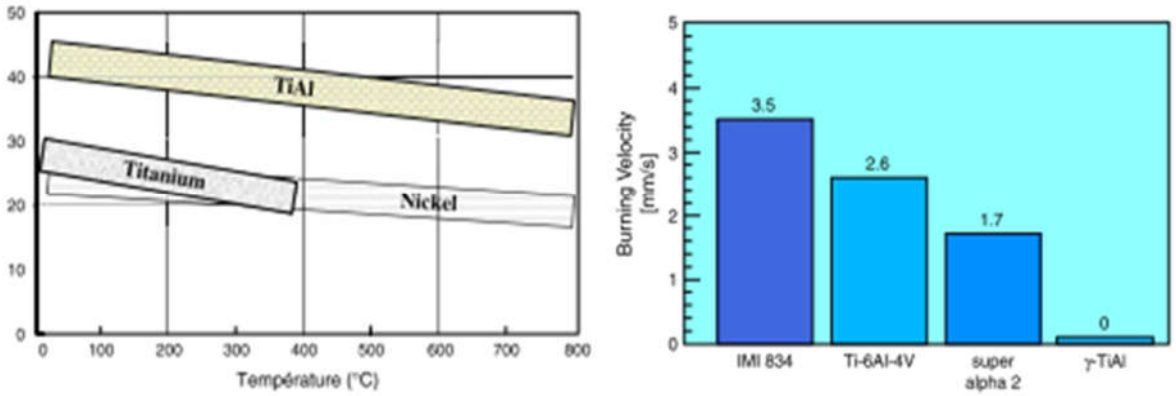

Figure 2.13. a) Specific elastic moduli of Ni and Ti based alloys compared to gamma TiAl and b) Burning velocity of γ-TiAl compared to that of various Ti alloys [5].

Subsequently, these two properties make the γ-TiAl relevant for applications as high pressure compressor casings. Furthermore, gamma alloys that exhibit high cycle fatigue properties; such as blades and shrouds of the high pressure compressor, are also interesting applications. For all of these applications, the expected weight saving is around 20% of small components

such as vanes, shrouds & blades, whereas a weight saving of 50% in the casings can be achieved [5].

To summarize, due to low toughness values of the γ-TiAl, care must be taken to avoid any defects such as porosity (casting), ceramic inclusions (casting, powder metallurgy), cracks (machining) and/or even handling defects (surface scratches). All these defects induce premature rupture of the components. However, Baudana et al. [2] reported that the alloy, when produced by electron beam melting, was amply consolidated with a small amount of build-up flaws, and further discovered a low loss of Al (lower than 2 wt%). Therefore, it is of interest in this research project that probabilistic methods should be used to predict the life of γ-TiAl components operating within high temperature environments fabricated by isothermal forging and hot rolling processes.

2.5. Simulation behavior of micro stress-strain curves

Fig. 2.14 illustrates the study of the Brockman finite element model [33]. The study demonstrated that each element has the freedom to glide on any of the γ or α_2 slip systems determined by the resolved local stress and slip-system harnesses [33].

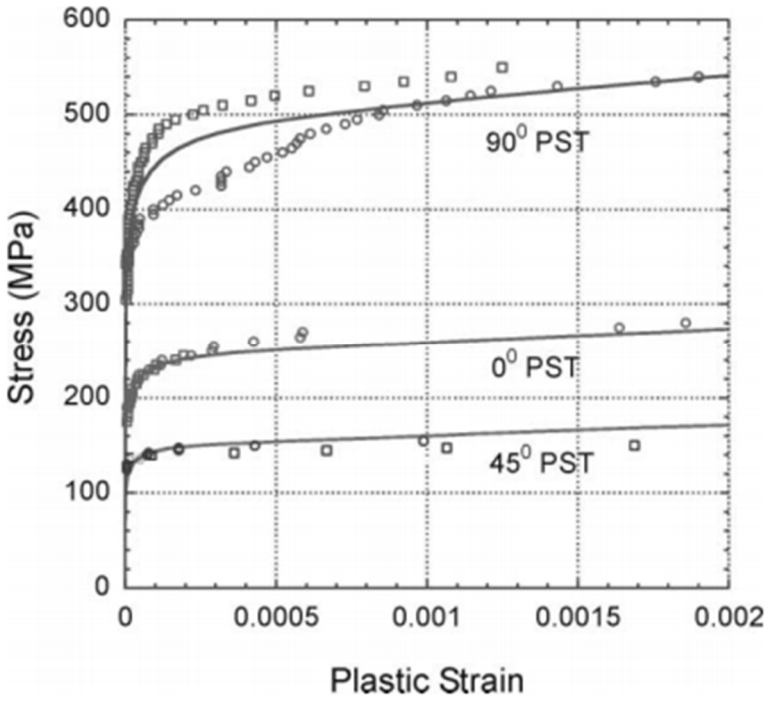

Figure 2.14. Finite element model for the flow behavior of poly synthetically twinned (PST) TiAl crystal compared with flow stress-strain data for the orientation 0°, 45°, and 90° [33].

2.6. Manufacturing and processing of bulk TiAl-based alloys

As noted in **Section 2.3.2**, one of the major problems which are holding back the production of engineering components from γ-based alloys is their processing. However, extrusion and forging techniques are utilized to manufacture compressor blades for engine testing, although the processing costs are expensive. The blades shown in **Fig. 2.15** are an example of this process route mainly manufactured by Thyssen, GfE, Leistritz, and GKSS for Rolls-Royce uses an alloy with the composition of Ti-45Al-8Nb and small amounts of C and B which provide good high temperature strength, as illustrated in **Fig. 2.16** [20]. Furthermore, the production routes for TiAl-based alloys have been complicated by heterogeneous microstructures in the blades. This difficulty is attributed to the compositional control of the ingots will be hard to pull-through if larger ingots are desired where segregation effects will be substantial [20].

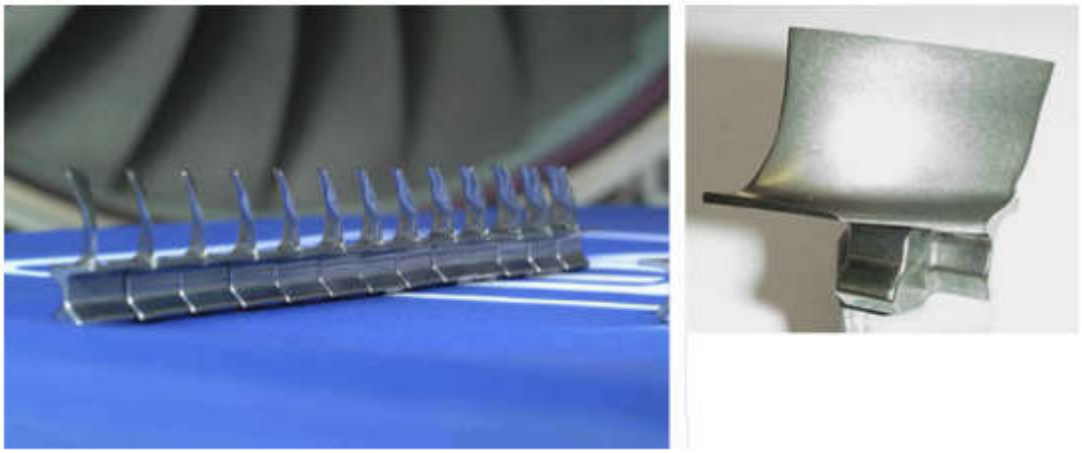

Figure 2.15. Compressor blades produced by forging process [20].

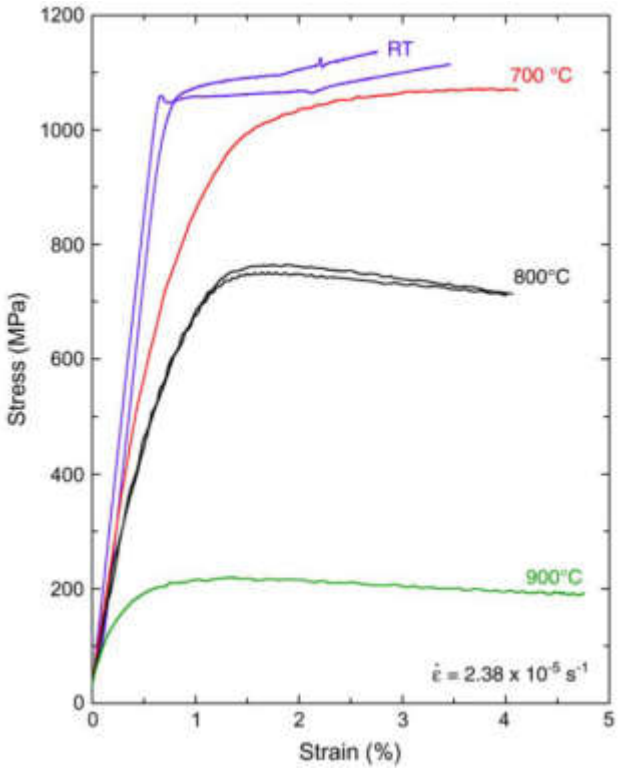

Figure 2.16. Mechanical properties as a function of temperature used for the manufacturing of compressor blades illustrated by Fig. 2.15 [20].

2.6.1. Melting and casting techniques

Wu [20] reported that there are two other techniques for component production viz.: casting and powder technology, which may offer lower processing cost. Powder processing is essential, especially for large component production (where there may be restriction of segregation which limits the homogeneity of products) but this process route is not covered entirely here but only the electron beam melting. Fundamentally, casting renders the production of complex shapes in a cost-effective way, since investment casting is a well-substantiated process. On the other hand, cold wall crucibles are thermally incompetent and provide superheating of only about 60 ºC, which is a drawback for the high reactivity of molten TiAl-based alloys. This has led to the necessity of pre-heated molds so improve filling. his resulted in slower cooling and larger alpha grain sizes, together with long lamellae. The resulting problem is well shown in **Fig. 2.17b,** which shows surface dimples formed on HIPing an investment cast turbine blade (**Fig. 2.17a**). These dimples however, revealed the extent of porosity present in the blades with a reject rate as high as 80% resulting in expensive components. Wu [20] further noted that the large fully lamellar structure shown in **Fig. 2.17c** had inherent low ductility, low fracture toughness and a significant scatter in properties, leading to an increased tendency to pre-yield cracking as illustrated in **Fig. 2.18** [20].

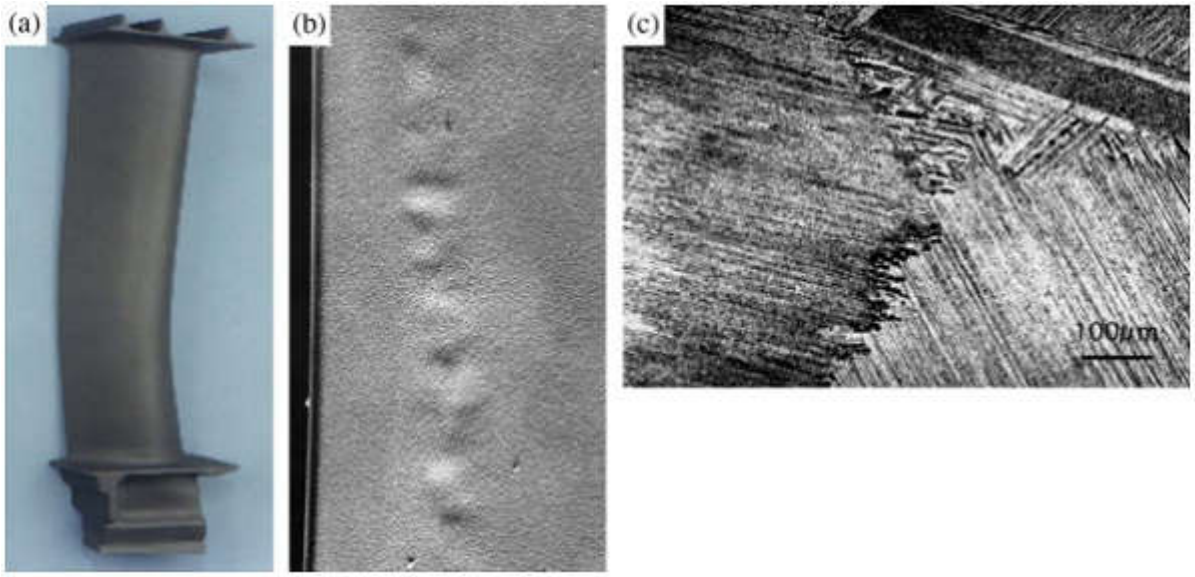

Figure 2.17. (a) Cast turbine blade, (b) dimples caused by collapse of porosity on HIPping such a blade and (c) the coarse-grained lamellar structure of the casting [20].

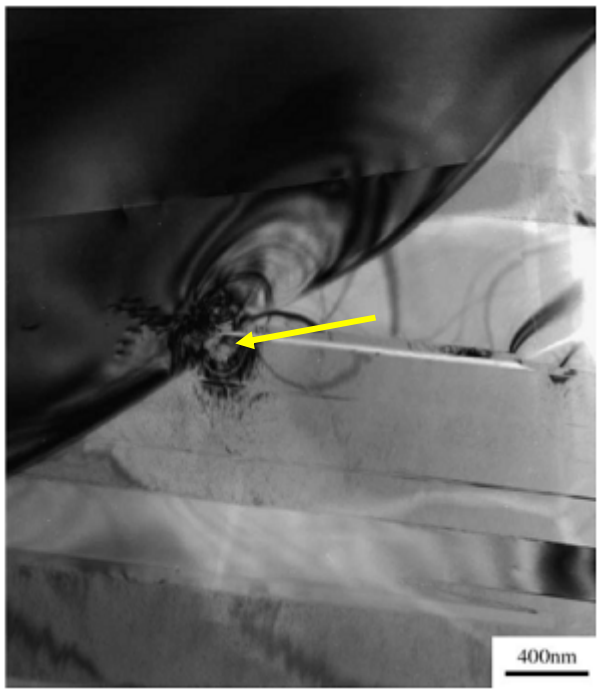

Figure 2.18. TEM micrograph showing internal cracks (arrow) in a component of Ti8Al8Nb1B stressed to 550 MPa [20].

As discussed above, the processing of titanium aluminides includes casting, hot extrusion, forging, powder metallurgy routes and electron beam melting. On the other hand, Franz [34] reported that there are two main production routes of titanium aluminides, viz.: Plasma Arc Melting (PAM) and Vacuum Arc Remelting (VAR). **Fig. 2.19** illustrates a titanium aluminide part's production routes.

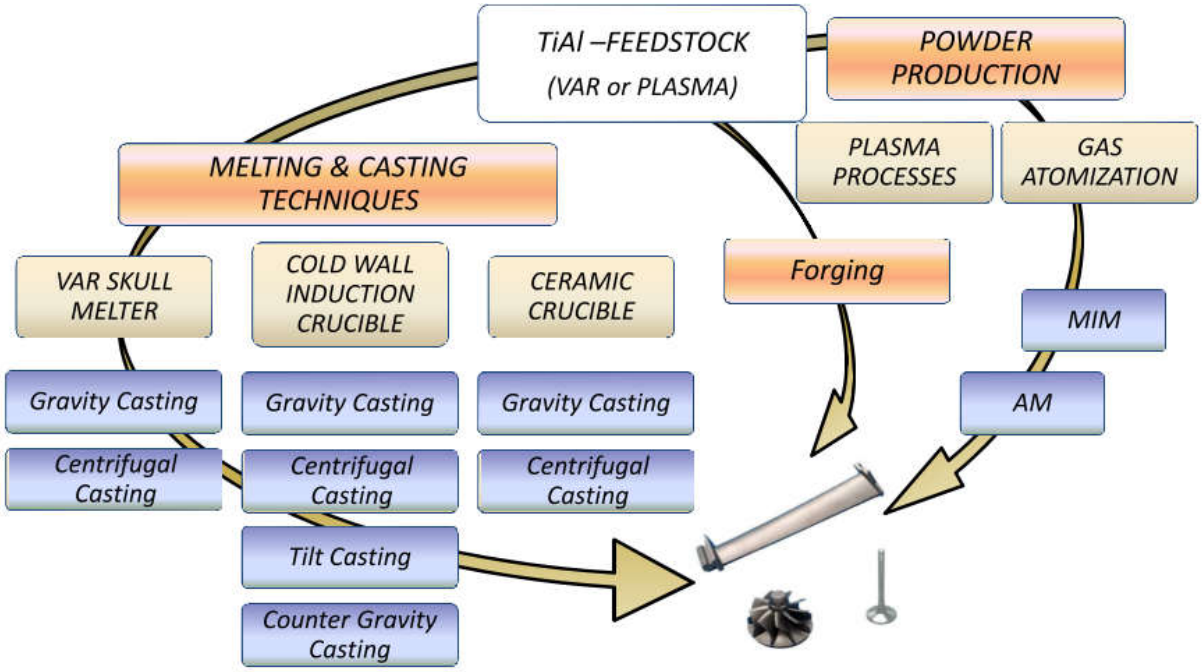

Figure 2.19. TiAl parts production routes [34].

Titanuim aluminide's melting and casting procedures can be summarized as follows [34]:

- For a customized feedstock of casting, suitable size and chemical composition is necessary.
- Melt superheat and turbulence during pouring influences casting yield i.e minimization of the local super-heat (heat of mixing) is likely to subdue loss of volatile elements which results in high casting yield and reduced costs.
- HIP and heat treatment of cast parts is necessary for improved mechanical properties.
- Investment casting/Shell system
    - Gating and feeding system is important (design by simulations).
    - Stress impact on cast parts during solidification and cooling should be minimized by mold-preheating at favorable intermediate temperatures to allow longer contact time between mold and melt, thus successively improve casting defects such as misruns.
- When melting in ceramic crucibles, there should be short cycle times, which then results in small batch weights.
- A combination of Cold Wall Induction Crucible (CIC) melting can allow in increased batch size, increased casting yield and reduced cost.
- Recycling technology with no and/or little risk of impurity pick-up is necessary in order to achieve increased batch size, which is associated with improved casting yield and low production cost.

According to ASM Metals Handbook, Volume 11 [35], investment casting is one of the processing routes that provides a cleaner metal and often superior properties. However, its primal use is for alloys that cannot be adequately cast in the air, such as the γ'-strengthened nickel-base alloys, some cobalt alloys, titanium alloys and refractory materials [35]. One of the major advantages of investment casting is its capacity to cast very thin walls. The technique involves the use of a hot mold, which is enhanced by specific casting methods, such as vacuum-assisted casting, pressurized casting, centrifugal casting and the counter-gravity casting [35]. In vacuum-assisted casting, the mold is placed inside an open chamber, which is then sealed with a plate and gaskets, leaving only the mold opening exposed to the atmosphere. A partial vacuum is drawn within the chamber and around the mold. The metal is poured into the exposed mold opening, and the vacuum serves to evacuate air through the porous mold wall and to create a pressure differential on the molten metal, both of which help to fill delicate detail and thin sections [35].

2.6.2. Forging Processes

In order to promote the application of the bulk TiAl alloys, determining the effective processing and production routes has become the main focus in the development of these alloys. As already mentioned in **Section 2.3.1**, titanium aluminide alloys have been found to offer elevated temperature characteristics that are competitive with those of super-alloys at a significantly reduced density. Schwaighofer et al. [36] found improved ductility of the final microstructure of the multi-phase γ-TiAl based alloys, as a result of the refinement of α_2 phase due to forging and subsequent heat-treatment. Initial α_2 alloys have been found to be workable by forging, while initial α alloys may not be workable by deformation processes such as forging. Moreover, preliminary α_2 titanium aluminide alloys have been found to display higher β phase volume fractions than existing α titanium alloys at temperatures between 1040 and 1150 °C. Furthermore, these preliminary α_2 alloys have deformation characteristics that are considerably more difficult than those of existing α titanium alloys and similar to those of nickel/cobalt-base superalloys [36]. However, under properly defined metal deformation conditions, some titanium aluminide α_2 alloys have been made to behave super-plastically. It appears that the necessary forging processes will be similar to those used for some difficult-to-fabricate titanium alloys, and that carefully controlled conventional hot-die and/or isothermal forging techniques will be necessary for successful forging fabrication [35].

Since there is only one family of (0001) planes in the alpha phase, Wu [20] recognized out that the γ/α lamellae produced during cooling extend across the diameter of the α-grains. This is mainly due to the alpha grain size formed during solidification being inherited in cast products. However, Wu [20]emphasized that if the sample was hot worked in the two-phase

region, the inherited structure was annihilated and a duplex structure comprising of gamma and lamellar grains, was formed after cooling. Moreover, for a fixed alloy composition, the ratio of gamma to lamellar grains is determined by the hot working temperature and the grain size is controlled by the extent of hot working. The grain size of alloys with a duplex microstructure is typically 20μm, which is smaller than the typical grain or colony size in an as-cast lamellar structure where grains of several hundred micro-meters are typical unless grain refiners are added. These distinct microstructures are shown in **Fig. 2.20** [20].

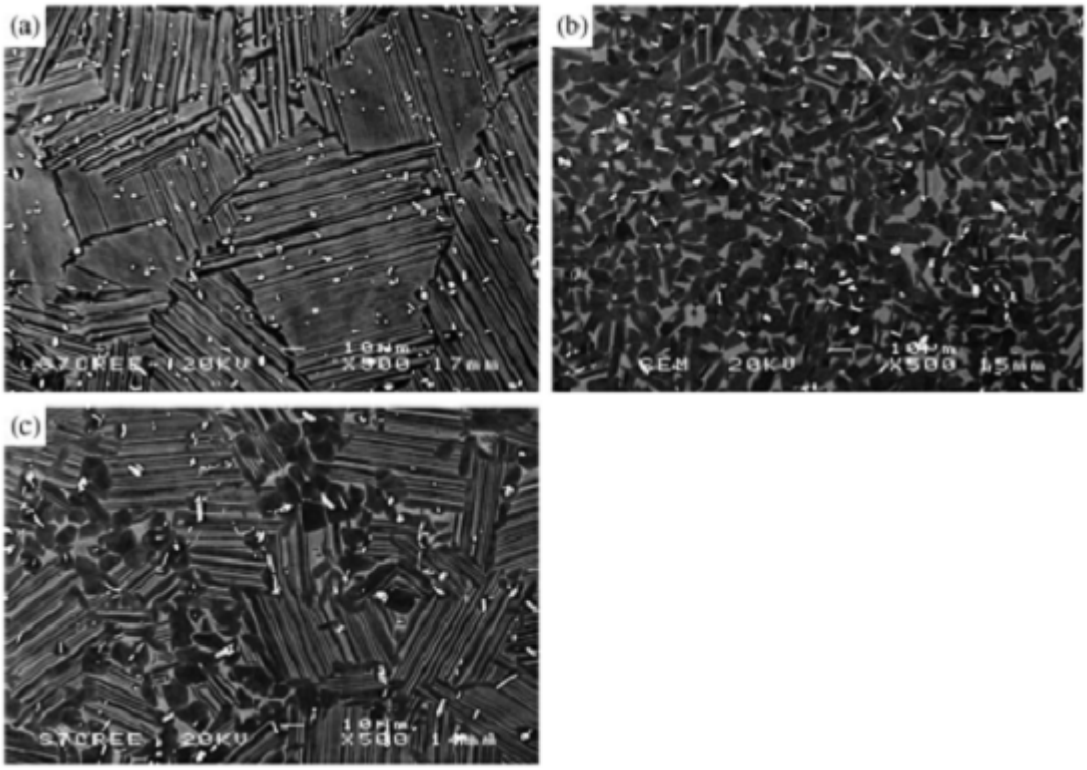

Figure 2.20. Three typical microstructures γ-Ti-44Al-8Nb-1B based alloy: (a) fully lamellar; (b) duplex and (c) nearly fully lamellar [20].

1.6.2.1 Types of forging processes

The process of forging (viz. Hot Die Forging & Isothermal Forging), and the heat treatment process after forging of titanium aluminide are as follows [33]:

- **Hot Die Forging and Isothermal Forging:** The die temperatures are significantly greater than those used in conventional hot-forging processes. This has the advantage of reducing die chill and results in a process capable of producing near-net and/or net shape parts. Therefore, these processes are also called near-net shape forging. These processing techniques are primarily used for manufacturing airframe structures and jet-engine components made of titanium and nickel-base alloys, but they have also been used in the manufacture of steel transmission gears and other components. The principal criterion for selecting these processes in production is the economic advantage

offered because of reduced input material and/or reduced machining costs. Therefore, they are primarily used for expensive and difficult-to-machine alloys such as titanium and nickel-base alloys.

Moreover, Huang [37] described isothermal forging is an effective processing route for the manufacturing of TiAl products with tailored microstructures considering the TiAl production routes including investment casting, forging, rolling and powder metallurgy. As a matter of fact, TiAl-based compressor blades of aerospace and subscale turbine engine compressor disc and blades have been produced by isothermal and closed die forging processes [37].

- **Heat treatment:** The majority of titanium aluminide based alloy forgings are thermally treated after forging with heat treatment ranging from stress-relief annealing to multiple-step processes of solution treating, quenching, aging, and/or annealing, which are designed to modify the microstructure of the alloy, in order to meet specific mechanical properties [37]. Selection of the heat treatment for titanium aluminide alloy forgings is based on the alloy, forging configuration, and mechanical property objectives. The furnaces used to thermally treat these alloy forgings are either continuous or batch gas-fired, electric, fluidized-bed, vacuum, or other specially designed equipment. Titanium aluminide forgings that are heat treated in furnaces other than vacuum furnaces can be processed with or without ceramic pre-coats (in order to provide protection from reaction during the thermal processes). Factors such as the specific heat-treating equipment, conventional versus precision forging type, and process/material specification should be taken into consideration [37].
- **Annealing:** Annealing is used on forgings of most types of titanium aluminide based alloys in order to remove the deformation and/or thermal stresses imparted as a result of forging hot-working processes and/or post forging cooling rates. Annealing is generally done in the temperature range of 595 °C to 925 °C, depending on the specific alloy. It does not cause a significant microstructural modification and is applied to conventional cast titanium aluminide alloy forgings, primarily to facilitate the subsequent fabrication of the forgings, including machining [37].

Bartels et al. [38] recognized that the main aim of thermomechanical treatments is to develop a controlled fine-grained, and homogeneous microstructure, which is suitable for secondary processing operations or succeeding heat-treatments. However, in many cases thermomechanical processing of γ-TiAl alloys is conducted within the (α+γ) phase field, e.g. hot rolling, whereas annealing within the α-phase field and subsequent cooling is used to produce a fully lamellar microstructures.

2.6.3. Electron beam melting

One of the emerging fabrication technologies for metal parts is additive manufacturing (AM), also called, rapid prototyping, or solid free-form fabrication, and/or rapid manufacturing [12]. The AM technologies are able to produce complex shaped parts using three dimensional computer aided design (CAD) data, starting from a precursor powder that is consolidated layer-by-layer, which gives high geometrical freedom and the possibility to create very complex parts with internal cavities and channels [12]. The consolidation can be achieved by sintering or by melting using either a laser or an electron beam as an energy source [12]. Murr et al. [39] emphasized the EBM fabrication process as the technique that produces components to near net shape geometrically complex prototypes.

Biamino et al. [12] did a preliminary assessment of the mechanical properties of γ-TiAl alloy fabricated by EBM and found the following results:

- Very low impurity pickup (oxygen and nitrogen) from the vacuum environment coupled with a limited (1 wt.%) aluminium loss from evaporation in the starting powders;
- Very low residual micro-porosity (below 2%, maximum dimension of defects 200 μm) after EBM which is then even halved by HIP;

2.6.4. Very fine and homogeneous microstructures, due to extremely low levels of internal defects

Among the methods mentioned above, which have been studied extensively in the recent past years is elemental powder metallurgy (EPM) which is a technique for producing defect-free TiAl. However, Lee et al. [40] reported that one of the basic problems to overcome in this manufacturing process is Kirkendall porosity. For instance, the after-effect of transient phases such as $TiAl_2$ and $TiAl_3$ with respect to Kirkendall porosity and the detrimental effect of the beta-phase formation for high temperature mechanical properties are not well apprehended.

The present study seeks to delineate the reaction sequence among the elemental powders comparing two production routes i.e. the consolidation by elemental powder compaction and via the melting route. In addition, the physical properties of some elemental powders are shown in **Table 2.4**.

Table 2.4. Materials constants and properties of some metallic powders used in the manufacturing of TiAl alloys [41].

Properties	Ti (α)	Al	Nb	Cr
Crystal Structure	HCP	FCC	BCC	BCC
Density (g/cm^3)	4.5	2.7	8.6	7.2
Atomic diameter (nm)	0.289	0.286	0.292	0.260
Melting temperature (°C)	1668	660	2468	1875
Thermal expansion (ppm/°C)	8.4	23.8	7.2	6.5
Yield strength	200	75	170	100

2.7. Grinding of bulk γ-TiAl intermetallic alloys

Beranoagirre and López de Lacalle [42] mentioned in their work that grinding is a material removal and surface generation process utilized to shape and finish components made of metals and other materials. Further, the authors pointed out that the grinding modes for γ-TiAl alloys are all the same, whereby an abrasive surface is pressed against a work surface with a force that is perpendicular to the contact zone (normal direction), and thereafter a material is removed from the work and the wheel. This is true and applicable for grinding wheels and belts, using conventional abrasives such as aluminium oxide or silicon carbide, super-abrasives such as cubic boron nitride (CBN) or diamond, and/or the newest abrasive i.e. the seeded gel. In addition, there are three factors that determine how much material will be removed, viz. [42]:

- surface of the abrasive surface
- magnitude of the normal force
- durability of the abrasive component

2.8. The machining of bulk γ-TiAl intermetallic alloys

Machinability of the bulk γ-TiAl alloys is insignificant compared to most of the work-piece materials used in industry. Furthermore, damage is caused by the machining process on the titanium surfaces, i.e. plastic deformation regions, heat-affected zones and cavities can be found close to the surface of the work-piece. However, comparing titanium alloys (such as Ti-6Al-4V) with γ-phase alloys in terms of productivity, temperatures, cutting forces and tool wear/life, it has been found that the machining of gamma based TiAl alloys is more difficult [42].

2.9. Oxidation and nitridation behavior of bulk γ-TiAl based alloys

The bulk γ-TiAl based intermetallic cannot be employed as single phase alloys since it has low ductility and fracture toughness at ambient temperature, as a result the promising alloys are near-γ alloys; whereby the presence of α_2 permits the control of the microstructure [43]. In addition, these alloys are limited to low and intermediate temperature applications due to their insufficient oxidation resistance above 800 °C. Pilone and Felli [43] reported that when TiAl based alloys are exposed to oxidation in air, the scale became a mixture of Al_2O_3 and TiO_2, instead of the protective alumina layer (Al_2O_3). However, the oxidation resistance of TiAl based alloys has been improved by the addition of Mo, W and Nb. Furthermore, this doping effect supresses the formation of rutile (TiO_2), which is porous and allows the inward diffusion of oxygen [43].

Abba et al. [44] showed that oxidation in the presence of nitrogen follows a linear mass gain rate of 0.02 mg/cm^2/h controlled growth rate, and inner mixed scale of TiO or TiN and Si was expected to form. The stability diagram, **Fig. 2.21** demonstrates this. The diffusion process is described by the Fick's law relationship, **Eq. 2:**

$$J = -D\frac{\Delta c}{\Delta x} \qquad (2)$$

where *J* is the flux of atoms, D is the diffusion coefficient, Δc/Δx is the concentration gradient [45]. The linear oxidation at high temperature is time dependent and yields the change in the weight as described by **Eq. 3:**

$$\Delta m = K_L t \qquad (3)$$

where Δm is the change in weight monitored with time (t) with positive k_L when weight is gained.

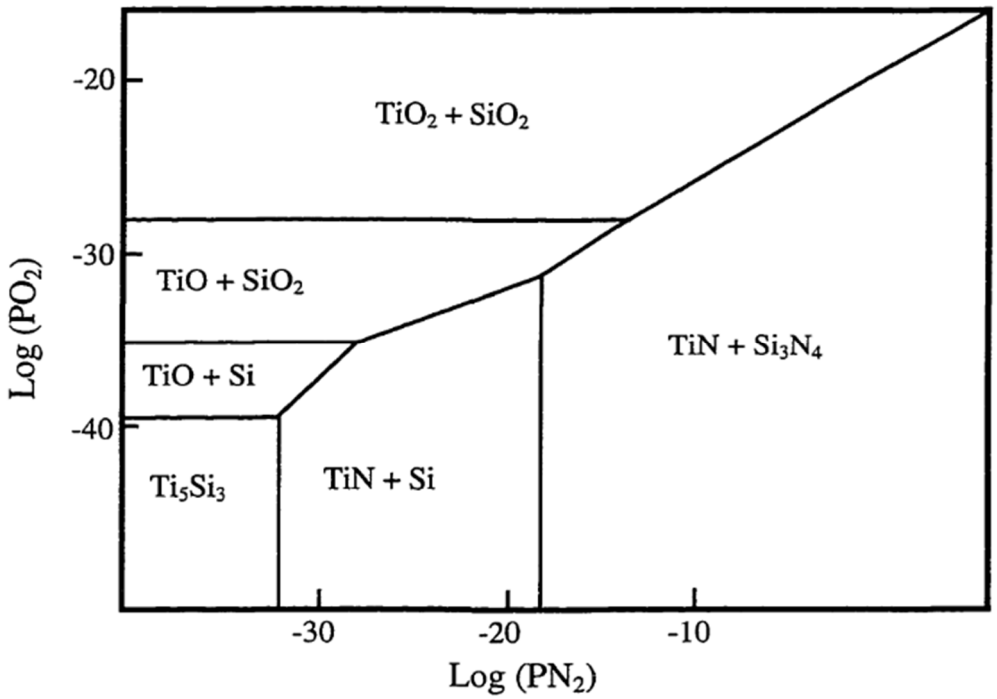

Figure 2.21. Stability diagram for 5Ti + 3Si indicating partial pressures of nitrogen and oxygen [44].

Moreover, the parabolic rate of a law of diffusion-controlled oxidation is represented in **Eq. 4**:

$$(\Delta m/A^2)=kp.t \quad (4)$$

where (Δm/A) is the weight gain per unit area, kp is the parabolic rate constant depending on oxidation temperature and is calculated from the slopes of the $(\Delta m/A)^2$ versus treatment time graphs [46]. The relationship between parabolic rate constant kp and temperature T can be expressed by an Arrhenius-type in **Eq. 5**:

$$D = D_0 exp\left(\frac{-Q}{RT}\right) \quad (5)$$

where D_0 is a constant, Q is an activation energy ((J/mol) for oxide formation, R is gas constant (8.314 J/mol.K) and T is the absolute temperature (K). The rate of the internal interfacial reaction which is also equal to the Ti flux across the oxide layer is represented in **Eq. 6**:

$$\frac{dn}{dt} = \frac{DCi}{x} \quad (6)$$

where D is the diffusion coefficient in the layer, C_i is the concentration of defects Ti_i at the internal interface. The growth of pure TiO_2 layer in the binary Ti-Al alloy is implied in **Eq. 7**:

$$\frac{dn}{dt} = \frac{1}{V_{TiO2}}\frac{dy}{dt} \quad (7)$$

where V_{TiO2} is the molar volume of TiO_2 [44].

2.10. Heat treatment processes of bulk TiAl based alloys

Wu [20] reported that alternative methods for microstructural refinement in cast products is due to rapid cooling from the alpha phase-field (**Fig. 2.1**) which results in massively transformed γ-phase. Subsequent ageing in the two-phase region gives rise to α precipitation on all four {111} planes of the γ-phase, resulting in the grain refinement of the structure, and the typical microstructures are illustrated in **Fig. 2.22 a-b**. Examples of the improvement in properties of some TiAl-based alloys heat treated by this and other approaches are indicated in **Table 2.5.** Cooling rapidly to produce a fully massive structure can lead to quench-cracking. However, there are two techniques which have been investigated to avoid cracking. The first is to quench into a salt bath to a temperature above the ductile to brittle temperature, but below the massive transformation temperature and, the second is to develop alloys which will transform massively using slower cooling rates. These two approaches have been shown to allow samples up to 25mm in diameter to be transformed massively without cracking.

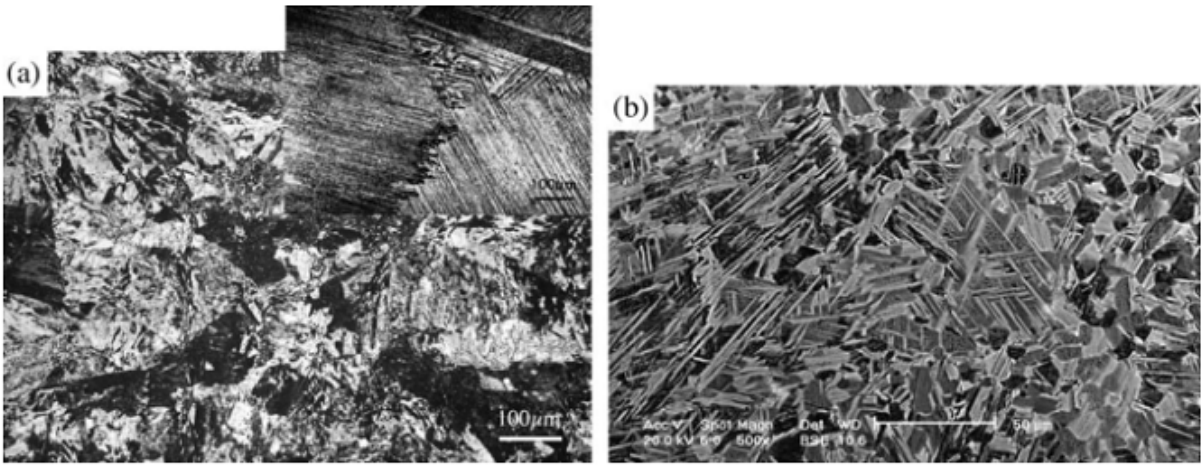

Figure 2.22. Optical and SEM micrographs of samples of Ti48Al2Nb2Cr showing (a) massive microstructure formed after oil quenching and (b) fine microstructure formed after HIP as alpha precipitates on the four {111} in the γ-phase [20].

Table 2.5. Mechanical properties of TiAl-based alloys obtained using various processing routes [20].

Alloy	Treatment	0.2% Proof stress (MPa)	UTS (MPa)	Ductility (MPa)
Ti48Al2Cr2Nb	Forged	312	347	0.5
Ti48Al2Cr2Nb	Forged/cast/OQ/HIP[a]	425	622	1.3
Ti46Al8Nb	Cast/HIP	–	537	0.1
Ti46Al8Nb	Cast/SBQ/HIP	523	567	0.5

The properties of TiAl intermetallic compounds strongly depend on the microstructures, especially the morphology of γ-TiAl and α_2-Ti_3Al phases. As mentioned in **Section 2.6.2**, there

are four types of microstructures in γ-TiAl based alloys viz. fully lamellar, nearly lamellar, duplex and equi-axial near-γ. The duplex and fully lamellar microstructures have a good combination of mechanical properties. Fully lamellar microstructures are most attractive for their good fatigue resistance, fracture toughness, creep resistance and high temperature strength retention, but with deficit ductility, whereas, duplex microstructures exhibit better strength and ductility, but retain poor creep resistance [47],[48].

Crofts et al. [21] has attempted to quantify the microstructure of bulk TiAl intermetallic alloys in terms of a set of parameters, of which the most considered are listed below. However, one could ideally wish to vary each of these parameters independently, but in general, heat treatments or thermomechanical processing alters more than one of them [21].

- Colony size
- Lamellar thickness
- Proportion of α_2
- Serration of the grain boundaries
- Nature of the lamellar interfaces

Fig. 2.23 illustrates the Ti-Al binary phase diagram pointing out the region of concern indicated by the arrow. The phase transformations occur between the ordered f.c.t. γ phase and hcp phase (i.e. the disordered α or ordered α_2). During the heat treatment process, the cooling sequence of lamellar morphology is formed via the following reaction: $\alpha \rightarrow \alpha+\gamma \rightarrow \alpha_2+\gamma$ or $\alpha \rightarrow \alpha_2 \rightarrow \alpha_2+\gamma$ depending on the Al content. Generally, alloys with Al contents greater than 45% follow the first reaction [49].

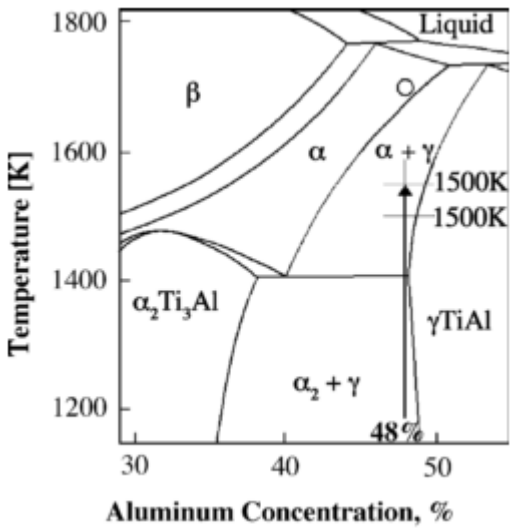

Figure 2.23. Ti-Al phase diagram showing the relevant section with the employed heat treatment temperature plotted on it [49].

Beddoes et al [50], **Fig. 2.24** illustrated a variety of microstructures such as a mixture of α_2 (ordered hcp) + γ-TiAl (ordered fct), duplex microstructure which favors good tensile properties, whereas the fully lamellar structure improves fracture toughness and creep resistance.

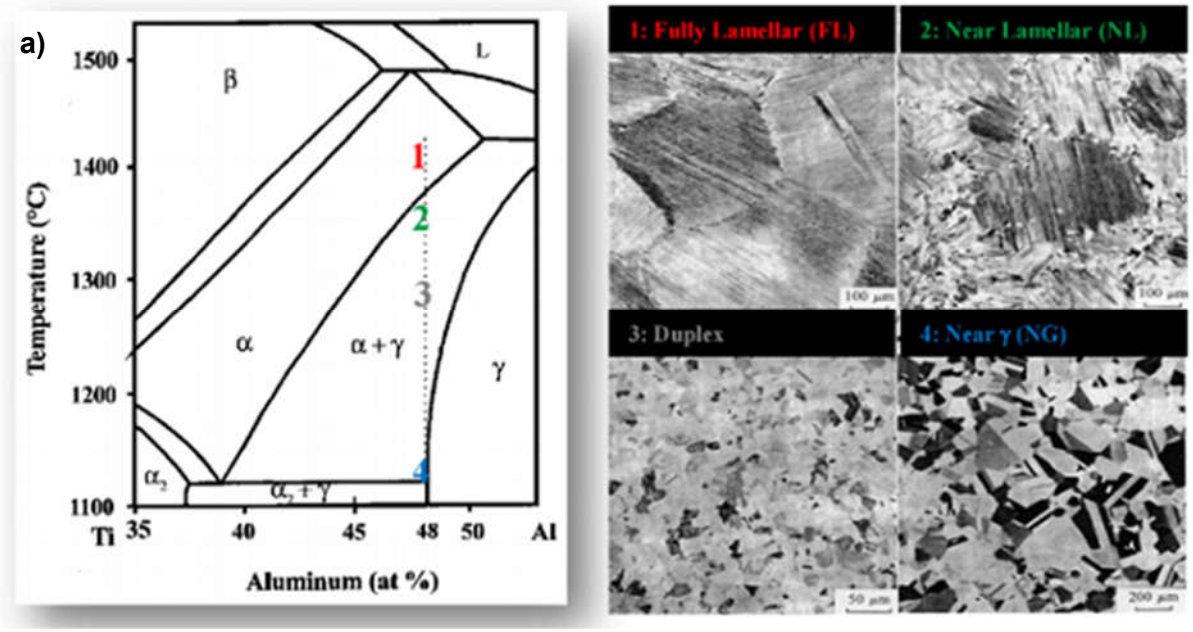

Figure 2.24. (a) TiAl phase diagram with corresponding various microstructures [50].

The composition of conventional engineering γ-TiAl based alloys, the allegedly 2nd generation alloys can be summarized as follows (in at. %) Ti-(45-48) Al- (1-3)X-(2-5)Y-(<1)Z, where X= Cr, Mn, V; Y=Nb, Ta, W, Mo; Z=Si, B, C [50]. These alloying elements change the position of the phase boundaries of the Ti-Al phase diagram. For example, Nb and Mo shift the α-transus line to the Al-rich side, thus narrowing (α +γ) phase field, as shown in **Fig. 2.25** [11].

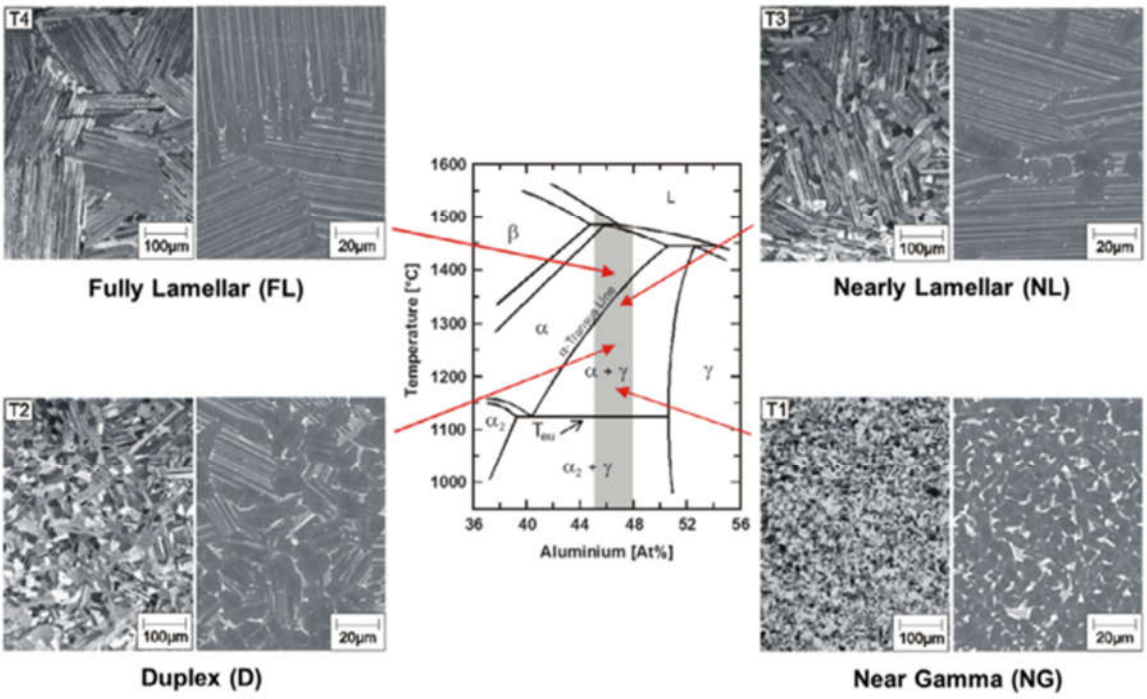

Figure 2.25. Mid-section of TiAl binary phase diagram showing different types of microstructures attained by means of heat treatments within the α and (α+γ) phase field conducted on a Ti-46.7Al-4(Cr, Nb, Ta, B) alloy (in at. %). The left half of the microstructural image illustrate a light optical microscope image, whereas the right half is the scanning electron microscope image taken in back-scattered electron mode, γ-appears dark and α_2 shows a light contrast. Heat-treatments: a little above eutectoid temperature (T_{eu}) → near gamma microstructure (NG) microstructure; between T_{eu} and α-transus temperature Tα → duplex (D) microstructure. The volume fraction of lamellar grains depends on the heat-treatment temperature relative to Teu and Tα; just below Tα→nearly lamellar (NL) microstructure. A NL microstructure exhibits a defined volume fraction of globular γ-grains; and lastly above Tα→fully lamellar (FL) microstructure [11].

Zhu et al. [49] found that as the cooling rate increased from 6×10^{-2} to $4Ks^{-1}$ for a Ti-48Al alloy, the microstructure changed from a sub-duplex structure comprised mainly of lamellar grains, through a fully lamellar structure to a very fine lamellar structure with Widmannstätten-type morphology. However, if the cooling rate exceeded $10Ks^{-1}$, a very fine Widmannstätten lath structure was formed, consisting of γ phase produced by massive transformation. Dey at al. [51] defined Widmanstätten laths as lengthy straight lamellar packets with approximately no orientation relationship between themselves, but are embedded in the lamellae with different spatial orientation. These structural laths were observed under various intermediate cooling rates, such as air, sand and oil quenched specimens. **Fig. 2.26** illustrates development

mechanisms of a range of structures generated during heat treatment of the (α_2+γ) TiAl based alloys from α phase field.

The cooling rate was inversely proportional to the lamellar spacing of the fully lamellar structure, and the creep rate reduced with increased lamellar spacing. On the other hand, fast cooling to obtain fine lamellar spacing of a fully lamellar structure, resulted in α_2 volume fractions far from thermodynamic equilibrium. Corresponding, non-equilibrium conditions contributed one of the driving forces responsible for microstructural degradation during creep deformation: as a result the creep strength deteriorated. Consequently, enhancement of creep resistance by reducing lamellar spacing by fast cooling is restricted [49]. Appel and Wagner [52] demonstrated that microstructural optimisation gave a plausible trend in mechanical properties for a fully lamellar microstructure with colony sizes below 200μm.

During heating a reverse phase transformation from γ to α occurs. If the initial microstructure is duplex and near-γ, four {111} habit planes of each γ grain are available for the precipitation of α phase from the γ matrix, resulting in the Widmannstätten-type structure. However, if the starting microstructure is lamellar, α phase can nucleate and grow during heating at pre-existing α laths. Thus, α and γ lamellae present at high temperature, would transform to the γ/α_2 lamellar structure after subsequent cooling. As a result, the morphology of α and γ lamellar phases before cooling may influence the final lamellar structure, which influences the creep property of TiAl alloys. However, less attention has been paid to this reverse phase transformation during heating in lamellar microstructure control of TiAl alloys [52].

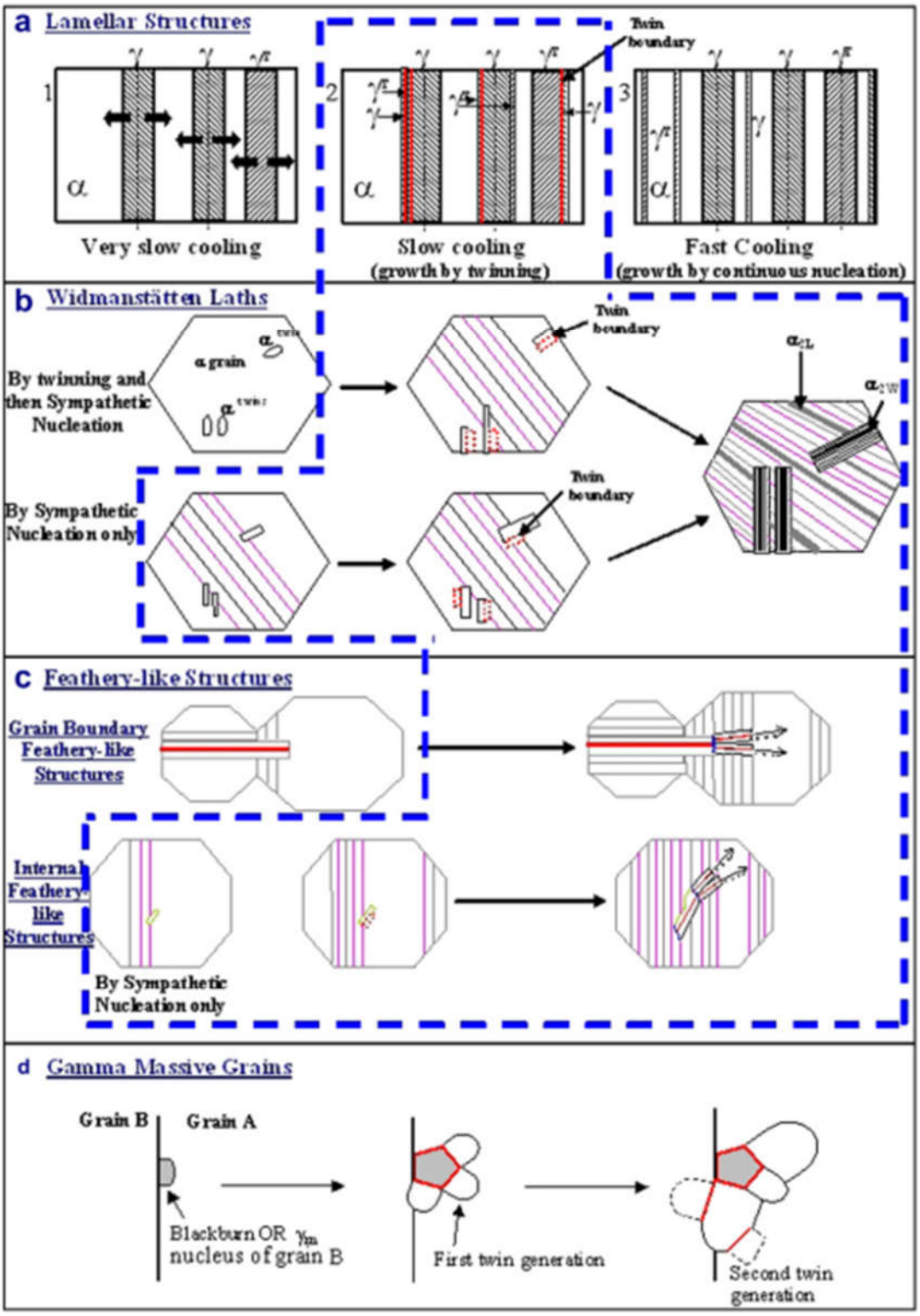

Figure 2.26. Schematic representation of development mechanism of a variety of structures generated during heat-treatment of the (α_2+γ) TiAl-based alloy from high temperature α domain [51].

As recognized by Ge [47], the lamellar structure can coarsen in two ways during heat treatment: 1) continuous coarsening which is governed by body diffusion, and 2) discontinuous coarsening which is governed by the α_2/γ interface. The author reported that coarsening of the

lamellar α_2 phase depended on the migration of interface defects, where the α_2 phase spheroidization occured as a result of Raleigh's breakdown. On the other hand, the α_2 phase boundary is not straight, thus providing the condition for instability of decomposition. In two-phase (γ + α_2) alloys, the ratio of lamellar to equiaxed γ must be controlled. A lamellar volume fraction of about 30% gives a good combination of properties with excellent creep resistance, adequate tensile strength and usable ductility. However, the optimum structure for enhanced ductility has been suggested to consist of adjacent regions of lamellar and equiaxed morphologies [53].

To conclude, the processing of TiAl-based alloys requires the further development prior manufacturing of good quality components acceptable for aero-engine applications at a tolerable cost. Thermo-mechanically processed samples are exceedingly costly; the resulting ingot heterogeneity limits the size of the manufactured parts. Moreover, casting technology should, however, be enhanced and the microstructural control aimed at refining the microstructure entails further work.

2.10.1. Phase transformation mechanism

During processing of γ-TiAl based components, variations in cooling rate where the thin parts exhibit extremely high cooling rates, leave a heterogeneous microstructure in the component. In such cases, annealing process at intermediate temperatures is mandatory for the components to stabilize the microstructure and release internal stresses. It is commonly reported that the as-cast and forged microstructures of Nb-containing TiAl alloys, although slowly cooled to room temperatures, are non-equilibrium structures. Consequently, phase transformations may occur during annealing at 700 ^{o}C -900 ^{o}C [54]. According to Schwaighofer et al. [36], forming procedures such as hot extrusion and forging contribute to the final microstructural evolution. An increased dislocation density may refine coarse constituent of the microstructure by means of recrystallization. Subsequent multi-step heat-treatments can result in optimized mechanical properties. Heat-treatments within single β-phase help achieve chemical and microstructural refinement and, reach tolerable mechanical properties without engaging hot forming process.

Bystrzanowski et al. [13] reported that controlling a fully lamellar entails a heat-treatment in a single α-phase with subsequent fast cooling through the (α+γ) phase field, and leads to phase compositions far from thermodynamic equilibrium. This provides a driving force for thermal instabilities of the lamellar microstructure and causes dissolution of the α_2 lamellae and dynamic recrystallization.

Saari et al. [55] simulated the development of the directionally solidified γ-TiAl structures. The study showed that the alloys solidified with β as the primary solidification phase, indicated by the four fold symmetry of the primary dendrites, **Fig. 2.27**.

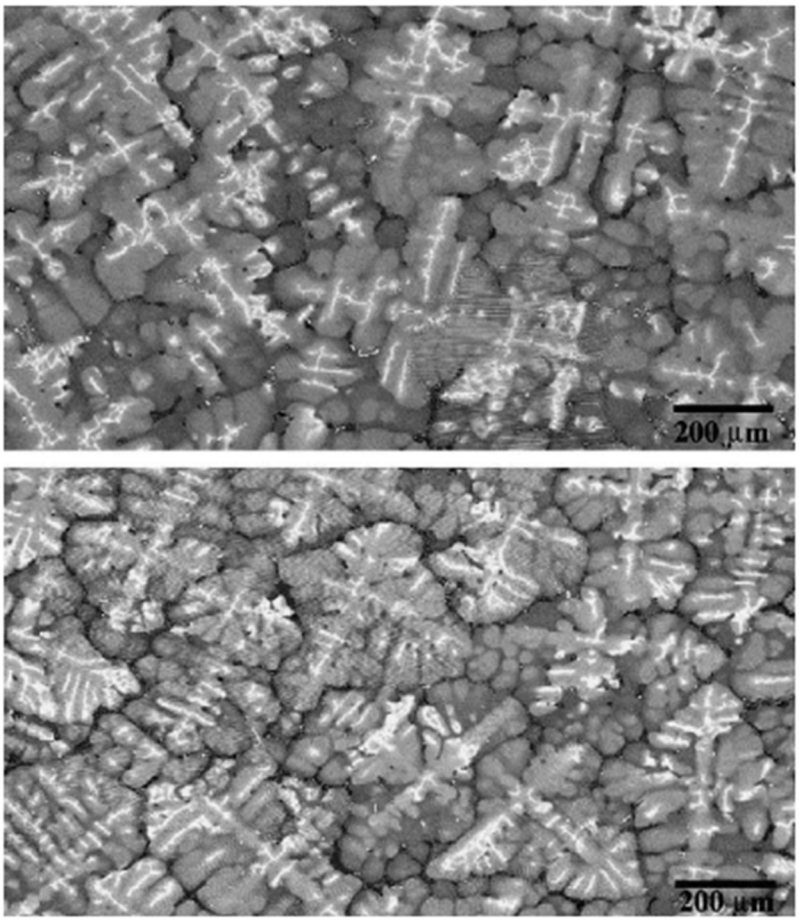

Figure 2.27. SEM-BSE of transverse sections of two castings processed under low (top image) and high (bottom image) withdrawal rates [55].

Franzén and Kalsson [56] found that as the γ-TiAl of about 48 at. % Al, cools down from the liquid, from the phase diagram in **Fig. 2.24a**, three primary solidification phases and two peritectic reactions are possible. When the γ-TiAl based alloy is heated into the α single phase region, the Al becomes effectively dissolved in the hexagonal closed packed Ti. If the pre-existing microstructure is the γ-phase segregated with α-phase, the dendritic segregation will dissolve and the microstructure will become homogeneous. Heating in this area induces grain growth of the α-grains generated as the γ-grains dissolves. It was found that the γ-grains dissolve through diffusion controlled dissolution [56], as shown in **Eq. 8**:

$$\frac{dD_\alpha}{dt} = k^* \left[\left(\frac{1}{D_\alpha}\right) - \left(\frac{1}{D_\alpha^L}\right)\right]^{P-1} \quad (8)$$

where Dα denotes grain size of the α grain as a function of time, k* denotes the rate constant, $D\alpha^L$ denotes the α grain size limit, and p denotes the grain growth exponent.

2.11. *Ab initio* calculations of γ-TiAl based alloys

2.11.1. First principles calculations: Geometry analysis

Computer simulation and geometry analysis techniques are used in such a way that, the method offers a way of investigating properties of materials using computers, whereby the simulator builds a model of an experimental system and explores its behavior. The commonly known computational technique is the *ab initio* method (employed in this study), also known as the Vienna ab Initio simulation package (VASP) which is a group of methods that enables the determination of properties of materials viz. the fundamental constants and atomic positions. First principle calculations are performed using projector augmented wave (PAW) pseudopotentials within the generalized gradient approximation (PW91-GGA), AS implemented in the (VASP) code [24]. An energy cutoff of 500 eV was used, as it was sufficient to converge the total energy of the TiAl alloys. For the exchange-correlation functional, the generalized gradient approximation of Perdew and Wang (GGA-PBE) [57] was chosen. The Brillouin zone integrations were performed for suitably large sets of k-points according to Monkhorst and Pack [58]. The phonon dispersion spectra were evaluated using PHONON code [59] as implemented by Materials Design within their MedeA software, VASP code. All the calculations were done at 0 K. Yongwang et al. [60] reported that for doped (alloyed) systems, geometry optimisation is performed to obtain a stable structure with minimum total energy. In addition, the geometry optimization process was performed on all atomic positions that were relaxed, until forces are less than 0.05 eV/Å and stresses less than 0.1 GPa. However, in the present study, the geometry optimization for the Ti-Al-$X_{(Nb, Cr, Si)}$ based alloys were performed within generalized gradient approximation using the energy cut-off of 500eV, and the lattice parameters allowed to vary.

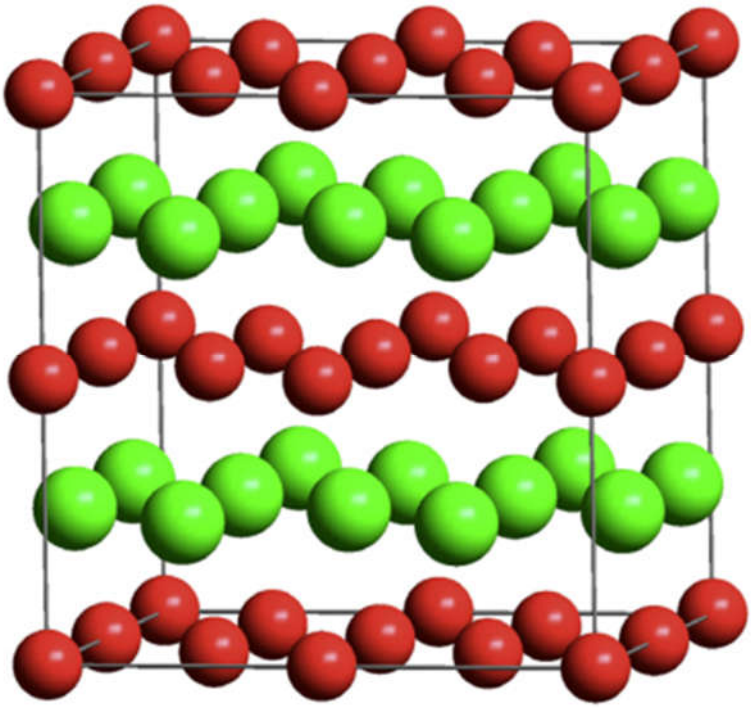

Figure 2.28. 32-atom TiAl supercell. Red and green spheres represents Ti and Al atoms, respectively [24].

A first principle supercell approach was used to obtain the formation of enthalpies of isolated point defects in $L1_0$ TiAl, using a 32-atom 2×2×2 super-cell (**Fig. 2.28)** has been employed in the work done by Jiang [24], whereby each cell contained a single point defect (vacancy, antisite or ternary element in its center). In this work, the semi-core 3p electrons of Ti, Cr, and the semi-core 4p electrons of Nb; the interstitial atoms of Si were explicitly treated as valence. The plane wave cut-off energy is set at 500 eV. The k-point meshes for Brillouin zone sampling are constructed using the Monkhorst-Pack scheme, and a 9×9×9 k-point mesh for the 32-atom supercell (corresponding to 75 irreducible k-points in the Brilloiun zone) is found to be sufficient to give fully converged point defect energetics.

2.11.2. Elastic constants

The calculated elastic constants aided to obtain the macroscopic mechanical parameters of all systems, e.g. bulk modulus K, shear modulus G and elastic modulus E. However, for all crystal structures, K, G and E of polycrystalline materials are predicted by the following Voight **Eq. 9-13** [60]:

$$K=1/9\ (C\_11+C\_22+C\_33)+2/\ (9)\ (C\_12+C\_13+C\_23) \quad (9)$$

$$G=1/15\ [(C\_11+C\_22+C\_33)-(C\_12+C\_13+C\_23)]+1/5(C\_44+C\_55+C\_66) \quad (10)$$

$$E=9KG/\ ((3K+G)) \quad (11)$$

The tetragonal system such as the γ-phase, there are six independent elastic constants viz. (c11=c22, c12; c13=c23, c33; c44=c55, c66) shown in **Table 2.6**. Thus, the elastic modulus equation of the tetragonal system can be written as [60]:

K=1/9 (2C_11+C_33) +2/ (9) (C_12+2C_13 (12)

G=1/15(2C_11+C_33-C_12+2C_13+⟦6C⟧_44+⟦3C⟧_66) (13)

Table 2.6. Summarizes the elastic moduli obtained using Eqs. (12) - (13) [60].

	Pure β-Nb5Si3	Ti-Nb-Si	Cr-Nb-Si
C_{11}	359.58	350.10	356.05
C_{22}	359.58	350.10	356.05
C_{33}	308.86	315.05	324.87
C_{44}	84.16	87.55	90.70
C_{55}	84.16	87.55	90.70
C_{66}	129.37	130.00	126.98
C_{12}	127.03	122.96	123.47
C_{13}	107.26	104.00	106.02
C_{23}	107.26	104.00	106.02
K	190.13	186.35	189.78
G	105.30	106.64	108.44
E	266.67	268.67	273.27

2.12. FIB-SEM analysis

A focused ion beam-scanning electron microscope (FIB-SEM) uses ions instead of electrons for analysis of sample materials. Generally, a Ga source is used to create Ga+ ions, which are projected onto the sample. These projected atoms scatter away from the sample surface. Backscattered ions can be analyzed using the same principal as backscatter electron (BSE) in the SEM. Additionally, the FIB approach can be utilized to remove material from the sample either to polish or etch [58].

The FIB column is directed right on the sample with the SEM at an angle of 58° vertically and 32° horizontally shown in **Fig. 2.29**.

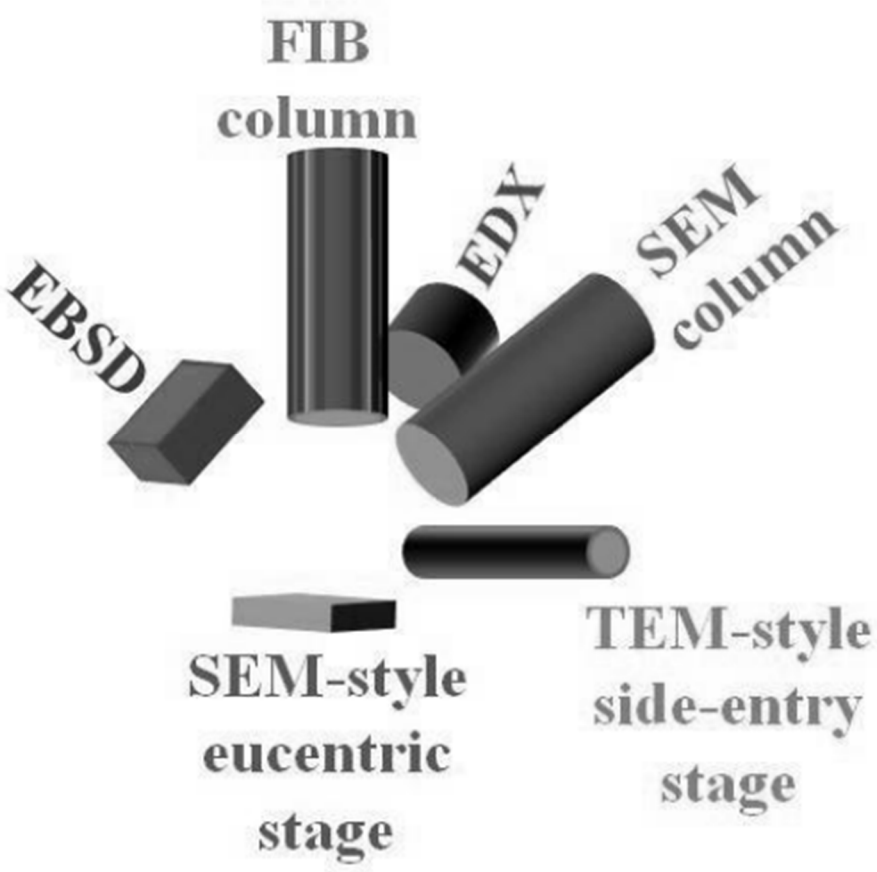

Figure 2.29. FIB-SEM setup at Oak Ridge National Laboratory [56].

For examination of γ-TiAl based alloys, pre-cuts were made by the FIB technique. An analysis covering an area of about 50μm was polished, as observed in **Fig. 2.30**.

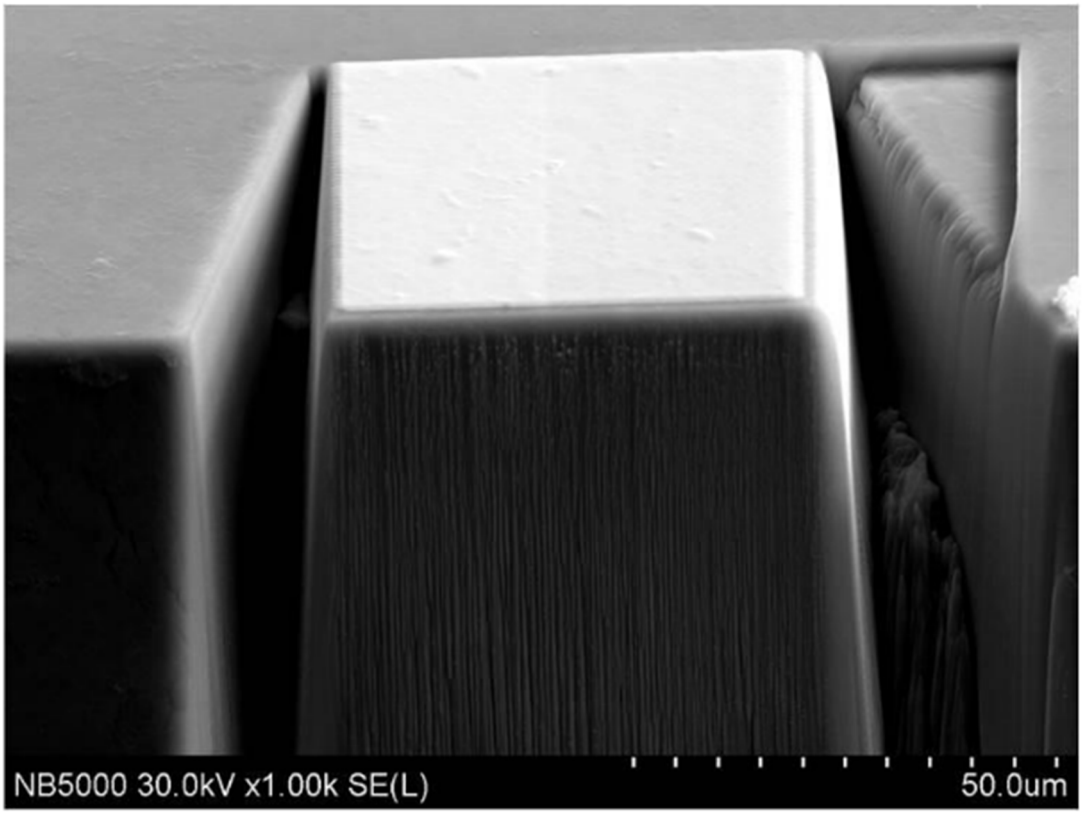

Figure 2.30. Cut-out of TiAl alloy using FIB [56].

2.13. Characterization of order domains in γ-TiAl

2.13.1. Orientation variants by electron backscatter diffraction

Phase transformation to γ-TiAl usually occurs during cooling from the hexagonal α-phase domain, and occurs according to the Blackburn orientation relationship, which give rise to six dissimilar orientation variants, shown in **Fig. 2.31** [61].These variants are grouped into two groups of three, with a mutually perpendicular *c* axes. The variant triplets are called order variants, generated by a 120° rotation around the (111) plane normal [61]. In typical lamellar structure, each grain comprises of all the six γ-variants. The γ-phase deploys a domain structure of twin-related lamellae, which contain of one to three order variants [61]. On one hand, for the coherent twin created by a 180° rotation around ⟨111⟩, two pseudo-twin relations exist. The pseudo-twins are related by a ±60° rotation around ⟨111⟩, and across the pseudo-twin interface, to create an order fault is created with addition to change of stacking order [61].

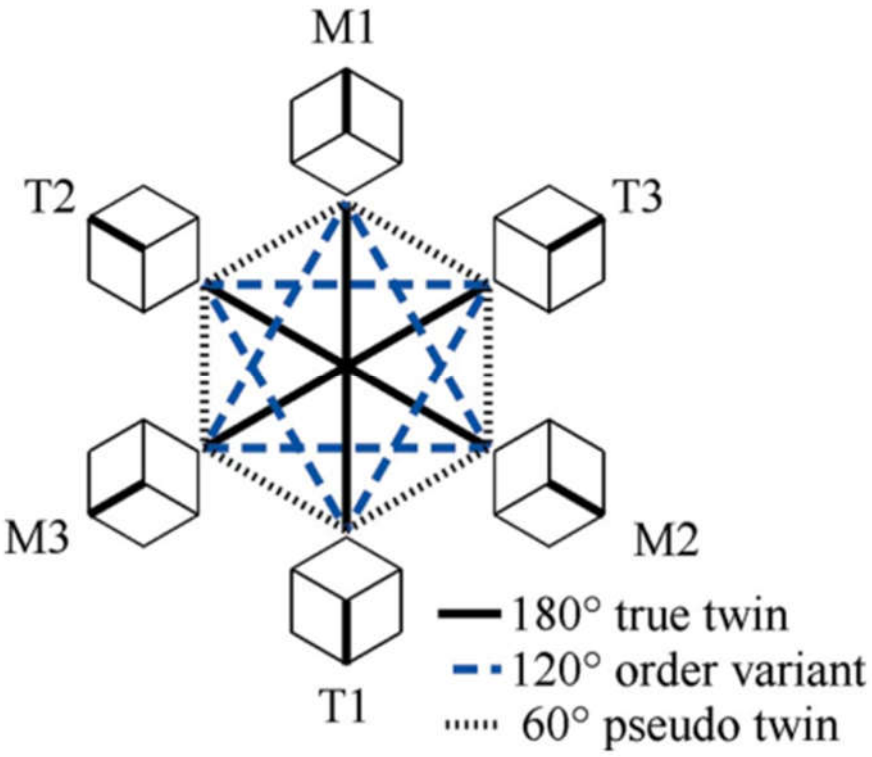

Figure 2.31.Six orientation variants in γ-TiAl. Opposing variants are in a true-twin relationship, *e.g* T1 and M1. The designation of the twin (T) and matrix (M) labels are arbitrary [61].

2.13.2. γ/γ interface relations by TEM Kikuchi patterns

Dey et al. [62], reported that due to the near-cubic lattice of the tetragonal γ-phase (*c/a*~1.02), the Kikuchi patterns of three γ-variants belonging to the same twin group are nearly identical. These interchangeable γ-variants can be differentiated by specific positioned superlattice reflection bands in their respective Kikuchi patterns. These superlattice reflections appeared from the planes following the rule: $h + k = 2n$ where *h*, *k*, *l* are neither all even nor all odd. **Fig. 2.32** shows Kikuchi patterns of six γ-variants with their orientation related α_2 phase.

During cooling, the $\gamma+\alpha_2$ lamellar microstructure is formed by decomposition of the α-phase (hexagonal structure, A3) into lamellar precipitates of the γ-phase (ordered tetragonal structures, $L1_0$ shown in **Fig. 2.33a**); and by ordering of the remnant α-phase, giving rise to lamellae of α_2-phase (ordered hexagonal structure, $D0_{19}$ shown in **Fig. 2.33b**) [63]. The α_2 lamellae in a given grain have the same orientation, since there is only one viable orientation variant for the $\alpha \rightarrow \alpha_2$ transformation.

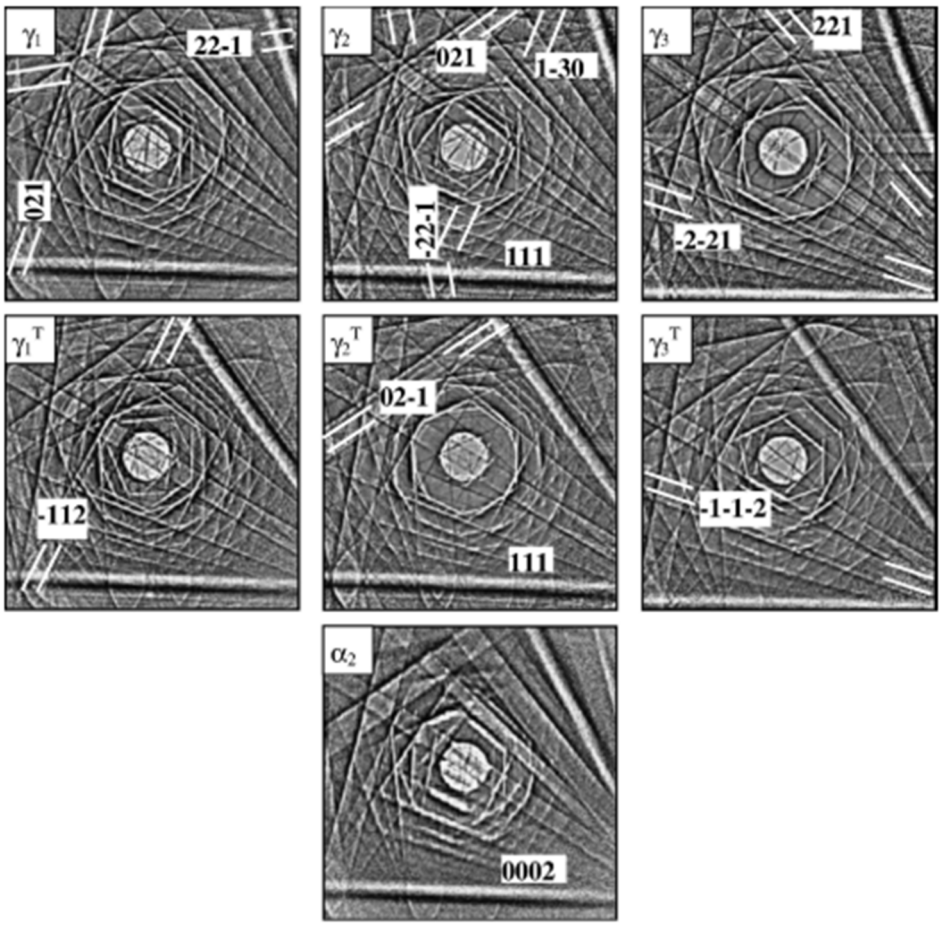

Figure 2.32. Kikuchi diffraction patterns of six γ-variants and α_2 phase of a given alpha grain. Variable γ-variants can be distinguished by their superlattice bands which are marked by white lines. [62].

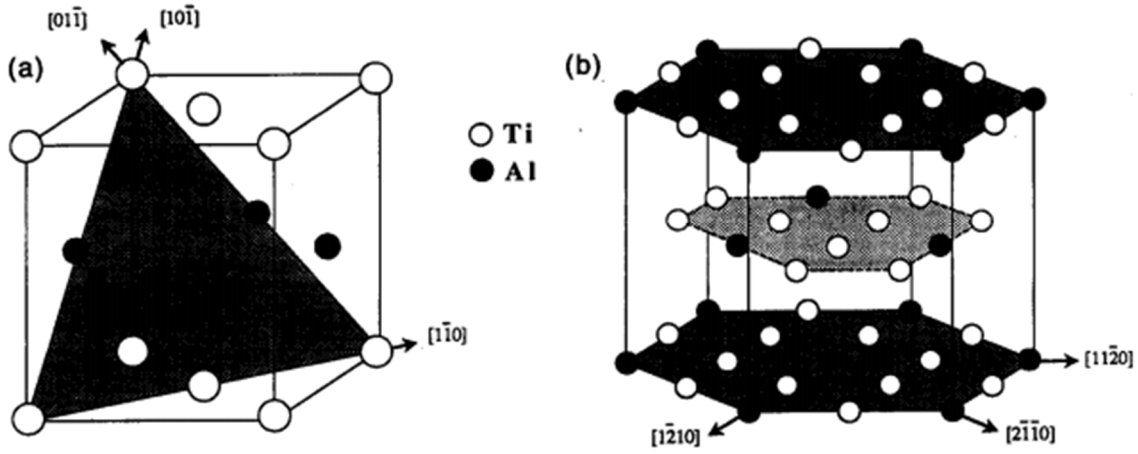

Figure 2.33. a) $L1_0$, and b) $D0_{19}$ structures [63].

As mentioned in **Section 2.13.1**, the γ-precipitation follows the Burgers orientation:

{111}γ // (0001)α_2 and ⟨110⟩γ // ⟨1120⟩α_2, and the habit planes are the most compact planes of the two structures: (0001) for α2, and {111} for γ-phase [63]. During this transformation, the

ABABABAB… stacking sequence of the hexagonal structure is altered into ABCABC… stacking sequence of the fcc structure, and the ordering of the fcc lattice gives rise to the tetragonality of the $L1_0$ structure. The orientations of lamellae for which the sequence is ABCABC are referred to as the group of orientations γ_I, and those for which the sequence is ACBACB are in the group of orientations γ_{II} depicted in **Fig. 2.34**. As a consequence of the tetragonality in the $L1_0$ structure, the ⟨110] direction, and the other two ⟨011] directions are not equivalent to one another. **Fig. 2.33a** indicate the atomic rows parallel to the ⟨110] direction comprising of only one type of atom, whereas those parallel to the ⟨011] directions are created by alternating Ti and Al atoms. Moreover, the ordering of the fcc lattice into the $L1_0$ structure is succeeded by a decrease in crystal symmetry giving rise to stacking sequence, to the formation of three possible positions of the ⟨110] direction in the habit plane **Fig. 2.34** [63].

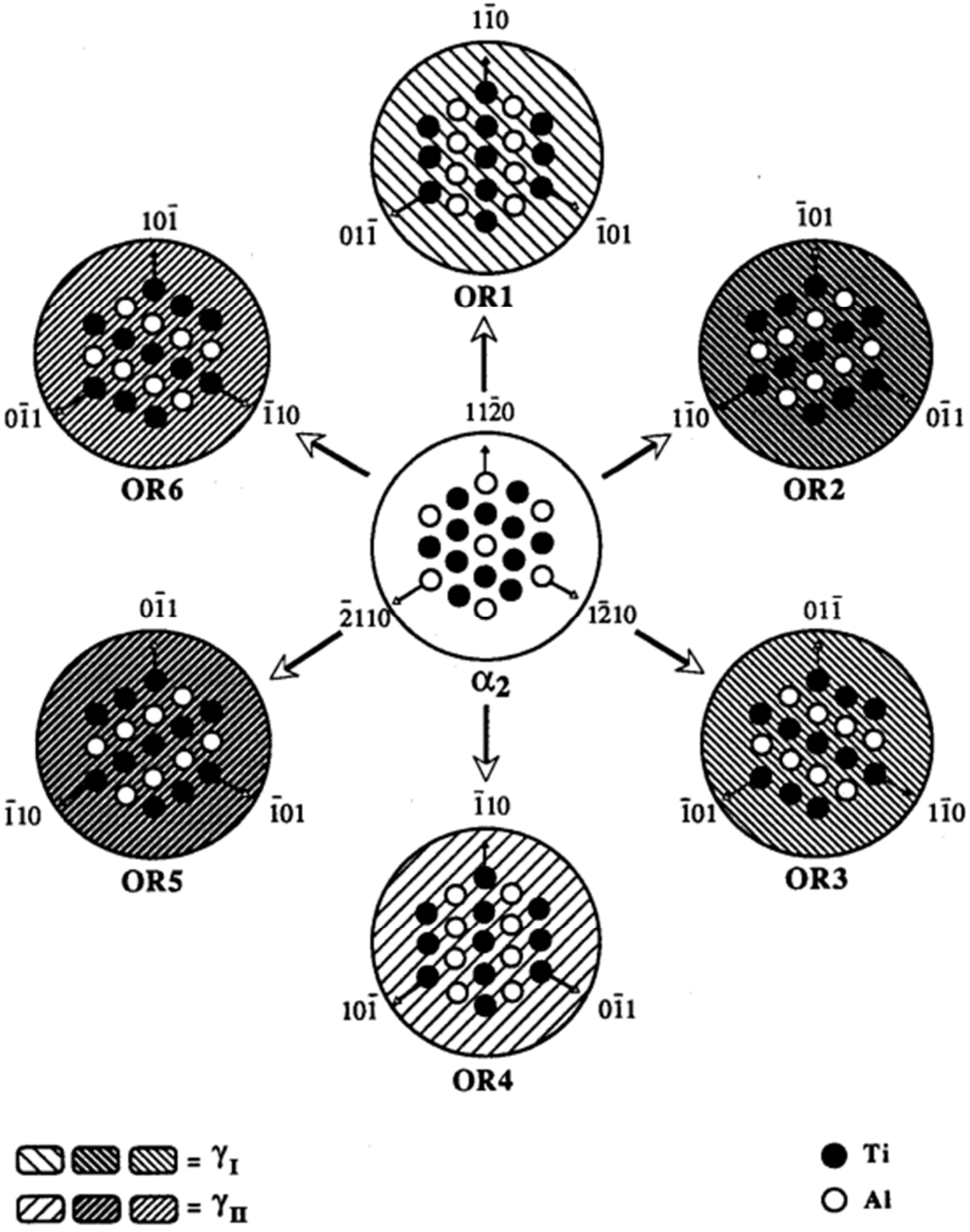

Figure 2.34. Schematic representation of the six orientation variants of the γ-phase with respect to the basal plane of the α2-phase taken as a reference and situated at the centre. Tilting either to the left or right in the hatching of the background patterns represents the two possible stacking sequences. The arrangement of the atoms species in the habit plane is also represented for the six orientations [63].

2.13.3. Numbering crystallographic variants in phase transformation

Orientation of a single crystal is denoted by a macroscopic coordinate system K_A coincident with a microscopic coordinate system K_B attached to the lattice, called orthogonal transformation. Such a transformation is either a rotation or a rotation followed by an inversion. However, in practice, the rotation *g* can be decomposed into a set of elementary rotations of angles φ_1, ϕ, φ_2, called Euler's angles shown in **Fig. 2.35** around specific axes of intermediary reference frames [64].

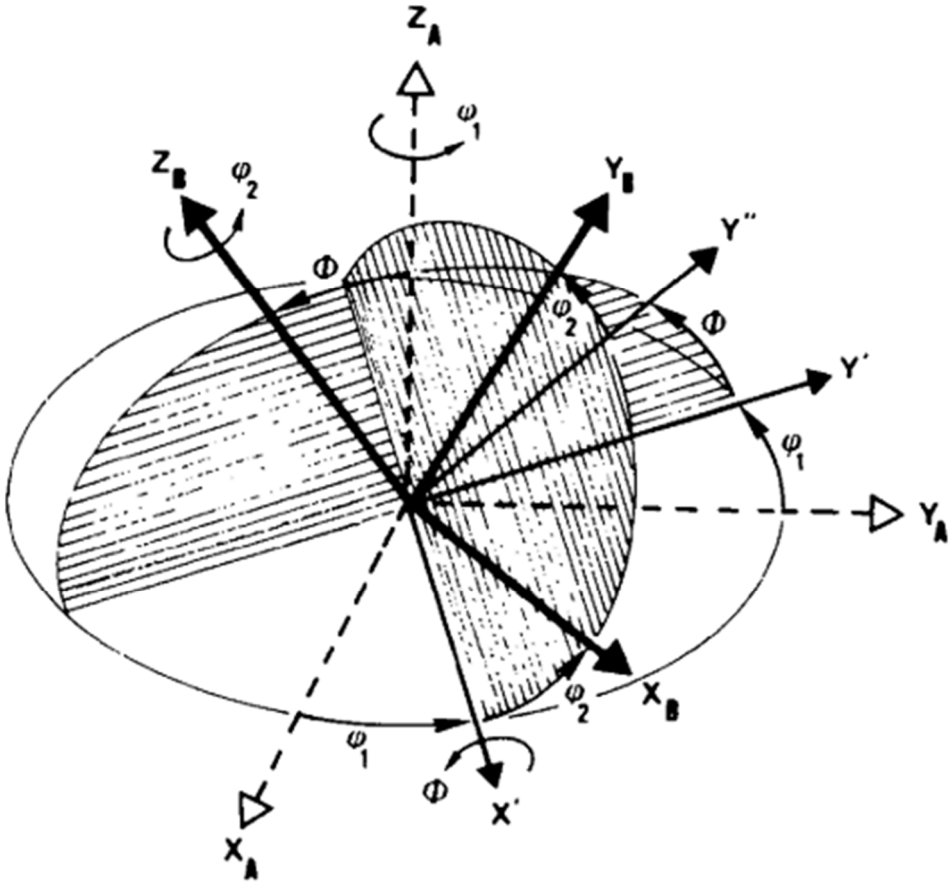

Figure 2.35. Decomposition of rotation *g* into three elementary rotations of angles φ_1, ϕ, φ_2 around the Z_A, *X'*, Z_B, respectively [64].

Humbert et al. [64] stipulated that a set of symmetrically equivalent reference frames K_{Bi} can be derived from an arbitrary chosen reference frame K_B by the rotation S_i of the rotational symmetry group G_B of the respective lattice, which is represented in **Eq. 14**:

$$K_A \xrightarrow{g} K_B \xrightarrow{S_i} K_{B_i}$$
$$g_i = S_i g. \qquad (14)$$

An orientation is therefore defined by the family of rotations $\{g_i = S_i g\}_{S_i \in G_B}$ generated by the whole set of the rotating elements S_i of G_B [64].

2.13.4. Interaction between a parent and the inherited orientations

The orientation of a parent β crystal is distinguished by rotation G, which alters the sample coordinate system into the crystal coordinate system. This is followed by a rotation S_i^{β} that belongs to the rotational elements of the symmetry group, G^{β}, of the crystal. Therefore, an orientation is resolved by one of the rotations $S_i^{\beta}G$ [65]. The orientation relation between a parent β orientation and an inherited α-orientation is ordinary given in terms of a family of rows and planes that remain parallel in both phases. The Burgers relation observed in the transformation between bcc-hcp is [65]:

$(110)_{bcc}||(0001)_{hcp}$

$[\bar{1}1\bar{1}]_{bcc}||[2\bar{1}\bar{1}0]_{hcp}$

This is expressed as a rotation D by Euler angles:D ≡ (135 °, 90 °, 354.74 °). Additionally, the corresponding matrix D of the coordinate transformation, expresses the components of hcp vector in the bcc reference frame, [65] and is shown in **Eq. 15**:

$$D = \begin{bmatrix} -\frac{1}{2}\left(1+\frac{1}{6^{1/2}}\right) & \frac{1}{2}\left(\frac{1}{3^{1/2}}-\frac{1}{2^{1/2}}\right) & \frac{1}{2^{1/2}} \\ \frac{1}{2}\left[1+\frac{1}{6^{1/2}}\right] & -\frac{1}{2}\left[\frac{1}{3^{1/2}}-\frac{1}{2^{1/2}}\right] & \frac{1}{2^{1/2}} \\ -\frac{1}{2}\left[1-\frac{2}{6^{1/2}}\right] & \frac{1}{2}\left[\frac{1}{3^{1/2}}+\frac{2}{2^{1/2}}\right] & 0 \end{bmatrix} \quad (15)$$

2.14. Micro/macro-texture determination by electron backscatter diffraction

2.14.1. Pattern formation

Electron backscattered patterns are produced by the interaction of the primary electron beam with a tilted specimen, called electron backscattered diffraction patterns (EBSP). In order to view the diffraction patterns, there are two conventional prerequisites of topographical information necessary for SEM operation. The first requirement is that the angle between the incident beam and the specimen surface be about 10 to 30^{o} in order to minimize the amount of signal which is absorbed, and to maximize the amount the diffraction proportion. The second requirement is associated to specimen preparation viz. the beam/specimen interaction depth is ~10nm, and this layer must be proportionally strain free, and clean for patterns to be obtained, and where necessary, electrical conduction is amended by deposition of a thin layer of carbon [66].

Dingley and Randle [66], reported that the EBSPs are basically Kikuchi patterns and they are formed in the SEM when the stationary probe is focused on the specimen. The subsequent elastic scattering of the divergent electrons by the crystal planes forms an array of Kikuchi cones whenever the Bragg condition is satisfied. If the distribution of diffracted intensities is recorded by the interception of Kikuchi cones by photographic film or a recording screen, the resulting EBSP can be viewed as shown in **Fig. 2.36**.

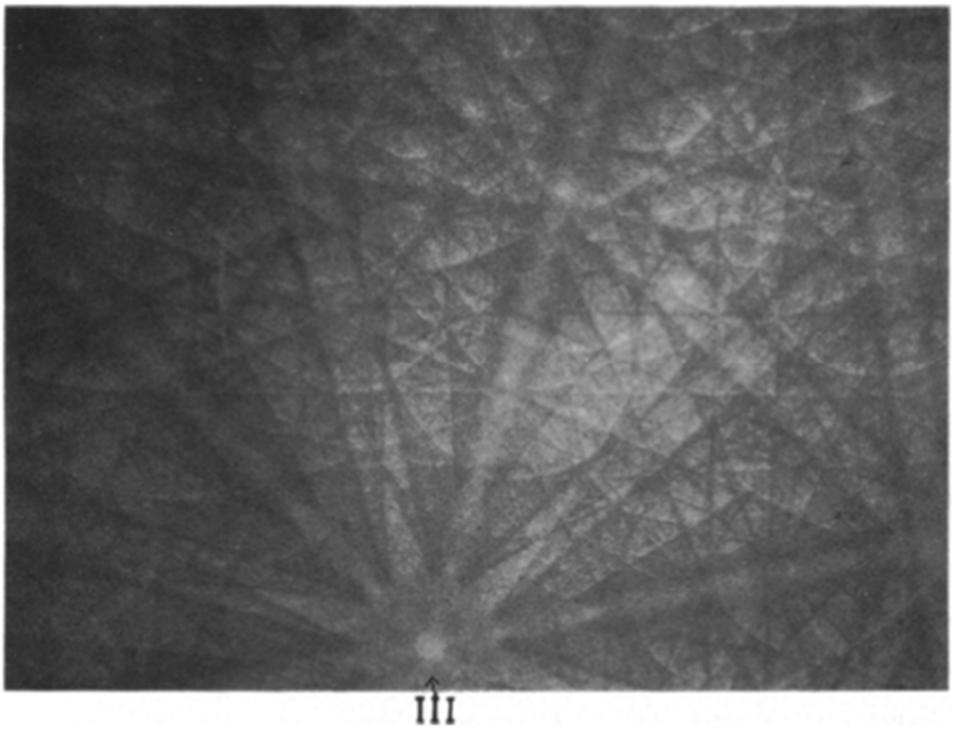

Figure 2.36. EBSP obtained from tungsten filament. The crystal structure is body centered cubic. Some major zone axes are marked [66].

The method involves the employing a calibration specimen of known orientation, i.e. a parallel, sectioned single Si crystal wafer polished such that the [001] is normal to the surface. The wafer is mounted in a precision pre-inclined holder such that the beam strikes the specimen at an angle of 70.6 ± 0.5°, with respect to the surface normal, shown in **Fig.2.37a**. In addition, it is necessary to know the orientation, and to define accurately a set of reference axes within the specimen, and to know the relationship between these axes and those of the imaging phosphor screen. The *XYZ* axes of the specimen are *Z* which is normal to the specimen surface, whereas *X* and *Y* are parallel to the two orthogonal horizontal lines in the specimen surface see **Fig. 2.37b**. The electron beam of the microscope, is defined by the microscope *Z*-axis, *MZ*, whereas *MX* and *MY*, are the two orthogonal directions normal to *MZ* which may be parallel to the *X* and *Y* transverses of the specimen stage also shown in **Fig. 2.37b**. Alternatively, if the screen is tilted normal to the specimen normal, the pattern center is situated by the position of the [001] zone axis. Therefore, the specimen to screen distance, *L* can be calculated using the following relationship **Eq. 16** [66]:

$$L = N / \tan \phi \qquad (16)$$

where N and ϕ are shown in **Fig. 2.37b**. The origin of MZ axis depends on the focal point of the specimen beneath the objective lens, and this is subject to change, depending on the height at which the sample was mounted in the specimen stage. It is necessary to attain a calibration figure which converts the specimen height to changes in the pattern centre

coordinates. This is conducted by using the computer cursor to track the position of the zone axis defining the pattern center in the pattern from the calibration specimen as the specimen height is changed by known amount, **Fig. 2.37c** [66].

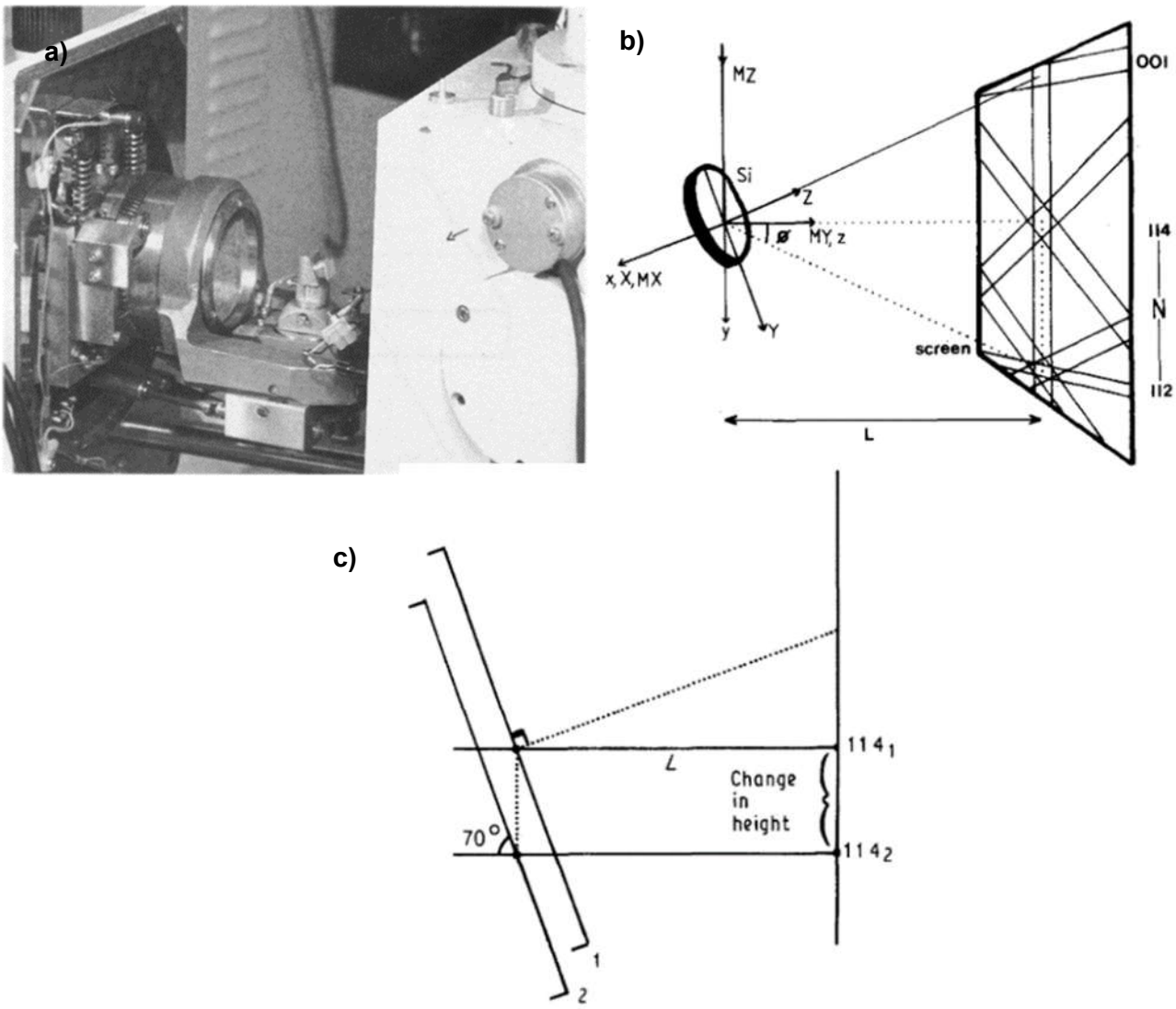

Figure 2.37. a) Photograph of specimen mounted on its holder pre-inclined at 70.6 °, prepared to be inserted into the microscope chamber; b) Diagram showing the calibration geometry for a Si calibration standard having [114] normal to the screen and the parameters ϕ, N and L (Eq. 16), The pattern centre is [114]; c) height change part of the calibration routine. The distance between 1141 and 1142 is measured in screen coordinates [66].

Fig. 2.38a shows an example of a diffraction pattern from a face centered cubic nickel-based alloy, and that of **Fig. 2.38b** shows a closed packed hexagonal zirconium-based alloy. The conventional operating conditions are typical for most metals and alloys: acceleration voltage of 20-30 kV, and a beam current of 1-6 nA [66].

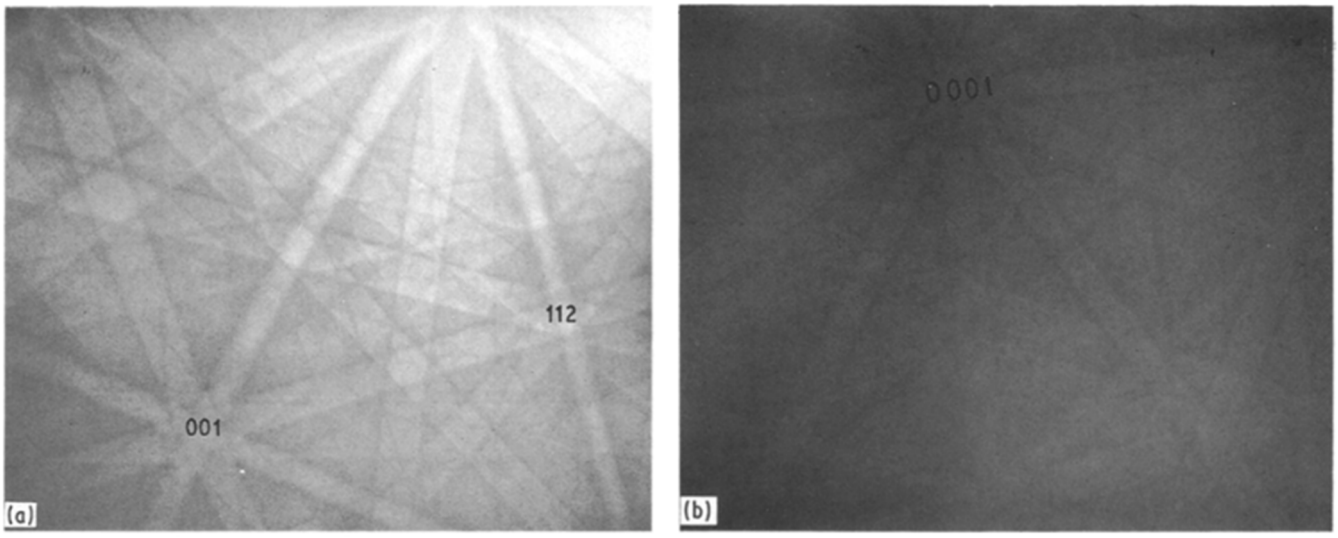

Figure 2.38. EBSD patterns: a) a face centred cubic material (nickel), and b) a closed packed hexagonal material (Zircaloy). Some major zone axes are marked [66].

2.14.2. Comparisons between X-ray and EBSD-determined textures

Fig. 2.39 illustrates a comparison between pole figures attained by X-ray and EBSP results for hexagonal Zircaloy both for [0001] and [$10\bar{1}0$] cases. The total number of grains sampled using EBSD was 420. Each position admits the positions of three [$10\bar{1}0$] zone axes to be calculated so that the total number of pole positions reflects six-fold symmetry of the material [66].

Another example of a comparison between X-ray and EBSD generated textures, is in the form of macrotextures orientation distribution function (ODF) shown in **Fig. 2.40a**, and EBSD microtexture ODFs in **Fig. 2.40b-c** from 160 grains [66]. There are two substantive differences between X-ray and EBSD determination of a pole figure. The first is that X-ray method gives the orientation distribution of a plane averaged over several thousands of grains, whereas the EBSD method is specific to single grain both interms of its orientation and its environment. The second difference relates to what is being measured in both cases. The X-ray case measures the orientation of a plane (a two dimensional entity), whereas that of the EBSD case measures the orientation of the crystal which is a three dimensional information [66].

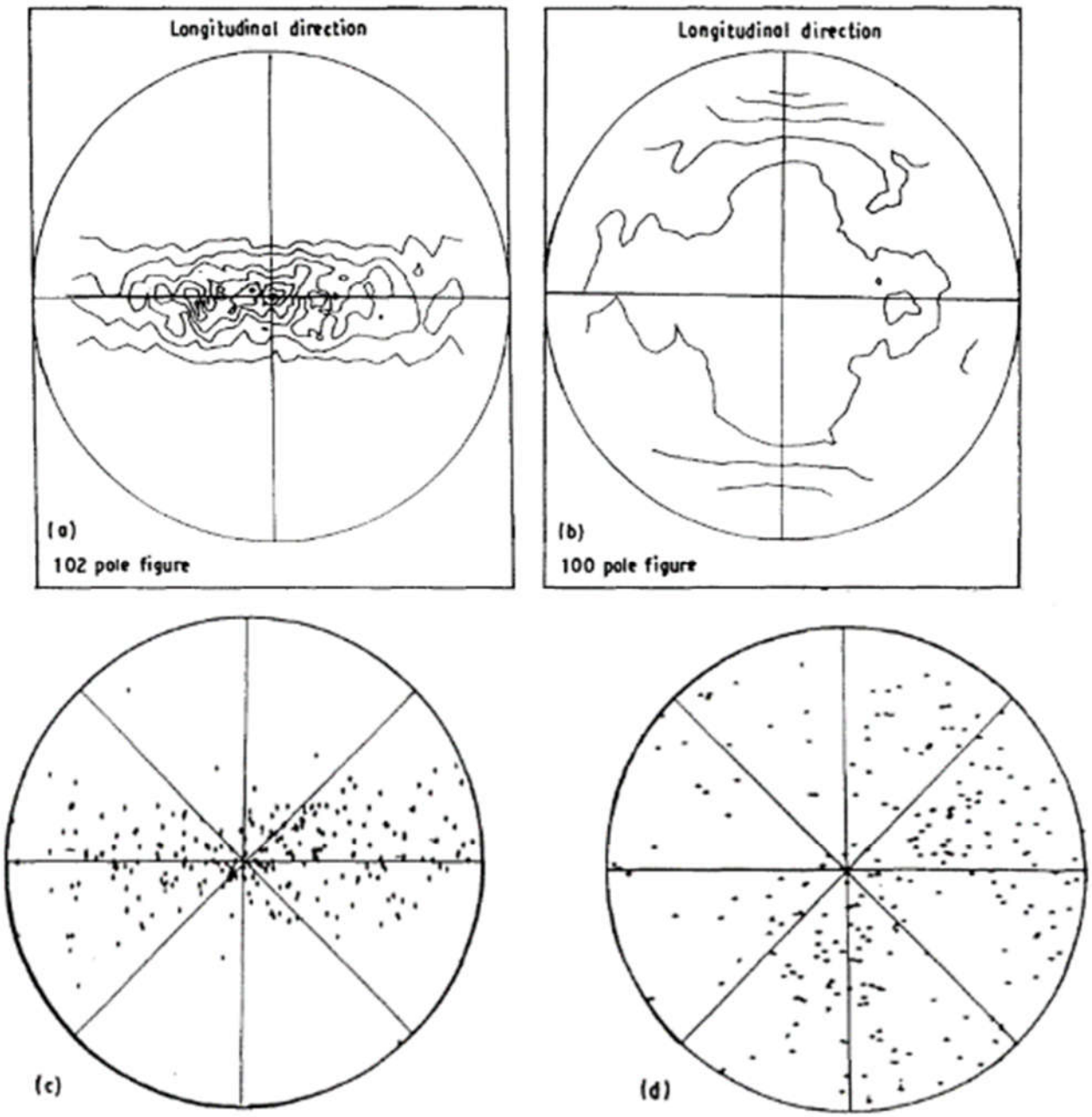

Figure 2.39. (a,b) [0001 and [10$\bar{1}$0] X-ray generated pole figures, for Zircaloyand EBSD generated pole figures for the same zone axes (c, d) [66].

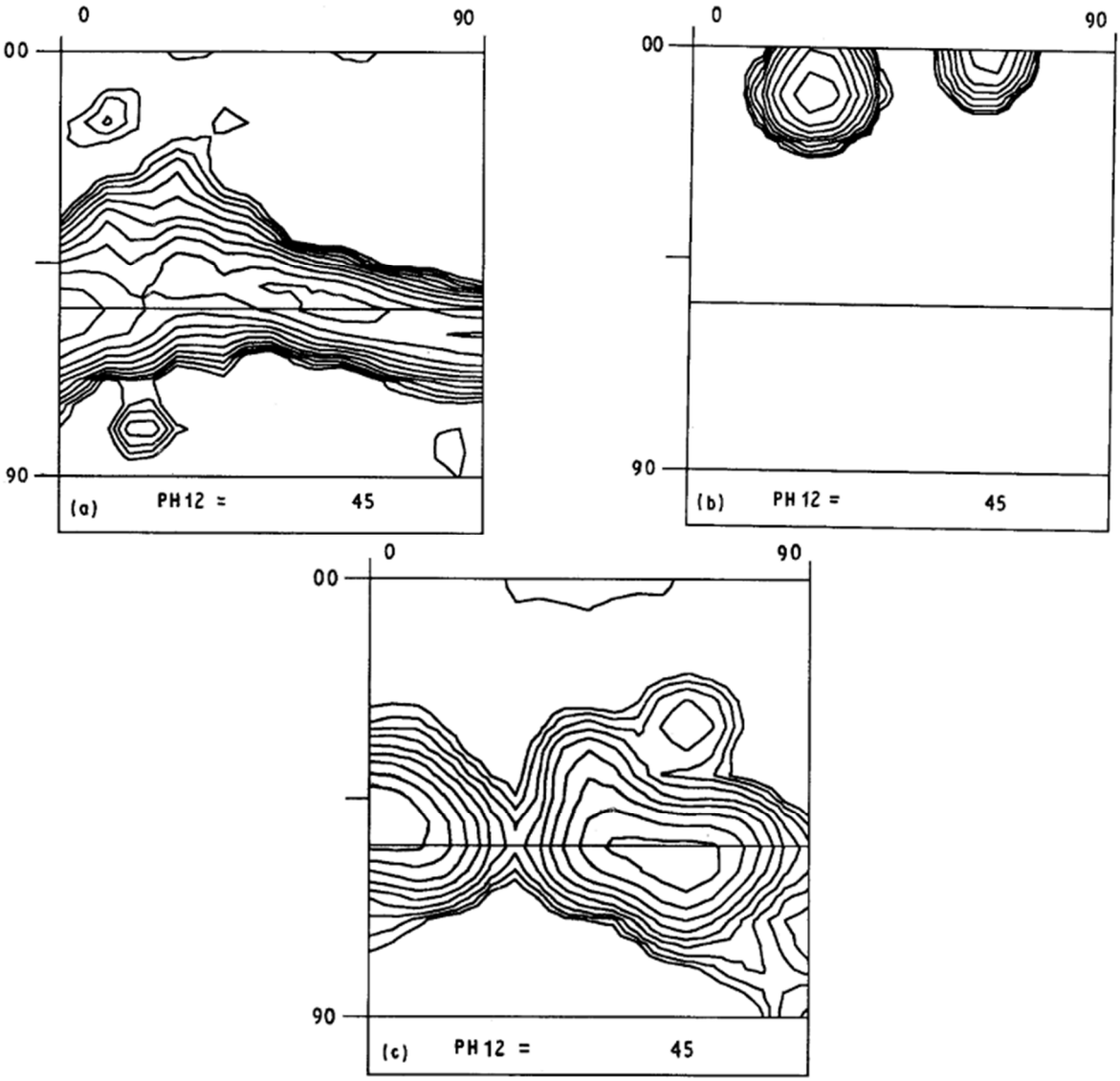

Figure 2.40.ϕ_2 = 45° sections of ODFs from a rolled and annealed steel sheet; a) X-ray generated macrotexture, b,c) EBSD generated microtexture from b) of only smallest grains, and c) all other grains in a 160 grain sample population [66].

Some essential crystallographic orientations and texture fibers relevant for fcc textures are represented in **Fig. 2.41**.

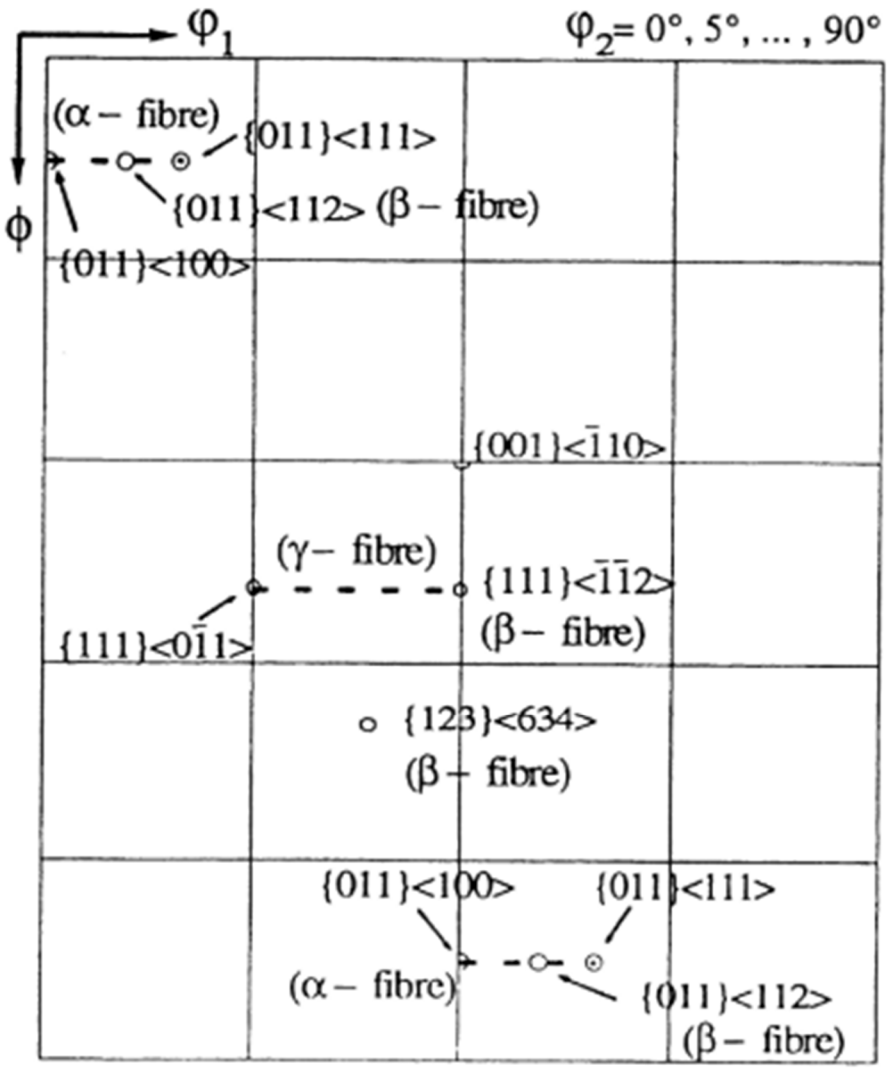

Figure 2.41. Schamatic display of some relevant texture fibers for fcc textures, and components drawn in φ2-sections through the reduced Euler space [67].

2.14.3. Texture measurement in γ-TiAl based alloys

Hasegawa and Fukutomi [68] used Schulz reflection technique mainly for measuring textures, employing nickel filtered Cu Kα radiation. They investigated the lamellar orientation of the Ti-45Al-10V (mol.%) alloy by high temperature compression in the α and (α + γ) phase regions. The X-ray intensities were measured on the 0002, $20\bar{2}0$,$20\bar{2}1$, and $20\bar{2}2$ reflections in α_2-Ti_3Al, and using 111 reflection in γ-TiAl. The (0001)α_2, $\{10\bar{1}0\}\alpha_2$, $\{20\bar{2}1\}\alpha_2$, and $\{10\bar{1}1\}\alpha_2$ pole figures; and the (0001) α_2 + {111}γ, $\{10\bar{1}0\}\alpha2$, $\{20\bar{2}1\}\alpha2$ and $\{10\bar{1}1\}\alpha2$ pole figures were constructed for the α_2-Ti_3Al single phase domain, and for the (α_2 + γ) lamellar two-phase regions. Using these pole figures, an orientation distribution function (ODF) of α_2-Ti_3Al was calculated using the Dahms-Bunge method [68], whereas, the main components and ODF of the texture were established by inverse pole figure from the calculated ODF. **Fig. 2.42(a, c)** illustrates the

(0001) α_2 pole figures of the Ti-45Al-10V (mol.%) alloy in the α-phase region. Formation of fiber texture was observed in these pole figures, whereas the inverse pole figures demonstrates the distribution of pole densities of the compression plane in **Fig. 2.42(b, d)** [68].

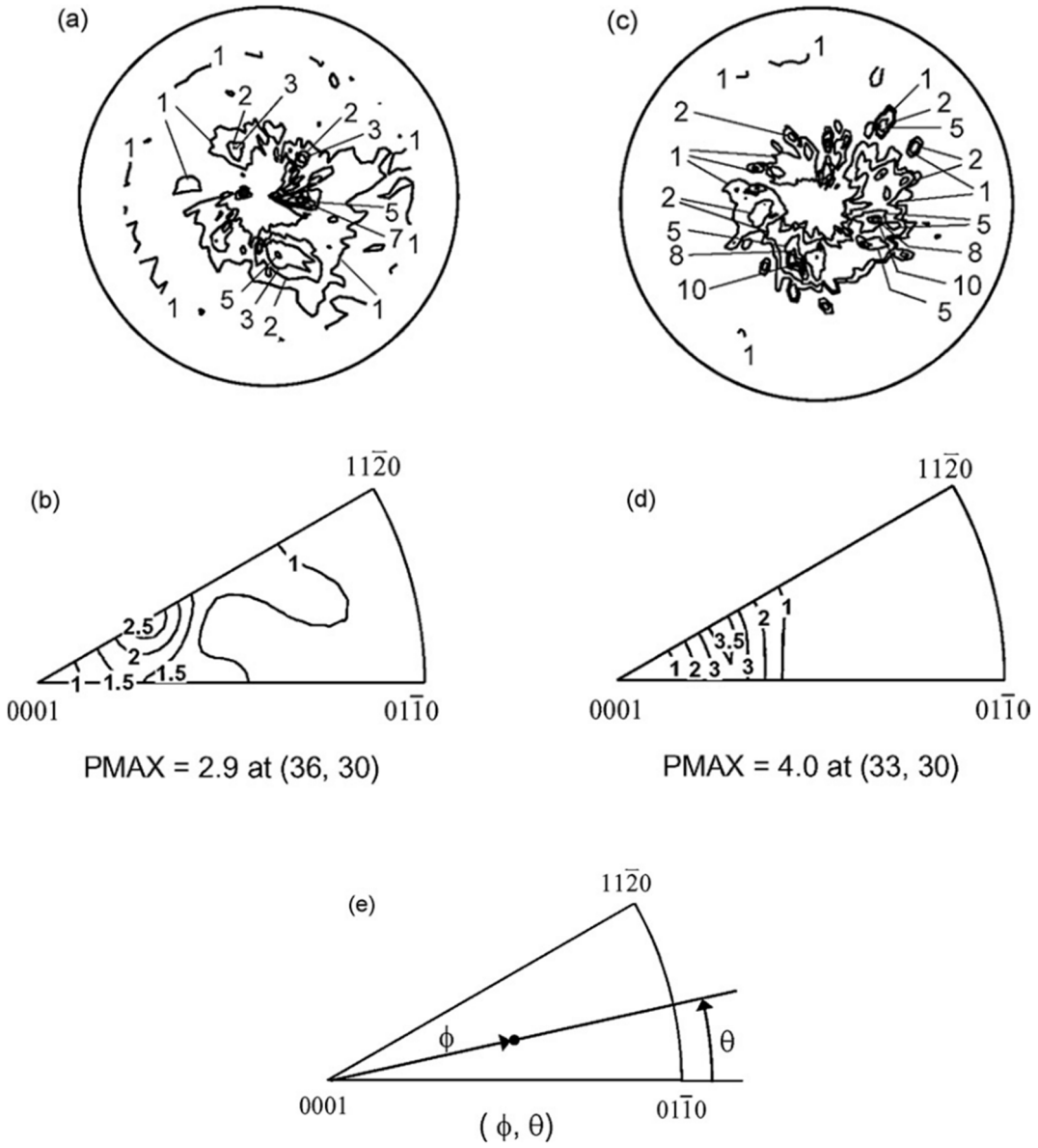

Figure 2.42. (0001) $\alpha 2$ pole figures and inverse pole figures showing the distribution of pole densities of the compression plane. The average density is used as a unit. The compression was conducted at T=1553K up to ε=1.2 with several true strains rates: (a and b) $\dot{\varepsilon}=5.0 \times 10^{-3}$ s $^{-1}$ and (c and d) $\dot{\varepsilon}= 5.0 \times 10^{-4}$ s^{-1} . The value of maximum pole density and its position (ϕ,θ) are given below the inverse pole figures. Definitions of ϕ and θ are given in (e) [68].

Pole figures have a drawback in terms of non-cubic crystal symmetry because different orientations, which are created by rotating a crystal about its plane normal, are identical [69]. However, the introduction of orientation distribution function (ODF) resolved this problem, because it is a function by which the complete distribution of crystal orientations within a sample can be described [69]. **Fig. 2.43** demonstrates the definition of ODF, and a distribution of N crystals is given. The volume of their unit cells is proportional to the frequency or volume fraction dV of the respective orientation gi (i = 1..N). For $N \rightarrow \infty$ and $\Delta g \rightarrow 0$ the orientation distribution function f(g) is introduced, which is defined by **Eq. 17**:

$$f(g)dg \sim dV_g / V, f(g) \geq 0 \quad (17)$$

where V= sample volume, and V_g = volume fraction of crystals having an orientation within g and g + dg with dg = sin (Φ) dΦdφ_1dφ_2. The $\varphi_1\Phi\varphi_2$ are Euler angles, and according to Bunge notation the crystal coordinate system (CS) is rotated with respect to the sample CS [69].

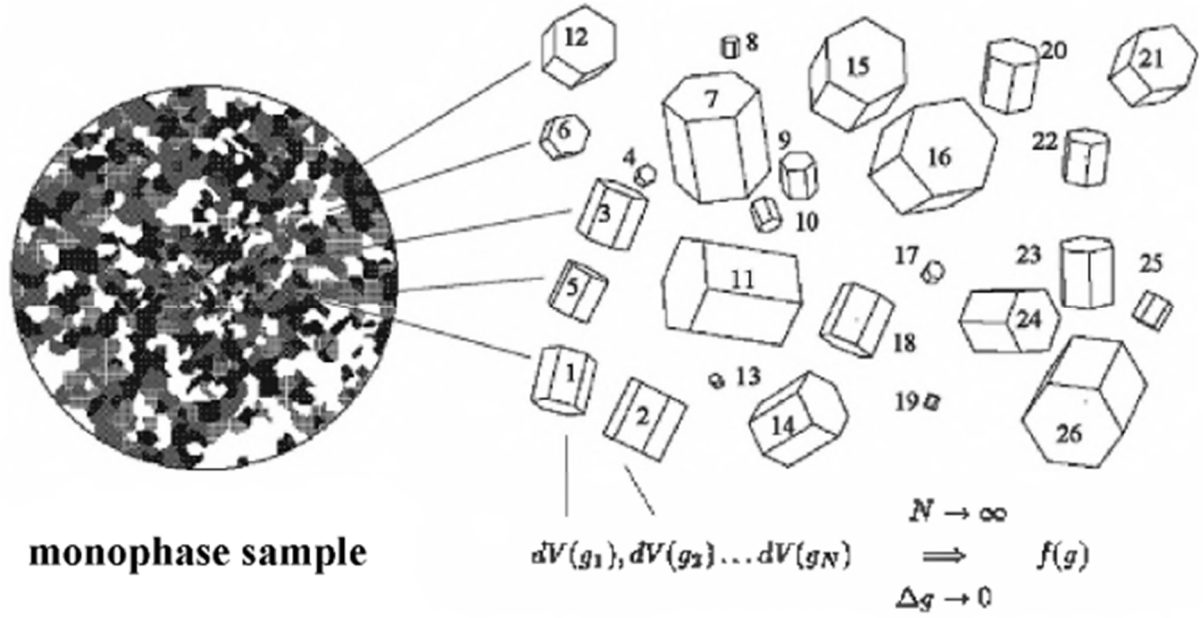

Figure 2.43. Definition of the ODF [69].

Zambaldi [70] reported that orientation pile-up formation conform to a projection of the 3D anisotropic plasticity of the material into a 2D height distribution around the indent. However, compared to the to the measurement of crystallographic texture, i.e. the orientation distribution function (ODF), the resulting representation is not complete by measuring one pile-up topography or pole figure. Alternatively, measurements of more than one indentation axis have to be performed in order to compile a 3D understanding of plastic anisotropy. However, Zambaldi [70], pointed out that for the indentation pile-up, the mathematical tools for what is called pole figure inversion in the domain of texture still have to be developed [70]. In the work by Weaver and Calhoun, [71] emphased was made that due to the tetragonality of the γ unit cell, the <100], and [001] reflections are non-equivalent, and their peak locations in the 2θ

scans overlap. Likewise, the <110] and <101] reflections also overlap. In order to separate the overlapping peaks, the sample orientation distribution (SOD) was computed from a set of incomplete pole figures. Therefore, recalculation of the complete pole figures for each overlapping reflection and calculations of the inverse pole figures was then attained from the SOD [71].

Fig. 2.44a shows the (0001)α_2 + {111}γ pole figure of a Ti-45Al-10V (mol.%) alloy, processed in the α-phase region, followed by annealing in the (α + γ) two-phase region, at *T*=1553 K up to ε = -1.2 under a true strain rate, $\dot{\varepsilon}$, of 5.0 × 10^{-3} and 5.0 × 10^{-4} $s^{-}1$, respectively. The pole densities are projected onto the compression plane and the mean pole density is used as a unit. Formation of fiber texture is observed in these pole figures. Furthermore, independent of true strain rate, $\dot{\varepsilon}$, the (0001)α_2 plane normal is tilted about 35° away from the compression axis. **Fig. 2.44b** indicates the inverse pole figure of α_2 phase showing the distribution of pole densities of the compression axis. This inverse pole figure was formed by calculation of ODF using three peaks from the $\{10\bar{1}0\}\alpha_2$, $\{20\bar{2}1\}\alpha_2$ and $\{10\bar{1}1\}\alpha_2$ reflections which do not overlap with the reflections from the γ-phase. The PMAX value shows that the results show that the texture formed by the compression process in the α single-phase region did not change during heat-treatment in the (α + γ) two-phase region for 1.8ks.

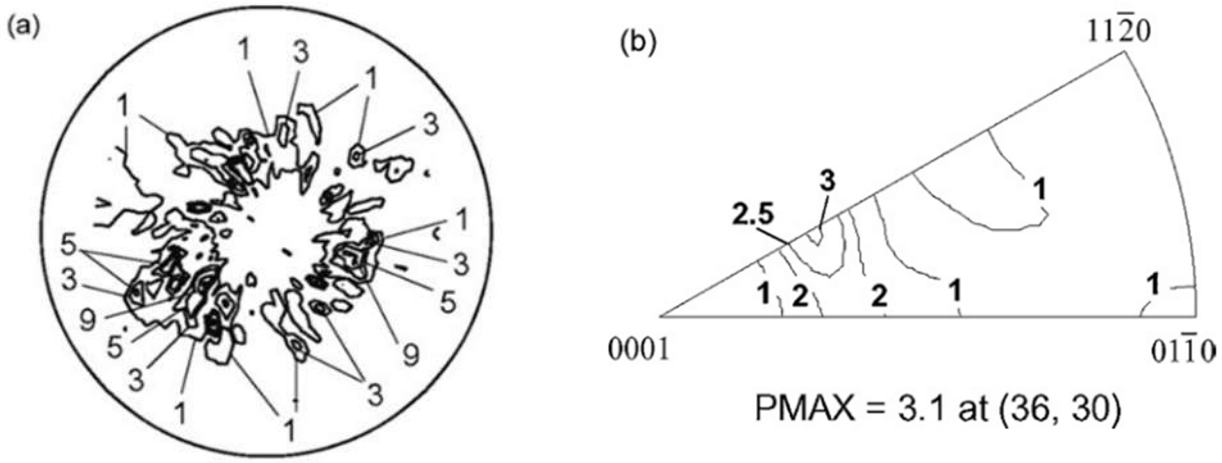

Figure 2.44. (a) (0001)α2 + {111}γ pole figure, and (b) inverse pole figure of Ti-45Al-10V (mol. %) alloy specimen processed at α phase region (T= 1553K, $\dot{\varepsilon}$= 5.0 × 10-4 s-1, ε=-1.2), and kept for 1.8ks in the (α + γ) two-phase region (T= 1453K) [68].

Shen et al. [72] investigated the corresponding textures of high-Nb TiAl sheet with 75% reduction, presented in **Fig. 2.45** in terms of the ODF sections. The main component was a modified cube texture, generated in all γ-TiAl based alloys by recrystallization during rolling passes with alignment of the c-axes [001] in the γ-phase along the transverse direction of the sheet [72].

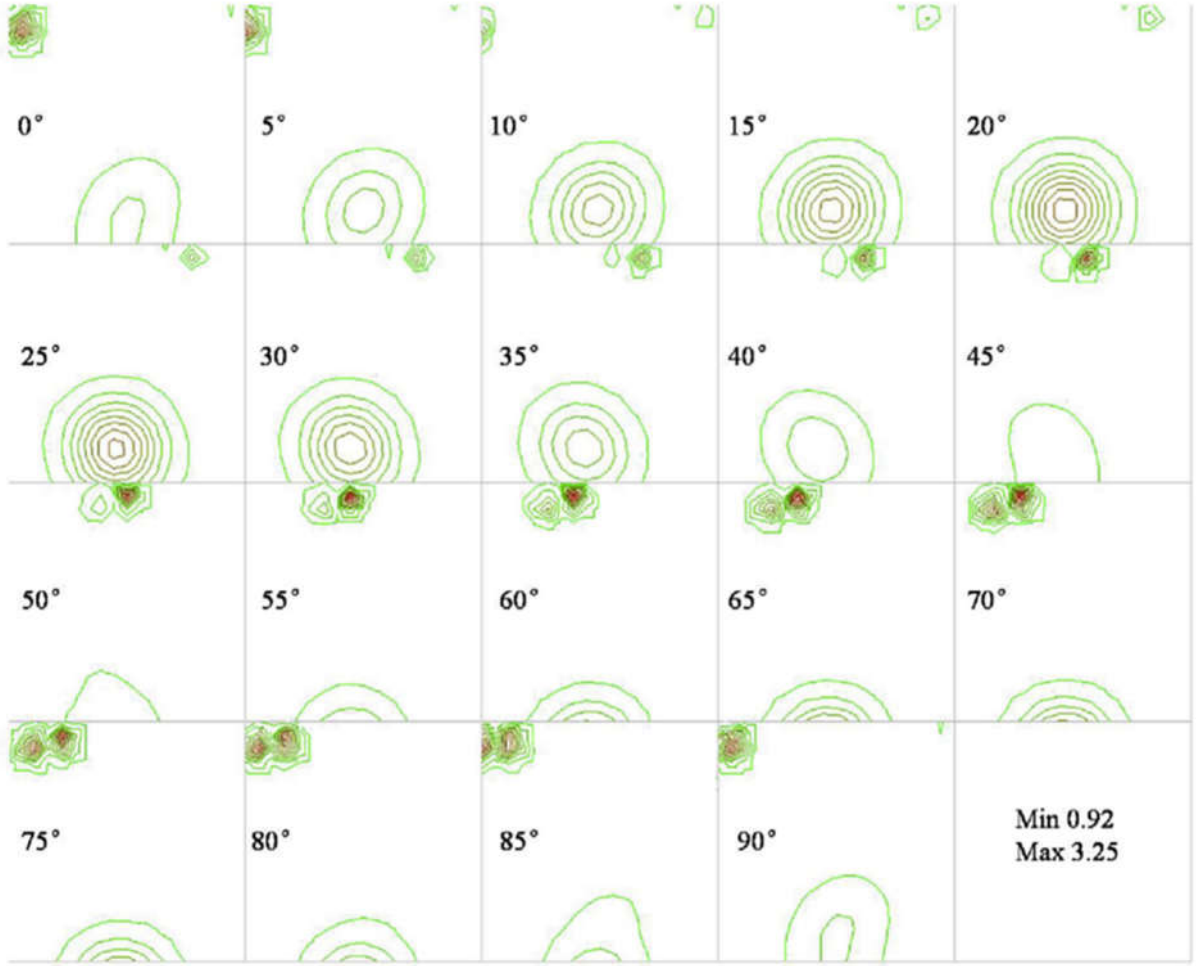

Figure 2.45. The orientation distribution function (ODF) sections of high Nb-TiAl alloy sheet [72].

The orientation distribution function (ODF) is a quantitative description of texture beyond the common orientation of pole figures. This technique articulates the probability of a crystallite with orientation described by Euler angles that associate specimen axes with crystal axes. There is generally a greater precision because of the use of data from several pole figures. Measurements of more than one indentation axis were performed to compile a 3D knowledge of plastic anisotropy. In addition, the orientation dependent pile-up formation corresponds to a projection of 3D anisotropy plasticity of the material into a 2D height distribution around the indent [70]. Therefore, measurement of crystallographic texture, i.e. ODF, was completed by measuring pile-up topography (pole figure) employing more than one indentation axis. However, the misorientation g_{ij}^{m} for the γ-phase can be calculated between the orientation g_i of a grid point, and its nearest neighbor g_j using **Eq. 18**:

$$g_{ij}m = g_i - 1g_j \quad (18)$$

the misorientation of the distribution function (M) ODF can be calculated from the texture coefficient, which are the coefficients of series expansion method according to **Eq. 19** for the calculation of coefficient C_l^{mn}:

$$C_l^{mn} = \frac{1}{n} \frac{\exp^{(\frac{-l^2 \Psi_0^2}{4})} - exp^{(\frac{-l+1^2 \Psi_0^2}{4})}}{1 - exp^{(\frac{-\Psi_0^2}{4})}} \cdot \sum_{i=l}^{N} T_l^{mn}(g_i) \quad (19)$$

where N is the Number of data points; Ψ_0= Gaussian half scatter width; l= highest harmonic, the upper cut-off of the series expansion; T= Generalised spherical harmonic function m, n the limits referring to crystal (m) and sample symmetry (n) [73].

2.14.4. Crystallographic texture measurement and analysis

A study of fundamental properties such as the nature of interatomic bonding, stability of crystal structures, elastic properties, dislocations, grain boundaries, interfaces, point-defects and diffusion is convenient to gain knowledge into the behavior of γ-TiAl intermetallic alloys, mostly under high temperature and mechanical loads. One of the *ab initio* studies on structural stabilities, elastic properties and nature of interatomic bonding have been reported for γ-TiAl, as well as other stoichiometric alloys in the Ti-Al binary system [74]. The mechanical properties of $L1_0$ TiAl, in either the single phase or lamellar form is still rather incomplete. However, it is known that the main deformation modes in γ-TiAl are slip and twinning, both of them operating on the closed-packed {111} planes. Slip occurs via two types of dislocation: ordinary dislocations with Burgers vectors $\frac{1}{2}$ <110> and super-dislocations with Burgers vector <101>. According to Appel and Wagner [52] the deformation behavior of γ-TiAl is closely related to its $L1_0$ structure, and the possible Burgers vectors are illustrated in **Fig. 2.46**.

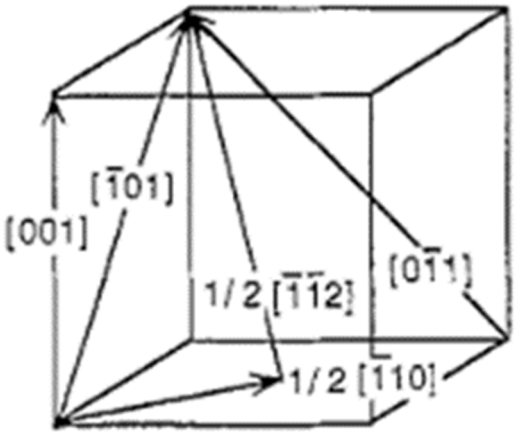

Figure 2.46. Burgers vectors of the ordinary ½<110] and <001> dislocations; and of ½ <112] and <011] super-dislocations [52].

On the other hand, twinning is of the {111} <112> type, similar to the fcc structure. However, it is not the low temperature deformation mode as in many materials but rather occurs at ambient and high temperatures [75].

Section 2.6.1 mentioned that the fabrication processing of the γ-TiAl alloys is a challenge. For example, Dey et al [51] reported that the drawbacks faced by as-cast microstructures are thein coarse columnar lamellar grains, producing strong solidification textures with anisotropic properties and low room temperature ductility. Therefore, casting with subsequent thermal treatments has been found as a feasible option to resolve such problems. Furthermore, various microstructure-property related studies suggested that small (α_2+γ) lamellar grains with fine lamellae spacing are an answer to these problems [51]. However, these alloys lack in crystallography/morphology correlation studies available among microstructures generated from thermal treatments. The authors further reported that, solidification and transformation paths depends on alloy compositions, and this path crosses the single α phase domain at high temperature. Additionally, at the final stage of cooling the rest of untransformed α phase domain inside the lamellar structure becomes the ordered α_2 phase with similar orientation. Following BOR, α_2 lamellae in a given ex-α grain can coexist with γ-tetragonal lamellae presenting six different crystallographic orientations called variants. Most often γ/γ, as well as γ/α_2 intefaces are encountered in lamellar structures. Therefore, there are three kinds of tetragonal γ/γ interface types which are possible: order-domain related, pseudo-twins and true-twins. However, EBSD is not capable to detect sub-structure lines present in the Kikuchi patterns of ordered intermetallic phases. Therefore, it is impossible to distinguish ordered-α2 phase from disordered α-phase, and also to separate the six variants of γ phase. Instead SEM/EBSD differentiates the γ-variants as two fcc orientations variants (γ and γ-twin). Usually, the determination of six tetragonal γ variants [54] is performed under transmission electron microscopy (TEM) using several techniques.

The Ti-47Al-2Nb-2Cr alloy is a first generation alloy with a very strong texture. The solidification sequence is first by a peritectic reaction i.e. L+ β → α. Under further cooling phase transformation occurs by the α (hcp)→α+β ($L1_0$)→α_2 (DO_{19}) + γ reaction where nucleation and growth of γ lamellae with Blackburn relationship is followed by α→α_2 ordering below the eutectoid temperature [15].

Dey et al. [51] recognized that the as-cast (α_2+γ) TiAl alloy, usually comprises coarse lamellar structure grains with a few γ monolithic (γ_{mono}) grains in between lamellar grains, generating a solidification texture and anisotropic properties, which may persist even at homogenization treatments.

2.15. Fracture of some Intermetallic alloys

The examples of common intermetallics include compounds between titanium and aluminium (titanium aluminides such as TiAl or Ti_3Al) or compounds between nickel and aluminium (nickel aluminides such as Ni_3Al or NiAl). The intermetallics have ordered or partially ordered structures, therefore it is difficult to achieve the five independent slip systems required for homogeneous plastic deformation in intermetallic systems [76]. Furthermore, room temperature fracture favors brittle cleavage or inter-granular fracture modes in most intermetallic systems, as shown in **Fig 2.47(a) & (b)**.

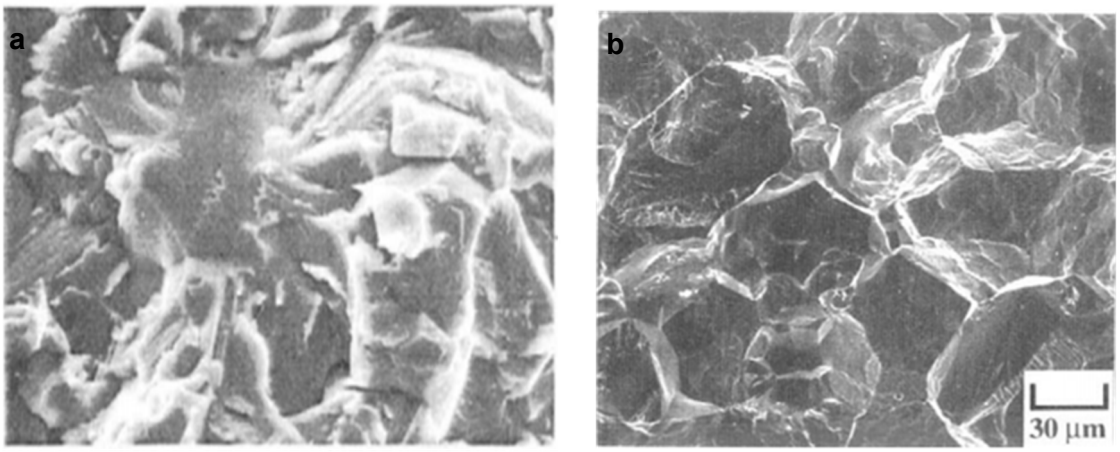

Figure 2.47. Room-temperature fracture modes in high-temperature intermetallics: (a) Cleavage in Ti–48Al; (b) intergranular fracture in NiAl [76].

Soboyejo [76] reported that grain boundary cohesion of some intermetallics can be improved by alloying, which results in increased room temperature ductility. Alloying with boron promotes a transition from intergranular fracture to ductile dimpled fracture. Fracture modes in most intermetallic systems have been determined to demonstrate strong temperature dependence. This is shown in **Fig. 2.48** illustrating fracture surfaces of Ti-48Al alloy.

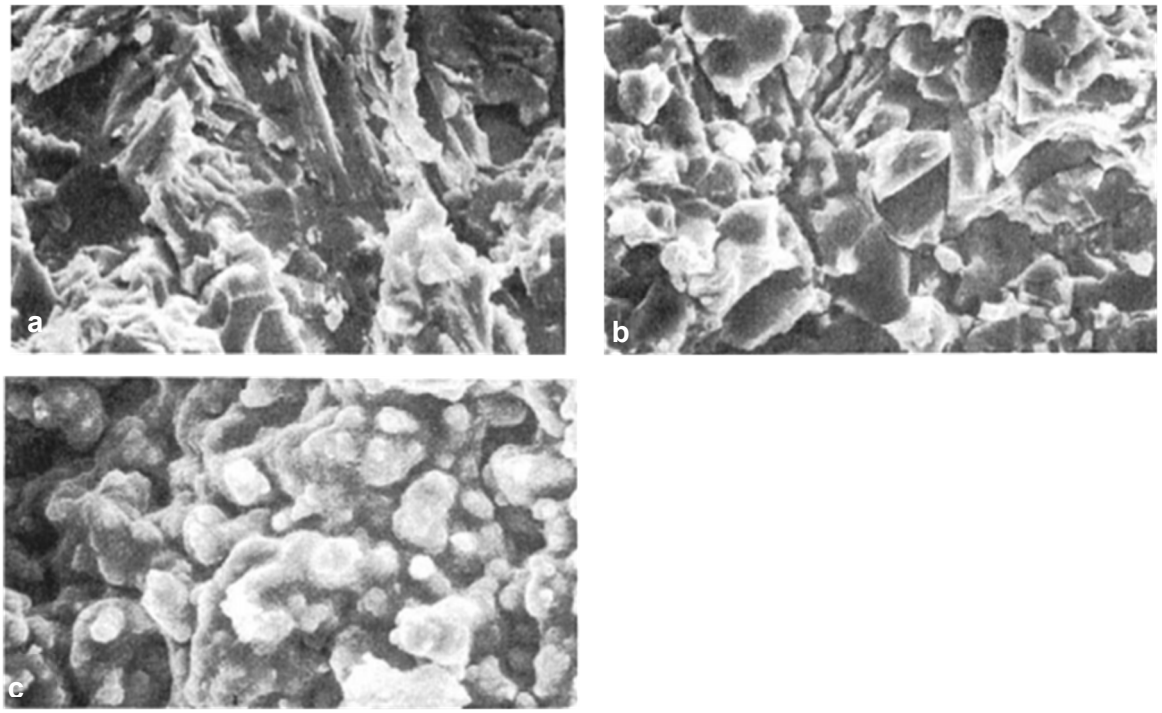

Figure 2.48. Effects of temperature on fracture modes in titanium aluminide alloys (a) cleavage and trans-lamellar fracture at 25 ºC; (b) intergranular fracture at 700 ºC; and (c) transgranular fracture at 815 ºC [76].

3. CHAPTER 3: EXPERIMENTAL PROCEDURE

The methodology of the development and microstructural evolution of the γ-Ti-48Al-2Nb-doped with (Sn, Cr, Mn, and Si) intermetallic alloys, and their mechanical properties which was followed during the course of this research studies described below.

3.1. Fabrication process

The alloys in this study were derived from precursor metallic powders of pure Ti, Al, Nb and Cr which were blended in a tubular mixer, cold pressed (shown in **Fig.3.1a and b**) and arc-melted in vacuum (**Fig.3.2**) to synthesize Ti-48Al, Ti-48Al-2Nb, Ti-48Al-2Nb-0.7Cr, and Ti-48Al-2Nb-0.7Cr-0.3Si alloys. The powder particle sizes are given in **Table 3.1**. The cold pressing was done using the Enerpac hydraulic press with 380 MPa pressure applied to the powder samples. Finite element analysis (FEA) [77] was utilized to predict the stress applied on powder metal, considering element size, mesh settings, mesh control, and surface contacts are useful parameters. Boundary conditions were studied using static stress analysis, varying uniformly distributed loads subjected to the same cross-sectional area and thickness of the sample. The bottom surface was fixed and compressive stress was applied to the samples with incremental pressures. The arc-melting furnace was operated under a high purity argon environment on a copper hearth. A non-consumable tungsten electrode, was used in order to protect the arc. Due to the samples containing alloying elements such as Nb, Cr and Si, the chemical analysis was performed such as to allow the elements to be acid dissolved using microwave digestion in order to get them in solution for inductively coupled plasma optical emission spectroscopy (ICP-OES) analysis. The final chemical compositions of the vacuum melted alloys given in **Tables 3.2 and 3.3** were found to be different from the nominal compositions. This might have been as a result of different vapor pressures of dissimilar components in the alloys due to melting process whereby, for example, Al with low melting point and being volatile, may have suffered the most burning loss [79].

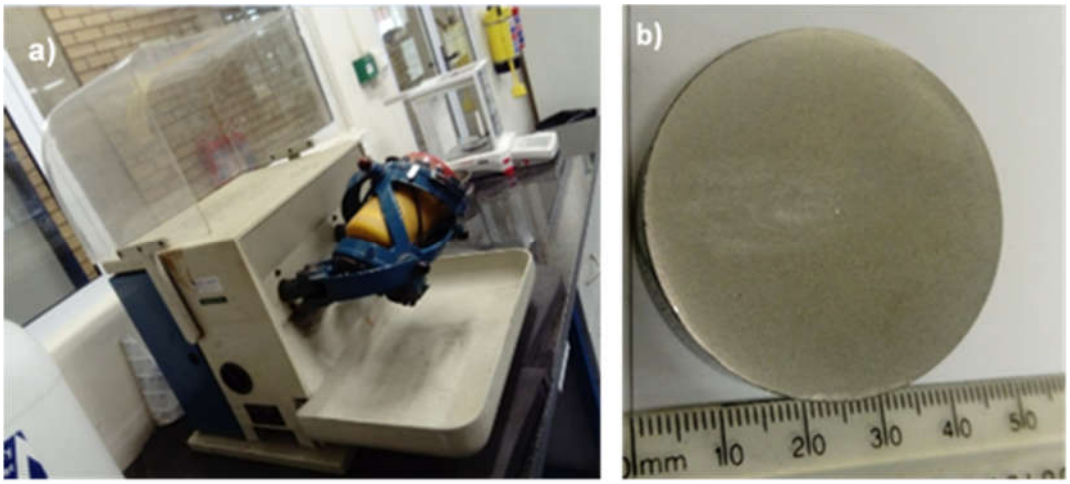

Figure 3.1. (a) Tubular mixer, and (b) Uniaxial cold pressed specimen.

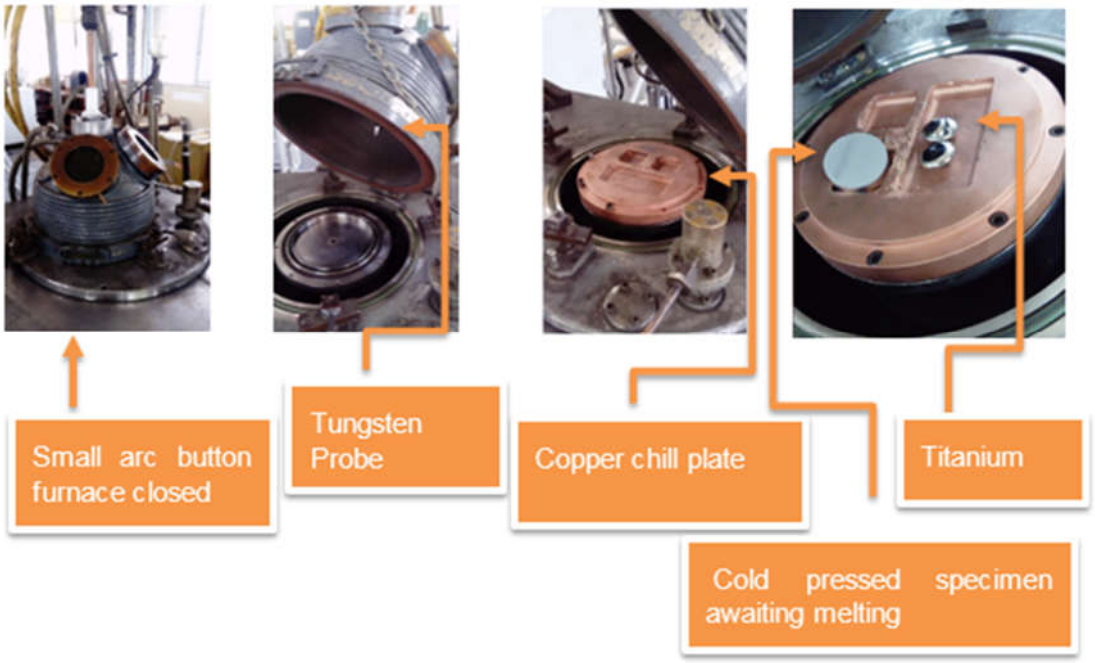

Figure 3.2. Images of the small vacuum arc melting furnace.

Table 3.1. Particle sizes and morphology of the powders.

Characteristic	Ti	Al	Nb	Cr	Si
Mean particle size (μm)	30.51	74.0	23.89	126	8.90
Morphology	Angular	Spherical	Angular	Angular	Angular

Table 3.2. Final chemical composition (at. %) of the Ti-Al, Ti-Al-Nb, Ti-Al-Nb-Cr, and Ti-Al-Nb-Cr-Si.

γ-TiAl based alloys	Ti	Al	Nb	Cr	Si
Binary	55.7	44.3	-	-	-
Ternary	53.1	45.8	1.8	-	-
Quaternary	51.0	46.4	1.9	0.7	-
Quinary	51.7	45.4	1.9	0.7	0.3

Table 3.3. Final chemical composition in (at. %) of γ-TiAl based Ti-Al-Nb-Si, Ti-Al-Nb-Sn-Si and Ti-Al-Nb-Sn-Mn-Si New alloys.

γ-TiAl based New alloys	Ti	Al	Nb	Sn	Mn	Si
Quaternary	52.5	45.3	2.0	-	-	0.3
Quinary	51.5	45.4	1.9	1.0	-	0.3
Septernary	50.8	45.3	2.0	1.0	0.7	0.3

3.2. Materials characterization

Metallographic examination was carried out using conventional techniques. Specimen surfaces were prepared by grinding to a mirror-like surface using grit papers up to 4000 followed by 1 µm alumina, colloidal silica and then etched in 24ml H_2O + 50ml glycerol +24ml HNO_3 + 2ml HF.

Microstructural analysis was done in a JEOL® JSM-6510 scanning electron microscope (SEM) back scattered electron (BSE) mode using energy dispersive X-ray spectroscopy (EDS) capabilities for micro-analysis. The average grain size was determined according to ASTM standard designation E112-96 using the line intercept method. Image j and Digimizer software were utilized to determine the size and volume fraction of phase constituents. The measurements were carried out based on a minimum of ten SEM-BSE micrographs which were randomly chosen. Phase identification was carried out using with X-ray diffraction (XRD) using CuKα radiation λ=1.54062 Å and 2θ from 20°-90° angles. The latiice parameters were obtained from PANalycal's X'Pert High score, a program with data organized in ASCII or

XRDML files, using the Scherer equation. The surface coating properties were examined by X-ray photoelectron spectroscopy (XPS) using a a Thermo ESCAlab 250Xi instrument employing Monochromatic Al kα (1486.7eV). Image j and Digimizer computer software's were employed in order determine the size and volume fraction of the phase constituents. A minimum of ten SEM-BSE micrographs were randomly selected for measurements. The surface roughness of the cyclically oxidized alloys were studied by atomic force microscopy (AFM) and X-ray photoelectron spectroscopy (XPS) analysis. Additionally, the transmission electron microscope (TEM) was employed to examine surface topography of an etched alloy specimen, prepared by replica technique. This technique comprised carbon deposition on the specimen surface from an arc source in a vacuum chamber. A dilute solution of (~2%) Formvar in chloroform was allowed to run over the surface and then to dry, to allow carbon film extraction on small copper grids. For surface coating analysis, a small spatula tip of the oxidized sample was dispersed in ethanol in order to yield a lightly dispersed solution, which was then ultrasonicated for ±30minutes at ambient temperature. Copper grid coated with carbon was dipped into the dispersed solution and left to dry overnight. Observations were conducted in a JEOL JEM 2100 high-resolution electron transmission microscopy (HRTEM) operating at 200kV. Chemical composition of the nano-sized particles was measured using a scanning transmission electron microscope (STEM) -EDS technique. Moreover, the density of the compacted and as-melted alloy parts was measured using the Archimedes method according to ASTM B962-08.

3.3. Vickers hardness measurements

Vickers hardness tests were conducted according to the requirements of ASTM standards E384-10. Prior the test, the specimens were ground and polished using 1µm diamond suspension, followed by final polishing using 50 nm colloidal silica. The applied load macro-hardness was 20 Kgf, and the dwell time was 10 seconds. Hardness profiles throughout the specimens were measured at 0.2 mm intervals and average of at least 15 measurements.

3.4. Tensile testing

Flat tensile specimens of 5mm × 3mm cross-section and 12mm gauge length were prepared for room temperature tensile tests. The specimens were machined from the center of the as-cast ingot button by electrical discharge machining. To prevent crack initiation, the tensile specimen were ground along the gauge length in the longitudinal direction with SiC grit paper in water. The dimensions of the tensile specimens are shown in **Fig. 3.3**. A uniaxial tensile test was conducted at room temperature using a MTS criterion C45 tensile machine at a constant crosshead speed of 0.25mm/min. Three tests were performed for each condition and average values were taken. However, it should be noted that due to size restriction of the

melted buttons, Barba's law (ASTM A370) was not adopted to tailor the ratio of gauge length to cross-sectional area according to Barba.

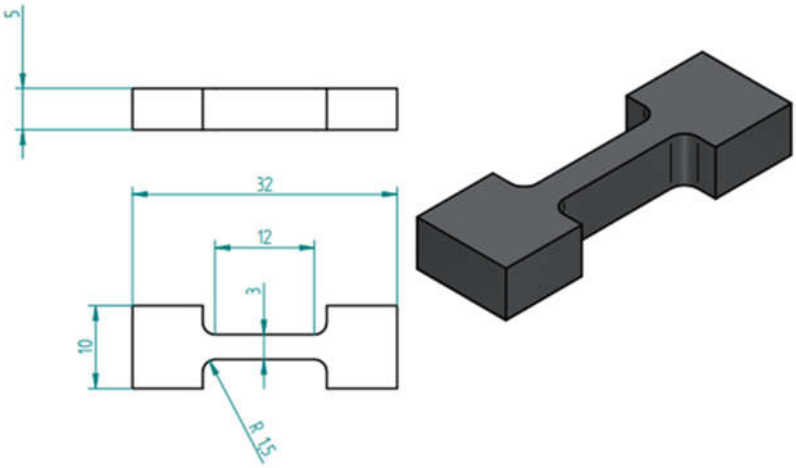

Figure 3.3. Dimensions of the tensile specimen for tensile testing.

3.5. Cyclic oxidation

The cyclic oxidation test was conducted at 900 °C in a static laboratory air up to a maximum of 9 cycles. Each cycle consisted of exposure for 100 hours at test temperature and 15 mins at ambient temperature, which was sufficient to cool the specimens below 50 °C. The specimens were put into and removed from the hot zone of the furnace within a few seconds. Changes in mass of the specimens were recorded after each thermal cycle. Prior to the oxidation test, the specimens used in the test were homogenized at 1100 °C for one hour, followed by grinding down to 600 grit SiC papers, and ultrasonically cleaned with acetone for 20 minutes to remove any organic substances. The stabilized/homogenized alloys in **Section 4.7** and **4.8** alloys were, induced under nitrogen at 900 °C for 3.6 hours at a rate of 1L/min prior to the cyclic oxidation test. The oxidized specimen surfaces were ground down to 1200 SiC grit papers to conduct metallographic examination. The morphology of the scale and specimen cross-section were investigated by SEM, and micro-analysis were performed by EDS.

3.5.1. Chemical analysis

The final as-melted chemical composition of the alloys are shown in **Table 3.4** [78]. The difference between the nominal and final chemical composition is thought to be the difference in vapor pressures of different components in the alloys, and aluminuim low melting point meant it was none likely to bevolatile may have suffered the most burning loss reported in our latest publication [79].

Table 3.4. Chemical composition (at. %) of the Ti-Al, Ti-Al-Nb and Ti-Al-Nb-Cr alloys.

γ-TiAl based alloys	Ti	Al	Nb	Cr
Binary	55.7	44.3	-	-
Ternary	53.1	45.8	1.8	-
Quaternary	51.0	46.4	1.9	0.7

3.6. Thermal analysis

High temperature differential thermal analysis (HTDTA) was performed on the solidified alloy ingot buttons in order to determine critical temperatures and provide insight into phase transformations. The DTA was conducted using a Shimadzu (DTA-50) instrument, on 3×3×3 mm size specimens cut by electro-discharge machining (EDM). Test specimen, were contained in high purity recrystallized alumina crucibles. The DTA cell was continuously evacuated and back-filled with ultra-high purity argon during the heating runs, which were all performed at a heating rate of 20 °C /min starting from room temperature to 1500 °C with subsequent furnace cooling.

In addition, phase transformation behavior was also studied using differential scanning calorimetry (DSC) on the as-cast specimens in order to characterize the solid state reactions. The heating rate was 10 °C /min from room temperature to 1500 °C β-transus temperature using a high temperature DSC Netzsch STA 449F3 Jupiter® simultaneous thermal analyzer. A sample size of 3×3×3mm cut by electro-discharge machining (EDM) was used. The crucibles consisted of Al_2O_3. An Y_2O3 suspension was used to improve the thermal contact between the samples and the crucible. The measurements were conducted under argon atmosphere, while the temperature measurements of the DSC setup was calibrated by means of enthalpy standards.

3.7. Heat-treatment

The heat treatment process was performed in tube furnace flushed with argon gas. The temperature profile for each microstructure is given in **Table 3.5**.

Table 3.5. Heat treatment parameters.

Microstructure	Isothermal treatment	Cooling route
Spheroidised laths	1335 °C / for 1h/ ramp to 1350/30mins 10 °C /min	Water quench
Widmanstätten laths	1335 °C / for 1h/ ramp to down to 1230/30mins at 10 °C /min	Air cooling from 1230 °C
Stabilized fully lamellar structure	1335 °C / for 1h/ ramp to 1380/30mins-ramp down to 900 °C /	Furnace cool

3.8. EBSD analysis

To determine crystal orientation behavior on the as-cast and heat-treated γ-Ti-48Al-2Nb-(Sn, Mn, Cr and Si)-doped intermetallic alloys, the SEM with electron backscatter diffraction (EBSD) was utilized. Due to the complexity of the phases in the alloy (i.e. γ-tetragonal, α_2-hexagonal, Ti_5Si_3 precipitates) computer simulation techniques using first principles density functional theory, especially the determination of atomic positions (Wyckoff notations) was performed, in order to enable entering crystallographic data to the Twist Software, while proceeding with the EBSD analysis. The specimens analyzed for EBSD was mechanically polished using colloidal silica and electro-polished in a solution of 600ml methanol, 360 ml butoxyethanol and 60ml perchloric acid. The parameters used to conduct EBSD analysis were: acceleration voltage of 20kV, and the specimen tilt angle of 70 °. The common way to distinguish EBSD is its color representation which is used as a tool to visualize local crystal orientations, which are expressed in Euler angles ($\varphi_1\phi\varphi_2$), and therefore a representation of successive conventional rotations to match the crystal orientation with a Cartesian co-ordinate system related with sample surface [51].

In addition, the research study discusses briefly the crystallographic textures that is beyond the scope of the study; however, the focus would be on the relative mis-orientations between pixels of a given mapped surface.

3.9. FIB-SEM preparations

Precipitation behavior and γ-variants were characterized by scanning electron microscope (SEM) in backscatter electron mode (BSE) deploying a focused ion beam (FIB) milling technique outsourced at the National Metrology Institute of South Africa (NMISA) corporation.

Electron transparent foils were prepared by grinding the exact cut slices of diameter of 3mm thickness, and with subsequent electronic thinning at -12 °C with an A3-electrolyte from Struers LectroPol-5 [80]. Electron micrographs and selected area electron diffraction (SAED) patterns were collected with an FEI Tecnai G^{2}20 FE-TEM. **Fig. 3.4** shows the overall sample layout of nominal composition Ti-48Al-2Nb-0.3Si and Ti-48Al-2Nb-1Sn-0.7Mn-0.3Si intermetallic alloys.

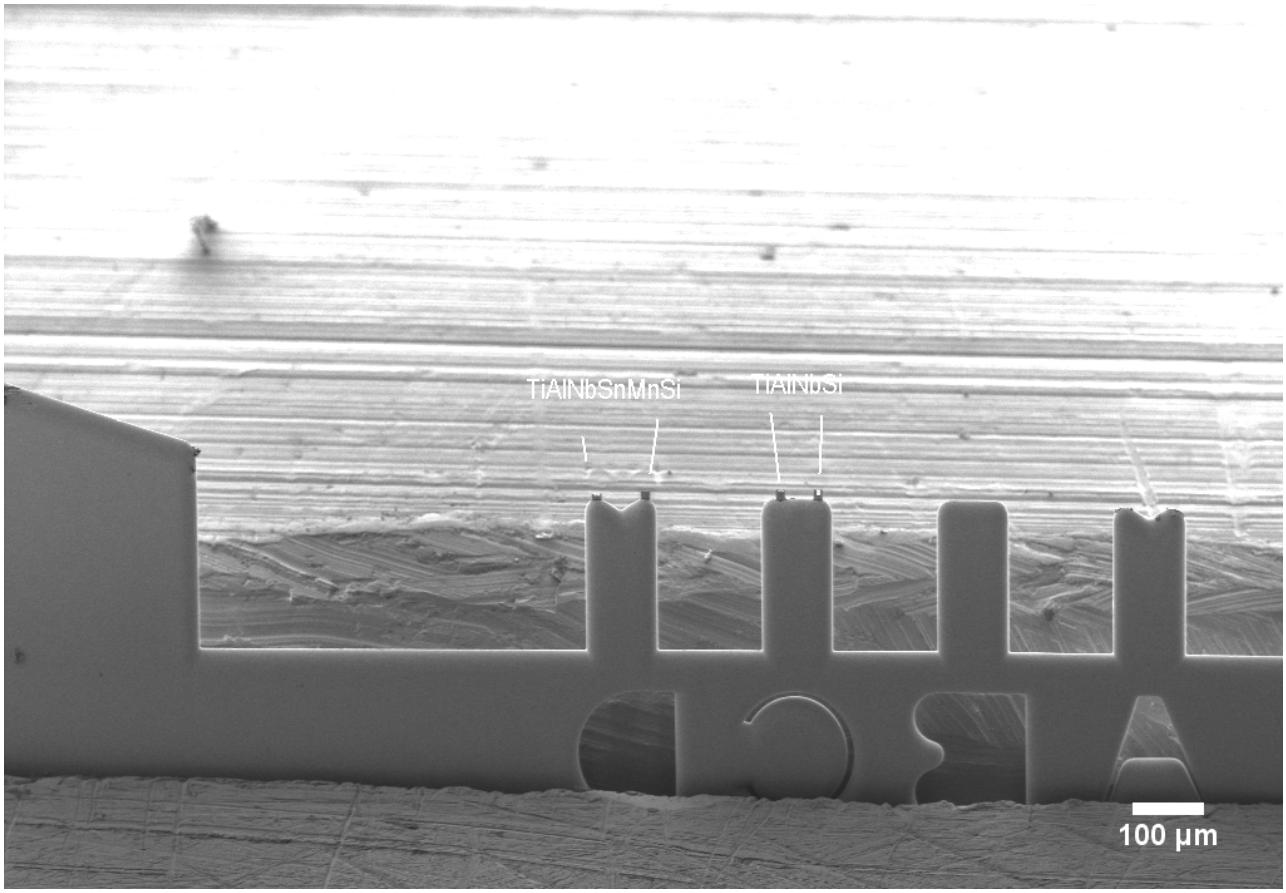

Figure 3.4. FIB-SEM Sample layout of TiAlNbSi, and TiAlNbSnMnSi alloys.

Fig. 3.5 show the sample preparation of the lamellar sectioning from FIB-SEM workstation. Sample mounting is shown in **Fig. 3.5a**, whereas sample undercut is shown by **Fig. 3.5b**, and lastly **Fig. 3.5c** demonstrates FIB with corresponding SEM sample extracted.

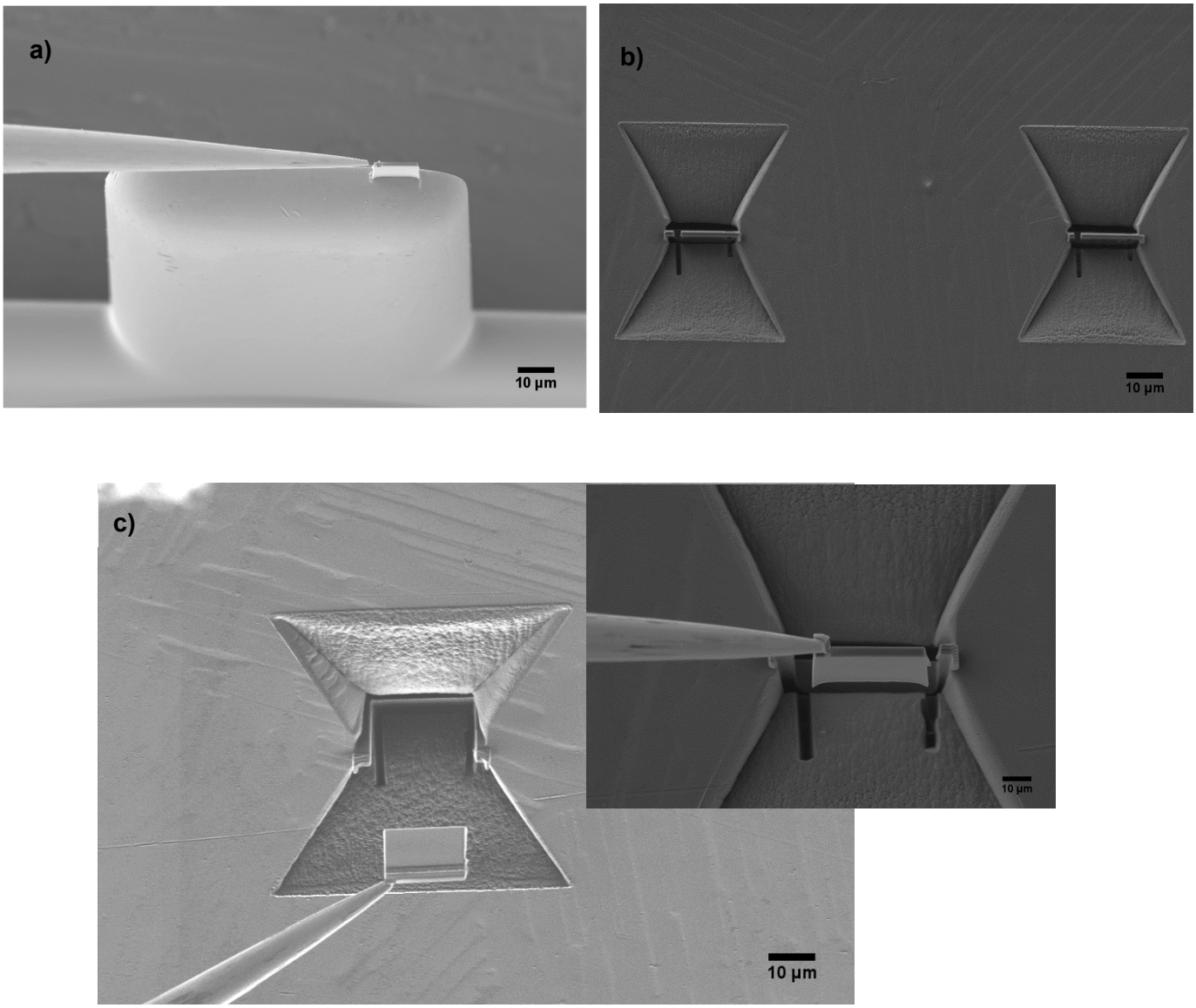

Figure 3.5. FIB-SEM preparation: a) sample mounting, b) sample under-cut, and c) sample extracted.

4. CHAPTER 4: RESULTS AND DISCUSSION

4.1. The development of γ-Ti-45Al-(Nb, Cr) based Intermetallic Alloys by arc melting: FCC and Rhombohedral phase transformation

4.1.1. Introduction

Alloying of pure Ti takes advantage of the α↔β phase transition as well as improving the low tensile ductility in the (Ti-hcp) that has high CRSS of different slip systems [81]. Alloying with Al helps to reduce the anisotropic deformation to improve mechanical performance [81]. The origin was that the {10−10} planes which were the preferred substitution prismatic planes for Al atoms [81]. Wu et al. [81], has established that the preferred substitution behavior of Al atoms produced a higher energy barrier against dislocation gliding on prismatic planes, thus rapidly hardening the prismatic slip. Due to low density, high specific stiffness, specific strength, good oxidation resistance and excellent creep properties, intermetallic γ-TiAl alloys have been considered for applications in aerospace and automotive engines [11], [82]–[85]. Despite the excellent intermetallic γ-TiAl based alloys properties, their inherent low room temperature ductility and lack of hot deformability gives major challenges in fabrication of complex geometries using the most conventional processing methods, hence becoming impractical to produce sound products [20], [86]–[88]. The biggest challenge for researchers is to control the brittle intermetallic compounds, i.e. Ti_3Al precipitates formed at Ti/Al through interfacial thermodynamic reactions [89],[90]. Titanium aluminides have a possibility of replacing the current Ni-based super-alloys [91]. The advantages will imply a significant increase in fuel efficiency, cost reduction and environmental effects. Other than forming an alloy, Ti-Al-Nb can be used as a coating material as a hard (Ti, Nb) Al_3 intermetallic surface coating [92]. Microstructures of Ti-Al based alloys are predominantly dominated by the lamellar structures which are refined by the combination of Al-supersaturated α_2-Ti_3Al grains and the introduction of dislocations prior to aging [93]. The α_2-Ti_3Al phase precipitates during the fabrication or aging of Ti-Al alloys, and the mechanism behind this is explained by [93]–[95]. In addition, Yang et al. [9], reported that TiAl-based alloys have a poorer castability, high chemical reactivity and larger solidification shrinkage rate than typical Al casting alloys, causing misrun defects on the surface of the components, shrinkage porosity and crack defects with poor ductility. In the current study, button arc melting was employed to develop γ-based alloys of nominal composition Ti-48Al (binary), Ti-48Al-2Nb (ternary) and Ti-48Al-2Nb-0.7Cr (quaternary). For the first time, **Section. 4.1**, show that the combination of Nb and Cr induce phase transformation accompanied by grain refinement.

4.1.2. XRD analysis

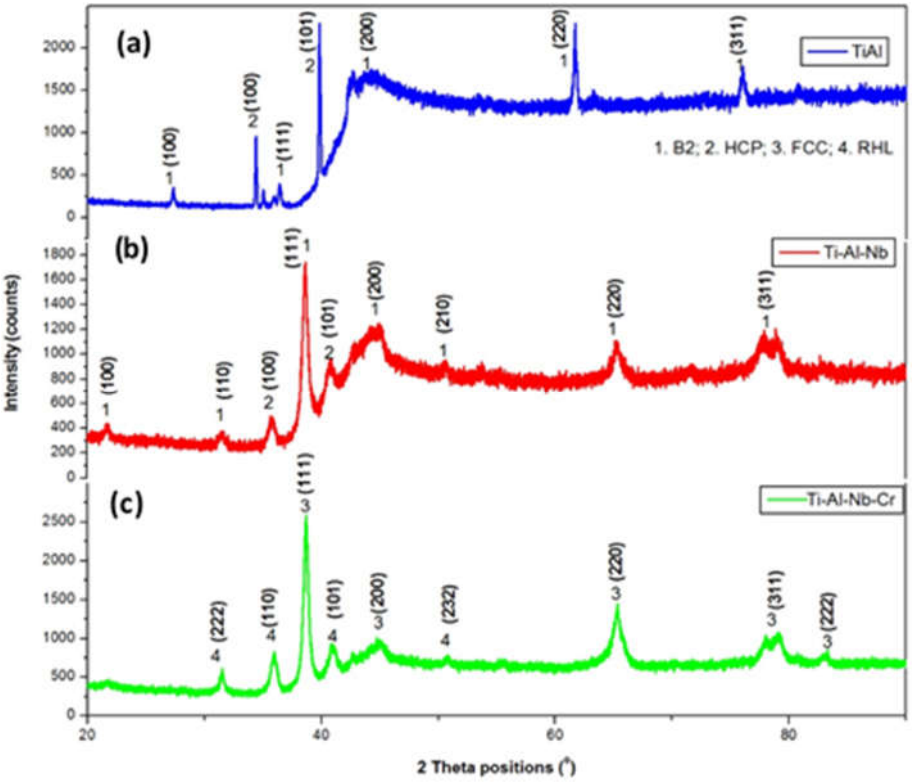

Figure 4.1. XRD patterns of (a) binary (Ti-Al), (b) ternary (Ti-Al-Nb) and (c) quaternary (Ti-Al-Nb-Cr) alloys.

The crystal structures of the as-cast binary Ti-Al, ternary Ti-Al-Nb and quaternary Ti-Al-Nb-Cr were analyzed by the XRD technique. The phase development of the alloys is shown in **Fig. 4.1**. The binary alloy in **Fig.4.1a** comprised BCC-B2 (β) with lattice parameters *a*=4.04 Å (*Pm-3m #221*) and HCP (α) of *a*=2.90 Å; *c*=4.58 Å *(P63/mmc #194)* space group and number. The calculated *c*/*a* ratio of the α-phase was 1.58. **Fig. 4.1b** shows the XRD pattern of the alloy upon Nb addition. Both the β and the α-phases were detected. The β-phase retained the *a*=4.04 Å while the HCP-phase was detected with *a*=2.89 Å; *c*=4.72 Å lattice parameters. The HCP *c*/*a* ratio increased from 1.58±0.36 in binary to 1.63±025 in the ternary alloy. The lattice parameter *c* increased at a higher rate, while the *a* lattice parameter slightly decreased. In the quaternary alloy, shown in **Fig. 4.1c**, two phases were detected. The FCT phase with lattice parameters *a*=2.81Å and *c*=4.08 Å with an *c*/*a* ratio of 1.45, the HCP α2-Ti_3Al phase with lattice parameters *a*=5.73 Å and *c*=4.64 Å with an *c*/*a* ratio of 0.81, and lastly a rhombohedral (RHL) phase with *R-3m #166* space group and lattice parameter *a*=5.96 Å were formed due to the addition of Cr. The FCT and RHL shared similar peaks; however, the peaks were named based on the most intense peaks. Similarity between FCC and RHL were previously simulated on pure Ti [96] and also observed in Ni-Ti-V alloys [97]. In the recent work done by Mathabathe et al. [79], the *c*/*a* ratios gave insight into the precipitation behavior

of the constituent phases $\alpha_2/\gamma/\beta$-B2. They demonstrated that the crystallization of the phases in the as-cast β/B2-containing γ-TiAl based intermetallic alloy follows a Blackburn orientation relationship (β-solidifying) = {110}β // {0001}α and <111>β // <2 $\bar{1}$ $\bar{1}$0>α.

4.1.3. Metallographic examination

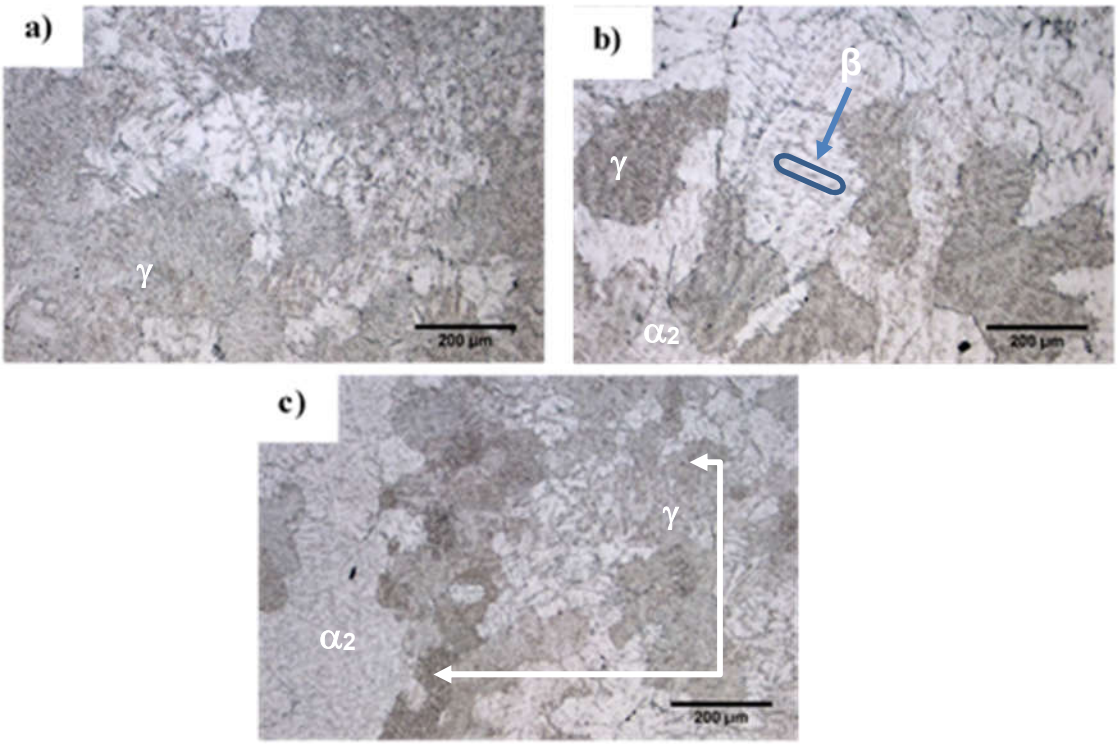

Figure 4.2. Optical micrographs of the (a) binary (Ti-Al), (b) ternary (Ti-Al-Nb) and (c) quaternary (Ti-Al-Nb-Cr) alloys.

Fig. 4.2 shows the optical microstructures of the γ-based alloys after arc melting. The binary Ti-Al alloy shown in **Fig. 4.2a** illustrates a two-phase microstructure. It comprised a lighter phase of network colonies around the major darker phase. The lighter phase was identified as to the B2 (β)-phase networking around the HCP-Ti parent phase. The effect of 2 at.% Nb on the TiAl alloy is demonstrated in **Fig. 4.2b**. It seems the lighter colonies were increased. The volume fraction of the lighter phase became more profound in **Fig. 4.2c**. According to Yan et al. [9], during solidification, Nb segregation to dendrite cores, and a few primary β-phases were retained with subsequent cooling to ambient temperature due to enrichment of β-phase stabilizer.

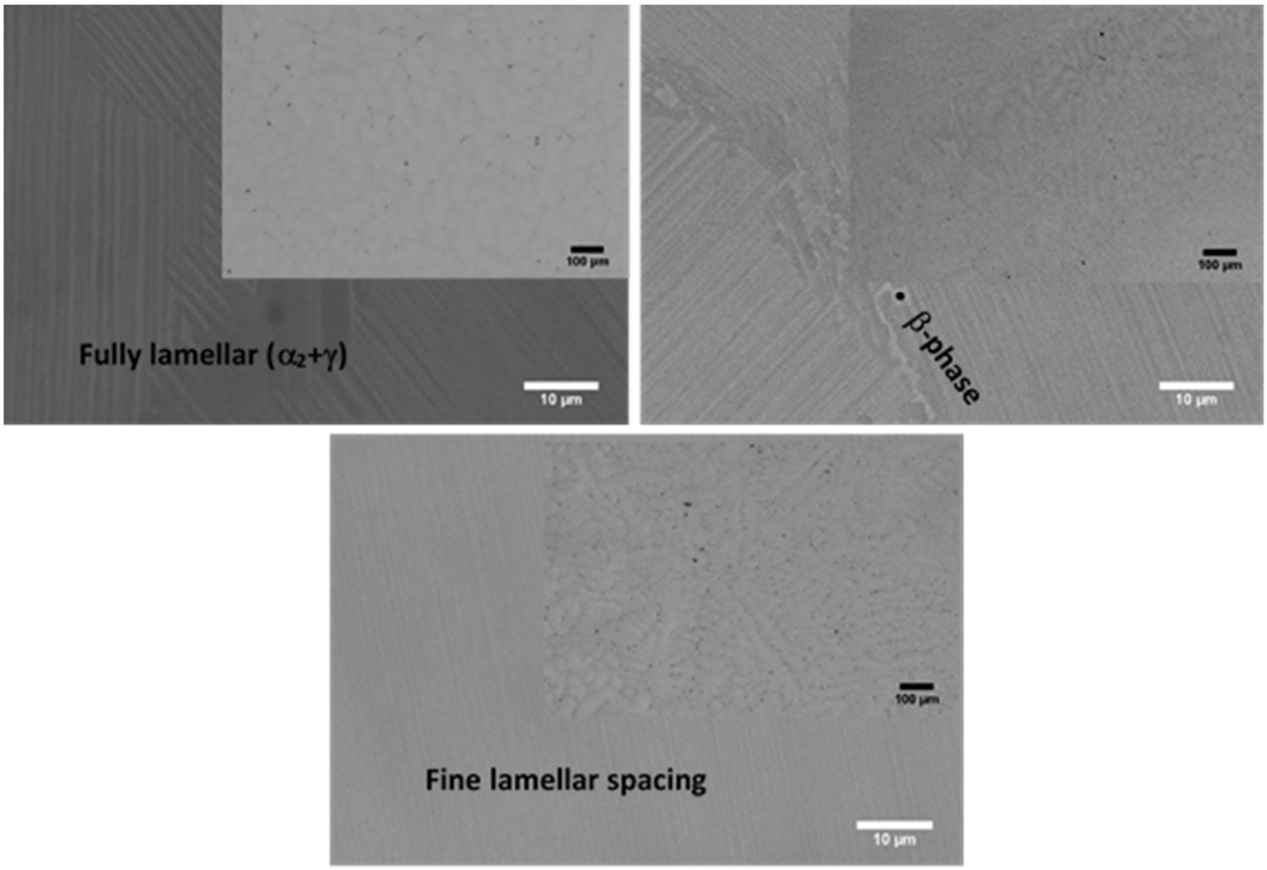

Figure 4.3. SEM-BSE micrographs of the (a) binary (Ti-Al), (b) ternary (Ti-Al-Nb) and (c) quaternary (Ti-Al-Nb-Cr) alloys.

Fig. 4.3 shows the SEM micrographs of the binary (TiAl), (b) ternary (TiAlNb) and (c) quaternary (TiAlNbCr) alloys, respectively. The microstructure of the binary alloy illustrated in **Fig 4.3.a** comprised lamellar α_2 (light-gray) and dark gray (γ) second phase segregated along grain boundaries. The chemical constitution of the binary alloy is displayed in **APPENDIX Fig.S1**. The addition of Nb (2 at.%) to the binary alloy led to solidification behavior different from the TiAl alloy system. Liu et al. [98], reported that the Nb addition increases the melting point by almost 100 ºC and promoted zone shifting of the β-phase to the steep Al direction and, therefore, induce (α_2/γ lamellar, B2 phase) multi-phase structures, for the favorable mechanical properties [99]. The TiAlNb ternary alloy microstructure in **Fig. 4.3 (b**) shows few elongated B2 (ordered-β) phase [10] that are usually observed in the inter-dendritic regions of the structure. The composition of the B2 structure is shown in **APPENDIX Fig. S2**. Lapin et al. [10], reported similar B2 phase in microstructures of the TiAl alloys with β-stabilizing elements. **APPENDIX Fig. S3** illustrates the composition of the lamellar structure comprising of (α_2+γ) phases. The EDX analysis indicates that the difference between the two phases is that the α_2-phase had higher Ti content than the γ-phase **(APPENDIX Fig. S3)**. The microstructure of the TiAlNbCr quaternary alloy is illustrated in **Fig. 4.3c** after addition of 0.7 at. % Cr. The as-cast quaternary alloy shows evidence of new development. The dendritic

orientation appears in a fishbone appearance typical of twinning behavior obtained in Ti with FCC structure [100]. Furthermore, the XRD analysis of this work detected the FCC crystal structure with a similar lattice parameter to that of the B2 phase. This new observation in the quaternary microstructure is attributed to the change in crystal orientation in agreement with the XRD analysis. The superimposed microstructure in **Fig. 4.3c** showing dendritic colonies, indicates Al segregation as is shown by the dark gray contrast formed in the inter-dendritic regions. These dendritic structures, according to Ding et al. [99], are presumed to be developed during directional solidification. It is observable at higher magnifications that some dendrites are aligned at inclined angles and the lamellar orientation in these dendritic regions remains aligned with that in the other dendritic regions. The solidification mechanism in TiAl alloys shows that when the peritectic temperature was achieved, the α phase nucleated and grew from the liquid. As the cooling continues, the solid state transformation will occur in the sequence $\beta \rightarrow \alpha$ forming the lamellar structure [99]. Furthermore, the consequential final lamellar orientation occurs when the peritectic α phase consumed the primary β phase [99], [55]. The results from this work indicate that addition of Nb and Cr in the quaternary alloy promoted phase transformation and refinement of the microstructure. Therefore this is an indication that that the quaternary alloy exhibited a minor remnant the β-phase, hence better percentage elongation in quaternary than the ternary alloy. The quaternary alloy composition of the lamellar structure and the β-phase is shown in **APPENDIX (Fig. S4-S5)**. The summary of the present phases in the alloys is illustrated in **APPENDIX (Table S1)**.

4.1.4. Grain size and macro-hardness analysis

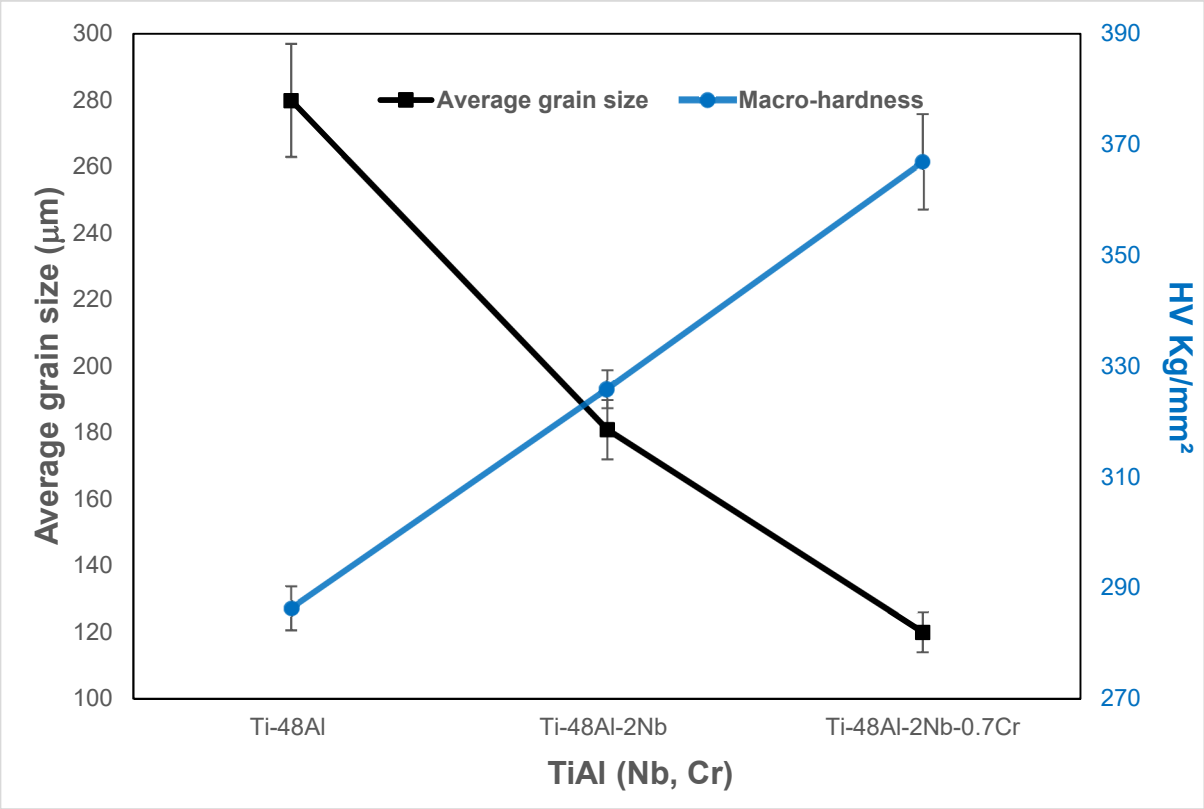

Figure 4.4. Average grain size and macro-hardness values of the Ti-Al, Ti-Al-Nb and Ti-Al-Nb-Cr alloys.

Fig. 4.4 shows the grain size and Vickers hardness measurements. The hardness of the alloys increased with the addition of the Nb and Cr, while the grain sizes decreased. The hardness values are reported to have a linear relation with the yield strength in solidified γ-based alloys [98]. The smaller grain sizes in the quaternary alloy agreed with the fine lamellae microstructure observed under SEM analysis. Therefore, it is apparent that 2 at. % Nb and 0.7at. % Cr both act as grain refiners for the Ti-Al alloy in addition to changing the crystal structure.

4.1.5. Tensile analysis

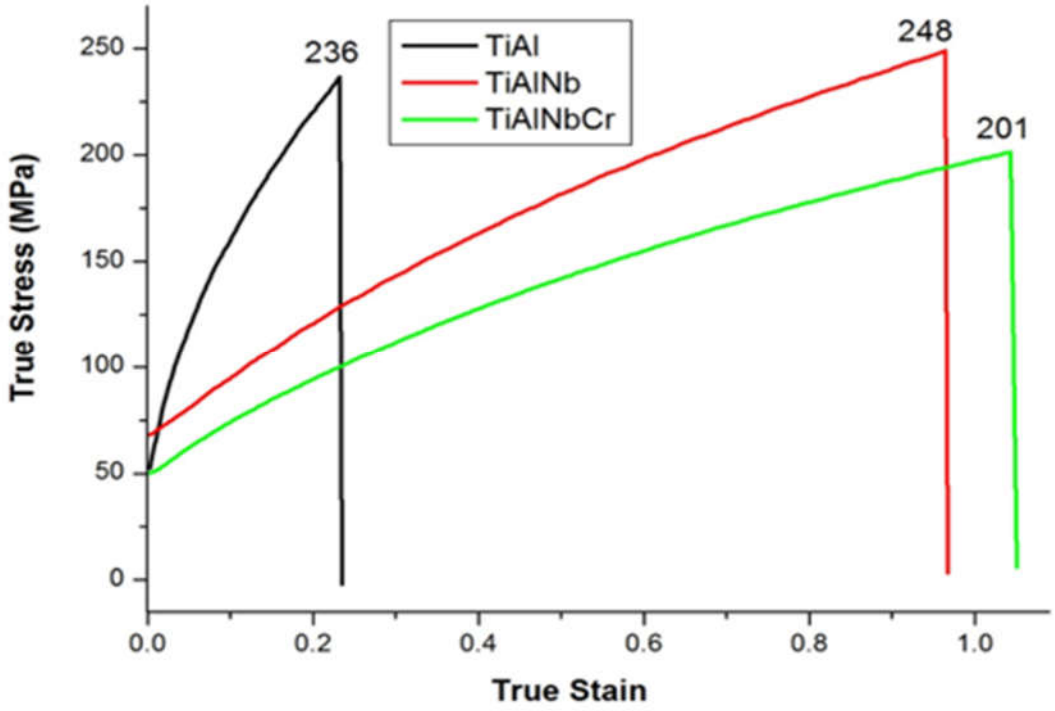

Figure 4.5. Room temperature tensile curves of the binary (Ti-Al), ternary (Ti-Al-Nb) and quaternary (Ti-Al-Nb-Cr) alloys.

Fig 4.5 shows the true stress-true strain curves of the binary (Ti-Al), ternary (Ti-Al-Nb) and quaternary (Ti-Al-Nb-Cr) alloys. The ternary Ti-Al-Nb had the highest UTS and elongation, comparable to that of the quaternary. Of the three alloys the quaternary alloy exhibited the lowest UTS. This behavior is attributed to the effect of great refinement induced by the addition of Cr. However, it is important to note that the contending mechanisms in these alloys are the twin and super-dislocation nucleation [17], depending on stacking fault energy. Furthermore, duplex structures favors twin deformation, because its fault energy is lower due to lower Al concentration or the presence of α_2 which absorbs and lowers the interstitial content in gamma (γ) [17]. When Cr atoms occupy Ti-sites in a single γ-phase alloy, the Ti-Al bond is slightly modified and plasticity is enhanced. In contrast, when Cr atoms occupy the Al sites in a duplex alloy, the overall covalency of Ti-Al bond is reduced and as a result favors plastic deformation [17] hence the lower UTS in the quaternary alloy.

4.1.6. Conclusions

The Ti-48Al binary alloy, Ti-48Al-2Nb ternary alloy and Ti-48Al-2Nb-0.7Cr quaternary alloy were investigated. Phase compositions and the microstructures of the alloys were studied by X-ray diffraction (XRD), optical microscopy (OM), and the scanning electron microscopy (SEM).

The addition of 2 at. % Nb influenced the HCP *c*/*a* ratio in Ti-Al alloy, i.e. it increased from 1.58 to 1.63 due to lattice parameter *c* expansion. The microstructure of the binary alloy comprised the lamellar structure and (β) second phase segregated along grain boundaries. The Ti-Al-Nb ternary alloy microstructure had some elongated B2 (ordered-β) phase that are usually found in the interdendritic regions of the structure. In the quaternary alloy, two phases were detected:.FCT phase with lattice parameter *a*=4.04 Å and a rhombohedral (RHL)-phase with R-3m #166 space group with a lattice parameter *a*=5.96 Å were formed due to the addition of Cr. The dendritic orientation of a fishbone appearance, typical of twinning behavior in FCC-Ti structure, was observed. The results from this work indicate that addition of Nb and Cr in the quaternary alloy promotes grain refinement and induced phase transformation.

4.2. Novel design of γTiAl based alloys with minimal Al vaporization by vacuum arc melting

4.2.1. Introduction

Despite the excellent properties of intermetallic γ-TiAl based alloys, their intrinsic lack of hot deformability poses major challenges in the fabrication of complex geometries using the most conventional processing methods, hence becoming impractical to produce sound products [20], [86]–[88]. The biggest challenge for researchers is to control the brittle intermetallic compounds, i.e. Ti_3Al precipitates formed during Ti/Al interfacial thermodynamic reactions [89], [90]. Work has been performed on alloys such as ternary Ti–Al–Nb elemental powder blends with minor additions of SiC, where the alloys were synthesized in a high energy ball mill in order to understand the structural evolution during mechanical alloying (MA) and subsequent thermal treatment [101]. Mechanical alloying (MA) of elemental powders has been extensively explored to develop the aluminides [102]–[104]. The current study comprised alloying TiAl with Nb and Cr to improve properties through powder metallurgical cold pressing followed by melting. The cold pressing technique was expected to reduce powder inter-particle distances in order to promote better efficiency during melting. The intermetallic tin-telluride (Sn-e) has been prepared in air and at room temperature by the repeated pressing operation of elemental granular Sn and shots Te precursors. The atomic structure of the reactant elements were cold deformed until the pressing action supplied enough mechanical energy by explosive reaction [105]. Additionally, the presence of stacking faults in metastable cobalt green-compacts obtained by compaction of reduced cobalt oxide induced transformation from (FCC) phase to (HCP) phase [106]. Bolokang et al. [107] confirmed the HCP to FCC phase transformation in pure Co using cold pressing process. In this work, the Ti-48Al, Ti-48Al-2Nb and Ti-48Al-2Nb-0.7Cr (at. %) alloys in were developed by combining both powder and ingot

metallurgy routes via uniaxial cold pressing and vacuum arc melting of the compacted powders. The alloys structural and microstructural characterization are presented.

4.2.2. Precursor metallic powders

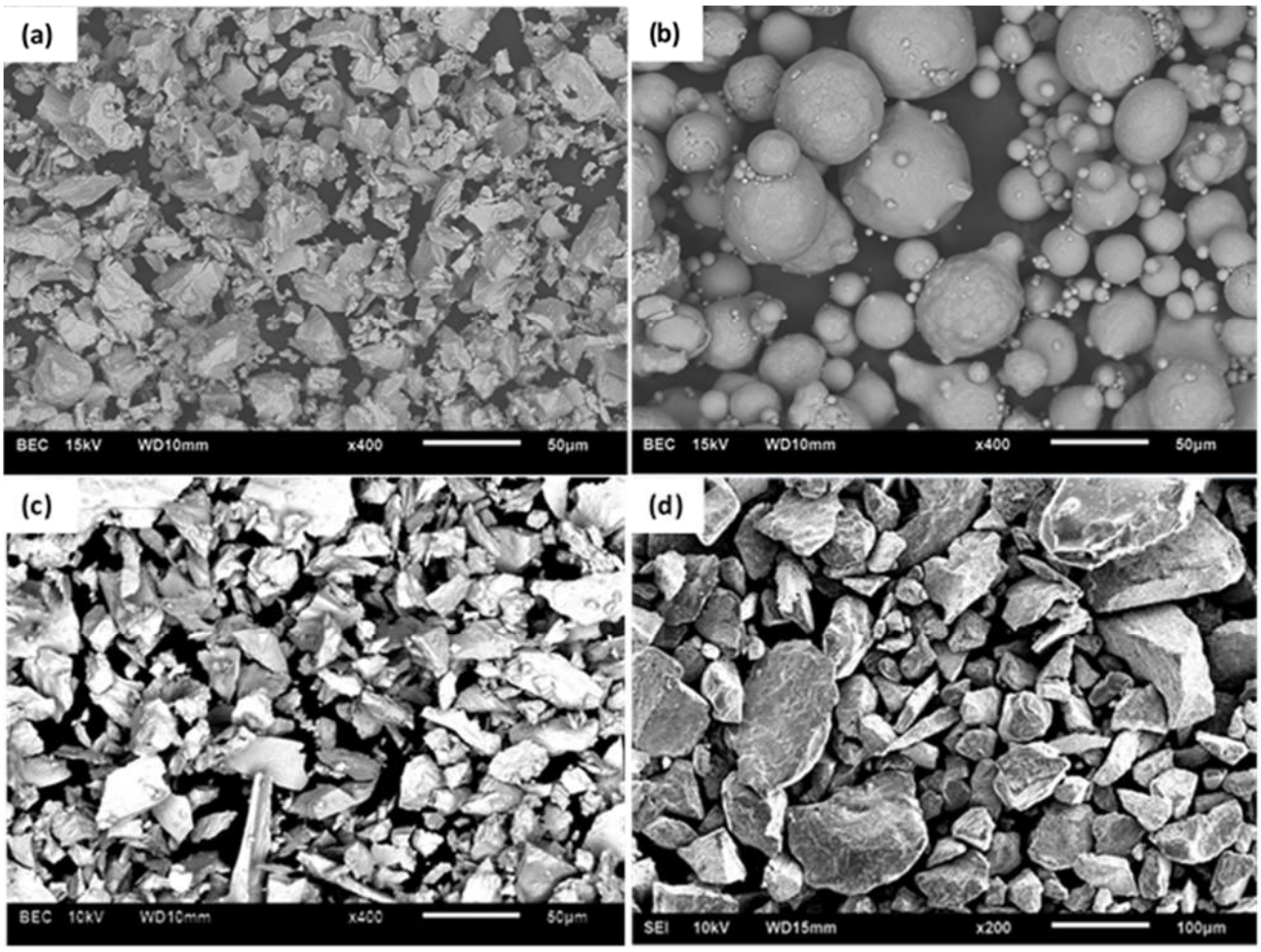

Figure 4.6. SEM micrographs of a) Ti, b) Al, c) Nb and d) Cr powder particles.

Fig. 4.6 shows the microstructure of the Ti, Al, Nb and Cr powder particles, respectively. The Ti, Nb and Cr powder particles had the angular, but irregular shape with various particle sizes. The average particles sizes were 31 µm, 24 µm and 126 µm for Ti, Nb and Cr powders. The Al powder exhibits a spherical morphology comprised of varying particle sizes. It seems that the smaller particles have agglomerated to form large particle sizes in Al powder. The average particle sizes of Al elemental powder 74 µm were measured. The particle distribution curves in **Fig. 4.7 a-d** are in agreement with the SEM analysis. Al powder show narrow particle distribution compared to Ti, Nb and Cr powder particles. The physical properties of these elemental powders are conferred in **Table 2.4**. These elemental properties contribute to the final TiAlNbCr alloy after chemical reaction during melting and casting amid alloy formation.

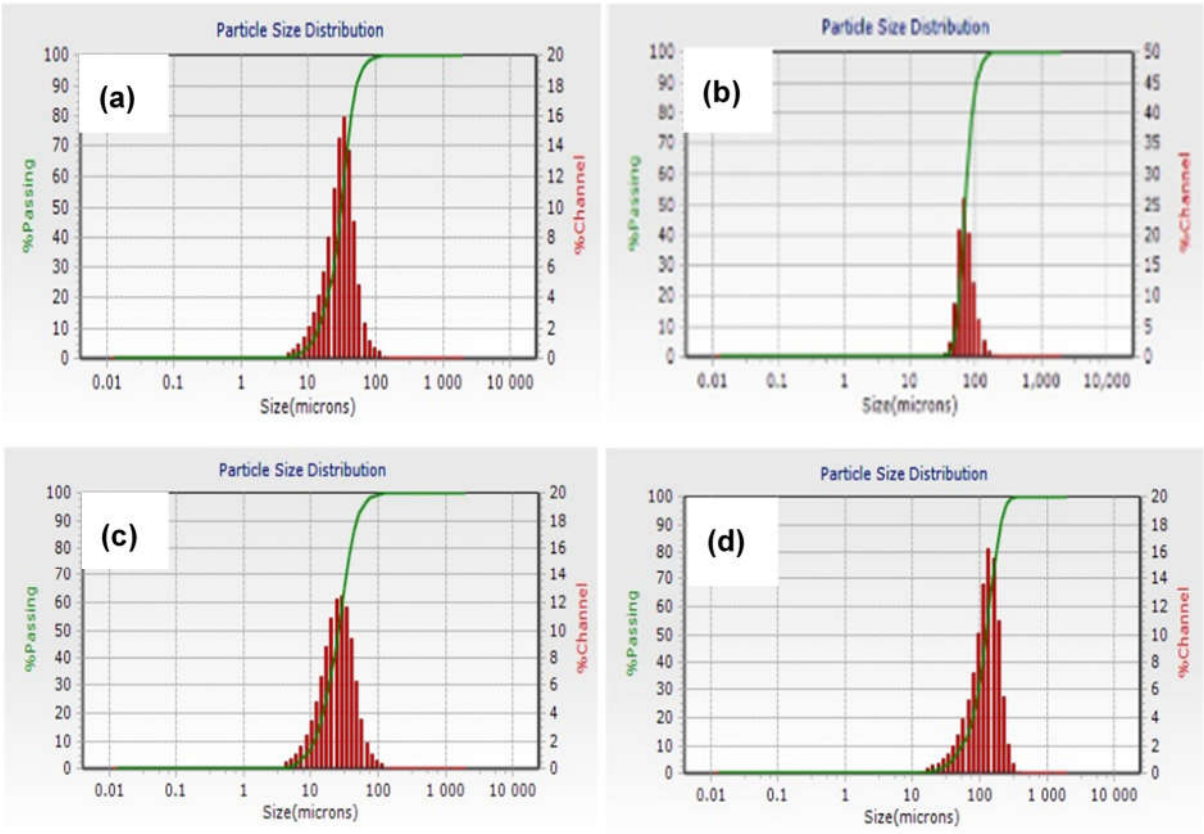

Figure 4.7. Particle size distribution of (a) Ti, (b) Al, (c) Nb and (d) Cr powders.

4.2.3. Uni-axial cold pressing analysis

The three cold compressed elemental alloy powder mixture micrographs are shown in **Fig. 4.8a-c**. Three 43 mm diameter compacts representing their corresponding alloys were cross-sectioned and analyzed to determine the effect of cold pressing and chemical homogeneity. In **Fig 4.8a** the cross sectional micrograph of the binary TiAl powder shows the two phase structure, the light phase on the surface and dark gray phase towards the center of the sample. It shows that during cold pressing, there was particle re-arrangement and evidence of particle welding as a result of compaction pressure. The mechanism of cold pressing is shown in **Fig. 4.9**. The corresponding EDX analysis confirmed high concentration of Al particles on the surface and less towards the center. This implies that, upon melting the γ-TiAl alloy compacts, the chemical reaction was ignited initially on the surface, being the first contact point, but also due to its high thermal expansion and low melting temperature shown in **Table 4.1**. However, Al will not necessarily melt first, but initiates the intermetallic phases as the temperature is increased. **Fig. 4.8b** represents a ternary TiAlNb elemental powder compact. The Al still dominated the surface due to its spongy characteristics with the presence of small amounts of Nb particles. During cold pressing the Al particles migrated to the surface in contact with die facets and formed a strong weld on particles upon the surface. The quaternary alloy

TiAlNbCr compact in **Fig 4.8c** followed the similar trend, but with no Cr detected on the surface structure.

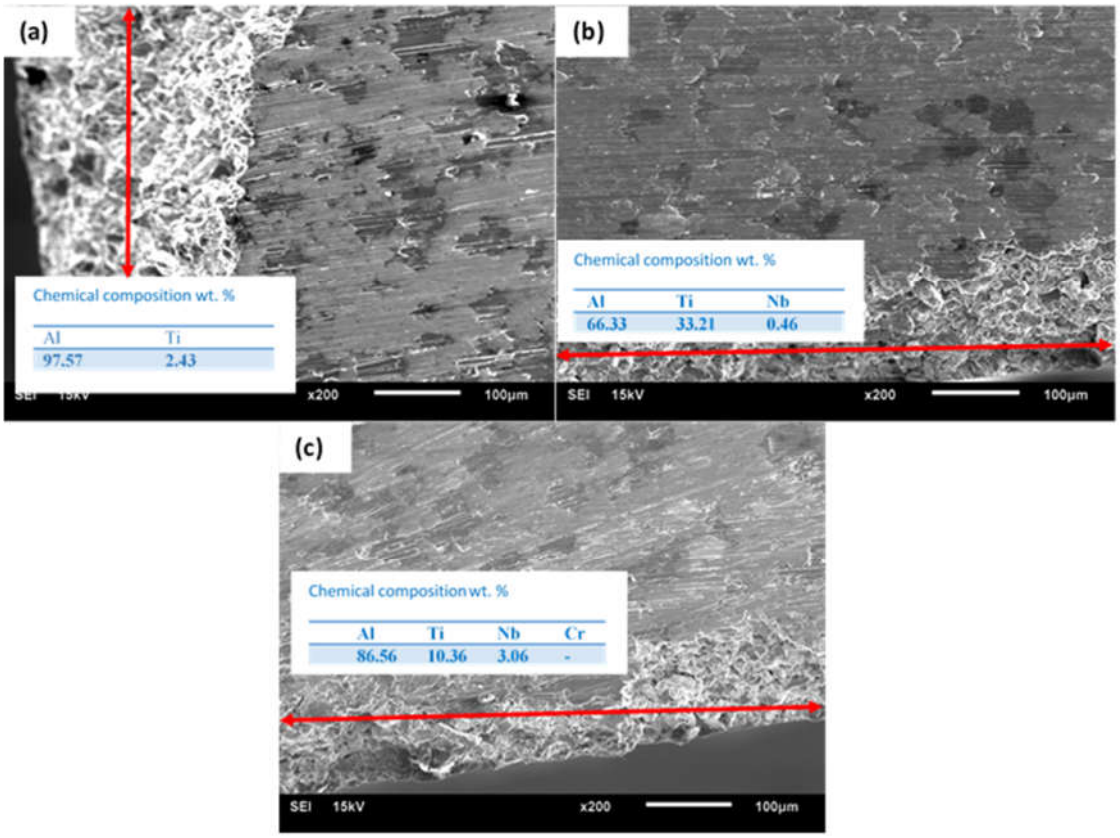

Figure 4.8. SEM-SEI micrographs binary Ti-48Al (b) ternary Ti-48Al-2Nb and (c) quaternary Ti-48Al-2Nb-0.7Cr compacted alloy powders.

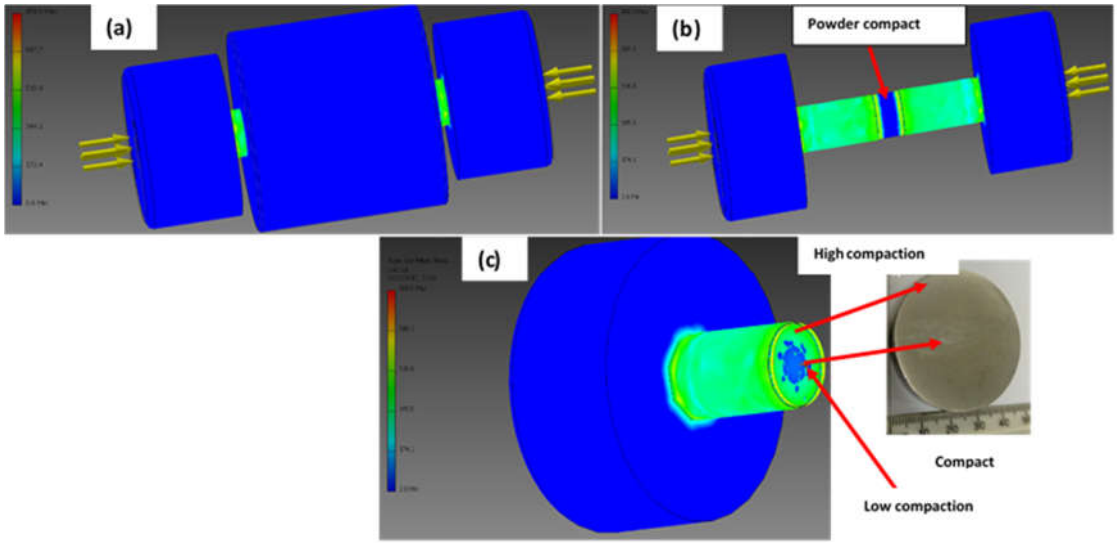

Figure 4.9. Illustration on formation mechanism of the finite element analysis (FEA) of the Die-powder compaction [77].

The composition profile of the compacted alloy powders far away from the surface is illustrated in **APPENDIX Fig. S6-8**. Supplementary to **Fig. 4.8**, the elemental maps with their

corresponding percentage composition far away from the surface, indicated that the Al atomic percentage was rather less compared to the surface of the compact. Moreover, **APPENDIX Fig. S8** illustrated that the atomic percentage of Cr was nil, on the contrary, the map profile indicated even distribution of Cr. This may have been due to the fact that, the added Cr in the compacted alloy was small about 0.7 (at.%).

The morphology of the elemental powder particles for Ti, Nb, Cr were irregular in shape as indicated in **Fig. 4.6a, c** and **d**, therefore it was observed that the inter-particle voids appeared to be more readily closed compared to the spherical Al powder **Fig. 4.6b**. The ability of particles to migrate depend highly upon the cohesive strength of the powder, and powders with little cohesive strength dilate more readily [108]. Ultimately, free flowing blends may segregate readily upon subsequent handling (e.g. mechanical compaction) especially if the different components of the blend do not adhere to one another [108]. Ultimately, air entrainment in the bulk powder blends will result, and cause compaction problems. Prescott and Barnum [108] reported that as a result of air entrapment, air will flow up and retard the flow of powder, limiting the feed rate. On one hand, the air has a potential to generate erratic flow by fluidizing a portion of the powder in the roll dies; and in the current work, the Al powder particles.

The particle size distribution in **Fig. 4.7** indicated that the precursor elemental powders exhibited a considerable size difference between them, and this aided in the average packing densities during compaction, correspondingly [103]. Contrary to this, the minor additions of Nb and Cr to the binary alloy did not have a significant effect on the green compacts, this was indicated by the percentage relative densities **Fig. 4.13**, where the graph showed a gradually decreasing curve as the alloying elements are added on the green compacts. However, the alloy density after melting, showed improved relative density as the ternary and quaternary elements are added to the binary system.

4.2.4. XRD and Raman spectra analysis

Fig. 4.10 shows the XRD patterns of the binary (TiAl), ternary (TiAlNb) and quaternary (TiAlNbCr) alloy cold pressed powders with lattice planes. The HCP-Ti and FCC-Al elements were detected in the binary alloy shown in **Fig. 4.10a**. The lattice parameters of all phases detected are presented in **Table 4.1**, and are comparable to literature. For the ternary compacted powder **Fig. 4.10b** the minor BCC Nb peaks were detected in agreement with the EDS analysis. Surprisingly, the compacted quaternary alloy powder **Fig. 4.10c** had additional peaks despite the absence of Cr element on the surface in contact with the die, which was also not detected by the EDX analysis. Instead, a rhombohedral (RHL) phase was detected and was attributed to the change in crystal structure due to the addition of BCC-Cr elemental on the bulk welded powder.

In addition, the compacted powders shown in **APPENDIX Fig. S9a-c** with their corresponding chemical composition for the γ-TiAl based alloys demonstrated flaky-like particles, which became larger as a result of flattening. This was presumably as a result of cold welding of the elemental crystalline powders during mechanical compaction. The light grey contrast was Ti rich, while the dark contrast was Al rich, in all the alloys **Fig. S9**. The pro-found white contrast composition observed in **Fig. S9b-c**, is an indication of the ternary and quaternary added on the alloys, respectively. The mechanical compaction in the current study, was employed to allow the powder particles to deform and alterate from elastic to brittle deformation, in order to constitute bonding between the particles; and not necessarily for alloying. The latter was achieved by melting technique shown by the arc melted buttons with their corresponding EDX chemical analysis in **Fig. 4.12**. By contrast, Zambaldi [70] reported that γ-TiAl has an $L1_0$ structure, which is a tetragonally distorted face-centered cubic lattice, whereby alternate (002) planes shown in **Fig. 4.10a-c** were occupied by two different species, presented in the work published by Mathabathe et al. [79]. From the discussion therein, strong and anisotropic bonding between Ti atoms on (001) planes was probably responsible for the c/a ratio being larger than unity in γ-TiAl [70], which was in agreement with c/a=1.45 found in [79].

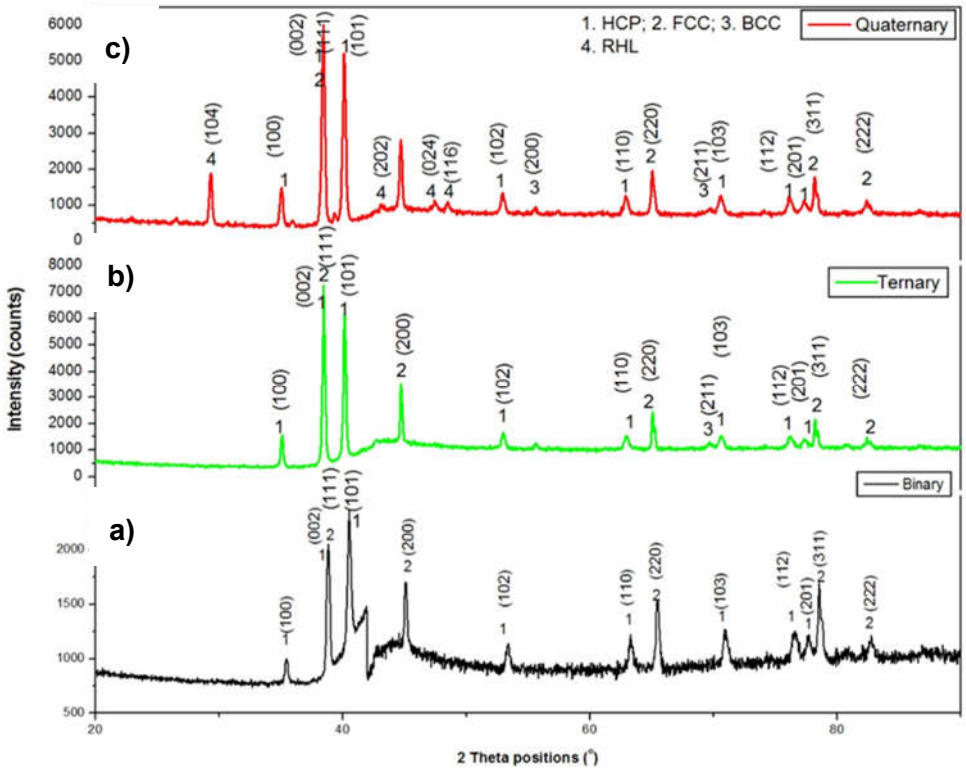

Figure 4.10. XRD pattern of TiAl, TiAlNb and TiAlNbCr alloy cold pressed powders.

Table 4.1. Crystal structure and lattice parameter of TiAl, TiAlNb and TiAlNbCr alloy cold pressed powders.

Alloy	Crystal Structure	Space Group	Lattice Parameters (Å)	
			a	***c***
Binary	HCP	*P63/mmc* # 194	2.590	4.682
	FCC	*Fm-3m # 225*	4.049	-
Ternary	HCP	*P63/mmc* # 194	2.590	4.682
	FCC	*Fm-3m* # 225	4.049	-
	BCC	*Im3m* #229	3.303	-
Quaternary	HCP	*P63/mmc* # 194	2.591	4.684
	FCC	*Fm-3m* # 225	4.052	-
	BCC	*Im3m* #229	3.303	-
	RHL	*R-3c* # 167	4.994	17.081

Raman scattering is a dominant and non-destructive technique used to evaluate the vibration modes of the microstructure [109]. Raman spectra collected along the reaction product surface layer after cold-pressing revealed varied features illustrated in **Fig. 4.11**, which compares the Raman spectra of the cold pressed binary, ternary, and quaternary powder mixture with those of melted alloys. The cold pressed binary powder mixture TiAl based alloys exhibited three Raman active modes at 841 cm^{-1}, 1006 cm^{-1} and 1036 cm^{-1}. The Raman peaks at 1006 and 1036 appeared as one peak split into two peaks, which is a representation of a double in this range. Like the binary (TiAl) compressed powder mixture, the same Raman peaks were observed in the ternary and quaternary cold pressed alloy powders, with additional strong Raman peak at 1372 cm^{-1}. These peaks could be attributed to the evolution of the RHL orientation detected by the XRD in alloys containing BCC elements. The Raman peak at 828 cm^{-1} and 1033 cm^{-1} are Ti related and slightly smaller to those obtained in pure Ti after water quenching [110]–[112]. The cast binary, ternary and quaternary alloys had only two peaks at 826 cm^{-1} and 1038 cm^{-1}. The broad peak at 828 cm^{-1} was closer to that observed at 600-750 cm^{-1} on Ti_2AlC due to Ti-C bonding vibration [113], [114]. On the contrary, the large broad hump at 826 cm^{-1} may be related to Al-Nb bonding, where Ti seems to have been etched away by compression mechanism on the surface layers confirmed by EDX analysis in **Fig. 4.8**.

Therefore, this Raman feature may be connected to the imperfection of the γ-TiAl-X (Nb, Cr) lattice in the studied alloys.

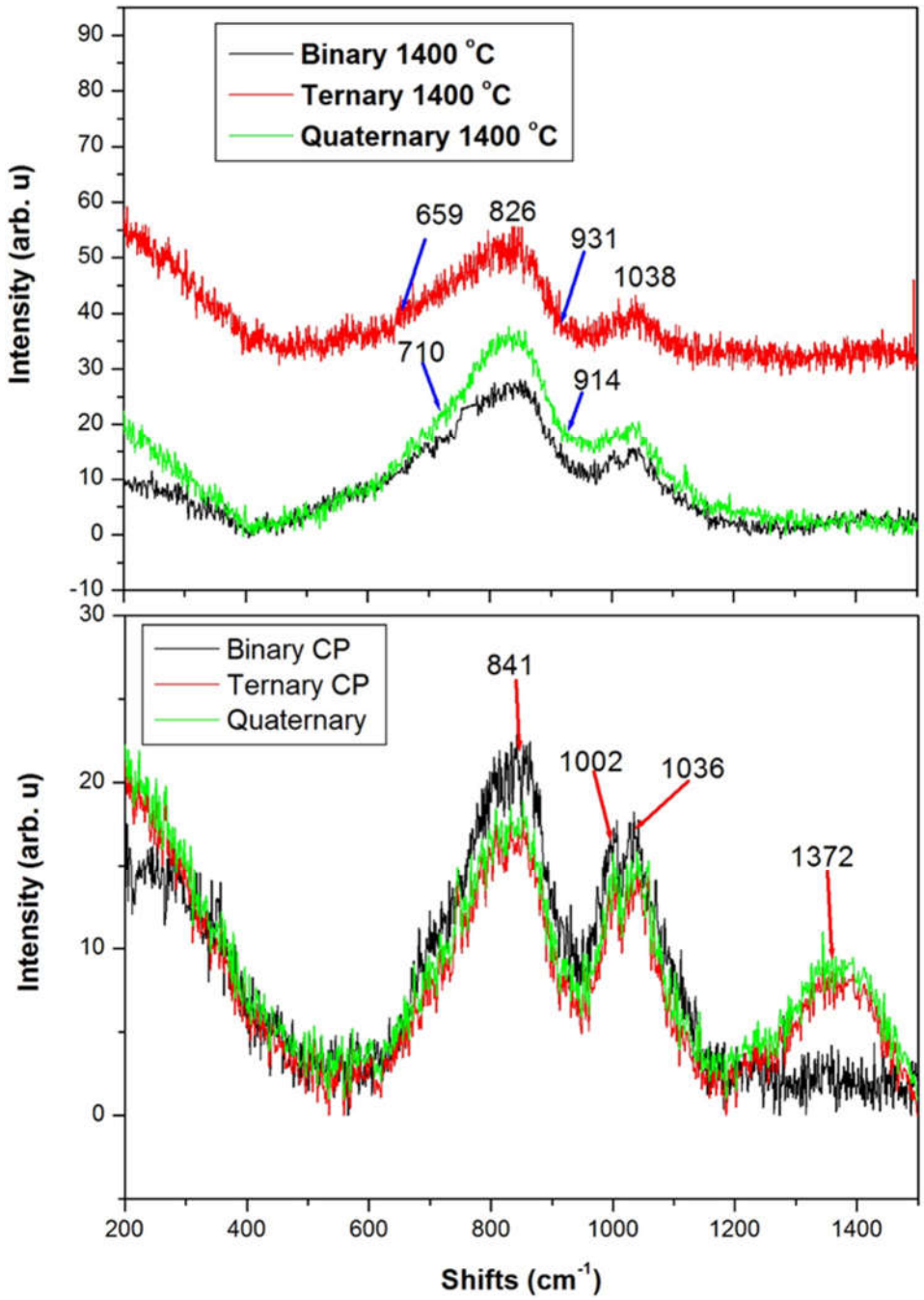

Figure 4.11. Raman spectra of TiAl, TiAlNb and TiAlNbCr alloy cold pressed powders.

4.2.5. Microstructure analysis

The microstructures of the arc-melted TiAl, TiAlNb and TiAlNbCr alloy are shown in **Fig. 4.12** with images of as-cast buttons (inset), with their corresponding bulk EDX chemical composition which was comparable to the final composition of as-vacuum melted alloy buttons shown in **Table 4.1**. All the three alloys showed dendritic structures associated with micro-segregation of alloying elements. Therefore, the deficiencies of as-cast γ-TiAl based alloys are

related not only to the intrinsic brittleness of (γ +α) phases but also to the microstructural evolution of the ingots during solidification. The addition of alloying elements (Nb and Cr) induces phase transformation by stabilizing the beta (β) phase in the microstructures. The binary alloy in **Fig. 4.12a** confers a coarse dendritic colony compared to the ternary and quaternary alloys. The addition of alloying elements (Nb and Cr) induces phase transformation by stabilizing the beta (β) phase in the microstructures, and as a result lead to grain refinement [78], [115]. For addition of 0.7 (at. %) Cr in the ternary Ti-48Al-2Nb alloy, **Fig. 4.127b**, the as-vacuum melted quaternary Ti-48Al-2Nb-0.7Cr alloy, **Fig. 4.12c**, shows evidence of new development whereby the dendritic orientation exhibit a fish-bone appearance attributed to a twinning behavior similar to the one obtained in γ-TiAl based alloys with FCT structure studied by [98].

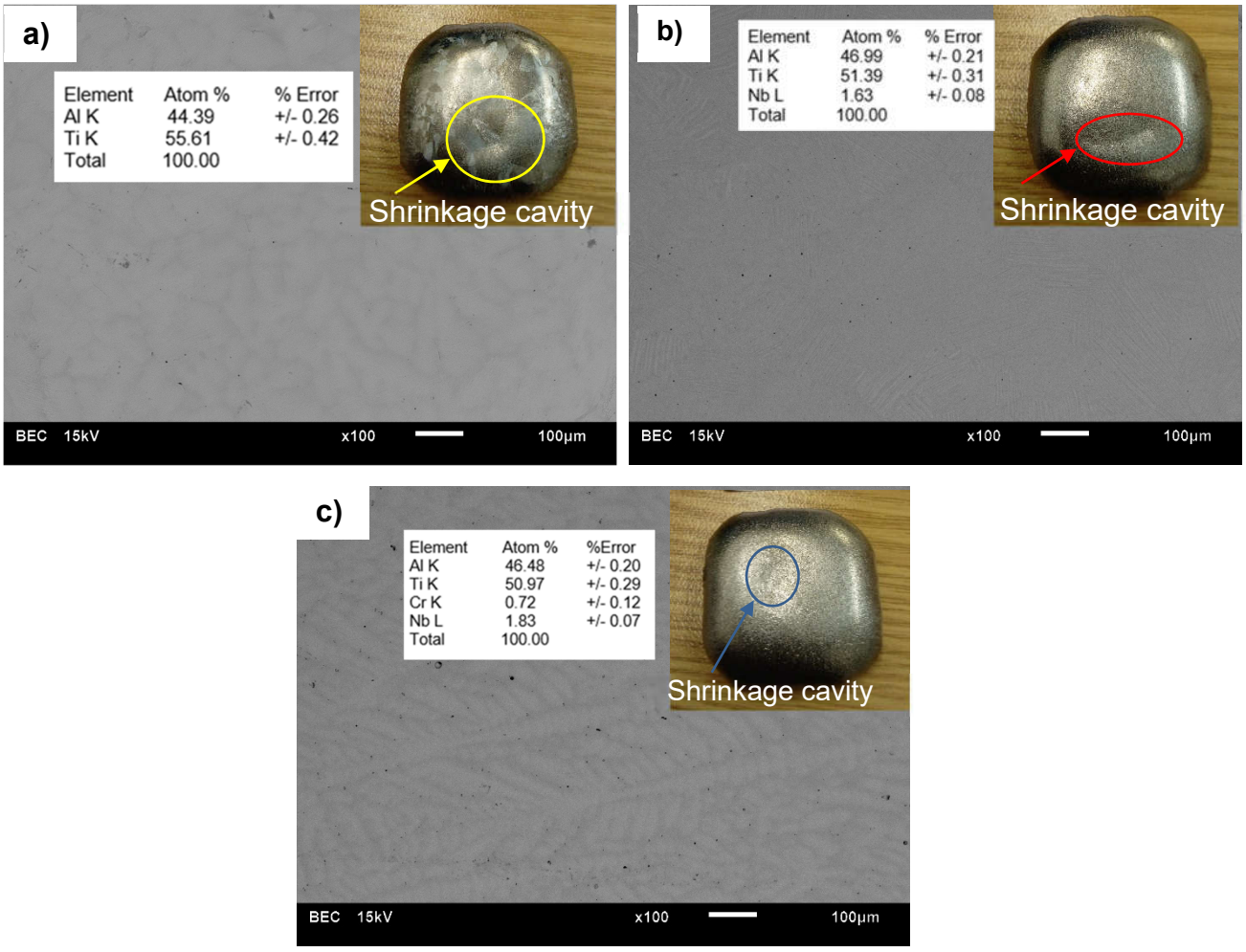

Figure 4.12. SEM-BSE micrographs of the arc-melted (a) binary, (b) ternary and (c) quaternary alloys.

The relative densities of the compacted specimens and the as-melted buttons are shown in **Fig. 4.13**. The relative densities in the green state were lower than the arc melted buttons. The melting process improved the relative densities by eliminating the porosity present on the cold pressed samples **Fig. 4.8**, and **Fig. 4.9** inset. However, emphasis should be made that the as-melted alloys could not achieve 100% densification, which was thought to be attributed to the presence of shrinkage cavities in **Fig. 4.12a-c**, comprising of a certain amount of pro-eutectoid Al-rich inter-dendritic γ-phase.

The arc-melted binary TiAl sample has the highest relative density compared to the ternary and quaternary sequentially. The slight decrease in the relative densities of ternary and quaternary alloys was attributed to the retained brittle β-phase at ambient temperature, which is enhanced by the β stabilizers viz. the Nb and Cr elements.

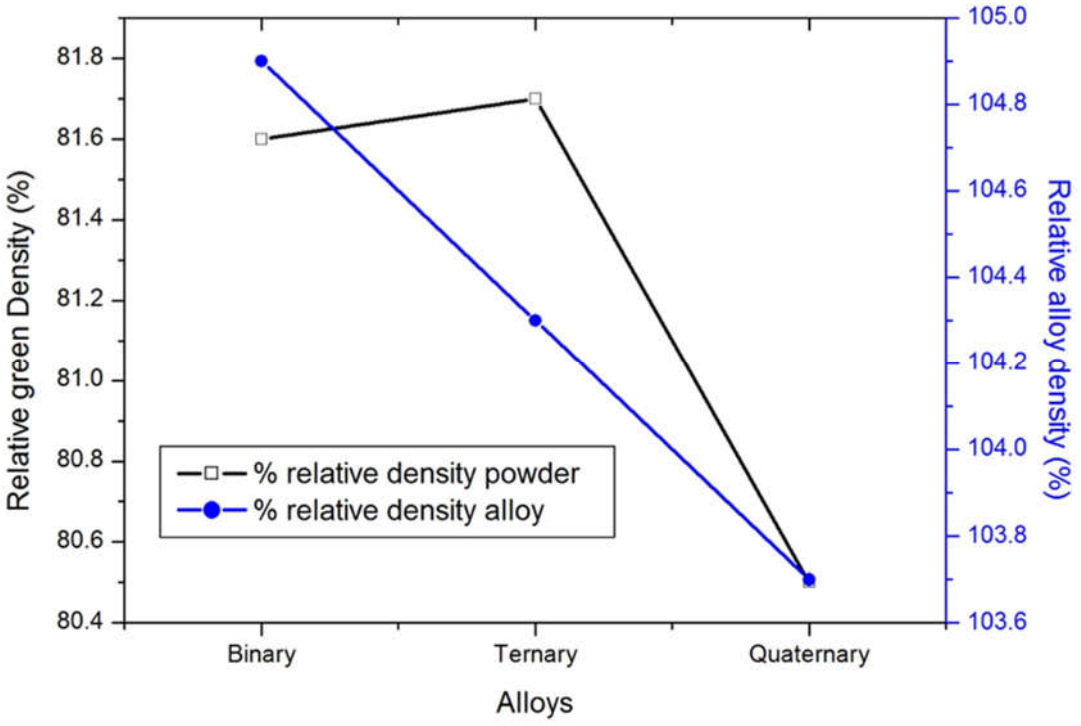

Figure 4.13. Comparative relative densities between the green compacts and the arc melted buttons.

The micro-analysis using SEM-EDX illustrated in **Fig. 4.14- 4.16**, shows that elemental maps were distributed evenly with the percentage elemental quantity that is more or less than the starting composition of binary, ternary and quaternary alloys, respectively. On the other hand, it has been shown [116] that the as-cast dendritic structures can be altered via thermal treatment in the α-phase domain, in order to produce homogeneous structures consisting of fully lamellar structures with spheroidal and Widmanstätten laths morphology.

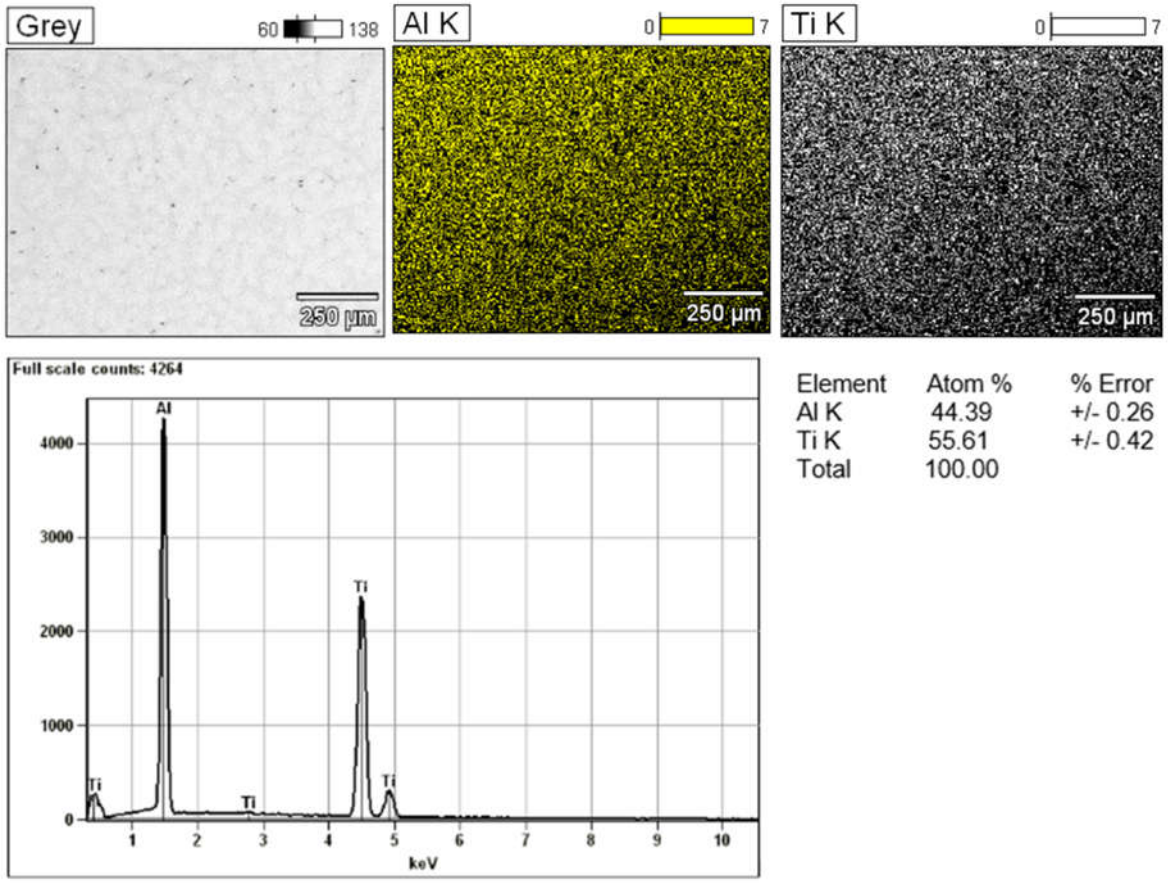

Figure 4.14. EDX spectra of the melted binary (TiAl) alloy.

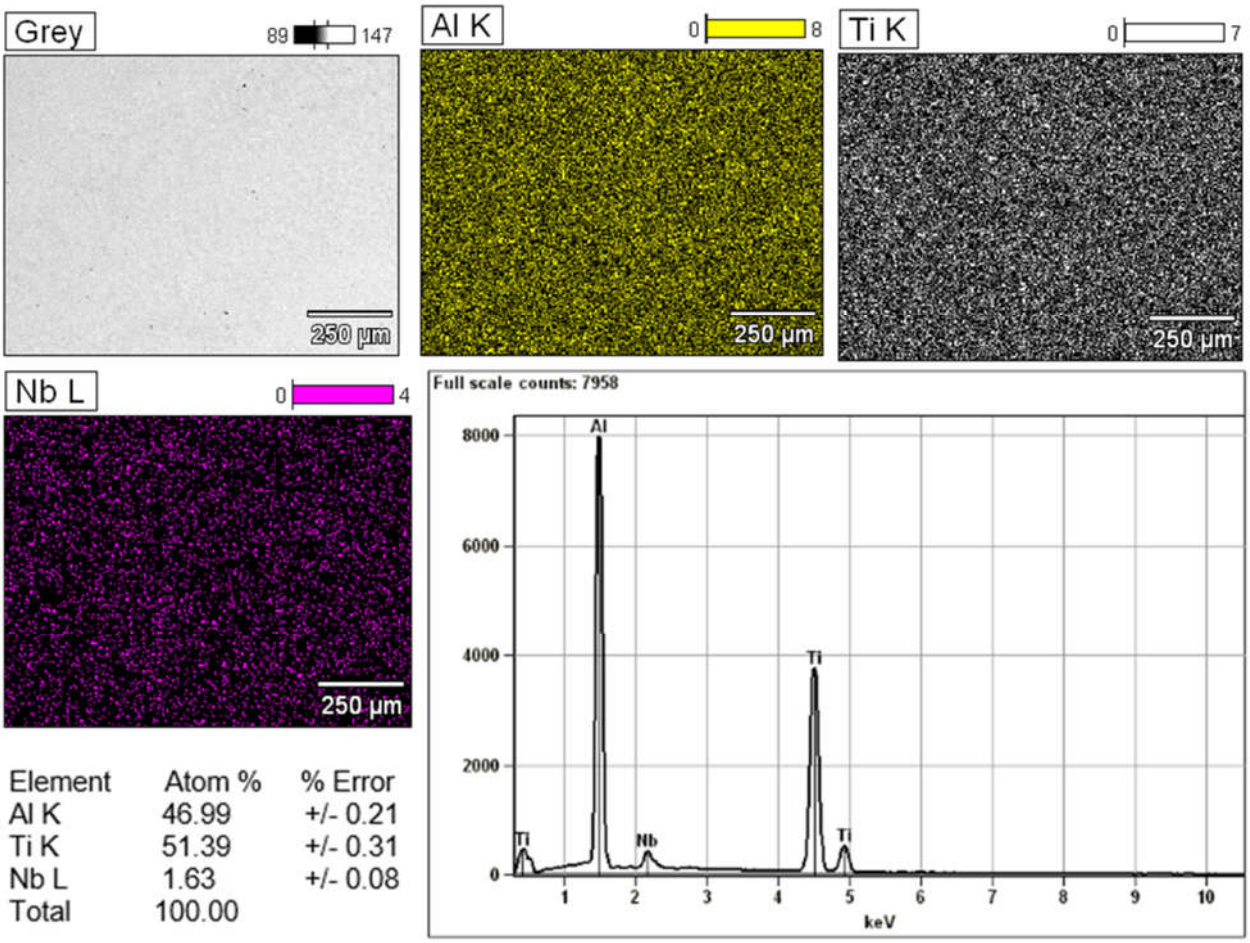

Figure 4.15. EDX spectra of the melted ternary (TiAlNb) alloy.

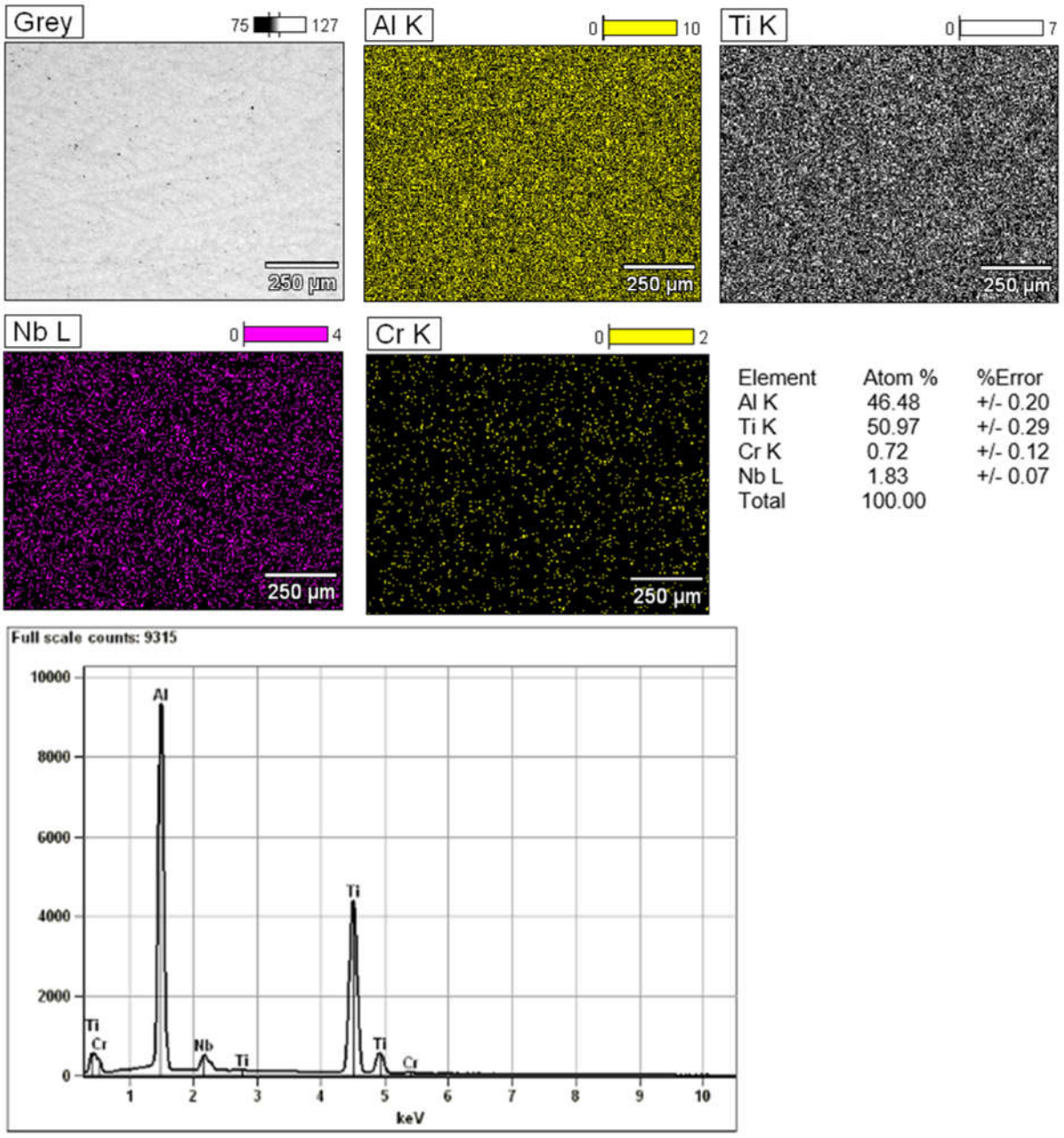

Figure 4.16. EDX spectra of the melted quaternary (TiAlNbCr) alloy.

4.2.6. EBSD analysis

EBSD mapping was conducted to characterize the as-vacuum melted γ-TiAl based alloys solidified from β-phase domain. The EBSD results revealed that stable phases at ambient temperature (RT) in the alloys were comparable to the one found in this work **Section 4.6** which is also published in [79], presented in **Table 4.2.** These results were comparable with experimental data found in [70], [16]. Also shown in **Table 4.2** is the HCP α_2-Ti_3Al with a DO_{19}– ordered structure, which was formed through an ordering reaction during solidification of high temperature, disordered α-phase [70].

Additional phases substantial at RT in the alloys are given in **Table 4.3**. Moreover, the Ti cubic structure was found in all the studied alloys, and the ternary and quaternary alloy exhibited the FCC structure.

Table 4.2. Phase acquisition.

Phase Name	*a* (Å)	*b* (Å)	*c* (Å)	α (°)	β (°)	γ (°)	Space group
α	3.20	3.20	5.20	90.00	90.00	120.00	194
α_2-(Ti_3Al)	5.72	5.72	4.64	90.00	90.00	120.00	194
α_2	5.73	5.73	4.64	90.00	90.00	120.00	194
γ	2.81	2.81	4.08	90.00	90.00	90.00	123

Table 4.3. Phase acquisition of the γ-TiAl based alloys.

Phase Name	a (Å)	b (Å)	c (Å)	α (°)	β (°)	γ (°)	Space group
Titanium cubic	3.19	3.19	3. 19	90.00	90.00	90.00	229
Aluminium FCC	4.05	4.05	4.05	90.00	90.00	90.00	225

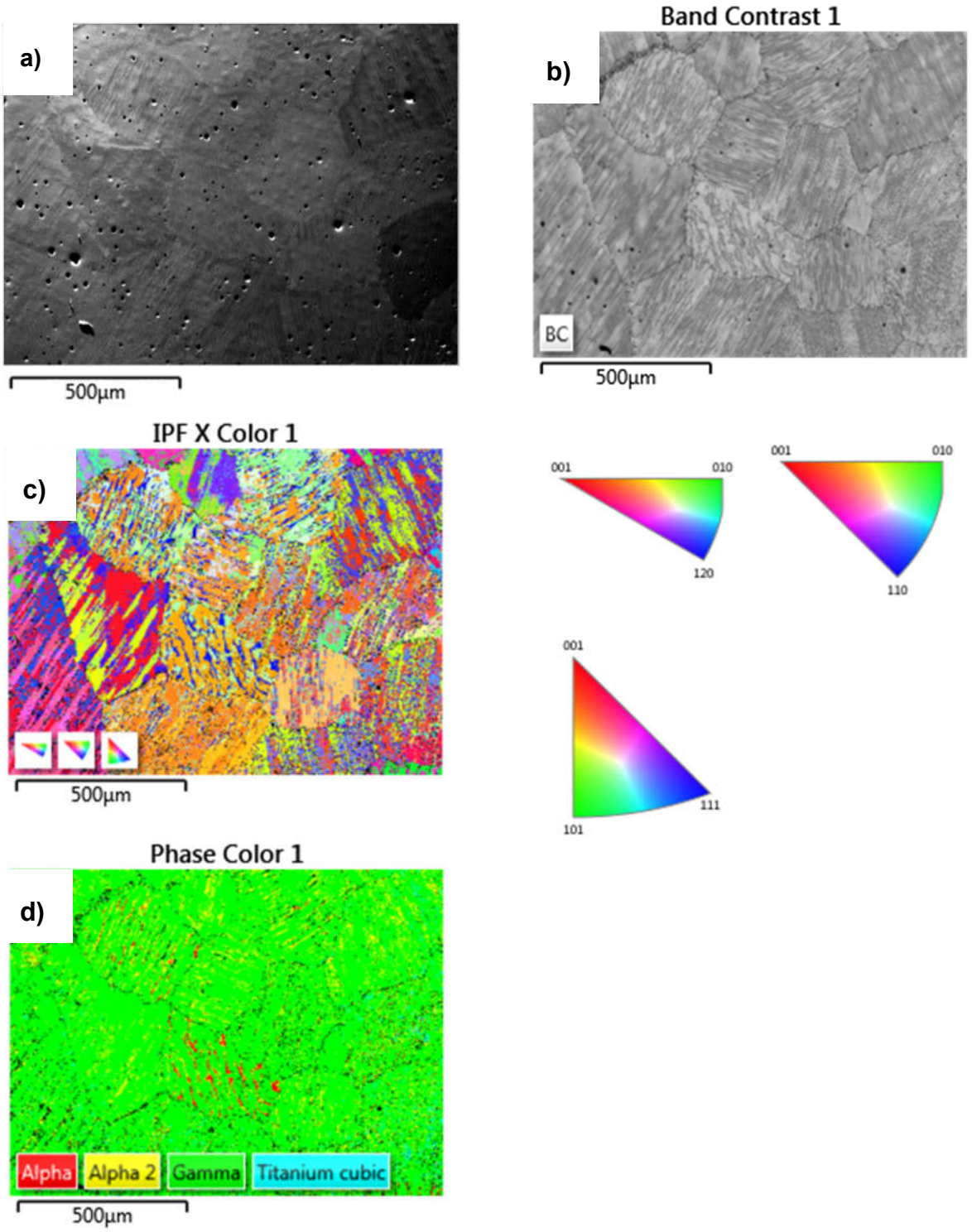

Figure 4.17. EBSD maps of the binary (Ti-44Al) alloy: a) electron image; b) band contrast; c) inverse pole figure (IPF) map and d) phase color map.

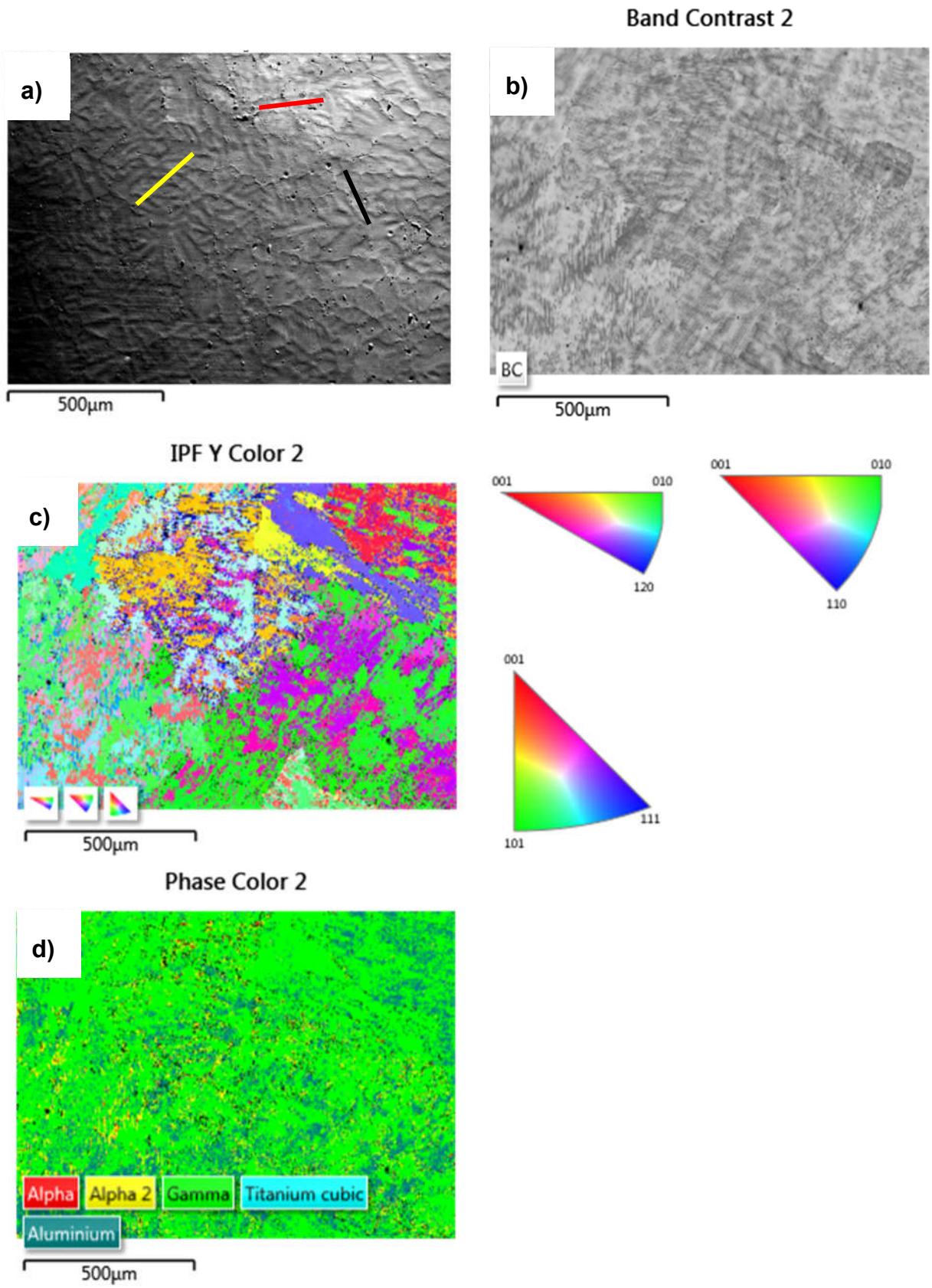

Figure 4.18. EBSD maps of the ternary (Ti-45Al-2Nb) alloy: a) electron image; b) band contrast; c) inverse pole figure (IPF) maps and d) phase color map.

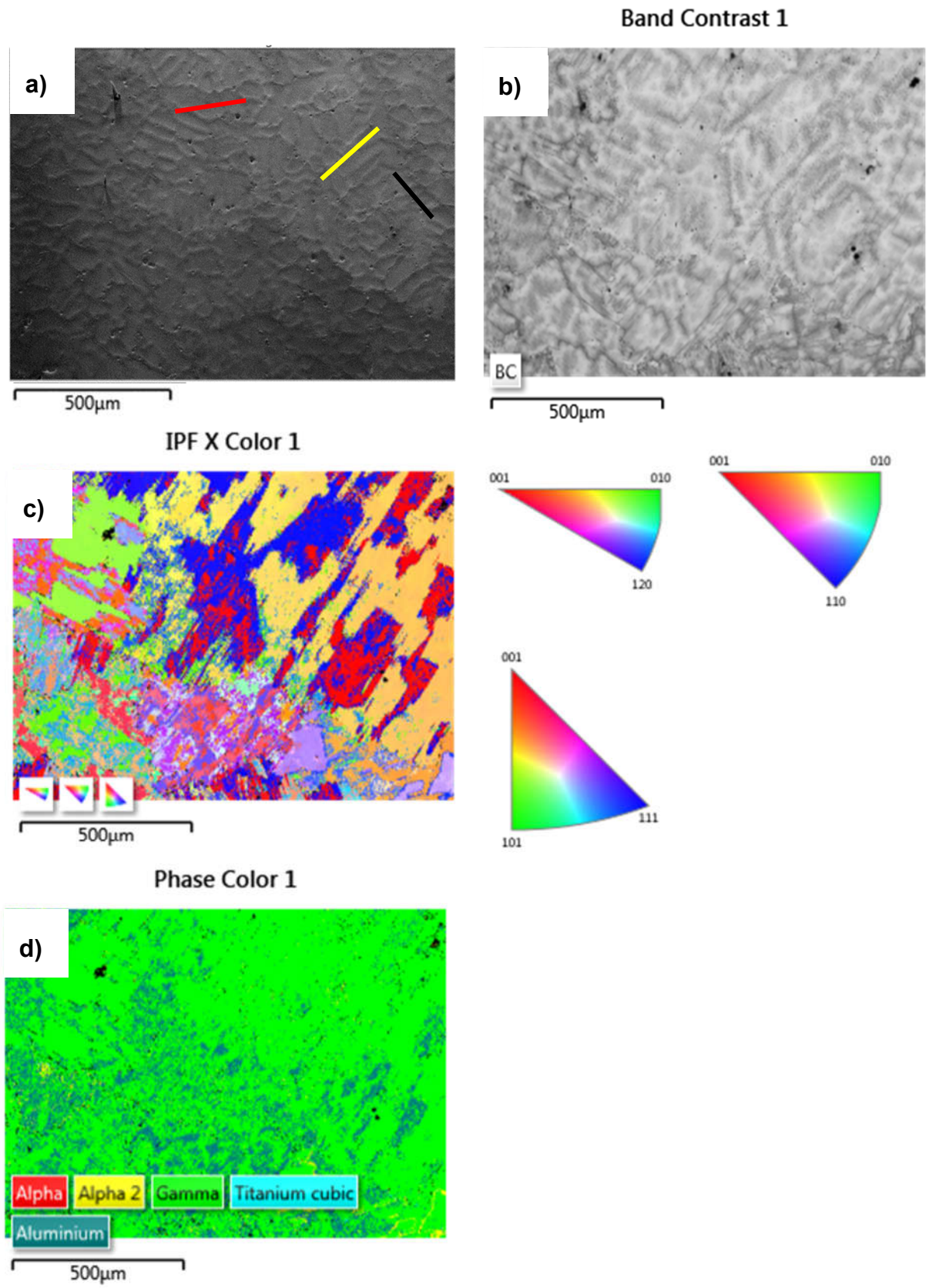

Figure 4.19. EBSD maps of the quaternary (Ti-45Al-2Nb-0.7Cr) alloy: a) electron image; b) band contrast; c) inverse pole figure (IPF) maps and d) phase color map.

Fig. 4.17-19 shows EBSD orientation maps of the binary (TiAl), ternary (TiAlNb), and quaternary TiAlNbCr alloys, showing that the dominant phase in the studied alloys was the γ-phase, indicated by **Fig. 4.17d**, **Fig. 4.18d,** and **Fig. 4.19d**. The phase acquisition of the respective alloys is represented in **Tables 4.2** and **4.3**. A considerable number of γ-grains are recrystallized. On one hand, it is shown in **Fig. 4.17c**, **Fig. 4.18c** and **Fig. 4.19c** that the grain orientation of the recrystallized γ-grains were relatively random, which imply that there is no obvious texture attained in the as-cast alloys solidified from β-phase domain, during arc melting technique. The γ-face centered tetragonal structure had *c/a*=1.45. The identified domain boundaries follow the lines of the band contrast in **Fig.4.17b**, **Fig. 4.18b** and **Fig. 4.19b**. The band contrast image for the binary alloy in **Fig. 4.17b** displays a larger colony size with a full lamellar structure composed of (α_2+γ) which had an average size of about 250 μm. However, the small colony size was the result of β-phase solidification which avoided the peritectic transformation in traditional TiAl alloy which had a colony size of 1000 μm [117].

Alloying elements such as Nb, Cr, W, Mo are added to TiAl alloys to improve elevated temperature resistance and lamellar structure stability, in addition to stabilizing the β-phase [118], [119]. **Fig. 4.18b** and **Fig. 4.19b** show band contrast structures of Ti-45Al-2Nb and Ti-45Al-2Nb-0.7Cr alloys, respectively. A large number of β/β_0 phase is distributed at (α_2+γ) lamellar colony boundaries and inside the (α_2+γ) colonies, and consequently divided the large lamellar colonies into many fine lamellar grains when Nb and Cr contents were 2 (at. %) and 0.7 at. %, respectively. There was no significant difference in the structures between the two alloys, except that the volume fraction of the β/β_0 may be slightly greater than Ti-48Al-2Nb alloy. Furthermore, it was noticed that the electron micrographs in **Fig. 4.18a** and **Fig. 4.19a** exhibited three orientations of the lamellar structure which were at 90°, 45°, and parallel to the primary growth direction of the β-dendrite (the black, red, and yellow lines, which represented the angle of 0°, 45°, and 90°, respectively). As the precipitation of α-phase at the parent β-phase follows a so-called Burgers OR ($\{111\}_\beta$ || $(0002)_\alpha$ and $<1\ \bar{1}\ 0>_\beta$ || $<1\ 1\ \bar{2}\ 0>_\alpha$) [79].

According to Singh et al. [120], the (α_2+γ) lamellar structure formed by the reaction of α→α_2+γ following the Blackburn OR which has the above three angles with the residual β/β_0-phase. Moreover, the preferential growth of β-phase during solidification is ⟨100⟩ axis, and the three equivalent directions, namely [100], [010] and [001] are indicated by inverse pole figure maps in **Fig. 4.17c**, **Fig. 4.18c** and **Fig. 4.19c** [116]**.**

4.2.7. Conclusions

The binary (TiAl), ternary (TiAlNb) and quaternary (TiAlNbCr) blended elemental powders were successfully mechanically compacted by uniaxial cold-pressing which constituted

bonding between particles, whereas alloying was achieved via arc-vacuum melting. The cold pressed samples were sectioned to study the particle arrangement and composition using the SEM/EDX technique. It was evident that the Al particles migrated to the surface in contact with the die facets. The FEA analysis [77] confirmed the high stress region to be the surface, while the core of the compact had low stress regions. The XRD analysis detected elemental Ti, Al and Nb on binary and ternary samples. However, on the quaternary sample the rhombohedral phase was detected and was attributed to the change in crystal orientation due to welding induced by cold pressing. The Raman analysis was consistent with the XRD results. Due to melting, the relative densities of the melted alloys were improved, compared to the green compacted specimens. However, Nb and Cr additions made the relative densities to be slightly lower than that of the binary as a result of β-phase formation.

4.3. The vacuum melted γ-TiAl (Nb, Cr, Si)-doped alloys and their cyclic oxidation

4.3.1. Introduction

Ti and its alloys are widely used and preferred materials for aerospace, medical, and nuclear field because of their attractive properties such as light weight but high strength as well as corrosion resistance. These alloys encounter challenges due to rapid gaseous corrosion at high application temperatures. The Ti-based alloys with emphasis on γ-TiAl intermetallic alloys are potential candidates for many high-temperature structural applications. It is one of the most important research material for scientists and engineers aiming to minimize the effect of both oxidation and oxygen embrittlement when these materials are in applications. One of the γ-TiAl intermetallic competitors' material for high temperature applications are NiAl alloys [121]–[123]. Different approaches have been adopted to resolve the high temperature oxidation, leading to the development of coatings to prevent the detrimental environmental effect on these alloys [124]–[126]. The heat and creep-resistant intermetallic substrates deposited with nanocrystalline γ-TiAl intermetallic TiAl-based coatings micro-alloyed with Cr atoms gave very good oxidation resistance at 1173 K [124]. $TiAl_3/Al_2O_3$ composite powders were prepared by high energy ball milling and subsequent heat treatment, then deposited on γ-TiAl intermetallic alloys, and decreased the oxidation rate of the γ-TiAl substrate [127] and Cr_2AlC coatings with better Al rich oxide scale [128]. The laser aided manufacturing of γ/β-Al_2O_3 coating on NiCrAlY coatings proved to withstand the operating temperature of 1200°C for ten cycles [129]. Another method of improving the properties of γ-TiAl alloys is to modify their chemical composition with alloying elements. For example, doping of traditional high temperature alloys such as β-NiAl to improve cyclic oxidation have been investigated [121], [130], [131]. Also, attempts to improve the oxidation resistance of Ti-Al intermetallic phase

based alloys showed positive results [132]–[136]. Ding et al. [137] investigated Nb-doped TiAl for cyclic deformation and microstructure evolution of high Nb containing TiAl alloy during high temperature low cycle fatigue. In this study, the investigation focused on the innovatively mixture of alloying elements to produce the binary, ternary, quaternary and quinary alloys by the addition of the Nb, Cr and Si γ-Ti-Al alloys. The arc button melting performed under vacuum was employed to manufacture the four γ-TiAl based alloys of nominal composition of Ti-48Al, Ti-48Al-2Nb, Ti-48Al-2Nb-0.7Cr, and Ti-48Al-2Nb-0.7Cr-0.3Si. The primary aim of this investigation was to analyze these novel alloys for improved oxidation resistance in air at 900 °C for 9 cycles of 900 h each.

4.3.2. Analysis of the structure and properties of the as-melted four alloys

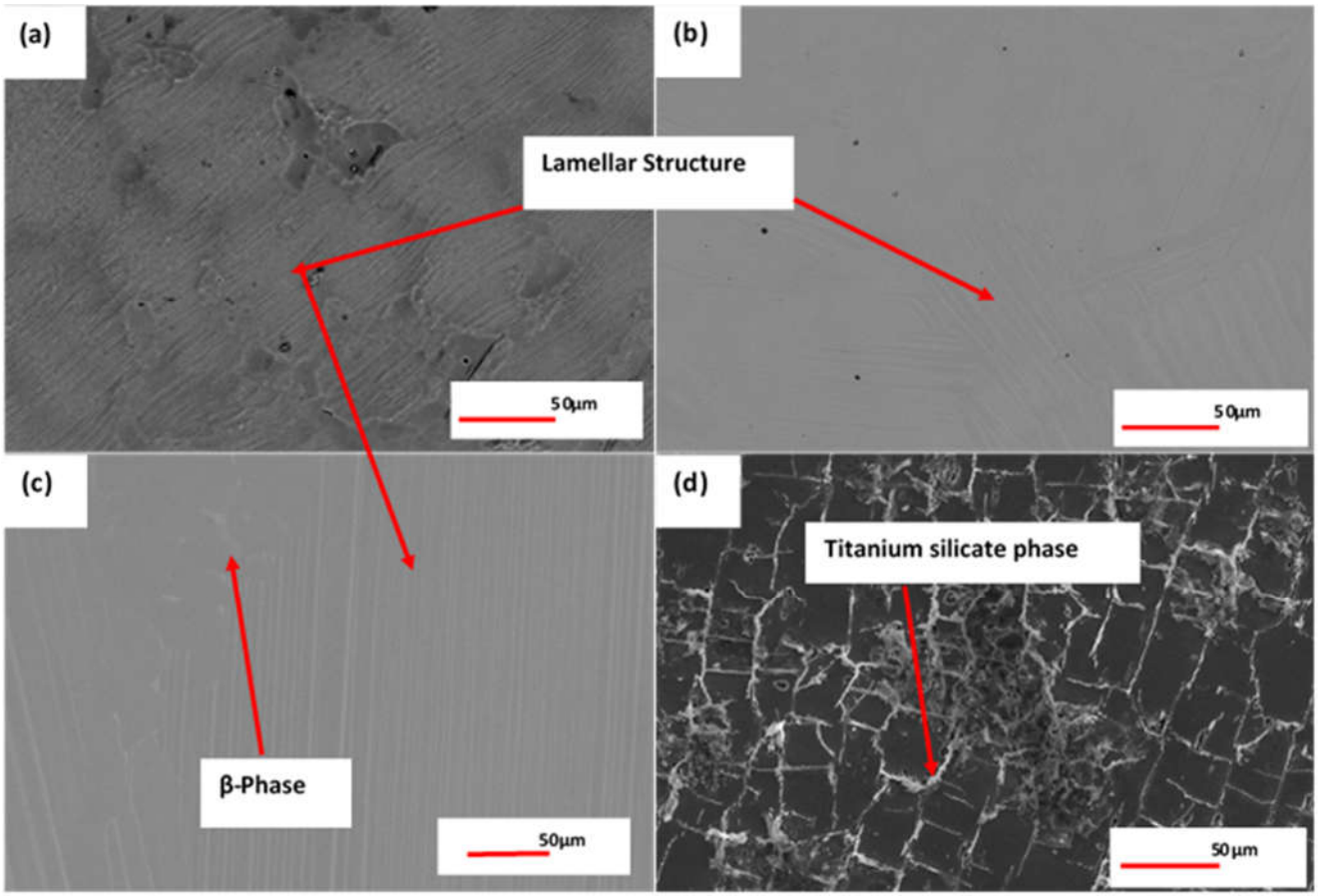

Figure 4.20. The SEM-BSE micrographs of (a) binary (TiAl), (b) ternary (TiAlNb), (c) quaternary (TiAlNbCr) and (d) quinary (TiAlNbCrSi) alloys.

Fig. 4.20 shows the microstructures of the binary TiAl, ternary TiAlNb, quaternary TiAlNbCr and quinary TiAlNbCrSi alloys. The multi-phase structures and the solute segregation were observed in the investigated γ-TiAl based alloys, which contributes to the mechanical properties of the corresponding alloys. The microstructures of the three alloys; binary TiAl, ternary TiAlNb, quaternary TiAlNbCr comprised γ-TiAl lamellar structure. The addition of Nb

to the TiAl phase diagram led to the solidification behavior that is different from that of binary TiAl alloy system. Liu et al. [98], reported that according to the partial TiAlNb phase diagram, the Nb addition can increase the melting point nearly 100 °C and promote β-phase zone shifting to the high Al zone in the Ti-Al binary system inducing the multi-phase structure (α_2/γ lamellar, B2 phase). As a result of this multi-phase microstructure, it quite challenging to optimize the mechanical properties of this TiAlNb [99]. As shown in **Fig 4.20b**, the ternary alloy displayed evidence of the elongated ordered β-phase found in the interdendritic regions of the structure. Furthermore, the quinary microstructure revealed block-layered structures. The chemical analysis of the four γ-TiAl based alloys synthesized by arc button melting are shown in **Table 4.4**.

Table 4.4. Chemical composition (at. %) of the binary (TiAl), ternary (TiAlNb), quaternary (TiAlNbCr) and quinary (TiAlNbCrSi) alloys.

γ-TiAl based alloys	Ti		Al		Nb		Cr		Si	
	At.%	Error	At.%	Error	At.%	Error	At.%	Error	At.%	Error
Binary	55.7	±0.41	44.3	±0.25	-		-		-	
Ternary	53.1	±0.35	45.8	±0.23	1.8	±0.06	-		-	
Quaternary	51.0	±0.29	46.4	±0.20	1. 9	±0.06	0.7	±0.08	-	
Quinary	51.6	±0.3	45.6	±0.2	1.9	±0.06	0.7	±0.08	0.3	±0.06

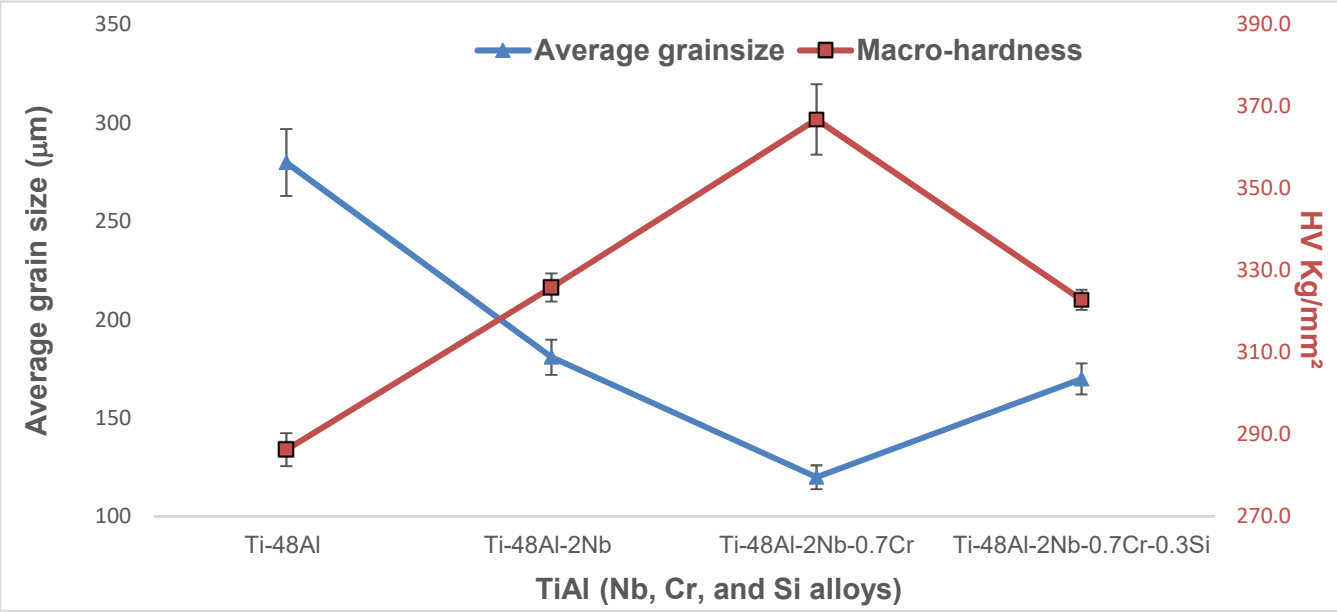

Figure 4.21. The macro-hardness and grain size of the as-cast binary (TiAl), ternary (TiAlNb), quaternary (TiAlNbCr) and quinary (TiAlNbCrSi) alloys.

Fig. 4.21 shows the relationship between the Vickers macro-hardness and grain sizes of γ-TiAl based alloys except the quinary alloy is added. The binary TiAl alloy had of the largest grain size of 370 μm and the lowest hardness value of 286 HV, respectively. It follows that addition of Nb in TiAl, to form a ternary alloy, reduced the grain size to 180 μm and increased hardness to 326 HV. Furthermore, the quaternary alloy showed the smallest grain size (120 μm) and high hardness (368 HV). This grain refinement behavior, proved to be as a result of the combinational effect of Nb and Cr on γ-TiAl alloy. The alloying elements Nb and Cr are solid solution strengthening elements or beta stabilizers while Si renders particle strengthening or precipitation elements [138]. In the current study, Nb and Cr evidently reduced the grain size of the TiAl alloy. The as-cast quaternary alloy microstructure was composed of the (α_2+γ) lamellar structure and isolated B2 phase. According to Liu et al. [98], the hardness values have a linear relationship with the yield strength in solidified TiAl alloys. The finer the grain size, the higher the hardness and strength, but the poorer the ductility. In the quinary alloy (TiAlNbCrSi), the addition of Si resulted in the slight increase in grain size (170 μm) and macrohardness of 315 HV, **Fig. 4.21**. This combination of hardness and grain size was attributed to the presence of second phase titanium silicate (Ti_5Si_3) along the grain boundaries of the quinary alloy. This novel chemical combination in the Ti-45Al-2Nb-0.7Cr-0.3Si quinary alloy in the as-cast condition yielded ultrafine lamellar spacing, **Fig. 4.20d**.

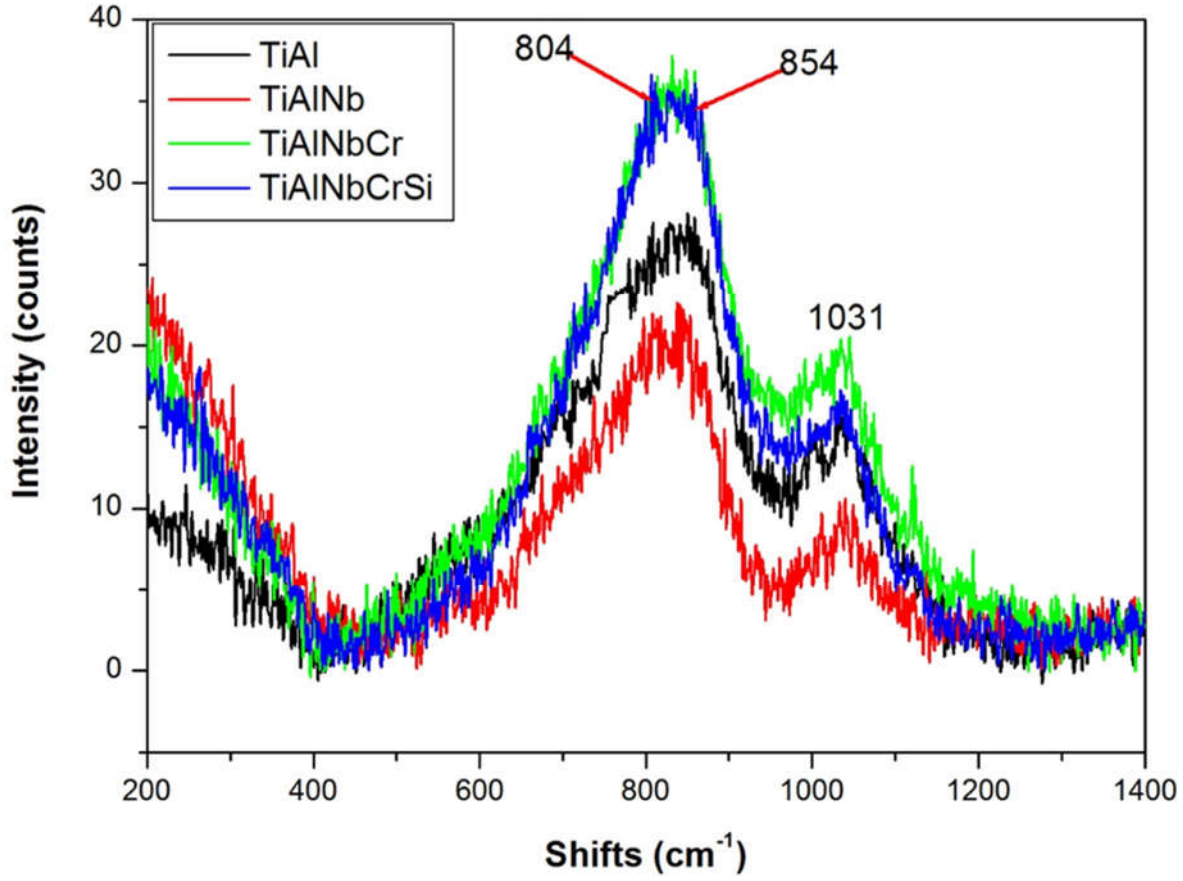

Figure 4.22. Raman spectra of the binary (TiAl), ternary (TiAlNb), quaternary (TiAlNbCr) and quinary (TiAlNbCrSi) alloys.

Raman scattering is a dominant and non-destructive technique used to evaluate the vibration modes of the microstructure [109]. **Fig. 4.22** shows the Raman spectra of the four as-melted alloys. All alloys, displayed similar Raman vibration peak positions. The first peak appeared as a split peak detected at 804 and 854 cm^{-1}, while the third peak was at 1031 cm^{-1} wavelength due to Ti-Al bonding vibration. The quaternary TiAlNbCr and quinary TiAlNbCrSi alloys had the most intense peaks. These alloys have more alloying elements which seem to increase the peak intensities. The ternary TiAlNb alloy has the shortest peaks. The Raman peak at 854 cm^{-1} and 1033 cm^{-1} were Ti related and previously found in Ti-based samples [110]–[112]. The as-melted binary, ternary and quaternary alloys exhibited two peaks at 826 cm-1 and 1038 cm-1, respectively. The peak positions are driven by the alloying element in Ti due to Ti /alloy bonding vibration [113],[114],[139].

4.3.3. Cyclic oxidation of the four alloys

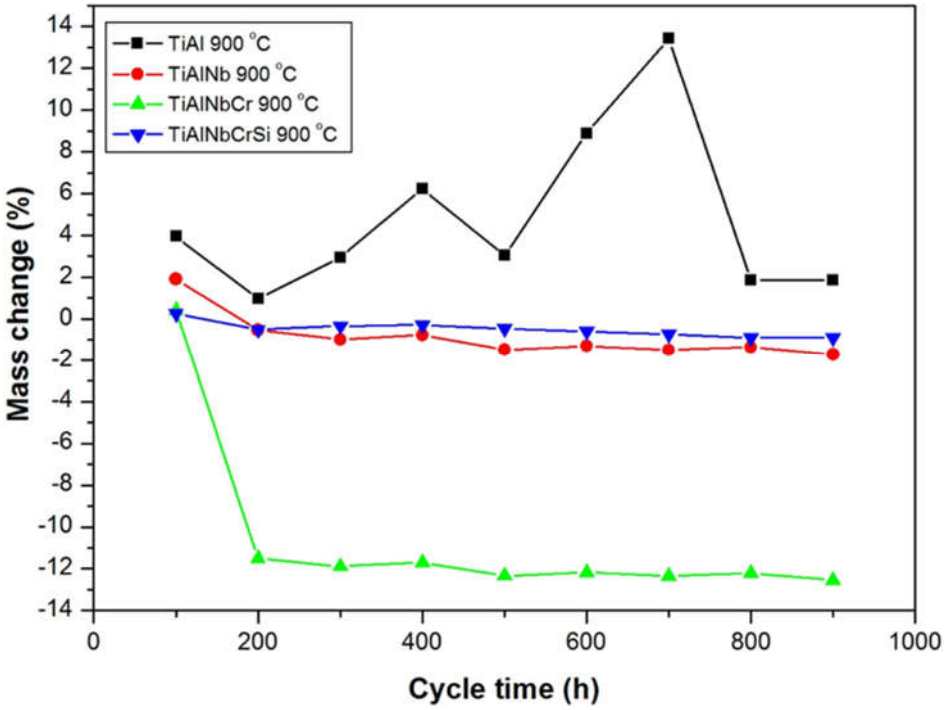

Figure 4.23. Cyclic oxidation performed at 900 °C for 900 h on the binary (TiAl), ternary (TiAlNb), quaternary (TiAlNbCr) and quinary (TiAlNbCrSi) alloys.

Fig. 4.23 shows the cyclic oxidation performed at 900 °C for 900 h on the binary (TiAl), ternary (TiAlNb), quaternary (TiAlNbCr) and quinary (TiAlNbCrSi) alloys. Due to oxide formation on the surface, the four alloys initially showed a sharp initial negative mass change during the first cycle (100 h) of oxidation. Following to longer exposure times erratic mass increase on the binary alloy was observed, but became stable between 800 and 900 °C. The binary alloy showed the rapid formation of the oxide scale. After the seven cycles, a significant mass loss associated with spallation and oxide regrowth has emerged. On the ternary alloy there was no measurable mass loss found. Although the quaternary alloy was stable from 200-900 °C, a large negative mass change was recorded from 100-200 h exposure time. Furthermore, the quinary alloy resembled the ternary alloy, since both showed more resistance to cyclic oxidation than the binary and quaternary alloys. Addition of 2 at.% Nb to γ-TiAl intermetallic alloys improved oxidation resistance and inhibited oxide growth at high temperatures by enhanced adherence of the oxide scale with the underlying substrate [140]. Furthermore, the quinary illustrated the best performance compared to all the alloys, its percentage mass change was negligible throughout the 900 h exposure time in the air. It indicated a slight reduction in mass change and remained constant until the end of 900 h cycle. Although air is comprised of a large quantity of nitrogen, Ti and Al have higher affinity for oxygen than nitrogen. However, nitrogen occupies oxygen vacancies, taking advantage of instability

caused by vibrations at high temperature on oxides to form titanium oxynitride (TiO_2-xNx). The oxynitrides layer formation reduced further oxygen diffusion into the surface [78].

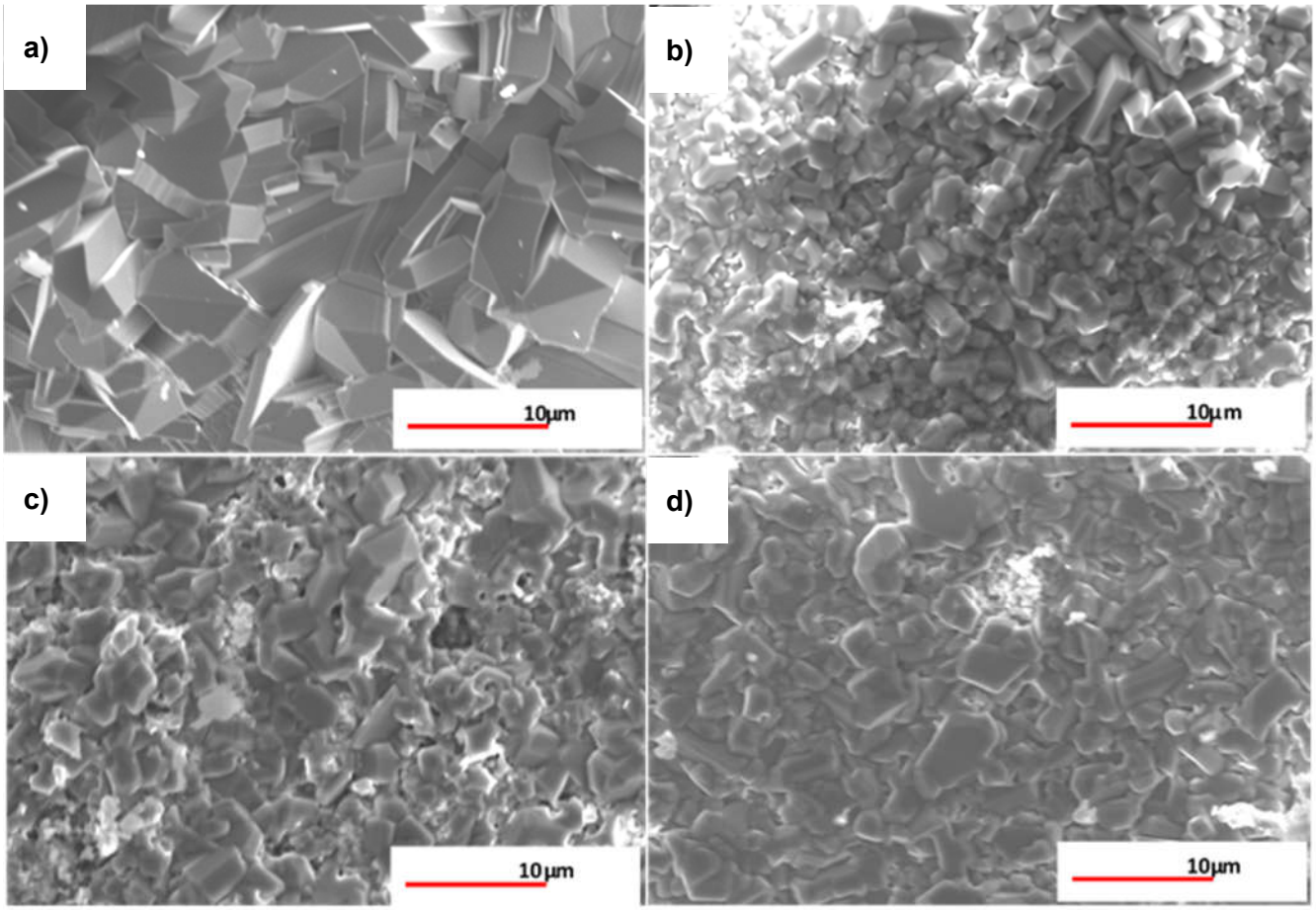

Figure 4.24. SEM-SEI images showing surface oxides formed on (a) binary (TiAl), (b) ternary (TiAlNb), (c) quaternary (TiAlNbCr) and (d) quinary (TiAlNbCrSi) alloys.

Fig. 4.24 shows the SEM micrographs of the oxide layers formed on the surface of the alloys. **In Fig. 4.24a**, a prismatic crystalline powder shows a well-defined smooth irregular thin but long particles. The Al content was negligible to induce Al_2O_3 particles on the surface of binary TiAl alloy. This is correlated to the severity of cyclic oxidation observed on the binary alloy shown in **Fig. 4.23**. The ternary alloy scale showed agglomeration of small particles mixed with few particles showing similar features such to those obtained in the binary alloy. This behavior was attributed to the mixed oxide formation in the ternary alloy. **Fig. 4.24c-d** demonstrate almost similar particles shape and orientation.

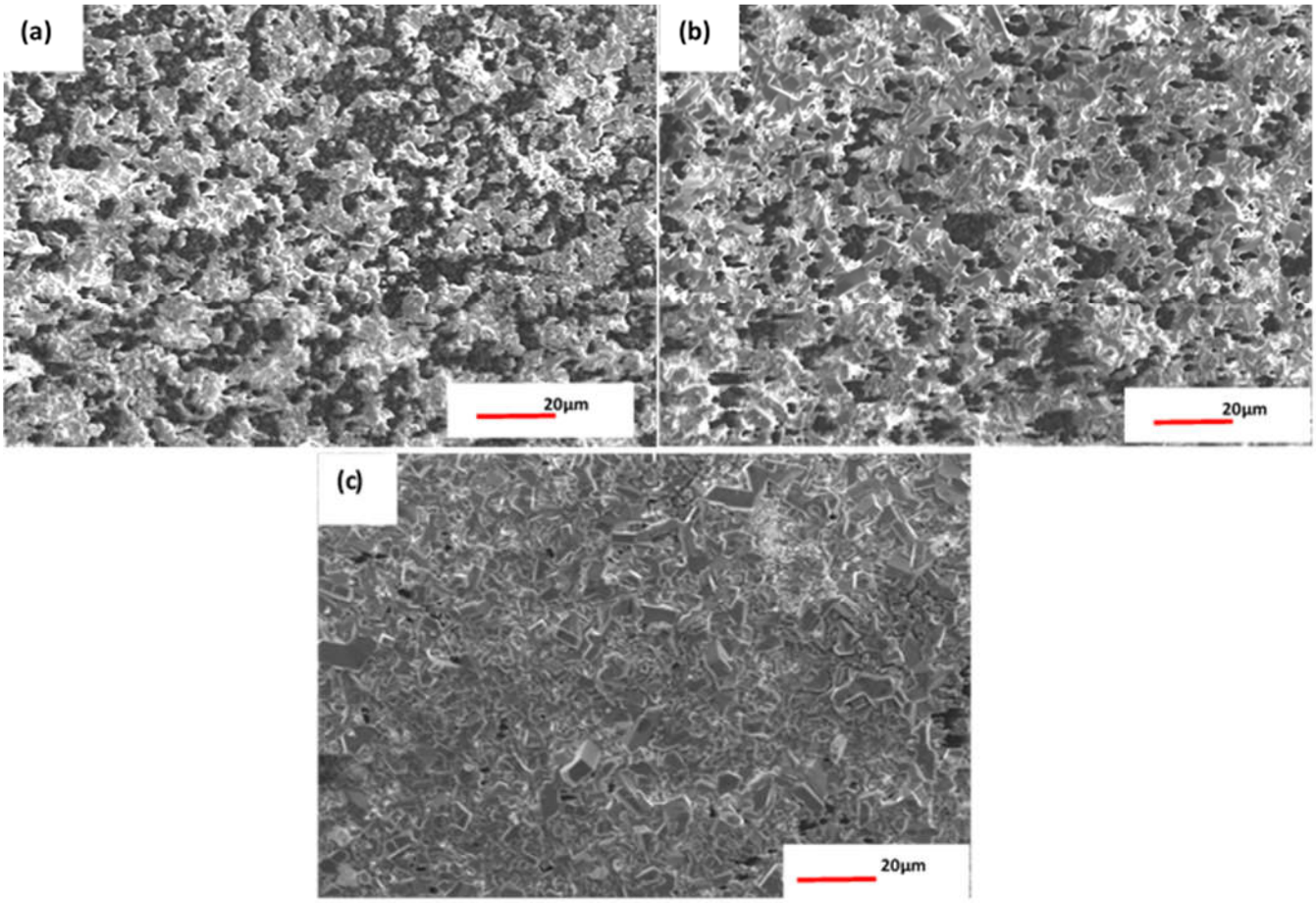

Figure 4.25. SEM-SEI images of Al_2O_3 formed on (a) ternary (TiAlNb), (b) quaternary (TiAlNbCr) and (c) quinary (TiAlNbCrSi) alloys.

The Al_2O_3 particles in the ternary, quaternary and quinary oxide scales are illustrated in **Fig. 4.25**. The ternary SAMPLE **(Fig. 4.25a)** shows a network of interconnected irregular particles. Additionally, the quaternary Al_2O_3 particles **(Fig. 4.25b)** were porous with spider web type shape with features of the ternary oxide. **Fig. 4.25c** shows the quinary Al_2O_3 particles. The morphology of the scale was different from those of ternary and quaternary. The particles were interconnected, non-porous and exhibited agglomeration but irregular in shape. These particles were attributed to nitrogen contamination of Al_2O_3 which improved corrosion resistance [141].

4.3.4. Analysis and characterization of the oxide layers

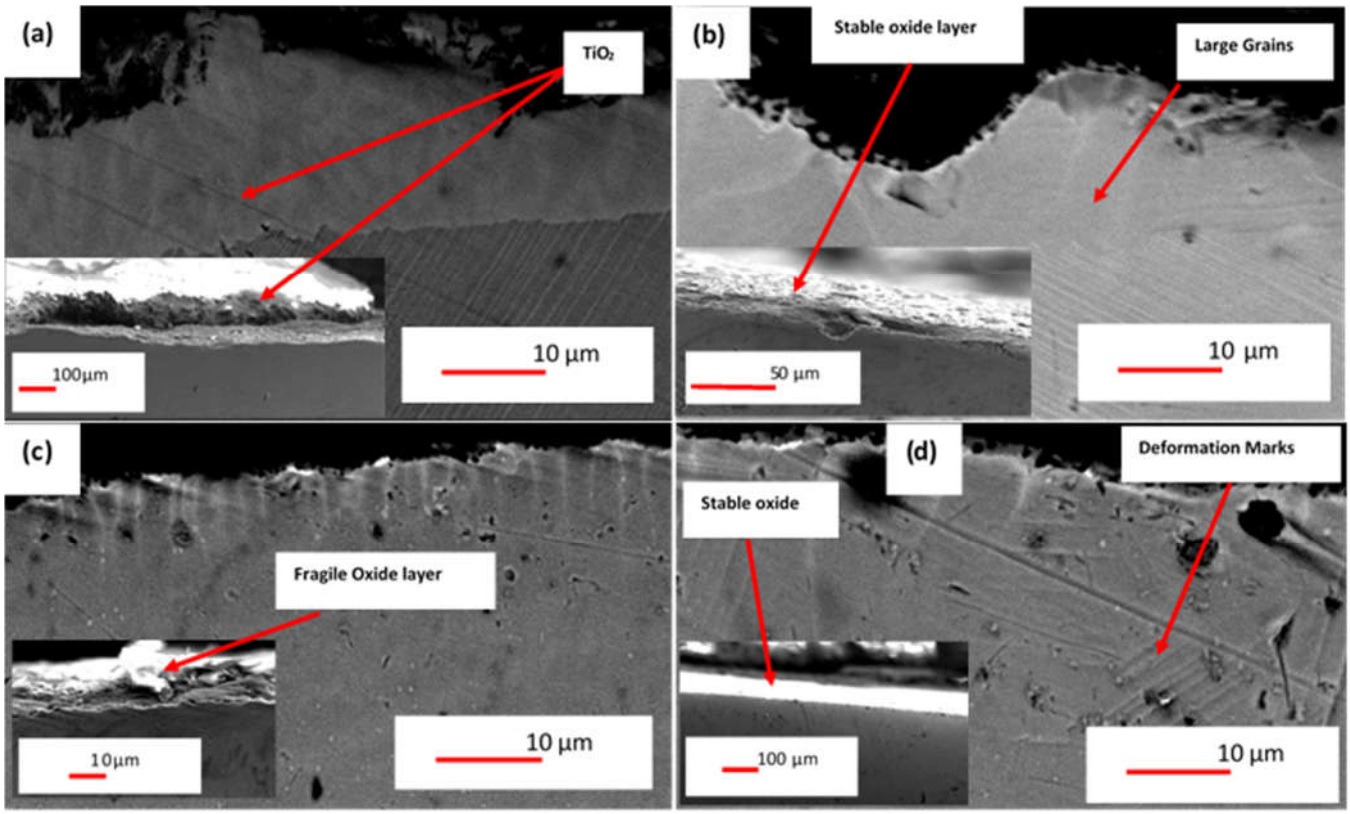

Figure 4.26. SEM images of the transverse sectioned γ-TiAl (a) binary (TiAl), (b) ternary (TiAlNb), (c) quaternary (TiAlNbCr) and (d) quinary (TiAlNbCrSi) alloys.

Fig.4.26 shows cross-sections of the four alloys subjected to cyclic oxidation with the BSE scale images (inserts). The EDX micro-analysis revealed that the primary constituent oxides dominating were alumina and titanium oxide/oxynitrides across the alloys. The binary TiAl alloy was comprised of rutile TiO_2 scale on the surface as shown in **Fig. 4.26a**. The layer displayed the alternating light and dark phases due the presence of nitrogen mainly enclosed in the core. The oxide showed poor adhesive behavior to the parent metal as shown by the chipping of the scale shown in the BSE contrast inserted image. In **Fig 4.26b,** the alternating oxide layers were more adherent due to the Nb presence on the surface of the parent metal influencing the diffusion process by decreasing the oxide scale. The oxide scale comprised layers of TiO_2 and Al_2O_3. Surprisingly, the chemical composition of the scale showed no significant amount of nitrogen. The initial stage of cyclic oxidation promoted Al-rich oxide scale to function as diffusion barrier by resisting the incoming oxygen, and effectively protected the parent metal from further oxidation. Furthermore, the alloy comprised large crystalline grains on the surface of the parent metal, making a clear boundary between the lamellar structure and enlarged grains. **Fig. 4.26c** shows the microstructure of oxidized TiAlNbCr alloy. The alloy oxide scale comprised mixed TiO_2 and Al_2O_3 with nitrogen impurities. The scale showed oxide surface chipping, peeling and was fragile as shown in the BSE inserted image. The initial scale

formation was rich in TiO_2 with alternating layers of Al_2O_3 in other regions of the parent metal surface. The oxides may have penetrated the alloy at weaker grain boundaries such as low angle boundries (LAGB). The TiAlNbCrSi alloy shown in **Fig. 4.26d** showed the most improved cyclic oxidation performance. It was well adhered to the parent metal throughout the cyclic oxidation period. Despite the similarity in cyclic oxidation performance of quinary and the ternary alloy, the quinary alloy demonstrated to its structural integrity by showing no major effect on the microstructure or any observed grain growth **Fig. 4.23**. Interestingly, the deformation marks were observed close to the alloy surface which are attributed to strain or compressive stresses induced by the oxinitride layer favoring the resistance to scale cracking due to mixed oxide/oxynitride structure [43]. Furthermore, the alumina scale exclusively grows by inward oxygen transport, appearing flat and adherent since the new oxide is formed nearly exclusively at the metal/oxide interface [43]. In the current study, the quinary alloy showed a low oxide growth due to the effect of Nb in the diffusion process by decreasing metal/oxygen transport [43], and the ability to form the oxynitride scale.

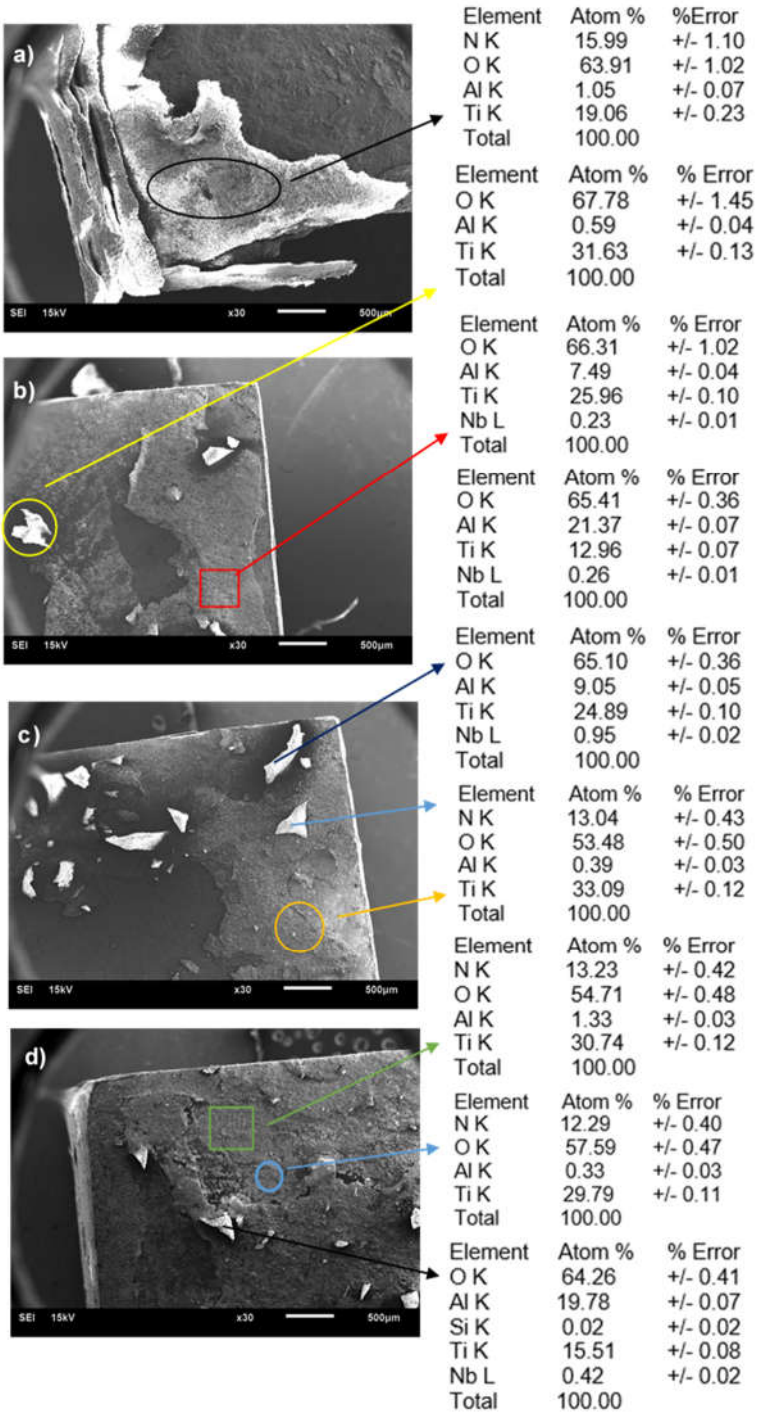

Figure 4.27. EDX analysis of the oxides formed on the (a) binary, (b) ternary, (c) quaternary and (d) quinary.

The EDX analysis was performed on the oxide scales. Since the cyclic oxidation experiment was performed in air, it is logical to consider nitrogen contamination. **Fig. 4.27 a-d** displays the SEM-SEI images of the surface oxides with their corresponding EDX chemical composition. The binary alloy shown in **Fig. 4.27a** resemble a homogeneous oxide scale throughout the specimen attributed to TiO_2 with small amount of Al and N. On one hand, the behavior of oxidation and surface morphology on ternary and quaternary appears similar **(Fig.**

4.27b-c). However, the quaternary alloy illustrated relatively large spallation of oxide particles from the surface of the specimen compared to the ternary alloy. On the other hand, the quinary alloy showed a homogeneous layer of oxide with some areas showing nodule-like pillar TiO_2 growth with the structure of the underlying substrate locally still noticeable. The varying compositions are indicated by the green, blue and black arrows in **Fig. 4.27d**. The light phases comprised low Al content similar to the composition of the binary alloy oxide scale. It is evident from the SEM micrographs of the γ-TiAl based alloys that the presence of Nb minimizes the formation of TiO_2. Fraction of the scale in **Fig. 4.27b-d** had a slightly higher amount of Al content, confirming the formation of Al_2O_3 oxide layer.

The formation of Al_2O_3 **(Eq. 20)** ΔHf = -1676.7 kj/mol is thermodynamically more feasible than the formation of TiO_2 **(Eq. 21)** ΔHf = -945 kj/mol at 900 °C. However, due to prolonged exposure to air, γ-alumina phase absorbs the nitrogen ions to form a stable AlON, which is a non-stoichiometric compound in nature and rich in defect structures [142]. Additionally, the formation of the oxynitride phases occurs through oxygen substitution by nitrogen. The AlON exhibits excellent stability, chemical and mechanical properties reported by Zhao et al. [141].

$$4Al + 3O_2 \rightarrow 2Al_2O_3 \quad (20)$$

$$Ti + O_2 \rightarrow TiO_2 \quad (21)$$

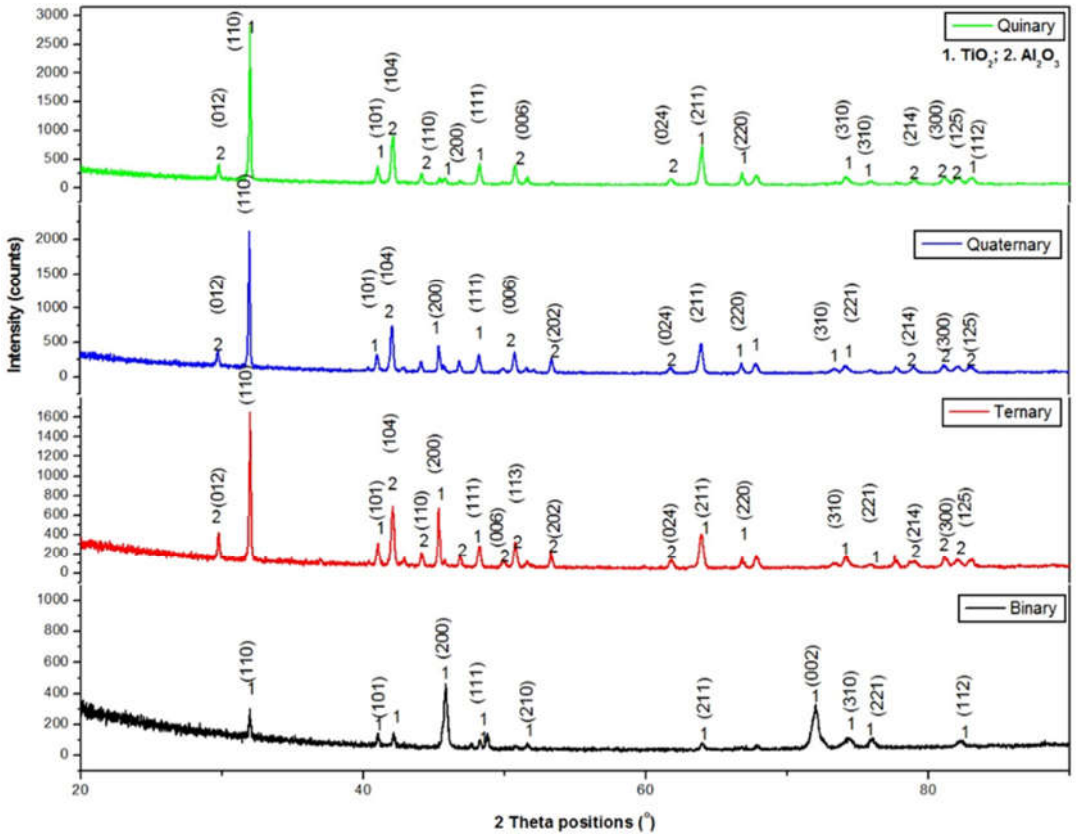

Figure 4.28. XRD pattern of the cyclic oxidation oxides formed on binary (TiAl), ternary (TiAlNb), quaternary (TiAlNbCr) and quinary (TiAlNbCrSi) alloys.

The structural analysis of the oxides formed during the cyclic oxidation of TiAl, TiAlNb, TiAlNbCr and TiAlNbCrSi alloys is shown in **Fig. 4.28**. The XRD analysis confirms the formation of two dominant oxides TiO_2 and Al_2O_3. Both oxide types were detected in the TiAlNb, TiAlNbCr and TiAlNbCrSi alloys with the exception of the TiAl alloy. These findings are in agreement with the SEM-EDX analysis. The TiO_2 belongs to rutile with tetragonal crystal structure and lattice parameters of *a*=4.593 Å; *c*=2.959 Å. The Al_2O_3 has rhombohedral structure of *a*=4.764 Å; *c*=12.997Å lattice parameters. These structures belong to both oxides and oxynitrides ($TiO_{2-x}N_x/Al_2O_{3-x}N_x$) phases due to the detected nitrogen content, especially on the quaternary and quinary alloys.

4.3.5. Hardness properties after cyclic oxidation

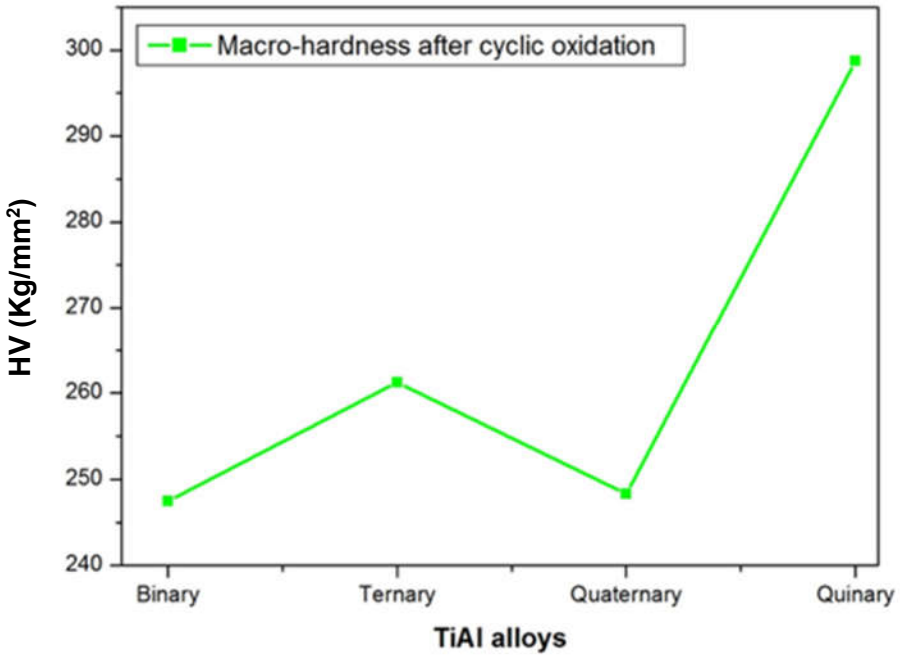

Figure 4.29. Macro-hardness of the binary (TiAl), ternary (TiAlNb), quaternary (TiAlNbCr) and quinary (TiAlNbCrSi) alloys after 900 h exposure at 900 °C in air.

The macro-hardness of TiAl, TiAlNb, TiAlNbCr and TiAlNbCrSi alloys after 900 h exposure at 900 °C was measured. **Fig. 4.29** shows drastic changes on TiAl, TiAlNb, TiAlNbCr when compared to **Fig. 4.21** (macro-hardness curve before cyclic oxidation). The binary TiAl hardness decreased from 286 to 247 HV while TiAlNb hardness was also reduced from 326 to 262 HV. Additionally, the highest rapid reduction in hardness was observed in the TiAlNbCr alloy from 368 HV to 248. This behavior is attributed to the grain growth as well as the brittleness induced by adsorption of oxides on the surface matrix of the alloy. On the contrary, the TiAlNbCrSi alloy reduction was negligible from 323 HV to 298 HV after 900 h at 900 °C. The alloy showed the best performance and these results are in agreement with cyclic oxidation results shown in **Fig. 4.23**.

4.3.6. Conclusions

The γ-TiAl based alloys with nominal compositionS Ti-45Al, Ti-45Al-2Nb, Ti-45Al-2Nb-0.7Cr, Ti-45Al-2Nb-0.7Cr-0.7Si were successfully synthesized by vacuum arc melting. These alloys were subjected to cyclic oxidation at 900 °C for 900 h and the conclusions were:

1. Both Ti-48Al-2Nb and Ti-48Al-2Nb-0.7Cr-0.7Si showed better properties when compared to Ti-48Al and Ti-48Al-2Nb-0.7Cr alloys.

2. In the quinary alloy (TiAlNbCrSi), addition of Si resulted in a slight increase in the grain size (170 μm) and lower hardness (315 HV) than that of the quaternary alloy due to the presence of the second phase (Ti_5Si_3) along the grain boundaries of the former.
3. Due to oxide formation on the surface, the four alloys initially showed a sharp initial weight loss at the beginning of the oxidation during the first cycle. Subsequent to longer exposure times, there was a rapid mass increase on the binary alloy which became stable between 800 and 900 °C. The binary alloy showed the rapid formation of the oxide scale, but after seven cycle's significant mass loss occured, which may be associated with spallation which was followed by oxide regrowth.
4. The Ti-45Al-2Nb and Ti-45Al-2Nb-0.7Cr-0.7Si exhibited improved cyclic oxidation properties, performed at 900 °C for the period of 900 h (9 cycles) compared to the binary and quaternary alloys. However, the Ti-45Al-2Nb-0.7Cr-0.7Si had the best properties among all four alloys due to the Al_2O_3 and oxynitride scale with better adhesion to the parent metal. Its percentage mass change was negligible throughout the 900 h exposure time in the air after 200 h. The alloy almost retained its hardness properties (323 HV-298 HV) and microstructure with deformation marks on the surface of the alloy induced by compressive stresses induced by the oxynitride scale.
5. The main oxide in all four alloys was rutile TiO_2 with some presence of nitrogen in it.

4.4. Effect of Nb, Cr, Si alloying on the microstructure and fracture mode of the new developed TiAl-based alloy

4.4.1. Introduction

The new contribution of high temperature materials with potential use as structural materials, shape memory alloys and coatings is of significance for a range of applications in the materials industry. Single-crystal nickel based super alloy are the most successful gas turbine materials due to their good high temperature mechanical properties obtained from the γ′-Ni_3Al ($L1_2$) phase in the fcc matrix [143]. However, ways to improve mechanical properties for better application of these alloys never cease [144]–[147]. Martensitic transformation and shape memory properties of Ti-50at%Pt are reported to show strain recovery during unloading in the martensite state for samples deformed at room temperature and at 1123 K [148]. Furthermore, iridium and aluminium doping of TiPt was investigated for high temperature properties [148]–[151]. Titanium aluminides aroused the research interest because an excellent combination of low density and high melting temperature with attractive mechanical properties at high temperature and noticeable corrosion resistance offer many fields for the application of α_2- and γ-based titanium aluminides [152]. Gamma-TiAl-based alloys are favorable materials for elevated temperature application due to their low density, high specific strength, stiffness,

oxidation resistance, however with limitation such as poor ductility and toughness [101]. Therefore, alloying γ-TiAl based alloys could improve the mechanical properties of titanium aluminides. The properties of nearly and fully lamellar NbTiAl alloys showed that an increase in creep strain reduces the microstructural stability and alters the microstructure, which reduces the creep life [153]. Section 4.4 addresses the effect of alloying TiAl with Nb, Cr and Si Ti-45Al, Ti-45Al-2Nb, Ti-45Al-2Nb-0.7Cr, Ti-45Al-2Nb-0.7Cr-0.3Si. The microstructural and fracture analysis before and after tensile testing are discussed.

4.4.2. Metallography analysis

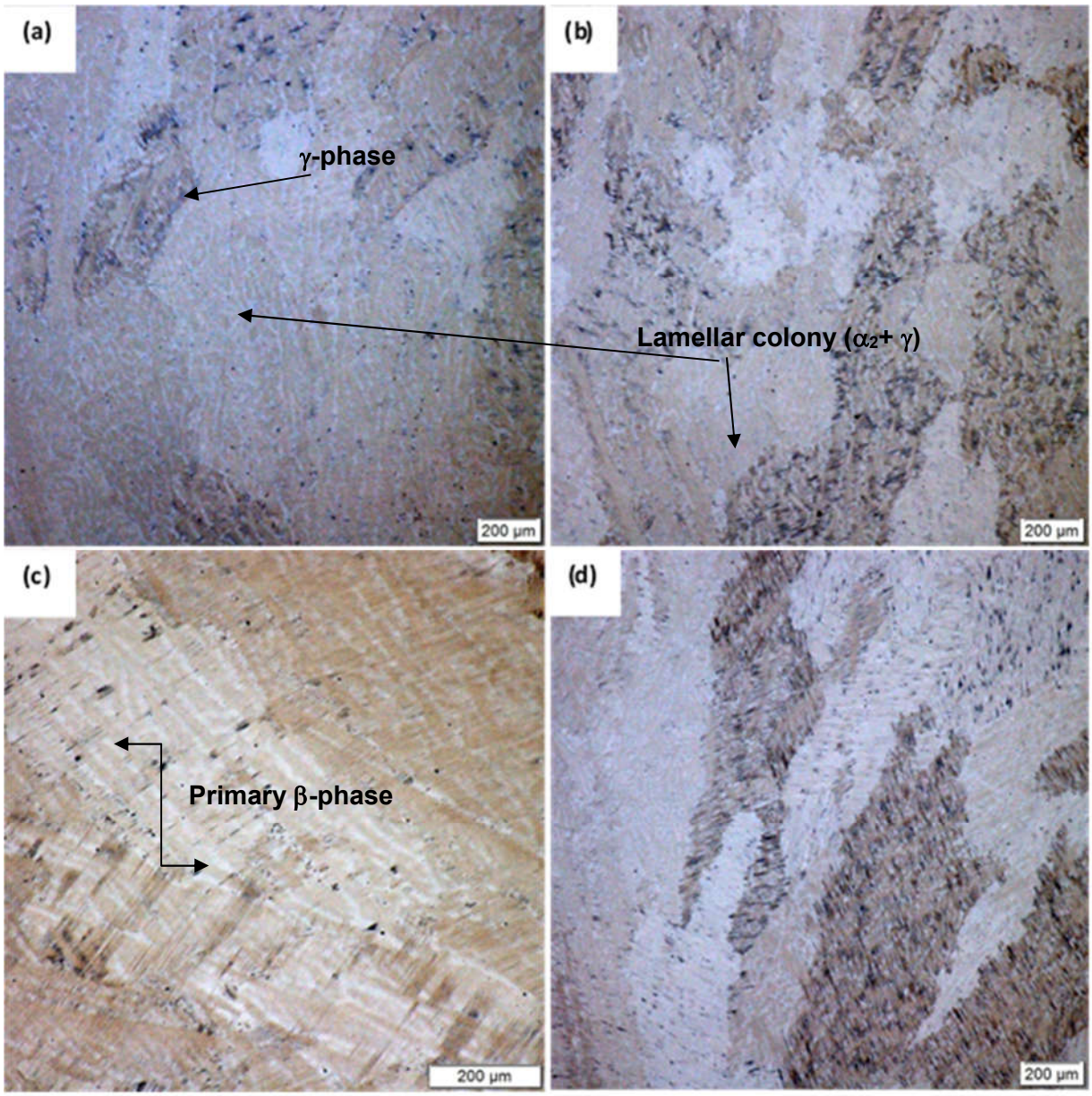

Figure 4.30. Optical images of the (a) binary (Ti-Al), (b) ternary (Ti-Al-Nb), (c) quaternary (Ti-Al-Nb-Cr) and (d) quinary (Ti-Al-Nb-Cr-Si) alloys.

Fig. 4.30 shows the optical microstructures of the binary Ti-Al, ternary Ti-Al-Nb, quaternary Ti-Al-Nb-Cr and quinary Ti-Al-Nb-Cr-Si alloys. In **Fig. 4.30a-c** the microstructures comprised a light network phase, the primary β-phase while the dark phase is the γ-phase. Due to addition of Si in **Fig. 4.30d**, the light phase in the quinary alloy is the titanium silicate precipitate (Ti_5Si_3). The β-phase grains were irregular in shape, together with fine γ-grains along grain boundaries. The micro-segregation of beta stabilizers Nb and Cr to the dendrite cores, possibly occurred during solidification, while a smaller volume fraction of the primary β-phases was retained after cooling due to enrichment in β-phase stabilizers [154].

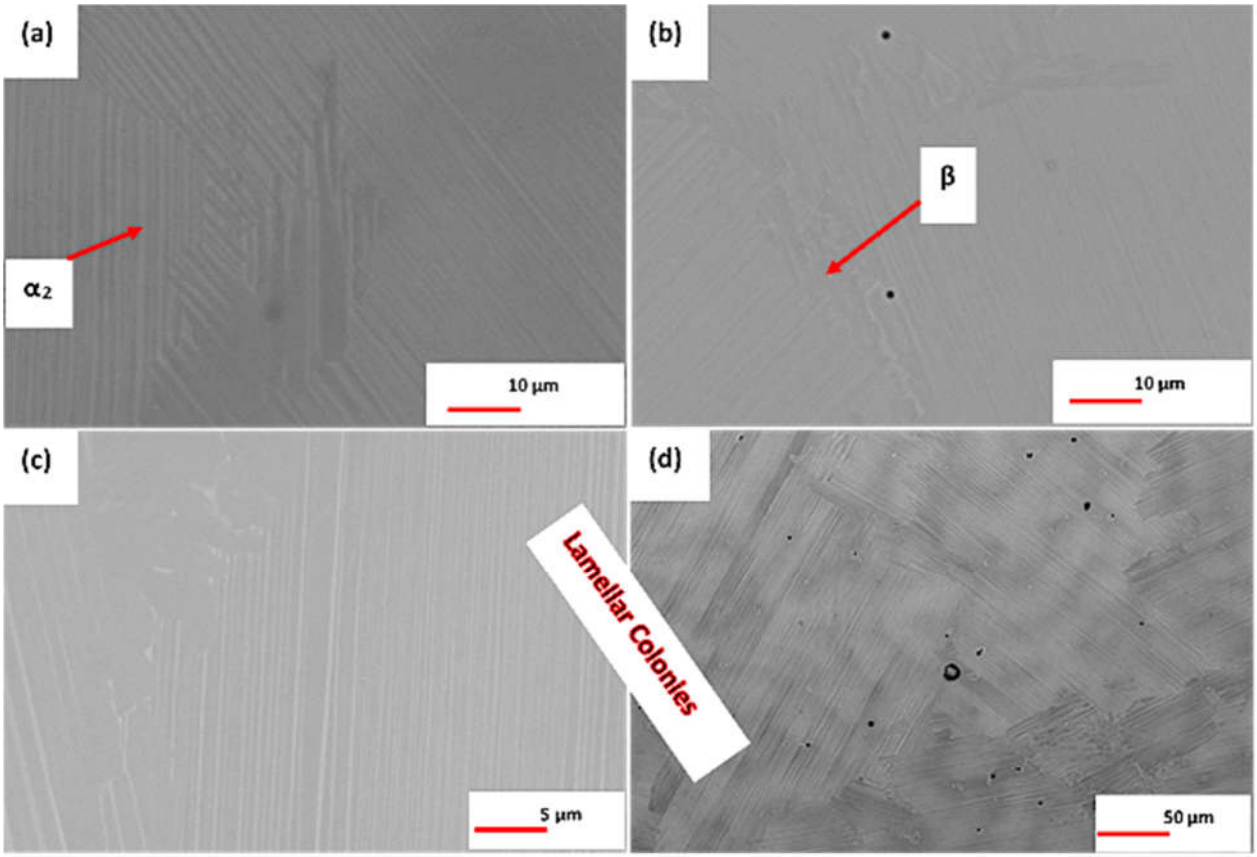

Figure 4.31. SEM images of the (a) binary (Ti-Al), (b) ternary (Ti-Al-Nb), (c) quaternary (Ti-Al-Nb-Cr) and (d) quinary (Ti-Al-Nb-Cr-Si) alloys.

The SEM images of the binary Ti-Al, ternary Ti-Al-Nb, quaternary Ti-Al-Nb-Cr and quinary Ti-Al-Nb-Cr-Si alloys are shown in **Fig. 4.31**. The micrographs of the binary TiAl alloy in **Fig. 4.31a** comprised the lamellar structure of (α_2+γ). The corresponding average chemical compositions of the lamellar structure in the binary, ternary, quaternary and quinary alloys are presented in **Table 4.5**. The lamellar colonies were evident, while the β-phase was segregated along the grain boundaries of the γ-phase. **Fig. 4.31b-d** confirms that the lamellar colonies become finer, with addition of more alloying elements.

Table 4.5. EDX chemical composition of the lamellar structure of the binary, ternary, quaternary and quinary alloys in at.%.

Alloy	Ti	Al	Nb	Cr	Si
Binary	57.13	42.87	-	-	-
Ternary	48.87	49.42	1.70	-	-
Quaternary	49.45	47.86	1.94	0.75	-
Quinary	49.39	48.04	1.72	0.69	0.15

4.4.3. Mechanical properties

Addition of Nb and Cr decreased the grain size of the ternary and quaternary alloys. As mentioned in **Section 4.1.5** and **4.3.2**, **Fig. 4.21** shows the effect of alloying element on the grain size and macro-hardness. The binary alloy had the largest grain size of 280 μm. Alloying TiAl with 2 at.% Nb reduced the grain size in the ternary alloy to 180 μm. An element such as Nb is known to be a β-phase stabilizer in TiAl alloy and plays two roles, i.e. reducing the grain size and stabilization of the β-phase. Additions of Nb (1-2 at. %) improves the strength of the γ-phase at room temperature [155], while addition of Cr improved the effect of grain refinement further. In the quinary alloy, the grain size slightly increased due to addition of Si implying that the ductility of the alloy was improved. **Fig. 4.21** follows the grain size-flow stress Hall Petch relationship in **Eq. 1**. Therefore, the smaller the grain size the higher the yield strength.

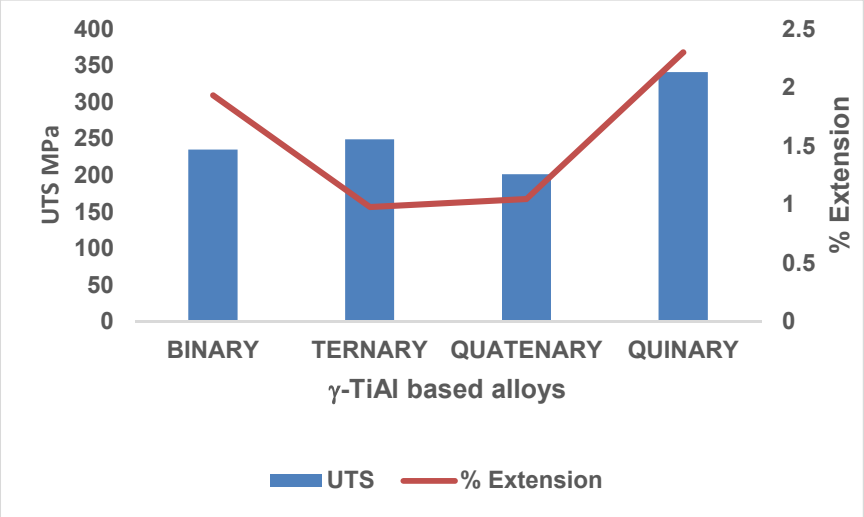

Figure 4.32. The tensile strength, and % elongation of the as-cast binary, ternary, quaternary and quinary alloys.

Fig. 4.32 shows the tensile strength and percentage elongation of the binary, ternary, quaternary and quinary alloys. The addition of Nb to binary TiAl has slightly increased the tensile strength. However, the quaternary alloy showed the lowest tensile strength due to alloying with Cr. The twin and super-dislocation nucleation are competing mechanisms in γ-TiAl alloys, depending on stacking fault energy [17]. Duplex structures favors twin deformation because its stacking fault energy is lower due to lower Al concentration or the presence of α_2 which absorbs and lowers the interstitial content in γ-phase [118]. The Cr atoms occupy Ti-sites in a single γ-phase alloy resulting in slight Ti-Al bond modification and plasticity enhancement. In contrast, when Cr atoms occupy the Al sites in a duplex alloy, the overall covalency of Ti-Al bond is reduced and plastic deformation is favored reducing the ultimate tensile strength in the quaternary alloy [156]. Furthermore, Si addition drastically increased the tensile strength and percentage elongation of the quinary alloy compared to binary, ternary and quaternary alloys, respectively. The improved properties in quinary alloy prove that the addition of Si in the TiAl based alloy enhances the room temperature ductility as a result of Ti_5Si_3 whisker formation during solidification process [156]. The interface between the strip/rod-like Ti_5Si_3 precipitates and matrix retard the motion of dislocations, leading to the improvement of strength [157].

4.4.4. Fractography analysis

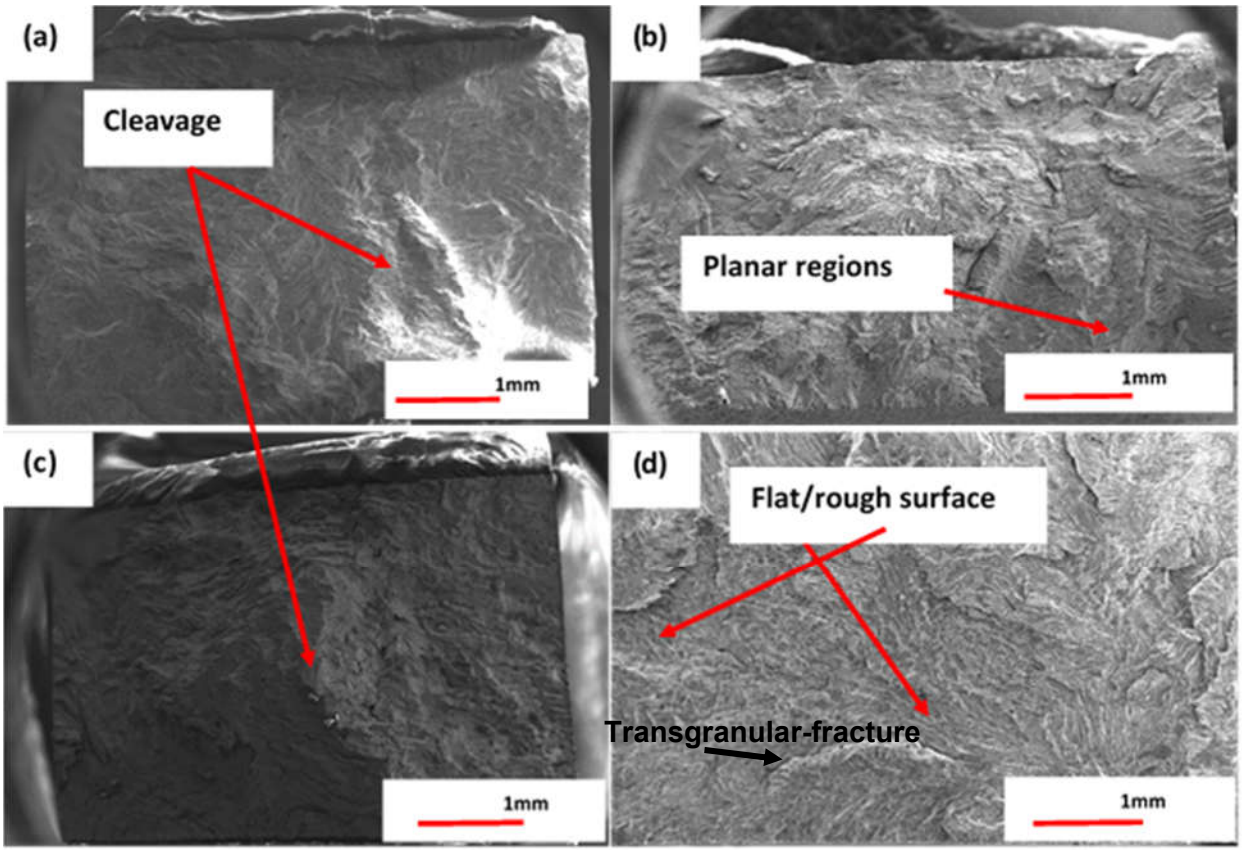

Figure 4.33. SEM-SEI images showing fracture surfaces after tensile testing of the binary, ternary, quaternary and quinary alloys.

The SEM secondary electron (SE) mode images of the fracture surface after room temperature tensile tests are shown in **Fig. 4.33**. A mixture of trans-granular and grain boundary failure for the binary alloy is shown in **Fig. 4.33a**. The duplex structure (α_2+γ) showed cleavage or lamellar interface failure. **Fig. 4.34b** reveals fracture surface was slightly flatter when compared with the binary and the quaternary alloy, although the fracture surface of the quaternary alloy **(Fig. 4.33c)** was slightly flat when compared to the binary alloy. The planar regions are illustrated by the arrows in **Fig. 4.33**. Furthermore, addition of Cr increased the probability for intra-granular failure in the duplex structure [17]. The quinary alloy in **Fig. 4.33d** had the most flat, but rough fractured surface with discontinuities. The glide and twinning at room temperature occurs more easily in globular γ-TiAl grains in the presence of fewer deformation obstacles, while in the case of lamellar microstructure, the dislocation movements are obstructed by many short range interfaces which collectively produce limited overall deformation [158].

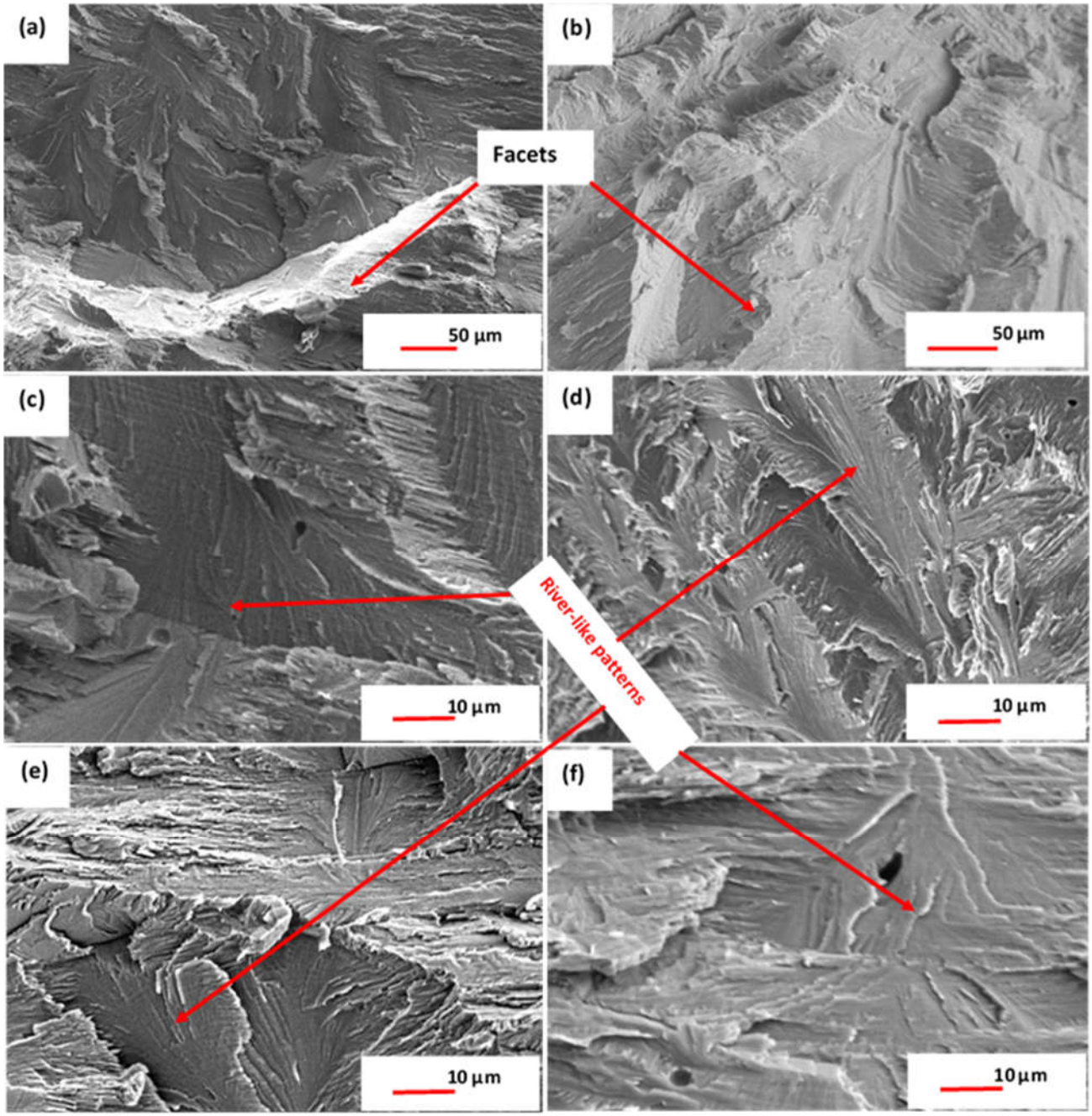

Figure 4.34. Fracture surfaces showing facets on the low tensile strength (a) binary (b) quaternary and river pattern in all alloys (c-f).

Fig. 4.34 shows the binary and quaternary alloys fracture surfaces showing the facets. These two alloys showed the lowest tensile strength of the four alloys. Infrequent inter-lamellar fracture and few facets were evident in these alloys. The fracture comprising of more facets suggested lower plasticity, which is an indication of the brittleness of the alloy and in turn corresponds to low tensile strength. Furthermore, the fracture surfaces of all specimens display features such as river-like patterns, “river marks” which are characteristic of cleavage fracture shown in **Fig 4.34c-f**. The cleavage fracture was a trans-lamellar fracture which occurred along a certain crystallographic plane at fast-paced rate [159]. A cleavage facet is a

crystallographic plane with the lowest surface energy, and crystallographic planes with lower indexes are generally not parallel in the polycrystalline metals. However, the cleavage steps form on the fracture surface when the cracks propagate across the grains, while the river-like patterns are the top view of the cleavage steps [159]. The “river” initiates from the grain boundary flaws in the grain and ends at the grain boundary of the same grain. Therefore, cracks originate in the interior of the specimens. In addition, secondary cracking along lamellar interfaces subsequent to room temperature tensile was occasionally observed in the ternary and the quinary alloy, as illustrated in **Fig 4.35a-b**. It was found that cracks initiated at the grain boundary and therefore extended by inter-lamellar propagation. The arrows indicate inter-lamellar secondary cracking. Regarding crack branching, the secondary cracks propagation along lamellar interfaces sought the path of least resistance. This meant that the lamellar structure of the alloys exhibited much stronger resistance against trans-lamellar fracture. Consequently, the ternary and quinary alloys had higher tensile strength when compared to the binary and the quaternary alloys.

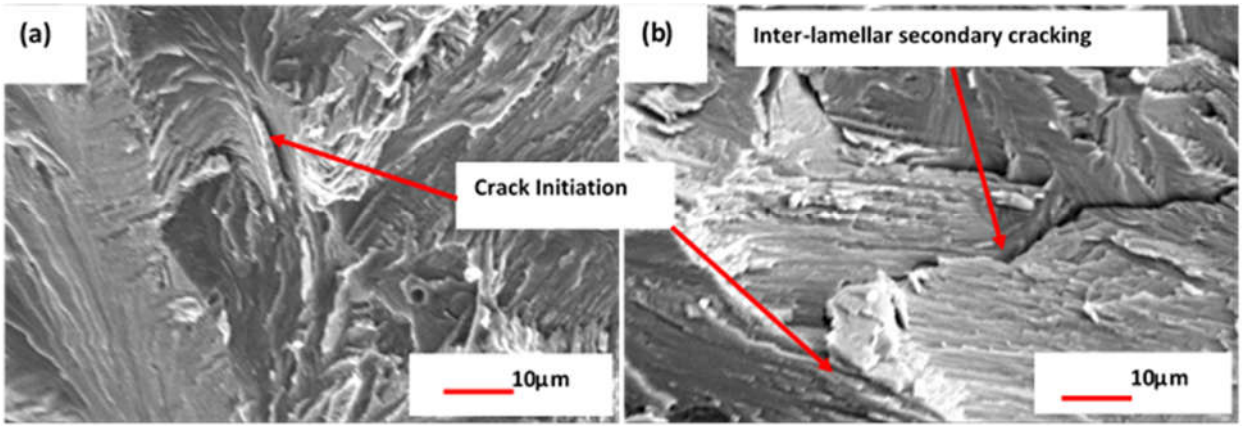

Figure 4.35. Trans-lamellar fracture with inter-lamellar secondary cracking in (a) ternary alloy and, (b) quinary alloy.

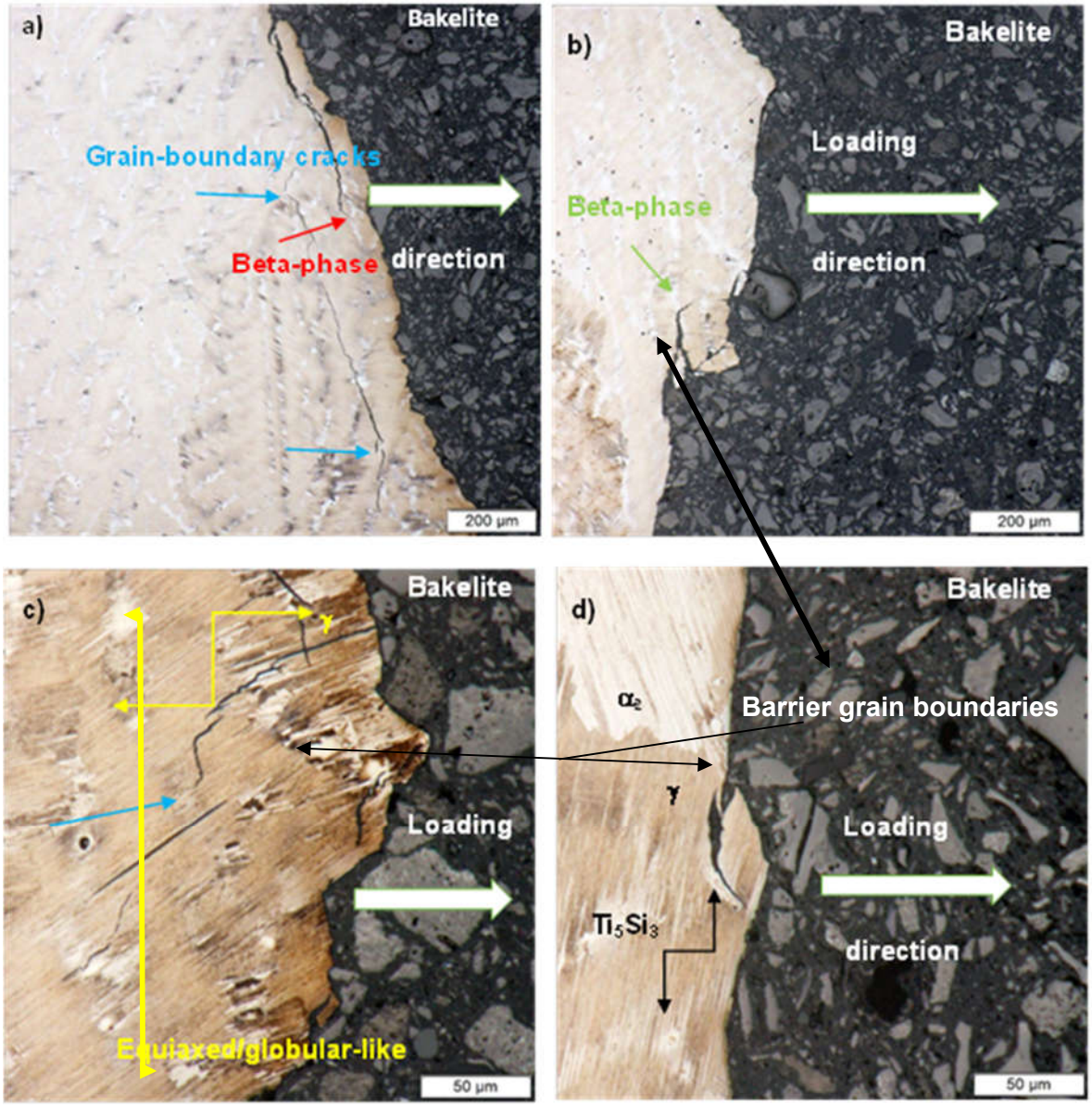

Figure 4.36. Optical images of a length section at/near the fractured surface after room temperature tensile failure of a) binary alloy, b) ternary alloy, c) quaternary alloy, and d) quinary alloy.

Fig. 4.36 shows cross-sections along the axis of the applied stress of the fractured specimens under the optical microscope. These micrographs were taken to further validate the fracture analysis results. The fracture analysis was carried out close to the fracture surface. Micro-cracks were associated with the presence of the β-phase for binary, ternary and quaternary (**Fig. 4.36a-c)** while for the quinary alloy (**Fig. 4.36d**), the presence of Ti_5Si_3 phase of which both acted as crack initiation points. These cracks initiated along the boundaries between γ-grains, γ-grains and lamellar colonies, and at the triple junctions of colonies and grains [153]. In addition, the length of the micro-cracks and the width of the crack opening distances suggested that the existence of the possible sites for crack initiation were the grain boundaries

between lamellar colonies and equi-axed γ-grains. On the contrary, when the crack stops at a barrier viz. the grain-boundary, a new crack initiated along lamellar interface behind the barrier grain. To expatiate on this, when a grain having lamellae perpendicular or inclined at a large angle to the crack propagation plane, the resulting crack is deflected to delamination mode (interlamellar fracture) (**Fig. 4.36a-c**) [153].

4.4.5. Conclusions

The following conclusions were drawn:

The β-solidifying γ-TiAl intermetallic alloys Ti-45Al (binary alloy), Ti-45Al-2Nb (ternary alloy), Ti-45Al-2Nb-0.7Cr (quaternary alloy), and the Ti-45Al-2Nb-0.7Cr-0.3Si (quinary alloy) were developed. Microstructural examination indicated that all the alloys comprised lamellar structures (α_2+γ) embedded in columnar dendritic cores in as-cast condition. However, there was a significant difference in the alloy microstructures in the binary, ternary and quaternary alloys, and the quinary alloy also had Ti_5Si_3 second phase. The addition of Nb to binary TiAl slightly increased the tensile strength. However, the quaternary alloy showed the lowest tensile strength due to alloying with Cr. Furthermore, the Si in the quinary alloy improved the tensile strength and elongation, compared to the other alloys. The improved properties in quinary alloy proved that addition of Si to the TiAl based alloys enhanced room temperature ductility as a result of Ti_5Si_3 whiskers formation during solidification process, inducing grain refinement. The binary and quaternary alloys showed more facets on the fracture surface, suggesting lower plasticity, which is an indication of the brittleness of the alloy and in turn corresponds to lowest tensile strength. Infrequent inter-lamellar fracture and few facets were evident in all alloys. The lamellar structure of the ternary and quinary alloys exhibited better strength against trans-lamellar fracture confirmed by higher tensile strength of ternary and quinary alloys.

4.5. Phase transformation behavior and microstructural control of an α-solidifying γ-Ti-45Al-2Nb-0.7Cr-0.3Si based intermetallic alloy

4.5.1. Introduction

The γ-TiAl based alloys are of particular interest for the production of rotating parts in gas turbine aero-engines and for automotive engine application such as engine valves and turbine wheels of turbochargers [2]. The main applications and material description for titanium aluminides are well described by Kothari et al. [3]. These intermetallic alloys offer a good combination of mechanical properties viz. low density, high specific modulus and strength, good creep and oxidation resistance. On the contrary, their limited use to date is due to property balance, cost and production quality. **Fig. 2.24** briefly illustrates various microstructures with corresponding heat-treatment.

Zambaldi [70] reported that the melting of titanium alloys is technologically challenging. Due to the high reactivity of γ-TiAl based alloys, the melting technique should exclude oxygen uptake or partial dissolution of the crucible material. Therefore, vacuum arc re-melting process is widely employed to melt titanium alloys. To establish homogeneity throughout the structure, three melting cycles was employed. In addition, alloy microstructure could also be controlled by heat treatment. Lapin and Nazmy [10] outlined that, depending on the chemical composition and heat-treatment process, γ-TiAl based alloys display four different types of microstructures: near-gamma, duplex, near lamellar and fully lamellar. The fully and near lamellar structures consist of TiAl (γ-phase) and a small volume fraction of Ti_3Al (α_2-phase) which gives good creep and crack-propagation resistance, along with higher fracture toughness. Additionally, higher tensile strength, ductility and longer fatigue life are therefore achieved for an alloy with a duplex structure. Moreover, the microstructure of Ti40Al-10Nb alloys studied by Zhan et al. [8], showed that the Widmanstätten laths are more creep resistant than the lamellar structure owing to their short mean free path of dislocation slip.

The mechanical properties of this class of alloys depend on microstructure. Various studies have shown that improved tensile strength and ductility for γ-TiAl based alloys can be obtained by grain refinement. Consequently, grain size plays an important role in as-cast γ-based alloys, considering that the microstructure often consists of coarse grains commenced from α solidification [154]. Clements et al. [160] reported that the solidification path via the β phase is complimentary to obtaining a fine-grained casting microstructure without significant texture and segregation. Additions of Nb, Mo, Cr, W, Ta and V alloying elements enlarge and stabilizes the β phase domain with a bcc crystal structure [161].

In the work done by Rajararn [162], during annealing of Ti-46.6Al-2.3V-0.9Cr alloy, found that the α plates spheriodized by continuous and discontinuous coarsening, by heat-tretment procedure resulting in near-γ structure. The evolution of the α plates is influenced by alloy composition and the morphology of the starting as-cast microstructure. Additionally, heat-treatments at slightly below Tα defined in **Fig. 2.25** can reduce the amount of γ grains, and limit the lamellar grain size in the near-fully lamellar structure, provided the time is short and air cooling is used. Increasing heat treatment time, however, does not eliminate the untransformed γ grains, which therefore tend to spheriodization. Furthermore, it is interesting to note that the spheriodized γ laths are located, not only at the lamellar grain boundaries but also within the lamellar grains, which shows that the γ grains do not always impede α grain growth during long time heat-treatment. Ramanujan [163], mentioned that the kinetics of globularization of Ti-45.5Al-2Cr-2Nb alloy were examined and found that spheriodization initiated and proceeded inward from prior α grain boundaries.

This research study aimed to investigate microstructure refinement of the Ti-45Al-2Nb-0.7Cr-0.3Si alloy generated from a two-step heat treatment process comprising of solution treating in α phase region, and solidifying into α_2 + γ stable phases at room temperature, with the aim of forming both the spheriodized and Widmanstätten laths.

4.5.2. As-cast Ti-45Al-2Nb-0.7Cr-0.3Si based alloy

Fig. 4.37 shows the as-cast structure revealed by macro-etching of the Ti-45Al-2Nb-0.7Cr-0.3Si alloy. **Fig. 4.37** shows the of coarse structure which was confirmed by the optical microscopy shown in **Fig. 4.38**, which demonstrated an inhomogeneous structure constituting of fine and coarse grains with irregular lamellae along with cellular-like dendritic structure formed after melting, indicated by the double red arrow. This is thought to be the micro-segregation of Nb, Cr to dendrite cores, which may have occurred during solidification with the resultant remnant primary β-phases after cooling to room temperature due enrichment of in β-phase stabilizers.

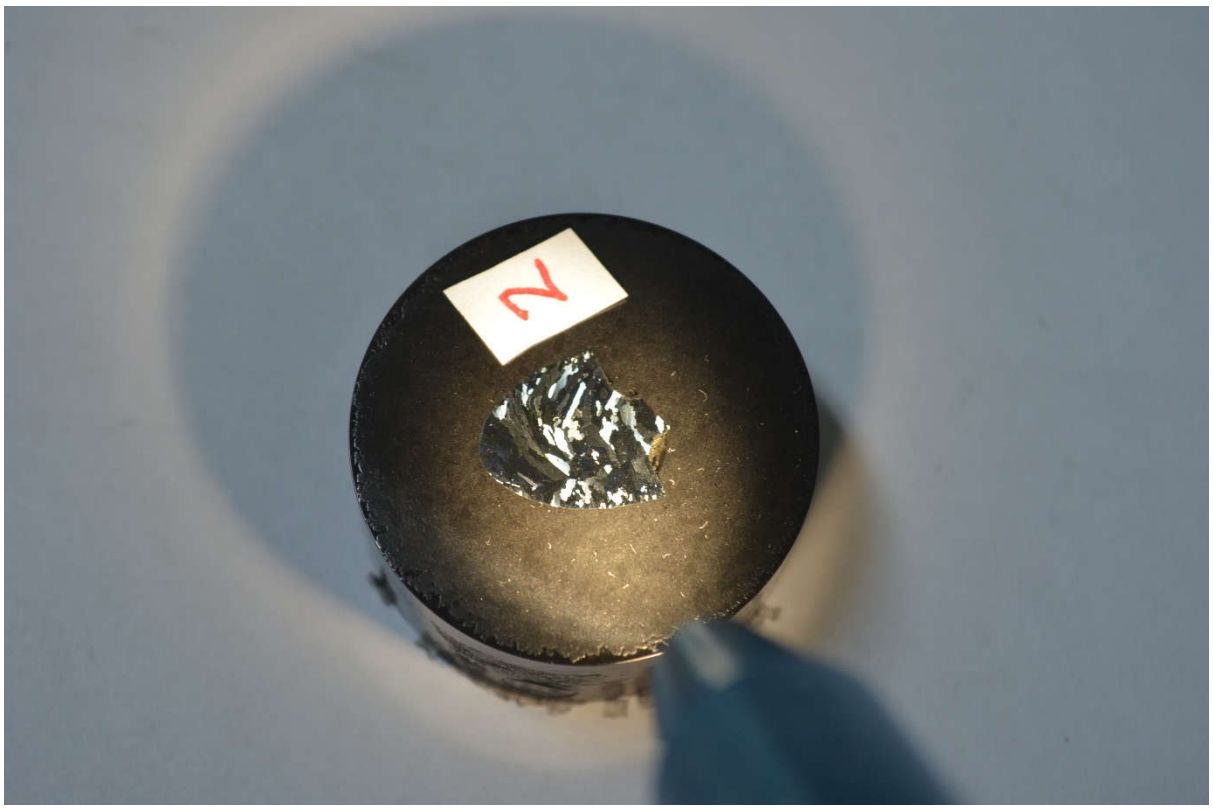

Figure 4.37. Structure of the as-cast γ-Ti-45Al-2Nb-0.7Cr-0.3Si based alloy shown by macro-etching..

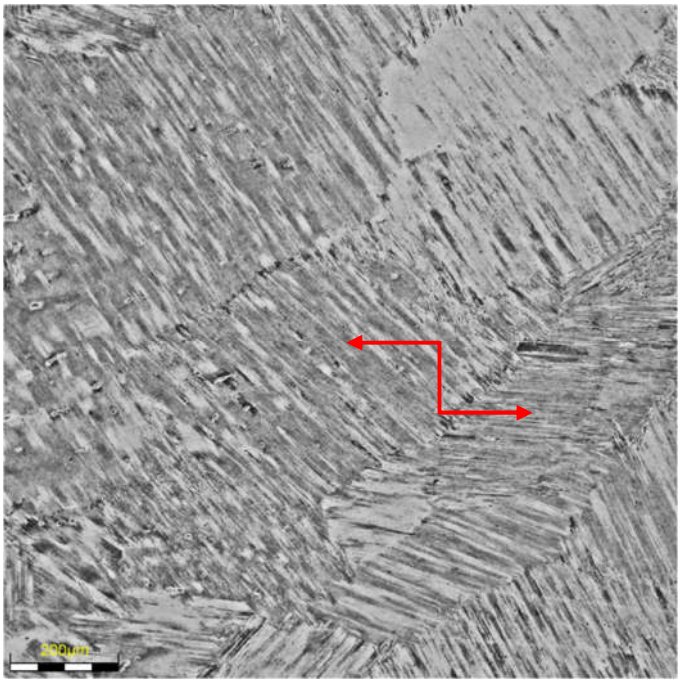

Figure 4.38. Optical micrograph of as-cast Ti-45Al-2Nb-0.7Cr-0.3Si alloy.

Fig. 4.38 is the optical micrograph of the as-cast γ-Ti-45A-2Nb-0.7Cr-0.3Si alloy, which demonstrate that the alloy seems to have solidified completely to β as the primary solidification phase, and according to Saari et al. [55], the resulting columnar grains should have a mixture

of parallel lamellar boundaries aligned at 45 ^{0} to the solidification growth direction. Moreover, Ding et al. [164], reported that β was the primary solidification phase provided that the secondary dendritic arms are orthogonal to the primary arms. Furthermore, during the primary β solidification, it may seem that Ti, Nb, and Cr are segregated into the dendrites, whereas the Al is rejected into the inter-dendritic regions. **Fig. 4.39** illustrates the electro-polished sample along with micro-analysis spectra. Wang Yan et al. [154], reported that the existence of different phases in γ-TiAl based alloys can be validated by BSE/SEM examination. The phases with different average atomic numbers in composition have different contrast in BSE-mode. **Fig. 4.39a** shows the conventionally etched SEM micrograph. The alloy solidified with β, as verified by the four fold symmetry of primary dendrites, **Fig. 2.27**. The mechanism according to Saari et al. [55], is that once the peritectic temperature is reached, the α phase will nucleate and grow from the liquid. As the cooling continues, the solid state transformation will occur, and according to Ding et al. [164], β to α, as a result, the lamellar structure forms. The final lamellar orientation occurs when the peritectic α phase consumes the primary β phase.

Zhang et al. [165] found no dendritic core regions and that suggested that core grains (lamellae) are enriched in Al and depleted in Cr and Mo, whereas the inter-grain regions (bright) phase were enriched in Ti, Nb, Cr, and may be Si too. However, the authors also suggested that the dark phase is the γ-TiAl because it was enriched with Al. The SEM-EDX micro-analysis was conducted and the red double arrow indicated in **Fig. 4.39a** shows the dark phase enriched in Al, where the chemical composition is shown in **Fig. 4.40a**. **Fig. 4.40b** shows the atomic composition of the β-phase indicated by the double blue arrow of **Fig. 4.39a**.

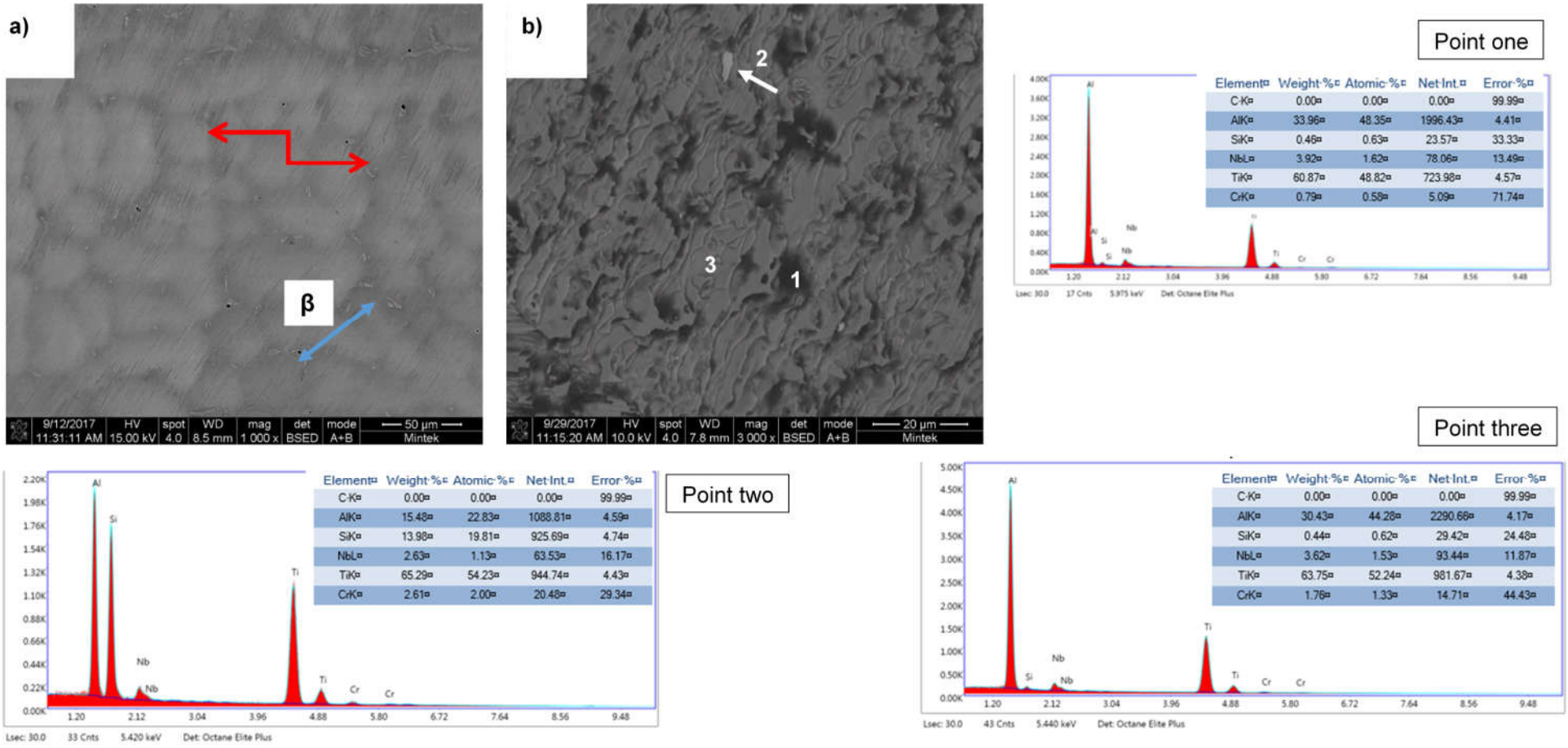

Figure 4.39. SEM-BSE micrographs with EDX spectra of the as-cast Ti-45Al-2Nb-0.7Cr-0.3Si (at. %) based alloy a) low magnification, b) high magnification.

a)

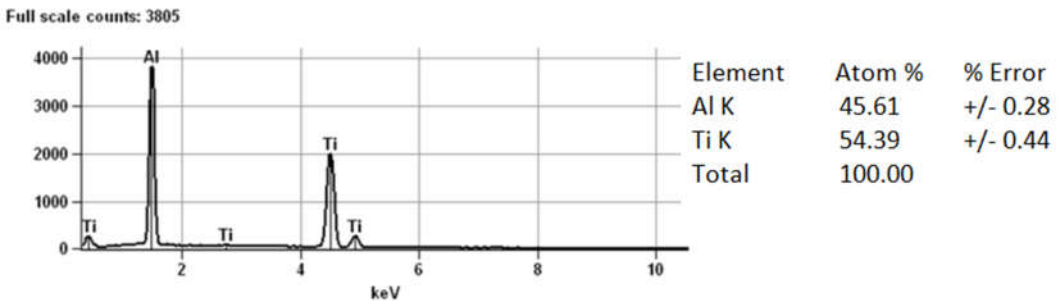

b)

Element	Atom %	%Error
Al K	48.85	+/- 0.89
Si K	1.60	+/- 0.38
Ti K	46.34	+/- 1.27
Cr K	0.17	+/- 0.34
Nb L	3.04	+/- 0.46
Total	100.00	

Figure 4.40. a) Elemental spectra and atomic composition enriched in Al; b) Atomic composition of the β-phase.

The electro-polished sample in **Fig. 4.39b**, shows quantitative EDX micro-analysis suggesting that the bright phase, point two, were enriched in Si content, and to some extent Cr and Nb alloying elements. Hence, the white colored network can be attributed to the retained primary β-phase, as seen in the optical image, whereby Clemens et al. [160], in their previous work further mentioned that Nb, Cr, Mo and W are β-stabilizers. In contrast, there was a dark gray region in the BSE micrograph of the as-cast γ-TiAl based alloy, point one, where the EDX atomic composition shows that the Ti and Al have slightly equal proportions which indicated of γ-TiAl phase. Conversely, the gray matrix in the microstructure, point three, had slightly higher Ti content than that of Al.

4.5.3. DTA determination of melting endotherms

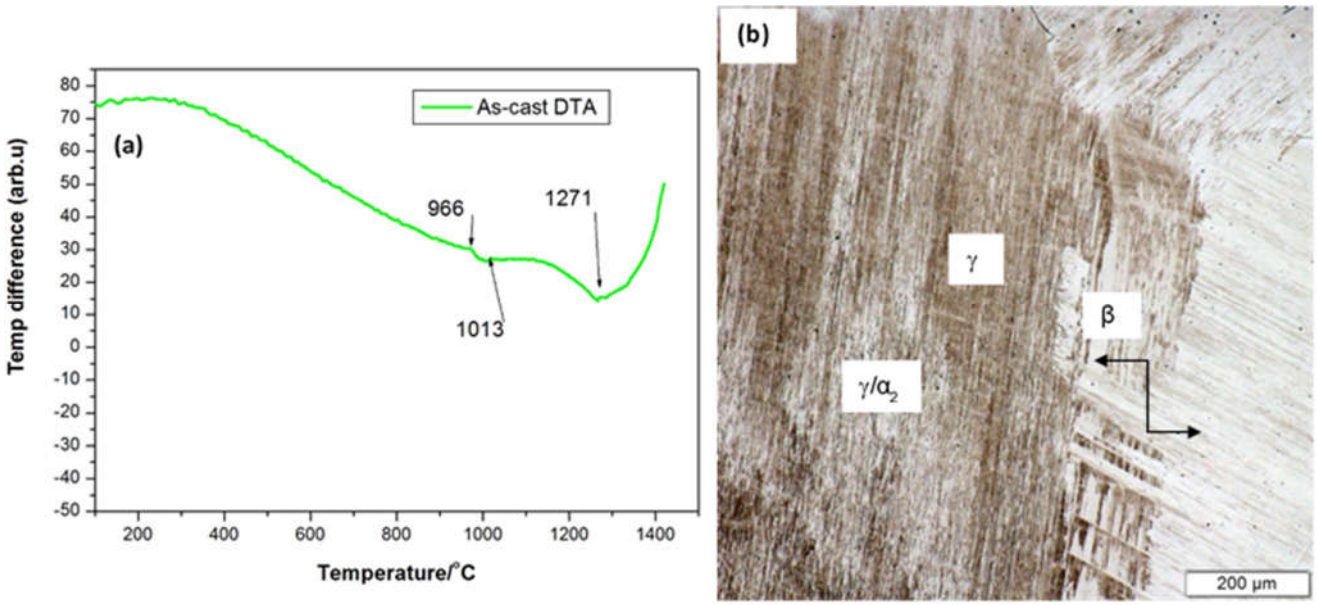

Figure 4.41. (a) DTA (heating curve of γ-TiAl based alloy; (b) DTA optical micrograph.

Fig. 4.41a shows a DTA curve for the Ti-48Al alloy, showing the solid state phase transformation are evident. There are two sets of melting endotherms within the temperature range between 900 and 1431 °C. The first temperature transition is indicated by the melting onset at 966 °C and completed at 1013 °C, which is thought to be 1) α_2 + γ. $\rightarrow$ α-phase transformation. The second melting endotherms' onset temperature is 1151 ^{0}C and was completed at 1431 °C, indicating second reaction 2) $\alpha \rightarrow \alpha + \beta$. However, this transition was broad compared to the first one; with evidence of more than one melting reaction, from an observation of a sudden change in slope at 1271 °C, indicating the occurrence of the major solid-state reactions. The metallographic examination of the as-DTAed specimen is illustrated in **Fig. 4.41b**, showing a inhomogeneous microstructure consisting of fine and coarse grains with irregular lamellar structure formed when heated to the β-phase domain at 1500 °C. The double arrow indicates the network of the β-phase.

4.5.4. Heat-treated alloy structure and EBSD analysis

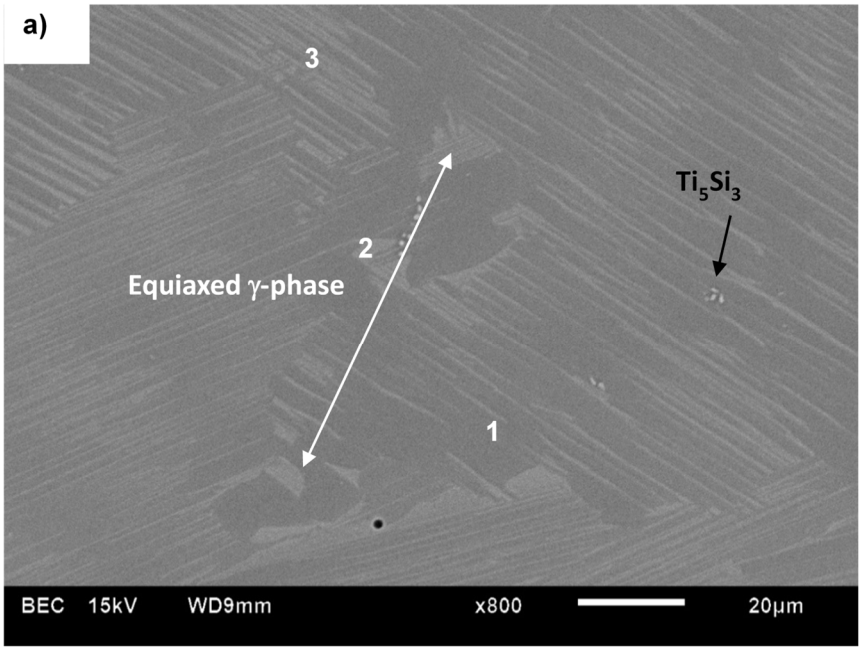

b)

Point 1

Element	Atom %	%Error
Al K	48.29	+/- 0.28
Si K	1.13	+/- 0.09
Ti K	48.27	+/- 0.40
Cr K	0.62	+/- 0.09
Nb L	1.68	+/- 0.10
Total	100.00	

Point 2

Element	Atom %	%Error
Al K	35.60	+/- 0.51
Si K	1.23	+/- 0.18
Ti K	60.20	+/- 0.97
Cr K	1.31	+/- 0.22
Nb L	1.66	+/- 0.21
Total	100	

Point 3

Element	Atom %	%Error
Al K	46.15	+/- 0.48
Si K	4.83	+/- 0.20
Ti K	46.88	+/- 0.70
Cr K	0.53	+/- 0.16
Nb L	1.61	+/- 0.19
Total	100.00	

c)

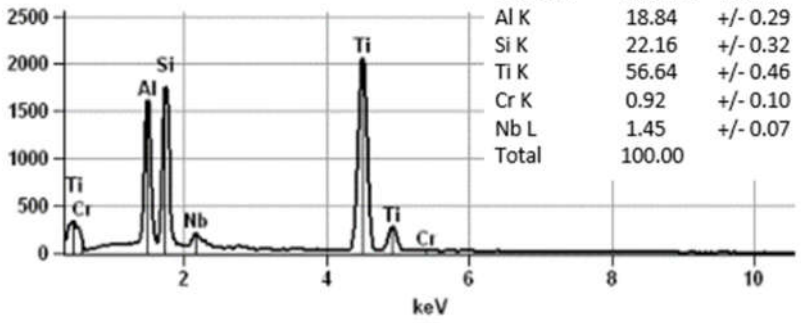

Element	Atom %	%Error
Al K	18.84	+/- 0.29
Si K	22.16	+/- 0.32
Ti K	56.64	+/- 0.46
Cr K	0.92	+/- 0.10
Nb L	1.45	+/- 0.07
Total	100.00	

Figure 4.42. a) Micrograph of sample spheriodized, b) Atomic phase composition of the spheriodized micrograph points 1 to 3, and c) Elemental spectrum and atomic composition of the Ti_5Si_3 precipitate.

Fig. 4.42a shows the as-cast Ti-45Al-2Nb-0.7Cr-0.3Si alloy after spheriodizing heat treatment followed by water quenching. The micrograph indicates lamellar structure ($\alpha_2+\gamma$) with some equiaxed γ-phase and Ti_5Si_3 precipitates. The microstructure of the α-solidifying water-quenched alloy exhibited a fine and homogeneous microstructure with no evidence of the β-

phase, compared to the as-DTA specimen. The phase compositions present in the sample are shown in **Fig. 4.42b (1-3)**, and that of the precipitate is shown in **Fig. 4.42c**. **Fig. 4.43a-d** shows the EBSD maps of the alloy. It was clear that a large number of γ-grains had recrystallized. However, grain orientation of the recrystallized γ-grains were almost random **(Fig. 4.43c)**, meaning no obvious texture was attained during the spheriodizing heat treatment. **Fig. 4.43d** illustrate the phase color map, with an evidence that the dominating phase is the γ-TiAl. Furthermore, **Fig. 4.43c** show the obtained orientation map with a tetragonal structure (c/a = 1.45), respectively. Zambaldi [70] pointed out that correct detection of order domain structure is given by the distribution of pattern quality. The position of order domain boundries is shown by reduced sharpness of the Kikuchi bands, which may result from misfit strain and defects along the boundaries, and therefore lower values in the pattern quality maps. In **Fig. 4.43c** the identified domain boundaries follow the lines of the band contrast **Fig. 4.43b**. The band contrast image in **(Fig. 4.43b)** display small spheriodized γ-phases between the lamellae structures. Moreover, the TEM micrograph in **Fig. 4.44** is the confirmation of the spheriodized laths in the lamellar structure.

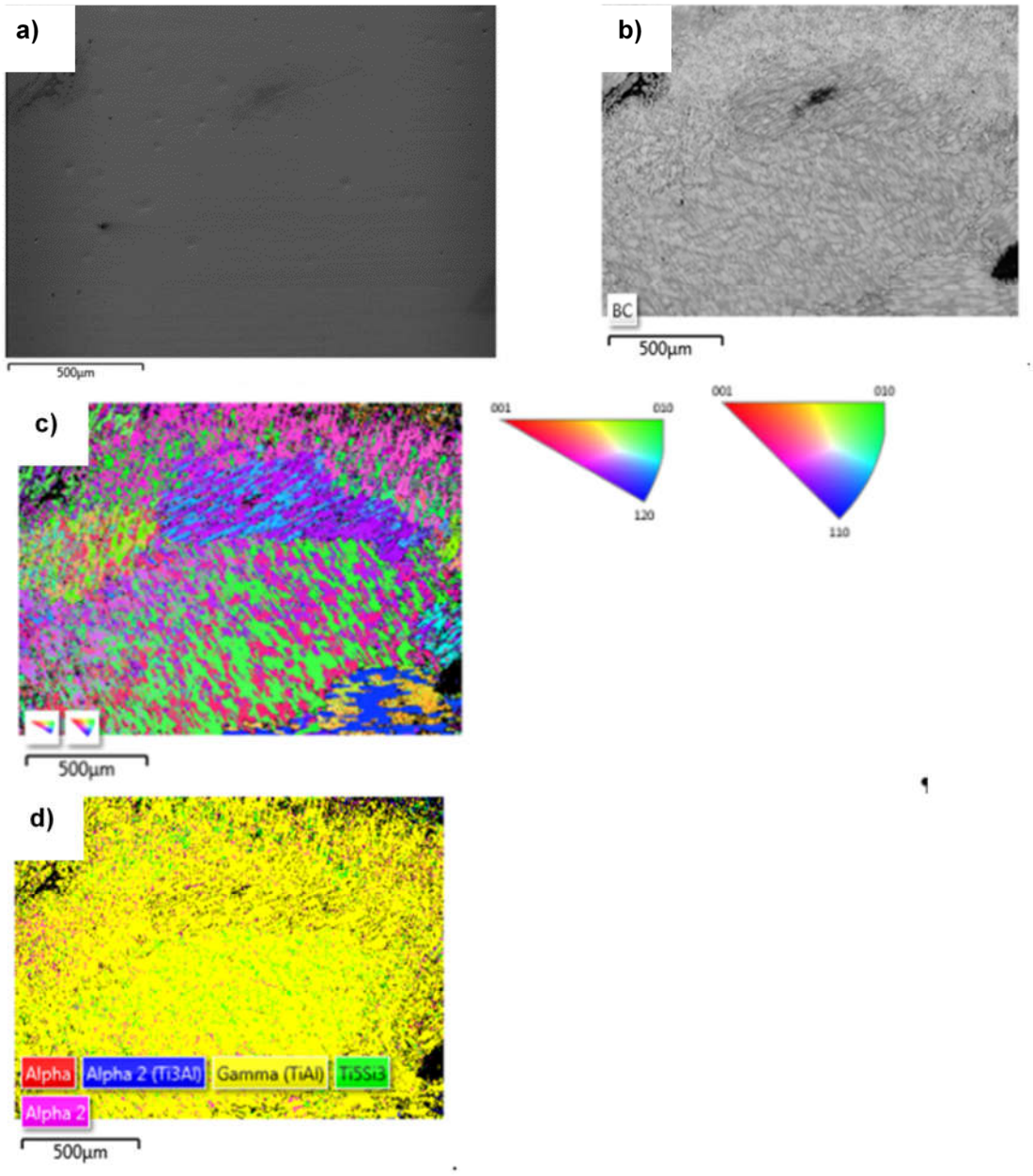

Figure 4.43. EBSD maps of the spheriodized Ti-45Al-2Nb-0.7Cr-0.3Si alloy: a) electron micrograph; b) band contrast image; c) inverse pole figure (IPF) maps and d) phase color map.

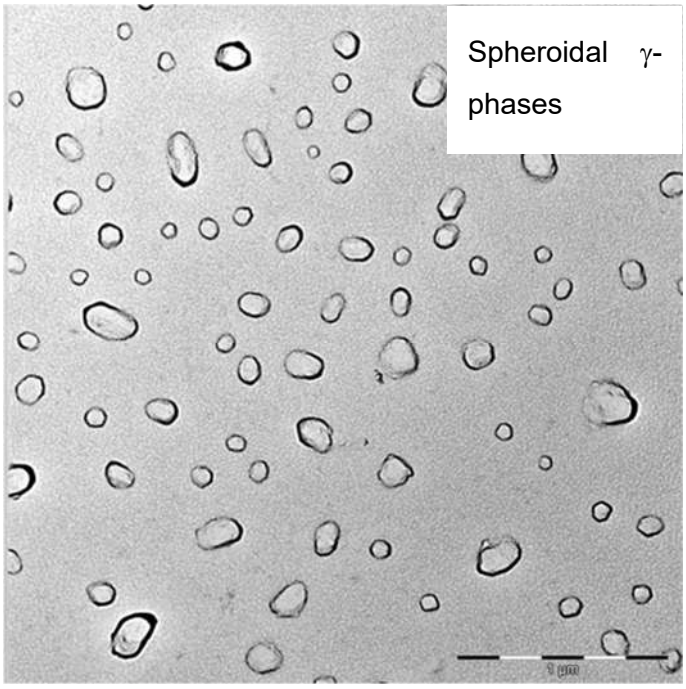

Figure 4.44. TEM image of the Ti-45Al-2Nb-0.7Cr-0.3Si alloy indicative of spheriodized laths.

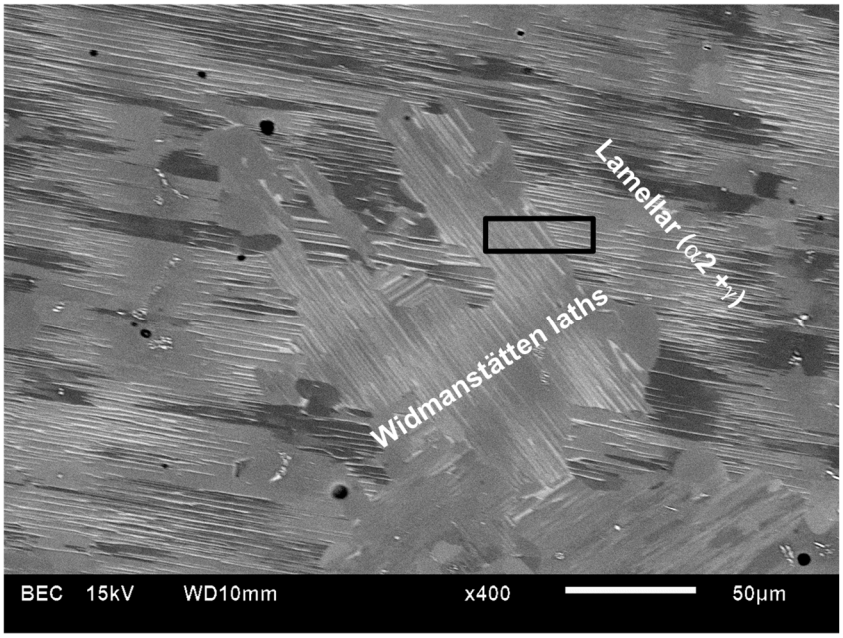

Figure 4.45. SEM-BSE micrograph representing Widmanstätten laths.

Fig. 4.45 is a SEM-BSE micrograph consisting of Widmastätten laths inside the lamellar structure. The growth mechanism of different structures which mainly depends on the cooling rate was previously reported in **Chapter 2 Fig. 2.26,** demonstrating the development of different structures which originated during heat treatment of the (α2+γ) TiAl-based alloy from an elevated temperature (α-domain). The marked region (blue dotted line) in **Fig. 2.26** showed the domain under the influence of sympathetic nucleation [51]. This complication in the lamellar structure is mainly observed along colony boundaries, and it is also considered that

they represent sites of increased internal stresses coupled with locally higher dislocation densities [166]. Moreover, Fransén and Kalsson [56] mentioned that Widmanstätten colonies (needle-like in a random direction) formed inside lamellar grains with small spacing. It was also argued that the Widmastätten colonies are formed through twinning or recrystallization, from the present α grains that had different orientation than the surrounding material. The driving force for such a structure is believed to be the super-cooling occurring at the applied cooling rate.

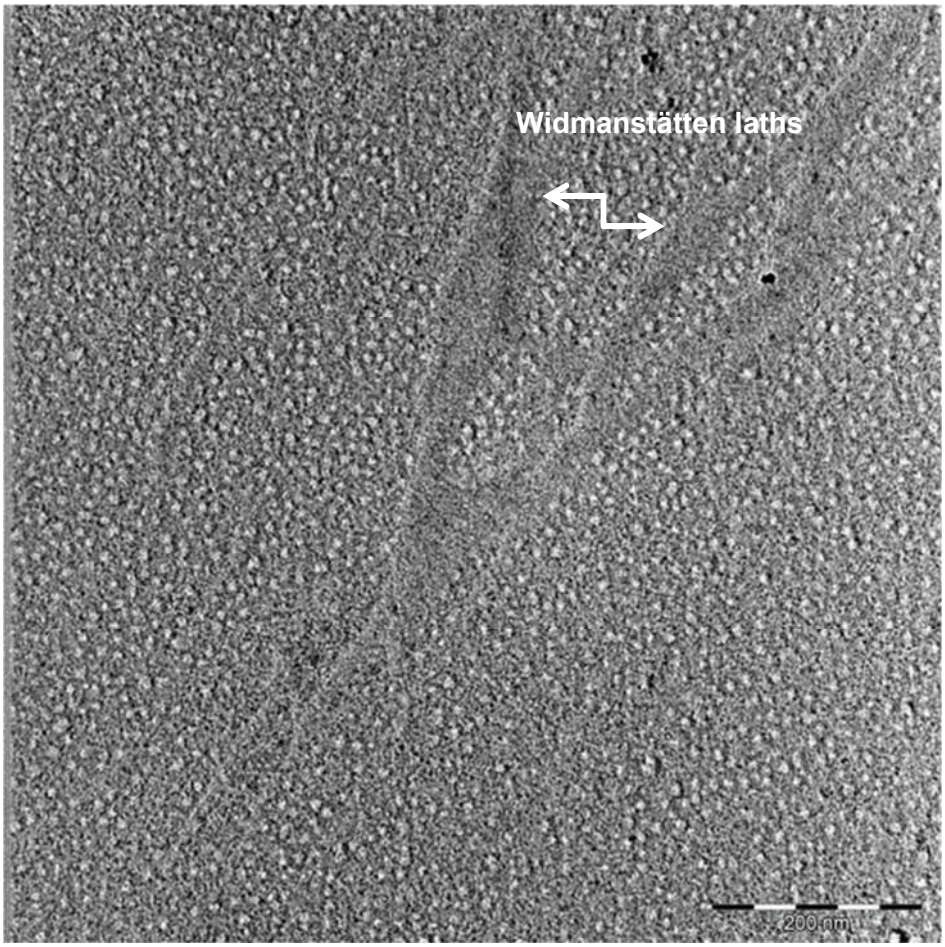

Figure 4.46. TEM micrograph of Ti-45Al-2Nb-0.7Cr-0.3Si alloy.

Fig. 4.46 Is a TEM micrograph, exhibiting long Widmanstätten colonies of needle-like laths in a random direction which is indicated by the double arrow.

4.5.5. XRD determination of phase diffraction angle

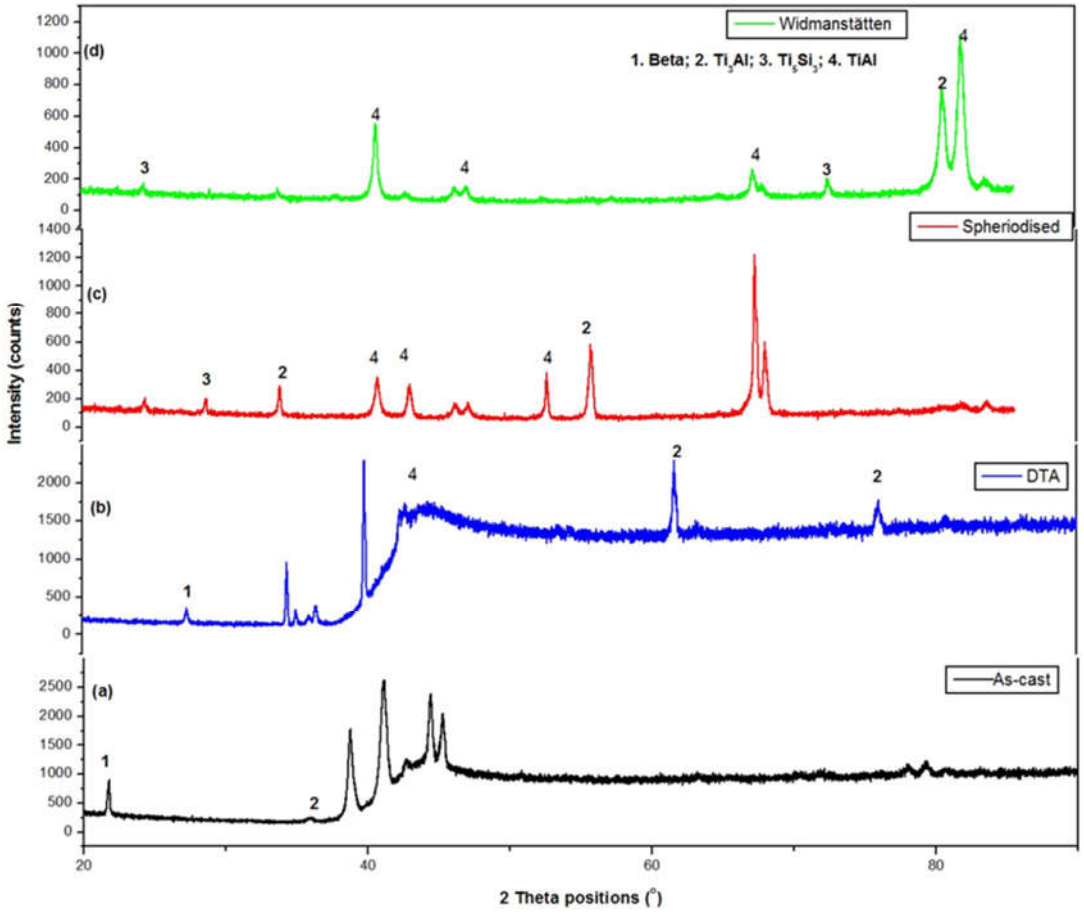

Figure 4.47. XRD patterns of the (a) as-cast, (b) thermally analyzed (c) spheriodized and (d) Widmanstätten induced Ti-45Al-2Nb-0.7Cr-0.3Si alloy.

The X-ray diffraction results in **Fig. 4.47** confirmed the phases present in the microstructures. The alloys exhibited ordered γ-TiAl with a tetragonal lattice, and ordered α_2-Ti_3Al with a close-packed hexagonal lattice. A few peaks of retained β-phase and Ti_5Si_3 were also detected. The β phase, was only seen in the as-cast and the as-DTA alloys and not the heat-treated alloys. This could be a result of the α-solidification which may have absorbed some if not all the β-phase. It is interesting to note that the spheriodized and Widmanstätten laths peaks have shifted to the right with respect to the as-cast alloy, which may be an indication of solid state transformation. Peak broadening at 2θ 81° diffraction angle is believed to be the formation of a phase that has a small crystallite size; hence the presence of γ-TiAl.

4.5.6. Macro-Vickers hardness profile

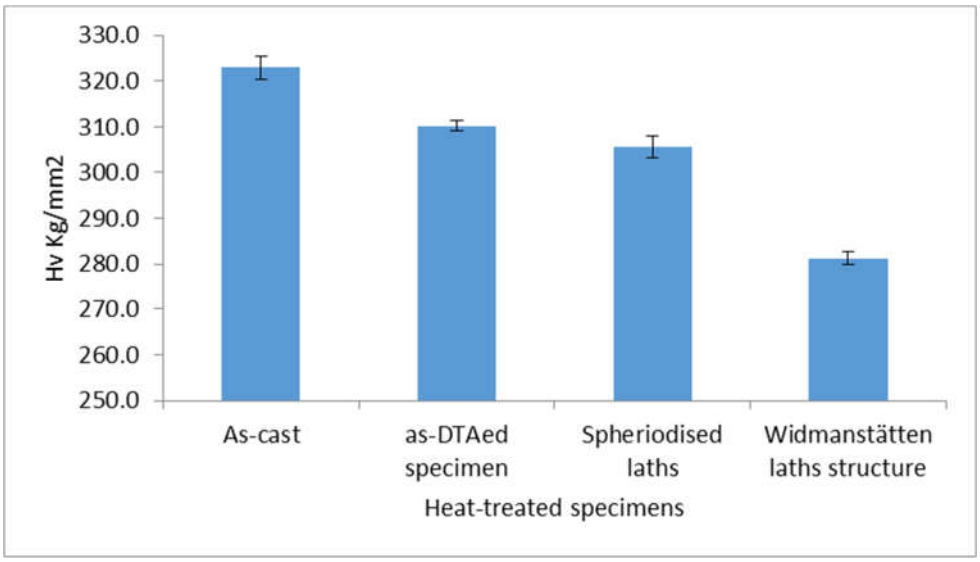

Figure 4.48. Macro-hardness of the γ-TiAl based alloys.

In theory hardness, values have a linear relationship to the yield strength in directionally solidified TiAl alloy [98], and in addition reflect the processing performance, which makes mechanical properties to be estimated easily. The hardness evolution can be attributed to the inhomogeneous phase compositions and solute segregation leading to the scatter of mechanical properties [161]. **Fig. 4.48** illustrates the macro-hardness of the Ti-45Al-2Nb-0.7Cr-0.3Si alloy in an as-cast, as-DTAed, spheriodized and as-Widmanstätten laths condition. The as-cast and the as-DTAed specimens had higher hardness values compared to that of the heat treated structures. The Widmanstätten lath structure exhibited the lowest hardness value compared to the rest; this may be attributed to be the existence of micro-cracks forming at the boundaries of the lamellar structure, along the grain boundaries or at equi-axed gamma grains due to hard transition of the dislocations, (in the as-cast alloy due to the presence of the β-phase), which therefore enhances the intergranular cleavage fracture [56]. Due to the high density of internal boundaries after the melting process, the as-cast's hardness was 323 HV was measured, **Fig. 4.48**, which was 12.9 % higher than that of the Widmanstätten lath structure. This may be due to the fact that high concentration of vacancies become mobile at elevated (α+γ phase domain) temperature, and Clemens et al. [160] reported that in this temperature range, recovery processes begin and diminish the number of defects and anti-phase boundaries, as well as internal stresses. Another reason may be due to Al-segregation in the inter-dendritic region and the Nb enrichment in the core of the dendrites suggested by Liu et al. [161]. This decreased the hardness in the TiAl-(Nb,) alloy which is mainly associated with the inhomogeneous phase compositions and the coarse lamellar spacing (as in **Fig. 4.42a**), which led to the variation of mechanical properties.

4.5.7. Summary of metallographic examinations

The as-cast ingot and the as-DTAed specimen exhibited coarse grained microstructure with lamellar colonies and γ-grains, as well as a few retained β-phases, which were attributed to: **1)** solidification path induced by the addition of Nb and Cr; and **2)** non-equilibrium solidification due to the melting method. Wang Yan et al. [154] reported that the solidification path of the γ-TiAl based alloys is influenced by the Al content and the addition of alloying elements. They also mentioned that since the preferential crystal growth is parallel to the *c* axis and there were no other orientations equivalent to the *c* axis in the hcp α-phase, the α-crystals tended to form columnar grains (as seen in **Fig. 4.38**) opposite to the direction of the heat extracted during solidification. For the alloy evaluated in this work, β-phase was contemplated both inside the lamellar structure and along the boundaries of the colonies, **Fig. 4.39a-b**. This indicated that the β-phase is the primary solidification phase. Moreover, the preferential growth of the β phase during solidification is the <100> axis and there are three equivalent directions, namely [100], [010], and [001]. As a result, the alloys demonstrated columnar characteristics which were much less pronounced than the case of α solidification [154], **Fig. 4.39a** and **Fig. 4.43**.

In order to obtain the spheriodized lath structure, the alloy was subjected to solution treatment in the α phase field at 1350 °C, with abrupt holding in the (α+γ)-phase region followed by water quenching. During cooling the α phase transformed to lamellar structure (α_2 +γ) or γ. The remnant β phase, when quenched from 1350 °C, decomposed into acicular alpha via secondary lath formation at high cooling rates as confirmed by the EBSD band contrast map in **Fig. 4.43b** and TEM in **Fig. 4.44** [175]. Moreover, the XRD results for spheriodized condition in **Fig. 4.47** confirmed that the sample was quenched from α + β phase field. The microstructure in **Fig. 4.42a** also showed $Ti_5(Si, Al)_3$ precipitates along the grain boundaries of the gamma-phase and the composition is indicated in **Fig. 4.42c**. This is in agreement with the observation by Sun and Froes [167] that $Ti_5(Si, Al)_3$ particles precipitated during the solid transformation in powder processing, whereas Ti_5Si_3 whiskers were formed during solidification in ingot metallurgy. The addition of Si to γ-TiAl based alloys improved room temperature ductility, oxidation resistance and creep properties at high temperatures.

Different manufacturing technologies bring about different microstructures. Franzén and Kalsson [56] showed that the as-cast materials may favor segregation as cooling occurs differently in the cast material. The proposed solidification sequence in this study is the $L\rightarrow\beta+L\rightarrow\beta+L+\alpha\rightarrow L+\alpha\rightarrow\alpha\rightarrow\alpha+\gamma\rightarrow\alpha_2+\gamma$.

4.5.8. Conclusions

In this study microstructure evolution, phase transition and hardness were investigated for the Ti-45Al-2Nb-0.7Cr-0.3Si alloy in as-cast, as-DTA and α-solidifying (heat-treated condition). The following conclusions might be drawn:

- The formation of β/B2 might have originated from the stabilization of retained β-phase during β→α transition and precipitation through α+γ→α_2/γ+β2 transition in the Nb-rich region. The β-phase occurred in the block, strip and cluster-shape distribution depending on the origin and solute enrichment.
- Spheriodized laths were ascertained by EBSD band contrast map. The TEM micrograph confirmed the spheriodized laths embedded inside the lamellae.
- The macro-hardness values of the samples exhibited near-gamma with B2 microstructure (as-cast and as-DTA) were high, and gradually decreased for the near-gamma/duplex/spheriodized/Widmanstätten laths with increased lamellar spacing and α_2-phase.
- Phase transformation and microstructural evolution of an α-solidifying Ti-45Al-2Nb-0.7Cr-0.3Si alloy was determined, and as a resulting homogeneous microstructure with spheriodized/ Widmanstätten laths along the lamellae were obtained.
- Widmanstätten laths were observed as long and straight laths embedded in the lamellar structure that assumed a partial orientation of their own.
- X-ray diffraction patterns confirmed the phases present, i.e. the α_2, γ, β and Ti_5Si_3. The higher macro-hardness value for as-cast structure was related to precipitation of the β-phase particles or a defect cluster interaction with dislocations. The decreased hardness in the heat treated alloy was believed to be due to elevated isothermal temperatures in the (α_2+γ) which may have brought about reduction in defects, antiphase boundaries and internal stresses.

4.6. Structure, property and orientation relationship of $\alpha_2/\gamma/Ti_5Si_3$ in as-cast and heat-treated γ-Ti-45Al-2Nb-0.7Cr-0.3Si intermetallic alloy

4.6.1. Introduction

The γ-titanium aluminide compound with an ordered $L1_0$ (space group *P*4/*mmm*, prototype CuAu) crystal structure, could potentially play an important role in the aerospace and automotive industries, in particular for engineering applications where weight reduction, improved fuel consumption and high temperature efficiency are essential requirements. However, applications of TiAl alloys are hindered by their lack of room temperature ductility and fracture toughness. In order to overcome these drawbacks, micro-alloying with ternary elements can be done. For example, Jiang [24] suggested that the intrinsic ductility of TiAl is due to directional Al *p*-Ti *d* covalent bonds, as a result ternary additions that can weaken the *p*-*d* interactions may effectively enhance the ductility of TiAl. Furthermore, Chubb et al. [168] proposed that alloying elements that can lower the axial *c*/*a* ratio of TiAl to close to unity may increase in the number of deformation modes, and consequently with improved ductility.

However, alloying with strong beta-stabilizing elements such as Cr, Nb, W and Mo may refine the grain structure and improve high temperature formability as a result of stabilized metastable B2 phase (ordered phase of β at low temperature). On the other hand, Fan et al. [28] reported that small additions of Si enhanced high temperature oxidation resistance, in particular the fine coherent Ti_5Si_3 particles formed during an eutectoid reaction along lamellar interfaces improved creep resistance. They also reported that the presence of coarse Ti_5Si_3 particles suggests that the particles may have precipitated directly from the liquid, that consequently reduced tensile properties. In order to gain fundamental understanding of the role of alloying elements in modifying the structural, electronic and mechanical properties of TiAl, specific knowledge of their lattice site occupancy behavior is crucial. The current work present the T= 0 K site preference of alloying elements viz. the 3*d* (Ti-Cu), 4*d* (Zr-Ag) transition elements and 6*g* (Si) in TiAl using first-principle calculations to thermodynamically model the developing microstructure.

It is of paramount importance to acquire knowledge of why, how, and what collective effect does the $\gamma/\alpha_2/Ti_5Si_3$ have on the arc button melted and heat treated γ-TiAl based intermetallic alloy. The present study summarizes the recent progress on the investigation of the combined effect of these compositional phases regarding the structure and property relationship. In this regard, EBSD was used for the orientation mapping. Thermal treatment was used to refine the coarse dendritic as-cast structure. Other investigations have proven that a fine grained, fully lamellar structure (FFLS) exhibited a good balance of mechanical properties [169]. Various methods have been used to obtain a FFLS in previous studies. However, Jin et al.

[169] reported two thermomechanical mechanisms of achieving this structure. The first method involved forging or extrusion at a lower temperature than the α transus temperature ($T\alpha$), then heat-treating at $T \geq T\alpha$ and/or directly extruding the alloy at $T \geq T\alpha$. Conversely, the second technique involved conversion of a coarse grained structure (originated from α-solidification) into a FFLS by cyclic heat treatment.

4.6.2. Crystal structure analysis

As shown in **Fig. 2.4** the crystal structures of $L1_0$, $D01_9$ and B2; with their representative crystallographic data analysis in **Table 2.1**, the calculated lattice parameters in the current work using ab initio simulation technique (out-sourced elsewhere [170]) are comparable to the experimental data indicated in **Table 2.1**, which were found to be: γ-phase, *a*=*b*=2.81295, *c*=4.08134, and the α/γ/β angle=90°; whereas for the α_2 phase *a*=*b*=5.72989, *c*=4.64225, whereby the α/γ=90°, β=120°. The structure of γ-TiAl based alloys is reviewed in detail by Braun et al. [171]. In the present study, the investigated alloy, of nominal composition Ti-45Al-2Nb-0.7Cr-0.3Si (at. %) comprised the Ti_5Si_3 precipitate in as-cast and heattreated condition. The Ti_5Si_3 crystal structure is hexagonal and it's prototype is Mn_5Si_3 with a space group of $P6_3/mcm$, shown in **Fig. 2.5**. In addition, extensive work has been done by researchers to determine the lattice parameters of titanium silicate (Ti_5Si_3), **Table 2.2** highlights some of this work.

The substitution of atoms changes lattice parameters due to differences in atomic radius, electronegativity etc. The calculated positions of the TiAl atoms are represented by **Table 4.6** and are denoted by the Pearson symbol *tP*2, **Table 4.7** represents α_2-Ti_3Al which is a closed packed hexagonal crystal structure denoted by Pearson symbol *hP*8 (which resembles the α crystal structure) and **Table 4.8** represent atomic positions of the supposedly Ti_5Si_3 precipitate in the Ti-45Al-2Nb-0.7Cr-0.3Si alloy. In addition, it was suggested that Ti_5Si_3 particles stable at room temperature in the Ti-45Al-2Nb-0.7Cr-0.3Si alloy, may have precipitated from the liquid during the melting [28]. However, in this work geometry optimization for the precipitate was performed and the calculated lattice parameters with their respective co-ordinate angles were found to be *a*=*b*=7.445, α=β=90°; and *c*=5.143, γ=120° which are comparable to the experimental data in Table 2. Therefore, this information (atomic positions and occupancy numbers) was helpful in determining the atomic positions of the predicted room temperature phases of the alloy in an as-cast condition using the EBSD software.

Table 4.6. Atomic positions (Wyckoff notation) in the $L1_0$ TiAl crystal structure.

Structure	Atom	Positions	X	Y	Z	Occupancy Number
$L1_0$	Al 1	1d	0.5	0.5	0.5	1
	Ti 1	1a	0.0	0.0	0.0	1

Table 4.7. Atomic positions (Wyckoff notation) in the DO_{19} Ti_3Al crystal structure.

Structure	Atom	Positions	X	Y	Z	Occupancy Number
DO_{19}	Ti 1	6h	0.16953	0.33906	0.25000	1
	Al 1	2d	0.33333	0.66667	0.75000	1

Table 4.8. Atomic positions (Wyckoff notation) in the Ti_5Si_3 crystal structure.

Structure	Atom	Positions	X	Y	Z	Occupancy Number
Hexagonal Ti_5Si_3	Ti1	6g	0.236	0.000	0.250	1
	Si1	6g	0.599	0.000	0.250	1
	Ti2	4d	0.333	0.667	0.000	1

Solidification and phase transformation depends on the alloy composition. It is believed that the γ-phase lamellae start precipitating inside coarse parent α-peritectic grains with the Blackburn orientation relationship (BOR) [51]:

$\{111\}_\gamma \parallel (0002)_\alpha$ and

$\langle 1\ \bar{1}\ 0\rangle_\gamma \parallel \langle 1\ 1\ \bar{2}\ 0\rangle_\alpha$.

Towards the last stage of cooling, the untransformed α phase, inside the lamellar structure, becomes ordered phase α_2 with the same orientation. The α_2 lamellae can coexist with γ (tetragonal) lamellae, presenting six different crystallographic orientations called variants. Often times, the γ/γ and γ/α_2 interfaces are found in lamellar structures [51]. Hecht et al. [172], pointed out that α-Ti can form (i) along peritectic reaction and transformation path, (ii) by solid

state growth from single phase β-Ti, and (iii) via both mechanisms. The authors further mentioned that solidification and phase transformation path strongly depended on alloy composition, but also on solidification kinetics and nucleation behavior of α-Ti. The α-Ti of which its prototype is Mg, has a space group like the α_2 crystal structure of *P*6_3/*mmc*. The calculated geometry optimization was performed on α-Ti and the lattice parameters with their respective co-ordinate angles viz. the *a*=*b*=3,202 Å, α=β=90°; and *c*=5.199 Å, γ=120° which is comparable to the experimental crystal data in **Table 2.1**. The atomic position of α-Ti is the same as the α_2 which is given in **Table 4.7**.

4.6.3. SEM-EBSD microstructure analysis

Transformation mechanism in the as-cast microstructure is illustrated in **Fig. 4.49a** indicating the present phases (γ+α_2) in the structure, and the double arrow shows the Ti_5Si_3 particles, mainly situated near the γ/α_2 interface boundaries. **Fig. 4.49b** shows X-ray diffraction (XRD) results: the pattern exhibited several diffraction peaks belonging to α-Ti_3Al and γ-TiAl, and some peaks of the Ti_5Si_3 second phase.

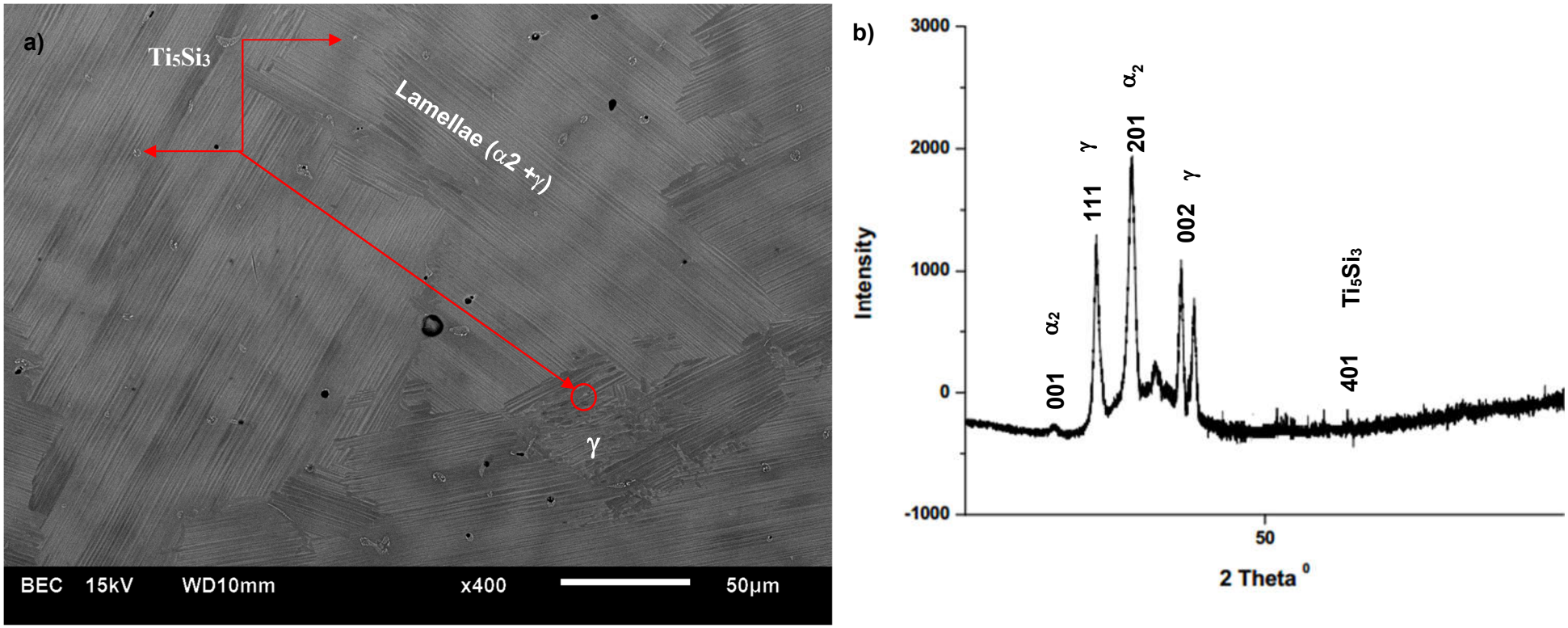

Figure 4.49. (a) As-cast microstructure; and (b) X-ray diffraction pattern.

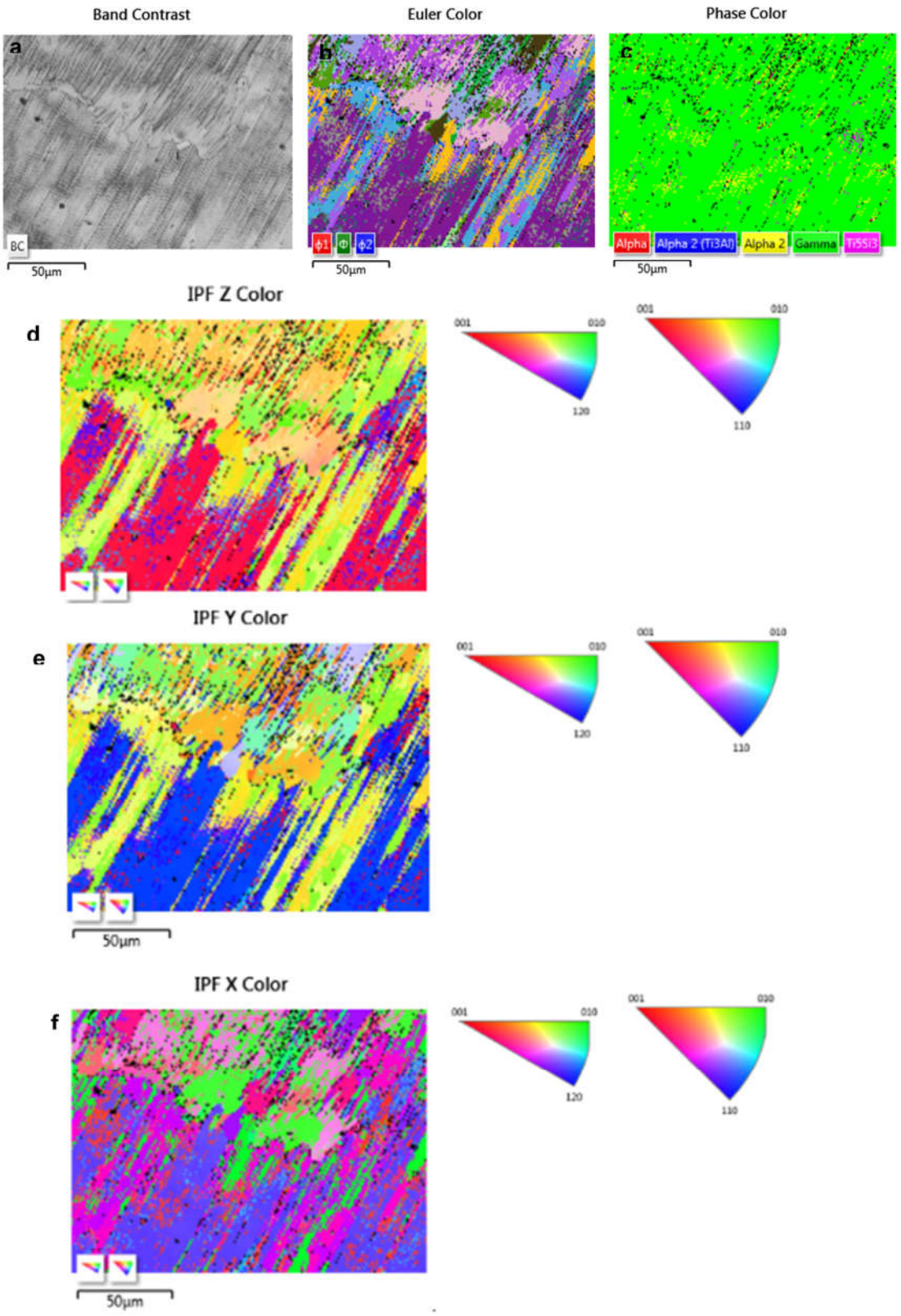

Figure 4.50. EBSD results of as-cast Ti-48Al-2Nb-0.2Cr-0.3Si alloy: (a) SEM-EBSD band contrast map (based upon quality of the acquired Kikuchi patterns shown in Fig. 4.51); (b) Euler angles; (c) phase constituents; (d)-(f) orientation maps mainly indicating the inverse pole figure maps.

Fig. 4.50 illustrates EBSD results of the as-cast Ti-45Al-2Nb-0.7Cr-0.3Si alloy. **Fig. 4.50a** is the SEM-EBSD band contrast image based on the quality of Kikuchi patterns on each point on the mapped surface. **Fig. 4.50b** is an indication of the three Euler angles which describes the orientation of the crystal lattice as determined by the indexing procedure. **Fig. 4.50c**, represents phase constituents which exhibited $\gamma/\alpha_2/Ti_5Si_3$ phases in the analyzed area, as marked by green, yellow and blue (α_2-with different lattice parameters shown in **Table 4.10** further below), and pink. **Fig. 4.50(d)-(f)** is a representation of orientation map superimposed with band contrast image of **Fig. 4.50a**, with their corresponding inverse pole figures in the x, y and z directions. Dey et al. [51], highlighted that the boundaries between lamellar grains were often escorted with equiaxed γ_{mono} grains. However, in this case, the lamellar grains were identified having mostly the γ phase (~90%), which is supported by phase fraction estimation shown in **Table 4.9**. Therefore, this may denote that the SEM-EBSD research studies do not illustrate the high temperature α solidification texture properly [51].

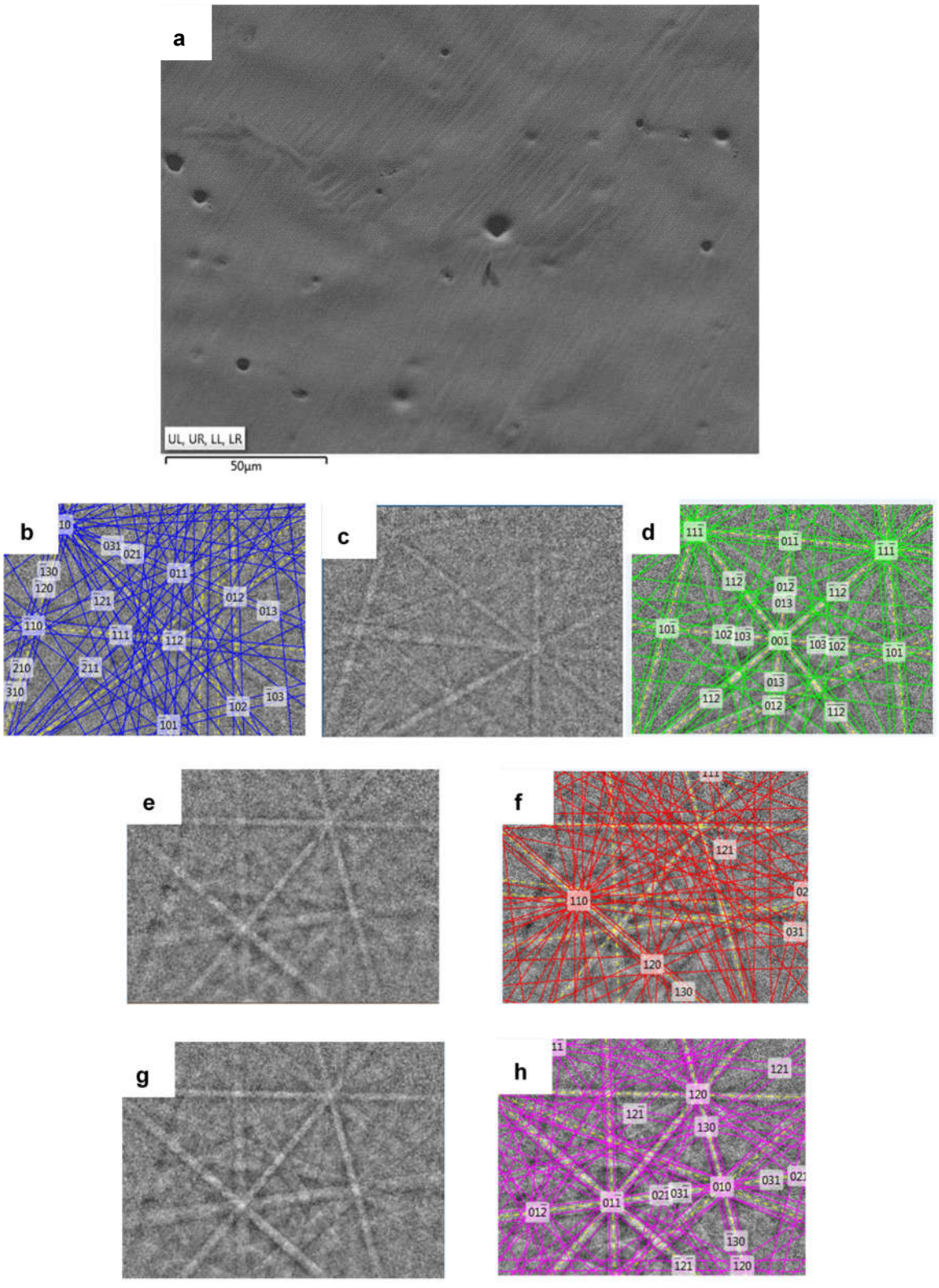

Figure 4.51. (a) Electron layered image of an electro-polished Ti-48Al-2Nb-0.7Cr-0.3Si intermetallic alloy (c), (e) and (g) are Kikuchi patterns with their corresponding indexed phases (b), (d), (f) and (h) according to the color coding in Fig. 4.50 (c).

Fig. 4.51a shows EBSD electron image showing the phase constituent (marked by different colors) in **Fig. 4.50c** whereby the phase fraction estimation is illustrated in **Table 4.9**, where MAD stands for mean angular deviation, and describes the quality of the fit of the solution. According to CHANNEL 5 Oxford Instruments [73], the smaller the mean MAD number, the better the match between the detected Kikuchi bands and the simulation. In general, a number under 1 ° is acceptable for most systems. As given in **Table 4.9**, the phase that had better match of the Kikuchi patterns was the γ-phase structure. Shown in **Fig. 4.51(c)**, **(e)** and **(g)** are the Kikuchi patterns with their corresponding indexed phases (**Fig. 4.51(b), (d), (f)** and **(h)**); for which the structural data are given in **Table 4.10**. **Fig. 4.49a** shows that Ti_5Si_3 was found along the γ-grain boundaries, and from **Table 4.10** shows that the *c*/*a* for the γ-TiAl was 1.4520 (which increased due to the addition of Si) and that of the Ti_5Si_3 was 0.6899; which is mostly similar to the work done by Sun et al [27] **Fig. 2.6a-c**. The images in **Fig. 2.6** represents Ti_5Si_3 particle with a polygonal shape in Ti_{52}-Al_{48}-$3Si_2Cr$ and Ti-45Al-2Nb-0.7Cr-0.3Si alloys, respectively. **Fig. 4.52** illustrates the semi-coherent Ti_5Si_3/γ interface. For some of the round Ti_5Si_3 particles in a γ matrix (**Fig. 4.49a**), there was no orientation relationship at the Ti_5Si_3/γ interface, it has been suggested to have nucleated at the vacancies [27].

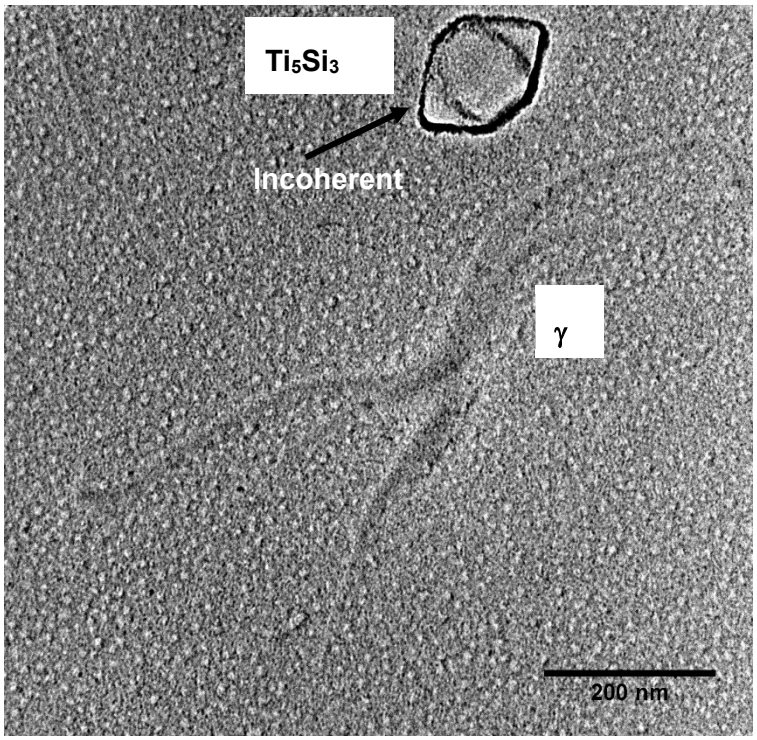

Figure 4.52. TEM micrograph showing incoherent Ti_5Si_3/γ interface in Ti-45Al-2Nb-0.7Cr-0.3Si.

The Ti_5Si_3/γ interface (marked with an arrow in **Fig. 2.6**) has an orientation relationship of $(011)_\gamma$ || $(0110)_{Ti5Si3}$ and $(233)_\gamma$ || $(0002)_{Ti5Si3}$. This was confirmed by the selected area

diffraction pattern (SADP) and the corresponding schematic diagram of a Ti_5Si_3/γ interface in Ti_{52}-Al_{48}-$3Si_2Cr$ represented in **Fig. 2.7**. Therefore, the needle-like Ti_5Si_3 particles precipitated along the γ/γ boundaries nucleated with an orientation relationship of $(101)_\gamma \parallel (1010)_{Ti5Si3}$.

The EBSD orientation mapping was not possible to detect sub-structure lines present in the Kikuchi patterns of the ordered intermetallic phases [51]. So it was impossible to differentiate ordered α_2 phase from disordered α phase and also to separate the six variants of the γ phase. However, the γ variants were distinguished as two fcc orientations i.e. γ and γ-twin. Furthermore, each fcc γ variant detected under EBSD represented three ordered domain tetragonal γ variants which sums to six. It is common practice to determine the six tetragonal γ under TEM using several techniques [51]. Most commercial EBSD systems, employ techniques which uses Hough's transform method which is used to convert electron backscattering patterns (EBSP) image into a different image where EBSPs are indicated by bright spot in the transformed image. However, it is important to note that the Oxford Instrument's HKL Channel 5 software [73] employed in this study used a rather advanced fit; for accurate results and beneficial for complicated phases such as γ-TiA, instead of Hough transform method which are not able to yield accurate results.

Table 4.9. Phase fraction estimation.

Phase Name	Phase Fraction (%)	Phase Count	Mean Band Contrast	Standard Deviation Band Contrast	Mean MAD	Standard Deviation MAD
α	0.33	76	103.62	11.57	1.15	0.37
α_2-(Ti_3Al)	0.05	12	110.08	17.43	1.26	0.42
α_2	4.56	1037	109.94	15.60	0.88	0.39
γ	89.84	20439	157.74	22.05	0.63	0.18
Ti_5Si_3	0.73	165	131.65	19.89	0.74	0.24
Zero Solutions	4.49	1021	114.80	23.17		

Table 4.10. Phase acquisition.

Phase Name	a	B	c	α	β	γ	Space group

α	3.20 Å	3.20 Å	5.20 Å	90.00 °	90.00 °	120.00 °	194
α_2-(Ti_3Al)	5.72 Å	5.72 Å	4.64 Å	90.00 °	90.00 °	120.00 °	194
α_2	5.73 Å	5.73 Å	4.64 Å	90.00 °	90.00 °	120.00 °	194
γ	2.81 Å	2.81 Å	4.08 Å	90.00 °	90.00 °	90.00 °	123
Ti_5Si_3	7.45 Å	7.45 Å	5.14 Å	90.00 °	90.00 °	120.00 °	193

4.6.4. Crystallography of phase domains

According to Yang et al. [115], the mis-orientation angles between the α grains arising from the same β grain can only be 10 ° 53′, 60 °, 60 ° 83′, 63 ° 26′,or 90 °, respectively. In addition, Hecht et al. [172] showed that if misorientation angles measured by EBSD between neighboring α grains differ from these ordinates, the grains cannot originate from the same parent β grain, or else the transformation does not obey the Burgers orientation relationship of $\{110\}_\beta$ // $\{0001\}_\alpha$ and $<111>_\beta$ // $<2\ \bar{1}\ \bar{1}0>_\alpha$. Therefore, the orientation angle can be applied to ascertain whether the α grain obeys the Burgers orientation relationship or not. However, when the misorientation angles between the neighboring α grains differ from other angles, these grains are non-Burgers α grains, and such a microstructure is regarded to be non-textured. Furthermore, misorientation axes can help clarify which crystallographic directions the misorientation axes align with for a given range of misorientation angles. However, in the current research study as shown in **Fig. 4.50d-f,** the misorientation axes in the form of four colors which shows the $\alpha/\alpha_2/\gamma$ grain boundaries and captures the orientation difference of neighboring grains viz. (8 °-12 °, blue; 57 °-63 °,green to yellow; 88 °-92 °, red); inverse pole figures. **Fig. 4.50c** shows two colors viz. green and red representing the γ and α phases, respectively. The orientation of the EBSD map was close to an angular tolerance of 20 °which is related to γ-variants of the lamellae in the structure. **Fig. 4.53** is the representation of the contoured pole figures for the γ + α phases; which illustrates that {111} // {10-10} and follows the Blackburn orientation, as discussed above. However, according to Dey et al. [51] the spatial and angular resolutions of transmission microscopy are required to distinguish the different γ lamellae and their variants. Nevertheless, in this study when assessing the EBSD-

orientation maps, it was important to analyze frequency distribution of misorientation angles (discussed below) between neighboring γ grains to ascertain γ variants that obey Burgers orientation relationship (BOR) relative to the peritectic alpha grains that occurred as a result of solidification during the arc button melting.

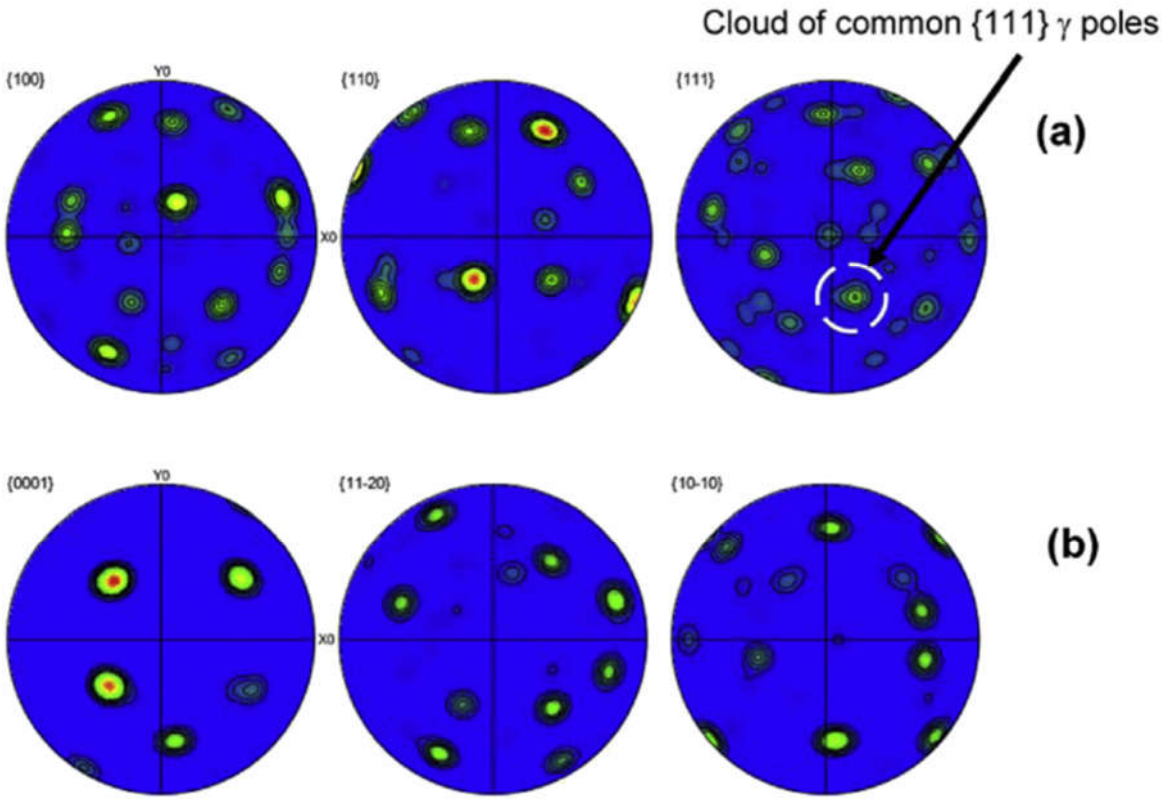

Figure 4.53. Pole figures (a) γ-phase, and (b) α-phase.

The Blackburn orientation relationship at interface between γ and α phase was: (111)γ || (0001)α and <1 $\bar{1}$0]γ || <11 $\bar{2}$0>α. Therefore, this may suggest that the γ-phase precipitated from the α-phase.

Fig. 4.54a shows misorientation axes for the γ-phase. These describe which crystallography directions the misorientation axes align with for a chosen range of misorientation angles. The observed misorientation axes are indicated by clusters between [001] and [010] in the 57- 63 ° section; another cluster is observed at about the [110] in the 88-92 °. This may be supplemented by **Fig. 4.54b** which is a representation of the relative frequency vs. misorientation angle, where the correlated (blue) and uncorrelated (red) misorientation plot are different from the random line and from each other. The difference between the uncorrelated and random distribution may be due to the strong fiber texture <111> shown in **Fig. 4.54c** (where colored grains in the texture map are Burgers γ grains and others are non-

Burgers γ grains). The correlated distribution exhibited a fairly large number of boundaries with misorientations below 15 ° compared to the uncorrelated distribution. Moreover, the results also showed that the correlated distribution exhibited a large number of boundaries with misorientations of 85-90 °. Clearly from these results, the low and high angle boundary may be a significant feature of the microstructure and not simply a product of strong texture.

The results shown in **Fig. 4.55a** are the misorientation axes of the α_2 phase, where clusters are seen between <011> and <010> at 8-12 ° angle, whereas clusters <010> were observed at 35-42 ° angle, also clustering of <101> at 57-63 ° and lastly clusters of <120> at 88-92 ° angle. **Fig. 4.55b** was the misorientation angle, where the correlated distribution exhibits a fairly large number of boundaries with misorientations below 15 ° compared to the uncorrelated distribution. Like the γ-phase, it can be seen that the low angle boundary maybe be a significant feature of the microstructure and not a product of texture **Fig. 4.55d**. **Fig. 4.55c (i)** is the γ-pole figure {110} which may be parallel to the α_2-phase in the <110> direction shown in **Fig. 4.55c (ii)**, as indicated by the blue circles. The two phases may exhibit a Burgers orientation relationship with the parent α-phase, also represented by the blue circle in **Fig. 4.55c (iii)** which illustrates the α pole figure in the <0001> direction. On the other hand, **Fig. 4.56(a)** is the misorientation axes (with accompanying color coding) of the Ti_5Si_3 precipitate; here there are no observable clusters of direction in the respective angles. However, like the α_2-phase, the misorientation angles of the precipitate in **Fig. 4.56b** exhibited a large number of boundaries with misorientation below 15 °, indicating that there was no preferential misorientations found in the second phase in the as-cast condition. **Fig. 4.56(c)** and **(d)** represents the pole figures of α and the (Ti_5Si_3) precipitate, both phases seemed to obey the Burgers orientation relationship, and therefore it can be concluded that the precipitate may have nucleated on the alpha phase. The reason behind this may have originated from the melting process (in the β-phase region), whereby the matrix began to solidify in Si-lean as a result of $L \rightarrow \beta + L_1$, and as cooling takes place a eutectic reaction occurs at about 1432 °C corresponding with $L_1 \rightarrow \alpha + Ti_5Si_3$. However, dendrite morphology in the in as-cast microstructure exhibited a hexagonal symmetry of the α dendrites, which is suggestive of a reaction L1 +β→ α that, took place immediately after solidification of L→β+L1. Betweeen these dendrites, the eutectic reaction L1→α+ Ti_5Si_3 occurred in the last solidified liquid (Si-rich) [167].

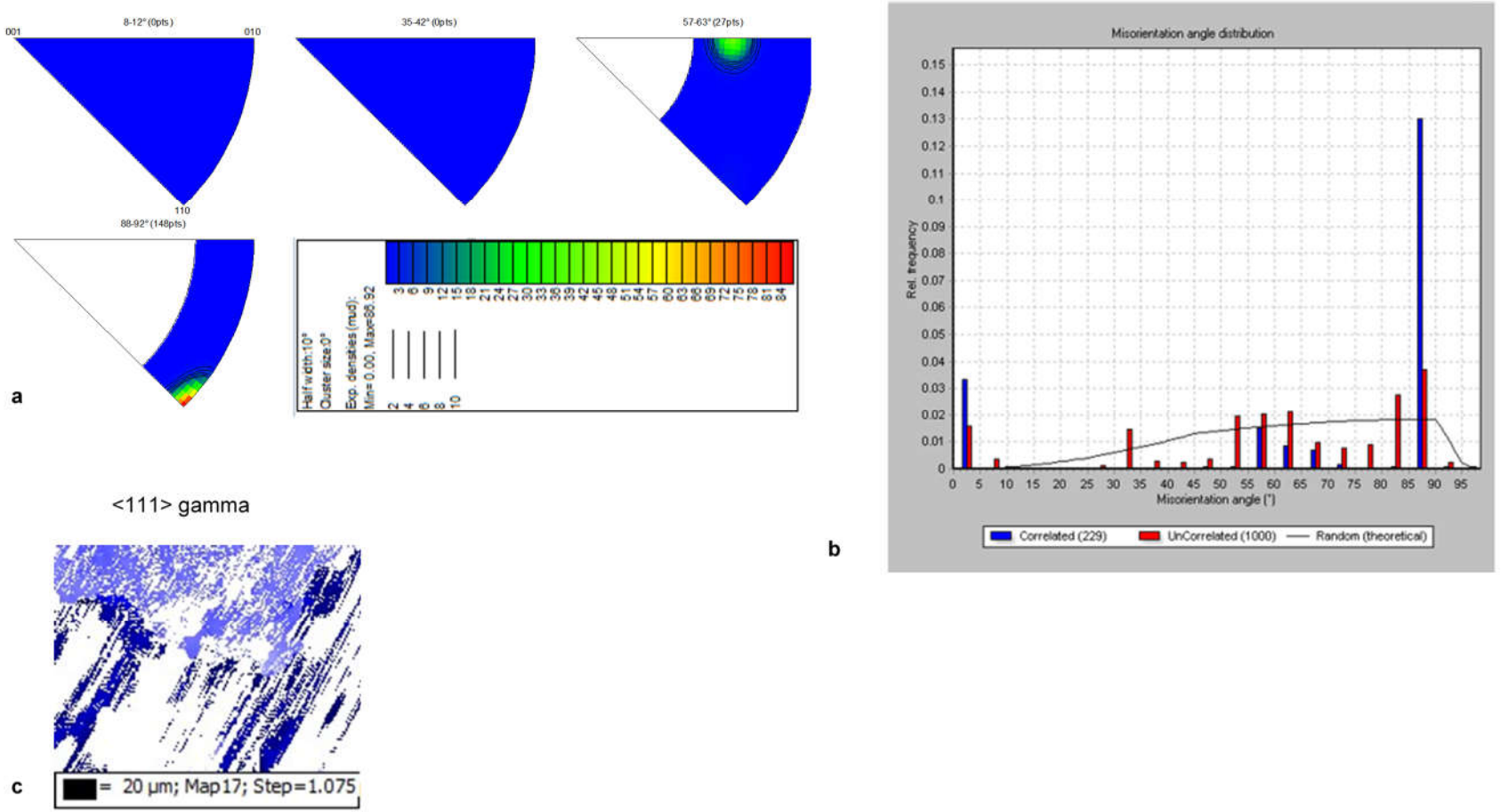

Figure 4.54. Misorientation data on the γ-phase: (a) Misorientation axes of the γ-phase with corresponding color coding; (b) Misorientation angle distribution; and (c) <111> fiber texture.

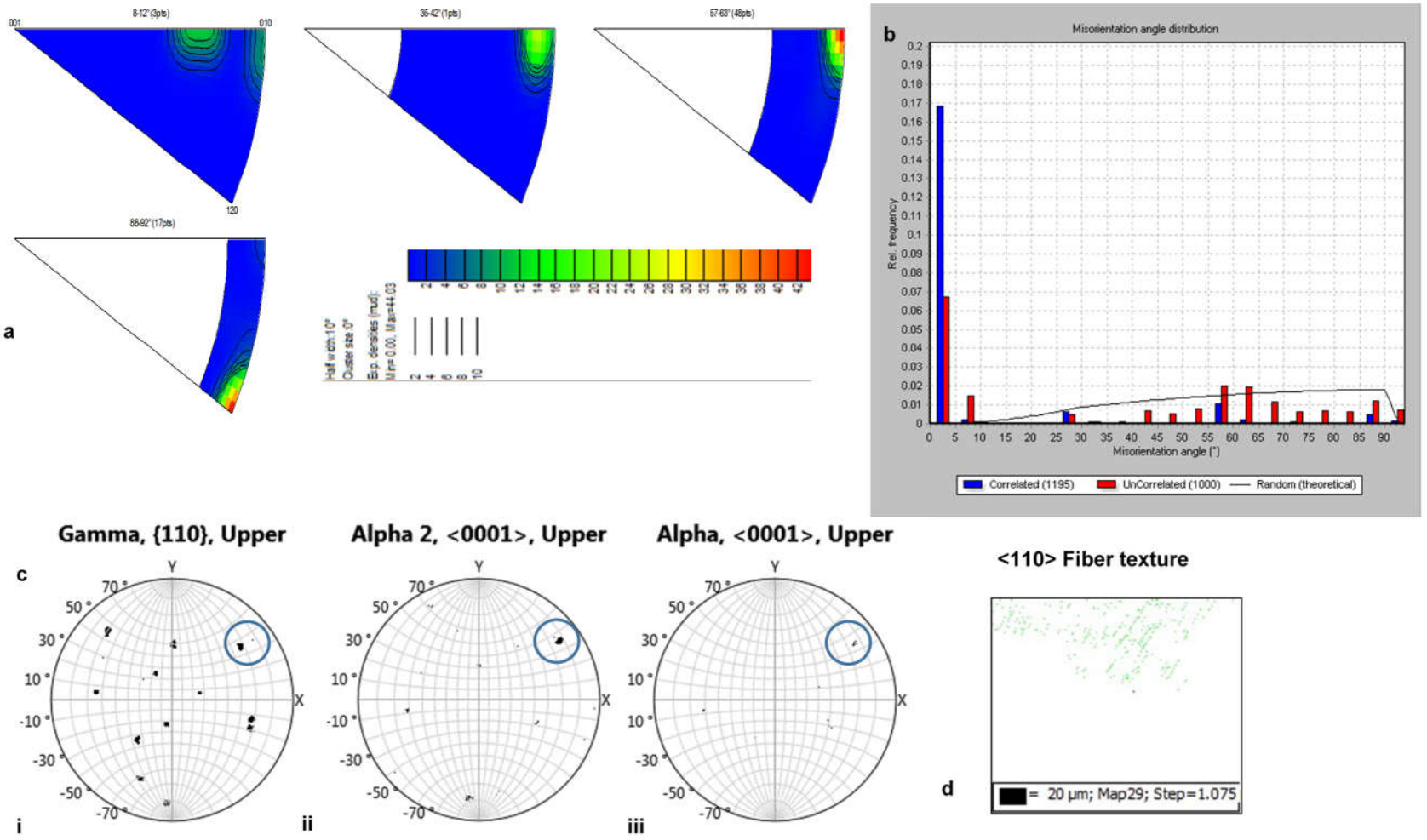

Figure 4.55. Misorientation axes of the α_2-phase with corresponding color coding; (b) Misorientation angle distribution (α_2); (c) Pole figures: i) of γ-phase, ii) α_2-phase and iii) α-parent phase; and (d) the <110> fiber texture (α_2).

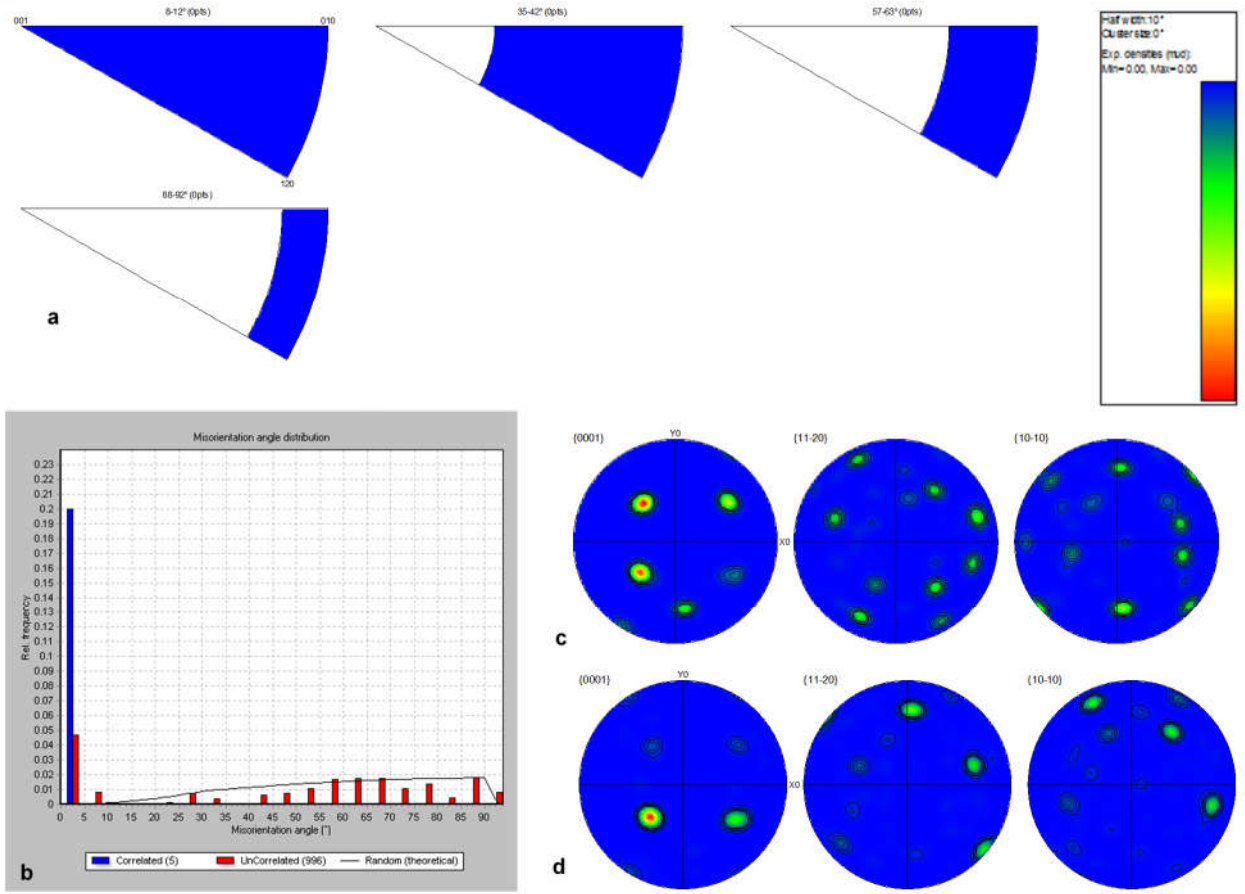

Figure 4.56. Misorientation axes of the Ti_5Si_3 second-phase with corresponding color coding on the far right; (b) Misorientation angle distribution (Ti_5Si_3); Pole figures of (c) α, and (d) (Ti_5Si_3).

4.6.5. SEM-EDS micro-analysis

To determine elemental mapping of the as-cast Ti-45Al-2Nb-0.7Cr-0.3Si alloy, SEM/EDS micro-analysis was employed. The spectrum mapping, shown in **Fig. 4.57** gives the distribution of the elements viz. Ti, Al, Nb, Cr and Si in the analyzed area of the alloy, shown in the top left image. The distribution of Cr in the alloy was close to nil, which is a clear indication that it was part of the dissolutioning process during melting of the alloy. The bottom right image, exhibits a spectrum map which is superimposed with the calculated wt %, which is closer to the initial composition. These results may display the likeness of homogeneity.

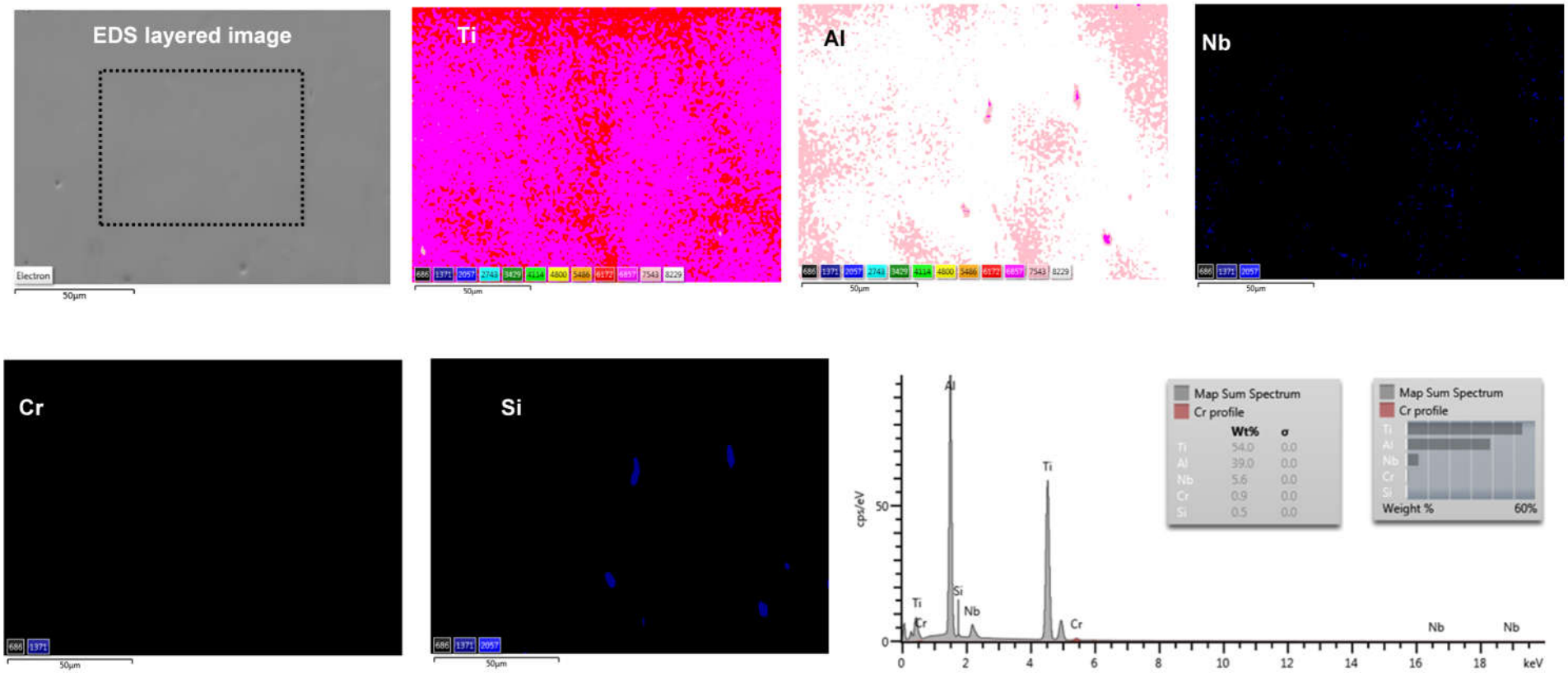

Figure 4.57. SEM-EDX elemental mapping of the γ-TiAl based alloy.

4.6.6. Heat-treated fully lamellar structure

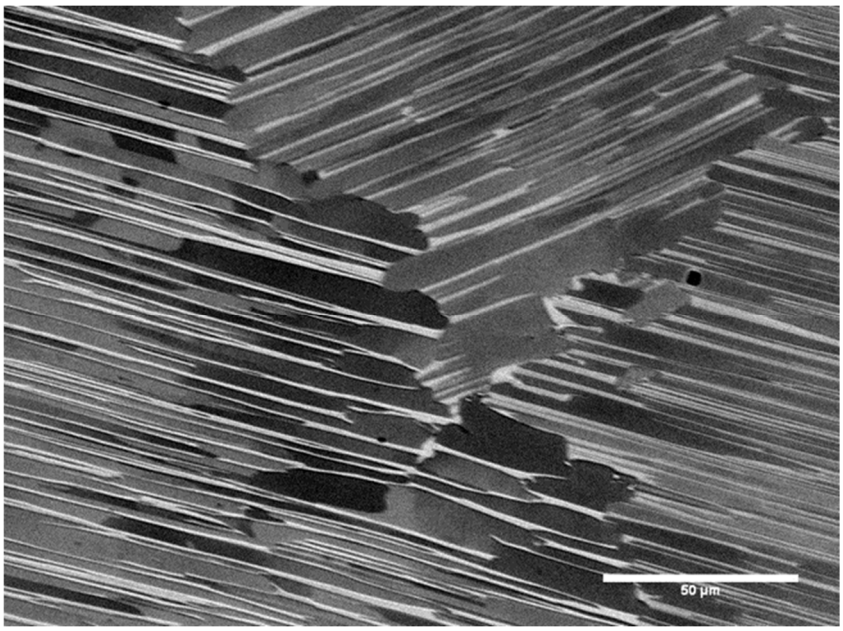

Figure 4.58. SEM-BSE micrograph showing a fully lamellar structure of the Ti-45Al-2Nb-0.7Cr-0.3Si.

The Nb and Mo shifted the α-transus temperature towards the Al-rich side, thus narrowing (α +γ) phase field, **Fig. 2.25**. **Fig. 4.58** illustrates a fully lamellar structure of the Ti-45Al-2Nb-0.7Cr-0.3Si alloy which had been heat treated in the α-phase domain with subsequent furnace cooling. The phase identification was done employing the X-ray diffraction shown in **Fig. 4.59**.

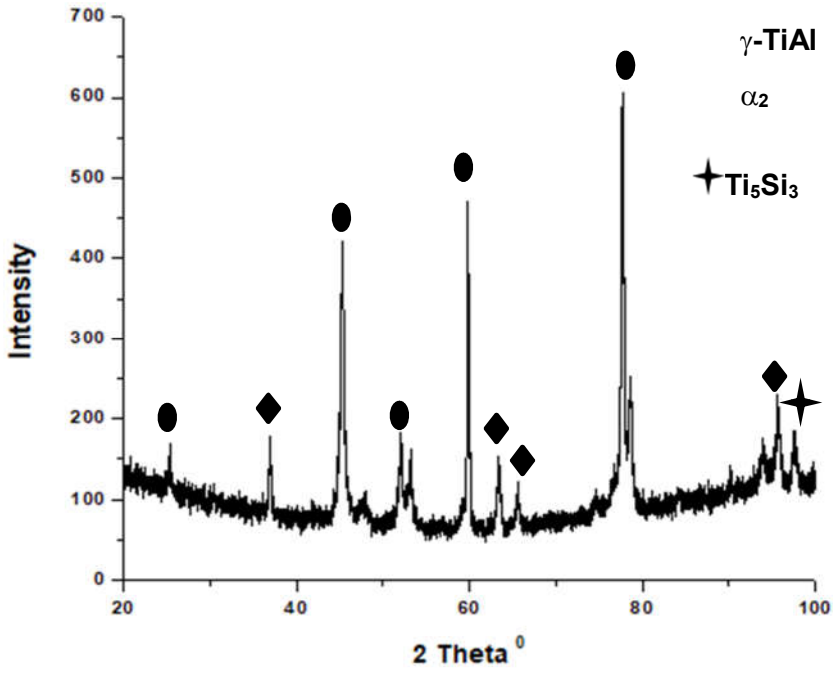

Figure 4.59. XRD results for the fully lamellar structure of the γ-TiAl based alloy doped with Nb, Cr and Si.

To clearly characterize this heat treated fully lamellar γ-TiAl based alloy, EBSD was used and the results are given in **Fig. 4.60**. The backscattered electron image and the band contrast results are shown **Fig. 4.60(a)** and **(b)** respectively. The lamellar ($\gamma+\alpha_2$) structure was almost random, suggesting that no texture formed attainable in the fully lamellar structure **Fig 4.60c**. **Fig. 4.60d** represents the phase color with the evidence (shown in **Table 4.9**) that the dominating phase is the γ-phase with a c/a ratio of 1.452.

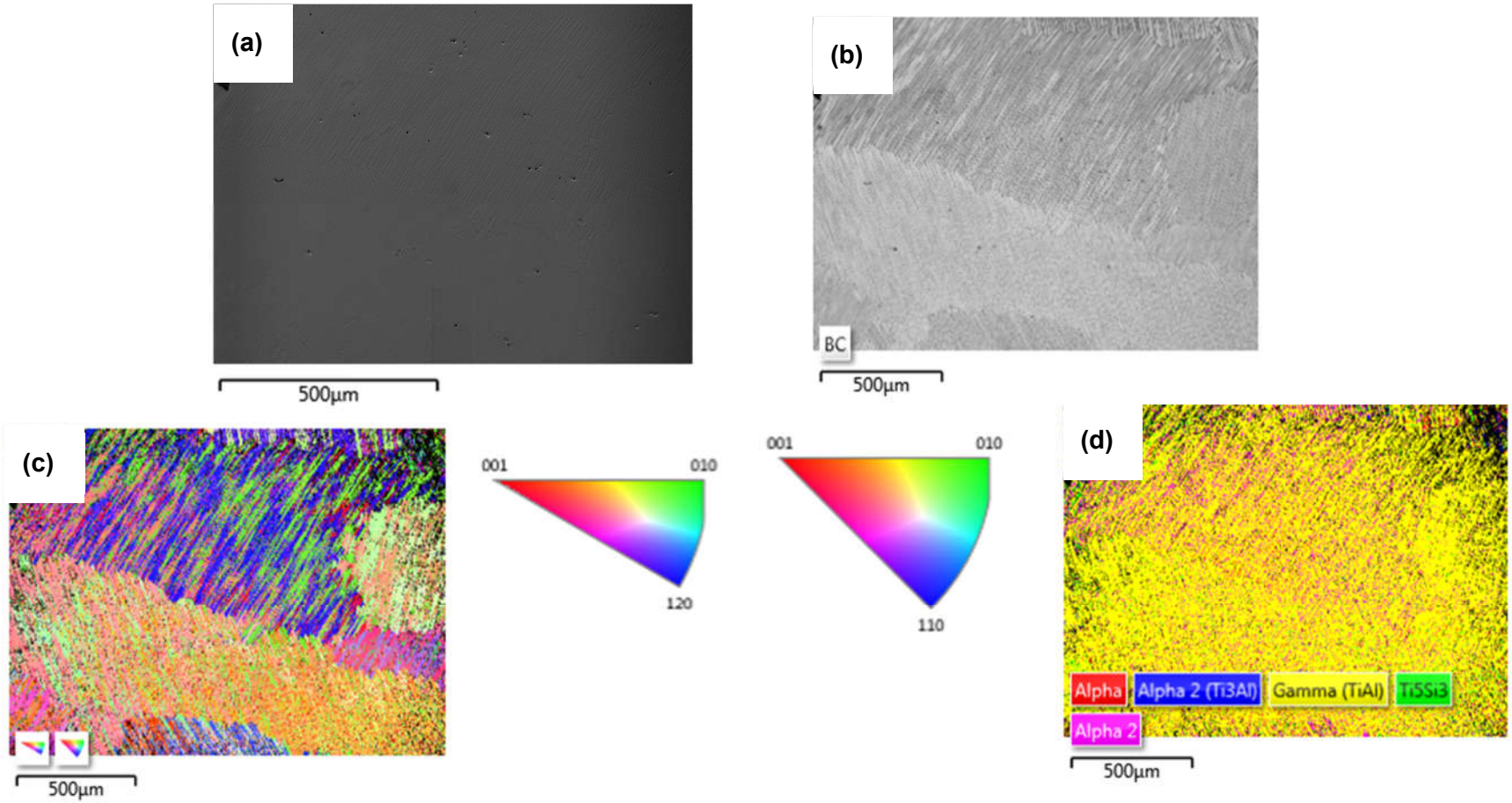

Figure 4.60. EBSD map of the fully lamellar Ti-45Al-2Nb-0.7Cr-0.3Si alloy: a) electron micrograph, b) band contrast image, c) grain orientation map, and d) phase color map.

4.6.7. Conclusions

The composition-structure-property relationship of the as-cast γ-Ti-45Al-2Nb-0.7Cr-0.3Si based intermetallic alloy was examined and the following conclusions were drawn:

- The phases stable at room temperature were found to be $\gamma/\alpha_2/Ti_5Si_3$. First principle approach (using VASP) was performed to study the stability of $L1_0$, DO_{19} and HCP-A3 atomic position and the Wyckoff notation and occupancy numbers obtained for the phases and were used for the EBSD analysis. The calculated lattice parameters were found to be in good agreement with the available experimental data.

- Grain orientation of $\gamma/\alpha/Ti_5Si_3$ phases were studied via EBSD, using its distinctive, advanced fit band detection and indexing algorithm, the HKL CHANNEL 5 invariably and correctly measured the orientation of the tetragonal γ-TiAl crystals. The formation of $\gamma/\alpha_2/Ti_5Si_3$ in the Ti-48Al-2Nb-0.7Cr-0.3Si intermetallic alloy followed the Blackburn orientation relationship for both the as-cast (β-solidifying) and heat-treated (α-solidifying) phases. The formation of $\gamma/\alpha_2/Ti_5Si_3$ follows the Blackburn orientation relationship (BOR): (β-solidifying) = $\{110\}^{\beta}$ // $\{0001\}^{\alpha}$ and $<111>^{\beta}$ // $<2\ \bar{1}\ \bar{1}0>^{\alpha}$ and (α-solidifying) = $(111)\gamma$ || $(0001)\alpha$ and $<1\ \bar{1}0]\gamma$ || $<11\ \bar{2}0>\alpha$. This relationship was precisely followed by$<1\ \bar{1}0]$ direction, while the $<\ \bar{1}01]$ directions showed deviations of 0.2 ° to 0.3 ° to the respective α_2-directions.
- The Ti_5Si_3/γ interface had an orientation relationship of $(011)_{\gamma}$ || $(0110)_{Ti5Si3}$ and $(233)_{\gamma}$ || $(0002)_{Ti5Si3}$Surface characterization of the cyclically oxidized γ-Ti-46Al-2Nb-0.7Cr alloy after nitridation.

These conclusions can form the basis of First principles studies to obtain isotropic physical properties of this specific alloy, which has not been done so far.

4.7. Surface characterization of the cyclically oxidized γ-Ti-48Al-2Nb-0.7Cr alloy after nitridation

4.7.1. Introduction

Alloying of the γ-TiAl results in mixed microstructure with improved ductility, fatigue properties and strength [173]. Full commercialization of these alloys depends on successful control of the microstructure and texture by thermomechanical processing, hence, the hot forming of these alloys needs to be optimized [174]. The oxidation behavior of TiAl alloys at high temperatures are critical for successful industrialization of this alloy in aerospace and other high-temperature applications. The oxidation rate of Ti-based alloys follows a logarithmic law at low temperatures and a parabolic law at higher temperatures [175]. To improve the surface properties of TiAl alloys, surface coating has been considered [176]**.** It has emerged that the formation of surface titanium oxynitrides is feasible [112] and it changes the surface properties and improves the fatigue and wear resistance [177]. According to Chu and Wu [177] the ion nitriding has a faster growth rate of nitride layers, easier control of the crystal structure of nitrided layers with fewer environmental problems compared to other industrial techniques. The nitride-coated materials are used in cutting tools due to their superior tribological and high oxidation resistance properties. For example, chromium nitride (CrN) has been extensively used, although an improvement in the oxidation resistance is still necessary for certain applications [177]. The FCC solid solutions such as AlCrSiN and AlCrN are used for coating tool steels for better performance and improved wear resistance [178]. The CrN composite is superior to TiN at elevated temperatures [179] in corrosion performance and wear properties [180]. Addition of W, B, C and N to titanium aluminides stimulates either dispersion or precipitation hardening in an efficient way [181]. The Cr containing titanium aluminide has revealed poor cyclic oxidation in an as-cast condition when exposed to 900 °C [78]. In the present study, the surface properties of the γ-Ti-48Al and Ti-48Al-2Nb-0.7Cr intermetallic alloy were improved by nitridation and subjected to cyclic oxidation.

4.7.2. Nitridation analysis of γ-Ti-48Al and Ti-48Al-2Nb-0.7Cr intermetallic alloys

The final chemical composition after casting is shown in **Table 3.2** for the binary (TiAl) and the quaternary (TiAlNbCr) alloys. The difference between nominal and final composition may be due to varying vapor pressures of different components in the alloys, and Al (low melting point)

being volatile may have experienced the highest burning loss [79]. However, there was not much difference on the microstructure, hence the main phases were the γ-TiAl, α-Ti_3Al, and remnant β,.

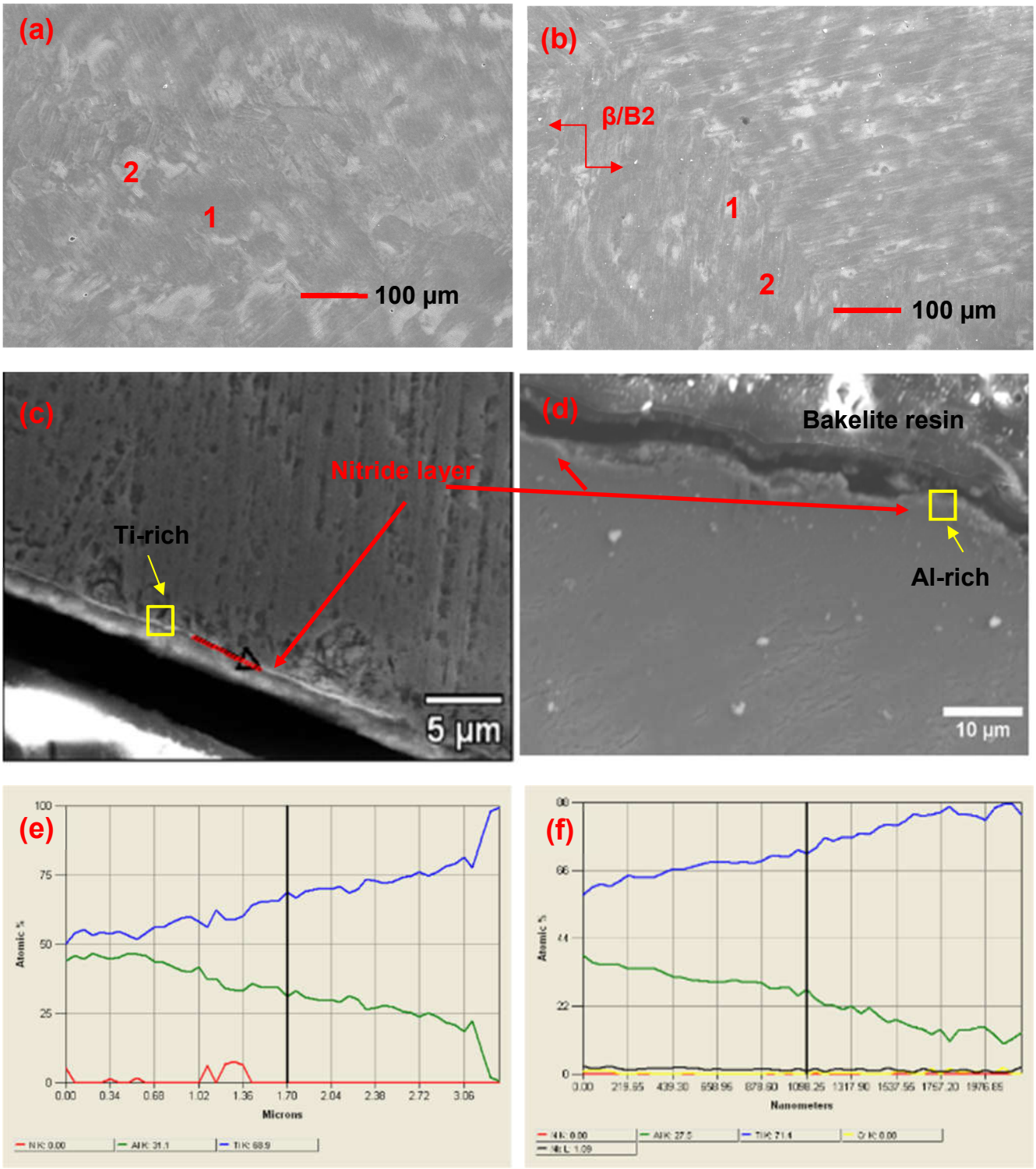

Figure 4.61. SEM-SEI micrographs of (a,c) as-stabilized and nitrided γ- Ti-48Al, (b,d) as-stabilized and nitrided Ti-48Al-2Nb-0.7Cr, (e) line traces of the nitrided γ-TiAl, and (f) line traces of the nitrided Ti-Al-Nb-Cr layers.

Fig. 4.61a shows the stabilized intermetallic γ-TiAl SEM secondary electron image (SEI) image. The elemental compositions of each phase are presented in **Table 4.11.** The predominant phases were γ-TiAl (dark contrast) and α_2-Ti_3Al (light contrast) which was in agreement with the annealing in the (α_2+γ) phase domain. The EDX elemental analysis of the stabilized alloys was similar to the as-cast compositions demonstrating the microstructural homogeneity. Each EDX analysis was obtained as an average of the values measured at more than five locations. The quaternary alloy in **Fig. 4.61b** exhibited the presence of remnant β/B2-phase. Alloying with Nb and Cr refined the alloy grains and stabilized the β-Ti phase [182] [183]. However, the combination of Nb and Cr did not yield the best cyclic oxidation results compared to when Nb was used alone in an as-cast condition [78]. The SEM micrographs of the nitrided intermetallic γ-TiAl and Ti-Al-Nb-Cr alloys cross-sectioned are shown in **Fig. 4.61c, d**. A thin nitride layer developed on γ-TiAl alloy is visible (**Fig. 4.61c),** revealing porosity next to the coated layer. Since N has a higher affinity for Ti than Al, the effect of annealing at 900 °C unstabilized the Ti-Al bonding due to atomic vibrations and selectively attacked the alloy and consequently promoted pores near the surface. **Fig. 4.61d** shows a nitride layer developed on the Ti-Al-Nb-Cr alloy surface,. which was thinner compared to the layer on the binary alloy (**Fig. 4.61e-f)**. There was no evidence of excessive porosity on the surface of the Ti-Al-Nb-Cr alloy, compared to the binary Ti-Al alloy.

Table 4.11.Elemental spot analysis of the γ-Ti-48Al based alloys (at. %).

Alloy	Ti	Al	Nb	Cr
TiAl	1. 54.2	45.8	-	-
	2. 53.0	47.0	-	-
TiAlNbCr	1. 52.5	45.0	2.0	0.5
	2. 51.4	46.1	1.5	1.0

The yellow rectangles in **Fig. 4.61c & d** are constituted in **Fig. 4.62-4.63** delineating surface layered scale showing the elemental distribution of the phases ascertained with the subsequent nitridation process of the Ti-48Al, and Ti-48Al-2Nb-0.7Cr alloys. The elemental distribution maps in **Fig. 4.62** shows that the overall scale was the Ti-rich phase, whereas in **Fig. 4.63** was the Al-rich phase. This is a clear indication that the Ti-48Al-2Nb-0.7Cr alloy had a mixture of TiO_2 and Al_2O_3 or rather Al_2O_3 in bulk compared to the Ti-48Al alloy. According to Gong et al. [184], a single or continuous Al_2O_3 outmost layer is the most desired oxide film

structure, whereas a single TiO_2 or a mixture of TiO_2 and Al_2O_3 is disadvantageous for oxidation resistance due to porous TiO_2, and the layer is susceptible to spalling.

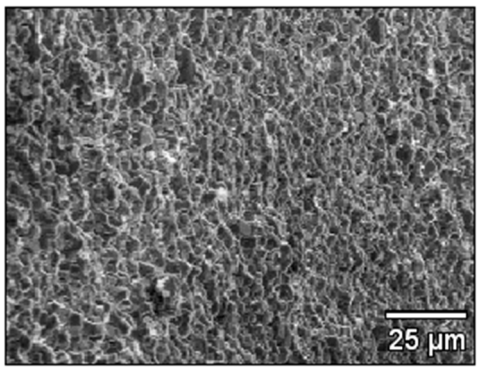

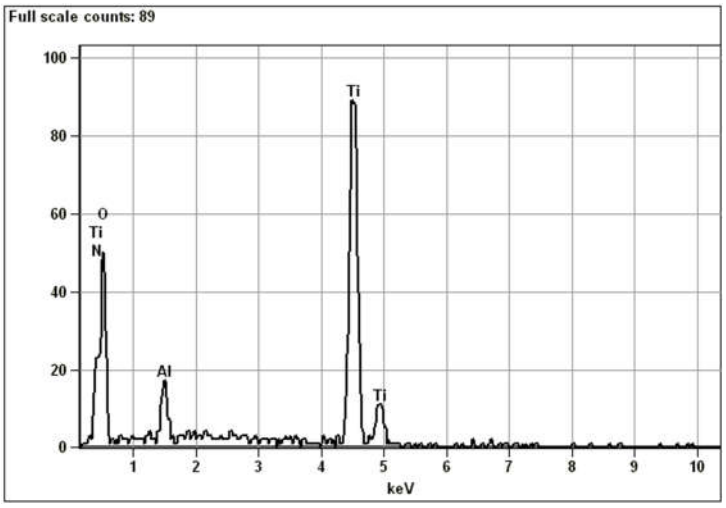

Element	Atom %	%Error
N K	24.69	+/- 2.02
O K	52.71	+/- 2.48
Al K	1.75	+/- 0.15
Ti K	20.85	+/- 0.59
Total	100.00	

Figure 4.62. Elemental distribution of phases of as-stabilized Ti-48Al alloy after nitriding, indicative of yellow rectangle in Fig. 4.61c.

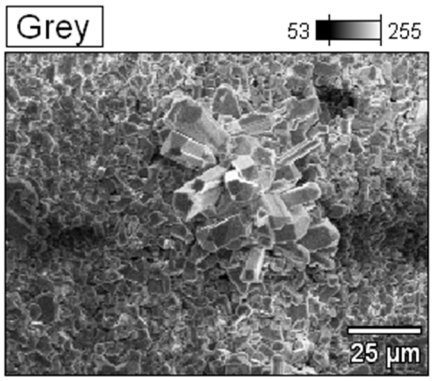

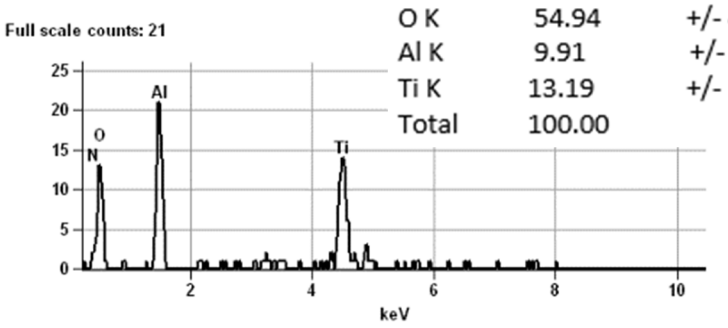

Element	Atom %	% Error
N K	21.96	+/- 4.99
O K	54.94	+/- 4.69
Al K	9.91	+/- 0.62
Ti K	13.19	+/- 1.20
Total	100.00	

Figure 4.63. Elemental distribution of phases of as-stabilized Ti-48Al-2Nb-0.7Cr alloy after nitriding, indicative of yellow rectangle in Fig. 4.61d.

4.7.3. Cyclic oxidation of the nitride γ-TiAl based alloys

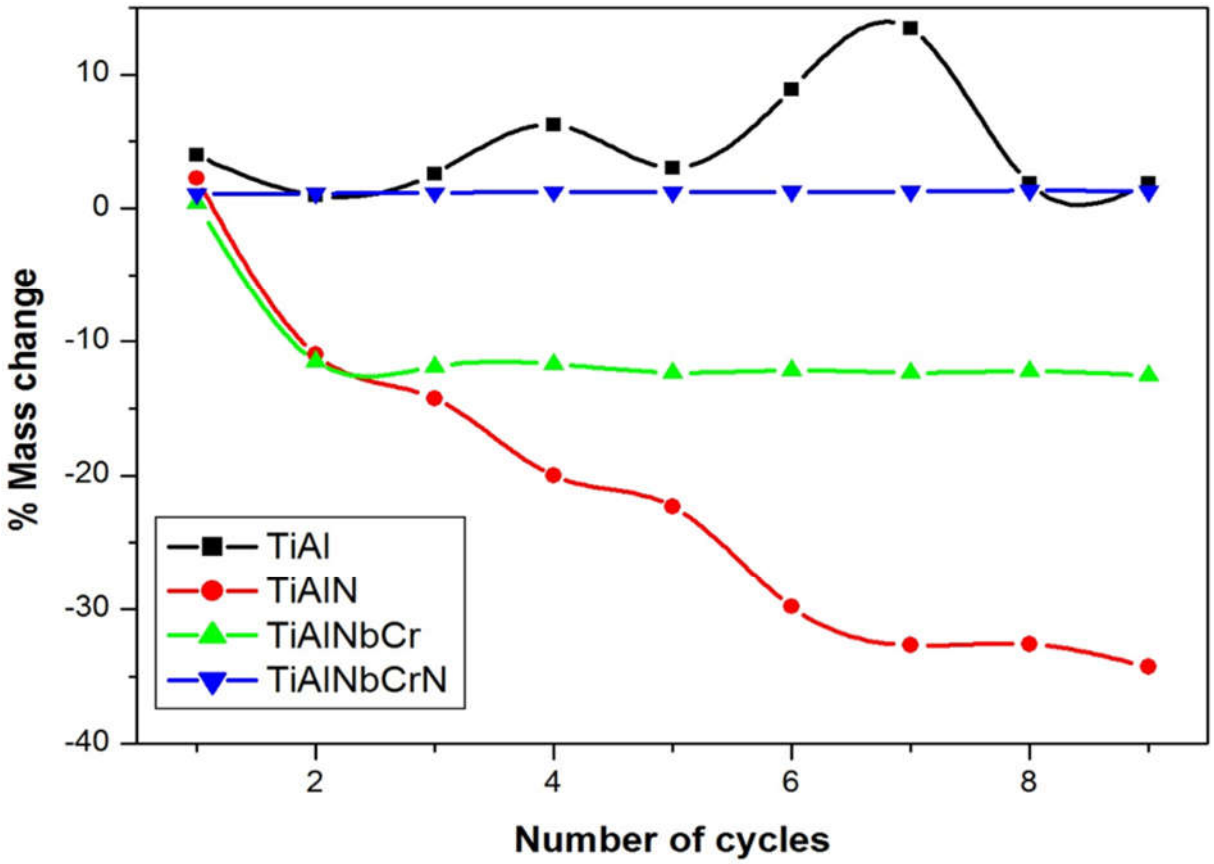

Figure 4.64. Cyclic oxidation conducted in air at 900 °C for 900 h on the nitrided Ti-48Al and Ti-48Al-2Nb-0.7Cr alloys compared with those in Section 4.3.3 without pre-nitridation.

As discussed in **Section 4.3.3**, the as-cast Ti-48Al-2Nb-0.7Cr alloy showed considerable mass loss during cyclic oxidation, while the Ti-48Al had the rapid formation of the oxide scale associated with spallation and oxide regrowth emerging [78]. The oxidation behavior of the as-cast Ti-48Al-2Nb-0.7Cr was improved by coating the alloy prior to cyclic oxidation. **Fig. 4.64** shows the nitrided Ti-48Al revealing poor cyclic oxidation performance with negative linear deteriorating behavior compared to the as-cast alloy. It confirms that porosity formation was promoted by nitridation. Upon oxidation at high temperature, a weak TiO_2 scale dominated the surface, which is porous and induces poor oxidation resistance [184]. Conversely, the nitrided Ti-48Al-2Nb-0.7Cr showed significant improvement compared with the as-cast alloy. This behavior was attributed to the formation of Ti-based oxynitride [78] as well as the presence of mixed CrN layer. Badini et al. [185] coated the Ti-48Al-2Cr-2Nb intermetallic alloy using a mixed titanium-aluminium nitride and the nitride coatings enhanced the oxidation resistance with excellent thermal shock properties [186]. The current findings revealed that even smaller Cr content of 0.7 (at.%) yielded good thermal oxidation. The oxygen diffusion probably formed a rich oxynitride scale with good bonding. The diffusion mechanism of the oxide layer is the rate determining factor for oxidation with kinetics described by the parabolic

rate of a law of diffusion-controlled oxidation in **(Eq. 4)**. Furthermore, the relationship between parabolic rate constant kp **Eq. 4** and temperature T can be expressed by an Arrhenius-type **Eq. 5** [46].

4.7.4. Characterization of oxide layers

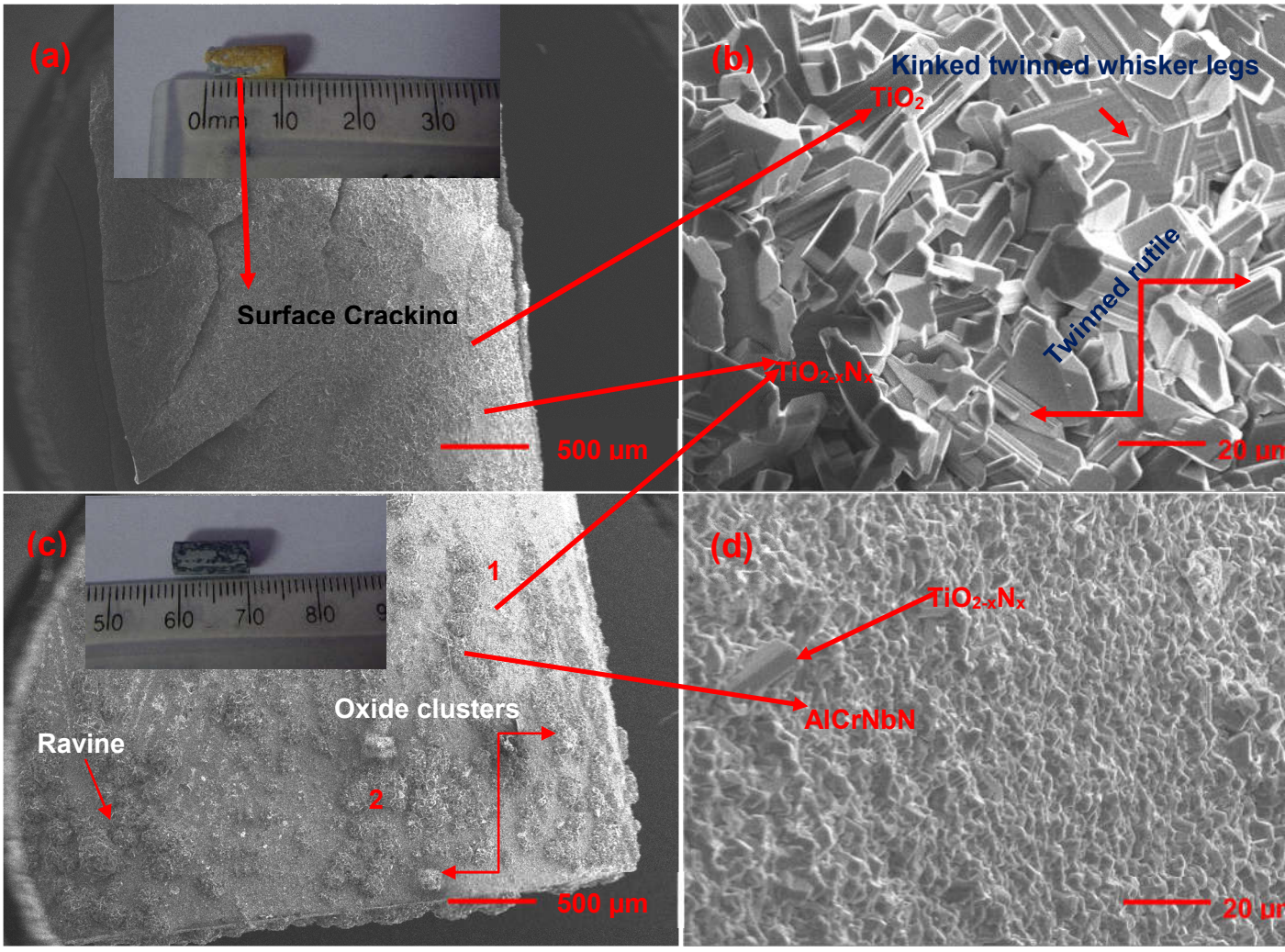

Figure 4.65. SEM-SEI micrographs of the cyclically oxidised pre-nitridated (a) Ti-48Al, (b) Ti-48Al scale (c) Ti-48Al-2Nb-0.7Cr and (d) its corresponding scale.

Fig. 4.65a shows the surface of the Ti-48Al intermetallic alloy surface condition after 900 h cyclic oxidation at 900 °C. An oxide scale throughout the specimen (inset) was attributed to the TiO_2 layer. The EDX micro-analysis of the layer (Point 1 of **Fig. 4.65a**) is shown in **Table 4.12**. Evidence of cracking and peeling of the surface scale showed that the layer was unstable. Formation of cracks allowed further diffusion of oxygen into the alloy, thus degrading the material oxidation resistance at high temperature. The small N content detected in the rutile-type oxynitride scale was revealed by the golden color displayed on the inset sample image. The crystal orientation varied from that of the as-cast Ti-48Al intermetallic alloy as shown in **Fig. 4.65b**. It revealed prismatic, smooth and regular long $TiO_{2-x}N_x$ rods rich in

oxygen. These particles display different crystal orientation depending on the N content in TiO_2. The morphology of the TiO_2 in the nitridated and cyclically oxidized binary alloy was distorted with a twinned appearance, unlike the relatively small platelet crystallites reported in [78] for the cyclically oxidized TiAl alloy without nitridation. The morphology of TiO_2 twinned crystal has been found, indicated by kinked/slipped stack of layers in **Fig. 4.65b**, and according to Guang-Lai et al. [187], there is a variety of equivalent {101} and {301} planes to form complicated TiO_2-rutile twinned crystals.

Table 4.12. EDX chemical analysis of the γ-Ti-48Al based alloy (Point 1).

Element	Atomic %	% Error
Ti	20.4	± 1.26
O	54.6	± 3.68
N	25.0	± 1.94

On the other hand, the continuous growth of TiO_2 (inset **Fig. 4.65a**) was influenced by the rate of the internal interfacial reaction which is also equal to the Ti flux across the oxide layer, equation **Eq. 6,** whereas the growing of pure TiO_2 layer in the binary Ti-Al alloy was implied in **Eq. 7**.

The oxide scale on the Ti-48Al-2Nb-0.7Cr alloy in **Fig. 4.65c** shows a two-structure, surface scale attributed to AlCrNbN and $AlTiO_{2-x}N_x$ layers. The chemical analysis of the oxidized layer designated (points 1 and 2 of **Fig. 4.65c**) are shown in **Tables 4.13 and 4.14**. Furthermore, the composition of TiO_{2-x} particles is negligible while the structure was dominated by the oxynitride particles. The representative inset sample image displays gray/black color on the surface with no excessive spallation and cracking compared to Ti-48Al **(Fig. 4.65a inset)**. Oxide layers appeared to be homogeneous throughout the surface of the specimens. The AlCrNbN scale in **Fig. 4.65c** comprised low Al content. Therefore, the presence of surface nitridation minimized the formation of $AlTiO_{2-x}$ in Ti-48Al-2Nb-0.7Cr alloy, but promoted AlCrNbN layer responsible for better cyclic oxidation performance. Recent studies by Mathabathe et al. [78] confirmed that the formation of Al_2O_3 is preferable to TiO_2 at 900 °C for the as-cast Ti-48Al-2Nb-0.7Cr alloy. However, the presence of AlCrNbN scale **Fig. 4.65d** appeared to have reduced the formation of Al_2O_3 scale, hence better oxidation properties. Therefore, due to prolonged oxidation times, the AlCrNbN absorbs a small amount of oxygen on the surface.

Table 4.13. EDX chemical analysis of the γ-Ti-48Al-2Nb-0.7Cr based alloy (Point 1).

Element	Atomic %	% Error
Ti	30.2	± 1.26
O	67.6	± 3.64
Al	2.2	± 0.44

Table 4.14. EDX chemical analysis of the γ-Ti-48Al-2Nb-0.7Cr based alloy (Point 2).

Element	Atomic %	% Error
Ti	74.2	± 1.89
N	0.4	± 0.67
Al	23.5	± 1.21
Cr	0.4	± 0.53
Nb	1.5	± 0.34

4.7.5. XRD analysis after cyclic oxidation

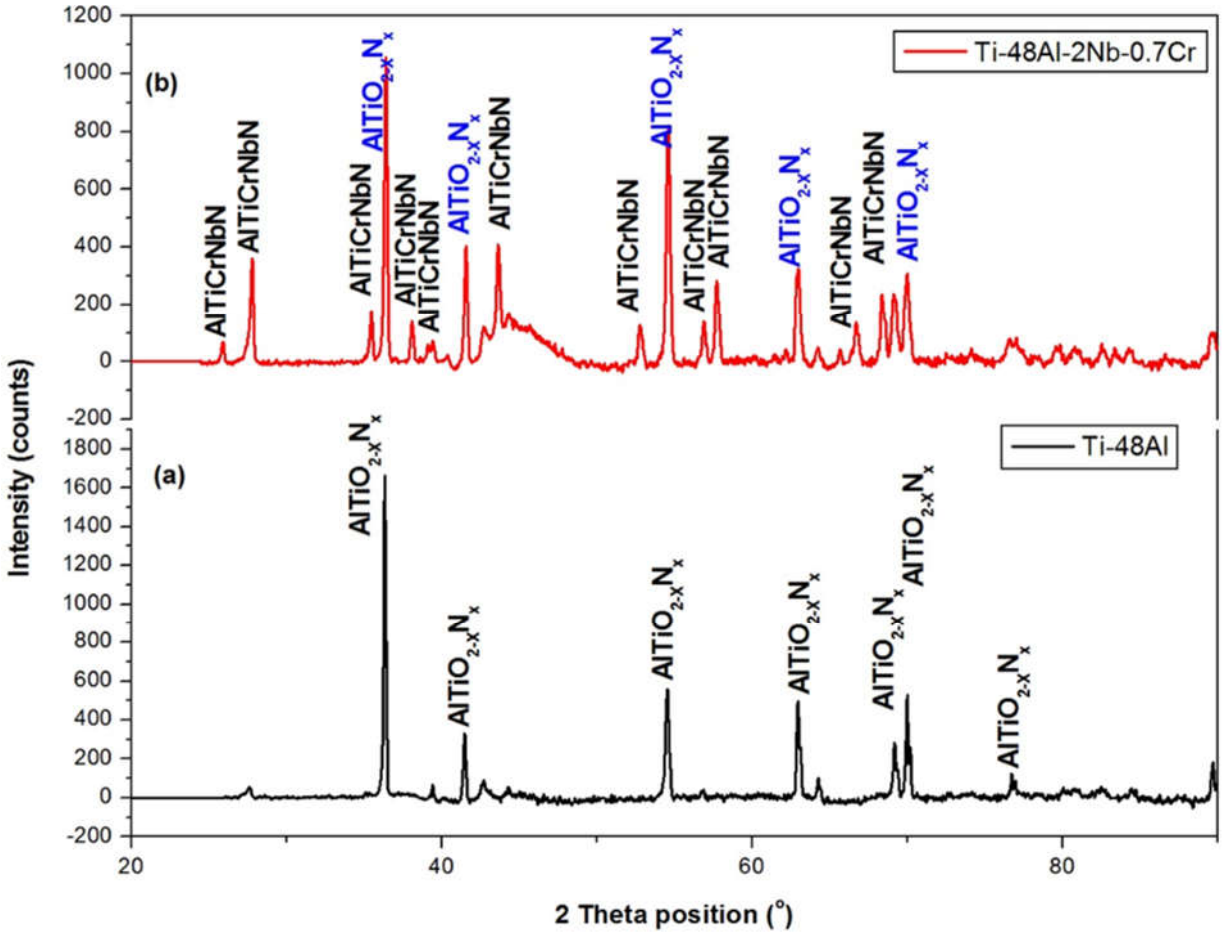

Figure 4.66. XRD patternS of the cyclically oxidized (a) Ti-48Al and (b) Ti-48Al-2Nb-0.7Cr intermetallic alloys.

The structural growth of the scale developed after cyclic oxidation is presented in **Fig. 4.66.** The XRD analysis was found to be in agreement with the SEM results. The tetragonal TiO_2 structure with lattice parameters *a*=4.566 Å; *c*=2.948 Å was detected in **Fig. 4.66a**. The scale developed on Ti-48Al-2Nb-0.7Cr comprised a two-phase structure in agreement with the detected peaks in **Fig. 4.66b**. Lattice parameters *a*=4.108 Å confirms the FCC crystal structure of the mixed AlNbTiCrN coating since the lattice parameter of pure CrN is *a*=4.14 Å [188]. Cubic TiN was ruled out due to its lattice parameter being *a*=4.24 Å [189]. Doping of CrN with other alloying elements slightly changed the lattice parameter as displayed in **Table 4.15**. The lattice parameter of CrN decreases from 4.14 Å to 4.113 Å, 4.099 Å, 4.111 Å with the addition of Al, Ti and Nb, respectively [190]. The lattice parameter of 4.108 Å obtained in the current study is representative of the coating chemical composition while the slightly smaller lattice parameter of the FCC phase is due to small amount of O dissolution on the surface. Additionally, the tetragonal Ti-rich $(AlTiCrNb)_{2-x}N_x$ with lattice parameters *a*=4.23 Å, *c*=9.43 Å was detected.

Table 4.15. Lattice parameters of the FCC CrN related solid solutions.

Compound	Lattice Parameter (Å)	Process	Reference
AlCrN	4.113	Deposition	[190]
AlCrTiN	4.099	Deposition	[189]
AlCrNbN	4.111	Deposition	[189]
AlN	4.120	PVD	[44]
CrN	4.140	PVD	[44]
CrN	4.150	ab initio & Experiment	[191]
$Cr_{0.52}Al_{0.48}N$	4.125	ab initio & Experiment	[191]
$Cr_{0.40}Al_{0.60}N$	4.117	ab initio & Experiment	[191]
$Cr_{0.31}Al_{0.69}N$	4.111	ab initio & Experiment	[191]
AlCrNbTiN	4.108	Annealing	Current work

4.7.6. Hardness properties

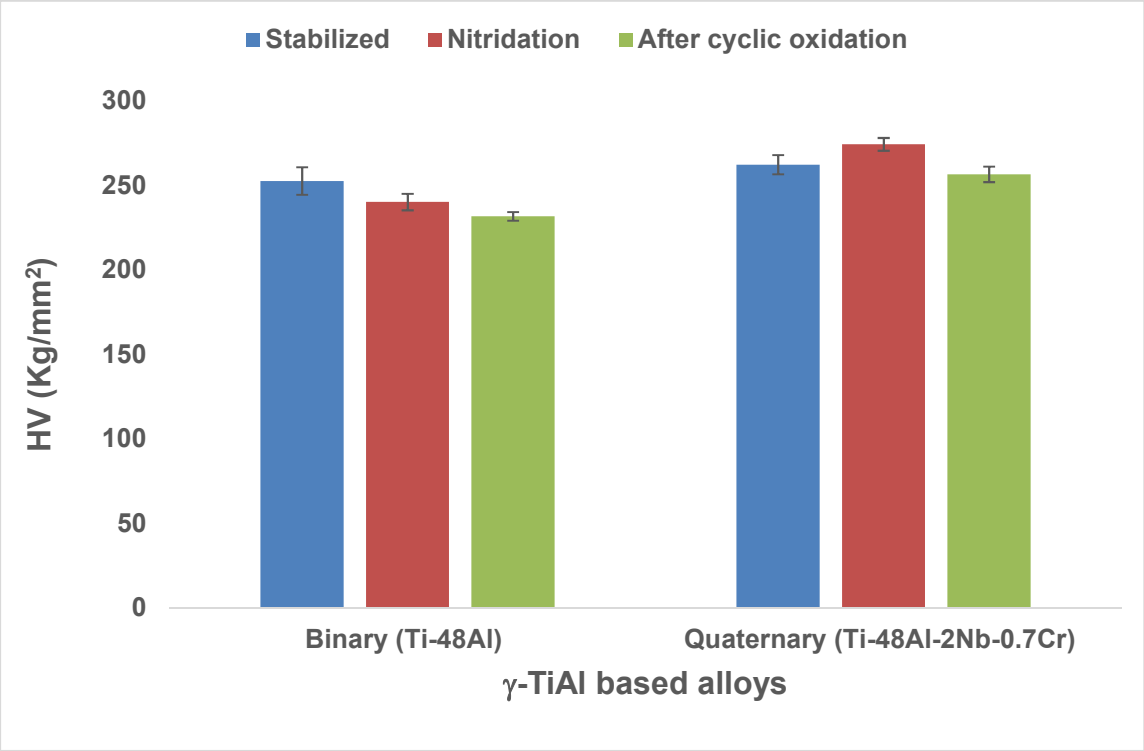

Figure 4.67. Macro-hardness profile of the γ-Ti-48Al and Ti48Al-2Nb-0.7Cr alloys.

Ti-48Al and Ti48Al-2Nb-0.7Cr intermetallic alloys macro-hardness graph for the as-cast stabilized annealing, pre-nitridation, and after cyclic oxidation are shown in **Fig. 4.67.** In general, the Ti-48Al displayed low hardness compared to the Ti48Al-2Nb-0.7Cr alloy: this was found to be attributed to poor nitradation layer. On the contrary, the nitrided sample exhibited a lower hardness than the as-cast alloy and this was attributed to surface porosity developed during annealing. Generally, prolonged exposure at high temperature will soften the alloy, hence the lower hardness after 900 h cyclic oxidation. Therefore, the surface cracking of the Ti-48Al oxide layer was not surprising. Contrarily, the nitrided Ti48Al-2Nb-0.7Cr alloy yielded high hardness due to the successful surface coating. This alloy contained small addition of Cr hence the formation of AlNbTiCrN. It has been reported that Cr_2N exhibits higher hardness, but is more susceptible to oxidation than CrN and can deteriorate the thermal stability of the coating [192]. This alloy displayed stability under cyclic oxidation at 900 °C. The surface layer formed on the Ti48Al-2Nb-0.7Cr alloy before being exposed to cyclic oxidation allowed the O diffusion through pores and cracks and, therefore, allowed regeneration of surface scale which resulted in the increase in mass gain and oxidation rate, Chen et al. [193]. Hence, a decreased hardness was obtained after cyclic oxidation. This oxynitride layer formation reduced further oxygen diffusion into the surface and it was softer than the mixed CrN layer [78]. Moreover, According to Chen et al. [193], once the oxide film is isolated from the substrate, the concentration of oxygen in the coating increases. The oxygen atoms therefore diffuse through

pores and cracks to form scales and in this case the $TiO_{2-x}N_x$., with the resultant increase in the mass gain and oxidation rate.

The formation of pores may have occurred during the vacuum melting of the metal powders. The compacted metal powders were melted and immediately cooled to room temperature. Transient phases such as Ti_3Al, TiAl, $TiAl_3$, and remnant β-B2 were retained due to non-equilibrium cooling. As suggested by Lee et al. [40], the first solid-state reaction during heating occurs between pure Ti and Al powder particles, whereby the layers of transient phases manifest at contact areas of the particles. The solid-state reaction coupled with the liquid-solid reaction yields the transient phases, prior to the main exothermic reaction between pure Ti and Al. At the maximum transformation temperature, this reaction is two-fold viz. 1) between pure Ti and Al powder particles, and 2) transient phases and pure Ti, through which pure Ti is embedded inside the layers of the transient phases. During this disposition, Al with greater mobility, diffuses towards Ti in the core faster than Ti in the opposite direction, thus leaving pores in the transient phases (Kirkendall porosity). During thermal annealing at intermediate temperatures there is an inducement of vacancies within the structure, therefore, according to Gong et al. [184], the diffusion of oxygen gas is fast through the pores/cavities, which will result in the fast growth of oxides; consequently the oxide clusters were instituted. Similar to the work of Gong et al. [184], the oxides were arranged in such a way that the deep ravines are between them (**Fig. 4.65c**). This morphology reduced the adherence of oxide scales because cavities were readily formed between the oxide clusters and the ravines.

4.7.7. Surface AFM analysis

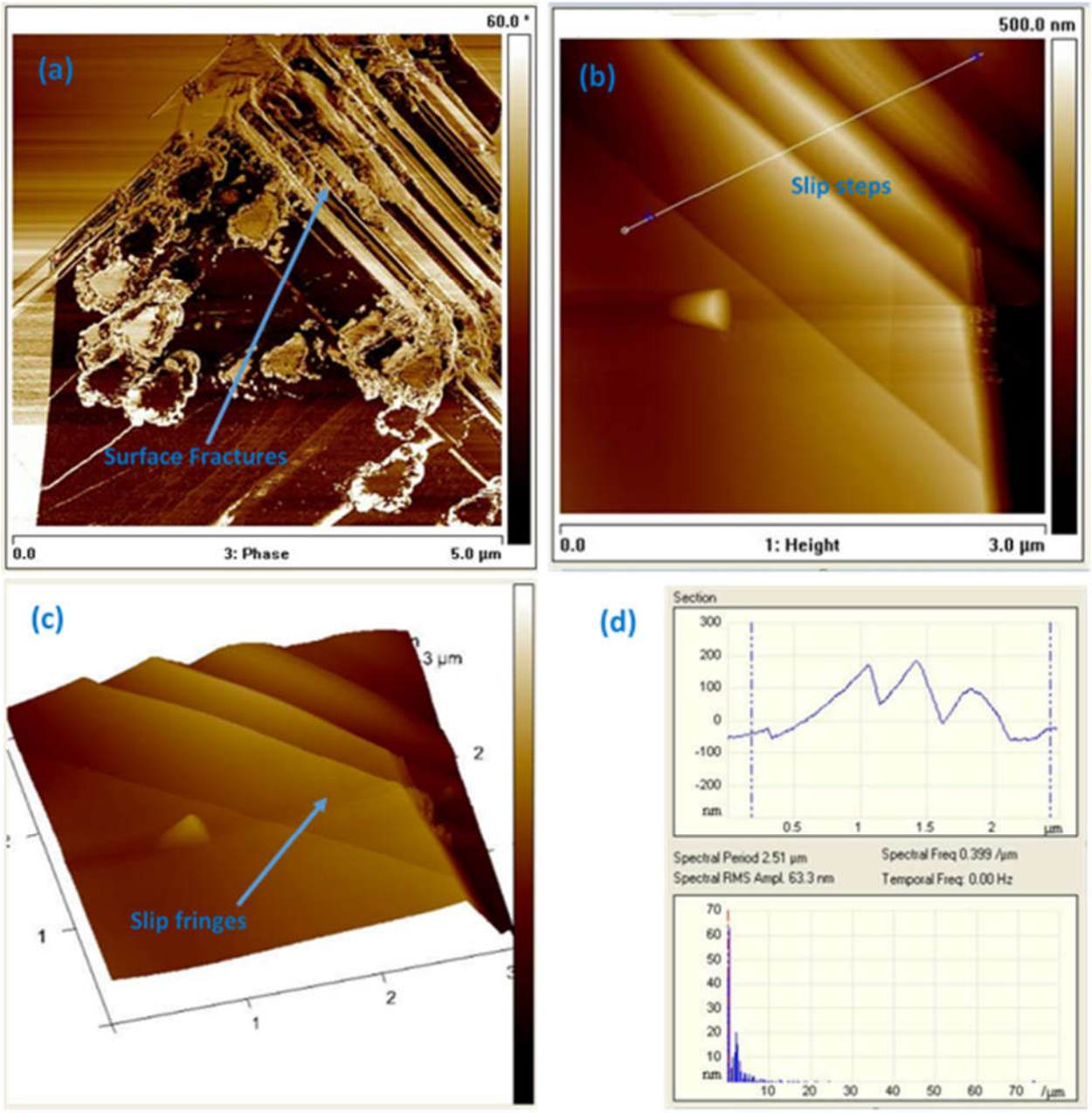

Figure 4.68. AFM images of the nitrided Ti-48Al alloy (a) deflection image, (b) a magnified view of slip steps corresponding to a pointed blue arrow in (a), (c) 3D surface topography of the oxidized scale layer, and (d) cross-sections corresponding to line traces a after cyclic oxidation exposure at 900 °C for 900 h.

Fig. 4.68a-d depicts the AFM images of the nitrided Ti-48Al alloy layer exposed to oxidation at 900 °C for 900 h. The nanoscale roughness, fracture and plasticity features were evaluated. The images show a marked difference in both localized plastic deformation and fracture as an outcome of cyclic oxidation at 900 °C in air. **Fig. 4.68a** reveals a cracking pattern along a scratch groove indicated by a blue arrow. **Fig. 4.68b** shows the AFM micrograph along slip step with corresponding quantitative measurements of the cross-section in **Fig.4.68d.** The 3D

topography in **Fig. 4.68c** shows peripheral slip fringes, with a maximum fringe height of about 200 nm **Fig. 4.68d**. The spectral root mean square (RMS) amplitude of the Ti-48Al oxide layer was 63 nm.

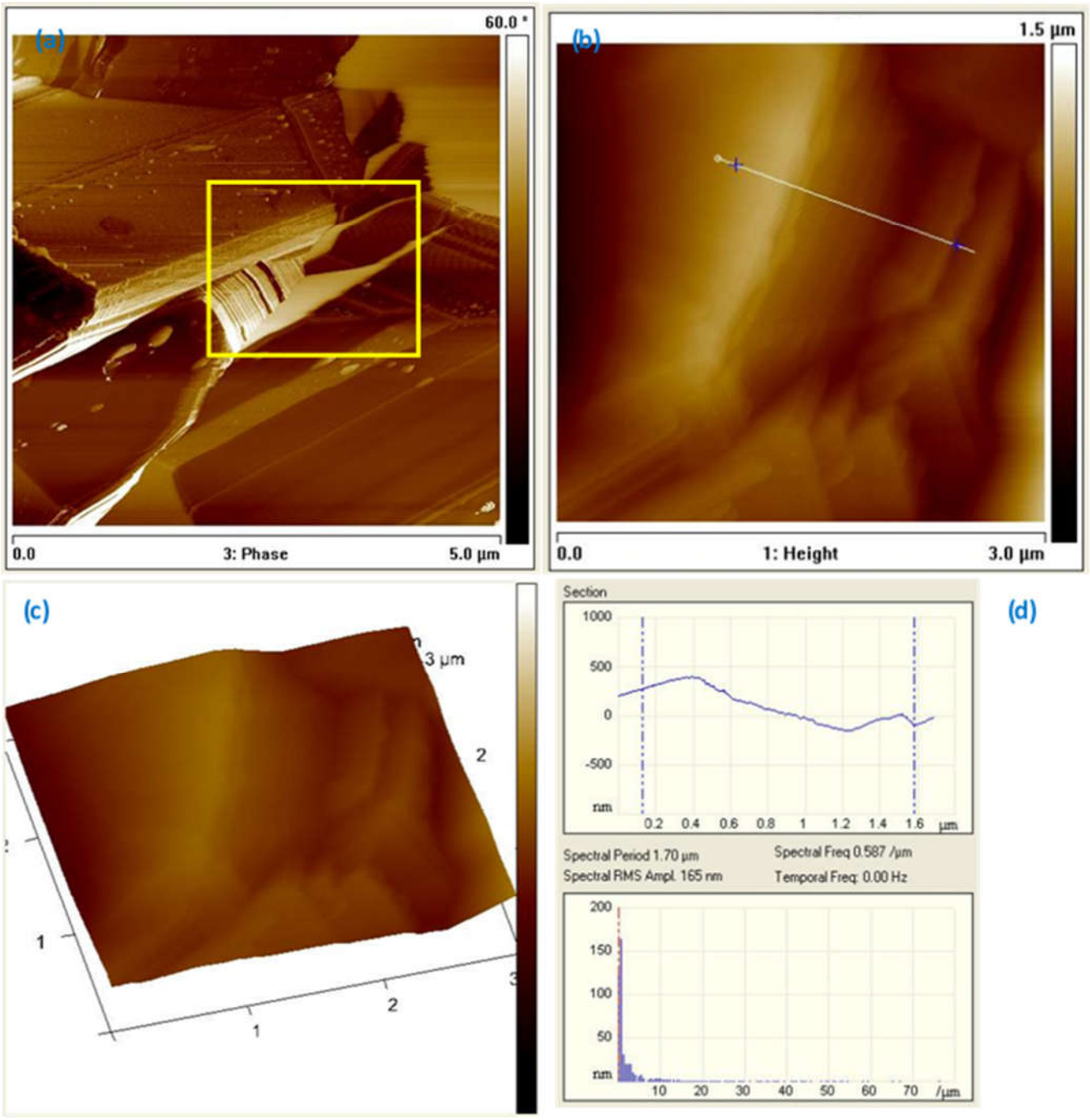

Figure 4.69. AFM images of the nitrided Ti-48Al-2Nb-0.7Cr alloy a) deflection image, (b) a magnified view of slip steps corresponding to a square area (c) surface topography of the oxidized scale layer and (d) cross-sections corresponding to line traces after cyclic oxidation exposure at 900 °C for 900 h.

Fig. 4.69a illustrate a slip-step pattern along a cracked groove indicated by a yellow square area. The AFM image along slip step and corresponding quantitative measurements of the cross-section are given in **Fig. 4.69b** and **d,** while a 3D topography with peripheral slip fringe is shown in **Fig. 4.69c** with a maximum fringe height of approximately 350 nm. Spectral root mean square (RMS) amplitude of the Ti-48Al-2Nb-0.7Cr oxide layer was found to be 165 nm which is higher than that of the Ti-48Al oxide layers by about 100 nm. This might have been due to the intermixed layers of the $(AlCrNbTi)_{2-x}N_x$ and the presence of the oxynitride coating. This also implies that the Ti-48Al oxide layer was more uniform and finer than the Ti48Al-2Nb-0.7Cr oxide layer, which showed oxide clusters **Fig. 4.65c**. Moreover, there was no major cracking in the scale (compared to **Fig. 4.65a**) attributable to the dominant AlNbTiCrN.

4.7.8. Conclusions

The characterization of the cyclically oxidation of the γ-Ti-46Al-2Nb-0.7Cr intermetallic alloy surface properties was carried and the following conclusions were drawn:

- The successful nitride coating was achieved by annealing the Ti-46Al-2Nb-0.7Cr intermetallic alloy at 900 °C under nitrogen.
- The surface hardness improved after nitridation.
- Due to surface porosity, the Ti-48Al surface coating was not successful and yielded low hardness.
- The pre-nitridated Ti-48Al-2Nb-0.7Cr showed improved cyclic oxidation at 900 °C after 900 h.
- The microstructures of the cyclically oxidized Ti-48Al-2Nb-0.7Cr surface revealed a two-phase structure comprised of B2 crystal structure and γ-Ti rich phases. The surface composed mostly of oxynitride multilayers.

4.8. Effect of nitridation treatment on cyclic oxidation of the γ-Ti-46Al-2Nb and Ti-46Al-2Nb-0.7Cr-0.3Si intermetallic alloys

4.8.1. Introduction

The traditional γ-TiAl based intermetallic alloys are faced with difficulties in material processing and machining. Alloying of the γ-TiAl intermetallic alloys with ternary, quaternary or even quinary constituent elements is of particular interest in an attempt to improve high-temperature applications for aerospace and automotive industry [194]. Improvement of alloys by the addition of alloying elements are enhanced primarily by the thermal control of microstructure. The research was conducted with the aim to overcome workability and machinability by producing a class of beta (β)/gamma (γ) alloys with improved properties [126]. Due to high temperatures in which these alloys are operating, oxidation resistance is an essential surface

property. In other applications, the surface properties are improved by materials coating which sometimes have the superior properties than the substrate. NavinŠek et al. [195], reported that hard coatings based on nitrides have been primarily applied in cutting tools on account of their superior tribological properties, as well as high oxidation resistance. During nitriding, diffusion of a nitrogen gas starts on the surface of a metal and form a nitride compound with the base metal at high temperature [196]. Surface modifications in Ti alloys such as Ti–6Al–4V [197] and γ-TiAl alloys [211] [112] [213] are widely used. Zhao et al. [200] revealed the benefits and limitations of the nitrided Ti–47Al–2Nb–2Cr–0.2Si intermetallic alloy. It emerged that the non-nitrided Ti–47Al–2Nb–2Cr–0.2Si alloys displayed better oxidation resistance than the nitrided alloys in the range of 800-1000 °C due to the dominant development of Al_2O_3 on the outer layer of the scales. They [200] further noticed that the nitrided alloys exhibited increased oxidizing rate with the prolongation of nitridation time at 800 °C but showing good oxidation resistance at more severe oxidizing conditions when nitrided at 940 °C for 50 h [200]. The alloy disobeyed the parabolic law at 900 and 1000 °C, which is an indication of the variation in uniformity of scale [201]. The Al-rich compositions was detected below the nitride/sub-layer interface whereby TiN and Ti_2AlN, η-Ti_3N_{2-x} and Ti_2N and Al_5Ti_2 intermetallic compounds [201] were detected. Nitridation with the aim of improving cyclic oxidation for Ti-Al-based alloys is relevant due to their exposure at high temperatures. Interventions were made to develop the model reference to the development of a TiN scale on a γ-TiAl substrate [202]. It revealed that the applied stress induces a large residual stress in the nitride scale owing to the mismatch of creep rates between the metal and the nitride scale. The large stress influences the diffusional flux of nitrogen vacancies, leading to deviation from the parabolic growth law [202]. The aim of **Section 4.8** was to investigate the effect of nitridation on cyclic oxidation of the γ-Ti-46Al-2Nb and Ti-46Al-2Nb-0.7Cr-0.3Si intermetallic alloys**.** Surface structural analysis and conditions of the two alloys were studied after cyclic oxidation.

4.8.2. As-stabilized γ-TiAl based alloys

The final chemical compositions of the as-cast vacuum melted Ti-48Al-2Nb, and Ti-48Al-2Nb-0.7Cr-0.7Si intermetallic alloys are shown in **Table 3.2** reporting previous work [78], [116]. As mentioned in **Section 4.7.2**, the difference between nominal and final composition may be due to varying vapor pressures of different components in the alloys, and volatile Al that suffers a burning loss [79].

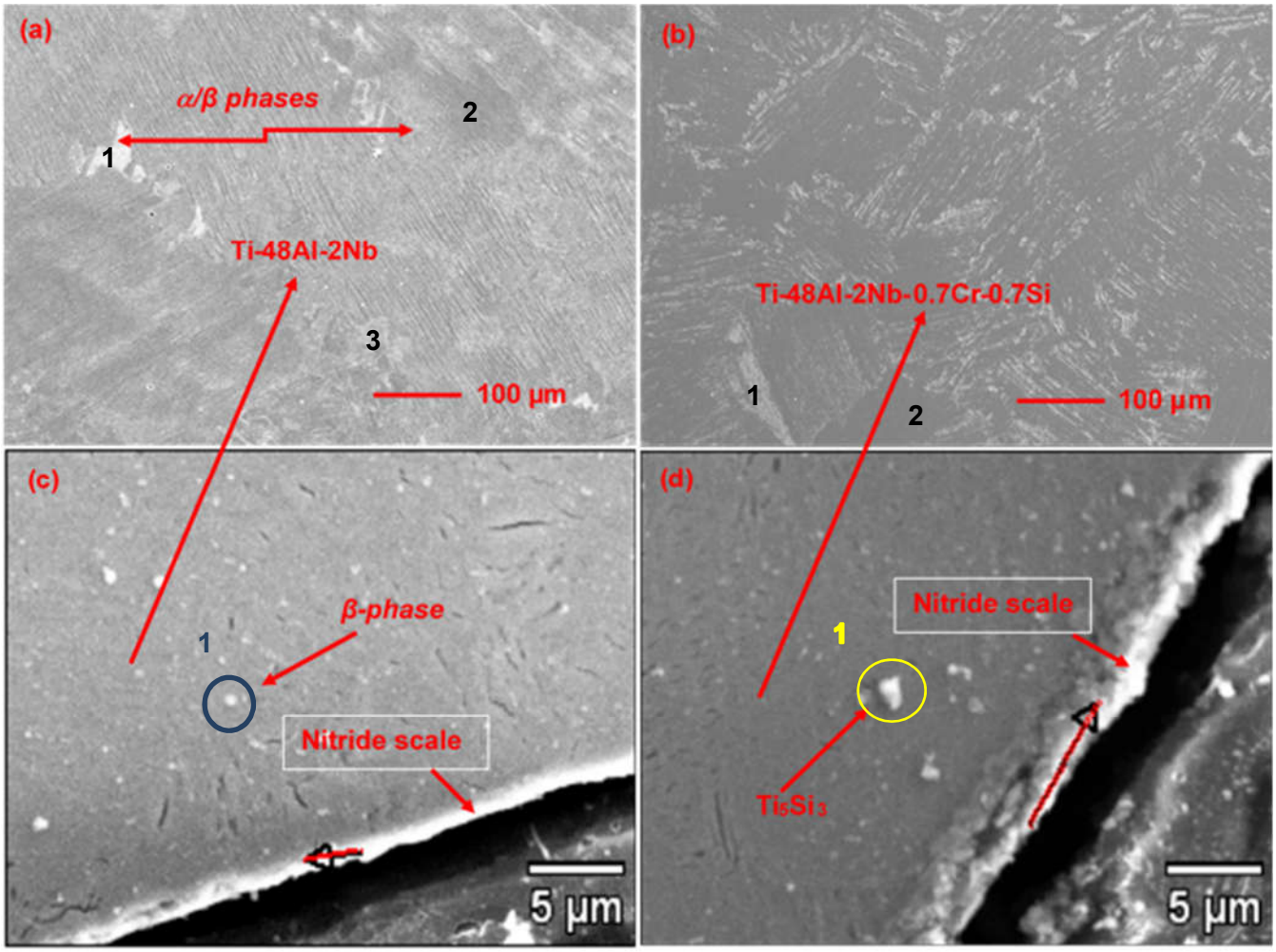

Figure 4.70. SEM-SEI micrographs of cross-sections of the as-stabilized γ-TiAl (a) Ternary Ti-46Al-2Nb (at. %), (b) Quinary Ti-46Al-2Nb-0.7Cr-0.7Si (at. %) alloys. Their corresponding nitrided images are shown in (c) and (d), respectively.

The cast alloy structures were stabilized at 1100 °C in the (α_2+γ) phase domain**. Fig. 4.70a** shows the SEM-secondary electron images (SEI) of the stabilized ternary γ-Ti-46Al-2Nb alloy microstructure. The main phases were the γ-(TiAl) and α_2-(Ti_3Al) the their EDS elemental analysis is in **Table 4.16** and is synonymous to the as-cast composition in **Table 3.2.** This may denote homogeneity of the alloys. Additionally, the ternary alloy revealed the presence of residual β or B2-phase. The white traces in **Fig.4.70a** indicated by the double red arrow, are typical products of α/β phases, and they are in the location where the last residual β-phase existed. It has been reported that these areas are enriched with beta-stabilizers such as Nb [203]. **Fig. 4.70b** also has the γ-(TiAl) and α_2 (Ti_3Al) phases. Moreover, the quinary Ti-46Al-2Nb-0.7Cr-0.7Si alloy exhibited Ti_5Si_3 precipitates illustrated in the microstructure. Both alloys demonstrated a lamellae structure with different grain orientations attributed to alloying elements and heat treatment applied. Surface coating for both Ti-46Al-2Nb and Ti-46Al-2Nb-0.7Cr-0.7Si (at. %) yielded different behavior. The micrographs of the cross-sectionsl in **Fig.**

4.70c, d show the as-nitrided Ti-46Al-2Nb and Ti-46Al-2Nb-0.7Cr-0.7Si intermetallic alloys. A thin coating of nitride was developed by annealing in the presence of N at 900 °C. However, both alloys revealed precipitates upon nitridation. The composition of the particles in **Fig. 4.70c** and **Fig. 4.70d** circled point 1 is demonstrated in **Fig. 4.71a-b** for the ternary and quinary alloy, respectively. The (at. %) composition of Ti and Al, corresponds to γ-phase composition.

Table 4.16. EDX spot analysies of the γ-TiAl based alloys (at. %).

Alloy	Ti	Al	Nb	Cr	Si
TiAlNb	1. 53.6 ±0.18	44.3 ±0.08	2.1 ±0.03	-	-
	2. 50.0 ±0.06	48.3 ±0.10	1.7 ±0.14		
	3. 50.1 ±0.21	48.3 ±0.13	1.7 ±0.05		
TiAlNbCrSi	1. 50.9 ±0.20	44.0±0.17	1.9 ±0.14	0.6 ±0.06	2.6 ±0.21
	2. 50.5 ±0.18	45.8 ±0.15	2.2 ±0.09	0.6 ±0.04	1.0±0.13

a)

Element	Atom %	%Error
Al K	49.95	+/- 0.15
Ti K	48.18	+/- 0.19
Nb L	1.87	+/- 0.05
Total	100.00	

b)

Element	Atom %	% Error
Al K	49.37	+/- 0.16
Si K	1.31	+/- 0.09
Ti K	46.55	+/- 0.20
Cr K	0.96	+/- 0.05
Nb L	1.82	+/- 0.05
Total	100.00	

Figure 4.71. Particles precipitated beneath the nitride layer on the a) ternary (β-phase) and b) quinary (Ti_5Si_3-phase) alloys.

4.8.3. Cyclic oxidation behavior

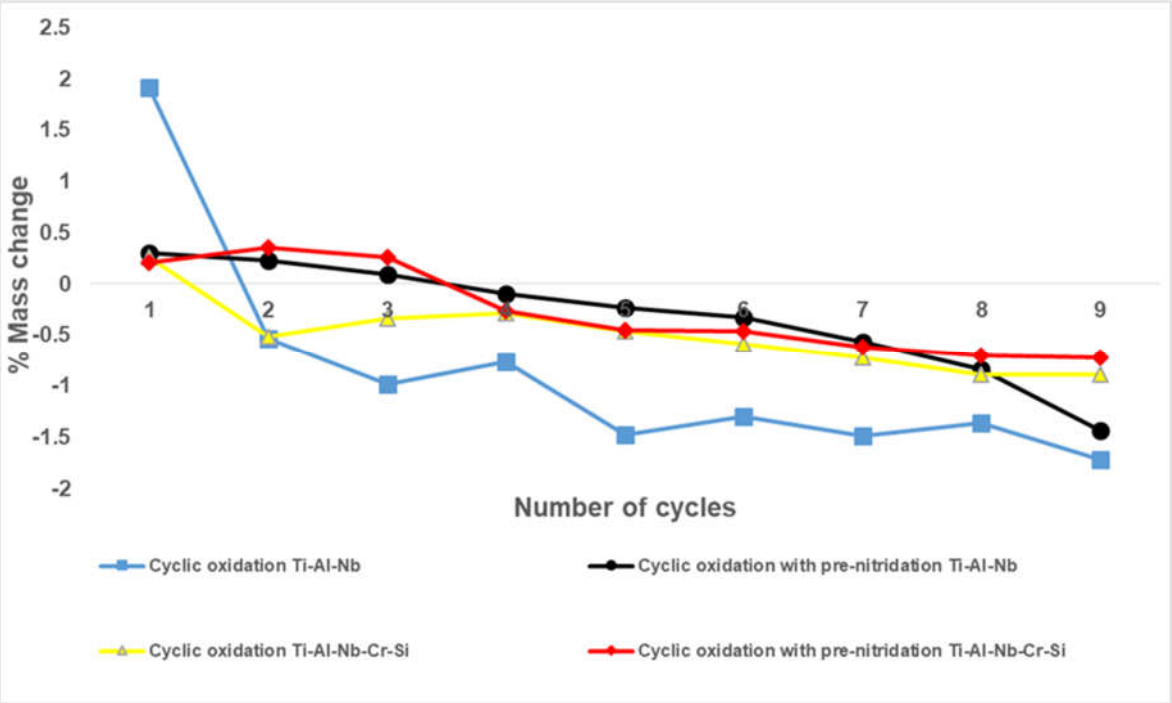

Figure 4.72. Cyclic oxidation conducted in air at 900°C for 900 h on the Ti-46Al-2Nb (ternary), and the Ti-46Al-2Nb-0.7Cr-0.3Si (quinary) alloys.

Fig. 4.72 is the cyclic oxidation graph demonstrating the Ti-46Al-2Nb and Ti-46Al-2Nb-0.7Cr-0.3Si alloy behavior. The cyclic oxidation of the nitrided alloys was compared with alloys without thermal nitridation treatment. The un-nitrided Ti-46Al-2Nb alloy showed a sharp initial negative mass loss during the first 100 h cycle and steadily continued to decrease to 900 h. This mass loss was indicative of rapid oxide growth (shown by initial positive weight gain) and spallation of the scale. Upon extensive exposure times, erratic specimen weight gain and loss, observed throughout the duration of oxidation, became stable 900h. In contrast, the nitrided Ti-46Al-2Nb alloy shows improved oxidation resistance and inhibition of the fast oxide growth during the initial stages of cyclic oxidation. It implies that the nitride coating played a significant role in prohibiting rapid development of the oxide layer. The Ti-46Al-2Nb-0.7Cr-0.3Si alloy, before nitridation, showed a narrow initial negative mass loss compared to the Ti-46Al-2Nb alloy in the initial 100 h cycle. However, the nitrided Ti-46Al-2Nb-0.7Cr-0.3Si alloy had a steady increase of the oxide scale and generally performed better than the as-cast alloy due to the protective oxide. The cyclic oxidation resistance of the Ti-46Al-2Nb-0.7Cr-0.3Si alloy was sustained up to 900 °C i.e. it was better than the nitrided Ti-46Al-2Nb alloy which showed a sharp drop between 800 and 900 h cycles. The reason behind this may be due to the presence of Ti_5Si_3 phase in the Ti-46Al-2Nb-0.7Cr-0.3Si alloy shown in **Fig. 4.70b** and **d**. At temperatures slightly below 900 °C, Ti_5Si_3 forms a mixed scale of crystalline TiO_2 (rutile) and amorphous SiO_2. The scale grows inwardly by diffusion of oxygen along grain boundaries or

through oxygen vacancies in rutile [26]. A linear mass gain rate of 0.02 mg/cm^2/hr controlled growth rate and inner mixed scale of TiO or TiN and Si was expected to form demonstrated by the stability diagram in **Fig. 2.21** [44]**.** Based on the stability diagram, it implies that the oxidation resistance of Ti_5Si_3 in Ti-46Al-2Nb-0.7Cr-0.3Si alloy improved due to the interstitial element (N) surface diffusion. The large improvement of oxidation resistance was due to higher SiO_2 content in the scale. Although the scale comprised rutile-SiO_2, the rutile was isolated such that no continuous diffusion path existed through the rutile to the Ti_5Si_3 interface. Furthermore, the Ti-46Al-2Nb-0.7Cr-0.3Si alloy showed a marginal positive mass gain throughout the 600 h to 900 h range cycle, relative to the Ti-46Al-2Nb alloy. This behavior was attributed to Cr contributing to the oxidation properties, where the formation of the nitride scale prohibited the diffusion between the alloy and the oxygen gas [204]. Moreover, Cr additions to the TiAl based alloy would have enhanced the stabilization of an Al_2O_3 scale, and it may also have decreased the solubility of interstitial atoms such as oxygen and nitrogen due to its high electron to atom ratio [134].

Although nitriding was carried out prior to the cyclic oxidation tests, the static laboratory air contained N and this resulted in the formation of $TiO_{2-x}N_x$. This oxynitride layer formation reduced further oxygen diffusion into the alloy [78].

4.8.4. XPS spectra analysis

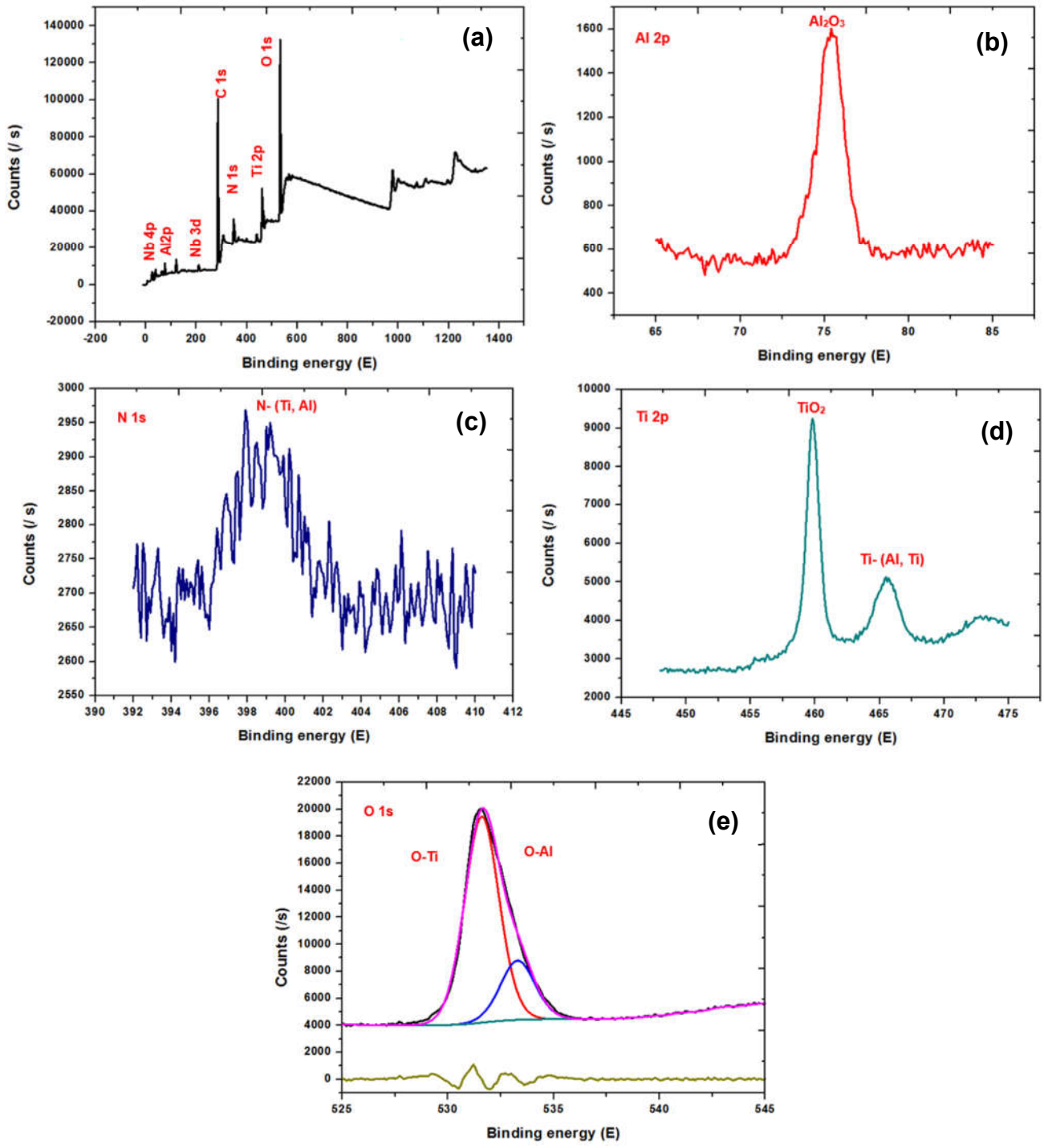

Figure 4.73. XPS survey scan of (a) nitrided Ti46Al-2Nb intermetallic alloy after cyclic oxidation at 900 °C for 900 h, and the corresponding experimental and fitted curves for normalized (b) Al 2p (c) N 1s, (d) Ti 2p, and (e) O 1s XPS spectra.

Fig. 4.73a shows a fully scanned spectra of the x-ray photoelectron spectroscopy (XPS) of the Ti46Al-2Nb alloy confirming the presence of Ti, Al, Nb, O, N, and C. The detected carbon was associated with the carbon tape during the sample preparation. In addition, the Nb 3*d* and 4*p* XPS spectrum was observed at 209.8 eV and 50 eV, corresponding to the Nb^{5+} $3d_{3/2}$ and Nb^{5+} $3d_{5/2}$ spin orbit peaks of the Nb_2O_5 phase of Li et al. [118]. **Fig. 4.73b-e** displays the XPS spectra of the Ti2*p* core-level of the nitrided Ti46Al-2Nb after cyclic oxidation. **Fig. 4.73b** shows the peak at 75.38 eV which is associated with Al-O (α-Al_2O_3) bonds [185]. Another peak of 397.3 eV, shown in **Fig. 4.73c**, was related to N-Ti-O ($TiO_{2-x}N_x$) bonds [110], [176]. This suggests that more oxygen vacancies were produced during annealing for N atoms to occupy. Partial Ti-O bonds on the TiO_2 surface layer may be broken due to annealing and oxygen is released from the TiO_2 lattice. **Fig. 4.73d** shows the peaks centered at around 459.8 eV and 465.5 eV assigned to Ti^{4+}(2*p*3/2), and Ti^{4+}(2*p*1/2) for TiO_2 layer [205]. **Fig. 4.73e** presents the O1*s* core level spectra of the TiO_2. Each O1*s* signal of the TiO_2 scale could be fitted into two symmetric peaks. The peaks located at 531.59 and 533.31 eV corresponds to the oxygen vacancy-Ti^{4+} and oxygen vacancy-Ti^{3+}.

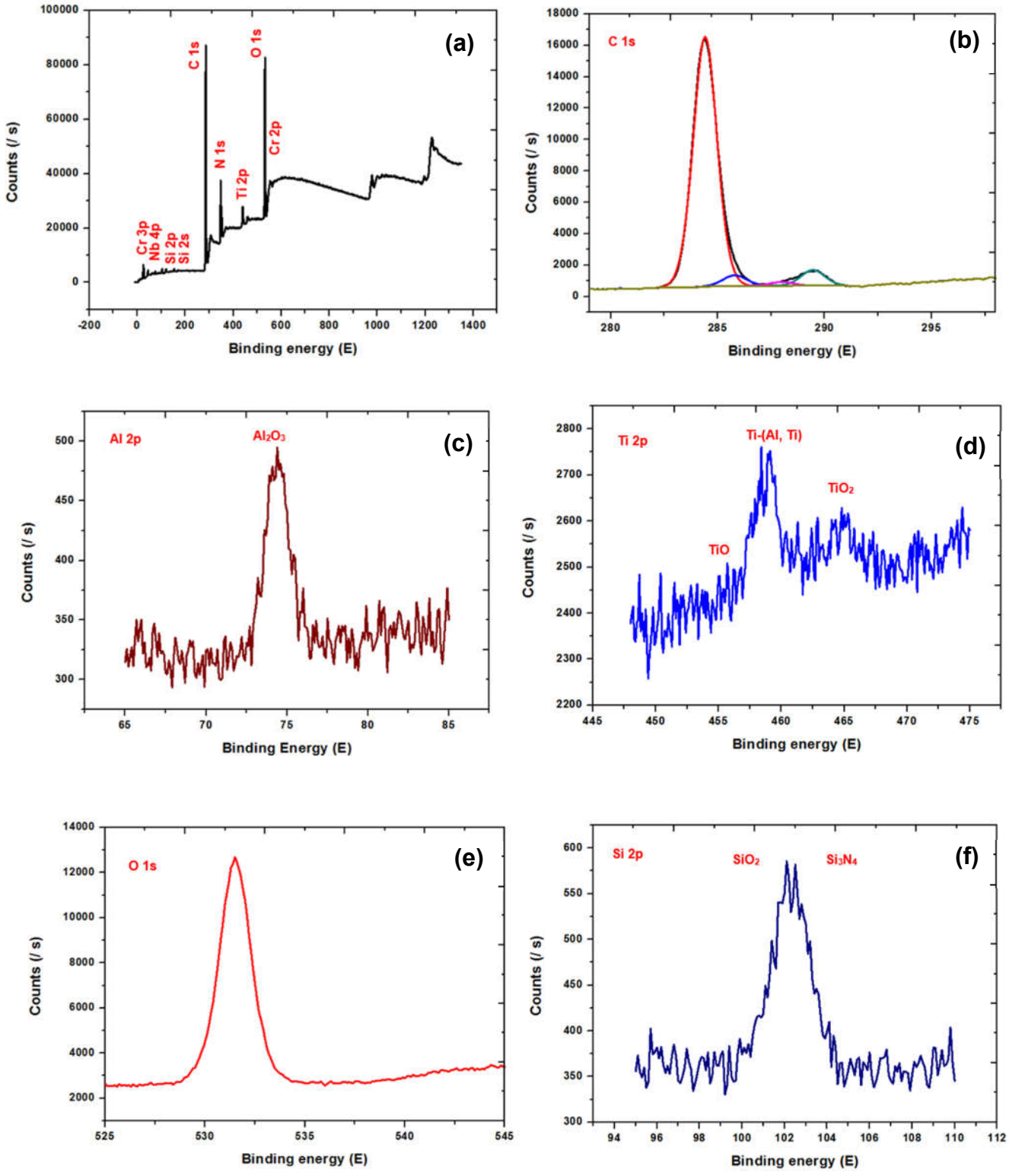

Figure 4.74. XPS survey scan of the (a) nitrided Ti46Al-2Nb-0.7Cr-0.3Si intermetallic alloy after cyclic oxidation at 900 °C for 900 h, and the corresponding experimental and fitted curves for normalized (b) C 1s, (c) Al 2p, (d) Ti 2p, (e) O 1s and (f) Si 2p.

Fig. 4.74 shows the XPS high-resolution surface spectra of the nitrided Ti46Al-2Nb-0.7Cr-0.3S intermetallic alloy after cyclic oxidation at 900 °C for 900 h. The Cr 2*p* spectrum in **Fig. 4.74a** is characterized by the Cr 2*p* 3/2 binding energy at 576.8 eV, which according to Chang et al. [206] is associated with the presence of Cr_2O_3. Like the Ti-46Al-2Nb alloy, the detected carbon in **Fig. 4.74b** was associated with the carbon tape used during sample preparation, whereas the peak of 75.38 eV in **Fig. 4.74c** was associated with Al-O (α-Al_2O_3) bonds [185]**.** The detected Nb 4*p*, and N XPS spectrum in **Fig. 4.74a** is similar to **Fig. 4.73a**. **Fig. 4.74d** represent the chemical composition of Ti, which yielded a pair of spin orbit viz. (Ti 2*p*3/2 and Ti 2*p*1/2) in the Ti 2*p* spectrum [185]. The spectrum consisted of broad peaks showing that the Ti-bonds occurred at the same time. According to Badini et al. [185], the Ti-O bonds in TiO_x, Ti_2O_3 and TiO_2 show bind energy (BE) that increases with titanium oxide state viz. Ti^{2+}, Ti^{3+} and Ti^{4+}. The authors recognized that TiO_x is a non-stoichiometric compound with compositions ranging from $TiO_{0.7}$ to $TiO_{1.3}$. The TiO_2 spin orbit doublet showed binding energies of 458.8 eV (Ti 2*p*3/2) and 464.6 eV (Ti 2*p*1/2). The peaks at 457.0 eV and 463.1 eV were attributed to Ti_2O_3 and TiO*x* was found at 455.3 eV and 461.5 eV [185]. The O 1*s* XPS depth profile in **Fig. 4.74e** shows that the oxygen was enclosed mainly as Al_2O_3 at the binding energy of 532.0 eV near the surface of the oxide layer. Moreover, minor SiO_2 at the binding energy of 532.9 eV, and Cr_2O_3 at the binding energy of 530.9 eV, were also located near the surface of the oxide [206]. **Fig. 4.74f** shows Si peaks, and a small fraction of SiO_2 near the surface of the Si 2*p* peak with a binding energy of 103.0 eV [206]. Therefore, a mixed oxide layer including Al_2O_3, Cr_2O_3 and SiO_2 was found near the surface [206].

4.8.5. Characterization of oxide layers

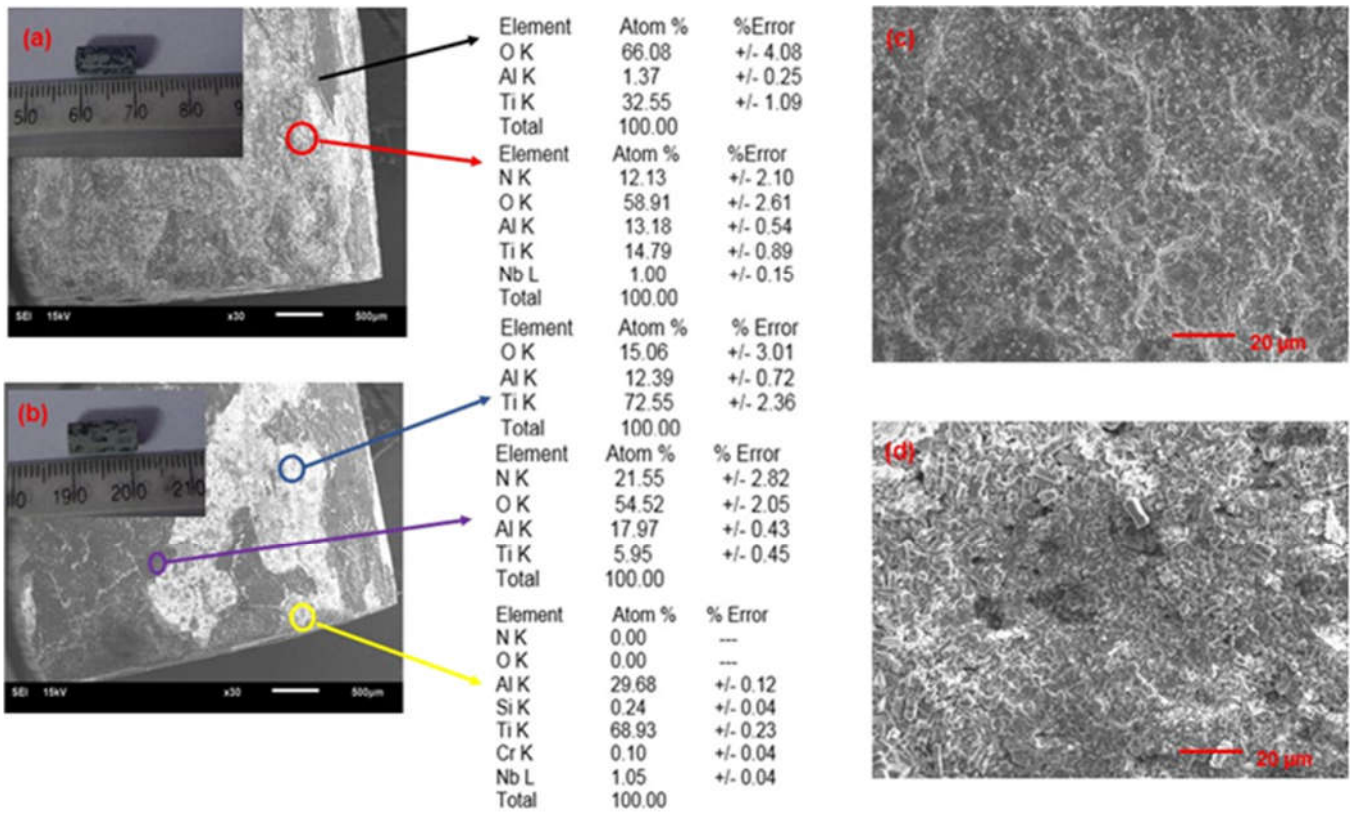

Figure 4.75. SEM-SEI images and EDX analysis of the surface scales of (a,c) Ti-46Al-2Nb and (b,d) Ti-46Al-2Nb-0.7Cr-0.3Si intermetallic alloys after cyclic oxidation

The surface scale images of the Ti-46Al-2Nb and Ti-46Al-2Nb-0.7Cr-0.3Si intermetallic alloys are shown in **Fig. 4.75**. Passive scales are shown by the black, red, yellow, purple and blue arrows. The Ti-46Al-2Nb scale in **Fig. 4.75a** confirms the formation of multiple layers, as well as spallation. The dark outer surface scale (black arrow) peeled off, leaving the underneath white scale exposed (red arrow). The formation of Al_2O_3 was thermodynamically more feasible than the formation of TiO_2 at 900 °C [5]. The same observation was made in the Ti-46Al-2Nb-0.7Cr-0.3Si alloy in **Fig. 4.75b**. However, due to prolonged exposure to at elevated temperatures, γ-alumina phase absorbed the nitrogen ions to form a stable AlON non-stoichiometric compound rich in defect structures. SEM-SEI images of the Ti-46Al-2Nb and Ti-46Al-2Nb-0.7Cr-0.3Si surface oxides are displayed in **Fig. 4.75c, d**,. The oxide layer of Ti-46Al-2Nb alloy in **Fig. 4.75c** showed a fibrous morphology of interconnected particles. It comprised valleys with the observed multiple layers formed during oxidation. The oxide film of the cyclically oxidized Ti-46Al-2Nb-0.7Cr-0.3Si in **Fig. 4.75d** revealed a mixture of rod and needle types and fibrous structures.

4.8.6. AFM analysis

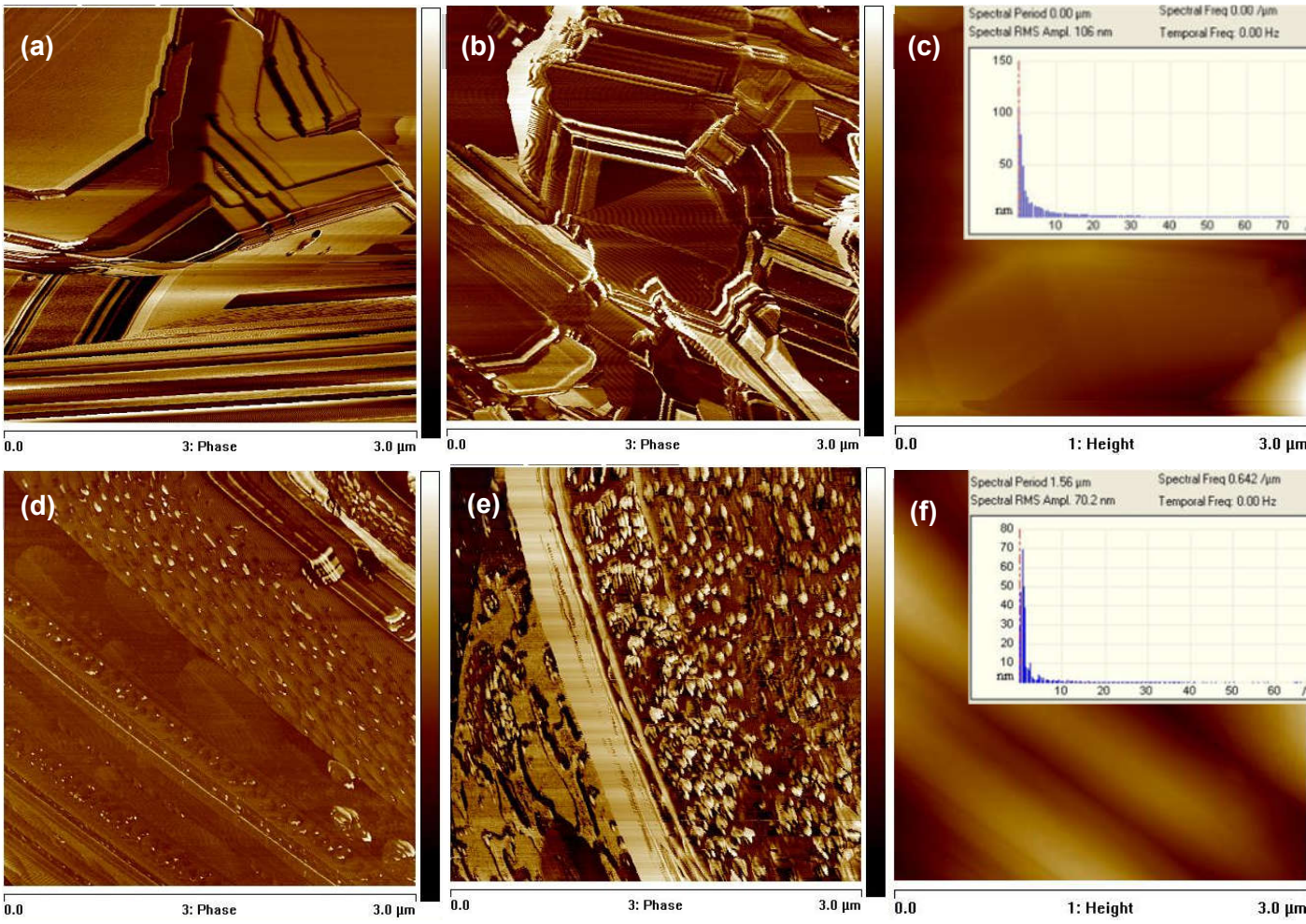

Figure 4.76. AFM surface topography images of the (a-c) Ti-46Al-2Nb and (d-f) Ti-46Al-2Nb-0.7Cr-0.3Si intermetallic alloys.

AFM surface topography oxide films shown in **Fig. 4.76a-f** revealed multiple slip-stepped surface structure having different orientations. The plastically deformed surface layers of the γ-TiAl based alloys are due to cyclic oxidation. **Fig. 4.76a, b** illustrates a slipping pattern with steps along a hill-valley groove on the Ti-46Al-2Nb surface. These were the alternating layers of the oxide/oxynitride compositions. **Fig. 4.76c** clearly shows slip steps of thin layers. The spectral RMS amplitude of the Ti-46Al-2Nb alloy oxide layer was 106 nm (inset of **Fig. 4.76c**) with a maximum fringe height of about 240 nm. AFM surface topography of the Ti-46Al-2Nb-0.7Cr-0.3Si oxide films is shown in **Fig. 4.76d-f.** On the contrary, the Ti-46Al-2Nb-0.7Cr-0.3Si alloy oxide film was comprised of a slip-step pattern of intermixed scale layers of different morphology **Fig. 4.76d, e**. The 3D topography in **Fig. 4.76e** has peripheral slip fringe with a maximum fringe height of 198 nm. The spectral RMS amplitude of the Ti-46Al-2Nb-0.7Cr-0.3Si alloy was 70.2 nm (inset of **Fig. 4.76f**) smoother than the Ti-46Al-2Nb surface film. This behavior was attributed to intermixed layers of oxides. This further proves that there was more

passive layer formation, which results in better restriction of oxygen diffusion into the Ti-46Al-2Nb-0.7Cr-0.3Si alloy than the Ti-46Al-2Nb alloy.

Moreover, TEM was conducted in order to examine the interfacial reaction of the oxide scales after oxidation at 900 °C for 900 h of the nitrided γTiAl based alloys. The oxide scales discussed are attributed to the oxide layers deliberated in **Section 4.8.5** and by XPS spectra analysis. **APPENDIX Fig. S10a** shows the TEM image with the corresponding zoomed out area indicating a facetted morphology. It can be seen from the micrograph that the particles were agglomerated on the carbon film and abroad the margin of the holes within the film. This makes the process of attaining high-resolution image complex because particles of interest are often unnoticeable by the overlapping particles [207]. The elemental mapping in **APPENDIX Fig. S10b** demonstrated that the scale was an oxynitride. The STEM did not pick-up Nb nor Al. In addition, the HRTEM image in **APPENDIX Fig. S10c** revealed evidence of surface reform on a single-crystal facetted particle with the d-spacing of 0.3259 nm. The corresponding SAED **APPENDIX Fig. S10d** suggests that the overall oxide layer is crystalline, despite the fact that the brightness and intensity of the other polymorphic rings are weak, which may have been an indication that the oxide film was partly amorphous.

APPENDIX Fig. S11a shows TEM images of the nitrided γ-Ti-46Al-2Nb-0.7Cr-0.3Si alloy with the complementary zoomed-out particle insert, meanwhile, the particle was characterised by STEM-EDS which was represented by elemental mapping in **APPENDIX Fig. S11b**. The elemental particles assumed a regular morphology. **APPENDIX Fig. S11c** shows the HRTEM of the facetted particle. Ordered lattice fringes are designated by the red arrow. The SAED in **APPENDIX Fig. S11d** validated the crystallinity of the particles. Similar findings by Rozita et al. **[26]** revealed facets that terminate with both (111) and (100) planes. They were ascertained at the end of the boundary and a partially disordered sub-surface visible in **APPENDIX Fig. S11d** back from the edge boundary. On the other hand, some part of the oxide scale of the γ-Ti-46Al-2Nb-0.7Cr-0.3Si alloy denoted the presence of $Ti_5Si_3(Nb_xAl_x)$ particles shown in **APPENDIX Fig. S12** which is in agreement with **Fig. 4.75b**.

APPENDIX Fig. S12a shows TEM images indicating an interfacial reaction between the oxidized film and the alloy. The corresponding elemental mapping in **APPENDIX Fig. S12b** clearly demonstrated that the observed oxide scale was the Ti_5Si_3 (Nb_xAl_x) film. Furthermore, the elemental mapping method validated the interfacial morphology designating that the reaction between the oxide film and the γ-TiAl based alloy occured. Moreover, the HRTEM image in **APPENDIX Fig. S12c** in concert with the SAED in **APPENDIX Fig. S12d** distinctly confirmed the Ti_5Si_3 (Nb_xAl_x) oxide film. In addition, **APPENDIX Fig. S12c** exhibited a facetted-type morphology of the scale illustrated by the red arrows.

4.8.7. Density analysis

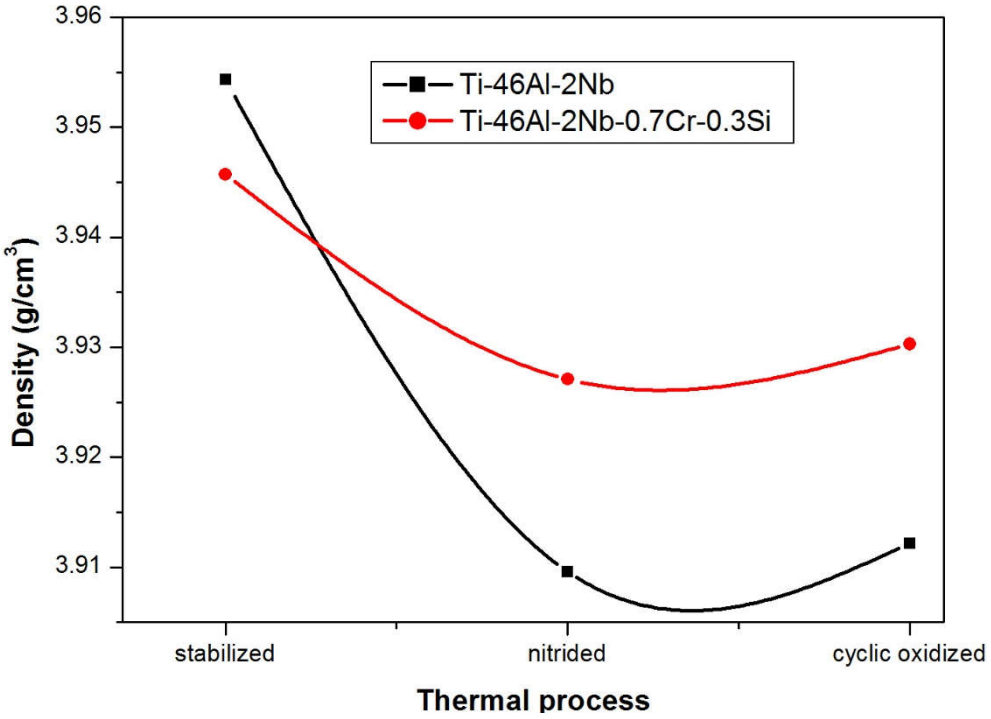

Figure 4.77. Density graphs of the measured Ti-46Al-2Nb and Ti-46Al-2Nb-0.7Cr-0.3Si intermetallic alloys after stabilization, annealing, nitridation and cyclic oxidation thermal treatment processes.

Fig. 4.77 illustrates the annealed Ti-46Al-2Nb alloy demonstrating a density of 3.954 g/cm^3 which decreased to 3.909 g/cm^3 after the nitridation process at 900 °C. A minute increase in the density of Ti-46Al-2Nb alloy to 3.912 g/cm^3 was observed after cyclic oxidation. This behavior agrees with the mass gain shown in **Fig. 4.72**. This variation of the alloy density, was rather negligible. For the Ti-46Al-2Nb-0.7Cr-0.3Si intermetallic alloy, the densities measured were 3.946 g/cm^3 and 3.919 g/cm^3 for the stabilized and cyclically oxidized samples. The Ti-46Al-2Nb-0.7Cr-0.3Si alloy also shows higher density after cyclic oxidation when compared to the nitrided sample. Moreover, the density variation between nitrides and cyclic oxidized ranges is negligible and smaller when compared to Ti-46Al-2Nb alloy. This behavior implies that the Ti-46Al-2Nb-0.7Cr-0.3Si was more stable after cyclic oxidation than the Ti-46Al-2Nb alloy where spallation was great in **Fig.4.72** between 700-900h.

4.8.8. Macro-hardness profile of the γ-TiAl based alloys

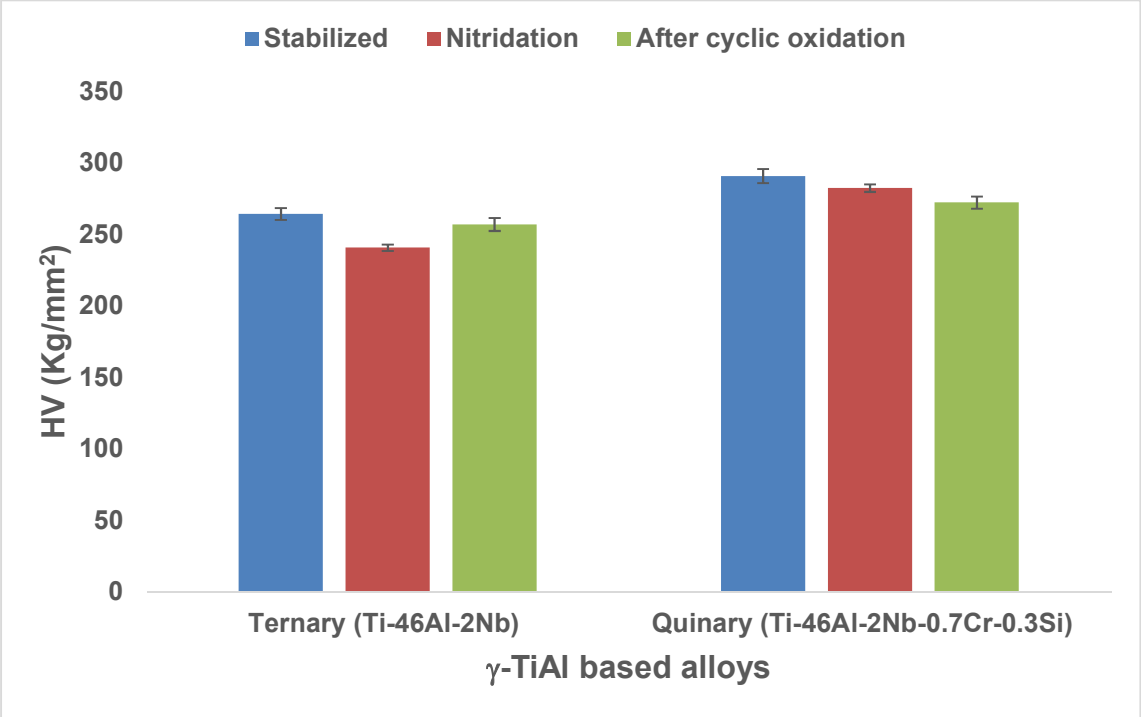

Figure 4.78. Macro-hardness profile of the γ-TiAl based alloys.

Fig. 4.78 illustrates the macro-Vickers hardness of the Ti-46Al-2Nb and Ti-46Al-2Nb-0.7Cr-0.3Si alloys of the stabilized, nitrided and cyclically oxidized conditions. The stabilized samples demonstrated higher hardness values than all the other samples for both alloys. Moreover, the bulk hardness results show that surface for the Ti-46Al-2Nb alloy were the lowest of all samples shown in **Fig. 4.78**. The nitrided Ti-46Al-2Nb-0.7Cr-0.3Si alloy hardness was also lower than that of the stabilized sample. Cyclic oxidation improved the hardness of the nitrided Ti-46Al-2Nb, but softened the Ti-46Al-2Nb-0.7Cr-0.3Si alloy. Chang et al. [206] reported comparable results and found that the coexisting of Al_2O_3 and SiO_2 near the surface delayed the diffusion of oxygen into the $Cr_{0.38}Al_{0.56}Si_{0.06}N$ coating, resulting in improved oxidation behavior. In the case of the quinary alloy, it was believed that the Al might have been incorporated into the CrN structure (B1-fcc), which decreases the grain size, by modifying its preferred crystalline orientation from (200) to (111), and inhibit the formation of hexagonal chromium nitride (Cr_2N) phase [206].

4.8.9. Micro-hardness profile of the γ-TiAl based alloys

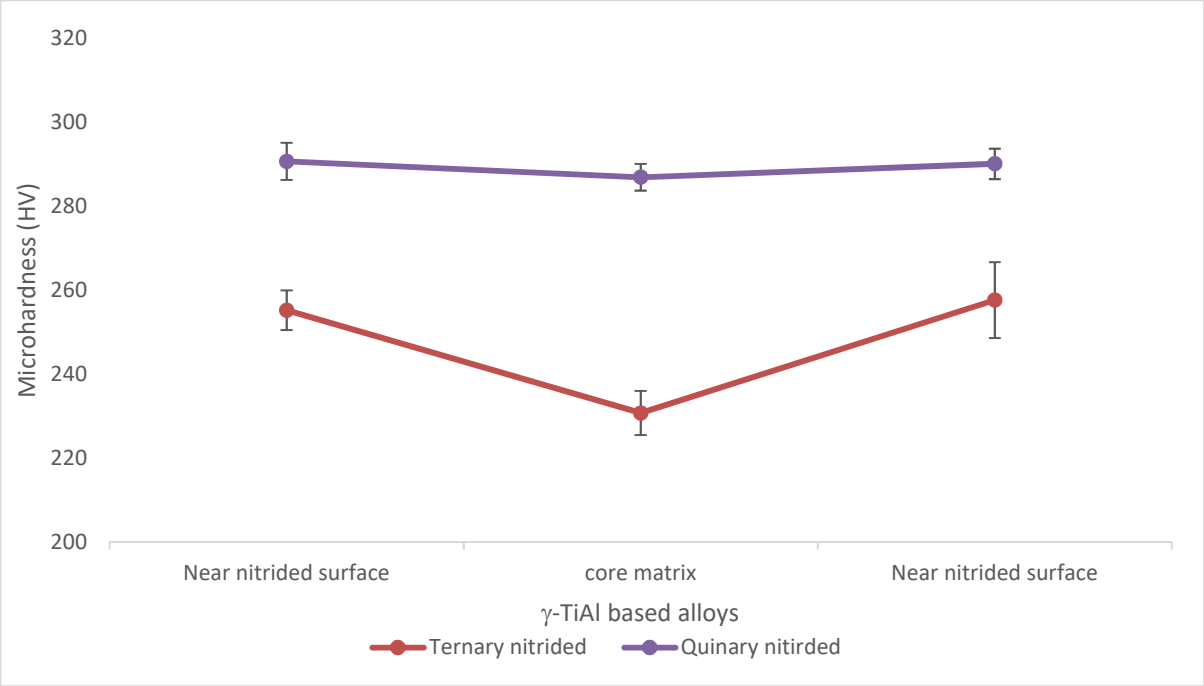

Figure 4.79. Micro-hardness profile of the γ-TiAl alloys.

The micro-hardness profiles of the Ti-46Al-2Nb and Ti-46Al-2Nb-0.7Cr-0.3Si alloys of the nitride samples are given in **Fig. 4.79**. The micro-hardness evaluation was conducted on the nitride surfaces and core matrix. Generally, the hardness measurements obtained near the nitrided surfaces were slightly higher than the core matrix. This was a result of the difference in the cooling effect between the core matrix and the surface of the sample. Abd El-Rahman [208] reported that surface hardness primarily depends on the treatment temperature, and that surface enhancement is attributed to the formation of the nitride layer on the surface. However, the variation in surface hardness of the alloys was due to the relative substrate effect on the treated layer; along with small variations in the microstructure as a consequence of different alloying elements in the alloys. Moreover, the high affinity of TiAlNb alloy for carbon and oxygen has been scrutinized by Menand et al. [209], which leads to increase the hardness.

Due to transition elements such as Al and Si in the quinary hard coatings **Fig. 4.75b**, improved oxidation resistance was obtained due to the generation of protective oxides on the surface of the coating which hindered ionic diffusion. As a result, hardness was increased compared to the TiAlNb alloy, due to strengthening by grain size refinement and solid solution hardening [210].

4.8.10. Conclusions

The ternary (Ti-46Al-2Nb), and quinary (Ti-46Al-2Nb-0.7Cr-0.3Si) alloys were developed, thermally treated at 1100 °C to stabilize and homogenize the structure ($\alpha_2+\gamma$), prior to nitriding and cyclic oxidation treatment and following conclusions were drawn:

- Due to surface coating in N/Ar atmosphere, oxidation properties of ternary, and quinary alloy improved significantly compared to the results reported elsewhere [78].
- The surface hardness of the quinary alloy was significantly greater than the ternary alloy with post-cyclic oxidation. This was due to the protective hard coatings viz. $Ti_{1-0.6893x}Al_{1-0.2968x}Cr_{1-0.001x}Si_{1-0.002x}Nb_{1-0.0105x}N_x$ and $Ti_{1-0.0595x}$ $N_{1-0.2155x}$ $O_{1-0.5452x}$ $Al_{1-0.1797x}$. This was confirmed by the micro-hardness profile values where the hardness near the nitride surface was higher than the core.
- The ternary alloy showed the most surface roughness with a spectral RMS amplitude of 106nm, while that of the quinary alloy was 70.2nm which was ascribed to the homogenous protective intermixed layers of SiO_2 and Al_2O_3 oxide scales. Moreover, TEM was further utilised to investigate the crystallinity, morphology and size of the particles constituted in the oxide films.
- Density measurements were in agreement with the obtained cyclic oxidation curves where weight gain and loss is concerned.
- The γ-Ti-46Al-2Nb-0.7Cr-0.3Si alloy showed improved hardness results compared to γ-Ti-46Al-2Nb alloy as a result of strengthing by grain size and solid-solution.

4.9. Microstructural evolution of a multi-phase γ-Ti-45Al-2Nb-0.3Si based intermetallic alloy solidified from β-phase domain

4.9.1. Introduction

Titanium aluminides (γ-TiAl) are strategic important research materials for scientists and engineers for high temperature application in aerospace. The well-known competitive high temperature alloys to γ-TiAl intermetallic are NiAl alloys [121]–[123]. These high temperature intermetallic alloys are also beneficial when used as coatings to enhance other industrial alloys' performance at elevated temperature application [124]–[126]. In particular, TiAl intermetallic alloys offer the best combination of mechanical properties versus low density, high specific modulus and strength, good creep and oxidation resistance [154]. On the contrary, their limited use to date is property balance, cost and production quality. The mechanical properties of this class of alloys are microstructure driven. Various studies have shown that improved tensile strength and ductility for γ-TiAl based alloys are obtained by grain refinement. Consequently, grain size plays an important role in as-cast γ-based alloys

considering that the microstructure often consists of coarse grains from solidification [154]. The Ti-48Al-2Nb-0.7Cr-0.3Si alloy was produced by electron beam melting (EBM) and comprised both equiaxed fine and coarse grains, which were altered after heat treatment [211]. Recently, Ti-48Al-2Nb and Ti-48Al-2Nb-0.7Cr-0.3Si alloys showed improved mechanical and cyclic oxidation properties, better than Ti-48Al-2Nb-0.7Cr alloy [78]. Therefore, the presence of Cr without Si did not contribute the best mechanical properties. The Ti-48Al-2Nb-0.7Cr-0.3Si alloy yielded the best properties due to the presence of Ti_5Si_3 phase along the grain boundaries. Additionally, the Ti-48Al-2Nb-0.7Cr-0.3Si intermetallic alloy had the ultrafine lamellar spacing, high tensile strength and percentage elongation [78]. The resultant heat treatment products were spheriodized and Widmanstätten laths [116]. In the current investigation, the effect of Cr in γ-Ti-48Al-2Nb-0.7Cr-0.3Si alloy, previously reported [78], [116], was compared with γ-Ti-48Al-2Nb-0.3Si alloy in terms of mechanical properties. Additionally, the high resolution electron back scattered diffraction (HREBSD) analysis of the heat-treated γ-Ti-45Al-2Nb-0.3Si alloy structures was employed to study the evolution of the β-solidified γ-TiAl based alloy.

4.9.2. DSC analysis

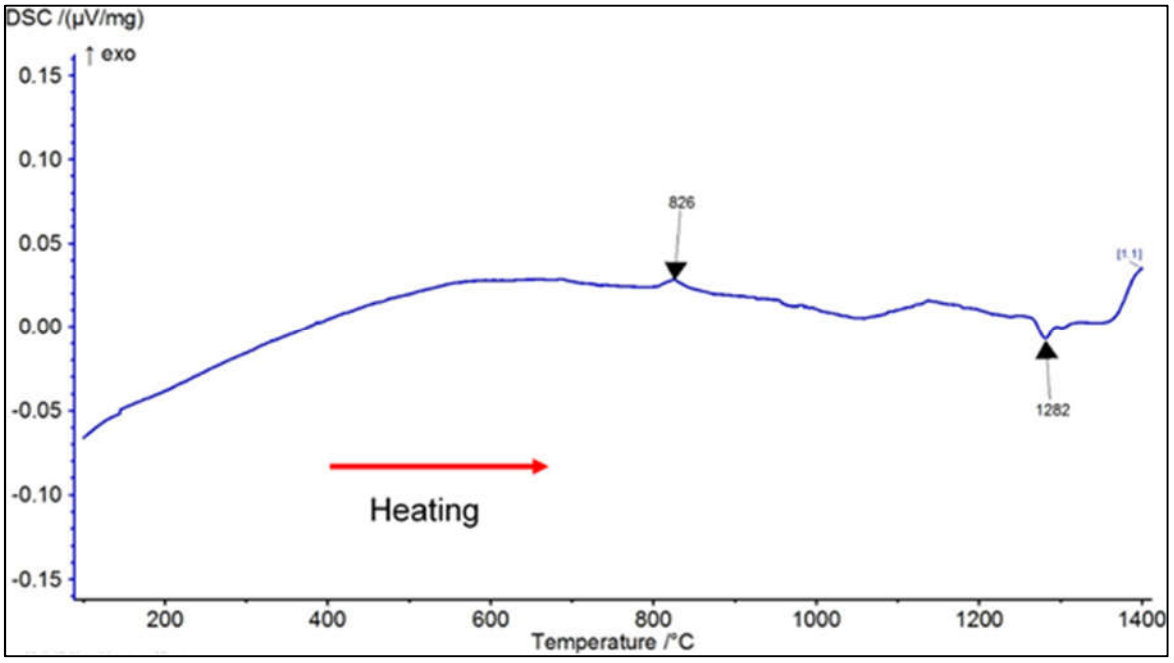

Figure 4.80. DSC curve of the as-cast Ti-45Al-2Nb-0.3Si alloy.

Fig. 4.80 shows the DSC heating curve of the as-cast Ti-45Al-2Nb-0.3Si alloy. There are two exothermic peaks emerged at 826 and 1120 °C indicating crystallization. Furthermore, at 1282 °C endothermic peak attributed to the transition $\alpha_2 + \gamma \rightarrow \alpha$ phase was observed. Therefore, the transformation temperature was determined to be about 1273 °C by the tangent method, which is almost similar to the value reported by Wang et al. [154]. The origin of such transformation in Ti based alloys is inherited from the pure Ti which shows α→β phase transition HCP→BCC [111]. The thermal analysis curve served as a guide for the selection of heat treatment temperatures in these alloys, which was above 1335 °C.

4.9.3. As-cast and heat-treated microstructures

The as-cast Ti-45Al-2Nb-0.3Si alloy was heat-treated according to **Table 3.5** for a stabilized fully lamellar structure. The final chemical composition is shown in **Table 4.17**.

Table 4.17. Final chemical composition (at. %) of the alloys.

γ-TiAl based alloy	Ti	Al	Nb	Cr	Si
γ-Ti-48Al-2Nb-0.3Si	52.5	45.3	2.0	-	0.3

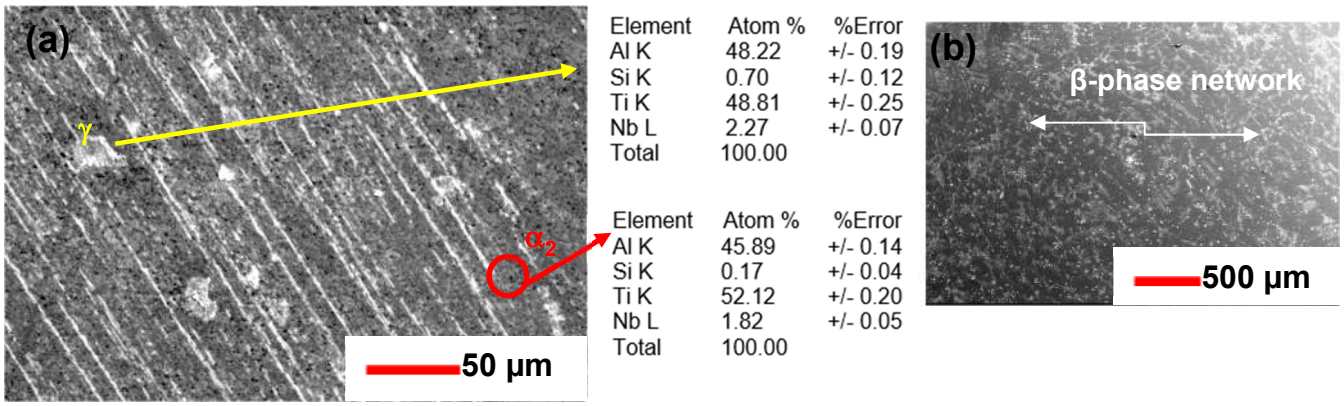

Figure 4.81. SEM-SEI EDX images of the as-cast Ti-45Al-2Nb-0.3Si intermetallic alloy.

Fig. 4.81 shows the SEM secondary electron images (SEI) of the as-cast, as well as heat treated, microstructures of γ-Ti-45Al-2Nb-0.3 Si intermetallic alloy. The microstructure of as-cast Ti-45Al-2Nb-0.3Si alloy have the lamellar (α_2/γ) structure (**Fig. 4.81a)** with partial isolated equiaxed γ-grains evenly distributed across the matrix. In the previous investigation, the microstructures of Ti-45Al-2Nb-0.7Cr-0.3Si comprised γ-TiAl lamellar structure [78]. Non-uniform microstructures are shown at low and intermediate magnifications, especially for the as-cast structure in **Fig. 4.81b**, which is indicative of micro-segregation, including solidification segregation which is characterized by high Al and low Nb contents in inter-dendritic regions, as a result an inhomogeneous microstructure forms causing poor and unstable mechanical properties. The residual β/B2 phase stable at room temperature was caused by the coring effect during $\beta \rightarrow \alpha$ transformation with subsequent growth of α-phase [115]. The corresponding chemical composition of the alloy related to phases formed was illustrated next to their corresponding microstructures.

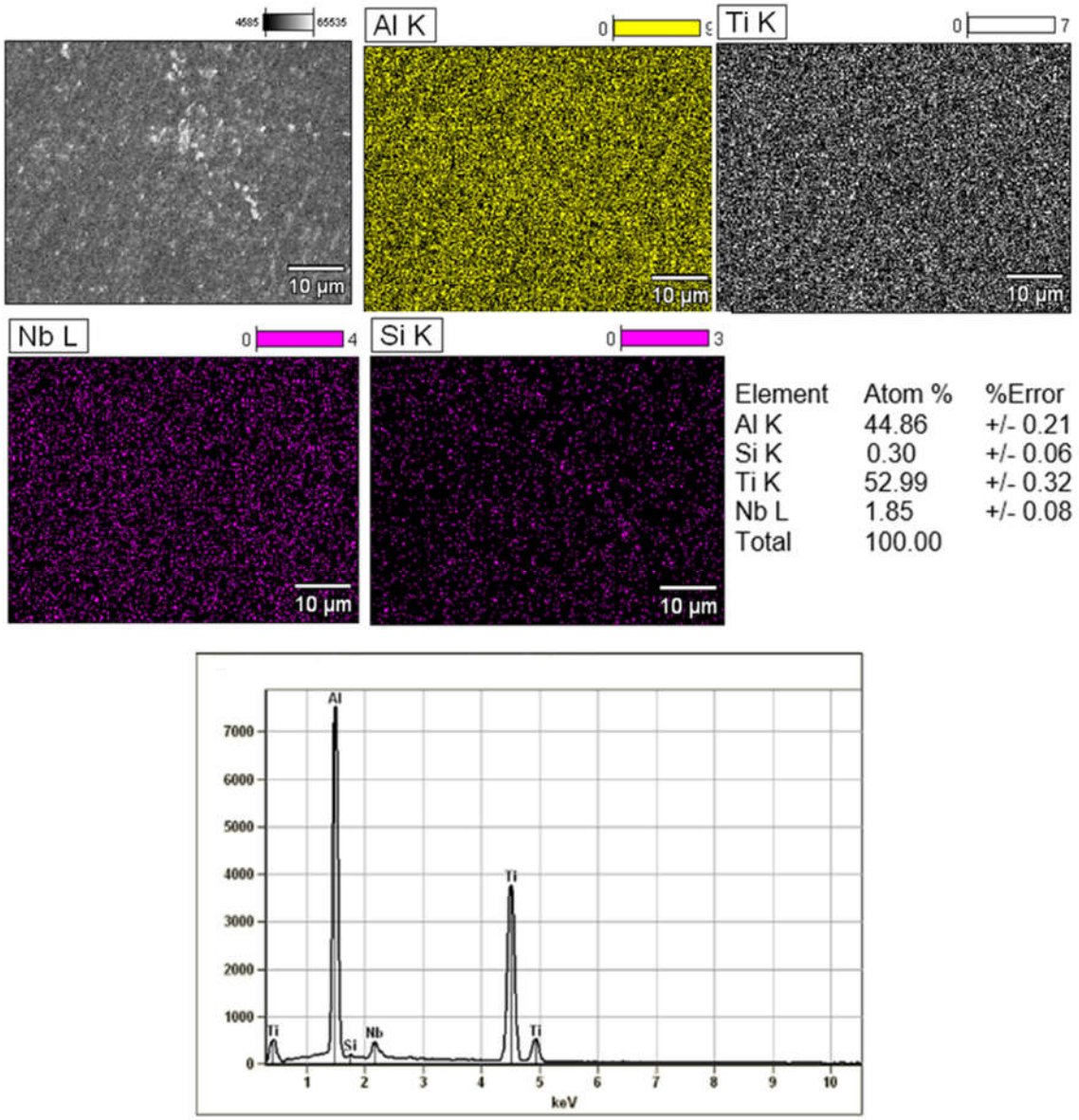

Figure 4.82. SEM-BSE images of the as-heat treated Ti-45Al-2Nb-0.3Si intermetallic alloy with corresponding elemental maps.

Heat-treated SEM-backscatter electron image (BSI) **Fig. 4.82,** with the corresponding elemental mapping of the electron image. Subsequent heat-treatment process, resulted in the homogeneity of Ti-48Al-2Nb-0.3Si alloy as shown by the elemental mapping indicating even distribution of the phases. The phases were also confirmed by the XRD pattern in **Fig. 4.83** for the microstructurally evolved γ-Ti-45Al-2Nb-0.3Si alloy. The XRD results verify the multi-phases stable at room temperature, viz. $\alpha_2/\gamma/Ti_5Si_3$ precipitates and some remnant β/B2, respectively. In addition, crystallographic orientation relationship and acquisition of the phases are consummately explained in **Section 4.10.4** (EBSD analysis).

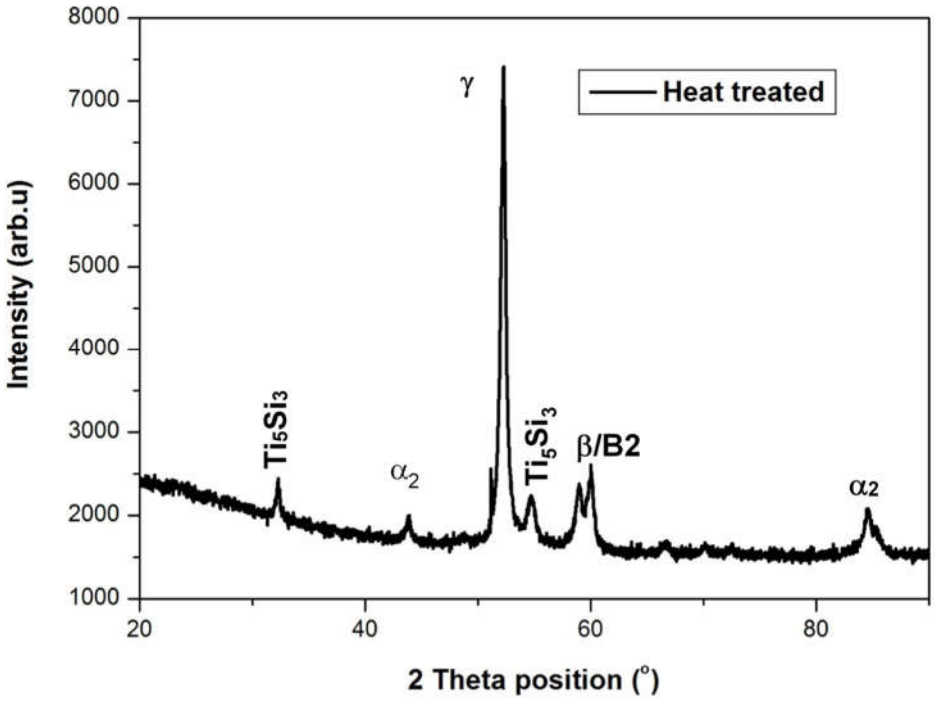

Figure 4.83. XRD pattern of the heat-treated γ-Ti-45Al-2Nb-0.3Si based intermetallic alloy.

4.9.4. Macro-hardness and tensile analysis

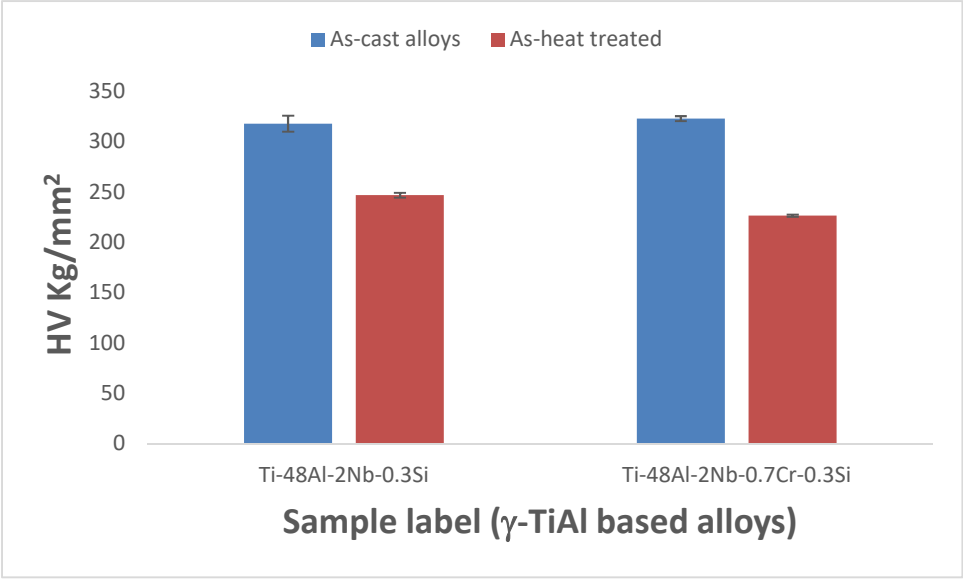

Figure 4.84. Comparison of the macro-hardness of the as-cast and heat treated Ti-45Al-2Nb-0.3Si compared with Ti-45Al-2Nb-2 Cr0.3Si alloy found in [78].

Fig. 4.84 illustrates the macro-hardness of the Ti-48Al-2Nb-0.3Si intermetallic alloy in the as-cast and heat-treated conditions. For comparison, the Cr containing alloy is also presented. The hardness values of the heat treated alloys were lower than the as-cast alloys. The Ti-45Al-2Nb-0.3Si alloy hardness decreased from 318 HV to 247 HV. Additionally, it was observed that Ti-45Al-2Nb-0.7Cr alloy without Si yielded a hardness of 368 HV much harder

than the former [78]. Furthermore, In the case of Ti-48Al-2Nb-0.7Cr-0.3Si alloy, it seemed Si reduced the value to 323 HV as the ductility of the alloy improved [78]. It implies that the presence of Cr mainly improved grain refinement of the alloy. Supplementing the hardness values is the summary of the room temperature tensile properties in **Fig. 4.85**. The Ti-45Al-2Nb-0.7Cr-0.3Si alloy exhibited higher UTS of 341 MPa and 0.0227 % extension [78] than the Cr-free Ti-45Al-2Nb-0.3Si alloy with 260 MPa and 0.017 % UTS and extension, respectively. The extension values appeared to be hardly beyond the point of plastic yielding, which suggested that dislocation movement may have been largely absent before fracture took place. On the other hand, addition of Cr increased the volume fraction of Ti_5Si_3 particles and decreases the γ-lamellar spacing prevailed during the solidification process. Furthermore, the presence of Ti_5Si_3 particles spheriodal-like (**Fig. 4.82a**) may retard the motion of dislocations, leading to the improvement of strength. The twin and super-dislocation nucleation are competing mechanism in γ-TiAl alloys, depending on stacking fault energy [78], [157], [27], [216], and [17]. In addition, when the lamellar boundaries are aligned parallel to the tensile direction, a good combination of room temperature strength, ductility, toughness and creep strength can be obtained Ding et al. [99].

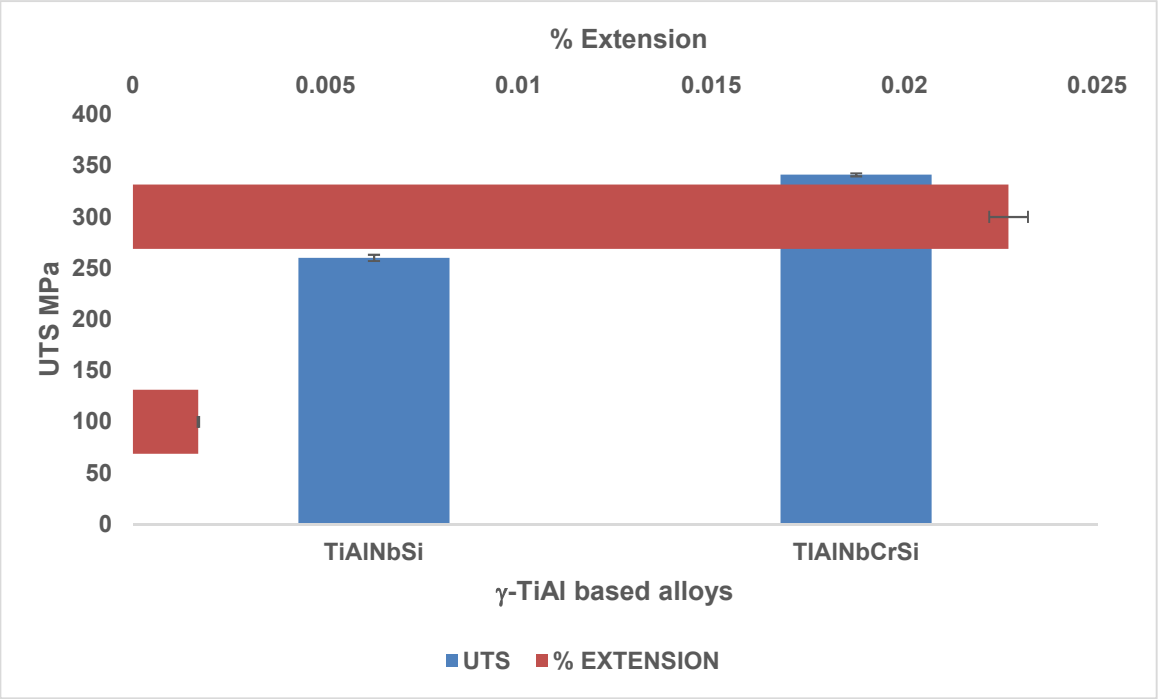

Figure 4.85. Room temperature tensile properties for the Ti-45Al-2Nb-0.3Si, and the Ti-45Al-2Nb-0.7Cr-0.3Si intermetallic alloys.

4.9.5. SEM-EBSD analysis

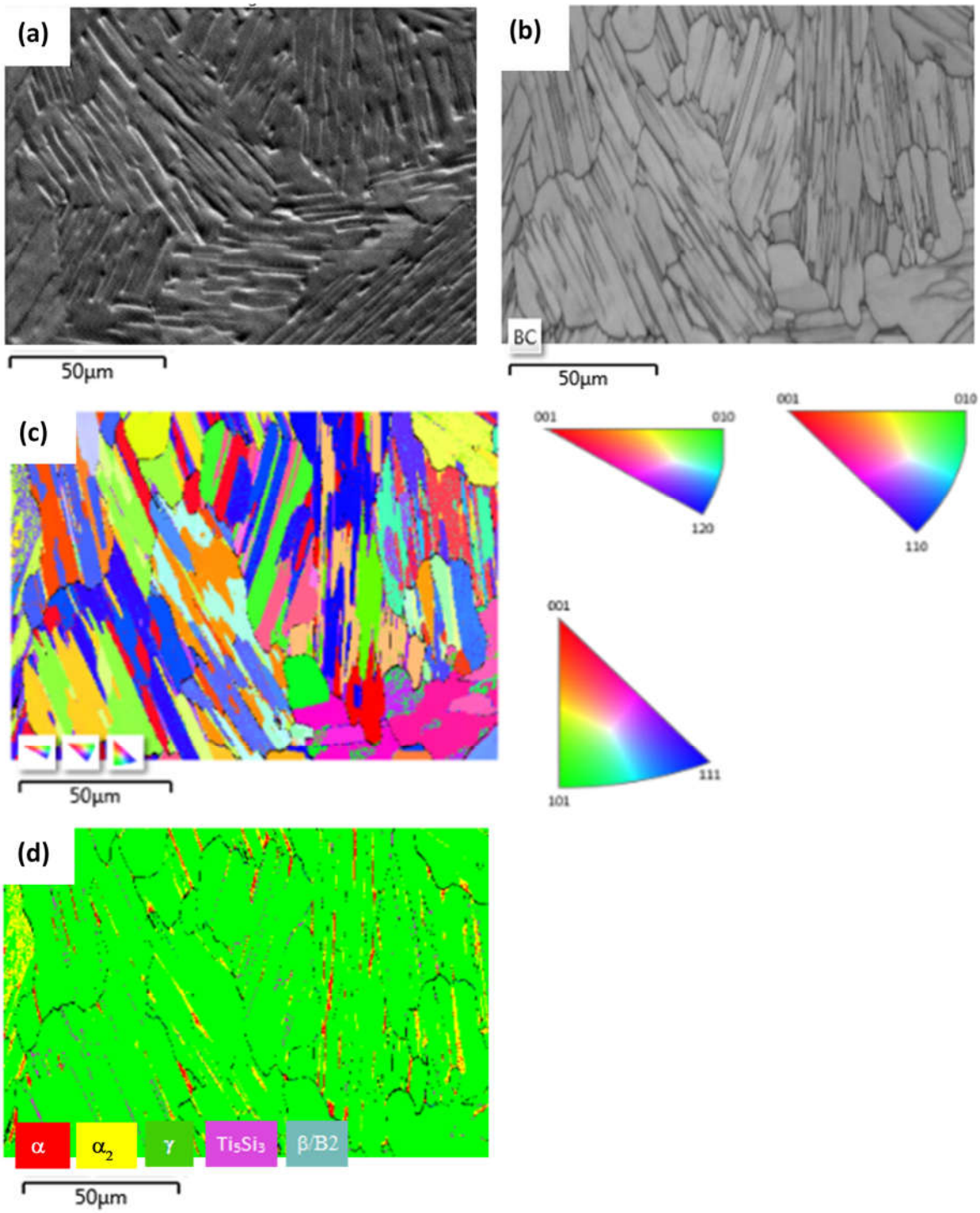

Figure 4.86. EBSD maps of Ti-45Al-2Nb-0.3Si alloy: (a) electron image, (b) band contrast maps, (c) inverse pole figure (IPF) maps and (d) phase color map.

Fig. 4.86 shows EBSD maps of the Ti-45Al-2Nb-0.3Si alloy. In **Fig. 4.86a** the area of mapping in the form of a backscattered electron image is illustrated with corresponding band contrast maps displayed in **Fig. 4.86b**. **Fig. 4.86c** is the orientation map with their corresponding inverse pole figures (IPF). **Fig. 4.86d** shows the phase color map which uses a five color key.

In addition, supplementary grain map **Fig. 4.87a** captures orientation difference between the neighboring grains, but does not represent crystal orientations. Meanwhile, **Fig. 4.87b** confirms the distribution function of the neighboring grains. The blue and the yellow color contrast is the representation of the α/α_2 (*c/a* = 2.012) matrix, while the pre-dominant phase (green) is the gamma phase *c/a* = 1.45. The B2 phase is represented by NiAl prototype which has a *c/a*= 1, and it is located in the α/α_2 phases. It implies that α_2 may have nucleated from B2 phase and grew as elongated precipitates. As shown in the supplementary **Fig. 4.87c**, the orientation relationship between the α/α_2 -matrix and the B2 phase was;

$$\{0001\}_{\alpha} \parallel (100)_{B2} \text{ and } \langle 10\text{-}10\rangle_{\alpha} \parallel [110]_{B2}$$

demonstrating that the B2 phase precipitated from the α-matrix. During the remnant $\beta_{(primary)} \rightarrow \alpha$ transformation at an isothermal temperature of 1380 °C, B2 phase can perform as preferential heterogeneous nuclei of the α-phase. Therefore, if α-phase heterogeneously nucleates on the B2 phase following the orientation relationship;

$$\{0001\}_{\alpha} \parallel (100)_{B2} \text{ and } \langle 10\text{-}10\rangle_{\alpha} \parallel [110]_{B2}$$

These α-phases are Burgers α-phase. Furthermore, on the analysis of EBSD-orientation maps, it is important to analyze the frequency distribution of misorientation angles between neighboring γ-grains in order to ascertain γ-variants that obey Burgers orientation relationship (BOR) relative to the peritectic α-grains that resulted due to the solidification process during the isothermal heat-treatment induced. This Blackburn orientation relationship [51] at interfaces between γ and α phase is: $(111)\gamma \parallel (0001)\alpha$ and $<1\ \bar{1}0]\gamma \parallel <11\ \bar{2}0>\alpha$. According to **Fig. 4.87c**, the orientation relationship between the α/α_2-matrix and the γ-phase is: $\{111\}\gamma \parallel \{0001)\alpha$ and $\langle 100\rangle\gamma \parallel \langle 11\text{-}20\rangle\alpha$. Therefore, this may suggest that the γ-phase precipitated from the parent α-phase. Meanwhile, the orientation relationship at interfaces between the Ti_5Si_3 with a *c/a* = 0.69, and B2 is $\{0001)_{Ti5Si3} \parallel \{111\}_{\beta/B2}$, and $\langle 11\text{-}20\rangle_{Ti5Si3} \parallel \langle\ 100\rangle_{\beta/B2}$. This suggests that the reaction L1 $+\beta\rightarrow\alpha$ took place immediately after solidification of $L\rightarrow\beta$+L1, with subsequent eutectic reaction $L1\rightarrow\alpha+ Ti_5Si_3$ which may have occurred in the last solidified liquid (Si-rich), according to Sun and Froes [156].

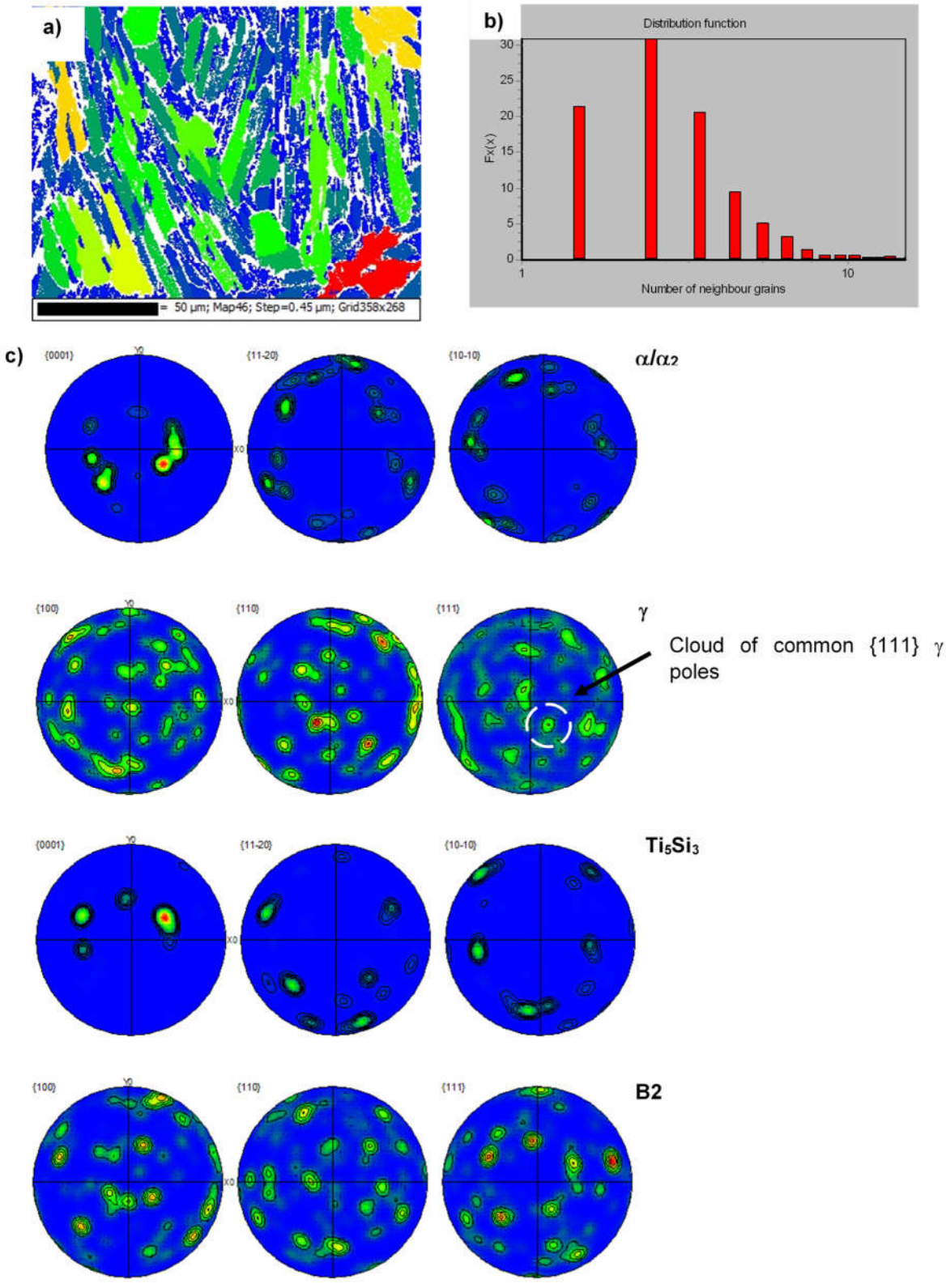

Figure 4.87. EBSD results of a) grain map, b) distribution function of the neighboring grains, and c) pole figures of α/α2, γ, Ti_5Si_3, and B2 phases.

The dominant phase was the gamma phase with a volume fraction of about 92 % and the *c/a* ratio = 1.45. The estimated phase fractions of all the phases present in the alloy are presented in **Table 4.18**. The phase acquisition for the alloy investigated is shown in **Table 4.19**.

Table 4.18. Phase fractions of Ti-45Al-2Nb-0.3Si alloy.

Phase Name	Phase Fraction (%)	Phase Count	Mean Band Contrast	Mean MAD	Standard Deviation MAD	Min MAD	Max MAD
α	1.49	1428	97.15	0.54	0.22	0.17	1.92
α_2	3.93	3767	103.13	0.62	0.34	0.16	1.99
γ	91.57	87858	142.92	0.39	0.12	0.13	1.86
Ti_5Si_3	0.68	648	109.84	0.64	0.20	0.24	1.98
β/B2	0.36	343	106.38	0.64	0.28	0.10	1.97
Zero Solutions	1.98	1900	96.70				

Table 4.19. Phase parameters of Ti-45Al-2Nb-0.3Si alloy.

Phase	*a* (Å)	*b* (Å)	*c* (Å)	Alpha (º)	Beta (º)	Gamma (º)	Space Group
α	3.20	3.20	5.20	90.00	90.00	120.00	194
α_2	5.73	5.73	4.64	90.00	90.00	120.00	194
γ	2.81	2.81	4.08	90.00	90.00	90.00	123
Ti_5Si_3	7.45	7.45	5.14	90.00	90.00	120.00	193
β/B2	2.89	2.89	2.89	90.00	90.00	90.00	221

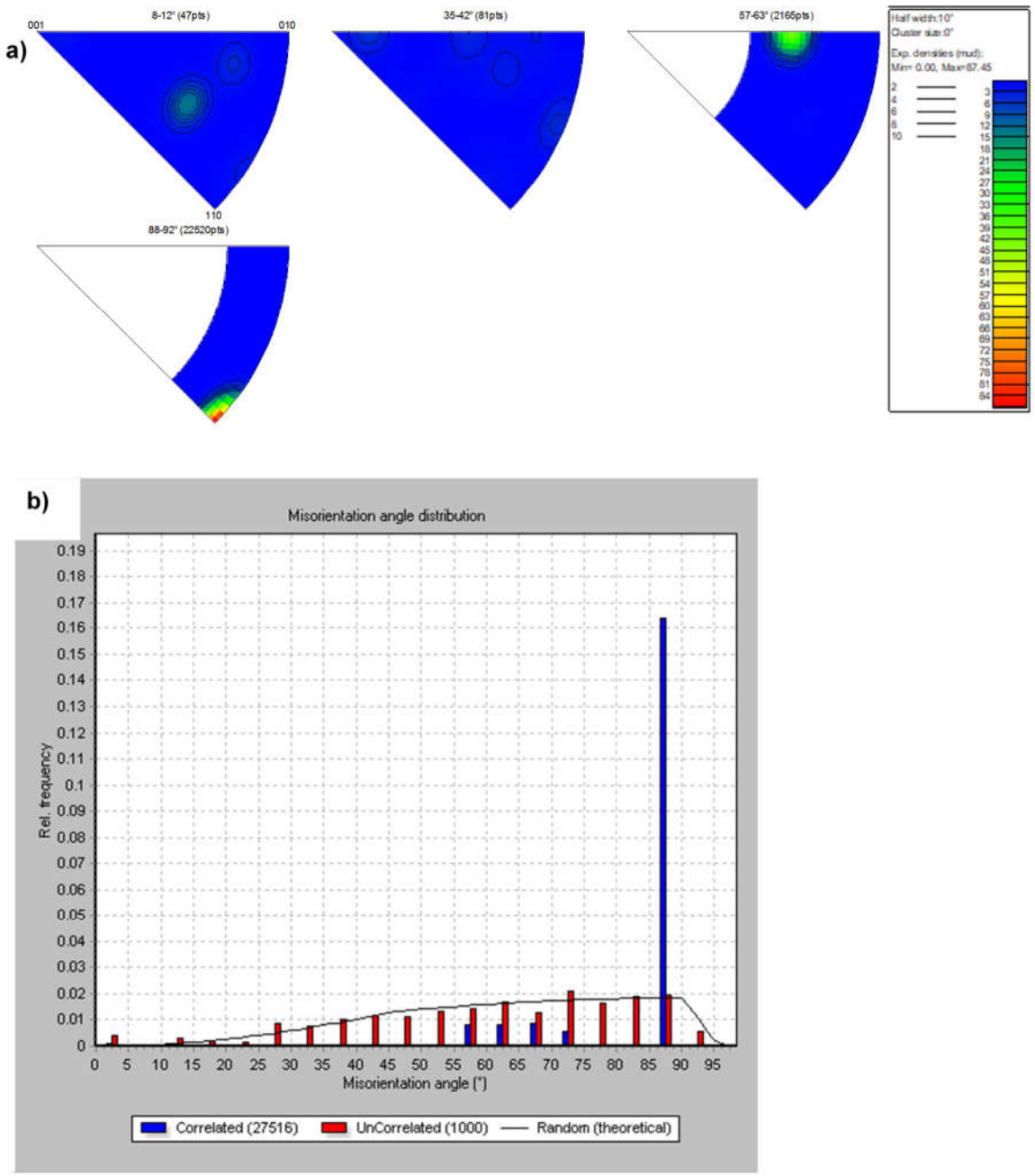

Figure 4.88. Misorientation data on the predominant γ-phase: a) Misorientation axes with corresponding color coding, b) Misorientation angle distribution.

Fig. 4.88a shows the misorientation axes in crystal co-ordinate system for the γ-phase. This describes which crystallography directions the misorientation axes align with for a chosen range of misorientation angles. The observed misorientation axes are indicated by clusters between [001] and [110] in the 8-12° section; another cluster between [001] and [010] in the 57-62°, and lastly at 88-92°. **Fig. 4.88b** demonstrate relative frequency versus misorientation angle, and there was not much difference between the uncorrelated and random distribution, which may be due to the absence of strong fiber texture <111>. The correlated distribution

exhibits a fairly larger number of boundaries with misorientations above a peak value of 85° compared to the uncorrelated distribution. Consequently, the high angle boundary may be a significant feature of the microstructure and not a product of texture, in a sense that microstructural evolution showed coarse elongated lamellar colonies via dynamic recrystallization high temperature heat-treatment process.

4.9.6. Conclusions

The γ-Ti-45Al-2Nb-0.3Si intermetallic alloy was developed. The DSC provided insight into phase transformation reactions prior to the heat treatment process and the following observations were made:

- The transformation temperature for the start and finish temperatures for the α to β phase transformation was found to be 1270 ºC and 1310 ºC, respectively.
- The addition of Cr to Ti-45Al-2Nb-0.7Cr-0.3Si alloy improved both the strength and percentage extension compared to the Cr-free Ti-45Al-2Nb-0.3Si alloy. It was suggested that the presence of Cr induced slight plasticity enhancement owing to Cr atoms occupying Ti-sites in the γ-TiAl phase based alloy which may have resulted in Ti-Al bond modification.
- The as-cast microstructure of the Ti-45Al-2Nb-0.3Si exhibited Ti_5Si_3 particles, and a grain boundary network of the β phase. Both the EBSD and XRD analysis demonstrated that the as-cast structures evolved into homogeneous microstructures, which exhibited multi-phases of α_2, γ, Ti_5Si_3, and B2. The results also showed that the phases obey the Blackburn orientation relationship.

4.10. EBSD texture analysis of the γ-Ti-45Al-2Nb-0.3Si intermetallic alloy solidified from the α-phase region

4.10.1. Introduction

As mentioned in **Section 2.3**, the γ-TiAl alloys are attractive structural materials, however, their inherent poor ductility and fracture toughness limits their use [116], [212]. However, Wei et al. [213] reported that the addition of α_2-Ti_3Al as the second phase of γ-TiAl based alloys improves ductility of TiAl. Therefore, the deformation mechanism of the TiAl/Ti_3Al interface behaviors will offer a useful reference to enhancing ductility of the γ-TiAl based alloys. It was reported that both experimental and theoretical approaches on the deformation of TiAl/Ti_3Al and TiAl/TiAl interfacial studies revealed that sliding occurred in $[11\bar{2}]$ direction in the (111) plane in TiAl, and the $[10\bar{1}1]$ direction on the (0001) in the Ti_3Al [3]. Mechanical properties of TiAl alloys depend on microstructural control via heat treatment and chemical composition [2, 4]. Lapin et al. [214] reported the microstructural stability of the Ti–46.5Al–2W–0.5Si (at.%)

alloy at 900–1000 °C annealing temperatures, where the initial γ/α_2-B2 structures destabilized into globular structures comprised γ-TiAl matrix, equiaxed globules of B2 and Ti_5Si_3 phases. Thermal treatment processes can convert the microstructure of the alloy to polycrystalline grains. It is therefore essential to study crystallography of specific orientation whereby its significance lies in the anisotropy of the alloys properties. As such, efforts have been made to provide quantitative texture data in conventionally accepted formats such as pole figure or orientation distribution functions (ODFs), employing electron backscatter pattern (EBSP) orientation measurement techniques which can challenge those obtained by X-ray methods in both speed and accuracy [215], [73]. The current **Section 4.10** reports on the texture component in the γ-Ti-45Al-2Nb-0.3Si alloy studied by EBSD in relation to ODFs, EBSP techniques.

4.10.2. Microstructural analysis

The Ti-45Al-2Nb-0.3Si alloy produced by vacuum arc melting was heat treated according to **Table 3.5** for a stabilized fully lamellar structure. The final chemical composition is displayed in **Table 4.17**.

The SEM-BSE images of the heat treated Ti-45Al-2Nb-0.3Si with the corresponding elemental mapping are shown in **Fig. 4.89a**. The chemical composition of the identified phases corresponding to TiAl, Ti_3Al, and Ti_5Si_3 are shown, also confirmed by the XRD analysis **Fig. 4.83**. Elemental mapping reveals the homogeneity of the Ti-48Al-2Nb-0.3Si alloy after heat treatment. The representative as-cast structure of γ-Ti-45Al-2Nb-0.3Si intermetallic alloy, is shown in the **APPENDIX Fig. S13** with columnar lamellar (α_2/γ) structures of an average size of approximately 100 μm.

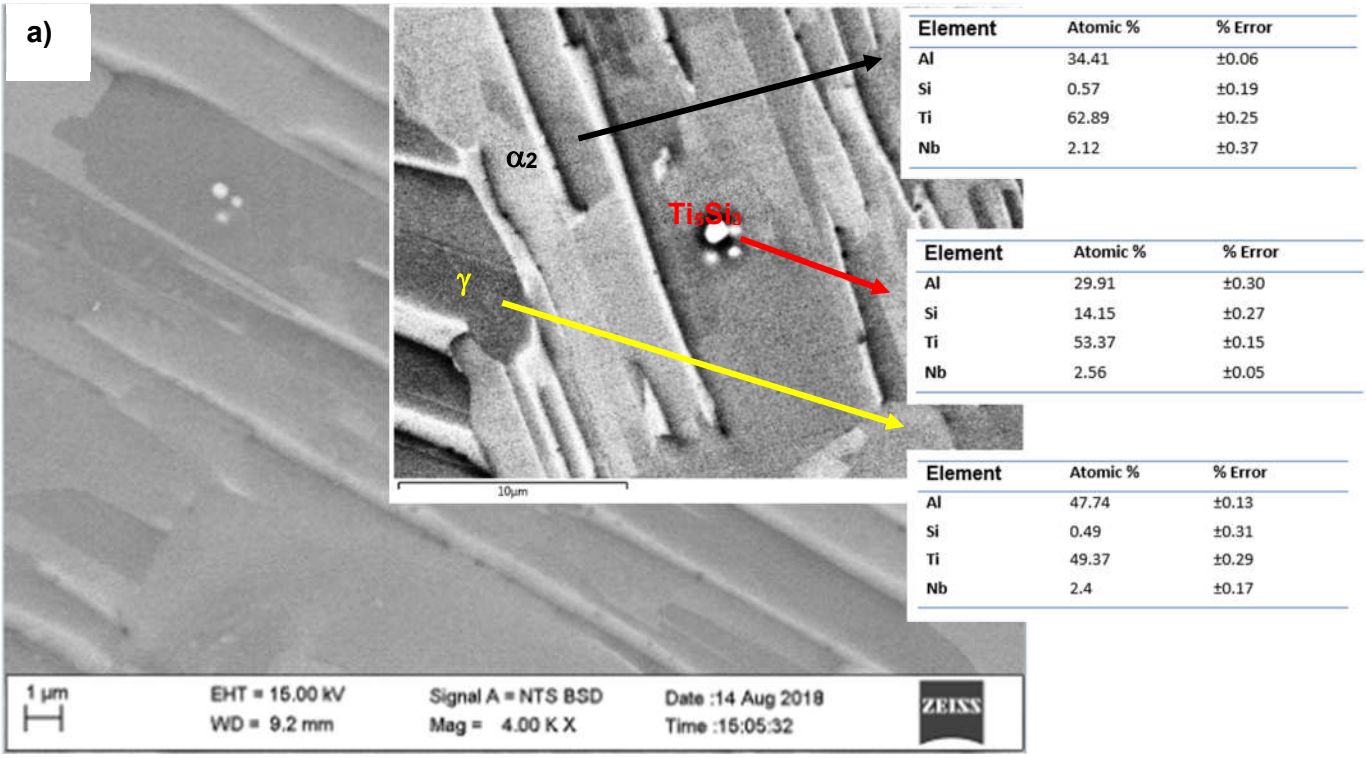

Element	Atomic %	% Error
Al	34.41	±0.06
Si	0.57	±0.19
Ti	62.89	±0.25
Nb	2.12	±0.37

Element	Atomic %	% Error
Al	29.91	±0.30
Si	14.15	±0.27
Ti	53.37	±0.15
Nb	2.56	±0.05

Element	Atomic %	% Error
Al	47.74	±0.13
Si	0.49	±0.31
Ti	49.37	±0.29
Nb	2.4	±0.17

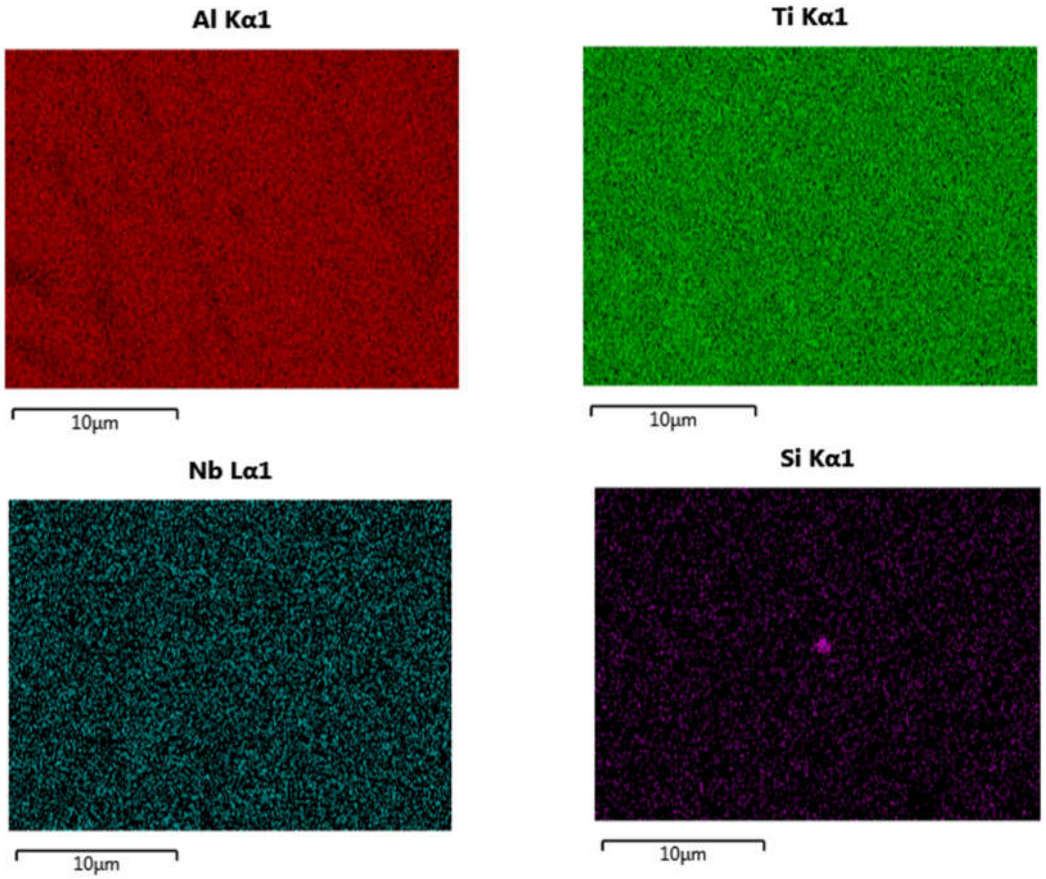

Figure 4.89. SEM-BSE images (a) heat treated Ti-45Al-2Nb-0.3Si intermetallic alloy with corresponding (b)-(e) elemental mapping images.

4.10.3. EBSD analysis

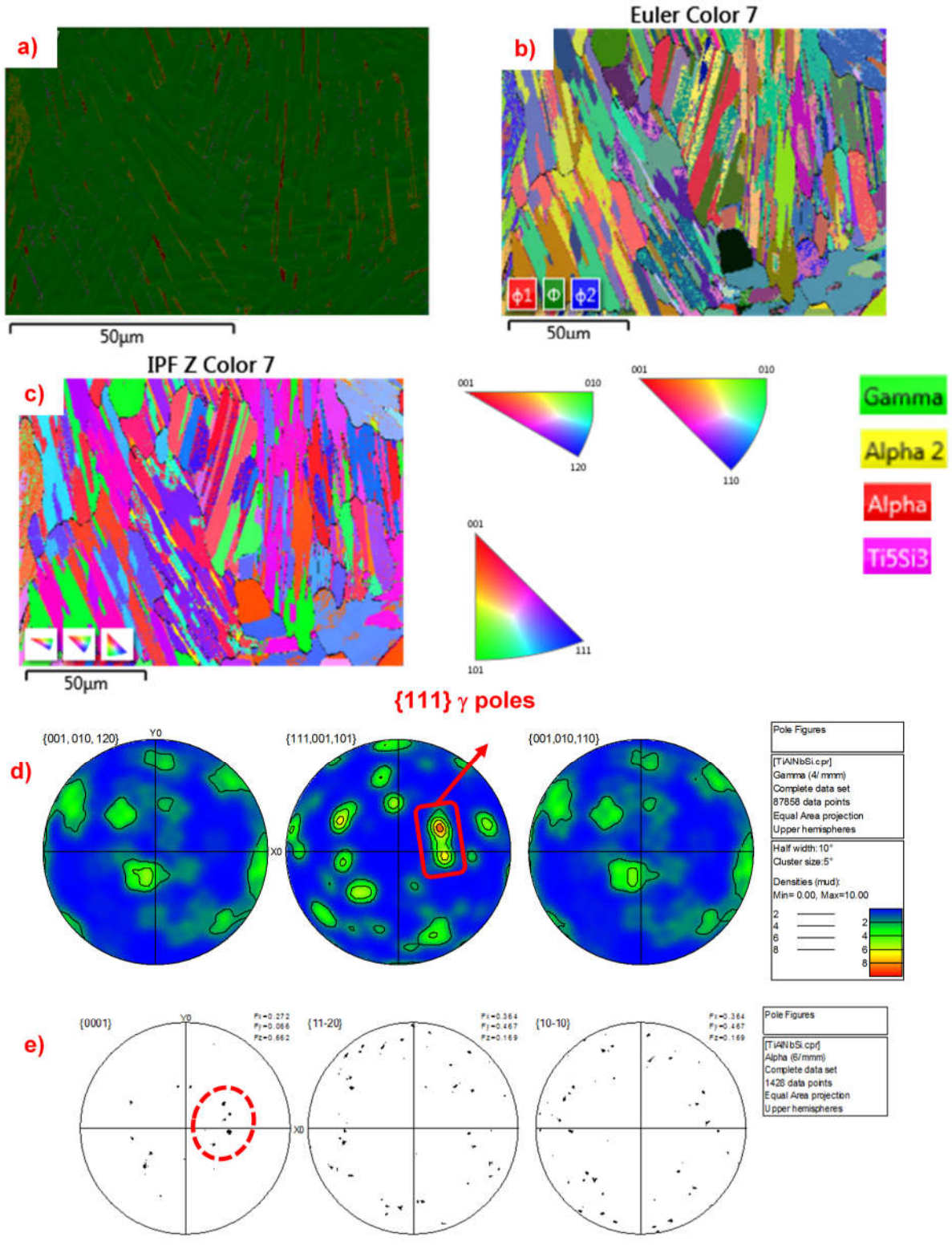

Figure 4.90. (a) EBSD layered electron image, (b) Euler angle map, (c) Inverse pole figure (IPF) map with corresponding phase color coding, (d) Pole figure maps of γ-phase, and (e) scattered pole figure maps of the α-phase.

The EBSD layered electron image **(Fig. 4.90a)**, Euler angle map (**Fig. 4.90b)**, inverse pole figure (IPF) maps (**Fig. 4.90c)** with corresponding color coding, and the IPF maps of the γ-phase **(Fig. 4.90d)** of Ti-45Al-2Nb-0.3Si alloy are shown in **Fig. 4.90.** The dominant phase was the γ-TiAl at about 91.57 %, the α_2-Ti_3Al (3.926%), Ti_5Si_3 (0.6754%) and the parent α-phase was 1.488%. **Fig. 4.90d** illustrates the IPFs, and **Fig 4.90e** shows that {111} γ-poles are parallel to the {0001} poles of the α-phase. Therefore, a representation of the Burgers orientation relationship (BOR) relative to the peritectic α-grains, resulted due to the solidification process during isothermal heat-treatment. This BOR at interface between γ and α phase is: (111)γ || (0001)α and <1-10]γ || <11-20>α. This is an indication that the γ-phase formed from the α-parent phase in the peritectic reaction [116].

4.10.4. γ-phase texture quantitative data

The strong fiber textures for ODF (see detail in **APPENDIX Fig. S14**) were found at densities of ϕ2=30°, 35°, 40°, 45°, 50°, 65°, 70°, 75° serial sections with black contour lines shown in **APPENDIX Fig. S15**. The misorientation of the γ-phase was calculated using **Eq. 18,** and the misorientation distribution function (M) ODF was calculated from the texture coefficient which are coefficients of series expansion method according to **Eq. 19**.

In the plane orientation convention for unique representation of pile-up profiles, it is determined by the choice of an initial orientation for the tetragonal structure of γ-Ti-45Al-2Nb-0.3Si alloy defined by c-axis || Z, a-axis || X, b-axis||Y, where Z, X and Y are the indentation direction. In the work reported by Zambaldi [70], the indenter axes in crystal coordinates is rotated into the [001]-[100]-[110] triangle by a rotation angle η around a rotation axis, viz. crystallographic *y*-axis around the crystallographic *z*-axes by the angle ς. These two are the angles between the crystallographic z_c-axis, [001] in case of γ-TiAl, the indentation axis (η), and the angle between the indentation axis projected into the x_c-y_c-plane, (001) for γ-TiAl, and the x_c-axis, here denominated by (ς). The current work, investigated the convention of an orientation interpreted in terms of Bunge Euler angles, (φ_1,Φ, φ_2).

Fig. 4.91 shows the misorientation distribution function MODF of the dominant γ-phase in the Ti-45Al-2Nb-0.3Si alloy both in the browser and 3D view **Fig. 4.91a** and **Fig. 4.91b**, respectively. The corresponding density profile **Fig. 4.91c** at the highest intensity is represented by the line scan of **Fig. 4.91a**. According to the density profile the dominant MODF and texture sharpness was strongly composed of {011} <21-2> and/or <623> orientation at (φ1,Φ, φ2)= (0°, 10°, 88°). The main component generated in γ-TiAl alloys is the cube texture with alignment of the c-axes [001]. Therefore, the corresponding textures of the Ti-45Al-2Nb-0.3Si alloy are presented in **Fig. 4.91d** in terms of the MODF sections (see details in

APPENDIX Fig. S16). In order to recognise common textures within Euler space and ODFs, ideal orientations were simulated (**Fig. 4.91d)** for the α-parent phase with one strong fiber texture which are simulations for the hexagonal <0001> fiber texture parallel to the specimen x-axis overlaid elliptical grid on the phi1 3D view.

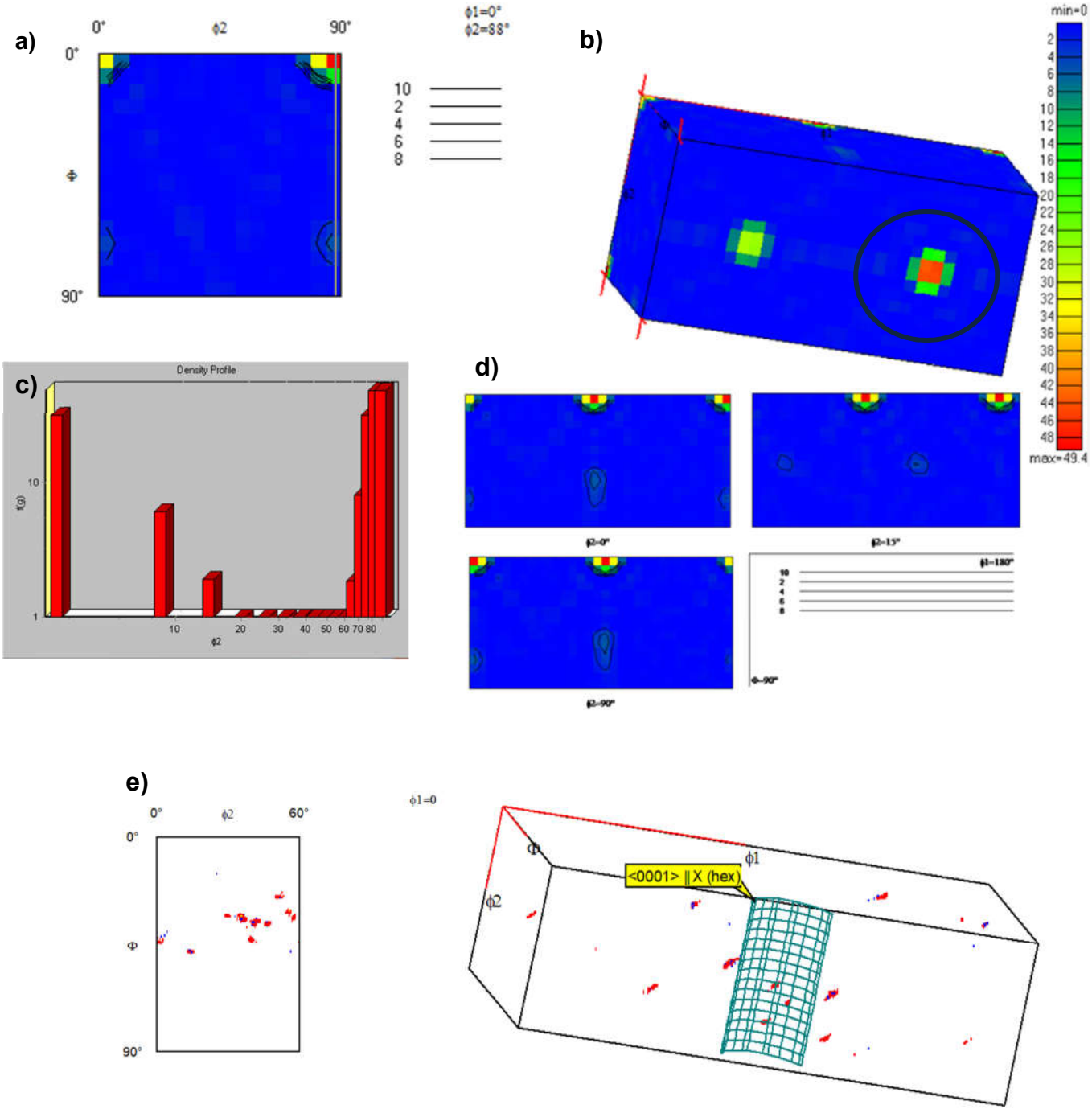

Figure 4.91. The γ-phase images of (a) browser section, (b) 3D contoured view MODF showing most intensity in Euler space circled in black, (c) corresponding density profile distribution graphs along vertical line in (a), (d) serial section through an ODF, and (e) ideal orientation of an α-parent phase in 3D scattered view.

4.10.5. TEM analysis for Ti-45Al-2Nb-0.3Si alloy

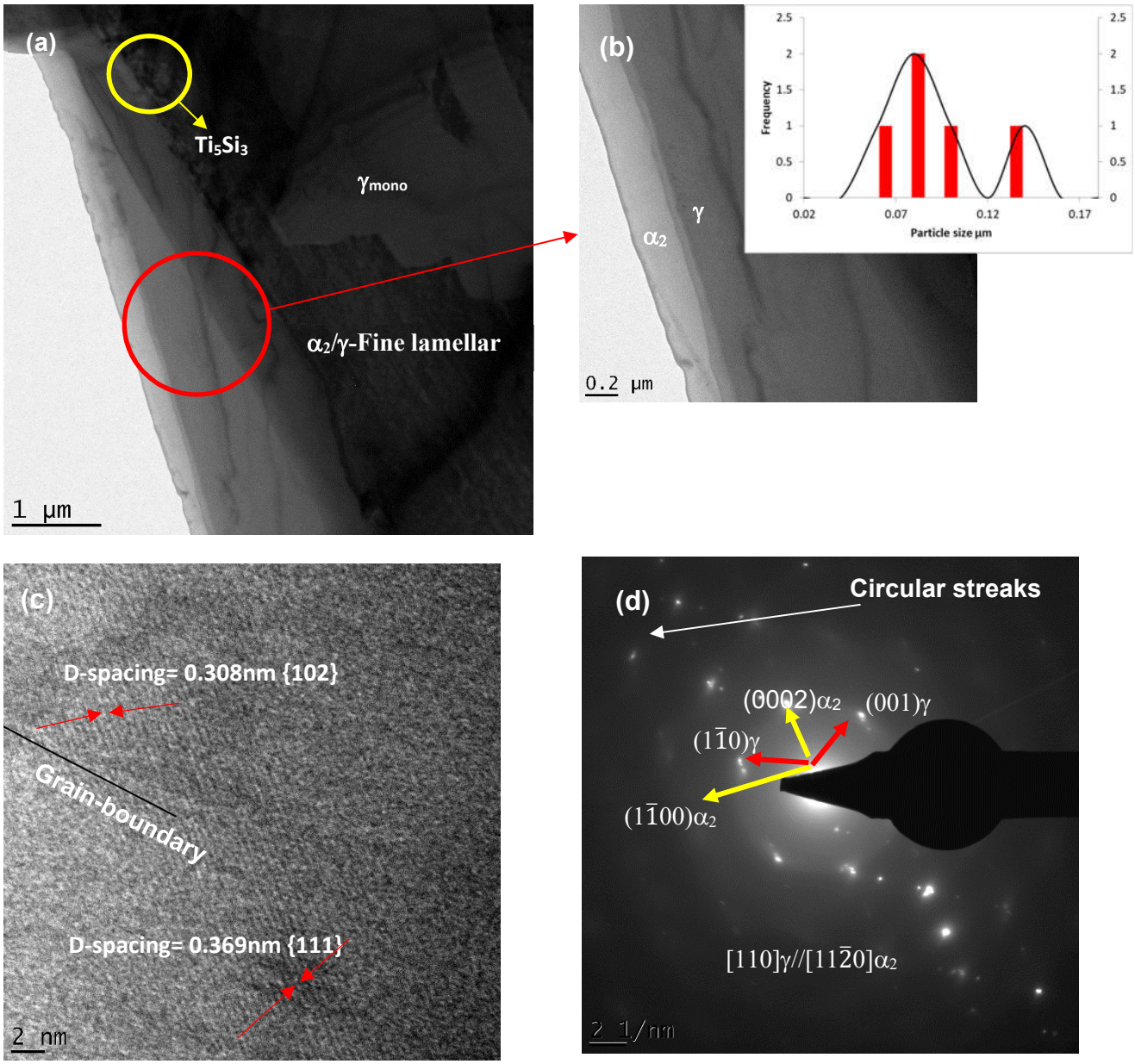

Figure 4.92. TEM bright-field images of the Ti-45Al-2Nb-0.3Si alloy: a) Ti_5Si_3 precipitate at α2/γ interface, γmono grain, both fine and coarse (α_2+γ) lamellar, b) coarse-grained (α_2+γ) lamellar colony with their corresponding lamellar distribution, c) high resolution transmission electron microscope (HRTEM) image, and d) selected area electron diffraction (SAED) pattern.

Fig. 4.92 illustrates the TEM microstructures of the Ti-45Al-2Nb-0.3Si alloy heat treated from the α-phase domain, with subsequent stabilization treatment in the (α_2+γ) two-phase region. The Ti_5Si_3 (based on **Fig. 4.89** and **Fig.4.90)**, some γmono grains and fine (α_2+γ) lamellar structures are shown in **Fig. 4.92a**. The coarse (α_2+γ) lamellar colonies circled (red) in **Fig. 4.92a**, is enlarged in **Fig. 4.92b** with the corresponding lamellar size distribution. **Fig. 4.92c** shows the high resolution transmission electron microscope (HRTEM) image of the overall γ-

TiAl based microstructure with D-spacings of 0.308nm for {102}, and 0.369nm for {111}. The selected area diffraction pattern (SADP) of the **circled** area (in red) taken from **Fig. 4.92a** is shown in **Fig. 4.92d**. Song et al, [54] reported that all of the variants of γ-laths are formed within a small region. Moreover, the circular streak diffraction along the [0001]α_2 direction **Fig. 4.92d**, which may have been indicative of intense planar defects in the lamellar colony [54]. Moreover, streaking along [0001] could also be due to other factors including the presence of various γ-variants depended upon the area covered by diffraction aperture. It can also be observed that [110]γ//[11$\bar{2}$0]α_2.

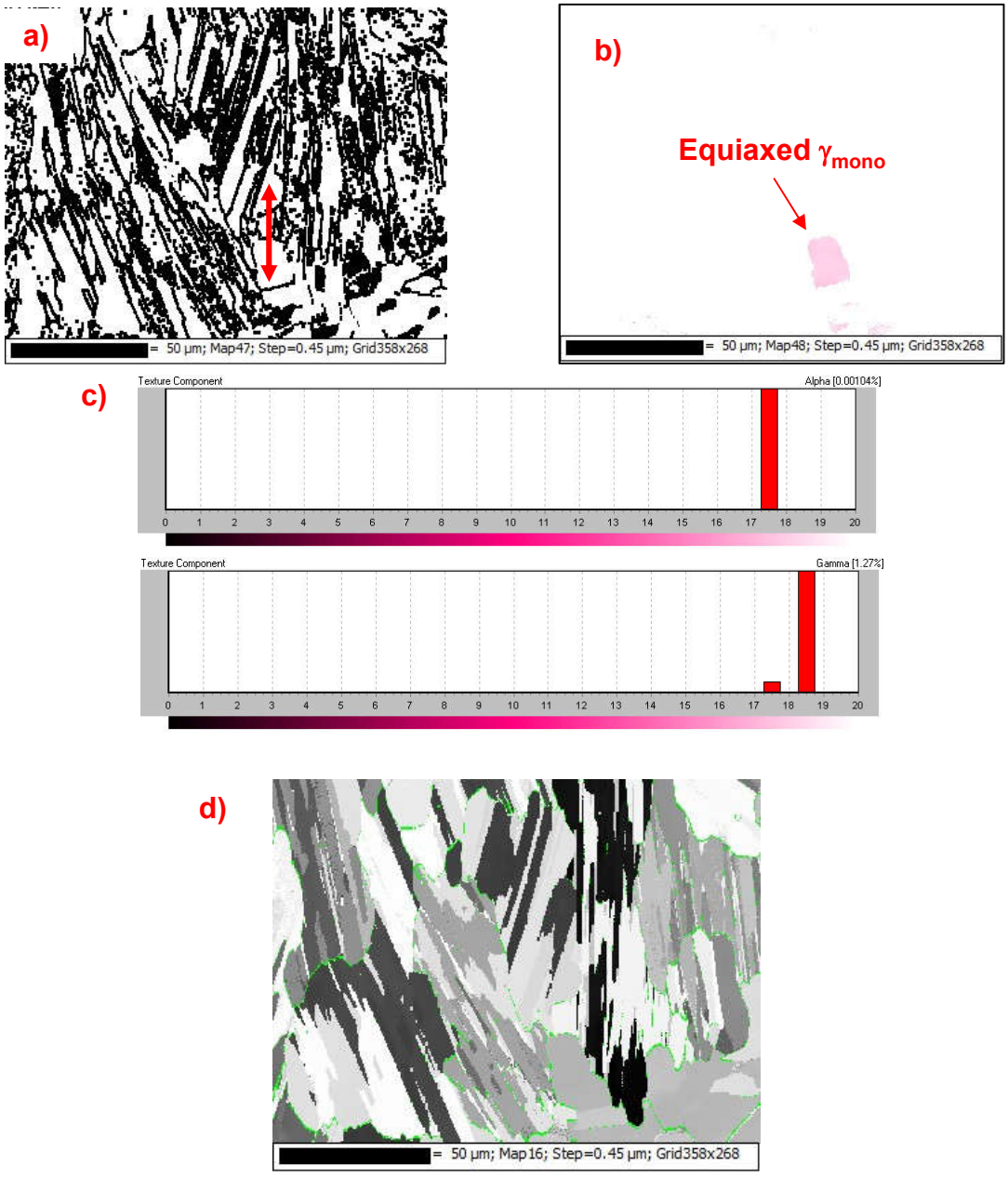

Figure 4.93. (a) Grain boundary component, (b) Texture component with their corresponding (c) phase fractions, (d) Schmid factor map.

Fig. 4.93a shows the boundaries between lamellar grains aligned with equiaxed γ_{mono} grains **Fig. 4.93b**. The lamellar grains are ascertained to have mostly γ-(fct) phase (~91.6%), with small amounts of α_2-phase (~3.93%), α-phase (~1.49%), Ti_5Si_3 phase (~0.675%) and B2-phase (~0.358%). The texture component emerged in the Schmid factor (the density of mobile dislocations within the crystal) and varies with the nature, sharpness and intensity of the crystallographic texture disclosed by the γ-grains. These observations indicate that the deformation modes operating in a certain γ-domain of the lamellar microstructure cannot be solely predicted on the basis of Schmid factor consideration, and this was never considered in the modelling studies [216]. The textured components in **Fig. 4.93c** indicates that only a fraction of about 1.27% γ-grains and 0.00104 α-grains were textured. Plastic deformation of titanium aluminides is attributable to the typical deformation behavior of other intermetallic compounds controlled by the core structure of dislocations; therefore, this section provides knowledge of operative slip systems and fine structure of dislocations. **Fig. 4.93d** illustrate the Schmid factor map of the Ti-45Al-2Nb-0.3Si alloy. The maximum of the locally effective shear stress results from the reciprocal Schmid factor, $M = 2$ which stipulates that both the slip plane and the slip direction be ideally orientated at 45^0 with respect to the stress axis [217]**.** The deformation behavior of γ-TiAl is closely related to its $L1_0$ structure, where the possible Burgers vectors are illustrated in **Fig. 2.46**. Due to the ordered structure, dislocations of type <100>, ½<110], and super-dislocations of type <011] and ½ <112], occur [52]. The Schmid factor analysis stipulated that the active slip system is: $\{1\bar{1}0\}$ <111> and that the Schmid factor calculated was 0.48. In addition, Burgers vectors ½<110], ½ <112] and <011], realizes glide on one of the {111} planes, whereas <100> dislocations seem to be involved at elevated deformation temperatures [100] [52], which is not the scope of the present study.

4.10.6. Conclusions

The microstructural control and evolution of the multi-phase α-solidified and stabilized γ-Ti-45Al-2Nb-0.3Si intermetallic alloy was developed, and characterized and the following conclusions can be drawn:

- The EBSD analysis demonstrated that the as-cast coarse columnar structures evolved into fine and homogeneous microstructures by heat-treating the alloy into a stabilized fully lamellar structure.
- The γ-phase transformation from the α-parent phase followed the BOR relationship with the three primary solidification phases and two peritectic reactions, as seen by solidification sequence in **Section 4.5.7**.
- It was found that the main texture component in the γ-Ti-45Al-2Nb-0.3Si alloy was the cube texture with the alignment of the c-axis [001].

- The parent α-phase had one strong <0001> fiber texture parallel to the specimen x-axis.
- The γ-phase with sufficient number of independent active slip system $\{1\bar{1}0\}$ <111>, acted as deformation accommodating phase.
- The TEM results indicated this alloy had a fully lamellar structure, with some γ-mono grains along with Ti_5Si_3 precipitates. The SAED patterns showed circular streaks along the $[0001]\alpha_2$ direction, and this was indicative of planar defects in the lamellar colony.

4.11. Development and microstructural control of the γ-Ti-48Al-2Nb (Sn, Mn and Si)-doped intermetallic alloy

4.11.1. Introduction

A similar approach was followed from the previous **Section 4.10**, except that the alloy was doped with both Sn and Mn. This section focuses on the development and microstructural control of the γ-Ti-48Al-2Nb-1Sn-0.7Mn-0.3Si based intermetallic alloy. High resolution electron back scattered diffraction (HREBSD) analysis of the heat-treated (α-solidified) γ-TiAl based alloy was employed to study microstructural evolution from a β-solidified state.

4.11.2. As-cast microstructures

The chemical analysis of the alloy is shown in **Table 4.20**. The alloy was heat-treated according to **Table 3.4** for a stabilized fully lamellar structure.

Table 4.20. Chemical composition (at. %) of the alloy.

γ-TiAl alloy composition	Ti	Al	Nb	Sn	Mn	Si
Nominal composition	48	48	2	1	0.7	0.3
Actual composition	50.7	45.4	1.9	0.9	0.7	0.3

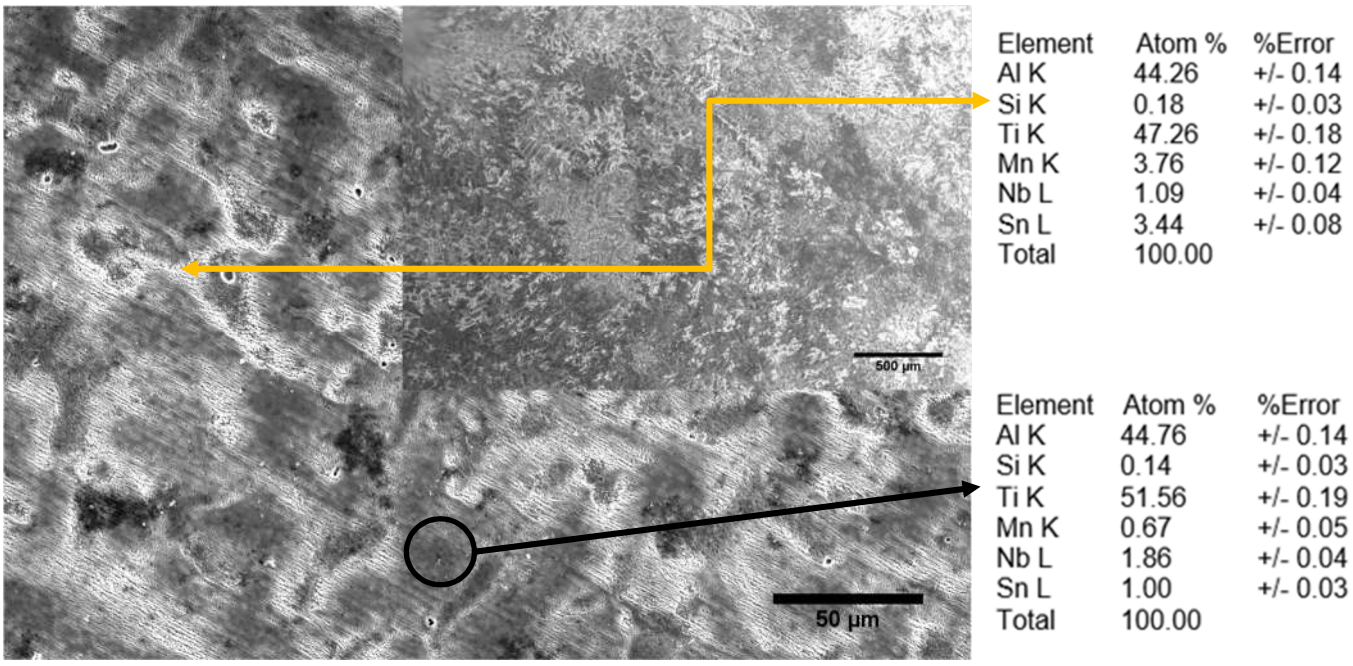

Figure 4.94. SEM-SEI EDX image of as-cast Ti-45Al-2Nb-1Sn-0.7Mn-0.3Si alloy.

Fig. 4.94 shows the as-cast microstructures of γ-Ti-48Al-2Nb doped with (Si-Sn-Mn) intermetallic alloy in secondary electron image (SEI). The dentritic microstructure shows the γ-TiAl (light/grayish phase) and α_2-Ti_3Al phases indicated by the yellow double arrow, and the circled black arrow, with their corresponding compositions, respectively. The actual composition in **Table 4.20** was suggestive of the precursor nominal composition prior to the casting process, which was a clear evidence that the alloy was successfully developed.

4.11.3. DSC analysis

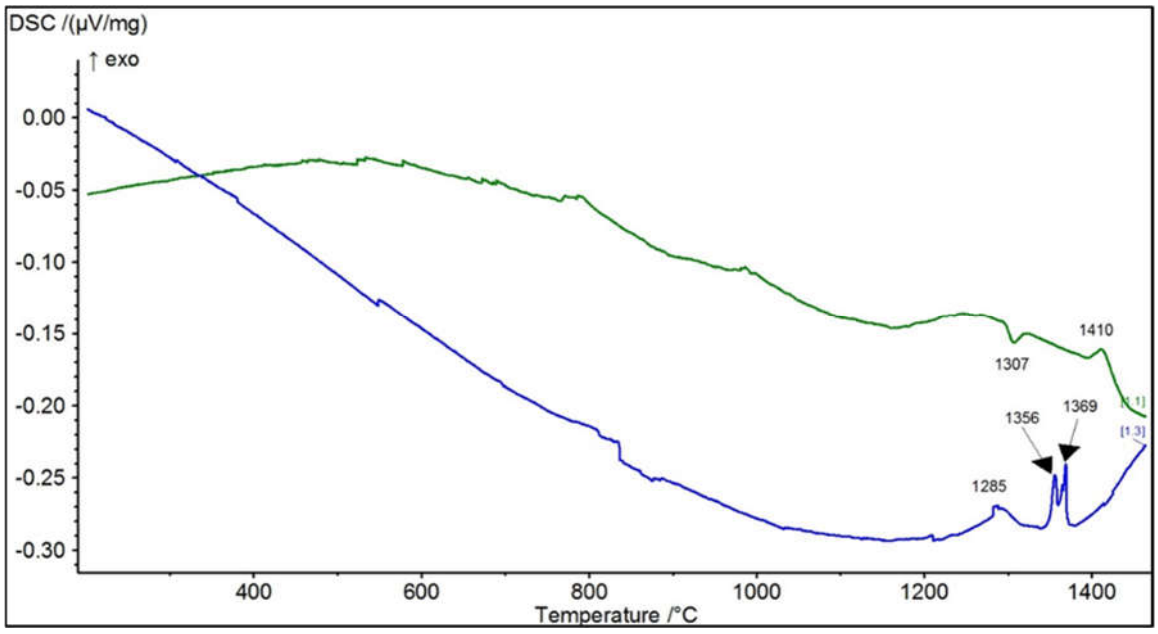

Figure 4.95. DSC curve of Ti-45Al-2Nb-1Sn-0.7Mn-0.3Si alloy.

Fig. 4.95 shows the DSC heating and cooling curves of Ti-48Al-2Nb-1Sn-0.7Mn-0.3Si alloy. The major thermal reaction occurs at the reversible endothermic temperature of 1307 °C on heating and exothermic on cooling at 1285 °C, which can be associated with the transition $\alpha_2+\gamma \rightarrow \alpha$. Furthermore, there was a crystallization exothermic peak at 1410 °C upon heating. On cooling two exothermic peak occured at 1369 °C and 1356 °C, respectively. Therefore, it can be assumed that the transformation temperature was 1307 °C by the tangent method. The exothermic peak at 1410 °C upon heating was considered to be associated with the $\beta \rightarrow \gamma$ transition. Therefore, a single broad exothermic peak appears between 1356 °C and 1285 °C, identified as the $\alpha \rightarrow \alpha_2+\gamma$ transition. DSC analysis indicated that the addition of Sn and/or Mn increased the transformation temperature of the γ-TiAl based alloy. The transformation temperatures of 1307 °C was found to be higher than that of Ti-45Al-2Nb-0.3Si which was found to be 1273 °C, **Section 4.9.2**.

4.11.4. Heat-treated microstructures

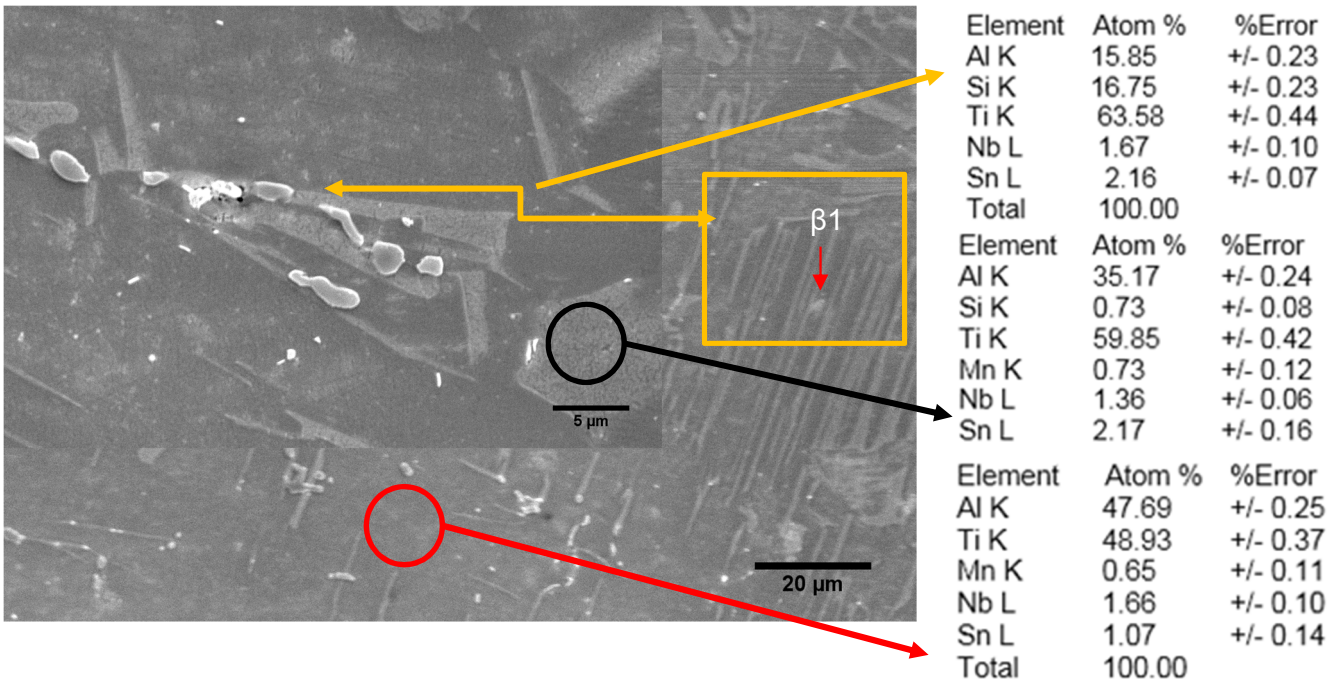

Figure 4.96. SEM-BEI of the Ti-45Al-2Nb-1Sn-0.7Mn-0.3Si intermetallic alloy.

Fig. 4.96 encapsulates the microstructural evolution via the heat treatment of the γ-Ti-48Al-2Nb doped with Sn, Mn and Si. The phases formed in the alloy studied were TiAl, Ti_3Al, and Ti_5SI_3. However, the precipitates appeared to be elongated rod-like Ti_5Si_3 (Al, Sn) along the light gray α_2-Ti_3Al phase (circled in black arrow) shown in **Fig.4.96**. The γ-phase is indicated by the red circled arrows showing near equal proportions between the Ti and the Al at.% contents. Moreover, homogeneity of the Ti-48Al-2Nb-1Sn-0.7Mn-0.3Si alloy with subsequent

heat treatment was examined by SEM-EDX technique and elemental maps were constructed to show the distribution of the elements shown in **Fig. 4.97**.

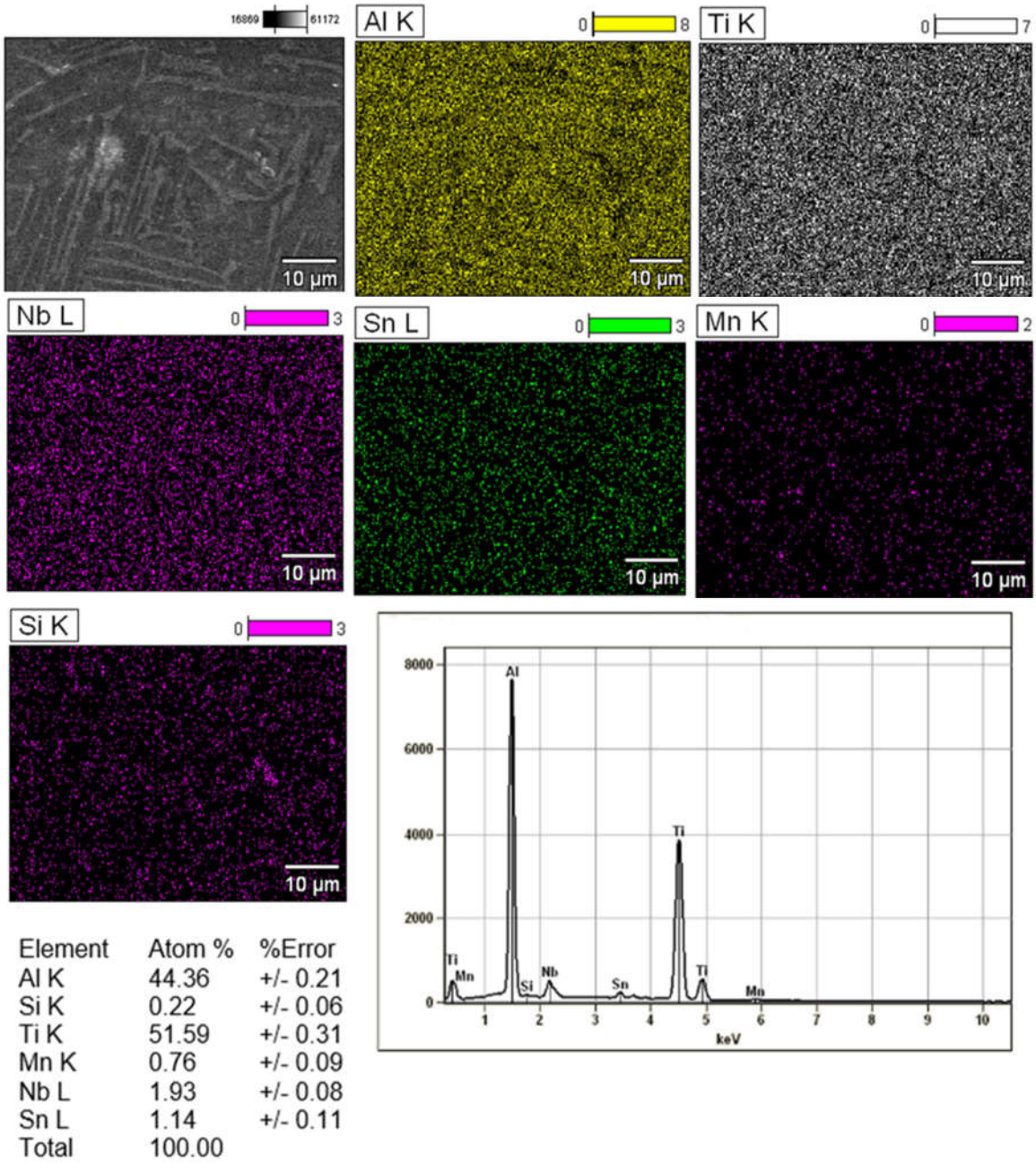

Element	Atom %	%Error
Al K	44.36	+/- 0.21
Si K	0.22	+/- 0.06
Ti K	51.59	+/- 0.31
Mn K	0.76	+/- 0.09
Nb L	1.93	+/- 0.08
Sn L	1.14	+/- 0.11
Total	100.00	

Figure 4.97. SEM-EDX elemental maps of the heat treated Ti-45Al-2Nb-1Sn-0.7Mn-0.3Si alloy.

4.11.5. EBSD analysis

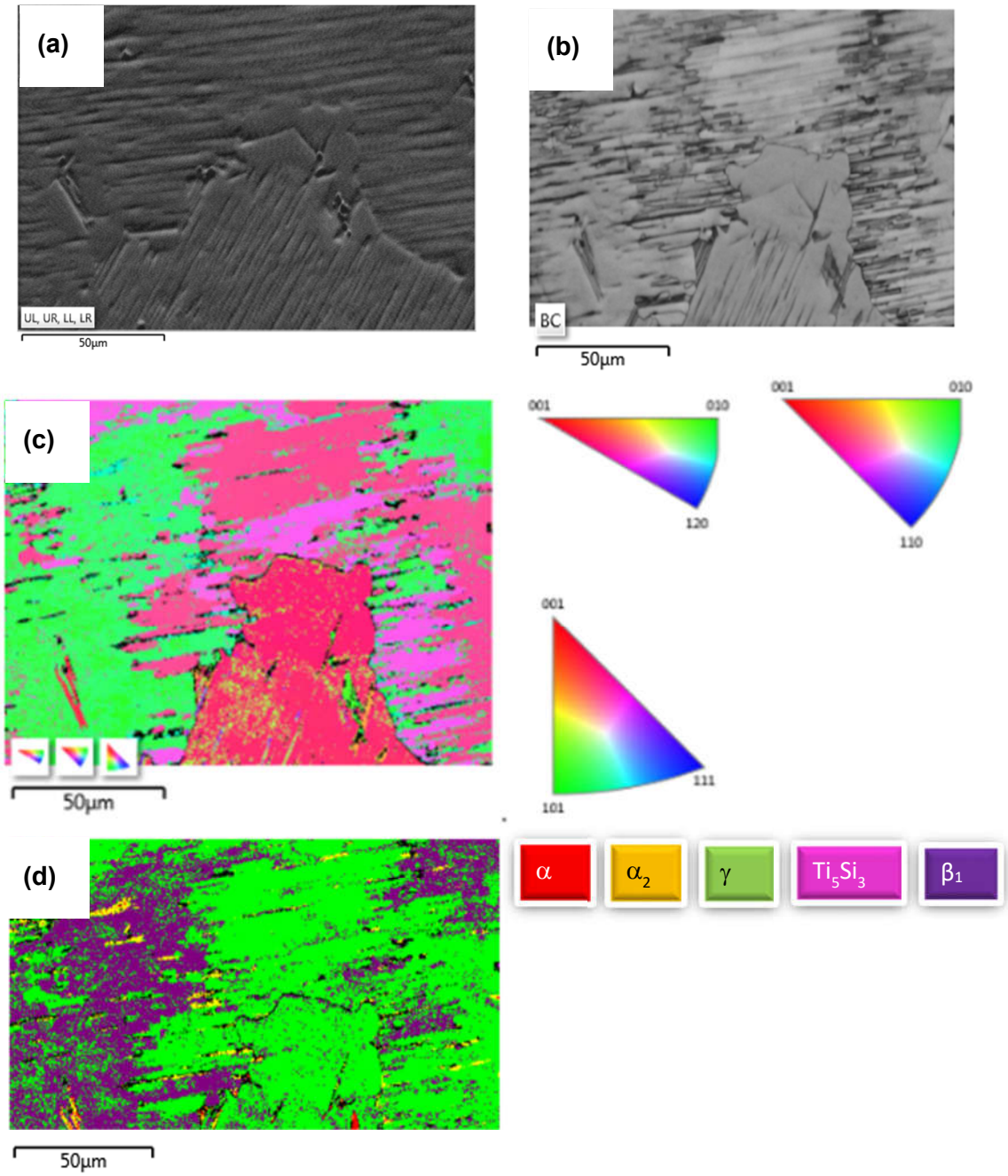

Figure 4.98. EBSD maps of the heat treated Ti-45Al-2Nb-1Sn-0.7Mn-0.3Si alloy: a) Electron image, b) Band contrast maps, c) Inverse pole figure (IPF) maps, and d) Phase color map.

Fig. 4.98 shows EBSD maps of the heat treated Ti-45Al-2Nb-1Sn-0.7Mn-0.3Si alloy. **Fig. 4.98a** illustrates the area of mapping in the form of a backscattered electron image, with a corresponding band contrast map displayed in **Fig. 4.98b**. **Fig. 4.98c** is the orientation map with its corresponding inverse pole figures (IPF). **Fig. 4.98d** is the phase color map, which uses a five color key, supplementing this is the grain map **Fig. 4.99a** which only captures orientation differences between the neighboring grains, but does not represent crystal

orientations. The pre-dominant phases were the γ, *c*/*a* = 1.45, and the β_1 (Ni_3Si-prototype) *c*/*a* = 1, with their corresponding phase fractions of 62% and 31%, respectively. Meanwhile, the residual α/α_2 (*c*/*a* = 1.63/0.81) was also observed. The volume fractions of the phases are shown in **Table 4.21** while their lattice parameters are shown in **Table 4.22**. The β_1 phase (also shown in **Fig. 4.96**) was located in the α/α_2 and γ/α_2 interfaces boundaries and this may suggest that β_1 phase acts as the precipitation sites of some phases.

Table 4.21. Phase fractions of Ti-45Al-2Nb-1Sn-0.7Mn-0.3Si alloy.

Phase Name	Phase Fraction (%)	Phase Count	Mean Band Contrast	Standard Deviation Band Contrast	Min Band Contrast	Max Band Contrast	Mean MAD	Standard Deviation MAD	Min MAD	Max MAD
α	0.40	383	91.40	15.94	44.00	136.00	0.71	0.22	0.31	1.79
α_2	2.60	2498	89.40	23.89	24.00	154.00	0.84	0.26	0.32	1.93
γ	61.94	59429	136.19	22.80	36.00	187.00	0.59	0.14	0.14	1.96
Ti_5Si_3	0.06	61	75.21	16.31	47.00	119.00	0.95	0.30	0.43	1.87
$\beta_1(Ni_3Si)$	30.97	29715	128.26	23.11	35.00	178.00	0.54	0.17	0.12	1.93
Zero Solutions	4.03	3665	73.97	21.59	0.00	151.00				

Table 4.22. Phase parameters of Ti-45Al-2Nb-1Sn-0.7Mn-0.3Si alloy.

Phase	*a* (Å)	*b* (Å)	*c* (Å)	Alpha (°)	Beta (°)	Gamma (°)	Space Group
α	3.20	3.20	5.20	90.00	90.00	120.00	194
α_2	5.73	5.73	4.64	90.00	90.00	120.00	194
γ	2.81 Å	2.81	4.08	90.00	90.00	90.00	123
Ti_5Si_3	7.45	7.45	5.14	90.00	90.00	120.00	193
$\beta_1(Ni_3Si)$	3.51	3.51	3.51	90.00	90.00	90.00	221

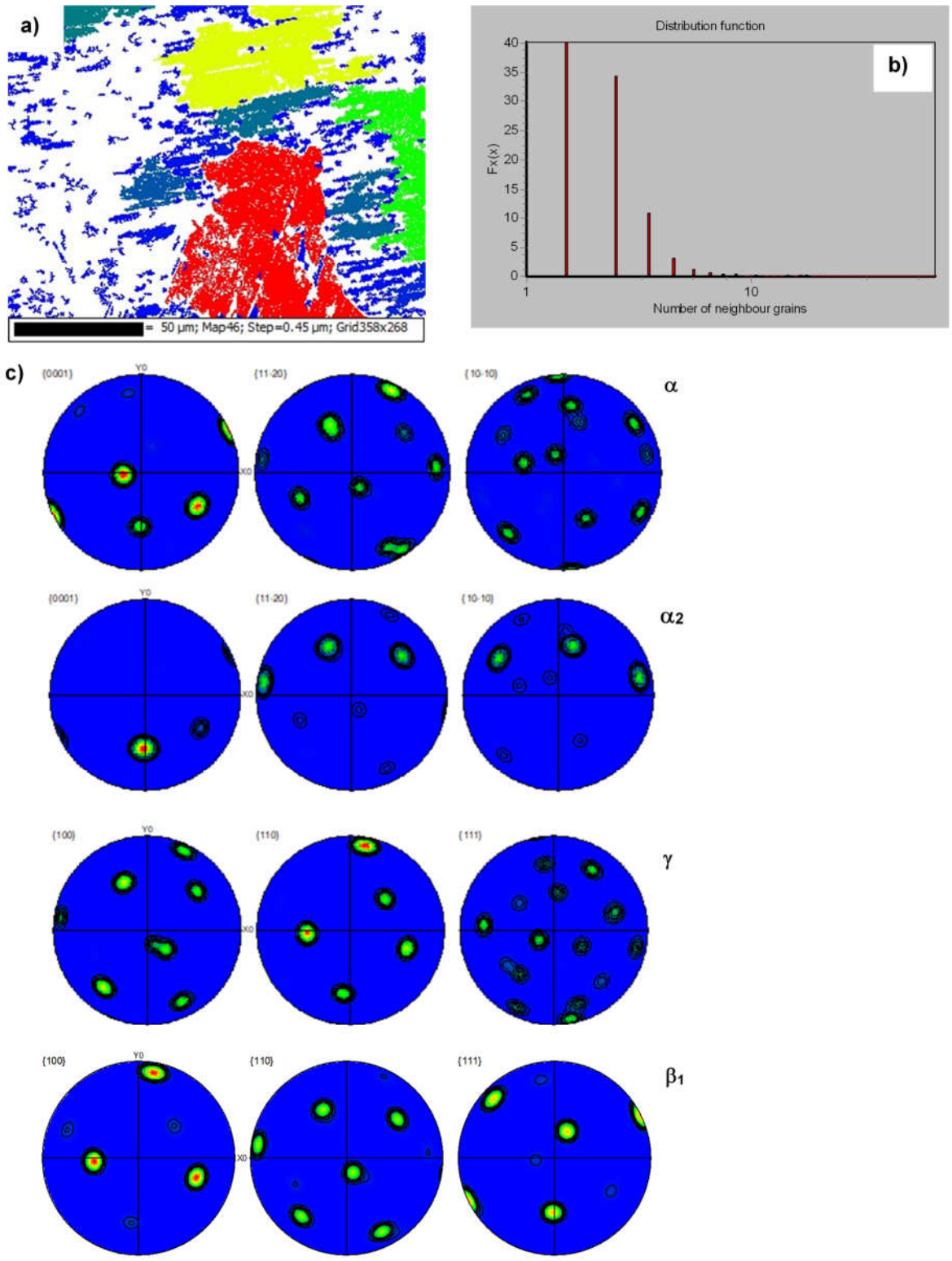

Figure 4.99. EBSD results of a) Grain map, b) Distribution function of the neighboring grains, and c) Pole figures of α/α2, γ, and β_1 phases.

Fig. 4.99a show the grain map of the Ti-45Al-2Nb-1Sn-0.7Mn-0.3Si alloy. **Fig. 4.99b** shows the distribution function of the neighboring grains. This suggested that, as the number of neighboring grains increased, the volume fraction of those grains decreased, and vice versa.

As shown in **Fig. 4.99c** the orientation relationship between the α/α_2 -matrix and the β_1 and/or β/B2 phase was observed to be $\{0001\}_{\alpha/\alpha2}$ || $(111)_{\beta1 \text{ or } \beta/B2}$ and $\langle 11\text{-}20\rangle_{\alpha/\alpha2}$ || $[110]_{\beta1 \text{ or } \beta/B2}$ demonstrating that the α/α_2 phase precipitated from the β_1. During the remnant $\beta_{(primary)} \rightarrow \alpha$ transformation at the isothermal temperature of 1380 ºC, the $\beta_{1 \text{ or}}$ β/B2 phase performed as preferential heterogeneous nuclei for the α- phase. Therefore, if α-phase heterogeneously nucleates on the β_1 phase following the orientation relationship $\{0001\}_\alpha$ || $(111)_{\beta1 \text{ or } \beta/B2}$ and $\langle 11\text{-}20\rangle_\alpha$ || $[110]_{\beta1 \text{ or } \beta/B2}$, these α/α_2 phases are BOR α.

Furthermore, from the EBSD-orientation maps, it was important to analyze the frequency distribution of misorientation angles between neighboring γ grains in order to ascertain the γ variants that obeyed the BOR relative to the peritectic alpha grains that resulted due to the solidification process during the isothermal heat treatment. This BOR between γ and α phase is (111)γ || (0001)α and <1-10]γ || <11-20>α [50]. According to **Fig. 4.99c**, the orientation relationship between the α/α_2 -matrix and the γ-phase was deduced to be {111}γ || {0001)α and ⟨100⟩γ || ⟨11-20⟩α and, therefore, this suggested that the γ-phase precipitated from the parent α-phase.

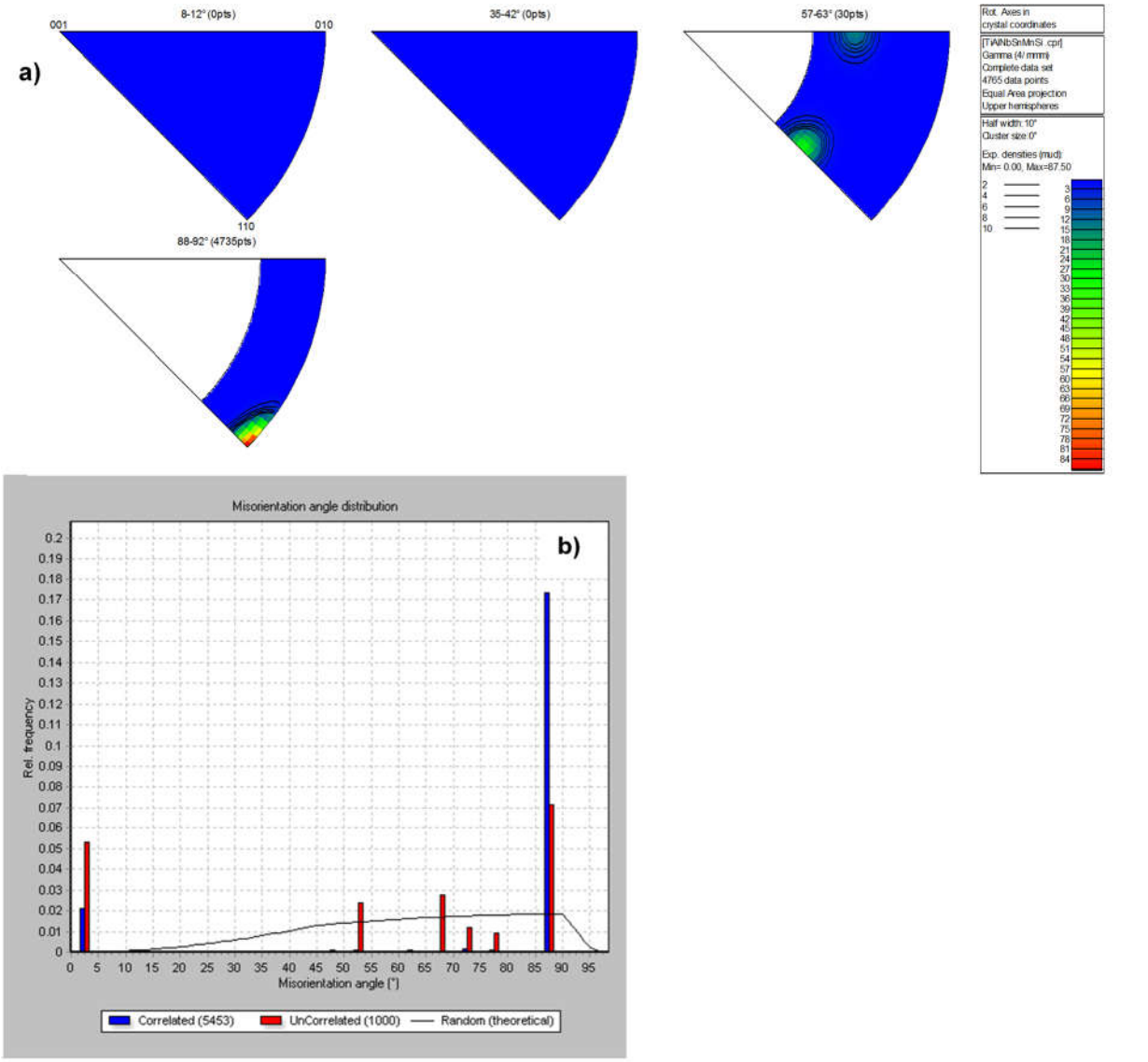

Figure 4.100. Misorientation data on the predominant γ-phase for the Ti-45Al-2Nb-1Sn-0.7Mn-0.3Si alloy: a) Misorientation axes with corresponding color coding, b) Misorientation angle distribution.

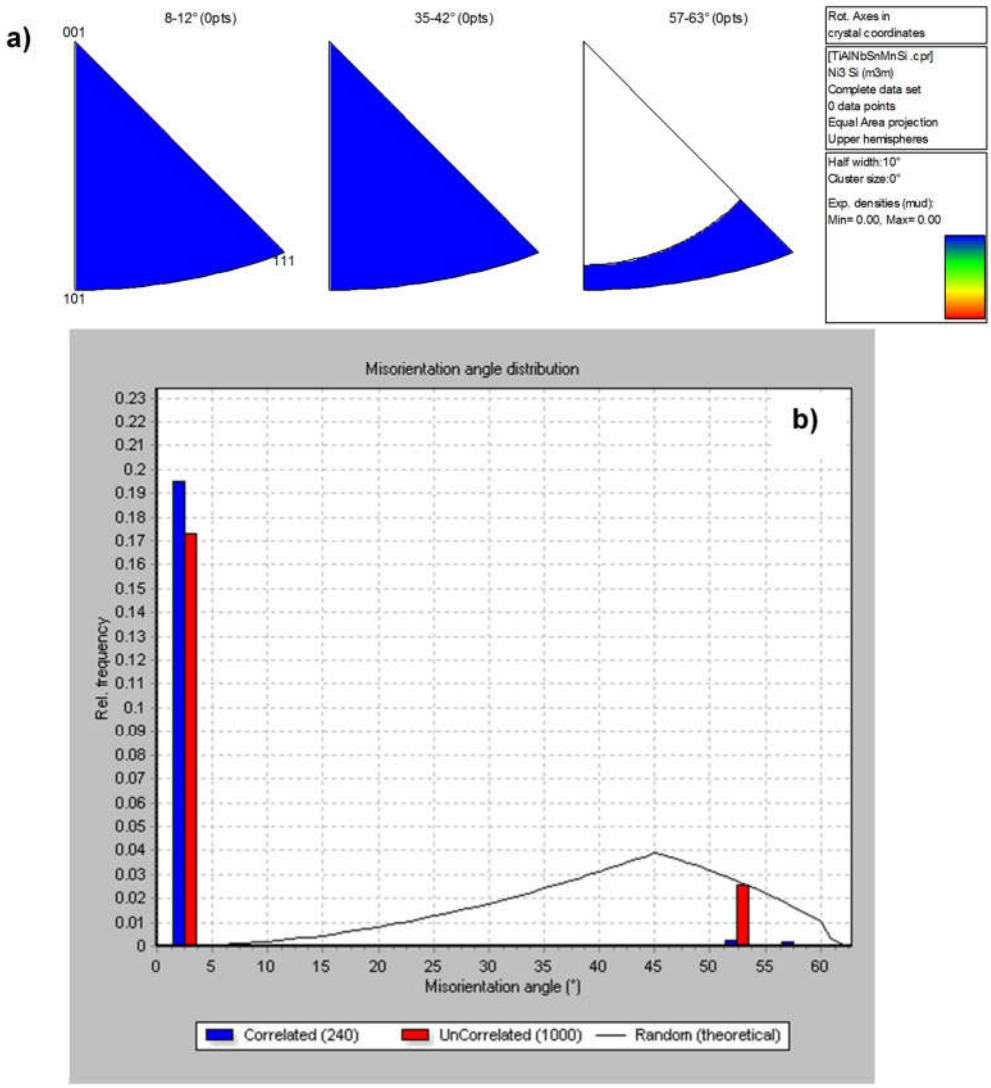

Figure 4.101. Misorientation data on the predominant β1-phase for the Ti-45Al-2Nb-1Sn-0.7Mn-0.3Si alloy: a) Misorientation axes with corresponding color coding, b) Misorientation angle distribution.

Figs. 4.100, and 4.101 show the misorientation data of the Ti-45Al-2Nb-1Sn-0.7Mn-0.3Si alloy, interms of the γ and β1/β-B2 phases. **Fig. 4.100a** illustrates misorientation axes in crystal co-ordinate system of the γ-phase, and describes which crystallographic directions, the misorientation axes align with for a chosen range of misorientation angles. The misorientation clusters are seen between [001] and [010] and [001] and [110] in the 57-63 °, and also observed at clusters of [110] in the 88-92 ° section. **Fig. 4.100b** is a representation of the relative frequency versus misorientation angle, where the correlated blue and uncorrelated red misorientation plot are different from the random line and from each other. This might have been due to strong fiber texture present in the microstructure. The correlated distribution exhibits a fairly large number of boundaries with misorientations below 15^0. Moreover, the results also show that the correlated distribution exhibited large number of boundaries with

misorientations enclosed by 85-90^0. Clearly from these results, the low and high angle boundary may be a significant feature of the microstructure and not simply a product of strong texture.

Misorientation axes in crystal co-ordinate system of the B2/β1-phase are shown in **Fig. 4.101** for Ti-45Al-2Nb-1Sn-0.7Mn-0.3Si alloy. There were no observed clusters for the β1-phase as shown in **Fig. 4.101a**. Moreover, **Fig. 101b** indicates that the large number of boundaries were low angle boundaries with misorientations below 15^0.

Fig. 4.102a illustrates the boundaries between lamellar grains were often aligned with equiaxed γ_{mono} grains in **Fig. 4.102b**. **Fig. 4.102c** indicates that only a fraction of about 0.215% γ-grains were textured.

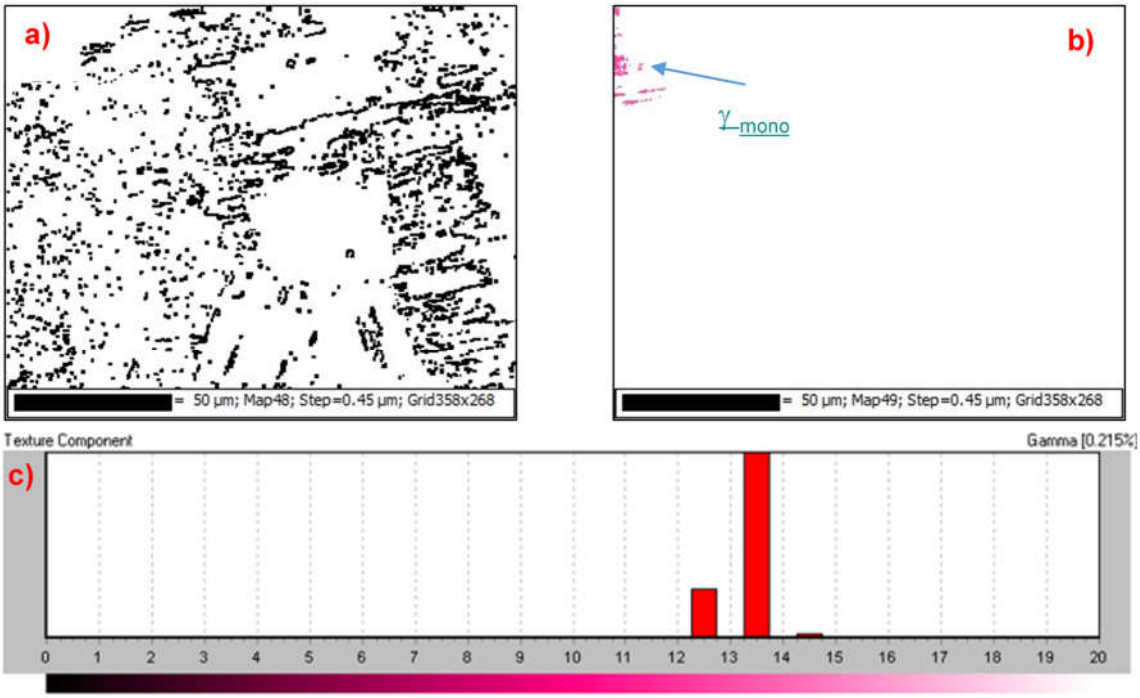

Figure 4.102. The γ-Ti-45Al-2Nb-1Sn-0.7Mn-0.3Si alloy a) Grain boundary component, b) Texture grain component with corresponding c) γ-phase texture component.

4.11.6. XRD analysis

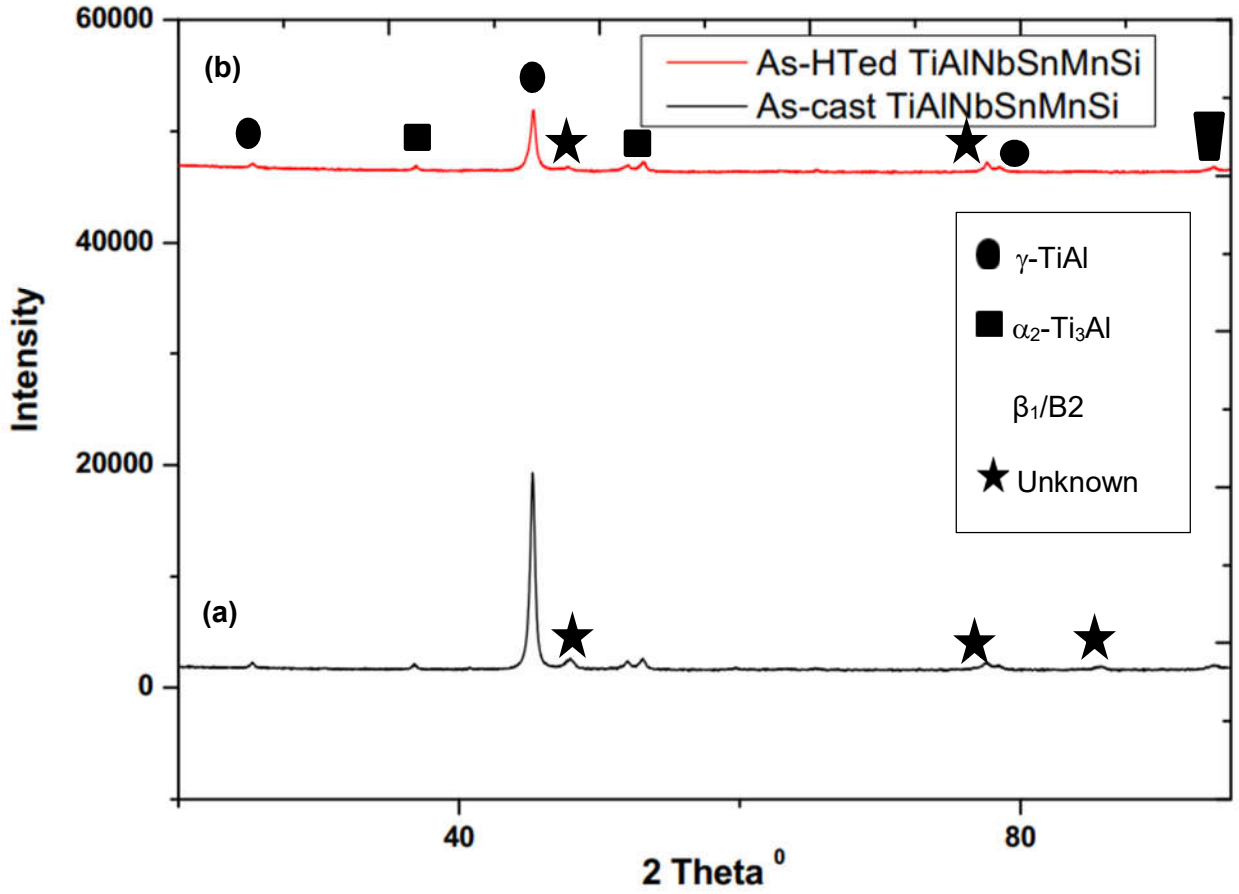

Figure 4.103. XRD analysis of the γ-Ti-45Al-2Nb-1Sn-0.7Mn-0.3Si alloy in the (a) as-cast, and (b) as-heat-treated conditions.

Fig. 4.103 illustrates the XRD patterns of the Ti-45Al-2Nb-1Sn-0.7Mn-0.3Si alloy in the as-cast, and heat treated conditions. These XRD results are in accordance with the phases obtained by the EBSD analysis in **Section 4.11.5**. Similar XRD patterns were seen in both the as-cast **Fig. 4.103a**, and heat treated **Fig. 4.103b** conditions; however, some patterns demonstrated unknown phases. Intermediate phases of unknown structures forms during β→α phase transition via melting process, and is stable at room temperature **Fig. 4.103a**. The phase at about 90 2theta angle in as-cast condition, disappears during α-solidifying to room temperature **Fig. 4.103b**. This preliminary investigation of phase transformation features in the present material may have denoted a feasible suppression of the α/γ boundaries of the equilibrium phase diagram to a lower temperature of an unknown new phase field. Therefore, the overall stable phases in both aforementioned conditions are γ-TiAl, α_2-Ti_3Al, β/B2, and the unidentified crystalline structures.

Furthermore, it is possible to distinguish unknown crystalline phases in metals with the assistance of their Bragg reflections (which is beyond the scope of this study), since its

crystalline material has its own characteristics Bragg angles [218]. For this purpose, a card file system (X-ray diffraction data index) has been published listing approximately thousand elements, and crystalline compounds, however, not only the Bragg angle of each Debye-Scherrer diffraction line but also its relative strength and intensity [218]. In addition, the identification of unknown crystalline phase in a metal can be made by matching powder pattern Bragg angle and reflected intensities of the unknown substance with the proper card of the index. The method is analogous to a fingerprint identification system, and constitutes an important method qualitative chemical analysis [218].

4.11.7. TEM analysis for the Ti-45Al-2Nb-1Sn-0.7Mn-0.3Si

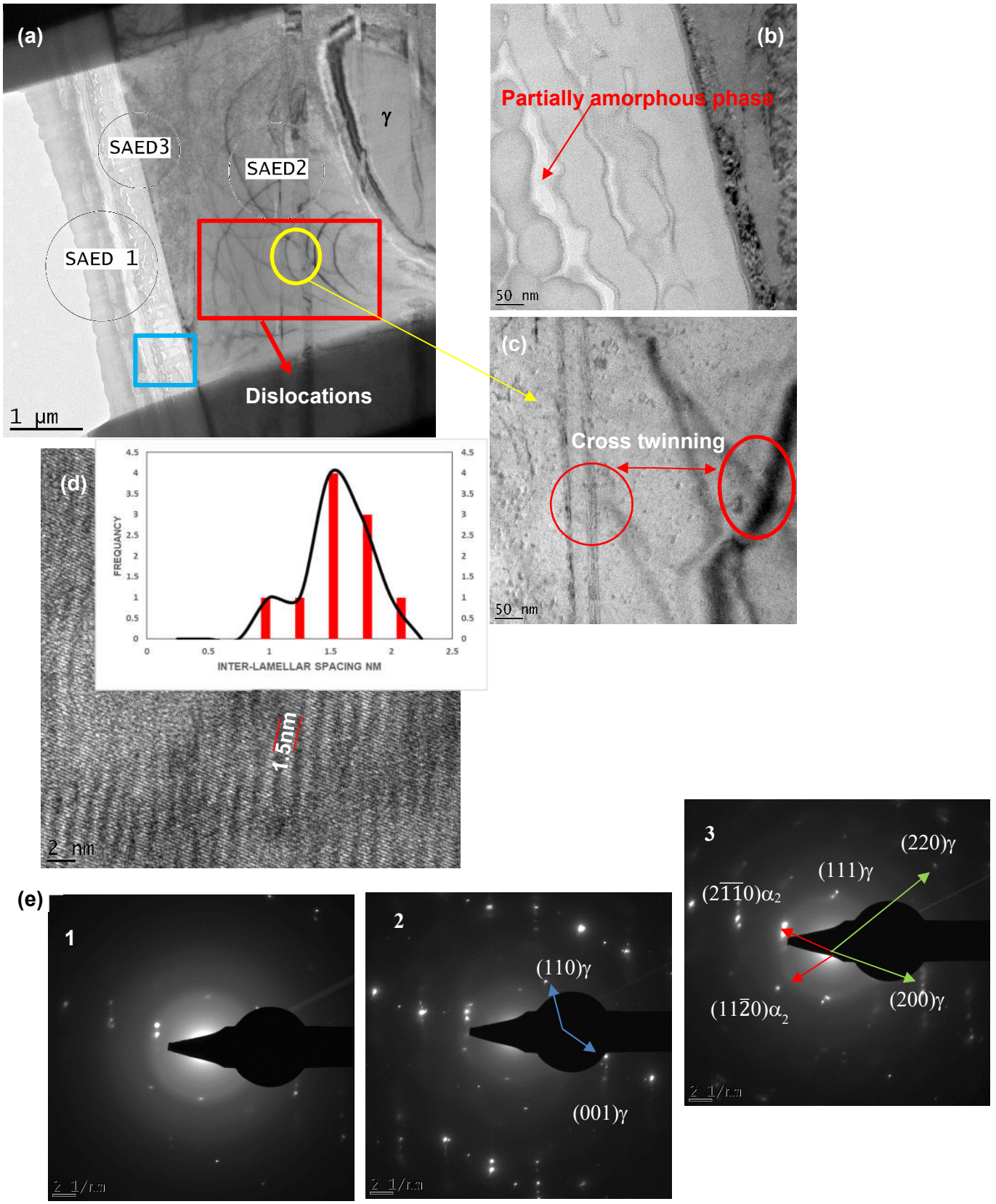

Figure 4.104. TEM bright-field images of the Ti-45Al-2Nb-1Sn-0.7Mn-0.3Si alloy: (a) α_2/γ lamellae (fine and coarse) with some dislocations along fine lamellae shown by the red

rectangle, (b) enlarged partially amorphous phase indicated by the blue square in Fig. 4.104a, (c) cross-twinning shown by the yellow circle in Fig. 4.104a, (d) is a high resolution transmission electron microscope (HRTEM) image showing lamellar striations with the corresponding inter-lamellar spacing distribution, (e) selected area electron diffraction (SAED) patterns labelled as per Fig. 4.104a.

TEM analysis proved that α-solidifying with subsequent stabilizing the Ti-45Al-2Nb1Sn-0.7Mn-0.3Si alloy resulted in refining the initial as-cast dendritic coarse grained structure, into nanoscale interlamellar spacing. This is shown in **Fig. 4.104** by the bright field images and diffraction rings. The microstructure in **Fig. 4.104a** was primarily composed of α_2+γ laths with some distorted structures along dislocations. The bright field (BF) image illustrates the presence of high densities of dislocations, and the grain boundaries appear to be curved, irregular or even ill-defined. This therefore, revealed that the grain boundaries introduced after the thermal treatment were distorted, and in a high energy non-equilibrium configuration. This entails that twinning along 1/6 <112]{111} and dislocations with Burgers vectors ½<110] and ½ <112] are active [88].

An enlarged view of the partially amorphous phase is shown in **Fig. 4.104b** with its corresponding SAED patterns shown in **Fig. 4.104e (1)**. It exhibited diffuse rings plus diffraction spots indicating a partially amorphous structure. It is important to note that the diffraction evidence obtained is consistent with the presence of an amorphous phase. This was confirmed by the XRD results in **Fig. 4.103** for the unknown phases at differing two theta angles of 43.038, 45.306, 47.835, 52.23, 78.306, with their corresponding d-spacing viz. 0.357nm, 0.375nm, 0.394nm, 0.428nm, 0.614nm, respectively.

The SAED patterns in **Fig. 4.104e (2)** revealed that the lamellar structures consisted of γ-TiAl twins. Evident linear diffusion streaks were also observed, besides the twinned diffraction patterns, suggesting the presence of significant amounts of two-dimensional defects. A HRTEM image of the γ-TiAl cross-twin boundaries is shown in **Fig. 4.104c**. Moreover, Cao et al. [88] pointed out that the presence of double diffraction indicates that the γ-TiAl phase contains twins.

The high-resolution transmission electron microscope (HRTEM) image **Fig. 4.104d** clearly indicates that the most common feature in the as-stabilized sample is a fine and uniform distribution of lamellar colonies, with an average inter-lamellar spacing of approximately 1.5nm, as measured by the inset.

Stipulated from **Fig. 4.104a** labelled SAED 3 is the α_2/γ interface. Indexing indicated that the twinning plane was (111). Furthermore, SAED patterns **Fig. 4.104e(3)** of γ-TiAl and α_2-Ti_3Al yielded the orientation relationship γ-TiAl {111} <110> || α_2-Ti_3Al (0001)<11$\bar{2}$0>.This

orientation relationship implicates the γ-TiAl phase to nucleate on the densely packed (0001) plane of α_2-Ti_3Al. According to Cao et al. [88] the changes in the stacking sequence from the ABABAB…in the α_2-phase to ABCABC…leads to the formation of the γ-structure. However, it was also suggested that to complete the transformation, $\alpha_2 \rightarrow \gamma$, a short range diffusion is needed. In addition to the crystallographic relation between the γ and the α_2 Xiao et al. [114] outlined that their lattice mismatch is relaxed by the ½ <110> perfect dislocations and the 1/6 <112> partial dislocation network at their interface. The perfect dislocation in γ may dissociate into partial ones such as ½ <01-1> = 1/6<-12-1> + 1/6 <11-2>. In addition, hot pressing process leads to movement of the interfacial dislocation and inhomogeneous deformation of γ-phase, that give rise to the ½ <01-1> to further dissociate into Shockely partials e.g. 1/6 <11-2> on {111} γ-phase for strain relaxation, which results in microtwins formation. Stacking faults and micro-twins which begin from grain boundary (phase boundary) can provide fast diffusion channels for interstitial atoms into the γ-TiAl grains. Therefore, twin boundary in TiAl grains can act as quick nucleation zone for precipitation [114].

4.11.8. Conclusions

The γ- Ti-45Al-2Nb-1Sn-0.7Mn-0.3Si based intermetallic alloy was developed and heat-treated into a stabilized structure. The DSC provided insight into phase transformation reactions prior to the heat treatment process. It was therefore ascertained that the transformation temperature for the alloy was around 1307 °C. The microstructural evolution the as-cast micro-segregated structures have evolved into homogeneous microstructures, via the heat-treatment process. The $\gamma/\beta_1/\alpha_2$ phases obeyed the Blackburn orientation relationship.

TEM results illustrated that the α-solidified and stabilized Ti-45Al-2Nb-1Sn-0.7Mn-0.3Si alloy constituted of a partially amorphous structure indicated by SAED patterns that exhibited diffuse rings plus diffraction spots, this was in agreement with the XRD results that confirmed unknown phases. The γ-TiAl and α_2-Ti_3Al lamellae yielded the orientation relationship γ-TiAl {111} <110> || α_2-Ti_3Al (0001)<11$\bar{2}$0>, and their lattice mismatch was relaxed by the ½ <110> perfect dislocations and the 1/6 <112> partial dislocation network at their interface.

5. Conclusions

- The binary (TiAl), ternary (TiAlNb), quaternary (TiAlNbCr), and quinary (TiAlNbCrSi) alloy powders were successfully uniaxially-cold pressed and melted. The cold pressed samples were sectioned to study the particle arrangement using scanning electron spectroscopy (SEM). It was evident that the Al particles migrated to the surface in contact with the die surfaces. The XRD technique was used to detect the phases on the cold pressed samples. The Raman analysis was consistent with the XRD results. As a consequence of melting, the relative densities of the alloys were improved compared to the compacted densities. However, Nb, Cr and Si additions made the relative densities slightly lower than that of the binary alloy due to the formation of the β-phase in as-cast structure.
- The alloys were fabricated as button melts by means of vacuum arc melting. Mechanical properties showed that it was apparent that 2 at. % Nb and 0.7at. % Cr acted as grain refiners for the Ti-Al binary alloy in addition to changing the crystal structure. The FCT phase with lattice parameter *a*=2.81 Å and a rhombohedral (RHL)-phase with *R*-3*m* #166 space group and the lattice parameter *a*=5.96 Å were formed.
- The cyclic oxidation of the beta (β) solidifying γ-TiAl intermetallic alloys were investigated. The quinary Ti-45Al-2Nb-0.7Cr-0.3 Si exhibited the best cyclic oxidation performance due to the Al_2O_3 and oxynitride scale with better adhesion to the parent metal. The ternary Ti-45Al-2Nb also showed improved cyclic oxidation properties. Doping with Cr and Nb of quaternary Ti-45Al-2Nb-0.7Cr yielded a fragile oxide layer that was prone to cracking and spalling. The quinary Ti-45Al-2Nb-0.7Cr-0.3 Si alloy showed the best performance and maintained the hardness properties.
- Due to prenitriding treatment at 900 °C under nitrogen, the γ-TiAl based intermetallic alloys showed improved cyclic oxidation.
- The γ-Ti-45Al-2Nb-0.7Cr-0.3Si based intermetallic alloy was developed and studied for microstructure evolution in as-cast, and heat-treated condition in order to produce spheriodized and Widmanstätten laths. Phase transformation and microstructural evolution of an α-solidification γ-Ti-45Al-2Nb-0.7Cr-0.3Si was determined. High temperature differential thermal analysis (HTDTA) was performed on the solidified alloy ingot button in order to determine critical temperatures and provide insight into phase transformations. EBSD mapping was employed to determine microstructural evolution. The results show that after heat-treatment, the microstructures were homogenized, compared to the dendritic as-cast structure. The spheriodized laths were seen embedded inside the lamellar structure; whereas the Widmanstätten laths

were observed as crossed/needle like (α_2+γ) laths of small spacing, with a spatial orientation with respect to the lamellar structure.

- Composition-structure-property relationship of the as-cast γ-Ti-45Al-2Nb-0.7Cr-0.3Si based intermetallic alloy was also examined and the γ, α/α_2, and Ti_5Si_3 were found to be stable at room temperature. The HREBSD was used to analyze the orientation relationships of both the as-cast (β-solidifying) and heat-treated (α-solidifying) phases. The results showed that the formation of $\gamma/\alpha_2/Ti_5Si_3$ follows the BOR: (β-solidifying) = $\{110\}^{\beta}$ // $\{0001\}^{\alpha}$ and $<111>^{\beta}$ // $<2\ \bar{1}\ \bar{1}0>^{\alpha}$, (α-solidifying) = (111)γ || (0001)α and $<1\ \bar{1}0]\gamma$ || $<11\ \bar{2}0>\alpha$.
- Due to surface porosity, the binary (Ti-48Al) alloy surface coating was not successful and yielded low hardness properties when compared to Ti-46Al-2Nb, Ti-46Al-2Nb-0.7Cr and Ti-46Al-2Nb-0.7Cr-0.3Si intermetallic alloys at 900 °C under nitrogen due to hard protective oxynitride layers.
- The γ-phase in the Ti-45Al-2Nb-0.3Si alloy exhibited the cube texture component with the alignment of the c-axis [001] and the γ phase demonstrated sufficient number of independent active slip systems $\{1\bar{1}0\}$ <111>, and therefore acted as deformation accommodating phase.
- The phase transformations temperatures in γ- Ti-45Al-2Nb-0.3Si and Ti-45Al-2Nb-1Sn-0.7Mn-0.3Si based intermetallic alloys were found to be about 1270 °C, and 1310 °C, respectively. In addition, the $\gamma/\beta_1/\alpha_2$/B2 phases exhibited the BOR with the α matrix.
- The TEM results indicated that the Ti-45Al-2Nb-0.3Si alloy had a fully lamellar structure, with some γmono grains along with Ti_5Si_3 precipitates. The SAED patterns showed circular streaks along the $[0001]\alpha_2$ direction, and this was indicative of planar defects in the lamellar colony.
- TEM results illustrated that the α-solidified and stabilized γ-Ti-45Al-2Nb-1Sn-0.7Mn-0.3Si alloy constituted of a partially amorphous structure indicated by SAED patterns that exhibited diffuse rings plus diffraction spots. This was in agreement with the XRD results that showed unknown phases. The γ-TiAl and α_2-Ti_3Al lamellae yielded the orientation relationship γ-TiAl {111} <110> || α_2-Ti_3Al (0001) $<11\bar{2}0>$, whereby the lattice mismatch was relaxed by ½ <110> perfect dislocations and the 1/6 <112> partial dislocation network at their interface.

References

[1] Z. Abdallah, M. T. Whittaker, and M. R. Bache, “High temperature creep behaviour in the γ titanium aluminide Ti–45Al–2Mn–2Nb,” *Intermetallics*, vol. 38, pp. 55–62, 2013.

[2] G. Baudana, S. Biamino, B. Klöden, A. Kirchner, T. Weißgärber, B. Kieback, M. Pavese, D. Ugues, P. Fino, and Claudio Badini, “Electron Beam Melting of Ti-48Al-2Nb-0.7Cr-0.3Si: Feasibility investigation,” *Intermetallics*, vol. 73, pp. 43–49, 2016.

[3] K. Kothari, R. Radhakrishnan, and N. M. Wereley, “Advances in γ titanium aluminides and their manufacturing techniques,” *Prog. Aerosp. Sci.*, vol. 55, pp. 1–16, 2012.

[4] T. Tetsui, “Development of a TiAl turbocharger for passenger vehicles,” vol. 331, pp. 582–588, 2002.

[5] A. Lasalmonie, “Intermetallics: Why is it so difficult to introduce them in gas turbine engines?,” *Intermetallics*, vol. 14, no. 10–11, pp. 1123–1129, 2006.

[6] Z. C. Liu, J. P. Lin, Y. L. Wang, Z. Lin, G. L. Chen, and K. M. Chang, “High temperature deformation behaviour of As-cast Ti-46Al-8.5Nb-0.2W alloy,” *Mater. Lett.*, vol. 58, no. 6, pp. 948–952, 2004.

[7] R. Pflumm, S. Friedle, and M. Schütze, “Oxidation protection of γ-TiAl-based alloys - A review,” *Intermetallics*, vol. 56, pp. 1–14, 2014.

[8] C. J. Zhan, T. H. Yu, and C. H. Koo, “Creep behavior of Ti-40Al-10Nb titanium aluminide intermetallic alloy,” *Mater. Sci. Eng. A*, vol. 435–436, no. 1, pp. 698–704, 2006.

[9] L. Yang, L. H. Chai, Y. F. Liang, Y. W. Zhang, C. L Bao, S. B. Liu, and J. P. Lin, “Numerical simulation and experimental verification of gravity and centrifugal investment casting low pressure turbine blades for high Nb–TiAl alloy,” *Intermetallics*, vol. 66, pp. 149–155, 2015.

[10] J. Lapin and M. Nazmy, “Microstructure and creep properties of a cast intermetallic Ti-46Al-2W-0.5Si alloy for gas turbine applications,” *Mater. Sci. Eng. A*, vol. 380, no. 1, pp. 298–307, 2004.

[11] F. Appel, H. Clemens, and F. D. Fischer, “Modeling concepts for intermetallic titanium aluminides,” *Prog. Mater. Sci.*, vol. 81, pp. 55–124, 2016.

[12] S. Biamino, A. Penna, U. Ackelid, S. Sabbadini, O. Tassa, P. Fino, M. Pavese, P. Gennaro, and C. Badini, “Electron beam melting of Ti-48Al-2Cr-2Nb alloy: Microstructure and mechanical properties investigation,” *Intermetallics*, vol. 19, no. 6, pp. 776–781, 2011.

[13] S. Bystrzanowski, A. Bartels, H. Clemens, R. Gerling, F. P. Schimansky, G. Dehm, and H. Kestler, “Creep behaviour and related high temperature microstructural stability of Ti-46Al-9Nb sheet material,” *Intermetallics*, vol. 13, no. 5, pp. 515–524, 2005.

[14] S. Tian, Q. Wang, H. Yu, H. Sun, and Q. Li, “Microstructure and creep behaviors of a high Nb-TiAl intermetallic compound based alloy,” *Mater. Sci. Eng. A*, vol. 614, pp. 338–346, 2014.

[15] M. Thomas and M.-P. Bacos, “Processing and Characterization of TiAl- based Alloys : Towards an Industrial Scale,” *Aerosp. Lab*, no. 3, pp. 1–11, 2011.

[16] C. Z. Qiu, Y. Liu, L. Huang, B. Liu, W. Zhang, Y. U. He, and B. Y. Huang, “Tuning mechanical properties for (B2)-containing TiAl intermetallics,” *Trans. Nonferrous Met. Soc. China (English Ed.*, vol. 22, no. 11, pp. 2593–2603, 2012.

[17] S. Huang and E. L. Hall, “The Effects of Cr Additions to Binary TiAl-Base Alloys,” *Metall. Trans. A*, vol. 22, no. November, pp. 2619–2625, 1991.

[18] J. Schwerdtfeger and C. Körner, “Selective electron beam melting of Ti-48Al-2Nb-2Cr: Microstructure and aluminium loss,” *Intermetallics*, vol. 49, pp. 29–35, 2014.

[19] A. Brotzu, F. Felli, and D. Pilone, “Effect of alloying elements on the behaviour of TiAl-based alloys,” *Intermetallics*, vol. 54, pp. 176–180, 2014.

[20] X. Wu, “Review of alloy and process development of TiAl alloys,” *Intermetallics*, vol. 14, pp. 1114–1122, 2006.

[21] P. D. Crofts, P. Bowen, and I. P. Jones, “The effect of lamella thickness on the creep behaviour of Ti-48Al-2Nb-2Mn,” *Scr. Mater.*, vol. 35, no. 12, pp. 1391–1396, 1996.

[22] Y. Mishin and C. Herzig, “Diffusion in the Ti–Al system,” *Acta Mater.*, vol. 48, no. 3, pp. 589–623, 2000.

[23] R. E. Smallman, “Modern Physical Metallurgy and Materials Engineering,”*Reed Educational and Professional Publishing Ltd*, pp. 448, 1999.

[24] C. Jiang, “First-principles study of site occupancy of dilute 3*d*, 4*d* and 5*d* transition metal solutes in $L1_0$ TiAl,” *Acta Mater.*, vol. 56, no. 20, pp. 6224–6231, 2008.

[25] R. W. Cahn,. and P. Haasen, “Physical Metallurgy,” *Elsevier Sci.*, vol. 3, pp. 2740, 1996.

[26] J. J. Williams, “Structure and high-temperature properties of Ti_5Si_3 with interstitial additions,” *Retrospective Thesis and Dissertations*, paper 12494, 1999.

[27] F. S. Sun, S. E. Kim, C. X. Cao, Y. T. Lee, and M. G. Yan, “A study of Ti_5Si_3/γ interface in TiAl alloys,” *Scr. Mater.*, vol. 45, no. 4, pp. 383–389, 2001.

[28] J. Fan, X. Li, Y. Su, J. Guo, and H. Fu, “Dependency of microhardness on solidification processing parameters and microstructure characteristics in the directionally solidified Ti-46Al-0.5W-0.5Si alloy,” *J. Alloys Compd.*, vol. 504, no. 1, pp. 60–64, 2010.

[29] C. J. Boehlert, “The effects of forging and rolling on microstructure in O+ BCC Ti-Al-Nb alloys,” *Mater. Sci. Eng. A*, vol. 279, no. 1, pp. 118–129, 2000.

[30] F. Appel, J. David, H. Paul, M. Oehring, D. O. De, and S. Wirtschaft, “Gamma Titanium Aluminide Alloys Materialwissenschaft : Metallische Werkstoffe Zu Inhaltsverzeichnis schnell und portofrei erhältlich bei,” 2011.

[31] R. J. Lancaster, W. J. Harrison, and G. Norton, “An analysis of small punch creep behaviour in the γ titanium aluminide Ti-45Al-2Mn-2Nb,” *Mater. Sci. Eng. A*, vol. 626, pp. 263–274, 2015.

[32] D. Johnson, Y. Masuda, T. Yamanaka, H. Inui, and M. Yamaguchi, “Creep deformation of TiAl-Si alloys with aligned γ/α2 lamellar microstructures,” *Metall. Mater. Trans. A*, vol. 10, no. 2, pp. 2463, 2000.

[33] D. M. Dimiduk, T. A. Parthasarathy, and P. M. Hazzledine, “Design-tool representations of strain compatibility and stress-strain relationships for lamellar γ titanium aluminides,” *Intermetallics*, vol. 9, no. 10–11, pp. 875–882, 2001.

[34] H. Franz, “Melting and Casting of Titanium Aluminides Challenges and Opportunities,”*Hilton Sorento Palace, Italy*, pp. 1-24, 2014.

[35] G. W. Kuhlman, “Forging of Titanium alloys,” *ASM Handb.*, vol. 14, p. 622, 1993.

[36] E. Schwaighofer, H. Clemens, S. Mayer, J. Lindemann, J. Klose, W. Smarsly, and V. Güther, “Microstructural design and mechanical properties of a cast and heat-treated intermetallic multi-phase γ-TiAl based alloy,” *Intermetallics*, vol. 44, pp. 128–140, 2014.

[37] Z. Huang, “Isothermal forging of γ TiAl alloys.” T*rans.Nonferrous Met.Soc. China*, pp. 1325–1328, 2003.

[38] A. Bartels, H. Kestler, and H. Clemens, “Deformation behavior of differently processed γ-titanium aluminides,” *Mater. Sci. Eng. A*, vol. 331, pp. 153–162, 2002.

[39] L. E. Murr, S. M. Gaytan, A. Ceylan, E. Matinez, J. L. Martinez, D. H. Hernandez, B.I. Machado, D. A. Ramirez, F.Medina, S. Collins, and R. B. Wicker, “Characterization of titanium aluminide alloy components fabricated by additive manufacturing using electron beam melting,” *Acta Mater.*, vol. 58, no. 5, pp. 1887–1894, 2010.

[40] T. Lee, E. Mosunov, and S. Hwang, “Consolidation of a γ TiAl–Mn–Mo alloy by elemental powder metallurgy,” *Mater. Sci. Eng. A*, vol. 239–240, pp. 540–545, 1997.

[41] R. German, Powder Metallurgy Science. *Metal Powder Industries Federation*, 1994.

[42] A. Beranoagirre and L. N. López de Lacalle, “Grinding of γ TiAl intermetallic alloys,” *Procedia Eng.*, vol. 63, pp. 489–498, 2013.

[43] D. Pilone and F. Felli, “Isothermal oxidation behaviour of TiAl-Cr-Nb-B alloys produced by induction melting,” *Intermetallics*, vol. 26, pp. 36–39, 2012.

[44] A. Abba, A. Galerie, and M. Caiilet, “High-Temperature Oxidation of Titanium Silicide Coatings on Titanium,” *Oxid. Met.*, vol. 17, no. 1, pp. 43–54, 1982.

[45] D. R. Askeland, *The Science and Engineering of Materials*. Springer US, 1996.

[46] C. Badini, S. M. Deambrosis, O. Ostrovskaya, V. Zin, E. Padovano, and E. Miorin, “Cyclic oxidation in burner rig of TiAlN coating deposited on Ti-48Al-2Cr-2Nb by reactive HiPIMS,” *Ceram. Int.*, vol. 43, no. 7, pp. 5417–5426, 2017.

[47] W. Ge, C. Guo, and F. Lin, “Effect of process parameters on microstructure of TiAl alloy produced by electron beam selective melting,” *Procedia Eng.*, vol. 81, no. October, pp. 1192–1197, 2014.

[48] K. Kothari, R. Radhakrishnan, N. M. Wereley, and T. S. Sudarshan, “Microstructure and mechanical properties of consolidated γ titanium

aluminides," *Powder Metall.*, vol. 50, no. 1, pp. 21–27, 2007.

[49] H. Zhu, J. Matsuda, and K. Maruyama, "Influence of heating rate in α+γ dual phase field on lamellar morphology and creep property of fully lamellar Ti-48Al alloy," *Mater. Sci. Eng. A*, vol. 397, no. 1–2, pp. 58–64, 2005.

[50] J. Beddoes, W. Wallace, and L. Zhao, "Current understanding of creep behaviour of near γ-titanium aluminides," *Int. Mater. Rev.*, vol. 40, no. 5, pp. 197–217, Jan. 1995.

[51] S. R. Dey, A. Hazotte, and E. Bouzy, "Crystallography and phase transformation mechanisms in TiAl-based alloys – A synthesis," *Intermetallics*, vol. 17, no. 12, pp. 1052–1064, 2009.

[52] F. Appel and R. Wagner, "Microstructure and deformation of two-phase γ-titanium aluminides," *Mater. Sci. Eng. R*, vol. 22, no. 5, pp. 187–268, 1998.

[53] F. H. Froes, "Titanium Aluminides: Science, Technology, Applications and Synthesis by Mechanical Alloying." Material science and technology, pp. 251–260, 1994.

[54] L. Song, J. Lin, and J. Li, "Phase transformation mechanisms in a quenched Ti-45Al-8.5Nb-0.2W-0.2B-0.02Y alloy after subsequent annealing at 800 deg C," vol. 691, pp. 60–66, 2017.

[55] H. Saari, J. Beddoes, D. Y. Seo, and L. Zhao, "Development of directionally solidified γ-TiAl structures," *Intermetallics*, vol. 13, no. 9, pp. 937–943, 2005.

[56] S. F. Franzén and J. Karlsson, "γ-Titanium Aluminide Manufactured by Electron Beam Melting," *Diploma Work No.37/2010, Master Program. Adv. Eng. Mater.*, p. 81, 2010.

[57] S. Plimpton, "Fast Parallel Algorithms for Short–Range Molecular Dynamics," *Phys. Rev. B*, vol. 117, pp. 1–19, 1995.

[58] H. and Monkhorst and J. D. Pack, "On Special Points for Brillouin Zone Integrations," *Phys. Rev. B*, vol. 13, no. 5188–5192, 1976.

[59] K. Parlinski, Z. Q. Li, and Y. Kawazoe, "First-principles determination of the soft mode in cubic ZrO2," *Phys. Rev. Lett.*, vol. 78, no. 21, pp. 4063–4066, 1997.

[60] Y. Kang, Y. Han, S. Qu, and J. Song, "Effects of Alloying Elements Ti, Cr, Al, and Hf on β-Nb5Si3 from First-principles Calculations," *Chinese J. Aeronaut.*, vol. 22, no. 2, pp. 206–210, 2009.

[61] C. Zambaldi, S. Zaefferer, and S. I. Wright, "Characterization of order domains in γ-TiAl by orientation microscopy based on electron backscatter diffraction," *J. Appl. Crystallogr.*, vol. 42, no. 111, pp. 1092–1101, 2009.

[62] S. R. Dey, A. Morawiec, E. Bouzy, A. Hazotte, and J. J. Fundenberger, "A technique for determination of γ/γ interface relationships in a (α_2+ γ) TiAl base alloy using TEM Kikuchi patterns," *Mater. Lett.*, vol. 60, pp. 646–650, 2006.

[63] S. Zghal, S. Naka, and A. Couret, "A Quantitative TEM analysis of the lamellar microstructure in TiAl based alloys," *Acta Mater.*, vol. 45, no. 7, pp. 3005–3015, 1997.

[64] M. Humbert, F. Wagner, and C. Esling, "Numbering the crystallographic variants in phase transformation," *J. Appl. Cryst*, vol. 25, pp. 724–730, 1992.

[65] B. Y. M. Humbert, F. Wagner, H. Moustahfid, and C. Esling, “Determination of the orientation of a parent β grain from the orientations of the inherited α plates in the phase transformation from body-centred cubic to hexagonal close packed,” *J. Appl. Cryst*, vol. 28, pp. 571–576, 1995.

[66] D.J. Dingley, and V. Randle, “Review Microtexture determination by electron back-scatter diffraction,” vol. 27, pp. 4545–4566, 1992.

[67] D. Raabe, “Examination of the iterative series-expansion method for quantitative texture analysis,” *J. Textures Microstruct.*, vol. 23, no. C, pp. 115–129, 1995.

[68] M. Hasegawa and H. Fukutomi, “Lamellar orientation control in TiAl base alloys by a two-step compression process at high temperature,” *Mater. Sci. Eng. A*, vol. 508, pp. 106–113, 2009.

[69] B. Kloden, “Microstructure and texture development during high-strain torsion of NiAl,”Dissertation, University of Dresden, 2006.

[70] C. R. Zambaldi, “Micromechanical modeling of γ-TiAl based alloys,” Aachen Univesity, PhD Dissertation, *Deutschen Nationalbibliografie*, pp. 1-201, 2010.

[71] M. L. Weaver and C. W. Calhoun, “Microstructure , texture , and mechanical properties of continuously cast γ TiAl,” *J. Mater. Sci.*, vol. 37, pp. 2483–2490, 2002.

[72] Z. Z. Shen, J. P. Lin, Y. F. Liang, L. Q. Zhang, S. L. Shang, and Z. K. Liu, “A novel hot pack rolling of high Nb e TiAl sheet from cast ingot,” *Intermetallics*, vol. 67, pp. 19–25, 2015.

[73] Oxford, “Oxford Instruments CHANNEL 5,” *User Manual.*, p. 527, 2010.

[74] R. R. Zope and Y. Mishin, “Interatomic potentials for atomistic simulations of the Ti-Al system,” *Phys. Rev. B*, vol. 68, no. 2, p. 024102-1 - 024102-14, 2003.

[75] S. Znam, D. Nguyen-Manh, D. G. Pettifor, and V. Vitek, “Atomistic modelling of TiAl I. Bond-order potentials with environmental dependence,” *Philos. Mag.*, vol. 83, no. 4, pp. 415–438, 2003.

[76] W. Soboyejo, "Mechanical Properties of Engineered Materials" *Marcel Dekker, Inc*. New York, Basel, 2003.

[77] F. Sishuba and A. S. Bolokang, “Finite element analysis (FEA) performed at Council of Scientific Industrial Research (CSIR) internal communication report,” Pretoria, 2018.

[78] M. N. Mathabathe, A. S. Bolokang, G. Govender, R. J. Mostert, and C. W. Siyasiya, “The vacuum melted γ -TiAl (Nb ,Cr ,Si) -doped alloys and their cyclic oxidation properties,” *Vacuum*, vol. 154, no. May, pp. 82–89, 2018.

[79] M. N. Mathabathe, A. S. Bolokang, G. Govender, R. J. Mostert, and C. W. Siyasiya, “Structure-property orientation relationship of a $\gamma/\alpha_2/Ti_5Si_3$ in as-cast Ti-45Al-2Nb-0.7Cr-0.3Si intermetallic alloy,” *J. Alloys Compd.*, vol. 765, pp. 690–699, 2018.

[80] T. Klein, M. Schachermayer, D. Holec, B. Rashkova, H. Clemens, and S. Mayer, “Impact of Mo on the wo phase in b-solidifying TiAl alloys : An experimental and computational approach,” *Intermetallics*, vol. 85, pp. 26–33, 2017.

[81] H. Wu, C. Zhang, G. Fan, L. Geng, and G. Wang, “Origin of reduced anisotropic

deformation in hexagonal close packed Ti-Al alloy," *Mater. Des.*, vol. 111, pp. 119–125, 2016.

[82] H. Zhou, F. Kong, K. Wu, X. Wang, and Y. Chen, "Hot pack rolling nearly lamellar Ti-44Al-8Nb-(W, B, Y) alloy with different rolling reductions: Lamellar colonies evolution and tensile properties," *Mater. Des.*, vol. 121, pp. 202–212, 2017.

[83] H. Wu, X. P. Cui, L. Geng, G. H. Fan, J. C. Pang, and L. S. Wei, "Fabrication and characterization of in-situ TiAl matrix composite with controlled microlaminated architecture based on SiC/Al and Ti system," *Intermetallics*, vol. 43, pp. 8–15, 2013.

[84] X. Cui, G. Fan, L. Geng, Y. Wang, H. Zhang, and H. X. Peng, "Fabrication of fully dense TiAl-based composite sheets with a novel microlaminated microstructure," *Scr. Mater.*, vol. 66, no. 5, pp. 276–279, 2012.

[85] H. Wu, G. H. Fan, X. P. Cui, L. Geng, F. Yuan, J. C. Pang, L. S. Wei, and M. Huang, "Mechanical properties of (Ti_2AlC+Ti_3AlC)-TiAl ceramic-intermetallic laminate (CIL) composites," *Mater. Sci. Eng. A*, vol. 585, pp. 439–443, 2013.

[86] K. N. Kulkarni, Y. Sun, A. K. Sachdev, and E. Lavernia, "Field-activated sintering of blended elemental γ-TiAl powder compacts: Porosity analysis and growth kinetics of Al_3Ti," *Scr. Mater.*, vol. 68, no. 11, pp. 841–844, 2013.

[87] Y. F. Wen and J. Sun, "Generalized planar fault energies and mechanical twinning in γ TiAl alloys," *Scr. Mater.*, vol. 68, no. 9, pp. 759–762, 2013.

[88] G. H. Cao, A. M. Russell, C. G. Oertel, and W. Skrotzki, "Microstructural evolution of TiAl-based alloys deformed by high-pressure torsion," *Acta Mater.*, vol. 98, pp. 103–112, 2015.

[89] B. Li, Z. Zhang, Y. Shen, W. Hu, and L. Luo, "Dissimilar friction stir welding of Ti-6Al-4V alloy and aluminum alloy employing a modified butt joint configuration: Influences of process variables on the weld interfaces and tensile properties," *Mater. Des.*, vol. 53, pp. 838–848, 2014.

[90] Y. Huang, J. Wang, L. Wan, X. Meng, H. Liu, and H. Li, "Self-riveting friction stir lap welding of aluminum alloy to steel," *Mater. Lett.*, vol. 185, pp. 181–184, 2016.

[91] E. A. Loria, "Gamma titanium aluminides as prospective structural materials," *Intermetallics*, vol. 8, no. 9–11, pp. 1339–1345, 2000.

[92] S. Valkov, P. Petrov, R. Lazarova, R. Bezdushnyi, and D. Dechev, "Formation and characterization of Al–Ti–Nb alloys by electron-beam surface alloying," *Appl. Surf. Sci.*, vol. 389, pp. 768–774, 2016.

[93] A. Radecka, J. Coakley, V. A. Vorontsov, T. L. Martin, P. A. J. Bagot, M. P. Moody, D. Rugg, and D.Dye, "Precipitation of the ordered α_2 phase in a near- α titanium alloy," *Scr. Mater.*, vol. 117, pp. 81–85, 2016.

[94] D. X. Wei, Y. Koizumi, M. Nagasako, and A. Chiba, "Refinement of lamellar structures in Ti-Al alloy," *Acta Mater.*, vol. 125, pp. 81–97, 2017.

[95] H. Wu, G. Fan, L. Geng, X. Cui, and M. Huang, "Nanoscale origins of the oriented precipitation of Ti_3Al in TiAl systems," *Scr. Mater.*, vol. 125, pp. 34–38, 2016.

[96] M. J. Phasha, A. S. Bolokang, and P. E. Ngoepe, "Solid-state transformation in nanocrystalline Ti induced by ball milling," *Mater. Lett.*, vol. 64, no. 10, pp. 1215–

1218, 2010.

[97] W. Soga, Y. Kaneno, and T. Takasugi, “Phase relation and microstructure in multi-phase intermetallic alloys based on Ni_3Al-Ni_3Nb-Ni_3V pseudo-ternary alloy system,” *Intermetallics*, vol. 14, no. 2, pp. 170–179, 2006.

[98] G. Liu, Z. Wang, T. Fu, Y. Li, H. Liu, T. Li, M. Gong, and G. Wang, “Study on the microstructure, phase transition and hardness for the TiAl-Nb alloy design during directional solidification,” *J. Alloys Compd.*, vol. 650, pp. 45–52, 2015.

[99] X. F. Ding, J. P. Lin, L. Q. Zhang, Y. Q. Su, H. L. Wang, and G. L. Chen, “Lamellar orientation control in a Ti-46Al-5Nb alloy by directional solidification,” *Scr. Mater.*, vol. 65, no. 1, pp. 61–64, 2011.

[100] A. S. Bolokang, M. J. Phasha, D. E. Motaung, F. R. Cummings, T. F. G. Muller, and C. J. Arendse, “Microstructure and phase transformation on milled and unmilled Ti induced by water quenching,” *Mater. Lett.*, vol. 132, pp. 157–161, 2014.

[101] S. Kumaran, T. Sasikumar, R. Arockiakumar, and T. Srinivasa Rao, “Nanostructured titanium aluminides prepared by mechanical alloying and subsequent thermal treatment,” *Powder Technol.*, vol. 185, no. 2, pp. 124–130, 2008.

[102] V. Y. Filimonov, M. A. Korchagin, I. A. Dietenberg, A. N. Tyumentsev, and N. Z. Lyakhov, “High temperature synthesis of single-phase Ti_3Al intermetallic compound in mechanically activated powder mixture,” *Powder Technol.*, vol. 235, pp. 606–613, 2013.

[103] H. W. Liu and K. P. Plucknett, “Titanium aluminide (Ti-48Al) powder synthesis, size refinement and sintering,” *Adv. Powder Technol.*, vol. 28, no. 1, pp. 314–323, 2017.

[104] K. Kasraee, A. Tayebifard, and E. Salahi, “Effect of substitution of Si by Al on microstructure and synthesis behavior of Ti_5Si_3 based alloys fabricated by mechanically activated self-propagating high-temperature synthesis,” *Adv. Powder Technol.*, vol. 25, no. 3, pp. 885–890, 2014.

[105] S. De la Torre, K. Ishihara, and P. Shingu, “Synthesis of SnTe by repeated cold-pressing,” *Mater. Sci. Eng. A*, vol. 266, no. 1, pp. 37–43, 1999.

[106] A. Kirin, A. Bonefacic, and D. Duzevic, “Phase transformation in pressed cobalt powder,” *J. Phys. F Met. Phys.*, vol. 14, no. 11, pp. 2781–2786, 1984.

[107] A. S. Bolokang, M. J. Phasha, D. E. Motaung, and S. Bhero, “Effect of Mechanical Milling and Cold Pressing on Co Powder,” *J. Metall.*, vol. 2012, no. Mic, pp. 1–7, 2012.

[108] J. Prescott and R. Barnum, “On powder flowability,” *Pharm. Technol.*, vol. 24, no. October, pp. 60–84, 2000.

[109] R. Cuscó, E. Alarcón-Lladó, J. Ibáñez, and Luis Artús, “Temperature dependence of Raman scattering in ZnO,” *Phys. Rev. B*, vol. 75, no. 16, p. 165202-1 - 165202-11, 2007.

[110] A. S. Bolokang, Z. P. Tshabalala, G. F. Malgas, I. Kortidis, H. C. Swart, and D. E. Motaung, “Room temperature ferromagnetism and CH_4 gas sensing of titanium oxynitride induced by milling and annealing,” *Mater. Chem. Phys.*, vol.

193, pp. 512–523, 2017.

[111] A. S. Bolokang, D. E. Motaung, C. J. Arendse, and T. F. G. Muller, “Formation of the metastable FCC phase by ball milling and annealing of titanium-stearic acid powder,” *Adv. Powder Technol.*, vol. 26, no. 2, pp. 632–639, 2015.

[112] A. S. Bolokang, D. E. Motaung, C. J. Arendse, and T. F. G. Muller, “Morphology and structural development of reduced anatase-TiO_2 by pure Ti powder upon annealing and nitridation: Synthesis of TiO_x and TiO_xN_y powders,” *Mater. Charact.*, vol. 100, pp. 41–49, 2015.

[113] M. Naguib, V. Presser, D. Tallman, J. Lu, L. Hultman, Y. Gogotsi, M. W. Barsoum, “On the topotactic transformation of Ti_2AlC into a Ti-C-O-F cubic phase by heating in molten lithium fluoride in air,” *J. Am. Ceram. Soc.*, vol. 94, no. 12, pp. 4556–4561, 2011.

[114] Z. Xiao, X. Zhu, Z. Chu, W. Xu, Z. Wang, and B. Wu, “Investigation of Ti_2AlC formation mechanism through carbon and TiAl diffusional reaction,” *J. Eur. Ceram. Soc.*, vol. 38, no. October 2017, pp. 1246–1252, 2017.

[115] G. Yang, H. Kou, J. Yang, J. Li, and H. Fu, “Microstructure control of Ti-45Al-8.5Nb-(W, B, Y) alloy during the solidification process,” *Acta Mater.*, vol. 112, pp. 121–131, 2016.

[116] M. N. Mathabathe, S. Govender, A. S. Bolokang, R. J. Mostert, and C. W. Siyasiya, “Phase transformation and microstructural control of the α-solidifying γ-Ti-45Al-2Nb-0.7Cr-0.3Si intermetallic alloy,” *J. Alloys Compd.*, vol. 757, pp. 8–15, 2018.

[117] S. Z. Zhang, Y. B. Zhao, C. J. Zhang, J. C. Han, M. J. Sun, and M. Xu, “The microstructure , mechanical properties , and oxidation behavior of β- γ TiAl alloy with excellent hot workability,” *Mater. Sci. Eng. A*, vol. 700, no. June, pp. 366–373, 2017.

[118] K. Li, Y. Li, X. Huang, D. Gibson, Y. Zheng, J. Liu, L. Sun, and Y. Q. Fu, “Surface microstructures and corrosion resistance of Ni-Ti-Nb shape memory thin films,” *Appl. Surf. Sci.*, vol. 414, pp. 63–67, 2017.

[119] A. V. Kartavykh, E. A. Asnis, N. V. Piskun, I. I. Statkevich, A. A. Stepashkin, M. V. Gorshenkov, and T. K. Akopyan, “Complementary thermodynamic and dilatometric assessment of phase transformation pathway in new β-stabilized TiAl intermetallics,” *Mater. Lett.*, vol. 189, pp. 217–220, 2017.

[120] A. K. Singh, K. Muraleedharan, and D. Banerjee, “Solidification structure in a cast γ alloy,” *Scr. Mater.*, vol. 48, no. 6, pp. 767–772, 2003.

[121] D. Li, H. Guo, D. Wang, T. Zhang, S. Gong, and H. Xu, “Cyclic oxidation of β-NiAl with various reactive element dopants at 1200°C,” *Corros. Sci.*, vol. 66, pp. 125–135, 2013.

[122] C. Zhao, Y. Zhou, Z. Zou, L. Luo, X. Zhao, F. Guo, and P. Xiao, “Effect of alloyed Lu, Hf and Cr on the oxidation and spallation behavior of NiAl,” *Corros. Sci.*, vol. 126, no. July, pp. 334–343, 2017.

[123] J. He, Y. Luan, H. Guo, H. Peng, Y. Zhang, T. Zhang, and S. Gong, “The role of Cr and Si in affecting high-temperature oxidation behaviour of minor Dy doped NiAl alloys,” *Corros. Sci.*, vol. 77, pp. 322–333, 2013.

[124] B. Wendler, M. Danielewski, K. Przybylski, A. Rylski, Kaczmarek, and M. Jachowicz, "New type AlMo-, AlTi- or Si-based magnetron sputtered protective coatings on metallic substrates," *J. Mater. Process. Technol.*, vol. 175, no. 1–3, pp. 427–432, 2006.

[125] X. Gong, R. Chen, Q. Wang, Y. Wang, N. Zhang, Z. Zhang and H. Fu, "Cyclic oxidation behavior and oxide scale adhesion of Al/NiCrAlY coating on pure titanium alloy," *J. Alloys Compd.*, vol. 729, pp. 679–687, 2017.

[126] D. J. Kim, D. Y. Seo, X. Huang, Q. Yang, and Y. W. Kim, "Cyclic oxidation behavior of a β-γ powder metallurgy TiAl-4Nb-3Mn alloy coated with a NiCrAlY coating," *Surf. Coatings Technol.*, vol. 206, no. 13, pp. 3048–3054, 2012.

[127] J. Wang, L. Kong, T. Li, and T. Xiong, "A novel $TiAl_3/Al_2O_3$ composite coating on γ-TiAl alloy and evaluating the oxidation performance," *Appl. Surf. Sci.*, vol. 361, pp. 90–94, 2016.

[128] Q. M. Wang, R. Mykhaylonka, A. Flores Renteria, J. L. Zhang, C. Leyens, and K. H. Kim, "Improving the high-temperature oxidation resistance of a β-γ TiAl alloy by a Cr_2AlC coating," *Corros. Sci.*, vol. 52, no. 11, pp. 3793–3802, 2010.

[129] M. Ansari, R. Shoja-Razavi, M. Barekat, and H. C. Man, "High-temperature oxidation behavior of laser-aided additively manufactured NiCrAlY coating," *Corros. Sci.*, vol. 118, pp. 168–177, 2017.

[130] H. Guo, Y. Cui, H. Peng, and S. Gong, "Improved cyclic oxidation resistance of electron beam physical vapor deposited nano-oxide dispersed β-NiAl coatings for Hf-containing superalloy," *Corros. Sci.*, vol. 52, no. 4, pp. 1440–1446, 2010.

[131] J. A. Haynes, B. A. Pint, Y. Zhang, and I. G. Wright, "Comparison of the cyclic oxidation behavior of β-NiAl, β-NiPtAl and γ-γ′ NiPtAl coatings on various superalloys," *Surf. Coatings Technol.*, vol. 202, no. 4–7, pp. 730–734, 2007.

[132] Y. Wu, K. Hagihara, and Y. Umakoshi, "Improvement of cyclic oxidation resistance of Y-containing TiAl-based alloys with equiaxial γ microstructures," *Intermetallics*, vol. 13, no. 8, pp. 879–884, 2005.

[133] B. G. Kim, G. M. Kim, and C. J. Kim, "Oxidation behavior of TiAl-X (X = Cr, V, Si, Mo or Nb) intermetallics at elevated temperature," *Scr. Metall. Mater.*, vol. 33, no. 7, pp. 1117–1125, 1995.

[134] T. Narita, T. Izumi, M. Yatagai, and T. Yoshioka, "Sulfidation processing and Cr addition to improve oxidation resistance of TiAl intermetallics in air at 1173 K," *Intermetallics*, vol. 8, no. 4, pp. 371–379, 2000.

[135] J. Małecka, W. Grzesik, and A. Hernas, "An investigation on oxidation wear mechanisms of Ti-46Al-7Nb-0.7Cr-0.1Si-0.2Ni intermetallic-based alloys," *Corros. Sci.*, vol. 52, no. 1, pp. 263–272, 2010.

[136] Y. Shen, X. Ding, and F. Wang, "High temperature oxidation behavior of Ti-Al-Nb ternary alloys," *J. Mater. Sci.*, vol. 39, pp. 6583–6589, 2004.

[137] J. Ding, Y. Liang, X. Xu, H. Yu, C. Dong, and J. Lin, "Cyclic deformation and microstructure evolution of high Nb containing TiAl alloy during high temperature low cycle fatigue," *Int. J. Fatigue*, vol. 99, pp. 68–77, 2017.

[138] E. Hamzah, M. Kanniah, and M. Harun, "Effect of chromium addition on microstructure, tensile properties and creep resistance of as-cast Ti-48Al alloy,"

J. Mater. Sci., vol. 42, no. 21, pp. 9063–9069, 2007.

[139] A. S. Bolokang, D. E. Motaung, C. J. Arendse, and T. F. G. Muller, "Production of titanium-tin alloy powder by ball milling: Formation of titanium-tin oxynitride composite powder produced by annealing in air," *J. Alloys Compd.*, vol. 622, pp. 824–830, 2015.

[140] V. A. C. Haanappel, H. Clemens, and M. F. Stroosnijder, "The high temperature oxidation behaviour of high and low alloyed TiAl-based intermetallics," vol. 10, pp. 293–305, 2002.

[141] X. J. Zhao, H. Q. Ru, N. Zhang, X. Y. Wang, and D. L. Chen, "Corrosion of aluminum oxynitride based ceramics by molten steel," *Ceram. Int.*, vol. 39, no. 3, pp. 3049–3054, 2013.

[142] X. Du, S. Yao, X. Jin, Y. Long, B. Liang, and W. Li, "Photocatalytic properties of aluminum oxynitride (AlON)," *Mater. Lett.*, vol. 161, pp. 72–74, 2015.

[143] X. L. Liu, S. L. Shang, Y. J. Hu, Y. Wang, Y. Du, and Z. K. Liu, "Insight into γ-Ni/γ′-Ni_3Al interfacial energy affected by alloying elements," *Mater. Des.*, vol. 133, pp. 39–46, 2017.

[144] Y. Sun, S. Xu, and A. Shan, "Effects of annealing on microstructure and mechanical properties of nano-grained Ni-based alloy produced by severe cold rolling," *Mater. Sci. Eng. A*, vol. 641, pp. 181–188, 2015.

[145] Y. K. Kim, D. Kim, H. K. Kim, C. S. Oh, and B. J. Lee, "An intermediate temperature creep model for Ni-based superalloys," *Int. J. Plast.*, vol. 79, pp. 153–175, 2016.

[146] X. Wang and J. A. Szpunar, "Ceria coating for controlling the isothermal oxidation behaviour of Ni-based alloy 625," *J. Alloys Compd.*, vol. 729, pp. 379–389, 2017.

[147] M. L. Bonnet, D. Costa, E. Protopopoff, and P. Marcus, "Theoretical study of the Pb adsorption on Ni, Cr, Fe surfaces and on Ni based alloys," *Appl. Surf. Sci.*, vol. 426, pp. 788–795, 2017.

[148] Y. Yamabe-Mitarai, T. Hara, S. Miura, and H. Hosoda, "Shape memory effect and pseudoelasticity of TiPt," *Intermetallics*, vol. 18, no. 12, pp. 2275–2280, 2010.

[149] Y. Yamabe-Mitarai, T. Hara, T. Kitashima, S. Miura, and H. Hosoda, "Composition dependence of phase transformation behavior and shape memory effect of Ti(Pt, Ir)," *J. Alloys Compd.*, vol. 577, no. SUPPL. 1, pp. S399–S403, 2013.

[150] X. Yan, A. Grytsiv, P.Rogl, H. Schmidt, G. Giester, A. Saccone, and X. Q. Chen, "Laves phases in the ternary systems Ti-{Pd, Pt}-Al," *Intermetallics*, vol. 17, no. 5, pp. 336–342, 2009.

[151] O. V. Zaikina, V. G. Khorujaya, D. Pavlyuchkov, B. Grushko, and T. Y. Velikanova, "Investigation of the Al-Ti-Pt alloy system at 1100 °C," *J. Alloys Compd.*, vol. 509, no. 28, pp. 7565–7571, 2011.

[152] A. Grytsiv, P. Rogl, G. Giester, and V. Pomjakushin, "Crystal chemistry of the G-phase region in the Ti-Co-Al system," *Intermetallics*, vol. 13, no. 5, pp. 497–509, 2005.

[153] J. H. Chen, G. Z. Wang, R. Cao, and J. Zhang, "Study on notch fracture of TiAl alloys at room temperature," *Metall. Mater. Trans. A*, vol. 35, pp. 439–456, 2004.

[154] Y. Wang, Y. Liu, G. Y. Yang, H. Z. Li, and B. Tang, "Microstructure of cast γ-TiAl based alloy solidified from bata phase region," *Trans. Nonferrous Met. Soc. China (English Ed.*, vol. 21, no. 2, pp. 215–222, 2011.

[155] S. Bulmer, "The Microstructures and Mechanical Properties of Powder Metallurgy (PM) Ti-48Al-2Cr-2Nb-(0-1)W," Carleton University, 2008.

[156] F. Sun and F. H. S. Froes, "Precipitation of Ti_5Si_3 phase in TiAl Alloys," *Mater. Sci. Eng A*, vol. 328, pp. 113–121, 2002.

[157] T. Liu, L. S. Luo, D. H. Zhang, L. Wang, X. Z. Li, R. R. Chen, Y. Q. Su, J. J. Guo, and H.Z. Fu, "Comparison of microstructures and mechanical properties of as-cast and directionally solidified Ti-47Al-1W-0.5Si alloy," *J. Alloys Compd.*, vol. 682, pp. 663–671, 2016.

[158] M. R. Kabir, M. Bartsch, L. Chernova, K. Kelm, and J. Wischek, "Correlations between microstructure and room temperature tensile behavior of a duplex TNB alloy for systematically heat treated samples," *Mater. Sci. Eng. A*, vol. 635, pp. 13–22, 2015.

[159] Q. Wang, H. Ding, H. Zhang, R. Chen, J. Guo, and H. Fu, "Variations of microstructure and tensile property of γ-TiAl alloys with 0–0.5 at% C additives," *Mater. Sci. Eng. A*, vol. 700, no. March, pp. 198–208, 2017.

[160] H. Clemens, A. Bartels, S. Bystrzanowski, H. Chladil, H. Leitner, G. Dehm, R. Gerling, and F.P. Schimansky, "Grain refinement in γ-TiAl-based alloys by solid state phase transformations," *Intermetallics*, vol. 14, no. 12, pp. 1380–1385, 2006.

[161] G. Liu, Z. Wang, T. Fu, Y. Li, H. Liu, T. Li, M. Gong, and G. Wang, "Study on the microstructure, phase transition and hardness for the TiAl-Nb alloy design during directional solidification," *J. Alloys Compd.*, vol. 650, pp. 45–52, 2015.

[162] S. Rajararn, "A heat-treatment procedure to produce fine grained lamellar microstructures in a P/M titanium aluminide alloy," *PhD Thesis*, 1996.

[163] R. V. Ramanujan, "Phase transformations in γ-based titanium aluminides," *Int. Mater. Rev.*, vol. 45, no. 6, pp. 217–240, 2000.

[164] X. F. Ding, J. P. Lin, L. Q. Zhang, H. L. Wang, G. J. Hao, and G. L. Chen, "Microstructure development during directional solidification of Ti-45Al-8Nb alloy," *J. Alloys Compd.*, vol. 506, no. 1, pp. 115–119, 2010.

[165] D. Zhang, E. Arzt, and H. Clemens, "Characterization of controlled microstructures in a γ-TiAl (Cr, Mo, Si, B) alloy," *Intermetallics*, vol. 7, no. 10, pp. 1081–1087, 1999.

[166] W. Schillinger, H. Clemens, G. Dehm, and A. Bartels, "Microstructural stability and creep behavior of a lamellar γ-TiAl based alloy with extremely fine lamellar spacing," *Intermetallics*, vol. 10, no. 5, pp. 459–466, 2002.

[167] F. Sun and F. H. S. Froes, "Solidification behaviour of Ti_5Si_3 whiskers in TiAl alloys," *Mater. Sci. Eng. A*, vol. 345, pp. 262–269, 2003.

[168] S. R. Chubb, D. A. Papaconstantopoulos, and B. M. Klein, "First-principles study of $L1_0$ Ti-Al and V-Al alloys," *Phys. Rev. B*, vol. 38, no. 17, pp. 12120–12124,

Dec. 1988.

[169] Y. Jin, J. N. Wang, J. Yang, and Y. Wang, “Microstructure refinement of cast TiAl alloys by β solidification,” *Scr. Mater.*, vol. 51, no. 2, pp. 113–117, 2004.

[170] G. Kresse and J. Furthmüller, “Efficiency of Ab-initio total energy calculations for metals and semiconductors using a plane-wave basis set,” *Comput. Mat. Sci*, vol. 6, pp. 15–50, 1996.

[171] J. Braun, Ellner, and B. Predel, “Experimental investigations of the structure and stability of the TiAl phase.” Zeitschrift fur Metallkunde, pp. 870–876, 1995.

[172] U. Hecht, V. Witusiewicz, A. Drevermann, and J. Zollinger, “Grain refinement by low boron additions in niobium-rich TiAl-based alloys,” *Intermetallics*, vol. 16, no. 8, pp. 969–978, 2008.

[173] A. Chlupová, M. Heczko, K. Obrtlík, J. Polák, P. Roupcová, P. Beran, T. Kruml, “Mechanical properties of high niobium TiAl alloys doped with Mo and C,” *Mater. Des.*, vol. 99, pp. 284–292, 2016.

[174] P. Erdely, P. Staron, E. Maawad, N. Schell, J. Klose, H. Clemens, and S. Mayer, “Design and control of microstructure and texture by thermomechanical processing of a multi-phase TiAl alloy,” *Mater. Des.*, vol. 131, pp. 286–296, 2017.

[175] P. Kofstad, “High-temperature oxidation of titanium,” *J. Less-Common Met.*, vol. 12, pp. 449–464, 1967.

[176] J. Sjölén, L. Karlsson, S. Braun, R. Murdey, A. Hörling, and L. Hultman, “Structure and mechanical properties of arc evaporated Ti–Al–O–N thin films,” *Surf. Coat. Technol.*, vol. 201, pp. 6392–6403, 2007.

[177] C. L. Chu and S. K. Wu, “Ion nitriding of titanium aluminides with 25-53 at .% A1 I : Nitriding parameters and microstructure characterization,” *Surf. Coat. Technol.*, vol. 78, pp. 211–218, 1996.

[178] W. Wu, W. Chen, S. Yang, Y. Lin, S. Zhang, T. Y. Cho, G. H. Lee, and S. C Kwon, “Design of AlCrSiN multilayers and nanocomposite coating for HSS cutting tools,” *Appl. Surf. Sci.*, vol. 351, pp. 803–810, 2015.

[179] P. Z. Shi, J. Wang, C. X. Tian, Z. G. Li, G. D. Zhang, D. J. Fu, and B. Yang, “Surface & Coatings Technology Structure, mechanical and tribological properties of CrN thick coatings deposited by circular combined tubular arc ion plating,” *Surf. Coat. Technol.*, vol. 228, pp. 534–537, 2013.

[180] X. Guan, Y. Wang, G. Zhang, J. Xin, L. Wang, and Q. Xue, “A novel duplex PDMS / CrN coating with superior corrosion resistance for marine applications,” *R. Soc. Chem. Adv.*, vol. 6, pp. 87003–87012, 2016.

[181] Y. W. Kim, “Ordered intermetallic alloys, part III: γ titanium aluminides,” *Jom*, vol. 46, no. 7, pp. 30–39, 1994.

[182] Q. Wang, C. Han, T. Choma, Q. Wei, C. Yan, B Song, and Y. Shi, “Effect of Nb content on microstructure , property and in vitro apatite-forming capability of Ti-Nb alloys fabricated via selective laser melting,” *Mater. Des.*, vol. 126, no. January, pp. 268–277, 2017.

[183] L. Slokar, T. Matkovic, and P. Matkovic, “Alloy design and property evaluation of new Ti–Cr–Nb alloys,” *Mater. Des.*, vol. 33, pp. 26–30, 2012.

[184] X. Gong, R. R. Chen, H. Z. Fang, H. S. Ding, J. J. Guo, Y. Q. Su, H. Z. Fu, "Synergistic effect of B and Y on the isothermal oxidation behavior of TiAl-Nb-Cr-V alloy," *Corros. Sci.*, vol. 131, no. December 2017, pp. 376–385, 2018.

[185] C. Badini, S. M. Deambrosis, O. Ostrovskaya, V. Zin, E. Padovano, and E. Miorin, "Cyclic oxidation in burner rig of TiAlN coating deposited on Ti-48Al-2Cr-2Nb by reactive HiPIMS," *Ceram. Int.*, vol. 43, no. 7, pp. 5417–5426, 2017.

[186] H. J. Grabke, "Oxidation of NiAl and FeAl," *Intermetallics*, vol. 7, pp. 1153–1158, 1999.

[187] G. L. Li, G. H. Wang, and J. M. Hong, "Morphologies of rutile form TiO_2 twins crystals," *J. Mater. Sci. Lett.*, vol. 18, no. 15, pp. 1243–1246, 1999.

[188] S. K. Mishra, S. Ghosh, and S. Aravindan, "Characterization and machining performance of laser-textured chevron shaped tools coated with AlTiN and AlCrN coatings," *Surf. Coat. Technol.*, vol. 334, no. July 2017, pp. 344–356, 2018.

[189] A. S. Bolokang and M. J. Phasha, "Formation of titanium nitride produced from nanocrystalline titanium powder under nitrogen atmosphere," *Int. Journal of Refractory Metals and Hard Materials*, vol. 28, no. 5, pp. 610–615, 2010.

[190] J. L. Endrino and V. Derflinger, "The influence of alloying elements on the phase stability and mechanical properties of AlCrN coatings," *Surf. Coat. Technol.*, vol. 200, pp. 988–992, 2005.

[191] B. Xiao, J. Liu, F. Liu, X. Zhong, X. Xiao, T. F. Zhang, and Q. Wang, "Effects of microstructure evolution on the oxidation behavior and high-temperature tribological properties of AlCrN / TiAlSiN multilayer coatings," *Ceram. Int.*, vol. 44, no. 18, pp. 23150–23161, 2018.

[192] E. Mohammadpour, Z. T. Jiang, M. Altarawneh, N. Mondinos, M. M. Rahman, H. N. Lim, N. M. Huang, Z. Xie, Z. Zhou, and B. Z. Dlugogorski, "Experimental and predicted mechanical properties of $Cr_{1-x}Al_xN$ thin films, at high temperatures, incorporating in situ synchrotron radiation X-ray diffraction and computational modelling," *RSC Adv.*, vol. 7, no. 36, pp. 22094–22104, 2017.

[193] R. Chen, X. Gong, Y. Wang, G. Qin, N. Zhang, Y. Su, H. Ding, J. Guo and H. Fu, "Microstructure and oxidation behaviour of plasma-sprayed NiCoCrAlY coatings with and without Ta on Ti44Al6Nb1Cr alloys," *Corros. Sci.*, vol. 136, no. March, pp. 244–254, 2018.

[194] C. G. McKamey, S. H. Whang, and C. Liu, "Microstructural characterization of a γ-TiAl-Ni alloy produced by rapid solidification techniques," *Scr. Metall.*, vol. 32, no. 3, pp. 383–388, 1995.

[195] B. Navinšek, P. Panjan, and I. Milošev, "PVD coatings as an environmentally clean alternative to electroplating and electroless processes," *Surf. Coatings Technol.*, vol. 116–119, no. September 1999, pp. 476–487, 1999.

[196] M. Song, M. Xiang, Y. Yang, Q. Zhu, C. Hu, and P. Lv, "Synthesis of stoichiometric TiN from TiH_2 powder and its nitridation mechanism," *Ceram. Int.*, vol. 44, no. 14, pp. 16947–16952, 2018.

[197] W. Zhu, D. Shi, Z. Zhu, and J. Sun, "Effect of the surface oxidization and nitridation on the normal spectral emissivity of titanium alloys Ti-6Al-4V at 800-1100 K at a wavelength of 1.5 μm," *Infrared Phys. Technol.*, vol. 76, pp. 200–

205, 2016.

[198] K. Sopunna, T. Thongtem, M. McNallan, and S. Thongtem, “Surface modification of the γ-TiAl alloys by the nitridation,” *Surf. Sci.*, vol. 566–568, no. 1-3 part 2, pp. 810–815, 2004.

[199] C. Boonruang, T. Thongtem, M. McNallan, and S. Thongtem, “Effect of nitridation and carburization of γ-TiAl alloys on wear resistance,” *Mater. Lett.*, vol. 58, no. 25, pp. 3175–3181, 2004.

[200] B. Zhao, J. Wu, J. Sun, B. Tu, and F. Wang, “Oxidation kinetics of the nitrided TiAl-based alloys,” *Mater. Lett.*, vol. 56, no. 4, pp. 533–538, 2002.

[201] B. Zhao, J. Sun, J. S. Wu, and Z. X. Yuan, “Gas nitriding behavior of TiAl based alloys in an ammonia atmosphere,” *Scr. Mater.*, vol. 46, pp. 581–586, 2002.

[202] A. M. Limarga and D. S. Wilkinson, “A model for the effect of creep deformation and intrinsic growth stress on oxide/nitride scale growth rates with application to the nitridation of γ-TiAl,” *Mater. Sci. Eng. A*, vol. 415, no. 1–2, pp. 94–103, 2006.

[203] C. Yang, D. Hu, A. Huang, and M. Dixon, “Solidification and grain refinement in Ti45Al2Mn2Nb1B subjected to fast cooling,” *Intermetallics*, vol. 32, pp. 64–71, 2013.

[204] C. M. Austin and T. J. Kelly, “Gas Turbine Engine Implementation of γ Titanium Aluminide,” *Superalloys 1996*, pp. 539–543, 1996.

[205] A. S. Bolokang, F. R. Cummings, B. P. Dhonge, H. M. I. Abdallah, T. Moyo, H. Swart, C. J. Arendse, T. F. G. Muller, and D. E. Motaung, “Characteristics of the mechanical milling on the room temperature ferromagnetism and sensing properties of TiO_2 nanoparticles,” *Appl. Surf. Sci.*, vol. 331, pp. 362–372, 2015.

[206] Y. Y. Chang, C. P. Chang, D. Y. Wang, S. M. Yang, and W. Wu, “High temperature oxidation resistance of CrAlSiN coatings synthesized by a cathodic arc deposition process,” *J. Alloys Compd.*, vol. 461, no. 1–2, pp. 336–341, 2008.

[207] Y. Rozita, R. Brydson, and A. J. Scott, “ An investigation of commercial γ-Al_2O_3 nanoparticles ,” *J. Phys. Conf. Ser.*, vol. 241, p. 012096, 2010.

[208] A. M. Abd El-Rahman, M. F. Maitz, M. A. Kassem, F. M. El-Hossary, F. Prokert, H. Reuther, M. T. Pham, and E. Richter, “Surface improvement and biocompatibility of TiAl24Nb10 intermetallic alloy using rf plasma nitriding,” *Appl. Surf. Sci.*, vol. 253, no. 23, pp. 9067–9072, 2007.

[209] A. Huguet and A. Menand, “interstitial solubility in γ and α_2 phases of TiAl-based alloys,” *Acta Mater.*, vol. 44, no. I, pp. 4729–4737, 1996.

[210] Q.-X. Fan, J. J. Zhang, Z. H. Wu, Y. M. Liu, T. Zhang, B. Yan, and T. G. Wang, “Influence of Al Content on the Microstructure and Properties of the CrAlN Coatings Deposited by Arc Ion Plating,” *Acta Metall. Sin. (English Lett.*, vol. 30, no. 12, pp. 1221–1230, 2017.

[211] O. Ostrovskaya, C. Badini, G. Baudana, E. Padovano, and S. Biamino, “Thermogravimetric investigation on oxidation kinetics of complex Ti-Al alloys,” *Intermetallics*, vol. 93, no. May 2017, pp. 244–250, 2017.

[212] S. Zeng, A. Zhao, L. Luo, H. Jiang, and L. Zhang, “Development of β-solidifying γ-TiAl alloys sheet,” *Mater. Lett.*, vol. 198, pp. 31–33, 2017.

[213] Y. Wei, Y. Zhang, H.-B. Zhou, G.-H. Lu, and H. Xu, “First-principles investigation on shear deformation of a TiAl/Ti_3Al interface and effects of oxygen,” *Intermetallics*, vol. 22, pp. 41–46, 2012.

[214] J. Lapin, A. Klimová, and T. Pelachová, “Softening of a cast intermetallic Ti-46Al-2W-0.5Si alloy during annealing at 700-800 °C,” *Scr. Mater.*, vol. 49, no. 7, pp. 681–686, 2003.

[215] O. Engler and V. Randle, "Introduction to TEXTURE ANALYSIS Macrotexture, Microstructure, and Orientation Mapping", *Taylor and Francis group*, 2010.

[216] F. Appel, H. Clemens, and F. D. Fischer, “Modeling concepts for intermetallic titanium aluminides,” *Prog. Mater. Sci.*, vol. 81, pp. 55–124, 2016.

[217] H. Christ and U. Siegen, “Cycl,” *ASM Met. Handb.*, vol. 19, no. 9, pp. 1689–1699, 1996.

[218] R. Abbaschian, L. Abbaschian, and R. E. Reed-Hill, Physical Metallurgy Principles Fourth Edition,. *Litton Educational publishing*, 2009.

APPENDIX

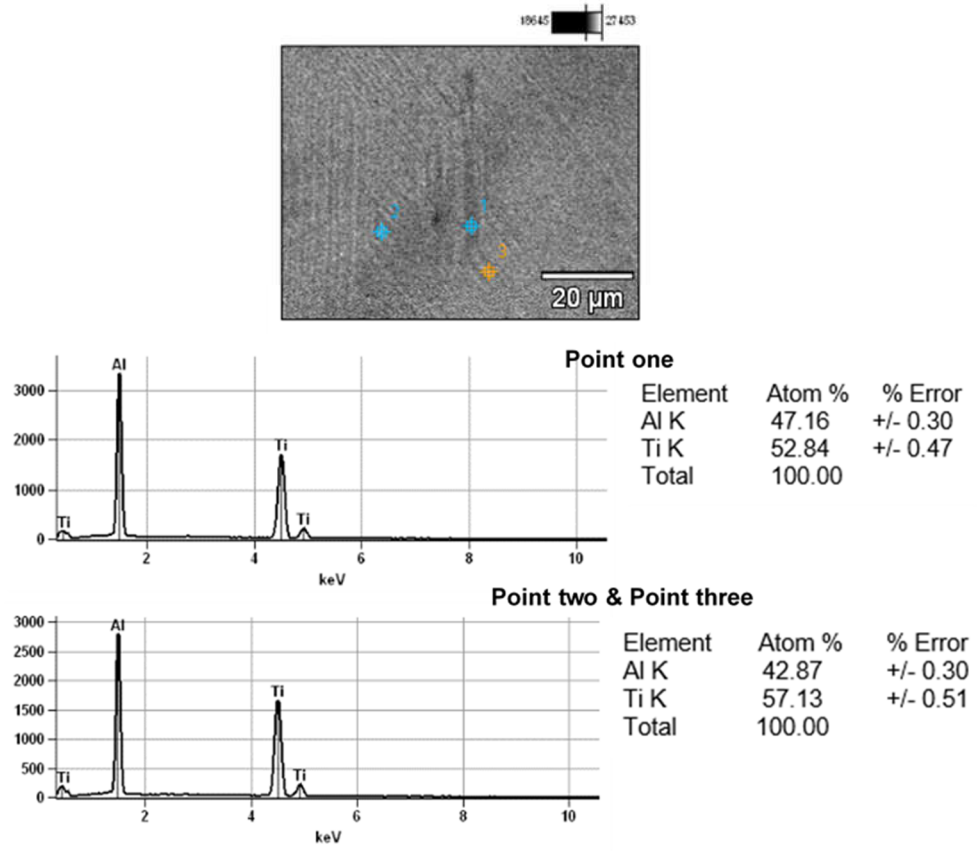

Figure S 1. Binary alloy

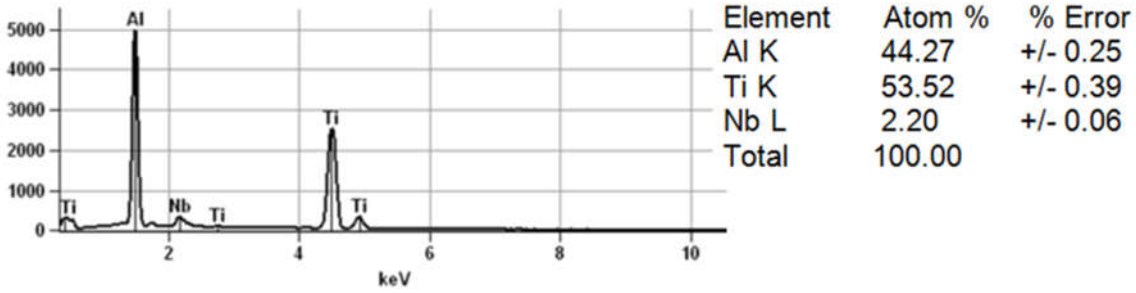

Figure S 2. Beta-phase composition of the ternary alloy

Table S 1.

Elements	Binary alloy			Ternary alloy			Quaternary alloy		
	α_2	γ	β	α_2	γ	β	α_2	γ	β
Ti	57.1	52.8		54.7	48.9	53.5	49.5	48.9	52.1
Al	42.9	47.2		43.3	49.4	44.3	47.9	48.4	45.1
Nb				2.0	1.7	2.2	1.9	2.0	1.6
Cr							0.8	0.6	1.3

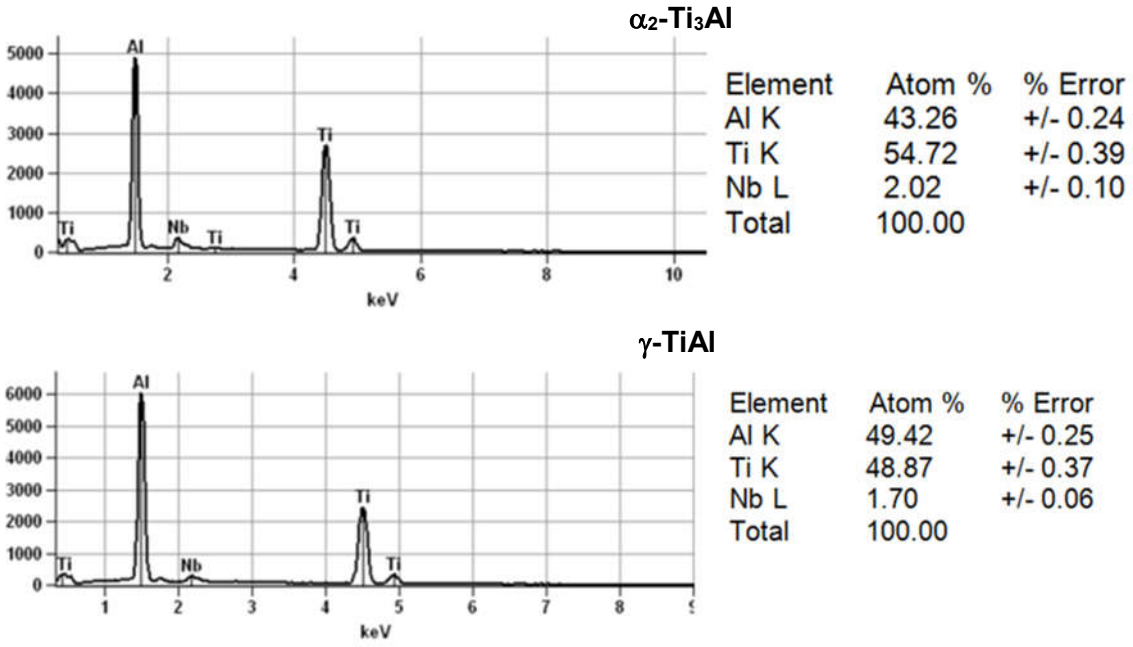

Figure S 3. Lamellae composition of the ternary alloy

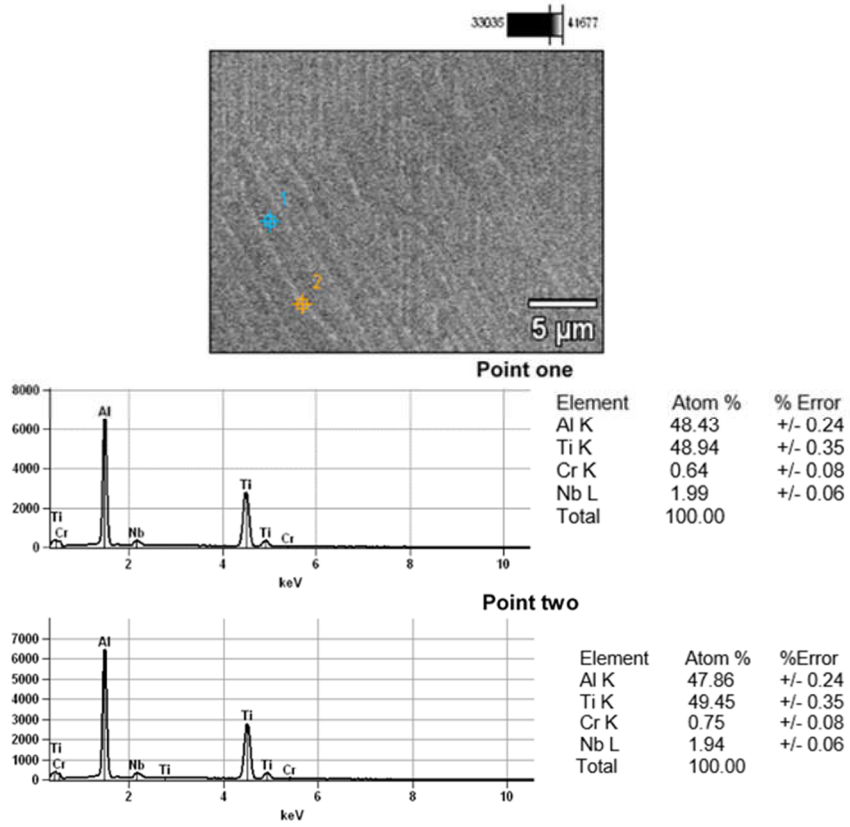

Figure S 4. Lamellar structure composition of the quaternary alloy.

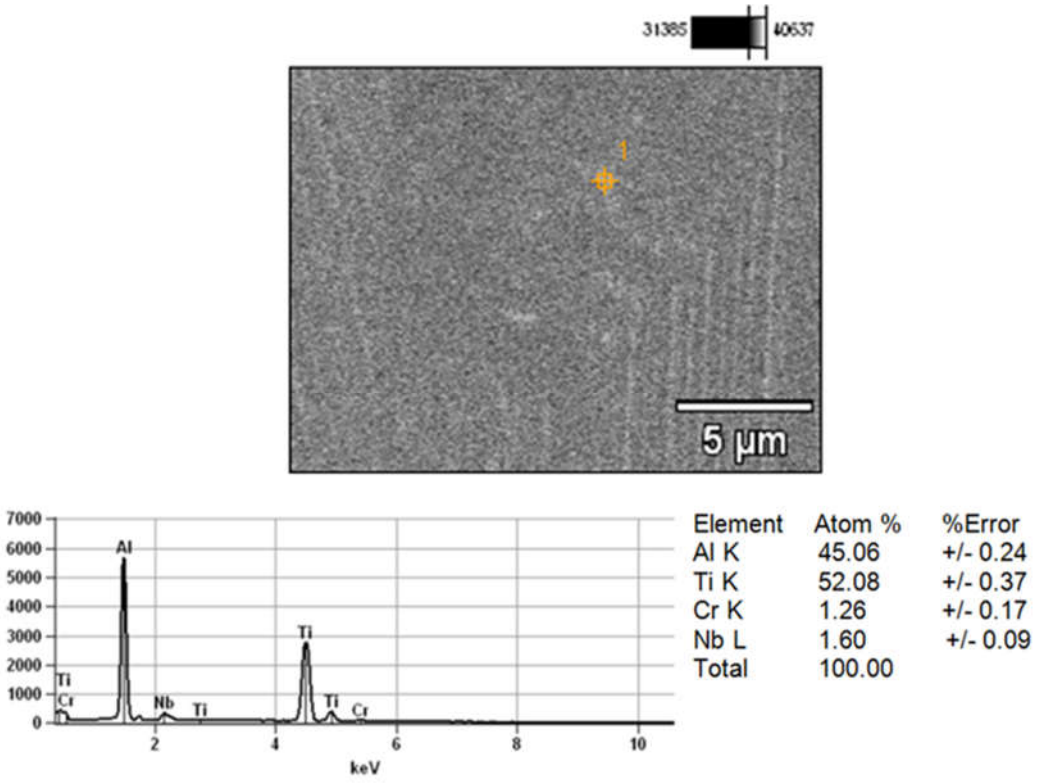

Figure S 5. Beta-phase composition of the quaternary alloy.

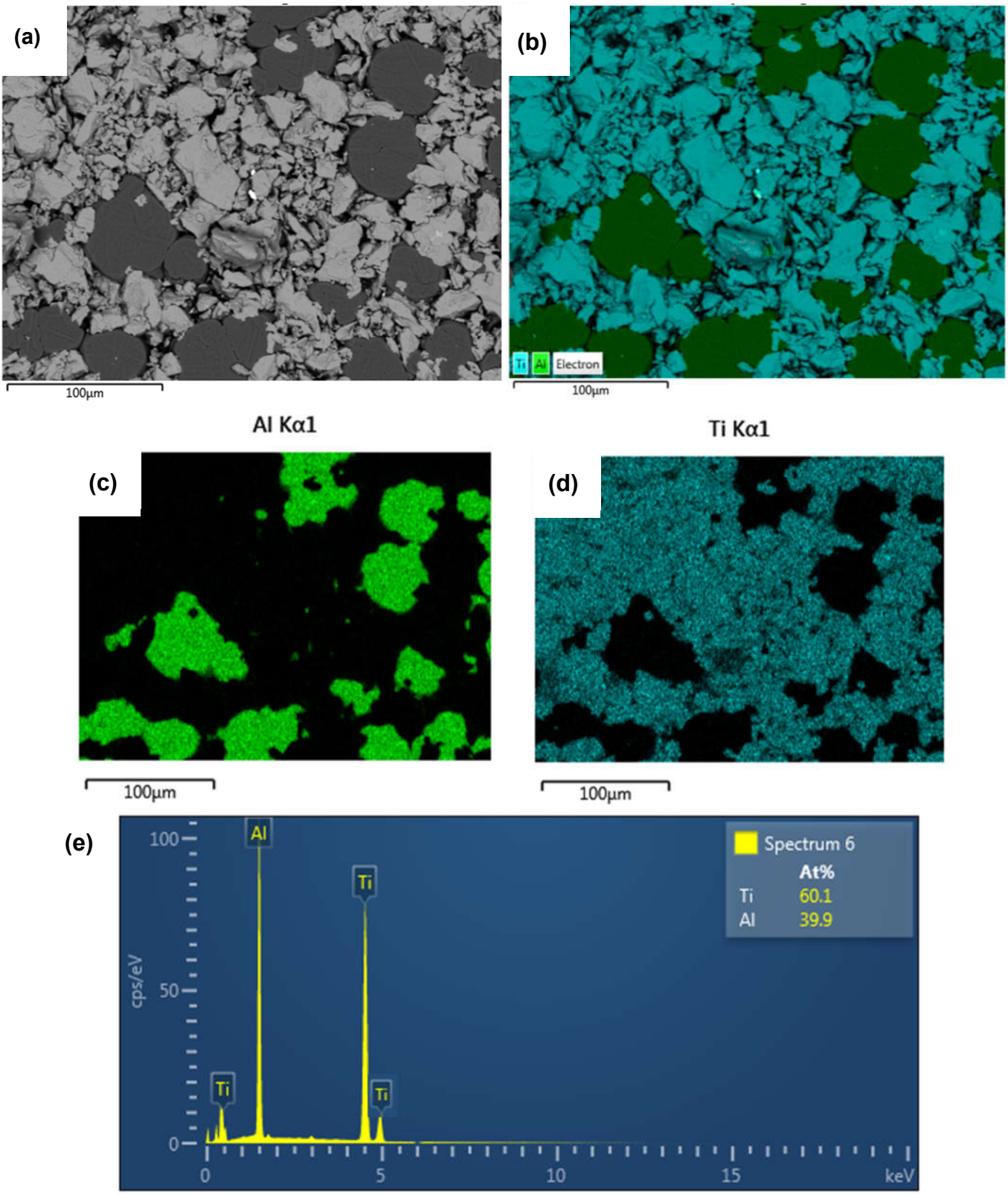

Figure S 6. SEM-EDS elemental map analysis for the Ti-48Al alloy: (a) electron image, (b) EDS layered image, (c) Al Kα, (d) Ti Kα, and (e) spectra with corresponding atomic composition.

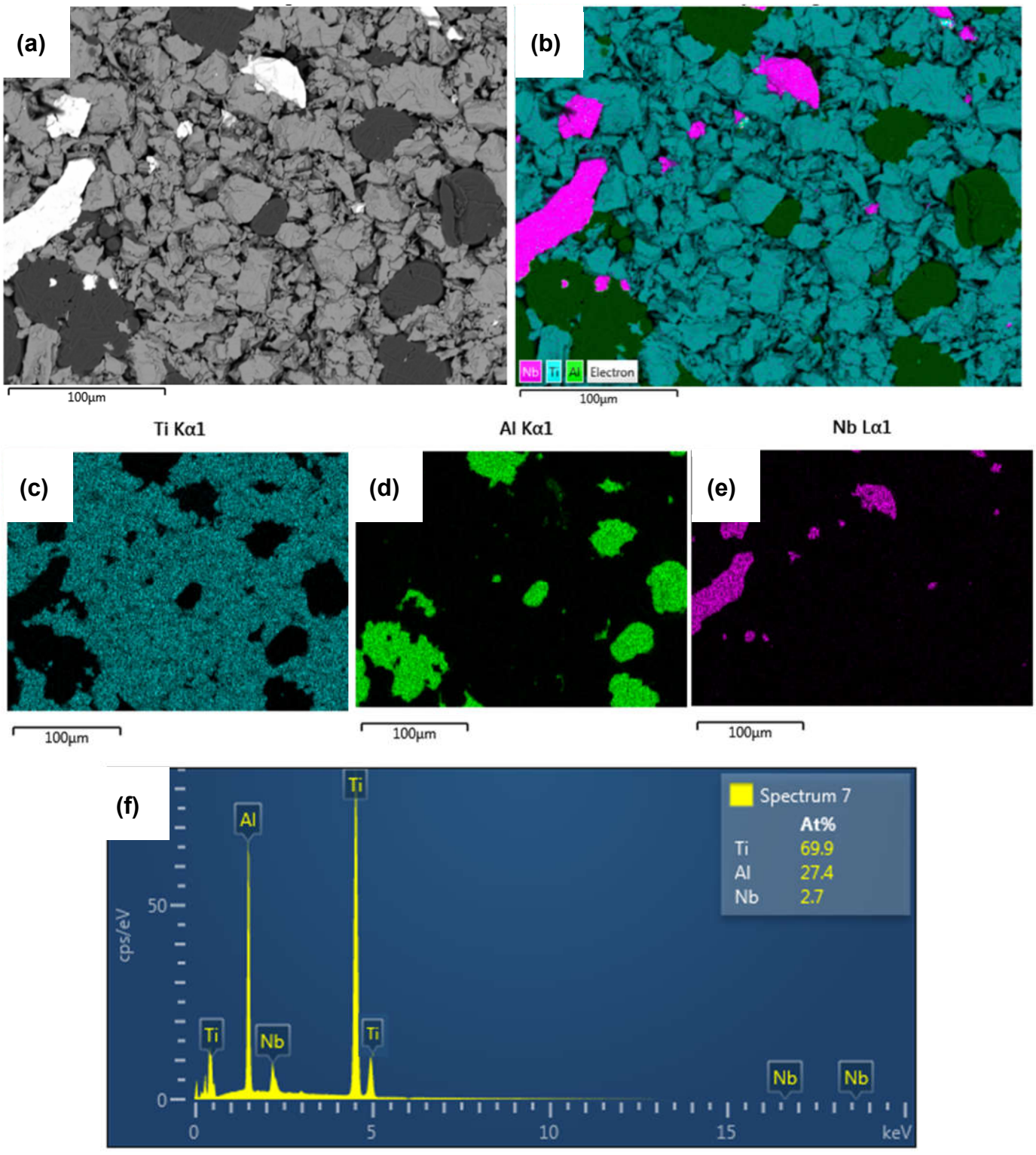

Figure S 7. SEM-EDS elemental map analysis for the Ti-48Al-2Nb alloy: (a) electron image, (b) EDS layered image, (c) Ti Kα, (d) Al Kα (e) Nb Kα, and (f) spectra with corresponding atomic composition.

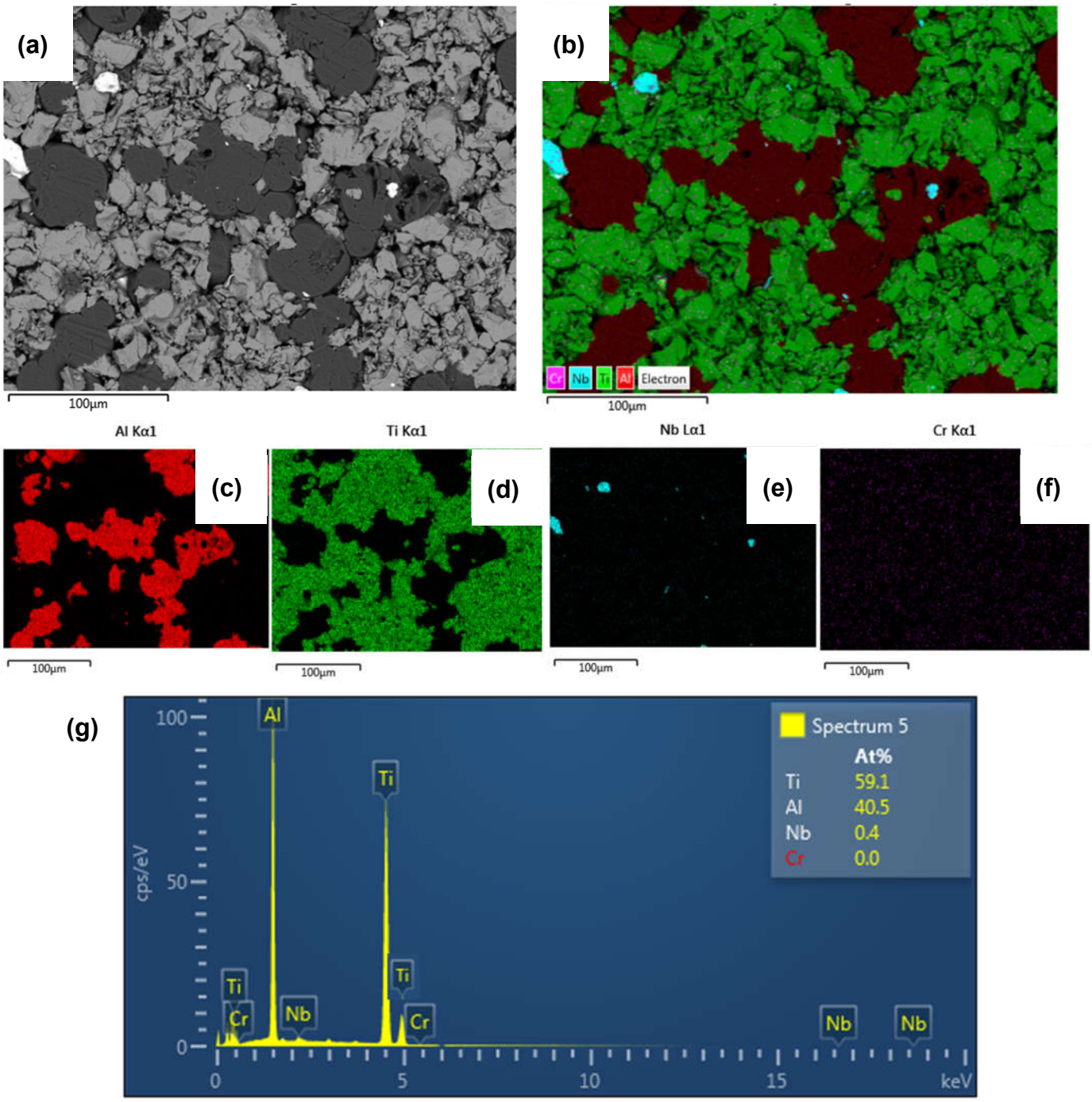

Figure S 8. SEM-EDS elemental map analysis for the Ti-48Al-2Nb-0.7Cr alloy: (a) electron image, (b) EDS layered image, (c) Ti Kα, (d) Al Kα (e) Nb Kα, (f) Cr Kα, and (g) spectra with corresponding atomic composition.

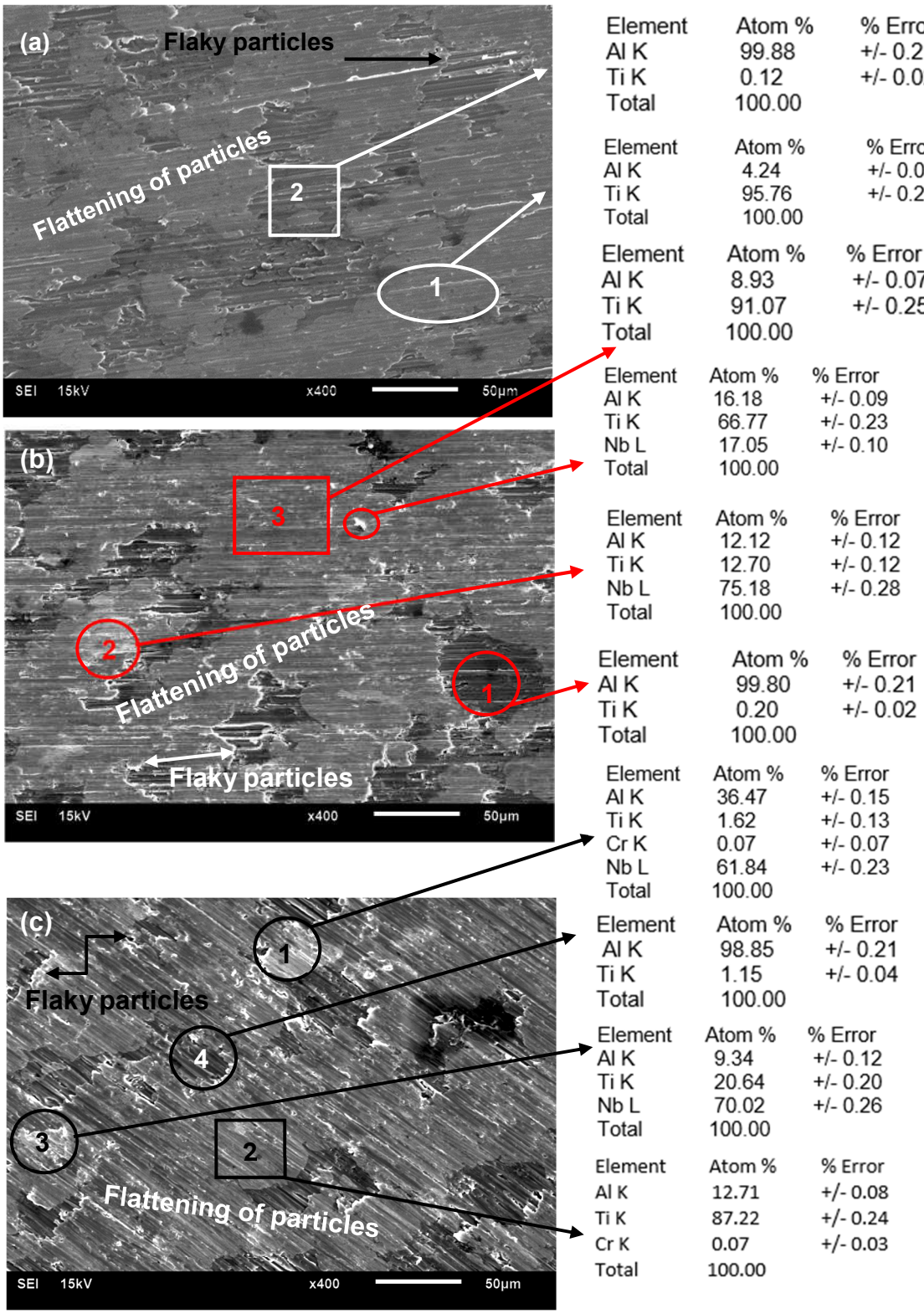

Figure S 9. SEM-SEI micrographs of a) binary Ti-48Al (b) ternary Ti-48Al-2Nb and (c) quaternary Ti-48Al-2Nb-0.7Cr compacted alloy powders, further away from the surface.

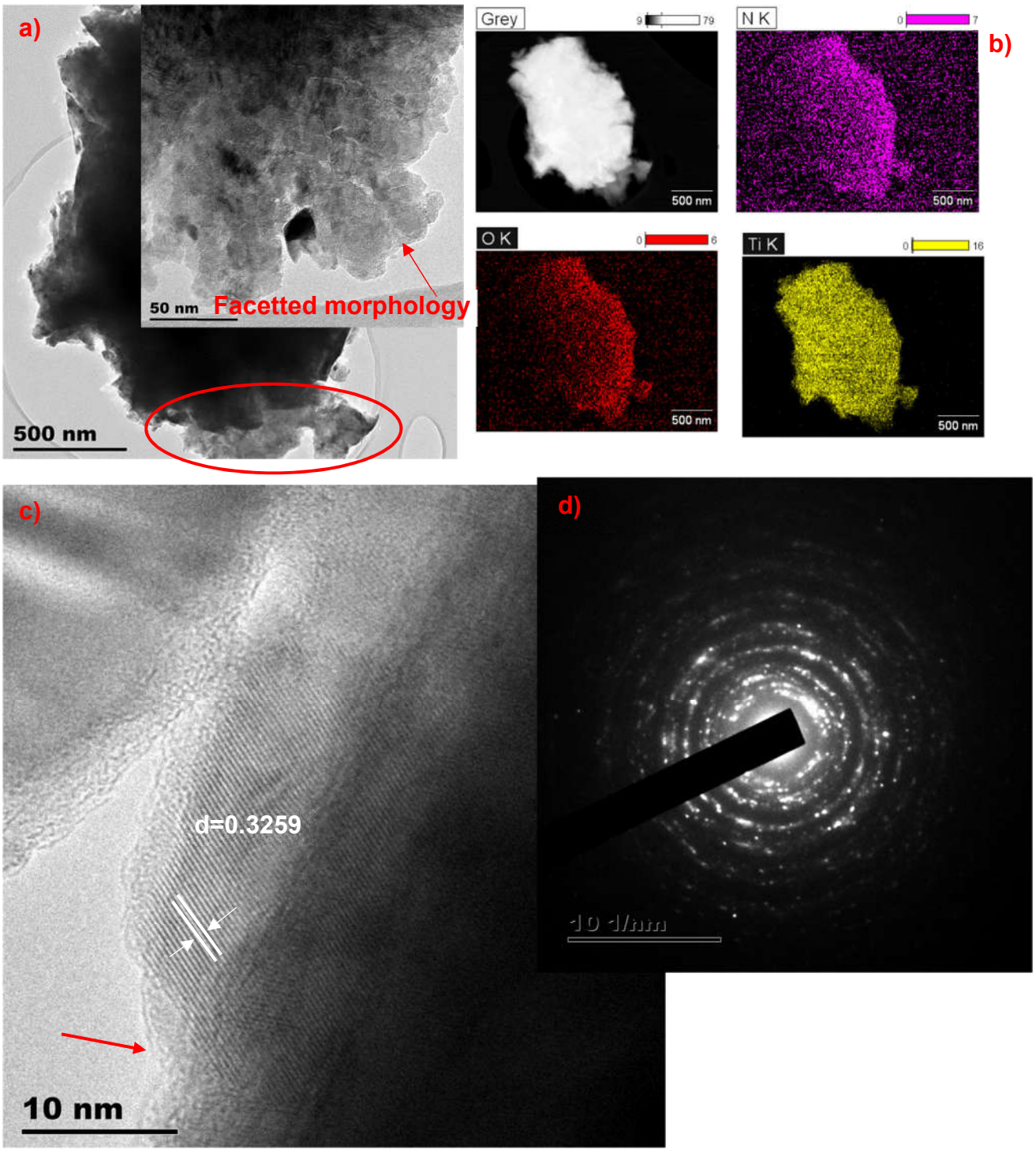

Figure S 10. The TEM images of the γ-Ti-46Al-2Nb alloy (a) with a corresponding insert indicated by a zoomed-out area marked with a red circle, (b) elemental mapping viz. (N, O, Ti) of the coating, (c) high-resolution TEM image of the facetted morphology indicated by the red circle in Fig. S10a (d) with the corresponding selected area electron diffraction (SAED).

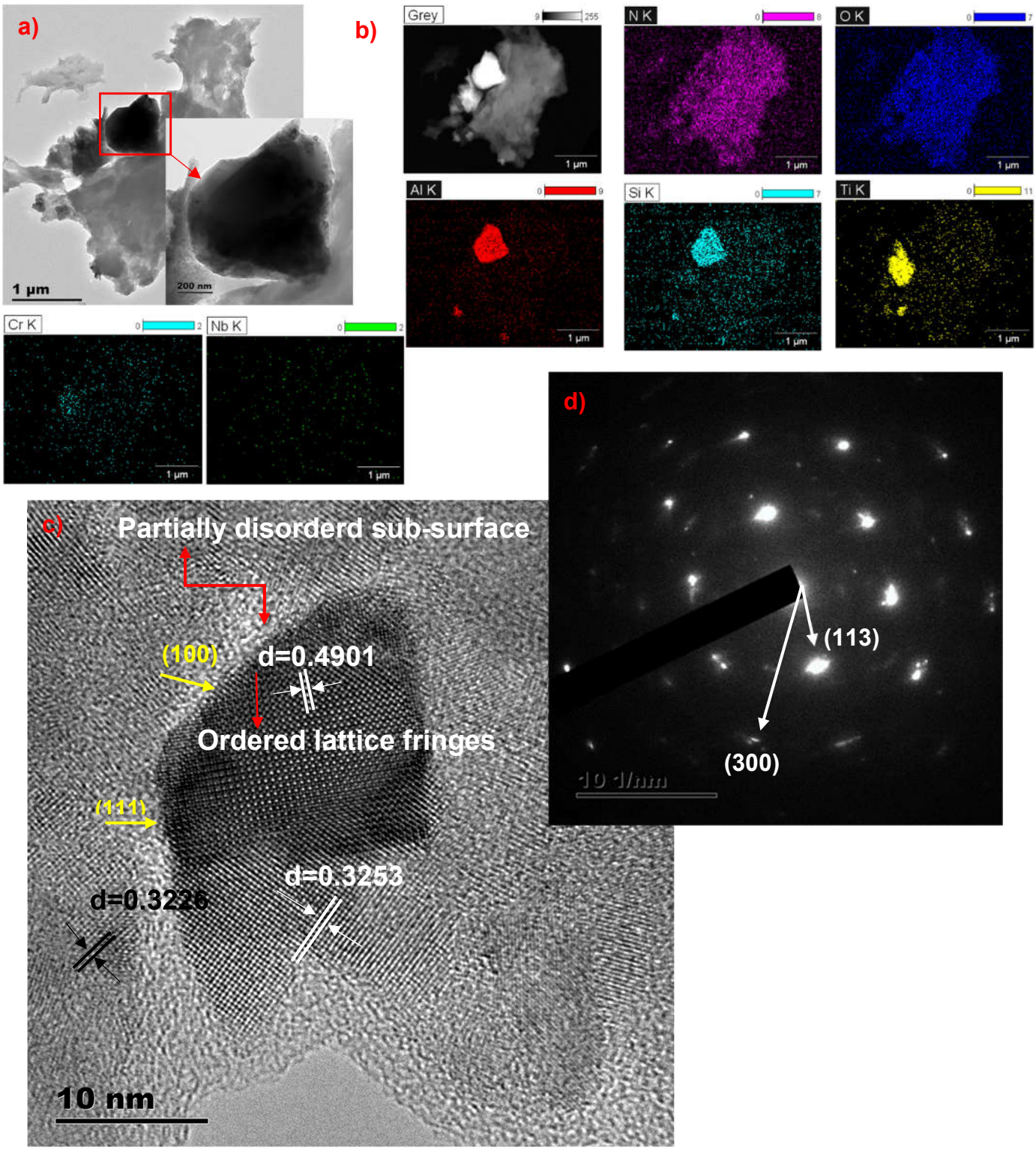

Figure S 11. TEM images of the nitrided γ-Ti-46Al-2Nb-0.7Cr-0.3Si alloy after cyclic oxidation at 900 °C for 900 h; with a corresponding insert of a zoomed-out particle is shown in (a), the elemental mapping (N, O, Al, Si, Ti, Cr, Cu, Nb) of the interface domain between the coating and the alloy (b), the high-resolution TEM indicating a facetted particle (c) with the corresponding SAED (d).

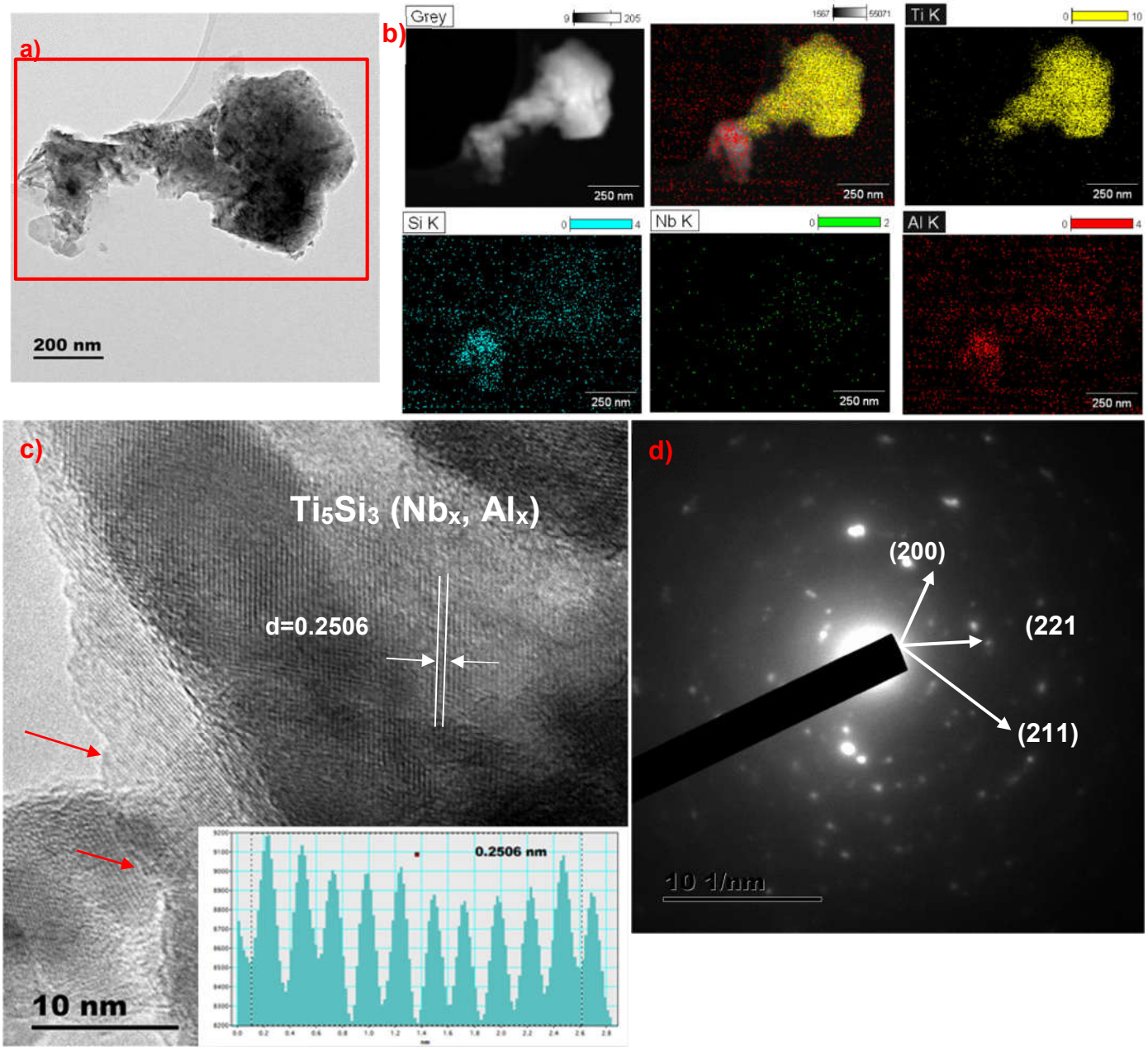

Figure S 12. TEM images of the nitrided γ-Ti-46Al-2Nb-0.7Cr-0.3Si alloy with subsequent cyclic oxidation at 900 °C for 900 h is shown in (a), elemental mapping viz. (Ti, Si, Nb, Al) of the interface domain between the Ti_5Si_3 (Nb_x, Al_x) coating and the alloy (b), the high-resolution TEM (c) with the corresponding selected area electron diffraction (SAED) of $Ti_5Si_3(Nb_xAl_x)$ (d).

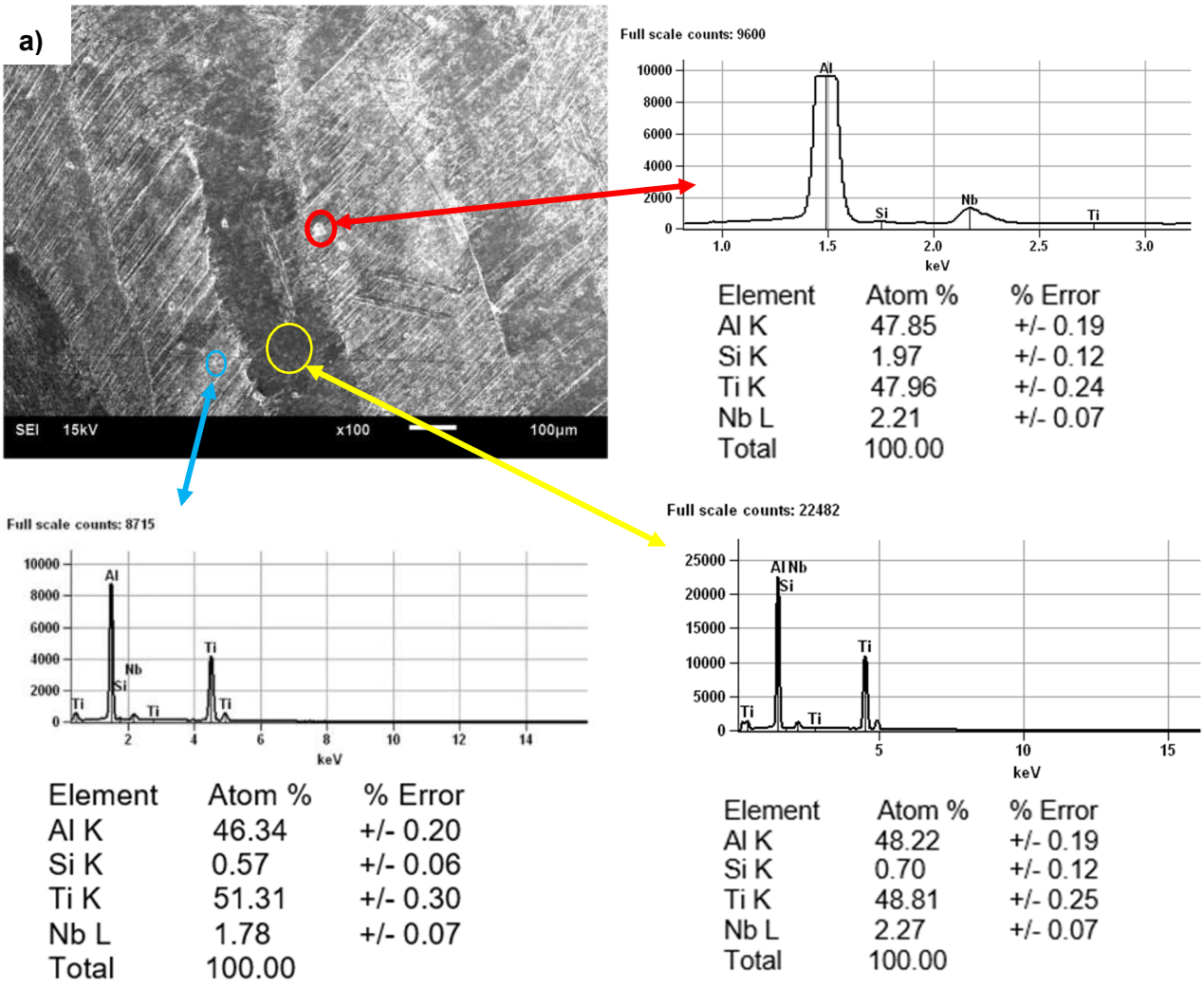

Figure S 13. SEM-SEI EDX image of the (a) as-cast Ti-45Al-2Nb-0.3Si intermetallic alloy.

Fig S.13 shows the SEM secondary electron image (SEI) of the as-cast microstructure of γ-Ti-45Al-2Nb-0.3Si intermetallic alloy. The main identified phases were the columnar lamellar (α_2/γ) structures, of an average size of approximately 100µm. The chemical composition of the gray network is the α_2-Ti_3Al phase shown by the circled blue double arrow, whereas that of the dark contrast is the γ-TiAl phase, indicated by the circled double yellow arrow. Moreover, within the lamellar colonies are the Ti_5Si_3 precipitates particles dissipated randomly throughout the structure illustrated by the circled double red arrow.

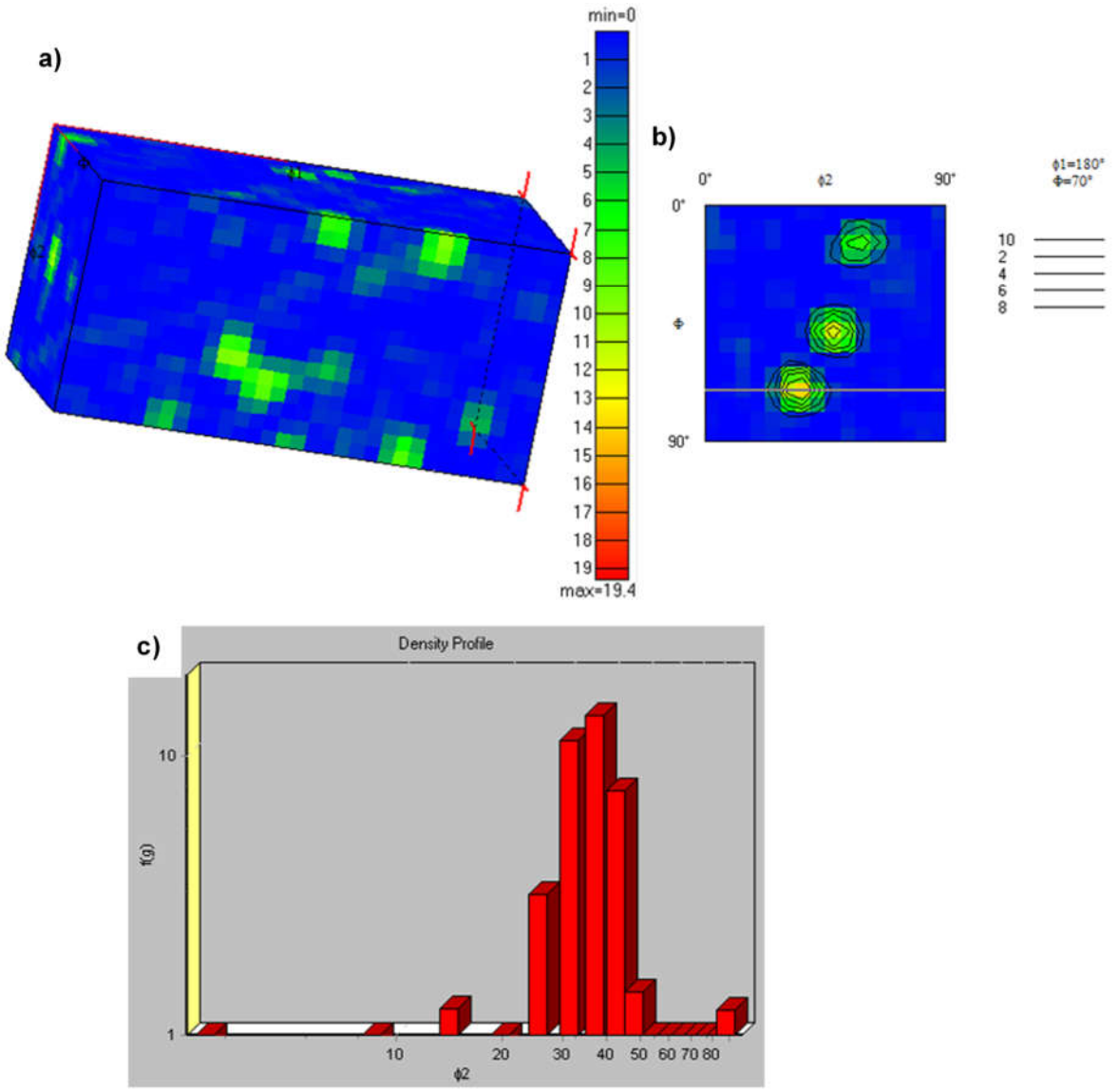

Figure S 14. γ-phase of Ti-45Al-2Nb-0.3Si alloy showing: (a) 3D view of scattered data and ODF intensities in Euler space with its corresponding browser section in (b), and (c) density profile distribution along a horizontal line in (b).

Fig S. 14 indicates that strong fiber textures for orientation distribution function (ODF) found at densities of ϕ2=30º, 35º, 40º, 45º, 50º, 65º, 70º, 75º serial sections with black contour lines shown in **Fig S. 15**.

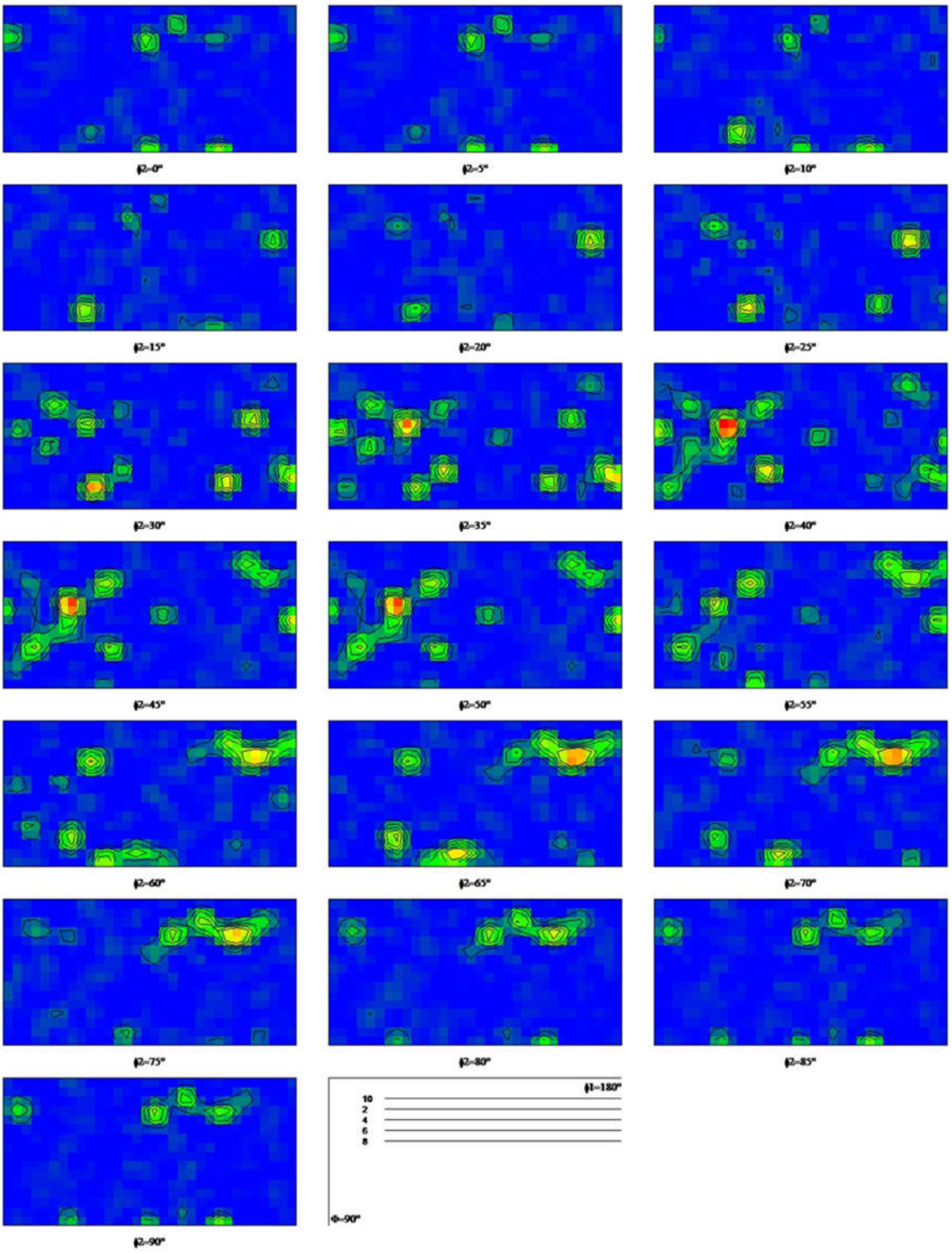

Figure S 15. Serial sections through an ODF of Ti-45Al-2Nb-0.3Si alloy (γ-phase).

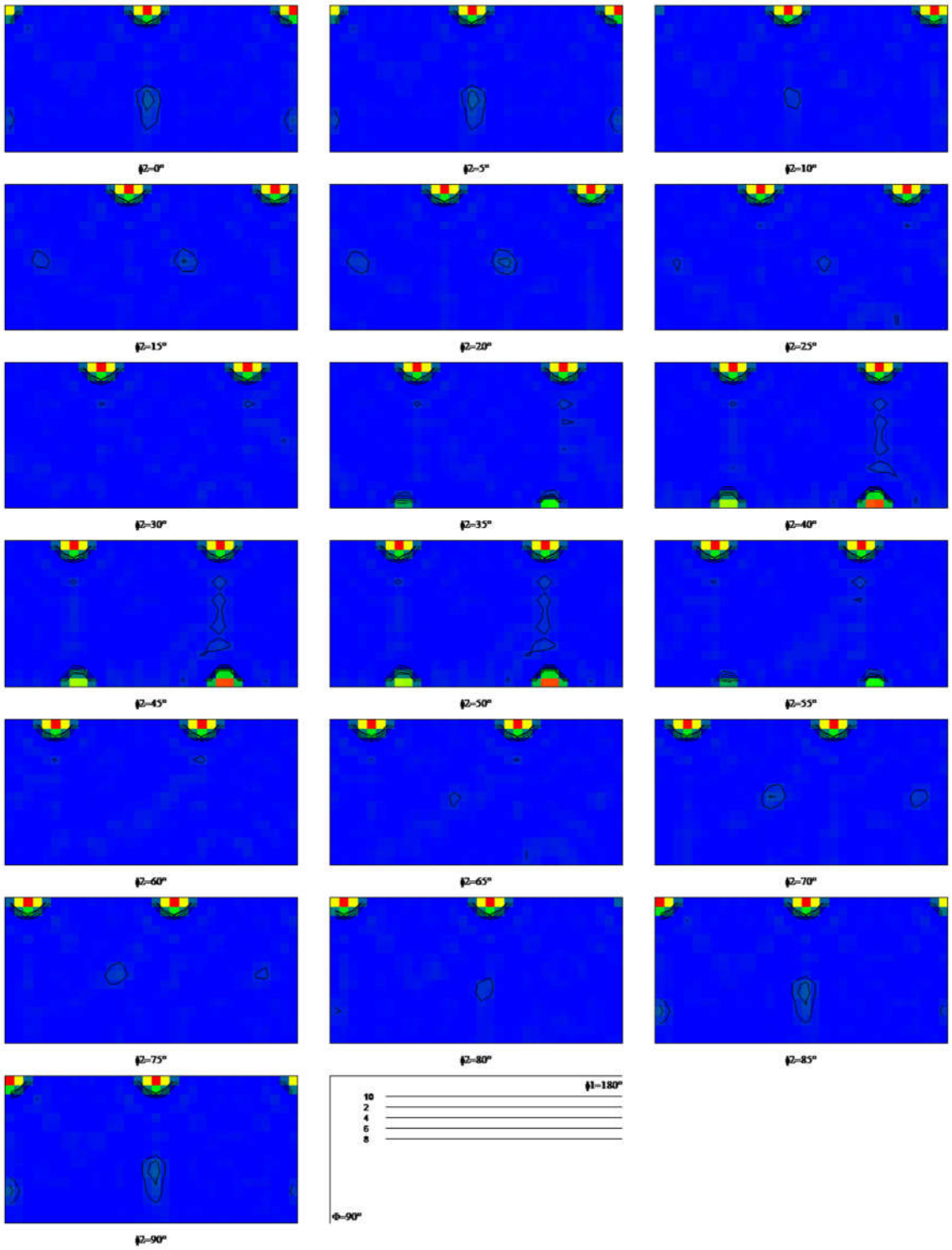

Figure S 16. Serial sections through an (M) ODF of Ti-45Al-2Nb-0.3Si alloy (γ-phase).

XRD phase analysis Fig. 4.1

Name and formula

Reference code: 01-088-2331

ICSD name: Molybdenum

Empirical formula: Mo

Chemical formula: Mo

Crystallographic parameters

Crystal system: Cubic

Space group: Fm-3m

Space group number: 225

a (Å): 4.0300

b (Å): 4.0300

c (Å): 4.0300

Alpha (°): 90.0000

Beta (°): 90.0000

Gamma (°): 90.0000

Calculated density (g/cm^3): 9.73

Volume of cell (10^6 pm^3): 65.45

Z: 4.00

RIR: 14.40

Subfiles and Quality

Subfiles: Inorganic

Alloy, metal or intermetalic

Modelled additional pattern

Quality: Calculated (C)

Comments

ICSD collection code: 041513

Test from ICSD: No R value given.

At least one TF missing.

References

Primary reference: *Calculated from ICSD using POWD-12++*

Structure: Haglund, J., Fernandez-Guillermet, F., Grimvall, G., Korling, M., *Phys. Rev. B: Condens. Matter*, **48**, 11685, (1993)

Peak list

No.	h	k	l	d [A]	2Theta[deg]	I [%]
1	1	1	1	2.32672	38.667	100.0
2	2	0	0	2.01500	44.950	45.2
3	2	2	0	1.42482	65.453	22.4
4	3	1	1	1.21509	78.684	22.5
5	2	2	2	1.16336	82.926	6.2

Name and formula

Reference code: 01-076-2366

ICSD name: Copper Iron Oxide

Empirical formula: CuFeO2

Chemical formula: FeCuO2

Crystallographic parameters

Crystal system: Rhombohedral

Space group:R-3m

Space group number: 166

a (Å): 5.9600

b (Å): 5.9600

c (Å): 5.9600

Alpha (°): 29.2600

Beta (°): 29.2600

Gamma (°): 29.2600

Calculated density (g/cm^3): 5.62

Volume of cell (10^6 pm^3): 134.26

Z: 1.00

RIR: 5.16

Subfiles and Quality

Subfiles: Inorganic

Corrosion

Modelled additional pattern

Quality: Calculated (C)

Comments

ICSD collection code: 037225

Test from ICSD: No R value given.

At least one TF missing.

References

Primary reference: *Calculated from ICSD using POWD-12++*, (1997)

Structure: Delorme, C., *Acta Crystallogr.*, **9**, 200, (1956)

Peak list

No.	h	k	l	d [A]	2Theta[deg]	I [%]
1	1	1	1	5.70089	15.531	4.3
2	2	2	2	2.85044	31.357	34.4
3	0	1	0	2.57756	34.777	8.5
4	1	1	0	2.49399	35.981	100.0

5	1	2	1	2.22609	40.490	34.4
6	2	2	1	2.07361	43.614	1.8
7	3	3	3	1.90029	47.827	1.2
8	2	3	2	1.78282	51.198	0.5
9	3	3	2	1.65318	55.544	26.5
10	-1	1	0	1.50535	61.555	18.8
11	1	2	0	1.45547	63.909	0.2
12	3	4	3	1.43007	65.183	13.5
13	4	4	4	1.42522	65.432	7.9
14	1	3	2	1.33113	70.716	10.8
15	-1	1	1	1.29990	72.681	0.4
16	0	2	0	1.28878	73.410	6.3
17	2	2	0	1.24700	76.300	3.1
18	1	3	1	1.21819	78.445	0.1
19	3	4	2	1.17998	81.507	0.7
20	4	5	4	1.17454	81.965	0.1
21	3	3	1	1.15018	84.091	0.1
22	5	5	5	1.14018	85.001	0.1
23	2	4	2	1.11304	87.588	3.9
24	5	5	4	1.10622	88.267	1.8